CENTRO INTERNACIONAL DE ESTUDOS
DE DOUTORAMENTO E AVANZADOS
DA USC (CIEDUS)

TESE DE DOUTORAMENTO

NEW PHYSICS IMPLICATIONS AND SEARCHES AT LHCB

Miriam Lucio Martínez

ESCOLA DE DOUTORAMENTO INTERNACIONAL

PROGRAMA DE DOUTORAMENTO EN FÍSICA NUCLEAR E DE PARTÍCULAS

SANTIAGO DE COMPOSTELA

ANO 2019

USC
UNIVERSIDADE
DE SANTIAGO
DE COMPOSTELA

DECLARACIÓN DO AUTOR/A DA TESE

New physics implications and searches at LHCb

D./Dna. Miriam Lucio Martínez

Presento a miña tese, seguindo o procedemento axeitado ao Regulamento, e declaro que:

1) A tese abarca os resultados da elaboración do meu traballo.
2) De selo caso, na tese faise referencia ás colaboracións que tivo este traballo.
3) A tese é a versión definitiva presentada para a súa defensa e coincide coa versión enviada en formato electrónico.
4) Confirmo que a tese non incorre en ningún tipo de plaxio doutros autores nin de traballos presentados por min para a obtención doutros títulos.

En Santiago de Compostela, 18 de febreiro de 2019

Asdo.
Miriam Lucio Martínez

USC
UNIVERSIDADE
DE SANTIAGO
DE COMPOSTELA

AUTORIZACIÓN DO DIRECTOR / TITOR DA TESE

New physics implications and searches at LHCb

D. Diego Martínez Santos
D. Xabier Cid Vidal
D. José Angel Hernando Morata

INFORMA/N:

Que a presente tese, correspóndese co traballo realizado por D/Dna. Miriam Lucio Martínez, baixo a miña dirección, e autorizo a súa presentación, considerando que reúne os requisitos esixidos no Regulamento de Estudos de Doutoramento da USC, e que como director desta non incorre nas causas de abstención establecidas na Lei 40/2015.

En Santiago de Compostela, 19 de febreiro de 2019

Asdo
Diego Martínez Santos

Asdo
Xabier Cid Vidal

Asdo
José Angel Hernando Morata

USC
UNIVERSIDADE
DE SANTIAGO
DE COMPOSTELA

Acknowledgements

A lot of people come to my mind when thinking about acknowledgements. This makes me think I have been very lucky during my time as a PhD. I apologise beforehand in case I forgot somebody. Memory is not my strong skill.

First, I want to thank my supervisors, Diego, Veronika and Xabi, for the excellent guidance and enormous support throughout this PhD. I would not have made it without them. I want to thank José Ángel for his support, and for introducing me to Diego and hence, being indirect responsible for this thesis. I would be working in something completely different if it was not for him.

I also want to thank the LHCb collaboration, a very good environment where I developed a lot of skills, both personal and technical. Special thanks go to the Rare Decays and B to Charmonia Working Group, in which I developed the two analyses present in this thesis. Moreover, I met excellent people along the way, that I can now consider friends. These include Jessica Prisciandaro: thanks for the support and the help, for always always being there and for taking me to VitamPark!, and Martino Borsato, with whom I shared drinks and bad jokes (mostly mine) during his time in Santiago. In a similar way, I want to thank all the members of the MasterCode collaboration, where I worked with bright and kind people always willing to help. It has been an honor. Thanks to Teppei Kitahara, Giancarlo D'Ambrosio, Kei Yamamoto and Nazila Mahmoudi, with whom I had the pleasure to collaborate. Thanks to all the friends that shared beers and dinners with me at CERN: Xuan, Álvaro.

I want to thank Marcos Seco, Francesco Dettori, John Ellis, Jeremy Dalseno, Giacomo Graziani and Diego Guadagnoli for kindly accepting being part of my thesis jury, as well as Martino Borsato and Marc-Olivier Bettler, for making the reports. Thanks to Marc-Olivier and Gino Isidori, for all the reference letters. I thank the financial support provided by the Xunta de Galicia during my PhD.

I am glad I have been a part of BSM-fleet, and want to thank all the people there, present and past. It has been a pleasure to work and share memorable moments with all of you. The same applies to the people from the Santiago LHCb group and IGFAE, all the professors and the PhD students. Special thanks to Marcos, for helping with everything, from SUSY to crashing codes.

USC
UNIVERSIDADE
DE SANTIAGO
DE COMPOSTELA

Agradecimientos

Me gustaría agradecer otra vez a Diego y a Veronika, por todas las horas dedicadas a mi tesis, el esfuerzo que hicieron por mí, pero sobre todo por estar ahí, por apoyarme y porque a nivel personal también se merecen una mención especial.

Gracias a mis compañeros de PhD, de despacho y de muchas horas al día: Alexandre, Adrián, Miguel, y a los de otros despachos: Antonio, María, Julián L, Bea, Óscar y Marcos, Dani, Brais. Por las cervezas, las comidas, las risas, los momentos de frustración frente al ordenador y todo aquello que hemos pasado juntos. Creo que Miguelito se merece aquí una consideración extra, porque sin quererlo se ha convertido en mi compañero de viaje estos 4 años. Gracias también a los que se fueron, Julián G, Carlos, Álvaro, Brais, Gonzalo. Gracias a Isa, porque lo que Mammoth ha unido que no lo separe nadie.

Gracias a los amigos que he hecho este tiempo en Santiago, y que son de lo mejor que me llevo. A Sabela, Erea, Alejandro, JC y Cris. Porque siempre están ahí cuando los necesito, y porque forman parte de muchos de mis mejores recuerdos en la ciudad, y sigo creando recuerdos con ellos. Gracias también a mis amigas de Ourense, fundamentales en mi vida y que siempre han sido un punto de apoyo. A Nadia, a Ana, a María gracias porque después de todo este tiempo aún somos amigas. A Paula Car y Paula Can, por *mochísimos* recuerdos inolvidables y un montón de aventuras que nos quedan.

Finalmente, quiero dar las gracias a las personas más importantes en mi vida: mi familia. Porque ellos me levantaron cuando me caí y porque sin ellos yo no hubiera podido llegar hasta aquí. Gracias a mis padres, por su amor y su apoyo incondicional. Por estar ahí siempre. Gracias a mis hermanas, por hacer de cada uno de mis destinos un sitio turístico. Gracias a mi hermana Rosalín, por su capacidad asombrosa para hacer maletas más compactas que CMS, porque siempre me escucha, está dispuesta a todo por mí y porque estoy muy orgullosa de ella y la considero un modelo a seguir. Gracias a mi hermana Fátima, porque sin ella yo no soy, y ella es la persona que siempre me hace sonreír. Gracias a mis cuñados Juan y Miguel, por hacerlas tan felices a ambas.

Esta tesis está dedicada a la memoria de mi tío Vicente y de mis abuelos, en especial de mi abuelo Manuel.

USC
UNIVERSIDADE
DE SANTIAGO
DE COMPOSTELA

Abstract

The Standard Model of Particle Physics (henceforth, SM) is a very successful theory. Nevertheless, it fails to explain some important questions present in nature. Therefore, a new model beyond the SM is needed. This is often known as New Physics, NP. Some of these alternatives are Supersymmetry (SUSY) and models with extra dimensions. This thesis represents a comprehensive study of NP searches and its implications, performed in a threefold manner.

Firstly, a study of NP implications in kaon physics is presented, through the $K_S^0 \to \pi^0\mu^+\mu^-$ sensitivity study at LHCb and phenomenological studies on $K_S^0 \to \mu^+\mu^-$. The former serves as important input for the SM prediction of the $K_L^0 \to \pi^0\mu^+\mu^-$ branching fraction, that is a relevant channel in models with extra dimensions. Concerning the latter, it plays a key role in scenarios where flavour violation does not originate from the CKM matrix, *non-minimal Flavour Violating* (non-MFV), where it carries information complementary to $B^0_{s(d)} \to \mu^+\mu^-$. A phenomenological study is shown under the simplest supersymmetrical extension of the SM, the *Minimal Supersymmetric Standard Model* (MSSM).

Secondly, a review of the CP violating phase ϕ_s is carried out. This is done via its measurement in $B_s^0 \to J/\psi\phi$ at LHCb, accompanied by a phenomenological study of this and more physics observables. The weak mixing phase ϕ_s measures the CP violation that happens in the interference between mixing and decay. The SM prediction for the $B_s^0 \to J/\psi\phi$ channel is very precise, making it a golden mode where to measure this observable. As for the phenomenological study, several physics observables, such as ϕ_s and the Electric Dipole Moments (EDMs), are computed under the MSSM paradigm.

To finalize, a more general study is done within the *minimal Anomaly Mediated Supersymmetry Breaking*, mAMSB, and the *Constrained Minimal Supersymmetric Standard Model*, CMSSM. In these scenarios, the prospects for the detection of dark matter, as well as for the prediction of the $(g-2)_\mu$ anomaly and flavour observables are presented, together with the available parameter space in light of the present experimental constraints.

USC
UNIVERSIDADE
DE SANTIAGO
DE COMPOSTELA

Resumen

El Modelo Estándar de la Física de Partículas (SM) es una teoría muy exitosa. Sin embargo, no explica algunas de las cuestiones más importantes de la naturaleza. Por lo tanto, se necesita un modelo más allá del SM. Ésto se denomina Nueva Física (NP). Algunas de estas alternativas son la Supersimetría (SUSY) y modelos con dimensiones extra. Esta tesis representa un estudio exhaustivo de búsquedas de NP y sus implicaciones, realizado de una manera triple.

En primer lugar, se presenta un estudio de las implicaciones de NP en la física de kaones, a través del estudio de la sensibilidad del LHCb a $K_S^0 \to \mu^+\mu^-$ y estudios fenomenológicos sobre $K_S^0 \to \mu^+\mu^-$. El primero constituye un importante input para la predicción del SM de la tasa de desintegración de $K_L^0 \to \pi^0\mu^+\mu^-$, un canal relevante en modelos con dimensiones extra. Respecto al segundo, juega un papel clave en escenarios en los cuales la violación de sabor no se origina de la matriz CKM, *non-minimal Flavour Violating* (non-MFV), donde proporciona información complementaria a $B_{s,d}^0 \to \mu^+\mu^-$. Se muestra un estudio fenomenológico realizado dentro de la extensión supersimétrica más simple del SM, el Modelo Estándar Supersimétrico Minimal (MSSM).

En segundo lugar se lleva a cabo una revisión de la fase de violación CP ϕ_s. Ésto se hace a través de la medida de ϕ_s en $B_s^0 \to J/\psi\phi$ en el LHCb, acompañada por un estudio fenomenológico de éste y de otros observables físicos. El ángulo débil de mezcla ϕ_s mide la violación CP que sucede en la interferencia entre mezcla y decaimiento. La predicción del SM para el canal $B_s^0 \to J/\psi\phi$ es muy precisa, lo que lo convierte en un modo estrella donde medir este observable. En cuanto al estudio fenomenológico, varios observables, como ϕ_s y los Momentos Dipolares Eléctricos (EDMs), se computan bajo el paradigma propuesto por el MSSM.

Para finalizar, un estudio más general se realiza dentro del *minimal Anomaly Mediated Supersymmetry Breaking*, mAMSB, y el *Constrained Minimal Supersymmetric Standard Model*, CMSSM. En estos escenarios se presentan las perspectivas para la detección de materia oscura, así como para la predicción de la anomalía $(g-2)_\mu$ y de observables de sabor, junto con el espacio de parámetros disponible en vista de las restricciones experimentales actuales.

USC
UNIVERSIDADE
DE SANTIAGO
DE COMPOSTELA

Resumo

O Modelo Estándar da Física de Partículas (SM) é unha teoría moi exitosa. Porén, non explica algunhas das cuestións máis importantes da natureza. Polo tanto, necesítase un modelo máis ala do SM. Esto denomínase Nova Física (NP). Algunhas destas alternativas son a Supersimetría (SUSY) e modelos con dimensións extra. Esta tesis representa un estudo exhaustivo de búsquedas de NP e as súas implicacións, realizado dunha maneira triple.

En primeiro lugar, preséntase un estudo das implicacións de NP na física de kaóns, a través do estudo da sensibilidade do LHCb a $K_S^0 \to \pi^0\mu^+\mu^-$ e estudos fenomenolóxicos sobre $K_S^0 \to \mu^+\mu^-$. O primeiro constitúe un importante input para a predición do SM da tasa de desintegración de $K_L^0 \to \pi^0\mu^+\mu^-$, unha canle relevante en modelos con dimensións extra. Con respecto ao segundo, xoga un papel clave en escenarios nos cales a violación de sabor non ten a súa orixe na matriz CKM, *non-minimal Flavour Violating* (non-MFV), onde proporciona información complementaria a $B_{s,d}^0 \to \mu^+\mu^-$. Móstrase un estudo fenomenolóxico realizado dentro da extensión supersimétrica máis simple do SM, o Modelo Estándar Supersimétrico Minimal (MSSM).

En segundo lugar lévase a cabo unha revisión da fase de violación CP ϕ_s. Esto faise a través da medida de ϕ_s en $B_s^0 \to J/\psi\phi$ no LHCb, acompañada por un estudo fenomenolóxico deste e doutros observables físicos. O ángulo feble de mestura ϕ_s mide a violación CP que ocorre na interferencia entre mestura e decaemento. A predición do SM para a canle $B_s^0 \to J/\psi\phi$ é moi precisa, o que a converte nun modo estrela onde medir este observable. En canto ao estudo fenomenolóxico, varios observables, como ϕ_s e os Momentos Dipolares Eléctricos (EDMs), compútanse baixo o paradigma proposto polo MSSM.

Para finalizar, un estudo máis xeral realízase dentro do *minimal Anomaly Mediated Supersymmetry Breaking*, mAMSB, e o *Constrained Minimal Supersymmetric Standard Model*, CMSSM. Nestos escenarios preséntanse as perspectivas para a detección de materia escura, así como para a predición da anomalía $(g-2)_\mu$ e de observables de sabor, xunto co espazo de parámetros dispoñible en vista das restriccións experimentais actuais.

USC
UNIVERSIDADE
DE SANTIAGO
DE COMPOSTELA

Contents

USC
UNIVERSIDADE
DE SANTIAGO
DE COMPOSTELA

Chapter 1

Introduction

The Standard Model (hereafter SM) of Particle Physics, mainly formulated in the 1970s, is a quantum field theory (QFT) that describes the strong and electroweak interactions. It is represented in Group Theory by [1]:

$$SU(3)_C \bigotimes SU(2)_T \bigotimes U(1)_Y, \tag{1.1}$$

where the strong interaction, described by Quantum Chromodynamics (QCD), is contained in the $SU(3)_C$ group (a symmetry group of *color*, C), and $SU(2)_T \bigotimes U(1)_Y$, where T and Y stand for weak isospin and hypercharge respectively, relates to the electroweak interaction (EW). The SM fermions (described in Section 1.1) consist of three families with two $SU(2)_L$ doublets (Q_L and L_L) and three $SU(2)_L$ singlets (U_R, D_R and E_R). In order to preserve the electroweak gauge invariance (and so, keep the SM renormalizable), the particles predicted by this Lagrangian have to be massless. This leads to the necessity of a spontaneously breaking of the symmetry into $SU(3)_C \bigotimes U(1)_{EM}$. Such breaking is done by the vacuum expectation value (VEV) of a scalar isospin doublet, with hypercharge 1/2, called *Higgs* [2]. More details on this mechanism are given in Section 1.2.

$$G_{SM} \xrightarrow{Higgs(1,2)_{1/2}} SU(3)_C \bigotimes U(1)_{EM} \tag{1.2}$$

1.1 Particle Content

The particle content of the SM is categorized as a function of the intrinsic angular momentum, or *spin*. Particles with half-integer spin are called *fermions*, while those with an integer value for the spin are *bosons*. The latter ones are the carriers of the different interactions that enter the SM Lagrangian:

$$\mathcal{L} = \mathcal{L}_{kin} + \mathcal{L}_{Higgs} + \mathcal{L}_{Yuk}, \tag{1.3}$$

where the first term accounts for the kinetic part of the interaction, and the two others describe the Higgs mechanism (described in Section 1.2) and its interaction with the

fermions. Regarding the latter, a further classification can be made depending on whether they are affected (*quarks*) or not (*leptons*) by the strong interaction. If affected, a quantum number, color, further characterizes the particle. Note that the electroweak interaction affects all the particles.

To distinguish among the different existing types of particles in the context of the quark model of hadrons, the quantum number *flavour* is used. There are three flavour families of quarks and leptons in the SM, represented in Figure 1.1. Each lepton (electron, e, muon, μ, tauon, τ) has associated a neutral particle, called the *neutrino*: ν_e, ν_μ, ν_τ. Even though they are predicted to be massless within the SM (so that there are not right-handed neutrinos in the SM and, equivalently, there are not left-handed antineutrinos), they are known to have mass [3].

The elementary particles of the SM are represented in Figure 1.1. For each of these particles, there exists another one with the same mass but opposite physical charges. Those are called *antiparticles*. Notice that some particles (e.g. the photon) are their own antiparticle.

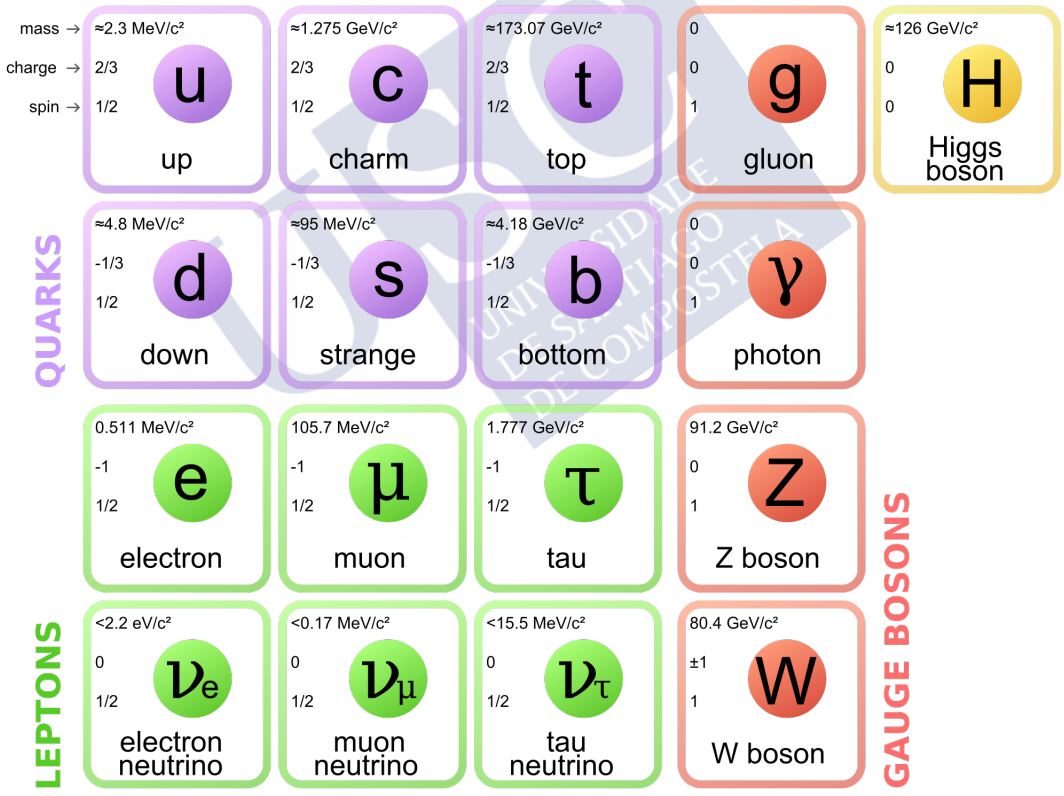

Figure 1.1: The SM particle content. Figure taken from Ref. [4].

Quarks form bound states named *hadrons* that have a quantum number associated called the baryonic number, $\mathcal{B}$. They can be *mesons* ($\mathcal{B} = 1$) formed by a quark and an antiquark or by 4 quarks, or *baryons* ($\mathcal{B} = 1$). The latter can be composed by three

quarks, or 4 quarks and an antiquark (the so-called *pentaquarks*, recently discovered by LHCb [5]). Given the spin that results of the *sum* of the quarks, baryons are fermions and mesons are bosons.

1.2 Higgs Mechanism

Similarly to what happens in the Ginzburg-Landau theory for superconductivity, the Higgs mechanism arises from the need of Electroweak Symmetry Breaking (EWSB), together with the requirement that gauge invariance is preserved in $\mathcal{L}_{SM}$. The Higgs field interacts with the particles corresponding to the elementary field, including gauge bosons. Resulting of this interaction, these particless acquire mass. As for the others, the Higgs field has associated at least one particle in the SM, the Higgs boson, a scalar particle. Within the SM, it is not possible to make a prediction of its mass, other than setting loose upper and lower limits, since it depends on a parameter that needs to be determined experimentally.

The term in the SM Lagrangian that accounts for the self-interaction of the Higgs field is the following:

$$\mathcal{L}_{Higgs} = \mu^2\phi^\dagger\phi - \lambda(\phi^\dagger\phi)^2,\ \mu^2 < 0, \lambda > 0, \tag{1.4}$$

where μ and λ are constants that go with the square and quadratic terms of ϕ respectively in the Higgs potential, represented in Figure 1.2, and ϕ denotes the (complex) Higgs Field :

$$\phi = \begin{pmatrix}\phi^+\\ \phi^0\end{pmatrix}, \tag{1.5}$$

a scalar isospin doublet with hypercharge +1/2. The initial symmetry of the system is broken for a non-zero value of this field:

$$\phi = \frac{1}{\sqrt{2}}\begin{pmatrix}0\\ v\end{pmatrix}, v = \frac{\mu}{\sqrt{\lambda}}, \tag{1.6}$$

leading to a Higgs particle, with mass $\sqrt{2\lambda v^2}$, neutral charge and hypercharge 1. It was discovered in 2012 by two LHC experiments, ATLAS [6] and CMS [7]. Its mass was measured to be $125.09 \pm 0.24\,\text{GeV}$.

The gauge fields $W^\pm$ and Z acquire mass through their interaction with the Higgs boson. Thus:

$$W^\pm = \frac{1}{\sqrt{2}}(W^{(1)} \mp W^{(2)}),\ Z = \frac{1}{\sqrt{g_I^2 + g_Y^2}}(g_I W^{(3)} - g_Y B), \tag{1.7}$$

where Z and $W^\pm$ are linear combinations of the weak and hypercharge bosons. Then:

$$m_{W^\pm} = \frac{v g_I}{\sqrt{2}}, m_Z = v\sqrt{\frac{g_I^2 + g_Y^2}{2}} \tag{1.8}$$

Notice that the relation between both masses is given by the so-called *weak-mixing angle*, θ_W

$$\frac{m_W^\pm}{m_Z} = \frac{g_I}{\sqrt{(g_I + g_Y)}} = \cos\theta_W, \tag{1.9}$$

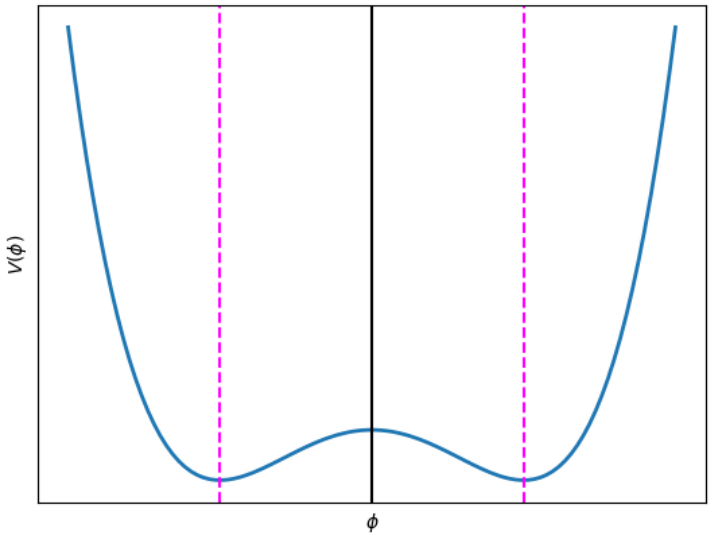

Figure 1.2: Higgs potential. The dashed-magenta vertical line indicates the two vacuum states. The black vertical line is located at the origin. The minimum is not at 0, and therefore the potential has a Vacuum Expectation Value (VEV).

measured experimentally to be $\theta_W \sim 0.50$ rad [1].

1.2.1 Coupling to fermions

The Lagrangian term corresponding to the Higgs (H)-fermions (f) interaction can be written as follows:

$$\mathcal{L}_{Hf} = -\lambda_e \bar{l}_L \phi e_R - \lambda_d \bar{q}_L \phi d_R - \lambda_u \bar{q}_L \phi^\dagger u_R + \text{h.c.}, \tag{1.10}$$

where l_L, q_L, u_R, d_R, are the corresponding fermion fields, and λ_e, λ_d and λ_u are the respective coupling constants (*Yukawa couplings*), different for each fermion. Substituting in this expression the VEV the fermion masses are found to have the form:

$$m_e = \frac{v\lambda_e}{\sqrt{2}}, \; m_u = \frac{v\lambda_u}{\sqrt{2}}, \; m_d = \frac{v\lambda_d}{\sqrt{2}} \tag{1.11}$$

Thus, they are proportional to the Yukawa couplings.

1.2.2 Coupling to photons and gluons

Both gluons and photons are gauge bosons of the strong and electromagnetic interactions, respectively. They have zero mass and spin 1. For the gluons, given that the color

symmetry SU(3) is not modified by the Higgs mechanism, they don't directly interact with the Higgs boson. The only way this interaction can happen is via quark loops. Contrary to what happens with the gluons, the photons can interact directly with the Higgs field. However, the introduction of the corresponding gauge field, A, doesn't lead to a term with a quadratic dependence on ϕ. Therefore, they don't acquire mass as a result of this interaction, $m_\gamma = 0$.

1.3 CKM Matrix

The Yukawa couplings generate off-diagonal terms that allow for the quarks to *mix* between the three generations. Diagonalizing the quark mass matrices, 4 unitary matrices are obtained, $V_{L,R}^{u,d}$, that determine the coupling of the $W^\pm$ bosons to the different quarks.

This diagonalization can be seen as the rotation from one basis (q) to another, hereafter called *mass basis* or *physical basis*, q'. These are related by the aforementioned matrices [8]:

$$u_L^i = V_u^{ij} u_L'^j \quad d_L^i = V_d^{ij} d_L'^j \tag{1.12}$$

With this, the weak current transforms from $\bar{u}_L^i \gamma^\mu d_L^i$ to $\bar{u}_L'^i \gamma^\mu (V_u^\dagger V_d)_{ij} d_L'^i \equiv \bar{u}_L'^i \gamma^\mu V_{\text{CKM}} d_L'^i$, where V_{CKM} is a non-diagonal, unitary matrix called the *Cabibbo-Kobayashi-Maskawa* (CKM) matrix. The most up-to-date measured values of its elements can be found in [1].

$$V^{\text{CKM}} = \begin{pmatrix} V_{ud} & V_{us} & V_{ub} \\ V_{cd} & V_{cs} & V_{cb} \\ V_{td} & V_{ts} & V_{tb} \end{pmatrix} \tag{1.13}$$

This matrix describes the transitions between different quark generations, that allow for processes in which there is change in the quark flavour. It also allows CP violation, that will be discussed in the following sections.

1.4 Need for New Physics

Even though the SM has shown to be a very successful theory, it lacks explanation for several phenomena present in nature.

1.4.1 Inclusion of gravity

The SM fails to include gravity as one of the interactions, as there is no quantum theory for it. This prevents the unification of forces, discussed in the next subsections. As it will be seen in the next chapter, within NP models such as Supersymmetry gravity can be included (*supergravity*), thus avoiding this problem.

1.4.2 Matter-antimatter imbalance

In order to have an excess of matter over antimatter in the early universe, a process known as *baryogenesis* [9], three requirements have to be fulfilled. These are known as the *Sakharov conditions* [10], and include a large CP-violation. The Higgs mass is too heavy to fulfill such conditions [11].

1.4.3 Dark matter and dark energy

Several experimental evidences, such as the rotational speed of spiral galaxies, gravitational lensing, or observed fluctuations in the Cosmic Microwave Background radiation (see for example references [12], [13]) have lead to a strong evidence of the existence of dark matter and dark energy, that take up the vast majority of the Universe composition and don't interact with light. The possible baryonic (MACHOs, MAssive Compact Halo Objects, such as black holes, and RAMBOs, Robust Association of Massive Baryonic Objects) percentage of dark matter is small. The rest cannot be explained within the SM, it is *non baryonic cold (hot) dark matter*, where cold (hot) refers to its non-relativistic (relativistic) nature. Possible candidates for cold dark matter entail weakly interacting sub-eV particles (WISPs), such as axions([14], [15], [16]), primordial back holes [17] and weakly interacting massive particles (WIMPs). Neutrinos are a possible candidate for hot dark matter.

1.4.4 Unification of interactions

The behavior of the three coupling constants at the order of TeV, *naturalness*, (Figure 1.3, left) suggests the existence of a *primary* interaction, represented by a higher symmetry group (e.g. SU(5) or SO(10)). Spontaneous symmetry breaking of this interaction would lead to the existence of the electromagnetic, weak, and strong interactions at lower energy scales. Nevertheless, in order for this to happen, there should be a matching of these coupling constants for such high energies, which is not perfectly achieved in the SM. This hints at the existence of new symmetries or fields (Figure 1.3, right). Some of these suggestions will be discussed in the following chapter.

More examples of some of the SM defficiencies are listed below.

- The number of fermion families. As mentioned earlier, the number of fermion families is not an observable, but rather an input for the theory. More generations could in principle be accommodated as part of the SM particle content.

- The gauge hierarchy problem. This is intrinsically related to the mass of the Higgs boson. Apart from the fact that it is not predicted by the theory, it requires fine-tuning in order not to diverge, leading to the enlargement of the EW scale. Also, it is very small compared to the gravity scale, given by the Planck mass: $M_{Pl} = \sqrt{\hbar c / G_N} = 1.2 \times 10^{19}\,\text{GeV}$, which is not fully understood.

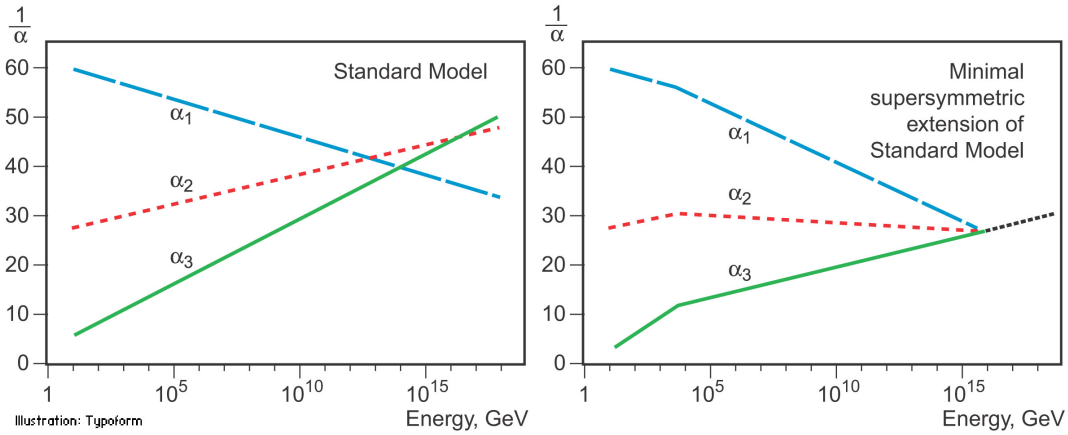

Figure 1.3: Running coupling constants as a function of the energy scale, for the SM (left) and in the context of supersymmetry (right). Figure taken from Ref. [18].

- Neutrino masses. As it was already mentioned before, neutrinos are massless within the SM model. Nevertheless, experimental observations such as the neutrino oscillations [3] prove this prediction wrong. Thus, a Beyond the SM (BSM) mechanism to give neutrinos mass is required. There are several proposals for this, such as the seesaw mechanism or the Majorana theory [19].

- Charge quantisation. The fact that the electron charge and the proton charge are of the same magnitude but opposite sign has no explanation in the SM.

- Fermion masses and mixing angles. Similarly to what happens with the number of fermion families, these quantities are not predicted by the SM. Moreover, the mass of the top quark, much bigger than the other quark masses, is an intriguing fact not explained by this theory.

- The magnetic dipole moment of the muon, whose experimental measurement [20] deviates more than 3σ from the SM predictions.

In addition to this, several results provided by the LHCb collaboration on flavour anomalies and lepton flavour universality studies (see for example references [21], [22]) contribute to the motivation of the search for BSM physics.

Several theories have been proposed to cope with the SM problems, that make this model look more like an effective low energy theory than a model itself. Among these, Supersymmetry and Minimal Flavour Violation (MFV) are of special importance and will be discussed in the following chapters. However, there are other alternatives, some of which are briefly discussed below.

- **Majorana neutrinos**: in the SM, neutrinos are supposed to be massless *Dirac* particles. However it has been suggested that they are instead its own antiparticle, *Majorana neutrinos*. Within this theory, they are allowed to acquire mass.

Several experiments search for a neutrinoless double beta decay that would prove this [23], [24].

- **Axions**: axions are hypothetical particles that compose DM, including the Peccei-Quinn mechanism [14] to solve the strong CP problem [25]. They would have been massively produced soon after the Big Bang. The couplings and masses of axions can cover several orders of magnitudes.

- **Two Higgs Doublet Models (THDM)**: in this scenario, there are two Higgs fields populating the vacuum instead of one.

$$\langle \phi_a \rangle_0 = \begin{pmatrix} 0 \\ \frac{v_1}{\sqrt{2}} \end{pmatrix}, \ \langle \phi_b \rangle_0 = \begin{pmatrix} 0 \\ \frac{v_2}{\sqrt{2}} \end{pmatrix} \tag{1.14}$$

  Where v_2 and v_2 follow the relation:

$$v \equiv (v_1^2 + v_2^2)^{1/2} \tag{1.15}$$

  The ratio between these two VEVs, $\tan\beta \equiv \frac{v_2}{v_1}$ is the most important parameter in this model. It describes the diagonalization of the mass-squared matrices of the charged scalars and of the pseudoscalars, resulting in 4 fields

$$\begin{gathered} \phi_1 = \sin\beta\phi_b + \cos\beta\phi_a \ \ \phi_2 = -\sin\beta\phi_a + \cos\beta\phi_b \\ \langle \phi_1 \rangle_0 = \begin{pmatrix} 0 \\ \frac{v_{SM}}{\sqrt{2}} \end{pmatrix}, \ \langle \phi_2 \rangle_0 = \begin{pmatrix} 0 \\ 0 \end{pmatrix} \end{gathered} \tag{1.16}$$

  The spontaneous symmetry breaking leads in this case to 5 physical Higgs particles: two neutral scalars linear combinations of $Re(\phi_1^0)$ and $Re(\phi_1^0)$, H^0 and h^0; a neutral pseudoscalar, $A^0 \propto Im(\phi_2^0)$ and two charged scalars $H^\pm = \phi_2^\pm$.

- **Models with extra dimensions**: models with extra dimensions (apart from the usual 4 from the observed spacetime) are motivated by the attempts made to unify electromagnetism and gravity within the Kaluza-Klein theory [26], [27]. There are several proposals, such as *string theory* or the *Randall-Sundrum model* [28], that gives explanation to hierarchy using 5 dimensions and predicts the existence of the *graviton*.

- **SM with fourth generation (SM4)**: one of the simplest extensions of the SM consists in the addition of a fourth generation of fermions requires the corresponding neutrino to be heavy, $m_{\nu_4} > M_Z/2$, to match the current experimental measurements on the number of light ν types, $N_\nu = 2.92 \pm 0.05$ [29].

- **Little Higgs Models (LHM)**: in these models, the Higgs is realised as a light pseudo-Nambu Goldstone boson of a broken global symmetry. They attempt to solve the gauge hierarchy problem. The minimal version of such models include 4 new heavy vector bosons, ($W'^\pm$, Z', B'), coupled to SM fermions, mixed with the SM

$W^{\pm}$ and Z; light Higgs doublet(s), with possibility of extra light scalar multiplets; heavy Higgs multiplets, coupled to Higgs/Goldstone pairs, decoupled from fermions, mixed with light Higgses, and heavy up-type quark(s), t'. An example spectrum for this scenario can be seen in Figure 1.4. Updated constraints in this model can be found in [30].

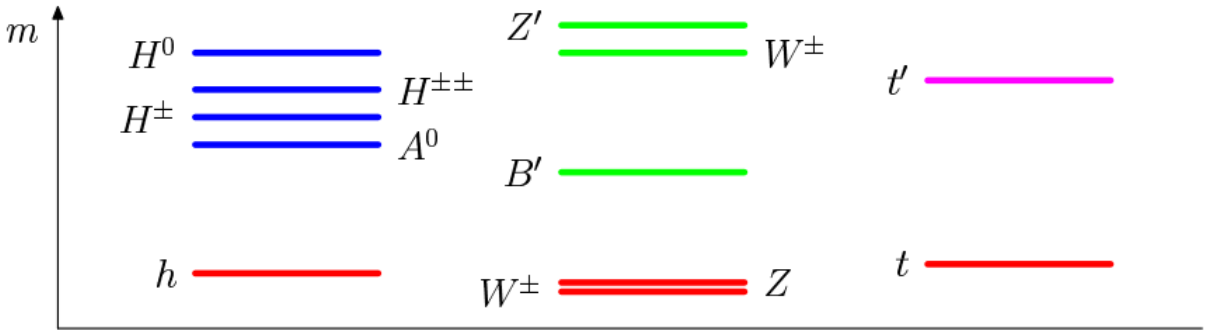

Figure 1.4: Example of mass spectrum for LHM. The new vector bosons, marked in green, have masses well above the SM ones (marked as red). The same happens for the heavy up-type quark, t', and for six heavy scalars, labelled using blue lines, with respect to their SM counterparts.

USC
UNIVERSIDADE
DE SANTIAGO
DE COMPOSTELA

Chapter 2

Supersymmetry

2.1 Introduction

Supersymmetry (henceforth SUSY) is a framework that constitutes one of the main alternatives for BSM Physics. Postulated in the 70s as a graded Lie algebra (with conmutators and anticonmutators), allowed by the Coleman-Mandula theorem [31], it possesses a unique mathematical nature that allows for the solution of several of the SM caveats that were discussed in the chapter before. It is being searched for in several experiments, and not yet discovered. Lower limits are set in the scale of SUSY breaking, the so-called scale of new physics.

SUSY can be seen as a generalization of space-time symmetries in QFT, establishing an invariance under the transformations of fermions to bosons, requiring their number to be the same in nature. Hence, for each boson (fermion) there is a superpartner of fermionic (bosonic) nature. If SUSY was not broken, the symmetry would be exact and the masses of the particles would coincide with those of their respective superpartners. None of the particles known to date fulfills the quality to be a superpartner, which leads to the conclusion that for Supersymmetry to exist there must be more particles than those seen so far (the double, in the simplest supersymmetric extension of the SM).

It is useful to introduce the quantum number R-parity, defined as:

$$R = (-1)^{3B+L+2S}, \tag{2.1}$$

where B is the baryon number, L the lepton number (both quantities conerved in the SM) and S the spin. Particles with R = 1 are SM particles, while their superpartners have R = -1. Models where R-Parity is conserved (hence, B-L invariance) predict the production of superparticles in pairs, and at least one stable supersymmetric particle, the Lightest Supersymmetric Particle (LSP), thus providing a good candidate for dark matter. There are also SUSY models where R-parity is violated (RPV models), allowing the LSP to decay to SM particles. An example of a RPV model is the bilinear RPV constrained Minimal Supersymmetrical Standard Model [32].

2.2 Points addressed by SUSY

As mentioned earlier, the interest in SUSY lies in the coverage of SM most important flaws. A summary of this is discussed in this section.

- **Inclusion of gravity**: as explained in Section 1, gravity is not included in the SM. Nevertheless, given that SUSY algebra is a generalization of Poincaré algebra, it is invariant under general coordinate transformation if it is local. With this, a theory including gravity (*supergravity*) can be obtained from SUSY.

- **Gauge hierarchy problem**: Supersymmetry (and supersymmetric partners) lead to the cancellation of quadratic mass terms causing divergences up to the SUSY breaking scale, M_{SUSY}, given the relation

$$\sum_{bosons} m^2 - \sum_{fermions} m^2 = M_{SUSY}^2 \tag{2.2}$$

  The origin of EWSB can also be explained from radiative electroweak symmetry breaking within SUSY, also explaining the difference between the scales (M_{SUSY} and the Higgs mass).

- **Unification of interactions**: as mentioned earlier, the behavior of the coupling constants at high energies hints a *great unification* of forces. This match, while not perfect in the SM, can be obtained in a supersymmetric scenario. This can be seen in Figure 1.3, thanks to the change in the parameters of the renormalization group equations.

- **Matter-antimatter imbalance**: leptogenesis, a scenario in which there is an asymmetry between leptons and antileptons in the early universe, can happen in supersymmetric models, being able to accommodate the total matter-antimatter imbalance.

- **Dark matter and dark energy**: as pointed out in Section 1.4.3, most of the origin of dark matter and dark energy remains unexplained in the SM. Supersymmetry can provide several candidates for this, provided R-parity is conserved.

2.3 Supersymmetry breaking

Supersymmetry breaking is inferred from experimental observation. Without it, the abundance and mass of partners and superpartners would be equal, as said in Section 1. Moreover, experimental constraints can help reduce the arbitrariness of the space parameters.

All global continuous symmetries can be broken with an *extra* component of the Lagrangian that breaks the symmetry of the larger part (Heisenberg-Wigner mode), with spontaneous symmetry breaking and the resulting appearance of Goldstone particles, or with a combination of these two methods. The Minimal Supersymmetric Standard Model is an example of the former, and will be discussed in more detail in the following section.

2.4 Minimal Supersymmetrical Standard Model (MSSM)

The Minimal Supersymmetrical Standard Model is the simplest supersymmetric extension of the SM, containing some general features that do not depend on the choice of model. Among said features is the fact that for each SM partner there is a *superpartner* (*gauginos* for bosons and *sfermions* for fermions), with a spin difference of 1/2. The particle content is summarized in Table 2.1.

Table 2.1: Particle content of the MSSM

SM	MSSM	Spin
gluon (g)	gluino $\tilde{g}$	1/2
Hypercharge & Weak bosons	$\tilde{W}^0, \tilde{W}^{\pm}, \tilde{B}^0$	1/2
leptons ($(\nu, l)_L$, e_R)	sleptons ($(\tilde{\nu}, \tilde{l})_L$, $\tilde{e}_R$)	0
quarks (q)	squarks ($\tilde{q}$)	0
Higgs field	Higgsinos ($\tilde{H}_u^{\pm}$, $\tilde{H}_d^{\pm}$, $\tilde{H}_u^0$, $\tilde{H}_d^0$)	1/2

The MSSM, as any supersymmetric scenario, requires the presence of 2 Higgs bosons in the SM with hypercharge -1 and 1, compatible with Flavour-Changing-Neutral-Current (FCNC) constraints, as it fulfills the Glashow-Weinberg/Paschos condition([33], [34]). Gauginos have spin zero in order to be matter scalars and not gauge bosons. As for the sfermions, the only consistent interacting field theory of spin 3/2 has to include gravity [35], hence they have spin 1/2. This theory, called *supergravity*, includes the superpartner of the *graviton*, known as *gravitino*. It is also worth mentioning that the MSSM, like the SM, fails to explain the number of fermion families.

The MSSM has some interesing features, such as the improvement in the unification of gauge coupling constants at some high energy scale, Λ, still undetermined but known to be in the order of 2×10^{16} GeV. This unification is kept if SUSY is broken at a scale $M_S \leq \mathcal{O}(1\text{TeV})$. Even if gravity is included, its coupling constant seems to roughly point to the same value at the same Λ.

The soft-explicit breaking of the MSSM (or the electroweak symmetry breaking itself) allows for mixing between different sparticles with the same charge and color to happen. This leads to the existence of *charginos* ($\tilde{\chi}^{\pm}_{1,2}$) and *neutralinos* ($\tilde{\chi}^0_{1,2,3,4}$), as a combination of gauginos and higgsinos for the former and neutral gauginos for the latter. Sfermion mixing can also occur. The mixing patterns and mass values of sparticle mass eigenstates depend crucially on the manner of supersymmetry breaking.

2.4.1 Dark Matter in the MSSM

As said before, within the SUSY framework there are several candidates to constitute DM. A common feature they share is their stability. These candidates are:

- Sneutrino: ruled out in the MSSM because of the current limits on the interaction cross section of dark matter particles with ordinary matter as measured by direct detection experiments.

- Lightest neutralino: the LSP for models conserving R-parity. Depending on its composition it can be of different natures. Said composition comes determined by a unitary 4x4 mixing matrix that diagonalizes the neutralino mass matrix ($M_{\chi_1^0}$), $M_{\chi_1^0}^{\text{diag}} = N^T M_{\chi_1^0} N$, as shown in Eq. 2.3, 2.4.

$$\begin{pmatrix} N_{11} & N_{12} & N_{13} & N_{14} \\ N_{21} & N_{22} & N_{23} & N_{24} \\ N_{31} & N_{32} & N_{33} & N_{34} \\ N_{41} & N_{42} & N_{43} & N_{44} \end{pmatrix} \tag{2.3}$$

$$\chi_1^0 = N_{11}\tilde{B} + N_{12}\tilde{W} + N_{13}\tilde{H}_d^0 + N_{14}\tilde{H}_u^0 \tag{2.4}$$

  1. Bino-like: when the term N_{11} dominates the neutralino diagonalization matrix, N, fulfilled for $M_1 < \mu$.
  2. Higgsino-like: when the off-diagonal elements in the mixing matrix $(N_{13}^2 + N_{14}^2)$ dominate, for $\mu < M_1$.
  3. Wino-like: when the term N_{12} dominates the neutralino diagonalization matrix, N, fulfilled for $\mu, M_{1,3} < M_2$.
  4. Mixed states of the above.

- Gravitino.

2.4.2 MSSM Lagrangian

The MSSM Lagrangian consists of two parts:

$$\mathcal{L}_{\text{MSSM}} = \mathcal{L}_{\text{SUSY}} + \mathcal{L}_{\text{SOFT}}, \tag{2.5}$$

where the first part is just a generalization of the SM Lagrangian, and the second part contains the supersymmetry breaking mechanism. The corresponding *superpotential* used in $\mathcal{L}_{\text{SUSY}}$ is of the form:

$$W = \epsilon_{ij}(y_{ab}^U Q_a^j U_b^c H_2^i + y_{ab}^D Q_a^j D_b^c H_1^i + y_{ab}^L L_a^j E_b^c H_1^i + \mu H_1^i H_2^j), \tag{2.6}$$

where Q, U and D represent the squark superfields, L and E the slepton ones, $y^{U,D,L}$ are the Yukawa couplings and $H_{1,2}$ the Higgs superfields. The only qualitative difference with respect to $\mathcal{L}_{\text{SM}}$ is the last term, that accounts for the Higgs mixing. Additional leptonic or baryonic number violating terms can be added to this superpotential in RPV models.

Because of gauge invariance, supersymmetry breaking in the MSSM cannot happen spontaneously. Thus, an explicit term accounting for this breaking appears in the Lagrangian, $\mathcal{L}_{\text{SOFT}}$, where *soft* refers to the dimension 2 and 3 of the operators. This breaking is the responsible for the SM particles not to be degenerate with their respective superpartners, as mentioned earlier, having these larger masses. Nonetheless this SUSY breaking, some properties from it remain.

A possible alternative to the soft-explicit supersymmetry breaking explained before consists in spontaneous symmetry breaking for a given scale, Λ_s, with a sector of fields that belong to a *hidden* sector which communicates with the *observable* sector with the exchange of fields known as *messengers*, as represented schematically in Figure 2.1. This type of supersymmetry has been extensively searched for in several experiments, with negative results so far.

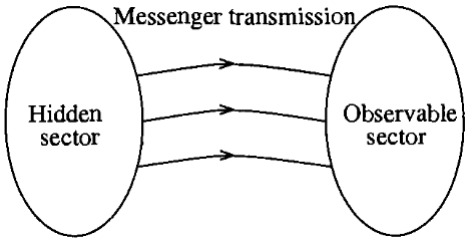

Figure 2.1: Schematic view of the hidden sector.

The MSSM has 124 free parameters, namely:

- 18 SM parameters
- 1 Higgs sector parameter, analogue to the SM Higgs mass
- 5 real and 3 CP violating phases in the gaugino/higgsino sector
- 21 squark and slepton masses
- 36 real mixing angles for squark and slepton mass eigenstates
- real mixing angles for squark and slepton mass eigenstates

The complex phases are usually considered small. Some experiments are capable of measuring some of these parameters individually. Nevertheless, in general this large amount of degrees of freedom spoils the predictive power of the model. In order to reduce it, *mass universality* is imposed to some particular cases that will be discussed further in this section. This implies that all spin 0 (1/2) sparticle masses are equal to a universal value m_0 ($m_{1/2}$). Another way of reducing the number of parameters is specifying the mechanism that breaks the symmetry, either with gauge fields (Gauge Mediated Supersymmetry Breaking, GMSB) or as a consequence of a dominating super-Weyl anomaly (Anomaly Mediated Supersymmetry Breaking, AMSB). Some of these models will be explained in more detail later.

2.4.3 CMSSM

The *constrained* MSSM (hereafter CMSSM) is one of the most popular subversions of the MSSM. In this model, the concept of mass universality introduced earlier is imposed, meaning that for a given GUT scale $\Lambda \sim 2 \times 10^{16}$GeV:

- All scalar masses are set to a universal scalar mass, m_0:

$$M_{\tilde{l}}^2(\Lambda) = M_{\tilde{q}}^2(\Lambda) \equiv m_0^2 I_3 \tag{2.7}$$

$$M_{\tilde{u}}^2(\Lambda) = M_{\tilde{e}}^2(\Lambda) = M_{\tilde{d}}^2(\Lambda) \equiv m_0^2 I_3 \tag{2.8}$$

$$m_{H_u}^2 = m_{H_d}^2 = m_0^2, \tag{2.9}$$

  where I_3 represents the 3x3 identity matrix

- All gaugino masses are set to have the same mass, $m_{1/2}$:

$$m_{\tilde{B}}(\Lambda) = m_{\tilde{W}}(\Lambda) = m_{\tilde{g}}(\Lambda) \equiv m_{1/2} \tag{2.10}$$

- The trilinear couplings are set to a single value, A_0:

$$A_{\tilde{u}}(\Lambda) = A_{\tilde{e}}(\Lambda) = A_{\tilde{d}}(\Lambda) \equiv A_0 I_3. \tag{2.11}$$

These requirements lead to the following relation between the gaugino masses at the TeV scale:

$$M_1 = \frac{\alpha_s}{\alpha} \sin\theta_W{}^2 M_2 = \frac{3}{5} \cos\theta_W{}^2 M_1, \tag{2.12}$$

which translates into the ratios:

$$M_1 : M_2 : M_3 \approx 1 : 2 : 6. \tag{2.13}$$

With these conditions, the CMSSM ends up with a set of 5 free parameters: (m_0, $m_{1/2}$, A_0, $\tan\beta = \frac{v_1}{v_2}$, sign($\mu$)). The last one refers to the sign of the Higgs self-coupling in the superpotential, while $\tan\beta = \frac{v_u}{v_d}$ is the ratio of the VEVs from the Higgs doublet. Since gaugino masses run in the same way as the gauge couplings, within the CMSSM the LSP is generally the lightest neutralino. The status of CMSSM in light of current experimental constraints will be reviewed in chapter 7.

A more restrictive version of CMSSM exists, mSUGRA, where supersymmetry breaking is gravity-mediated. Within this model, the gravitino mass is equal to the scalar mass, $m_{3/2} = m_0$, thus adding a new constraint on the parameters. On the contrary, there are models with more relaxed conditions. An example of these is when the universality condition on the Higgs masses is not applied, hence having Non Universal Higgs Masses (NUHM1 and NUHM2 [36]). This adds two extra free parameters, M_A, the mass of the CP-odd neutral higgs, A^0, and μ, the Higgs self-coupling.

2.4.4 AMSB

In the Anomaly Mediated SUSY Breaking (AMSB), the supersymmetry breaking occurs mainly via a loop-induced super-Weyl anomaly. In some scenarios, such breaking is assumed to take place in a different *brane* (a 5D volume with one dimension much smaller than the other 4) with respect to the *observable* sector, within the context of *Extra Dimensions*. The anomaly-mediated SUSY breaking parameters are RG-invariant, being the corresponding masses given as functions of the gauge and Yukawa coupling constants. This helps avoiding a SUSY flavor problem.

To generate the weak scale masses of the sparticles, the gravitino mass, $m_{3/2}$ must be fairly heavy (of the order of tens of TeV). Thus, it is not affected by Big-Bang nucleosynthesis bounds. The gaugino masses $M_{1,2,3}$ are suppressed by loop factors relative to this gravitino mass, and the wino-like states are lighter than the bino-like ones. The following approximate ratios hold:

$$|M_1| : |M_2| : |M_3| \approx 2.8 : 1 : 7.1 \tag{2.14}$$

Within this model, the soft supersymmetry breaking terms can be computed from the gravitino mass, and the soft terms are real and both flavor and renormalization group invariant. Despite its many advantages, AMSB has a strong drawback: renormalization leads to negative squared masses for sleptons. There are several proposals to cope with this, like the *minimal* AMSB (mAMSB), that will be discussed further.

2.4.4.1 mAMSB

In mAMSB, with the purpose of avoiding *tachyonic* sleptons in AMSB models, a constant contribution (m_0^2) is added to all squared scalar masses at the grand unified theory (GUT) scale, $\Lambda_{GUT} \sim 2^{16}$GeV. This addition can be mostly related to the presence of extra field(s) in the bulk [37], and destroys the aforementioned RG invariance, desirable in order to fulfill the FCNC constraint. Nevertheless some characteristics are inherited.

Both the μ term and the term to match soft bilinear Higgs coupling, B_μ, are parameters of this model too. Given that they determine the Higgs potential:

$$G_F = [2\sqrt{2}(v_2^2 + v_1^1)]^{-1} \simeq 1.7 \times 10^{-5}\text{GeV}^{-2} \tag{2.15}$$

The minimization of Eq. 2.15 leads to the determination of such paramaters as a function of $\tan\beta$. Hence, the mAMSB model has three continuous free parameters, (m_0, $m_{3/2}$, $\tan\beta$). In addition, the sign of the Higgsino mixing parameter, μ, is also free. The trilinear soft SUSY-breaking mass terms, like the gaugino masses, are determined by anomalies, therefore they are proportional to the gravitino mass.

This model has some interesting features, such as:

- The left and right sleptons are nearly degenerate ($m_{\tilde{l}_R} \approx m_{\tilde{l}_L}$), being stau the lightest slepton. As a consequence, the third and second generation L-R mixing angles become significantly larger, reaching the maximal limit at large $\tan\beta$.

- The lightest chargino and neutralino are also almost degenerate ($m_{\tilde{\chi}_1^\pm} \approx m_{\tilde{\chi}_1^0}$). This induces to a relatively long-lived $\tilde{\chi}_1^\pm$, that decays to a soft charged pion.
- Sfermion masses increase lineraly with m_0, but also depend on the precise value of $m_{3/2}$.
- The mass hierarchy between sleptons and gauginos depends on the input parameters.
- The squark masses are typically very heavy, as they grow with $g_3^4 m_{3/2}^2$.
- The stop masses are relatively high, because of the Higgs mass and the relatively low values of the trilinear couplings.
- The LSP (lightest neutralino) can be wino-, Higgsino-like or mixed.

The most up-to-date likelihood analysis of this model in light of current constraints can be found in [38], and will be discussed in detail in Chapter 7.

2.4.5 Renormalization Group equations

The renormalization grop equations (RGE) are applied within the MSSM to describe the evolution of gauge couplings, superpotential parameters and soft terms from a given *input* scale up to near the *electroweak* scale. The method used in the SM (dimensional regularization, DREG) cannot be used within SUSY, as it introduces a spurious violation of this symmetry. The most common method for it is the dimensional reduction, DRED, with modified minimal subtraction ($\overline{\text{DR}}$), as opposed to DREG with modified minimal subtraction ($\overline{\text{MS}}$). Figure 2.2 compares the RG evolution of the coupling constants both in the SM and in the MSSM [39]. As it can be seen, a better match at the electroweak scale is achieved within the MSSM, as discussed in Section 1.

The RGE are derived using what is known as the *supersymmetryc non-renormalization theorem*, that implies that the logarithmically divergent contribution to a particular process can always be written in terms of wave-function renormalizations [39]. One consequence derived from this is that for a given value of μ at tree-level, RG corrections to it will be proportional to the parameter itself and some combinations of dimensionless couplings, thus avoiding very large radiative corrections that could greatly enhance μ.

Within this framework, it is asumed that gauge couplings unify at a given scale, Λ. Hence, gaugino masses are considered to be unified near that scale as well (which come naturally in GUT models):

$$\frac{M_1}{g_1^2} = \frac{M_2}{g_2^2} = \frac{M_3}{g_3^2} = \frac{m_{1/2}}{g_\Lambda^2} \tag{2.16}$$

where g_Λ is the unified gauge coupling at Λ, and $m_{1/2}$ the unification value for the gaugino masses.

Some more consequences of the RGE are listed below.

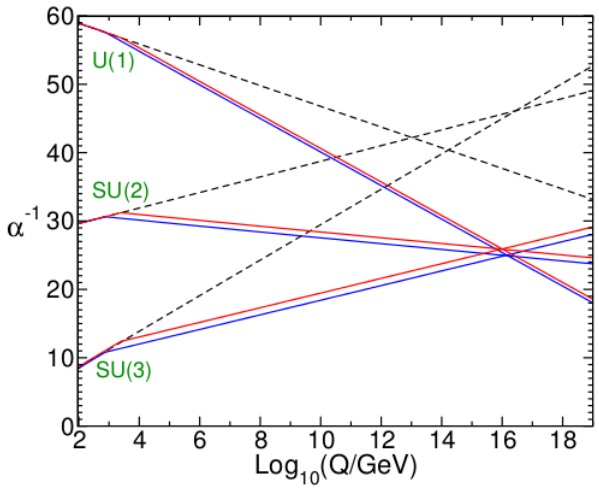

Figure 2.2: Two-loop renormalization group evolution of the inverse gauge couplings $\alpha_a^{-1}(Q)$ in the SM (dashed lines) and the MSSM (solid lines). In the MSSM case, the sparticle masses are treated as a common threshold varied between 750 GeV (blue line) and 2.5 TeV (red line), and $\alpha_3(m_Z)$ is varied between 0.117 and 0.120, respectively. Figure taken from Ref. [39].

1. Because they are not protected by the supersymmetric non-renormalization theorem, the soft parameters that describe the Yukawa couplings do not vanish at the electroweak scale, even if they are zero at the input scale.

2. The scalar squared masses will be almost diagonal, with the second family squarks and sleptons very nearly degenerate. The third-family squarks and sleptons will get normalized differently.

3. The scalar squared-mass parameters grow as they are RG-evolved, due to the gaugino masses effect on the RGE. Therefore, large masses can be obtained at the electroweak scale even if these are small or even zero at the weak scale.

4. Because of the contributions they receive from the RGE, the Higgs squared masses generally decrease at the electroweak scale with respect to the input scale. This can lead to a negative value of $m_{H_u}^2$, with the consequence of a non-zero Higgs VEV. This effect increases as the top Yukawa coupling does.

5. If the gaugino mass parameters M_1, M_2 and M_3 have non-zero values for a given input scale, all the soft terms will be generated via RGE. Otherwise, gauginos would be extremely light, causing the model to be inviable due to experimental measurements.

2.5 RPV Models

R-parity (or matter parity) conservation can be justified in terms of a grand unified theory or as a consequence of a residual symmetry of a superstring vacuum. However, it is not necessarily the existing scenario. Additional terms can be added to the superpotential in Eq. 2.6 that violate baryon number (B) or lepton number (L), namely:

$$W_{\Delta L=1} = \frac{1}{2}\lambda^{ijk} L_i L_j \overline{e}_k + \lambda'^{ijk} L_i Q_j \overline{d}_k + \mu'^i L_i H_u \tag{2.17}$$

$$W_{\Delta B=1} = \frac{1}{2}\lambda''^{ijk} \overline{u}_i \overline{d}_j \overline{d}_k, \tag{2.18}$$

where $i = 1, 2, 3$, depending on the fermionic family. Terms in Eq. 2.17 (2.18) violate lepton (baryon) number by one unit. If both terms accompanying λ' and λ'' were to exist (without suppression), proton decays to final products such as $e^+\pi^0$ would be feasible. Nevertheless, the lifetime for the proton is known to be $> 10^{34}$ years [40]. This, together with more experimental evidence , leads to the conclusion that one of these couplings must be zero or very small, being RPV models either B-violating or L-violating, with experimental upper bounds existing for both couplings.

One example of such type of RPV model is a scenario where R-parity is replaced by a *baryon triality*, Z_3^B,s defined as

$$Z_3^B = \exp\{2\pi i[B - 2Y]/3\}, \tag{2.19}$$

where Y is the hypercharge. The corresponding symmetry establishes that the product of the baryon trialities of the particles in any term in the superpotential must be 1. With this, proton decay and neutron-antineutron oscillation are forbidden processes, as they would violate triality. This symmetry does allow the LSP to decay.

Another alternative is the spontaneous R-parity symmetry breaking by particles, like sneutrinos in the context of MSSM([41, 42]). Strong experimental bounds exist on this. Either way, RPV scenarios greatly change the SUSY signatures in colliders, allowing processes like single sfermion production or exchange of sfermions to happen.

2.5.1 Consequences of RPV

Numerous consequences can be derived in the different possible RPV models. Some of them are briefly addressed below.

1. Within some of these models, there can be *leptogenesis* (asymmetry between leptons and antileptons in the early Universe), that would lead to the current matter-antimatter asymmetry discussed in Section 1.

2. The LSP can have color/charge, while fulfilling current constraints, and no longer needs to be stable.

3. Some RPV models include a seesaw mechanism that provides neutrinos with mass, while including sterile neutrinos [43].

4. A possible candidate for DM is the heavy gravitino, superpartner of the graviton. Even though it is unstable, its decay is heavily suppressed by the gravitational coupling, resulting in a lifetime bigger than the age of the Universe.

2.6 Experimental searches

Many experimental efforts have been done in the search for supersymmetry, both via direct searches of supersymmetric particles and by looking for indirect effects. A summary can be found in [44, 45], where bounds on the masses are set for different models, with data from ATLAS and CMS experiments, described in chapter 4. These put strong restrictions on the ability of SUSY or the MSSM to deal with the gauge hierarchy problem (what is known in the MSSM as *little hierarchy problem*).

With these experimental constraints, together with other experimental measurements, such as DM direct detection, results global fits can be made for different SUSY models. A specific case will be discussed in chapter 7. More of these fits can be found in References [46], [47–52].

USC
UNIVERSIDADE
DE SANTIAGO
DE COMPOSTELA

Chapter 3

Low E observables in SUSY

3.1 Minimal Flavour Violation

3.1.1 Motivation for Minimal Flavour Violation

The success of the SM in predicting flavour and CP violation effects leads to thinking that NP has to follow its pattern. Otherwise, experimental evidence of additional flavour violating structures should have appeared by now. Additionally, the hierarchy problem suggests $\Lambda <$ TeV, while in the case in which flavour violation is generated generically in SUSY, $\Lambda \sim \mathcal{O}$(TeV) [53]. An effective field theory (henceforth, EFT) becomes necessary in order to address the favour problem in SUSY, where the flavour violation predictions can largely exceed the experimental constraints and are *a priori* unrelated to the SM sources [54]. Minimal Flavour Violation (hereafter MFV) requires all flavour and CP-violating interactions to be governed by the known structure of the SM Yukawa couplings [55] in the low-energy regime. Hence, in any SM extension the amount of FCNC and CP violating process should be ruled by these. As for supersymmetry, MFV holds under the assumption of *mass universality*, and if the trilinear soft terms are proportional to the Yukawa couplings at the GUT scale. This MFV can be seen as the remnant of an underlying favor symmetry at the Λ scale [53].

3.1.2 MFV EFT

Minimal Flavour Violation (hereafter MFV) is constructed as a low-energy EFT [55], within which the SM is contained. Its main feature is that the only source of $SU(3)^5$ flavour symmetry breaking are the background values of fields transforming under the flavour group like the ordinary Yukawa couplings [55]. In he SM, the $U(3)^5$ flavour symmetry is the largest group of unitary field transformations that commutes with the gauge group. This can be decomposted [55] as: $U(3)^5 = [SU(3) \bigotimes U(1)]^5$. In the absence of Yukawa couplings, the SM presents an enhanced global symmetry [53,54], that commutes

with $U(3)^5$:

$$G_F = [SU(5) \bigotimes U(1)]^5 \equiv \bigotimes_{F=Q,U,D,L,E} [SU(3) \bigotimes U(1)]_F \tag{3.1}$$

Notice that the baryon, lepton and hypercharge numbers are not modified by Yukawa interactions. The $U(3)^5 = [SU(3) \bigotimes U(1)]^5$ group is broken by Yukawa interactions. Flavour invariance is recovered introducing dimensionless auxiliary fields, Y_U, Y_D and Y_E transforming under $SU(3)_q^3 \bigotimes SU(3)_l^3$ promoting to spurion fields in order for flavour violation to appear [54], thus leading to the Yukawa interaction terms of the SM Lagrangian as discussed in Section 1, consistent with flavour symmetry. These terms can be rotated such that:

$$Y_d = \hat{Y}_d,\ Y_e = \hat{Y}_e,\ Y_u = V^\dagger \hat{Y}_u \tag{3.2}$$

denoting $\hat{Y}$ diagonal matrices, and V being the CKM matrix. The notation in Reference [55] is followed.

In MFV all higher-dimensional operators are constructed from SM and Y fields, and are invariant under CP and the flavour group G_F. Therefore, they can be rewritten in terms of the SM Yukawa couplings [54]. Given that the top Yukawa coupling is considerably large with respect to the others, the only relevant non-diagonal structure in the low $\tan\beta$ regime is obtained contracting two Y_u, hence having:

$$(\lambda_{FC})_{ij} = \begin{cases} \left(Y_u Y_u^\dagger\right)_{ij} \approx \lambda_t^2 V_{3i}^* V_{3j} & i \neq h, \\ 0 & i = j \end{cases} \tag{3.3}$$

where $\lambda_t = (\hat{Y}_u)_{33}$ and subleading effects on the right hand side of Equation 3.3 are suppressed by powers of m_c/m_t [54] as the effective coupling ruling all FCNC processes with external down-type quarks. Such processes are governed by $\Delta F = 2$ and $\Delta F = 1$ (Higgs field, gauge fields and four-fermion) operators. Further details on this operators can be found in Reference [55].

3.1.3 MFV SUSY

Consider the MSSM (where R-parity is conserved) as a low-energy EFT. Differently to what happens in other non-supersymmetric MFV scenarios, there are renormalizable terms with non-trivial flavour structure, besides the ordinary Yukawa couplings. Within MFV, the off-diagonal entries in the soft terms (the genuinely new sources of flavour violation in the MSSM) are CKM-like [54].

According to MFV, the squark masses and trilinear couplings can be written as follows [55]:

$$\tilde{m}_{Q_L}^2 = \tilde{m}^2(a_1 \mathbb{I} + b_1 Y_u Y_u^\dagger + b_2 Y_d Y_d^\dagger + b_3 Y_d Y_d^\dagger Y_u Y_u^\dagger + b_4 Y_u Y_u^\dagger Y_d Y_d^\dagger) \tag{3.4}$$

$$\tilde{m}_{U_R}^2 = \tilde{m}^2(a_2 \mathbb{I} + b_5 Y_u Y_u^\dagger) \tag{3.5}$$

$$\tilde{m}_{D_R}^2 = \tilde{m}^2(a_3 \mathbb{I} + b_6 Y_d Y_d^\dagger) \tag{3.6}$$

$$A_u = A(a_4\mathbb{I} + b_7 Y_d Y_d^\dagger)Y_u \tag{3.7}$$

$$A_d = A(a_5\mathbb{I} + b_8 Y_u Y_u^\dagger)Y_d, \tag{3.8}$$

where $\tilde{m}$ and A set the mass scale of the soft terms, a_i and b_i are numerical coefficients and $\mathbb{I}$ is the 3x3 identity matrix. Quadratic terms of the first two families of Yukawas have been neglected. In the limit of low $\tan\beta$ the terms quadratic in Y_d can be dropped too. Under the assumption of mass universality and proportionality of trilinear terms, the b_i coefficients are zero at the GUT scale Λ and generated via RGE.

The squark mass matrices after the electroweak breaking and using the soft terms, 3.7 and 3.8 have the form [55]:

$$\tilde{M}_U^2 = \begin{pmatrix} \tilde{m}_{Q_L}^2 + Y_u Y_u^\dagger v_u^2 + (1/2 - 2/3\sin\theta_W{}^2)M_Z^2\cos 2\beta & (A_u - \mu Y_u \cot\beta)v_u \\ (A_u - \mu Y_u \cot\beta)^\dagger v_u & \tilde{m}_{U_R}^2 + Y_u^\dagger Y_u v_u^2 + 2/3\sin\theta_W{}^2 M_Z^2\cos 2\beta \end{pmatrix}, \tag{3.9}$$

$$\tilde{M}_D^2 = \begin{pmatrix} \tilde{m}_{Q_L}^2 + Y_d Y_d^\dagger v_d^2 + (1/2 - 1/3\sin\theta_W{}^2)M_Z^2\cos 2\beta & (A_d - \mu Y_d \tan\beta)v_d \\ (A_d - \mu Y_d \tan\beta)^\dagger v_d & \tilde{m}_{D_R}^2 + Y_d^\dagger Y_d v_d^2 - 1/3\sin\theta_W{}^2 M_Z^2\cos 2\beta \end{pmatrix} \tag{3.10}$$

From Eqs. 3.9 and 3.10 follows that the physical squark masses are not degenerate under the MFV assumption, but the mass splitting is severely constrained. The mass matrices in Eqs. 3.10 and 3.9 are then diagonalized using the expansions in Eqs. 3.4 - 3.8. Analogously to the SM case, it is possible to change to a *super-CKM* basis, where:

$$\hat{m}_u = \frac{v_d}{\sqrt{2}}\hat{Y}_u,\ \hat{m}_d = -\frac{v_u}{\sqrt{2}}\hat{Y}_d. \tag{3.11}$$

Notice that in this basis the Yukawa matrices are diagonal, but the trilinear coplings and the mass-matrices are still non-diagonal. Unitary matrices Z_U and Z_D are needed in order to change to a mass eigenstate basis. In the MFV scenario the off-diagonal entries of this matrices are not zero, but CKM-like [54].

3.1.4 MFV R-parity

MFV can be used instead of the R-parity conservation assumption [56]. Under this scenario the baryon number can be violated, while the lepton number violation is strongly suppressed and only possible with massive neutrinos. This is strongly discouraged by the proton lifetime, and bounds from $n - \bar{n}$ oscillation and dinucleon decay. In some specific models, extra suppression from the neutrino sector can help further alleviate this bounds. Under these models R-parity is obtained like an approximate symmetry as a side effect. The LSP decays fast and is not necessarily neutral. It can be a stop or sbottom (decaying to 2 bodies), a neutralino or chargino (decaying to 3 bodies) or a slepton (with the subsequent 4 body decay). A possible DM candidate is the gravitino.

3.1.5 MFV Characteristics

Given that the top Yukawa coupling is much larger than the others, in MFV all flavour-changing effective operators are proportional to the same non-diagonal structure. This greatly affects the predictability of this model, as will be discussed in Section 3.1.7. Within this approach, the squark masses in the physical eigenbasis are not degenerate, but the induced flavour violation is described in terms of the usual CKM parameters [55].

Strong assumptions need to be made in order to maintain MFV within different SUSY scenarios, such as supergravity. Other models with different susy-breaking mechanism (such as AMSB) can alleviate these conundrum [55]. As will be discussed in Section 3.1.8, the Universal Unitarity Triangle does not necessarily hold within the MFV scenario.

Within MFV, both the gaugino masses $M_{1,2}$ and the Higgs mixing parameter μ are real. Otherwise, given that they appear in the neutralino and chargino mixing matrices, they would induce new sources of CP violation, thus violating MFV. An alternative approach [57] consists in assuming the soft SUSY breaking sector to be CP conserving only in the limit of flavour blindness, while allowing CP violation to happen by the MFV-compatible terms. In this scenario, μ and the gaugino masses are real at low energies and the trilinear coupings (the only sources of CP-violation) are strongly hierarchical, being the Electric Dipole Moments (EDMs) the most important experimental constraints [53]. Nevertheless, in the case in which this *ansatz* holds not at the low scale, but at the GUT scale (determined by Λ), complex parameters can be generated via RGE [53], [57].

3.1.6 CMFV

The *constrained* MFV (cMFV) is a phenomenological definition of MFV, that uses the CKM matrix (instead of the Yukawa couplings) as the only source of flavour violation and retricts the set of relevant operators in the low-energy effective Hamiltonian to the SM ones [54] ($\mathcal{Q}_1$). Contrarily to the more general definition of MFV proposed in [55], it is not model-independent. In the limit in which $b_i \to 0$ in Equations 3.4-3.8, the cMFV is recovered from the general MFV. Nevertheless, it is worth mentioning that not all the scenarios are $\mathcal{Q}_1$-dominated, as it is assumed in cMFV. Indeed, in the limit of low $\tan\beta$ it is not always the case [54].

3.1.7 MFV Experimental bounds

Generic flavour-violating interactions at $\Lambda \simeq$ TeV are experimentally excluded. Within a MFV scenario, it is possible to relate various FCNC processes, such as rare B and K decays. Furthermore, CP-violation in the B_s system provides an excellent probe for non-CKM sources of flavour and CP-violation [54]. Besides, this constraint in the soft sector helps further reduce the number of parameters of the MSSM, thus improving its predictivity.

Experimental bounds to the generic MFV approach come mainly from:

- $\Delta F = 2$ processes that help further improve the precision for CKM matrix elements.

- The inclusive rare decay $B \to X_s\gamma$ to constraint the scale of the FCNC operators.
- Rare FCNC decays with a lepton in the final state, e.g. $K_L(B) \to l^+l^-$, $K^+ \to \pi^+\nu\bar{\nu}$, that provide constraints on several Wilson coefficients.
- Non-leptonic decays, provided electroweak contributions can be properly disentangled from the dominant effects coming from tree-level and gluon-penguin amplitudes.

3.1.8 Unitarity Triangle

The *universal unitarity triangle* [58] (henceforth, UUT) represented in Figure 3.1 is constructed using the CKM phases within the Wolfenstein parametrization [29]. It is characterized by not having any new operators beyond those present in the SM, hence only valid for cMFV models (see Section 3.1.6). Depending on the mass regime and the value of $\tan\beta$, variations up to the percent level can be found in a general MFV scenario [54]. In this triangle, no phases are beyond the CKM phase, hence they are not polluted by new physics contributions (since the quantities only depend on the CKM parameters). An advantage of the universal triangle is that it allows to separate the determination of the CKM parameters from the determination of new parameters present in the extensions of the SM. As an example, new phases could affect α, β and γ.

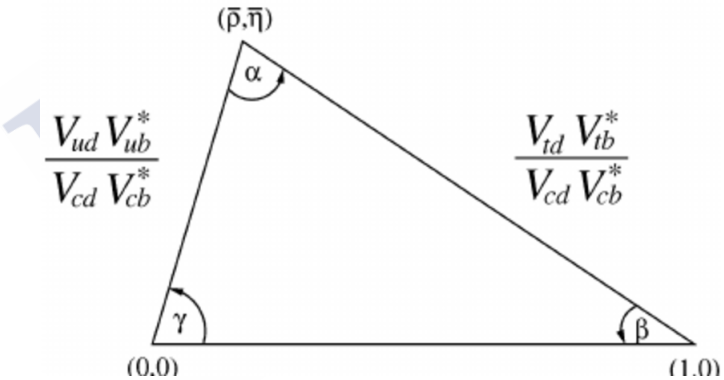

Figure 3.1: Unitarity Triangle, using the Wolfenstein parametrization [59]. Figure taken from Ref. [60].

Experimental measurements help determine the different values for the elements that define the triangle in Figure 3.1. Some of these measurements are $(\Delta M)_d/(\Delta M)_s$ (for R_t), $\sin 2\beta$, $B_d^0 \to J/\psi K_S^0$ (for β) and tree-level decays (for γ). As said before, NP contributions can affect these values, thus hinting at the existence of BSM Physics.

In order for this triangle to be *universal* to any SM extension, the requirement that new operators do not exist has to be fulfilled. Also, FCNC transitions should be ruled by the CKM eements. Hence, only the values of the functions describing top-mediated contributions to box and penguin diagrams can be modified by this new physics [58]. Under these conditions, the CKM matrix can be determined without further assumption

on the unknown BSM parameters, with the possibility of disentangling SM contributions from NP ones, looking for inconsistencies in the universal triangle or disagreements of the data with respect to the predictions made based on the UUT. As an extra feature, these parameters are not affected by hadronic uncertainties [58].

The most up-to-date determination of the elements of the UUT are shown in Figure 3.2.

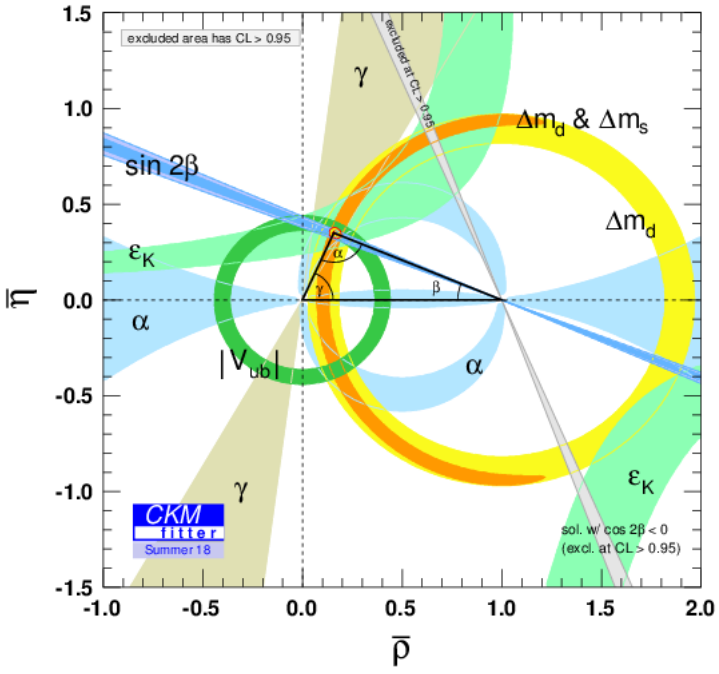

Figure 3.2: Experimental constraints on the UUT, using the Wolfenstein parametrization. Figure taken from Ref. [61].

3.2 Non Minimal Flavour Violation

The reachability of direct searches and searches in the quark flavour sector is strongly dependent on the NP scale, Λ. If this Λ is of the order of few TeV, or even greater, the only possibility to see it would be via indirect searches in quark flavour physics, provided there are new sources of Flavour Violation. Such new sources would not originate from the CKM matrix. Therefore, this scenario is called non-Minimal Flavour Violation (hereafter, non-MFV). They can be either slightly misaligned with respect to the MFV case (discussed in detail in the subsections above), or have an anarchic structure. The effects would be bigger for the latter. Within non-MFV , the soft mass and trilinear parameters of the SUSY-breaking Lagrangian are non-diagonal in flavour space. Generic SUSY models do not possess any symmetry preventing large off-diagonal elements in soft-SUSY parameters [62]. It should be noted that the *supersymmetrization* itself does not introduce any new flavor structures [63]. Thus, flavour breaking is related to more fundamental scales, differently to what happens in other theories (e.g., technicolor [64]).

3.2.1 Mass Insertion Approximation

In non-MFV, the squarks and sleptons mass matrices are not diagonal. The off-diagonal terms are often parametrized using the Mass Insertion Approximation, MIA. Such parameters (MI) that describe the matrix elements, labelled with δ, are assumed to be small. Different experimental signatures, as well as vacuum stability, constrain their values. The situation where all MI vanish would correspond to the MFV paradigm. For a given squark 6x6 mass matrix, $\mathcal{M}^2_{\tilde{Q}}$ in the super-CKM basis, the simplest MIA follows the expression:

$$\delta_{\tilde{Q}} = \frac{(\mathcal{M}^2_{\tilde{Q}})_{ij}}{\tilde{m}^2},\ i \neq j \tag{3.12}$$

Assuming one average squark mass, $\tilde{m}$ per matrix. Different conventions in this regard can be considered, and will be discussed in the following chapters. The same is true for sleptons.

Note that, in principle, flavour non diagonal terms would induce FCNC, in contradiction with experimental results [29]. To avoid this problem, flavour *blindness* is proposed in models like gauge-mediated SUSY breaking, in which the sfermion-mass matrice are flavour diagonal in the same basis as the quark matrices at the SUSY-breaking scale [65]. Nevertheless, because of RGE an amount of flavour mixing is foreseen.

3.2.2 Experimental signatures

As discussed before, precise measurements of low-energy observables can probe fundamental scales, icluding those beyond the "energy frontier" [63]. Furthermore, channels that impose bounds on mass insertions can shed light on the nature of SUSY.

Examples of such observables that have special interest in a non-MFV scenario include:

- $K^0 - \bar{K}^0$, $B^0 - \bar{B}^0$, $B_s^0 - \bar{B}_s^0$ and $D - \bar{D}^0$ mixing. These are meson mixings ($\Delta F = 2$ processes), that proceed via box diagrams in the SM. Therefore, sizeable NP contributions could induce a big deviation in the observables with respect to the SM predictions. They will be studied in detail in the following chapters.

- Flavor-changing decays: Higgs penguins. These are especially important in the large $\tan\beta$ regime [63].

- Electroweak penguins (inclusive $B \to X_s\gamma$, rare K, B decays, etc). Identifying contributions different from the SM sources would clearly hint NP [63].

- Lepton flavour violation. These decays are strongly suppressed in the SM, but not in SUSY scenarios. Therefore, stringent bounds MIs come from the study of these processes.

For all the above-metioned measurements, complementary to direct searches, high precision is needed in order to disentangle NP from SUSY effects. As it can be seen, in a non-MFV paradigm strange physics acquires an important role. This is because kaons have short-distance FCNCs with the strongest CKM suppression, making them more sensitive to anarchic structures of flavour violation [66].

Chapter 4

LHCb

4.1 LHC

The Large Hadron Collider (LHC) is the world's largest and most powerful particle accelerator. Located at CERN (*European Organization for Nuclear Research*), it consists of a 27 km ring of superconducting magnets with a number of accelerating units for charged particles.

Two proton beams travelling in opposite directions collide at different points of the ring. The protons are extracted from ion sources, and accelerated in a chain of preaccelerators, the last one of which is the Super Proton Synchrotron (SPS) (see Figure 4.1). The center of mass energy ($\sqrt{s}$) the protons reach is up to 13 TeV, in order to test the Standard Model and look for New Physics. One of LHC's main achievements has been the discovery of the Higgs boson, introduced in Refs [67], [68], the last piece of the Standard Model puzzle. Protons are sent in bunches containing up to 1.5×10^{11} particles, and crossing with a rate of 40 MHz. Special runs with heavy ions (e.g. lead) are also made periodically.

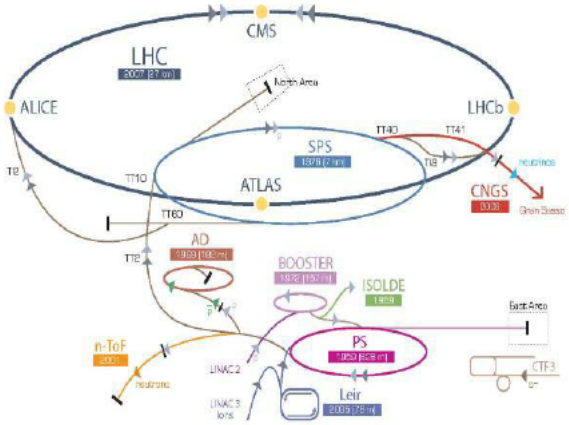

Figure 4.1: The LHC injection complex. Figure taken from Ref. [69].

Since it first started operating in 2008, the LHC has provided data with different center of mass energies, corresponding to 2 data-taking periods: Run 1 (2009-2013, $\sqrt{s} =$ 7, 8 TeV), and Run 2 (2015-2018, $\sqrt{s} = 13$, 14 TeV).

There are four interaction points within the LHC ring, corresponding to the four main experiments. In these points, the beams cross over to the other beam pipe and collide under a small angle. These four experiments are:

- **ATLAS** (*A Toroidal LHC ApparatuS*) [70]: a general-purpose 4π detector, focused mainly in the search of New Physics via direct searches and responsible of the Higgs boson discovery.
- **CMS** (*Compact Muon Solenoid*) [71]: also a general-purpose detector, with a physics program similar to ATLAS and a more compact layout.
- **ALICE** (*A Large Ion Collider Experiment*) [72]: the smallest of the four detectors, it focuses in heavy-ion studies.
- **LHCb** (*Large Hadron Collider beauty*) [73]: a single-arm forward spectrometer, initially designed for the study of particles containing b or c quarks. It is described in more detail in the following section.

4.2 LHCb

The LHCb detector [74, 75] covers the pseudorapidity range $2 < \eta < 5$. The detector includes a high-precision tracking system consisting of a silicon-strip vertex detector surrounding the pp interaction region [76], a large-area silicon-strip detector located upstream of a dipole magnet with a bending power of about 4 Tm, and three stations of silicon-strip detectors and straw drift tubes [77] placed downstream of the magnet. The tracking system provides a measurement of the momentum, p, of charged particles with a relative uncertainty that varies from 0.5% at low momentum to 1.0% at 200 GeV/c. The minimum distance of a track to a primary vertex (PV), the impact parameter (IP), is measured with a resolution of $(15+29/p_{\mathrm{T}})\mu$m, where p_{T} is the component of the momentum transverse to the beam, in GeV/c. Different types of charged hadrons are distinguished using information from two ring-imaging Cherenkov detectors [78]. Photons, electrons and hadrons are identified by a calorimeter system consisting of scintillating-pad and preshower detectors, an electromagnetic calorimeter and a hadronic calorimeter. Muons are identified by a system composed of alternating layers of iron and multiwire proportional chambers [79]. The online event selection is performed by a trigger [80], which consists of a hardware stage, based on information from the calorimeter and muon systems, followed by a software stage, which applies a full event reconstruction.

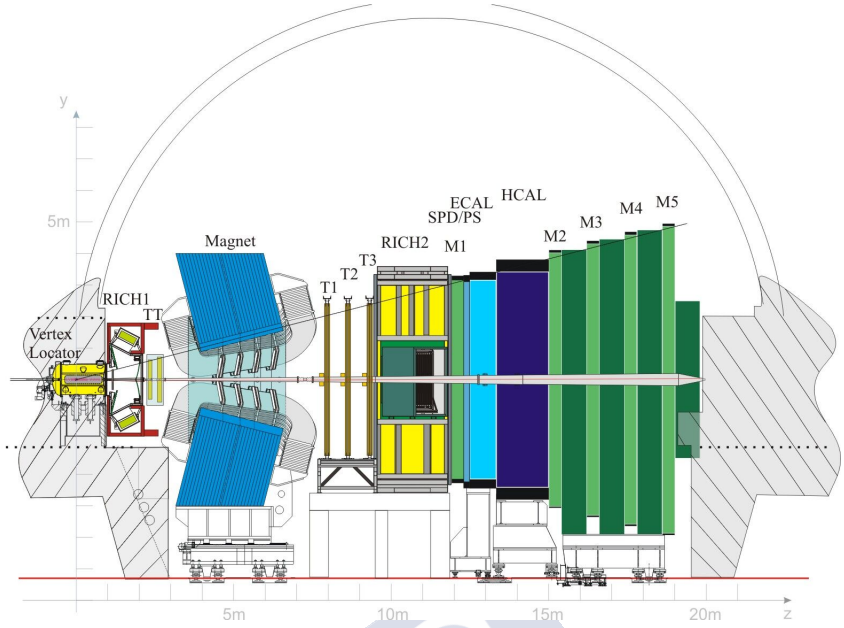

Figure 4.2: The LHCb detector. Figure taken from Ref. [81].

4.2.1 Beam pipe, vacuum chamber and BCM

The design of the beampipe (see Figure 4.3) is especially delicate, given the pseudorapidity region at which LHCb operates, where there is a high particle density. It is 19 m long and includes the forward window of the VErtex LOcator (VELO) and four main conical sectors. The three closest to the interaction point are made of beryllium, as it is highly transparent to particles resulting from collisions. The fourth one is made of stainless steel because of its good mechanical and vacuum properties. The beampipe support system consists of one fixed and one movable support, in order to reduce the background as much as possible. Two sector valves located at the cavern entrances isolate the experiment beam vacuum from the LHC.

The Beam Conditions Monitor (BCM) controls the LHC beam conditions, requesting a beam dump if necessary. It monitors the particle flux at two locations close to the vacuum chamber in order to protect the sensitive LHCb tracking devices. It is connected to the LHCb experiment control system and to the beam interlock controller of the LHC. The two stations consist of eight diamond sensors.

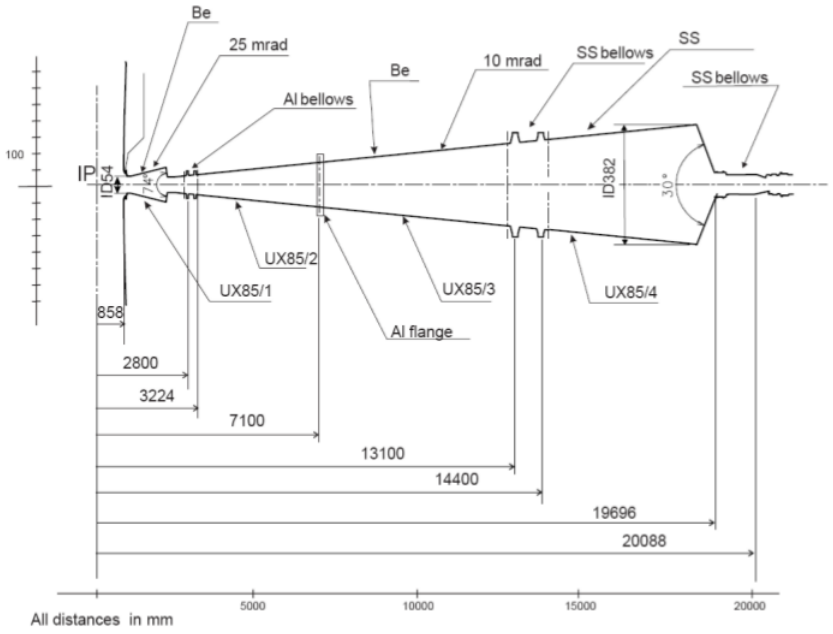

Figure 4.3: LHCb beam pipe.

4.2.2 Magnet

LHCb contains a dipole magnet (see Figure 4.4) that bends charged particles in order to measure their momenta. The measurement covers the forward acceptance of ±250 mrad verticaly and of ±300 mrad horizontally. Two identical conical saddle-shaped coils surround an iron yoke, producing a magnetic field of 4 Tm for tracks of 10 m length. These coils are made of pure Al-99.7. The magnet performance is monitored by the Magnet Control System and the Magnet Safety System assures its safe operation.

The precision with which the magnetic field is measured needs to be of the order of 10^{-4} so as to allow a precise measurement of the momentum resolution of the charged particles. In order to ensure this, field mapping campaigns in the tracking volume were made and obtained a value of about 4×10^{-4} (see Figure 4.4 right). In order to reduce the systematic effects of the detector, especially for CP studies, the polarity of the magnetic field is changed periodically.

4.2.3 Tracking

The tracking system of LHCb consists of two parts: the vertex locator (VELO) and four tracking stations: the *Tracker Turicensis* (TT) upstream of the magnet, and T1-T3 downstream of the magnet. The latter are composed by an Inner Tracker (IT) and an Outer Tracker (OT). Both IT and TT belong to a common project, the *Silicon Tracker* (ST).

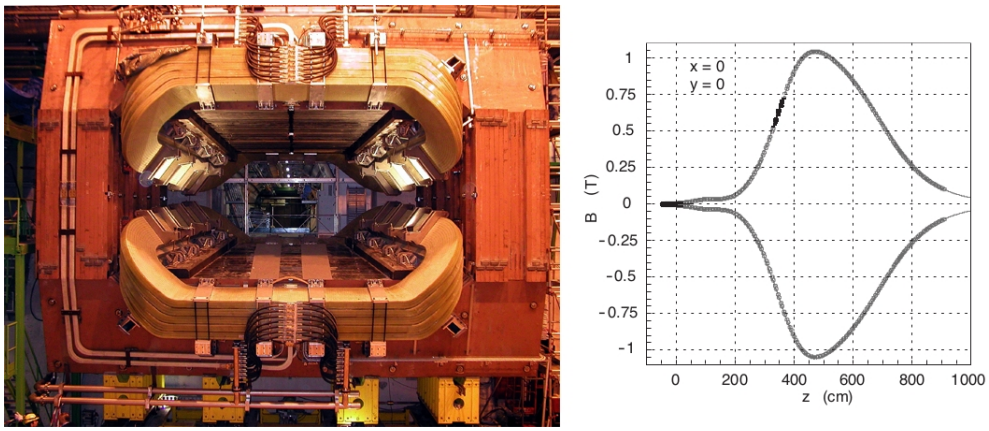

Figure 4.4: LHCb magnet (left) and magnetic field along the z axis (right).

4.2.3.1 VELO

The ability to reconstruct vertices with a high precision is a key feature of the LHCb detector. It allows precise measurement of decay lifetimes, the impact parameter and the flavour of the particles that are produced. Besides, detached vertices are of crucial importance for the High Level Trigger (see Section 4.2.5).

Such reconstruction is done in the VErtex LOcator (VELO), that provides measurements of the track coordinates close to the interaction region. It consists of 20 semicirular silicon modules located along the beam direction, each one providing measurement of cylindrical coordinates (r, ϕ) using microstrips, together with two planes perpendicular to the beam line, the *pile-up veto system*, as shown in Figure 4.5, that are then used to remove high multiplicity events. The minimum pitch at the innermost radius is 38μm, increasing linearly to 101.6μm at the outer radius of 41.9mm. These sensors must be retractable, as the distance from them to the beam is smaller than the one required from LHC during the injection phase. Vacuum inside the VELO is separated from the machine vacuum by corrugated aluminum foils, *RF-foils*. Polar coordinates are used in order to ensure fast reconstruction of tracks and vertices in the LHCb trigger [74].

4.2.3.2 ST

As said before, the Silicon Tracker (ST) refers to two different detectors: the Tracker Turicensis (formerly known as *Trigger Tracker*), TT and the Inner Tracker, IT (see Figure 4.6). Both use silicon microstrip sensors with a strip pitch of about 200 μm. The TT is a 150x130 cm high planar tracking station (covering the full LHCb acceptance), located upstream of the LHCb dipole magnet. The IT covers a 120x40 cm high cross shaped region in the centre of the three tracking stations downstream of the magnet.

The TT and each of the three IT stations have four detection layers, organized in an (x-u-v-x) configuration, with vertical strips in the first and the last layer (x-layers). Strips in the second and third layer are rotated by a stereo angle of $-5°$ and $5°$ respectively, so

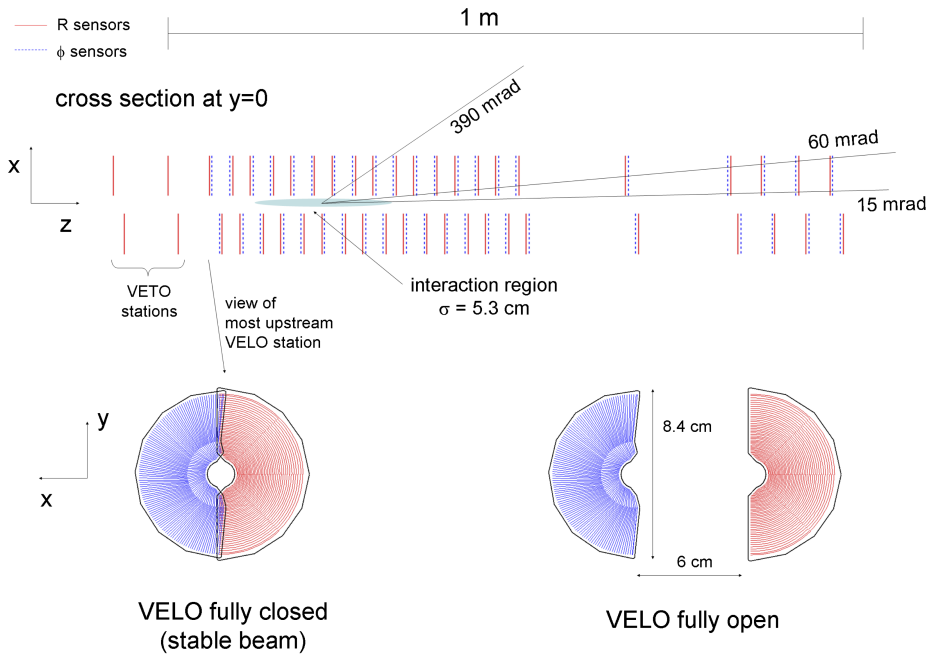

Figure 4.5: Cross section in the (x,z) plane of the VELO silicon sensors, at $y = 0$, with the detector in the fully closed position. The front face of the first modules is also illustrated in both the closed and open positions. Figure taken from Ref. [74].

as to get 3D reconstruction (u/v-layers). The pitch is about 200 μm which gives a single hit resolution of 50 μm. Momentum resolution is then dominated by multiple scattering. The active area is of about 8.4 m^2 for the TT and of 4.0 m^2 for the IT. A temperature below 5°C is maintained in both cases.

4.2.3.3 OT

The OT detector is designed for the tracking of charged particles, and the measurement of their momentum. Excellent momentum resolution and high tracking efficiency are needed for LHCb analyses. It consists of a drift-time detector, composed of an array of gas-tight straw-tube modules. For the gas, a mixture of argon (70%) and CO_2 (30%) is used. This ensures a fast drift time, as well as a sufficient drift-coordinate resolution.

The arrangement of the OT is shown in Figure 4.7. The modules are organized in three stations, each one consisting of four layers. The stations are further splitted in two halves, with two independently retractable units of two half layers (C-frames).

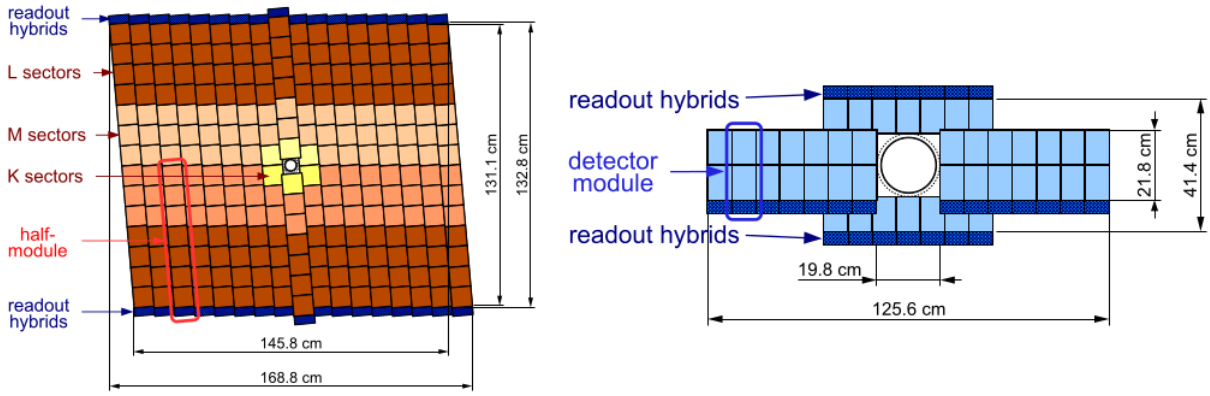

Figure 4.6: Layout of the third TT detection layer (left) and layout of an x detection layer in the second IT station (right). Figures taken from Ref. [74].

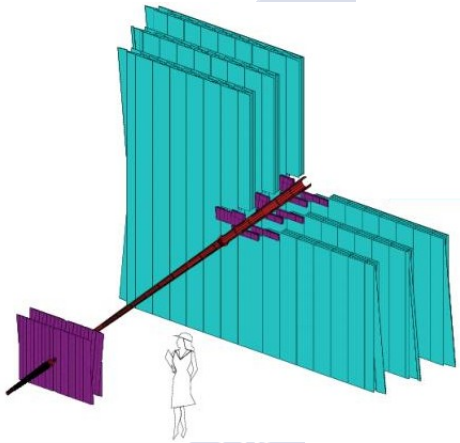

Figure 4.7: Arrangement of OT straw-tube modules in layer and stations. Figure taken from Ref. [74].

4.2.4 PID

Particle identification (PID) at LHCb is crucial in order to properly distinguish the different types of particles that are detected. Particularly, it is important to further reduce backgrounds from different decays, as well as at the trigger level (see Section 4.2.5). Three different subdetectors, described below, are used for PID.

4.2.4.1 RICH

There are two *Ring Imaging Cherenkov detectors* at LHCb, designed to cover a wide momentum range. RICH1 (Figure 4.8 left) covers the low momentum charged particle range ($\sim 1-60$GeV), while RICH2 (Figure 4.8 right) covers the high momentum charged

particle range ($\sim$ 15GeV up to and beyond $\sim$ 100GeV). In order to do this, RICH1 (located upstream, between the VELO and the Trigger Tracker) uses aerogel and C_4F_{10} radiators, while the downstream detector, RICH2, uses a CF_4 radiator.

While RICH1 covers the full LHCb acceptance, from $\pm$25 rad to $\pm$300 rad horizontal and $\pm$250 rad vertical, RICH2 has a more limited angular acceptance (where the high momentum particles are produced), of $\sim \pm$15 rad to $\pm$120 rad horizontal and $\pm$100 rad vertical.

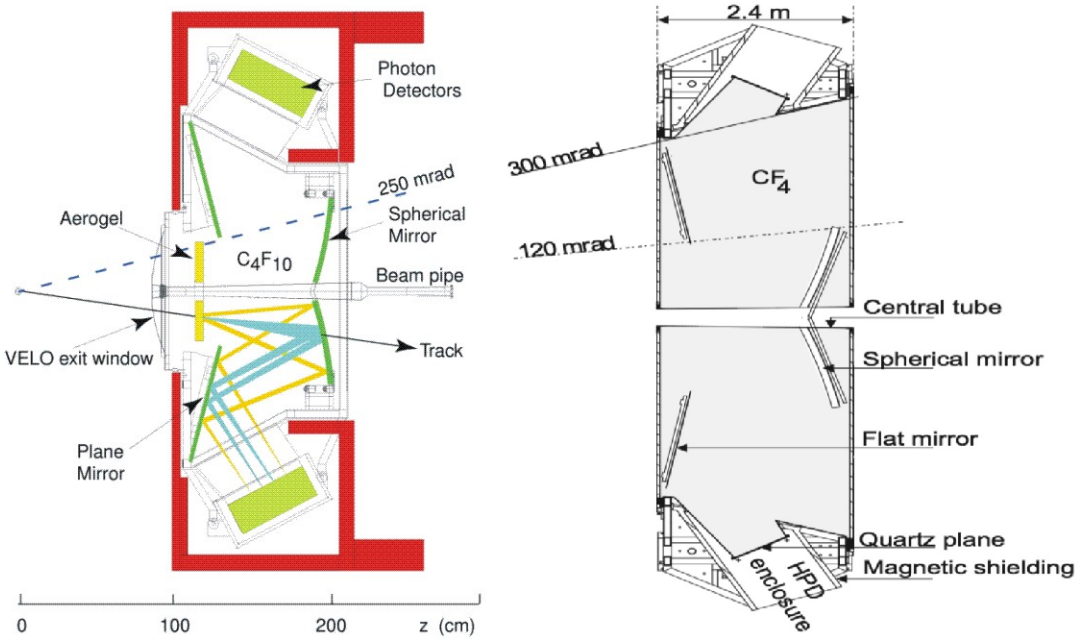

Figure 4.8: Schematic view of RICH1 (left) and RICH2 (right) detectors. Figures taken from Ref. [74].

Both detectors use spherical and flat mirrors to focus the Cherenkov light. The optical layout is vertical for RICH1 and horizontal for RICH2. Cherenkov photons in the wavelength range 200-600 nm are detected by Hybrid Photon Detectors (HPDs), which are outside the LHCb acceptance. These are surrounded by external iron shields that shield them from the marginal field of the LHCb dipole.

4.2.4.2 Calorimeters

The transverse energy of hadrons, electrons and photons is measured, selected in the calorimeter and passed to the L0 trigger (see Section 4.2.5). The energy and position is also measured, while avoiding the pass of those particles to the muon system. The proper identification of hadrons, electrons and photons is also of great importance for correctly identifying the flavour of the original meson in the decay (*flavour tagging*). This is done

taking into account that these particles deposit the energy in the different parts of the calorimeter in a different manner.

It consists of two separate parts: an electromagnetic calorimeter (ECAL) followed by a hadron calorimeter (HCAL), to identify electromagnetic and hadronic showers, respectively. A preshower detector (PS) is located before the ECAL, in order to eliminate a large background of charged pions that could be misidentified as elecrons. In front of the PS, a scintillator pad detector (SPD), used to select charged particles, is located. For all these parts a variable lateral segmentation is adopted, given that the hit density varies by two orders of magnitude over the calorimeter surface [74]. Because of the dimensions of the hadronic showers, the HCAL is segmented into two zones with larger cell sizes.

In all cases, the same principle of scintillation light transmitted to a Photo-Multiplier (PMT) (that turns the light into an electric signal) by wavelength-shifting (WLS) fibres is adopted. To have a constant transverse energy scale the gain in the ECAL and HCAL phototubes is set in proportion to their distance to the beampipe.

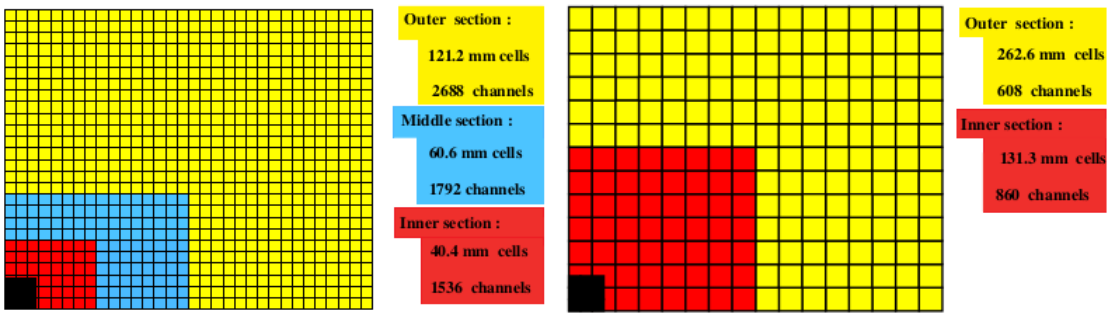

Figure 4.9: Lateral segmentation of the SPD/PS and ECAL (left) and the HCAL (right). One quarter of the detector front face is shown. Figures taken from Ref. [74].

4.2.4.3 Muon System

The muon system provides fast information for the high-p_T muon trigger at the earliest level (L0) and muon identification for the high-level trigger (HLT) and offline analysis [74]. Given that muons are present in final states of the most relevant channels for LHCb, this is of crucial importance.

It is composed of five rectangular stations (M1-M5), located along the beam axis, with a total of 1380 chambers and 435m^2 of coverage (see Figure 4.10). The inner and outer angular acceptances are 20(16) mrad and 306(258) mrad in the bending (non-bending) plane respectively [74]. All the stations are divided into 4 regions, R1-R4, with increasing distance from the beam axis. Their dimensions (scaling a factor two from one region to the next) and their geometry provide the same flux and channel ocupancy for all of them. Muti-wire proportional chambers (MWPC) are used for all regions except the inner region of station M1, where triple-GEM detectors (consisting of three gas electron multipliers) are used.

Stations M2 to M5 are placed downstream the calorimeters, interleaved with three iron filters. They have a threshold of $\sim$ 6 GeV/c for a muon to cross the five stations. Stations M1-M3 are used to define the track direction and to calculate the p_T of the candidate muon, due to their high spatial resolution along the bending plane. Stations M4 and M5 are focused on identifying penetrating particles. Station M1 is located in front of the calorimeters.

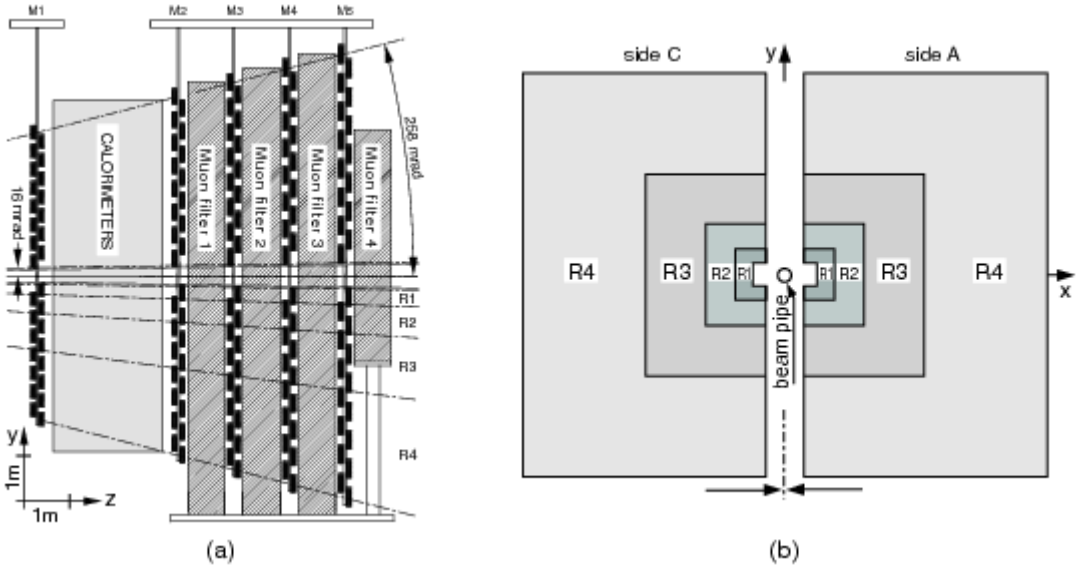

Figure 4.10: (a) Side view of the LHCb Muon Detector. (b) Station layout with the four regions R1-R4. Figures taken from Ref. [82].

4.2.4.4 PID performance

As explained in 4.2.4, particle identification at LHCb is performed in four different subdetectors. Each one of them gives a different performance that is then further combined into an overall PID performance.

For the calorimeters the main role is to distinguish photons, electrons and neutral pions. Electrons are differentiated from photons and π^0 by the fact that they have a track associated before the energetic deposit in the calorimeter, as they are charged particles. In order to separate photons from π^0, a neural network classifier is used, trained with samples as pure as possible. Non-converted photons are identified using a photon hypothesis likelihood, employing variables from the different subdetectors (PS and ECAL).

Both for photons and for electrons, the PID performance is assessed using the log-likelihood difference between the signal hypothesis (photon or electron) versus the background one (hadrons for electrons). Their associated likelihood is estimated using information from the ECAL, the PS and the HCAL. In the case of the electrons, this

log-likelihood is computed as the sum of log likelihoods:

$$\Delta \log \mathcal{L}^{\mathrm{CALO}}(e-h) = \Delta \log \mathcal{L}^{\mathrm{ECAL}}(e-h) + \Delta \log \mathcal{L}^{\mathrm{HCAL}}(e-h) + \Delta \log \mathcal{L}^{\mathrm{PS}}(e-h) \quad (4.1)$$

This is shown in Figure 4.11, for different cuts. As expected, the higher momenta particles have higher misidentification rates.

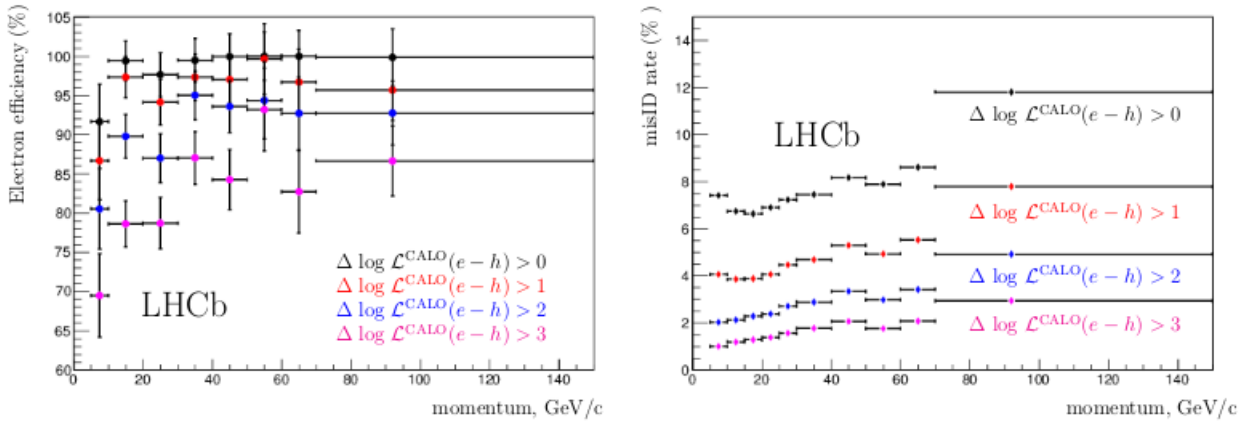

Figure 4.11: Electron identification performances for various $\Delta \log \mathcal{L}^{\mathrm{CALO}}(e-h)$ cut: electron efficiency (left) and misidentification rate (right) as functions of the track momentum. Figures taken from Ref. [75].

As for the RICH, its mission is to distinguish charged hadrons (π, K, p). The information thus obtained is used at the final analysis level and as part of the software level of the trigger. Complementary information on charged leptons can also be provided by the RICH. Its performance is evaluated using two variables:

- The Cherenkov angle resolution, $\theta(\sigma_C)$, defined as the resolution of the Cherenkov angle with which the emitted photons can be reconstructed.
- The photoelectron yield, defined as the average number of detected photons for each track traversing the Cherenkov radiator media.

Because of the high average track multiplicity in LHCb events, a reconstructed Cherenkov ring will generally overlap with several neighbouring rings. Figure 4.12 shows the Cherenkov angle as a function of particle momentum using information from the radiator for isolated tracks selected in data. Different bands represent different masses, hence different particles.

Figure 4.13 shows the kaon efficiency (kaons identified as kaons) and pion misidentification (pions misidentified as kaons) fraction achieved in LHCb data and simulation, as a function of momentum. The results are shown both optimising efficiency and minimising misidentification rate.

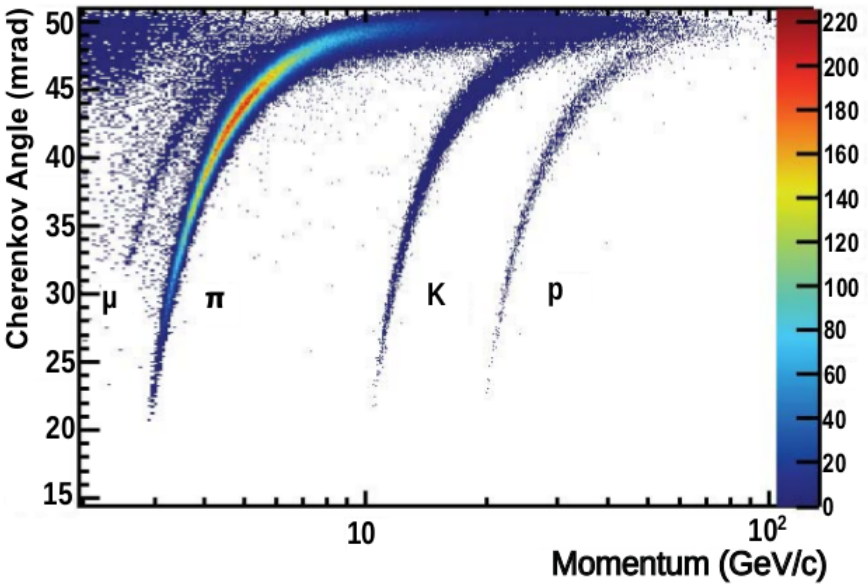

Figure 4.12: Reconstructed Cherenkov angle for *isolated* tracks, as a function of track momentum in the radiator. The Cherenkov bands for muons, pions, kaons and protons are clearly visible. Figure taken from Ref. [75].

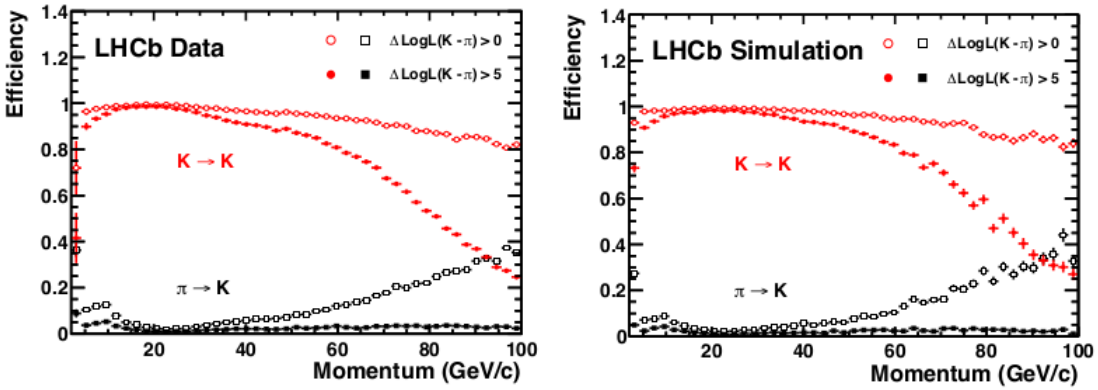

Figure 4.13: Kaon identification efficiency and pion misidentification rate as meaured using data (left) and from simulation (right) as a function of track momentum. Figures taken from Ref. [75].

Finally, muons are identified in the muon system. The algorithm is based on the association of hits around its extrapolated trajectory. In this case, the logarithm of the ratio between the muon and non-muon (protons, pions and kaons) hypothesis, $\Delta \log \mathcal{L}(\mu)$ is used as discriminating variable. Figure 4.14 shows, as a function of the track momentum and for different ranges of transverse momentum, the efficiency of the muon candidate selection, and the probabilities of incorrect identification of protons, pions and kaons as

muons.

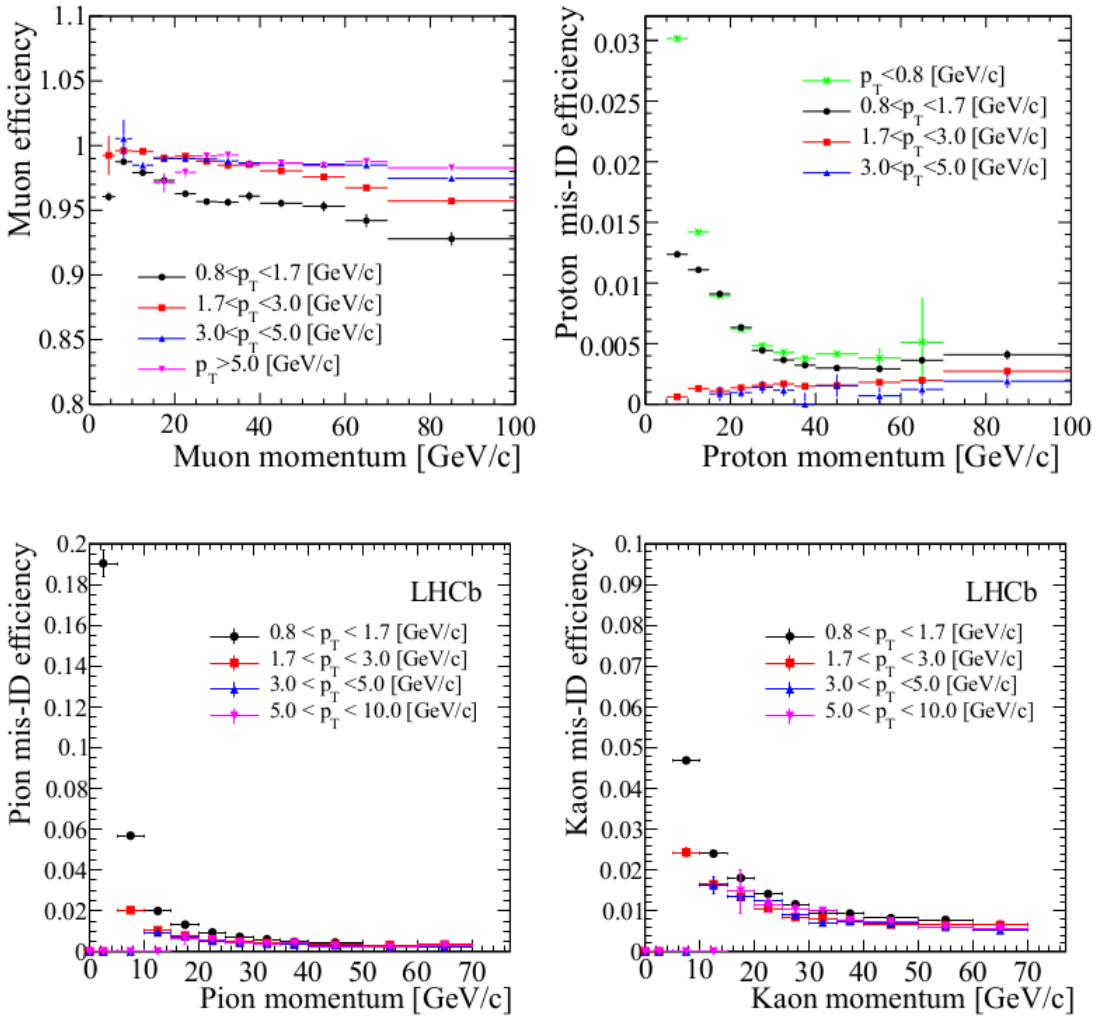

Figure 4.14: Top left: efficiency of the muon candidate selection based on the matching of hits in the muon system to track extrapolation, as a function of momentum for different p_T ranges. Other panels: misidentification probability of protons (top right), pions (bottom left), and kaons (bottom right) as muon candidate as a function of momentum, for different p_T ranges. Figures taken from Ref. [75].

The combined performance of the different PID subdetectors can be either be computed as a sum of the different likelihoods, or using multivariate techniques to get a single probability value for each particle hypothesis with different informations corresponding to each sub-system.

4.2.5 Trigger

The LHCb trigger is one of the most important parts of its infrastructure. It allows for a reduction of the crossing frequency with interactions visible by the spectrometer from 10MHz to about 2 - 5 kHz. At this rate the events are written to storage for further offline analysis [74]. It is composed of two levels: Level-0 (L0) and the High Level Trigger (HLT).

4.2.5.1 L0

The purpose of this first stage of the trigger is to obtain the highest efficiency for the events selected in the offline analysis, while avoiding storage of as many background events as possible. This is done reconstructing the highest E_T hadron, electron and photon clusters in the calorimeters, together with the the two highest p_T muons in the muon chambers, as B meson decay products are expected to have large p_T and E_T. A pile-up system in the VELO estimates the number of primary pp interactions in each bunch crossing. The calorimeters calculate the total observed energy and an estimate for the number of tracks, based on the number of hits in the SPD.

The L0 system is composed of three parts, all connected to a different part of the LHCb, and all connected to the L0 Decision Unit (DU) (see Figure 4.15):

1. The pile-up system: its purpose is to distinguish crossings with single and multiple visible interactions. For this, it uses four silicon sensors as the ones used in the VELO, that measure the radial position of the tracks. It consists of two silicon planes, situated upstream of the VELO and perpendicular to the beam-line, where the radii of track hits are measured. From this, the position of the track origin on the beam axis (the *vertex*) can be reconstructed.

2. The L0 calorimeter trigger: its goal is to look for high E_T electrons, photons, neutral pions or hadrons. This is done forming clusters by adding the transverse energy of 2x2 cells and selecting the cluster with the highest E_T. This zone is large enough to contain most of the energy, while avoiding overlap among different particles. Afterwards, such cluster is identified as one of the particle types using information from the SPD, PS, ECAL and HCAL subdetectors.

3. The L0 muon trigger: in the muon chambers muons are reconstructed with a p_T resolution of $\sim 20\%$. The L0 muon trigger selects the two muons with the highest p_T for each quadrant of the muon detector. The track finding is performed on the logical pads, searching for hits defining a straight line through the five muon stations and pointing towards the interaction point [74], also enabling the determination of the p_T of the track.

Multiplicities are measured by the SPD cells. A L0 Decision Unit (DU) collects all the information and derives the final L0 trigger decision for each bunch crossing to the Readout Supervisor, allowing for overlapping of several trigger conditions, as well as for prescaling.

The Readout Supervisor is in chrage of the ultimate decision about whether to accept an event or not.

The L0 uses custom made electronics, fully synchronous with the 40 MHz bunch crossing signal of the LHC. All L0 electronics uses fully custom-designed boards that use parallelism and pipelining in order to speed up the process. The time passed between a pp interaction and the arrival of the L0 trigger decision is of 4 μs. This time includes the time-of-flight of the particles, cable delays and all delays in the front-end electronics, leaving 2 μs for data processing in the L0 [74].

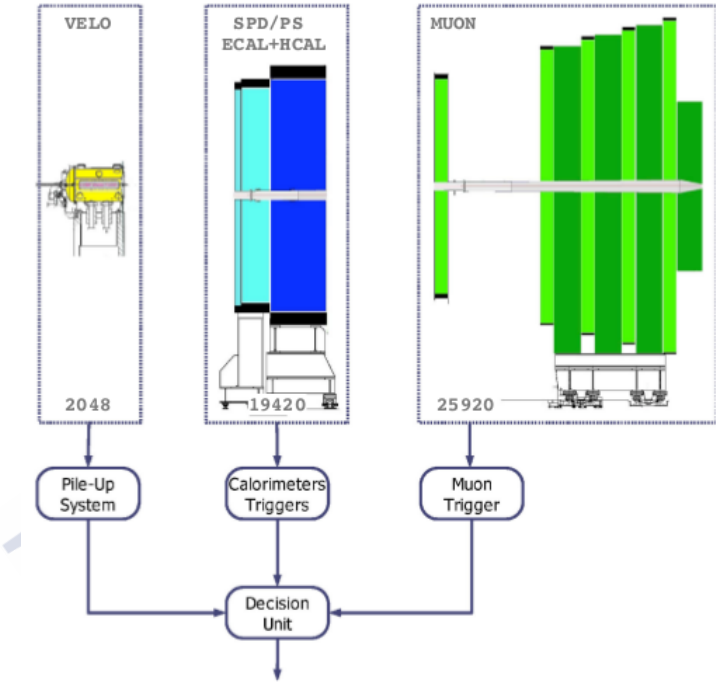

Figure 4.15: Overview of the L0. Figure taken from Ref. [74].

4.2.5.2 HLT

The High Level Trigger (HLT) reduces the event rate from 1 MHz down to 2 - 5 kHz, making use of the full event data. The HLT selected events are then saved on permanent storage. It is further subdivided into HLT1 and HLT2, each with different purposes.

It consists of a C++ application that runs on over 2000 computing nodes, the Event Filter Farm (EFF). Even though it can access all data in one event, the purpose is to discard uninteresting events using part of the full event data. In order to compute systematic uncertainties and trigger efficiencies, both levels can be fully emulated on stored data.

Both HLT1 and HLT2 summaries, containing the information of all tracks and vertexes that triggered events, are stored. This allows the study of the trigger performance, as well

as of the trigger source of each event. Furthermore, in order to ensure the traceability of the trigger conditions in the off-line analysis, the combination of trigger algorithms with their selection parameters are pre-loaded in the EFF before a fill in a Trigger Configuration Key (TCK).

4.2.5.3 HLT1

In the HLT1 step, the high-pT L0 candidate is confirmed, further adding information from other detectors [83], such as the tracking stations, the VELO or the muon segments [84]. The tracks must have a significant Impact Parameter with respect to all the primary vertices, or be matched to muon chamber hits by a fast muon identification algorithm that only runs over events triggered by a muon line in the previous step [75, 80]. As soon as a candidate is not confirmed in a sub-detector, the event is discarded [83].

4.2.5.4 HLT2

At this stage of the trigger, a set of tracks is selected with very broad cuts on their momentum and impact parameter, and used to form composite particles. These are then used for all selections to avoid duplication in the creation of final states. The selections can be exclusive or inclusive, depending on whether the full final state is reconstructed or not. The inclusive triggers are less dependent on the on-line reconstruction, while the exclusive one produces a smaller rate, thus allowing for a more relaxed set of cuts.

4.2.5.5 Trigger performance

As discussed in Section 4.2.5, the LHCb trigger is composed of two parts, in order to reduce the input rate to an output rate of 2 -5 kHz. The performance of each part is assessed using a data-driven technique with representative samples, to account for inefficiencies due to the simplified reconstruction algorithm, possible misalignments and reduced resolution.

In the trigger system, an event is considered to be *Trigger on Signal (TOS)* if the trigger objects that are associated with the signal candidate are sufficient to trigger the event. On the contrary, if the event has been triggered by trigger objects not associated with the signal, it is considered *Trigger Independet of Signal (TIS)*. Notice that events can be both TIS and TOS. The TIS and TOS efficiencies are defined as follows:

$$\epsilon^{\mathrm{TIS(TOS)}} = N^{\mathrm{TIS(TOS)}}/N^{\mathrm{SEL}} \tag{4.2}$$

where N^{SEL} represents the number of selected events.

4.2.5.6 L0 hardware trigger

The L0 trigger consists of three independent units:

- The L0-Calorimeter trigger, that uses information from the SPD, PS, ECAL and HCAL to compute E_T that particles deposit in clusters of 2x2 cells. From this, a candidate can be `L0Hadron`, `L0Photon` or `L0Electron`.

- The L0-Muon trigger, that looks for the two highest p_T muon tracks in each quadrant, with thresholds on the p_T^{largest} and $p_T^{\text{largest}} \times p_T^{\text{2ndlargest}}$.
- The L0-PileUp trigger, used for the computation of the luminosity.

Figure 4.16 shows the L0 hadron efficiency for the repreentative channels. As expected, it increases with the transverse momentum.

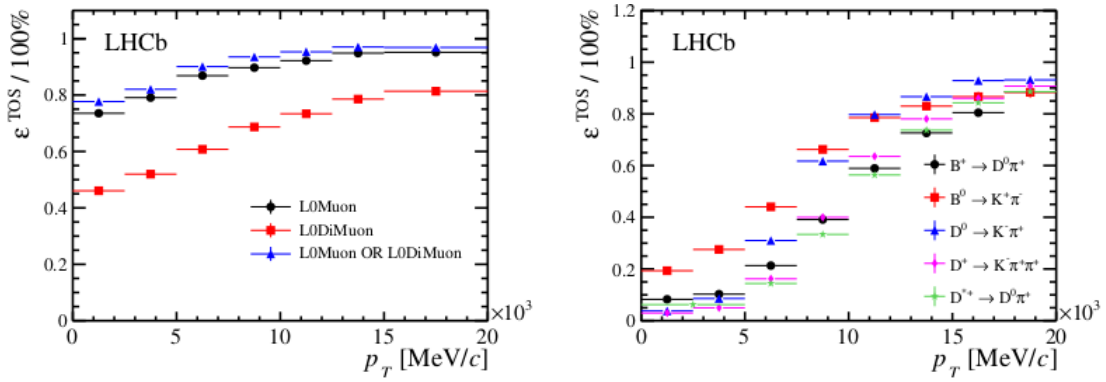

Figure 4.16: L0 muon trigger performance (left): TOS trigger efficiency for selected $B^+ \to J/\psi K^+$ candidates. (right) L0 hadron trigger performance (right): TOS trigger efficiency for different beauty and charm decay modes. Figures taken from Ref. [75].

4.2.5.7 High Level Trigger

The HLT has a variety of so-called trigger "lines" that consist of selection parameters for specific classes of events. In HLT1, a partial event reconstruction is performed, while in HLT2 the complete event is reconstructed.

In the first level (HLT1), vertices are reconstructed from a minimum of five intersecting VELO tracks. Vertices within a radius of 300 μm of the mean position of the pp-interaction envelope are considered to be primary vertices. During Run 1, the forward track search had a minimum momentum requirement that varied between 3 and 6 GeV/c. Dimuon candidates are either selected based on their mass without any displacement requirement, or based on their displacement without the mass restriction. The performance of HLT1 on muonic signatures as a function of p_T of the B^+ parent is shown in Figure 4.17.

In the second level (HLT2), long tracks are searched based on VELO seeds, thus simplifying the offline tracking algorithm (because of CPU restrictions). There is a generic beauty trigger, for any partially recontructed b-hadron decay, muon triggers, for decays with one or two muons, charm triggers and other exclusive and technical lines. Figure 4.18 shows the peformance of the J/ψ triggers.

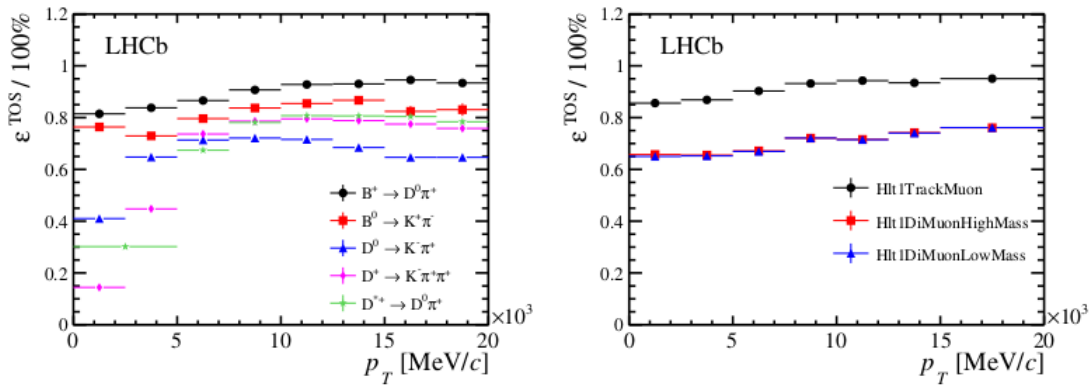

Figure 4.17: HLT1 inclusive track trigger performance: TOS efficiency for various channels as a function of B or D p_T (left). HLT1 muon trigger performance: TOS efficiency for $B^+ \to J/\psi K^+$. Figures taken from Ref. [75].

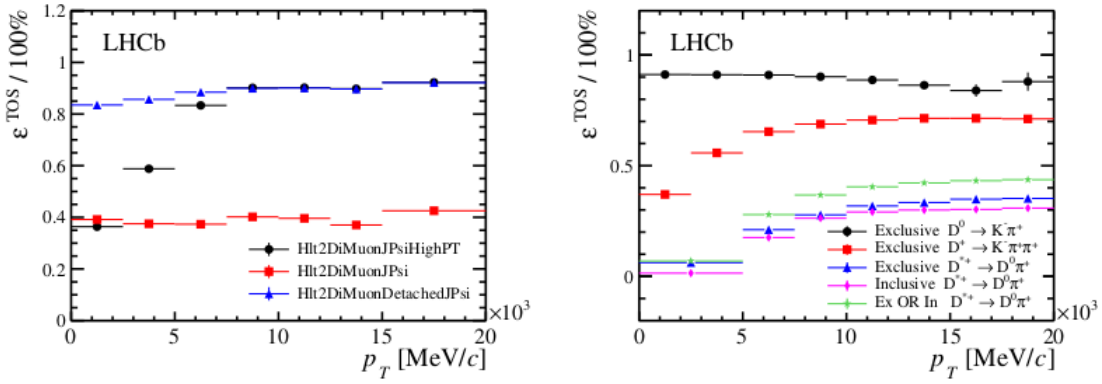

Figure 4.18: HLT2 muon trigger performance for the J/ψ trigger lines (left). HLT2 charm trigger performance for inclusive and exclusive selections (right). Figures taken from Ref. [75].

4.2.6 Tracking and Vertexing performance

In the track reconstruction software the hits in the VELO, the TT, the IT and the OT detectors are combined to form particle trajectories from the VELO to the calorimeters, with the purpose of finding all tracks in the event which leave sufficient detector hits. Depending on the subdetectors used for the reconstruction, offline tracks are classified in the following categories (see Figure 4.19):

- **Long tracks**: those that traverse the VELO, the TT and the T-stations, hence having the most precise momentum determination.
- **Upstream tracks**: those traversing only the VELO and TT stations. Generally, they have lower momentum and are bent out of the detector acceptance by the

magnetic field. Nevertheless, they pass through the RICH1 detector. Hence, they may generate Cherenkov photons, and can be used to understand backgrounds. Besides, they can also be used for flavour tagging, albeit their momentum resolution is poor.

- **Downstream tracks**: travering only the TT and T stations. The most relevant cases are the decay products of K_S^0 and Λ that decay outside of the VELO acceptance.
- **VELO tracks**: measured in the VELO only and typically with large angle, or backward tracks. They are useful for the primary vertex reconstruction.
- **T tracks**: the ones measured in the T stations, typically produced in secondary interactions, but useful for the global pattern recognition in RICH2.

For K_S^0 reconstruction, only long tracks and downstream tracks are used.

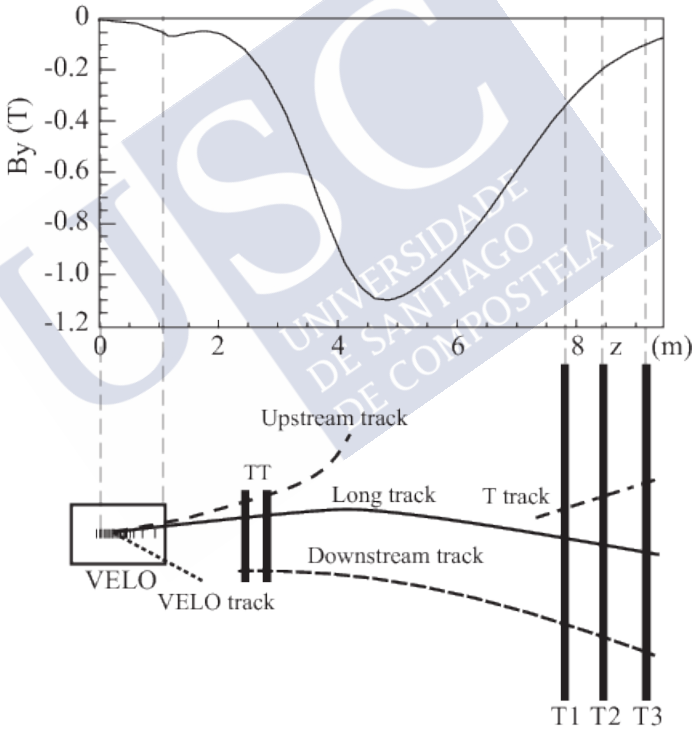

Figure 4.19: Schematic illustration of the various track types. For reference the main B-field component (B_y) is plotted above as a function of the z coordinate. Figure taken from Ref. [75].

For the track reconstruction algorithm, track *seeds* are used as starting points. These are the initial track candidates in the VELO and T stations, where the magnetic field is low. Their trajectories are refitted using the Kalman filter [85], that accounts for multiple

scattering and energy loss. The quality of such fitting is monitored using the χ^2 of the fit and the *pull* distribution for the different parameters.

The pattern recognition performance is evaluated in terms of efficiencies and ghost rates. The efficiencies are the ratio of successfully reconstructed tracks over the total amount of reconstructible tracks. A track is considered recontructible if it has a minimum number of hits in the relevant subdetector, and *successfully reconstructed* if at least 70% of such hits originate from a single MonteCarlo (simulated) particle. Otherwise, it is considered a *ghost track*.

Figure 4.20 shows this efficiency as a function of two kinematic variables, namely the momentum, p, and the pseudorapidity, η, for 2011 and 2012. The performance in the 2012 data is slightly worse, which is partially due to the higher hit multiplicity at the higher centre-of-mass energy [75]. The average efficiency is above 96% for $p < 200$ GeV/c, $2 < \eta < 5$, thus covering the full LHCb spacial angle.

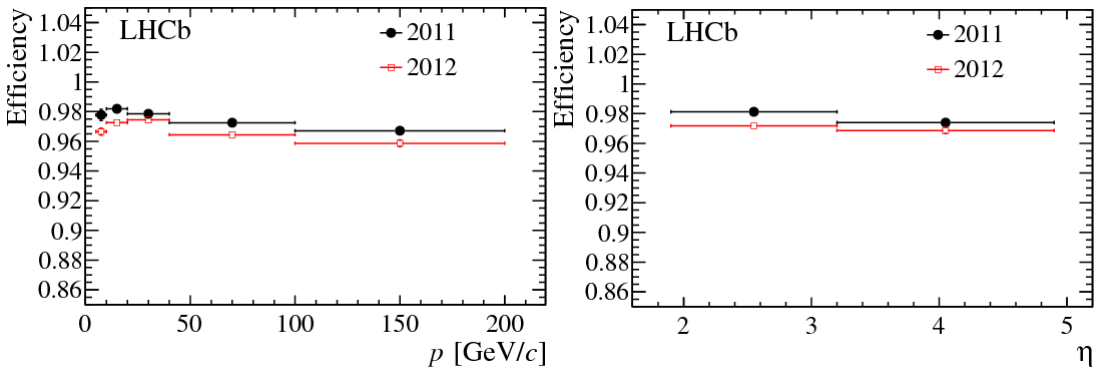

Figure 4.20: Tracking efficiency on muons from J/ψ as a function of momentum (left) and pseudorapidity (right). Black points correspond to 2011 data and red 2012 data. Figures taken from Ref. [75].

Regarding the relative momentum resolution, as it is shown in Figure 4.21 for two muons coming from a J/ψ, it is better (about 5 per mille) for low-momentum than for high-momentum (about 8 per mille) ranges. Hence, the best performances in terms of momentum resolution are achieved for long tracks, as said before.

In order to assess the vertexing performance at LHCb, two main quantities are examined: the PV resolution, and the track impact parameter. The PV resolution is measured by comparing two independent measurements of the vertex position in the same event. This is achieved by randomly splitting the set of tracks in an event into two and reconstructing the PVs in both sets.

The impact parameter (IP) of a track is defined as its distance from the primary vertex at its point of closest approach to the primary vertex. Particles resulting from the decay of long lived B or D mesons tend to have larger IP than those of particles produced at the primary vertex. Selections on IP and the IP χ^2 are extensively used in LHCb analyses to reduce the contamination from prompt backgrounds. Consequently, an optimal IP

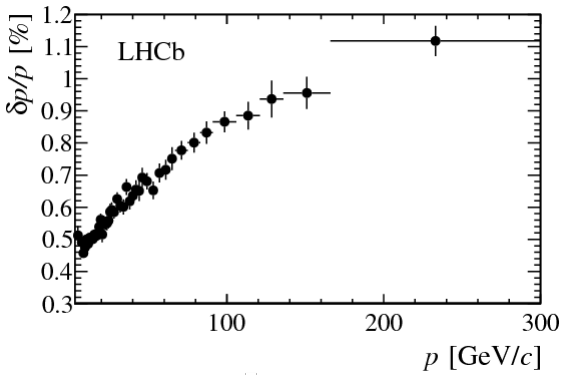

Figure 4.21: Relative momentum resolution versus momentum for long tracks in data obtained using J/ψ decays. Figure taken from Ref. [75].

resolution and a good understanding of the effects contributing to the IP resolution are of prime importance to LHCb performance [75].

The IP resolution is governed by three main factors: multiple scattering of particles by the detector material; the resolution on the position of hits in the detector from which tracks are reconstructed; and the distance of extrapolation of a track between its first hit in the detector and the interaction point. The minimisation of these factors is achieved in the design of the VELO [75].

The left part of Figure 4.22 shows the PV resolution in the x and y direction as a function of the number of tracks. It can be seen that in both cases it improves with the number of tracks. The right part shows the IP resolution in the x direction as a function of the inverse of the transverse momentum. Very good resolution is achieved in the VELO, thanks to the silicon strips.

4.2.7 The LHCb Upgrade

The LHCb detector has proven to be an outstanding general-purpose detector in the forward pseudorapidity region. Nevertheless, some of the measurements are still statistically limited. Therefore, in order to fully exploit the potential of LHCb, an increase in the luminosity is required. This leads to the need of upgrading some of the subdetectors, since the upgraded detector is expected to collect 50 fb^{-1} during 5 years of data-taking, with a 40 MHz readout (Phase-I of the Upgrade).

The changes made during the LHCb Upgrade will greatly benefit the sensitivity to rare strange decays, as the trigger limitation will disappear. Also, a significant improvement in the ϕ_s measurement is expected. Prospects for the flagship measurements on these fields can be seen in Table 4.1 [86].

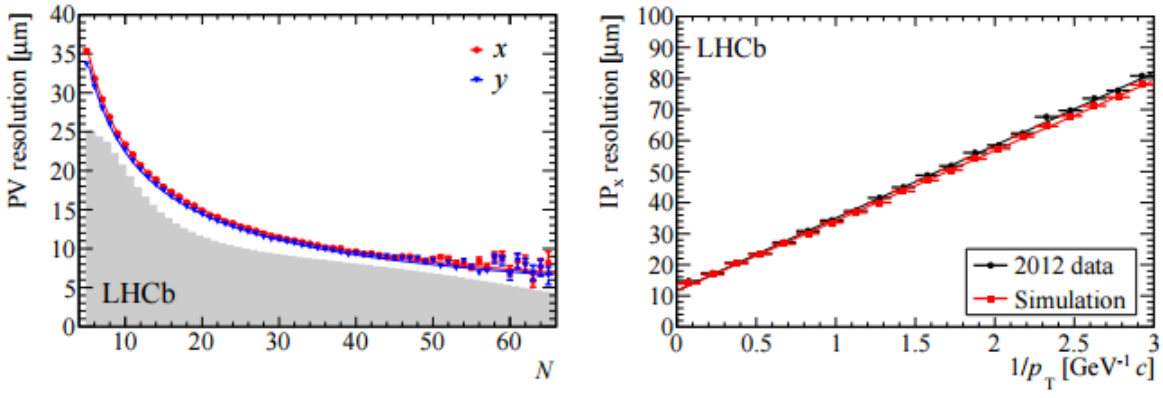

Figure 4.22: The primary vertex resolution (left), for events with one reconstructed primary vertex, as a function of track multiplicity. The x (red) and y (blue) resolutions are separately shown and the superimposed histogram shows the distribution of number of tracks per reconstructed primary vertex for all events that pass the high level trigger. The impact parameter in x resolution as a function of $1/p_T$ (right). Both plots are made using data collected in 2012. Figures taken from Ref. [75].

4.2.7.1 Trigger Upgrade

The main change that the LHCb trigger will undergo is the replacement of the L0 stage by a software one, the so-called *Low Level Trigger* (LLT), modified to run within the new readout architecture. It selects events containing clusters with high transverse energy in the calorimeters or tracks with high transverse momentum in the muon detector. A much larger LLT rate will be alowed, leading to a much larger rate to storage. Hence, the main limits will be processing power and bandwith. The front-end electronics will be upgraded as well to allow reading events at the LHC clock rate. More details can be found in [104].

4.2.7.2 VELO Upgrade

The LHCb upgrade requires the VELO to have an excellent vertex resolution and two track separation, with fast pattern recognition capabilities. Moreover, because of the high luminosity, it has to have a sufficient radiation hardness to guarantee the performance throughout all the data-taking period. Besides, the upgraded trigger discussed before strongly relies on this subdetector.

In order to cope with these requirements, two alternatives were proposed:

- A fine-pitched silicon strip detector, similar to the current design, with improved cooling and a new ASIC.
- A hybrid pixel detector, called *VeloPix*, that uses the Timepix chip [105].

The second was chosen for the Upgrade. The layout of the upgraded VELO can be seen in Figure 4.23.

Table 4.1: Summary of prospects for future measurements of selected flavour observables for LHCb, Belle II and Phase-II LHCb. The projected LHCb sensitivities take no account of potential detector improvements, apart from in the trigger. The Belle-II sensitivities are taken from Ref. [87].

Observable	Current LHCb	LHCb 2025	Belle II	Upgrade II
R_K $(1 < q^2 < 6$ GeV$^/$c$^4)$	0.1 [88]	0.025	0.036	0.007
R_{K^*} $(1 < q^2 < 6$ GeV$^/$c$^4)$	0.1 [22]	0.031	0.032	0.008
R_ϕ, R_{pK}, R_π	-	0.08,0.06,0.18	-	0.02,0.02,0.05
γ, with $B_s^0 \to D_s^+ K^-$	$(^{+17}_{-22})^\circ$ [89]	4°	-	1°
γ, all modes	$(^{5.0}_{-5.8})^\circ$ [90]	1.5°	1.5°	0.35°
$\sin 2\beta$, with $B^0 \to J/\psi K_S^0$	0.04 [91]	0.011	0.005	0.003
ϕ_s, with $B_s^0 \to J/\psi\phi$	49 mrad [92]	14 mrad	-	4 mrad
ϕ_s with $B_s^0 \to D_s^+ D_s^-$	170 mrad [93]	35 mrad	-	9 mrad
$\phi_s^{s\bar{s}s}$, with $B_s^0 \to \phi\phi$	154 mrad [94]	39 mrad	-	11 mrad
a_{sl}^s	33×10^{-4}	10×10^{-4} [95]	-	3×10^{-4}
$\lvert V_{ub}/V_{cb}\rvert$	6% [96]	3%	1%	1%
$\mathcal{B}(B^0 \to \mu^+\mu^-)/\mathcal{B}(B_s^0 \to \mu^+\mu^-)$	90% [97]	34%	-	10%
$\tau_{B_s^0 \to \mu^+\mu^-}$	22% [97]	8%	-	2%
$S_{\mu\mu}$	-	-	-	0.2
$R(D^*)$	0.026 [98,99]	0.0072	0.005	0.002
$R(J/\psi)$	0.24 [100]	0.071	-	0.02
$\Delta A_{CP}(KK - \pi\pi)$	8.5×10^{-4} [101]	1.7×10^{-4}	5.4×10^{-4}	3.0×10^{-5}
$A_\Gamma (\approx x \sin\phi)$	2.8×10^{-4} [102]	4.3×10^{-4}	3.5×10^{-4}	1.0×10^{-5}
$x \sin\phi$ from $D^0 \to K^+\pi^-$	13×10^{-4} [103]	3.2×10^{-4}	4.6×10^{-4}	8.0×10^{-5}
$x \sin\phi$ from multibody decays	-	$(K3\pi)$ 4.0×10^{-5}	$(K_S^0\pi\pi) 1.2 \times 10^{-4}$	$(K3\pi) 8.0 \times 10^{-6}$

4.2.7.3 PID Upgrade

As discussed before, the PID performance is crucial for the LHCb physics programme. Thus, its upgrade is of great importance.

The overall structure of the RICH will remain unchanged. In RICH1, the aerogel will be removed, as the efficiency gained by its removal outweighs the improvement on the PID provided by it. The HPDs will be replaced by commercial multianode photomultipliers (MaPMTs), with external readout electronics. Alternatively a lens system may be used there, to re-focus the Cherenkov images onto the 1-inch tubes and thus reduce the number of tubes required. A new subdetector, still under development, is being considered in order to recover the low momentum particle identification performance. It consists in a time-of-flight system, Time Of internally Reflected Cherenkov Light, TORCH.

As for the calorimeter, the electronics will be upgraded according to the new requirements. Also the PMTs gains will be reduced (and compensated by a gain increase in the electronics) to ensure a longer lifetime. Regarding the radiation hardness, studies have

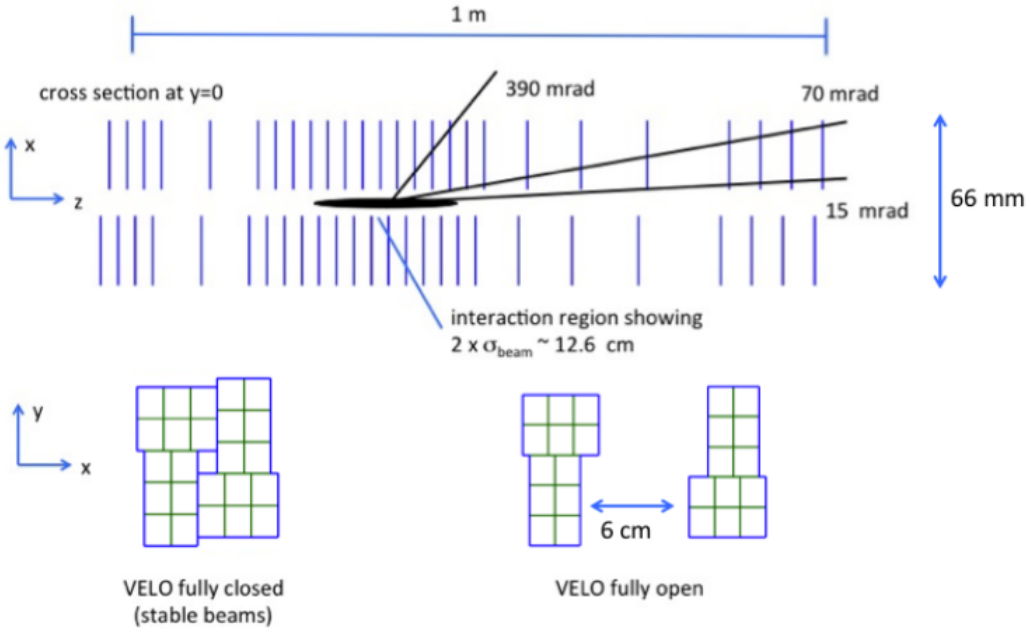

Figure 4.23: Schematic layout of the upgraded VELO. Figure taken from Ref. [106].

found the calorimeter resistent enough, even though some of the elements (such as the cells in the inner region of the ECAL) will need replacing in the long-term scale. Both the SOD and the PS will be removed, as they mainly contribute to the L0 trigger.

Finally, the muon system will have its first station removed, and additional shielding around the beam pipe in front of station M2. Similarly to the calorimeter, the electronics will be modified to comply with the new conditions.

4.2.7.4 Tracking Upgrade

The TT stations will be replaced by a tracking detector composed of new, high-granularity silicon micro-strip planes with an improved coverage of the LHCb acceptance, the *Upstream Tracker* (UT). Behind the magnet, a *Scintillating Fibre Tracker* (SFT) will be built, which is composed of 2.5 m long fibres read out by silicon photomultipliers at the edge of the acceptance, replacing the current OT and IT stations. Both new subdetectors are shown in Figure 4.24.

4.2.8 Analysis workflow

Raw data from collisions is taken at LHCb at a rate of several million events per second. A fast, efficient treatment and distribution of such data is thus needed to perform an offline analysis of a given decay channel. For this, C++ tools and algorithms embedded

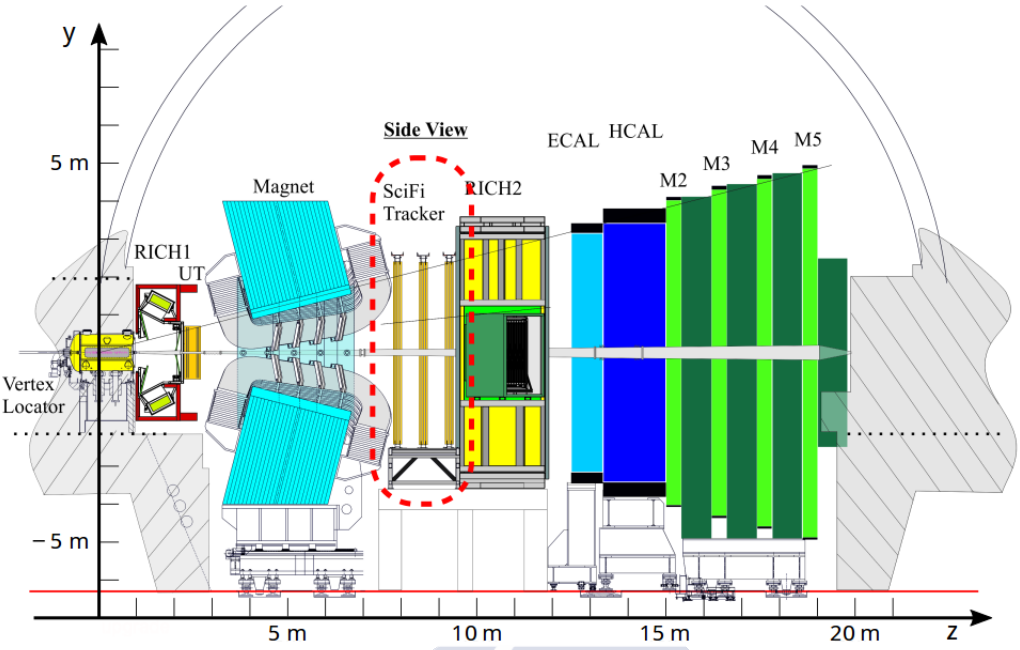

Figure 4.24: Side view of the upgraded LHCb. Figure taken from Ref. [107].

inside the Gaudi [108] project are used. The steps that are followed, together with their correspondance to the different projects inside such framework, are summarised below.

1. As explained in Sections 4.2.5, 4.2.5.5, a first loose selection is applied to the recorded data with the trigger. The trigger algorithms constitute what is known as the Moore project [109].

2. After data is recorded, it is necessary to convert the electronic signals to track and vertices. This was discussed in Sections 4.2.3 and 4.2.6. Particle identification (Sections 4.2.4, 4.2.4.4) is also required to properly assign each of these variables to a given type of particle. This whole process is called *reconstruction*, and the group of C ++ LHCb libraries which contain the relevant tools, Brunel [110]. Proper knowledge alignment of each subdetector is also of great importance at this stage, for which tools under the Alignment project [111] exist.

3. Once all triggered events have been reconstructed, a process is necessary to properly separate them offline according to their physics content. Such process, called *stripping*, consists on a splitting procedure that selects the different decays according to their specific features (final state, PV, mother particle, etc.). Each of the selection criteria are contained in a *stripping line*. The LHCb libraries that take part of this stage are DaVinci [112] and Erasmus [113].

4. In order to allow the access to the data, while keeping a backup of it, a distributed system, *Grid* [114] is used by LHCb. Both stripped events and raw data are stored,

so as to have the possibility of performing re-stripping and re-reconstruction if needed. Such system is of great computational power, and its spread in computing centers worlwide.

5. Finally, to properly understand the effects from the detector and the steps before on data, simulation is used. Another important reason for which simulation is crucial is the need of training analysis tool on well-known states. Simulated Monte Carlo events (MC) are employed for this, mimicking as much as possible the data. The C++ libraries at LHCb dedicated to the MC production are contained in Gauss [115], which is a collection of libraries for physics simulation based on Gaudi and with especialised algorithms and tools for generators (PYTHIA [116], EvtGen [117] ...) and detector simulation (Geant4 [118]). The MC events can be further classified as follows:

   - Minimum Bias: keep all events generated by PYTHIA: elastic, diffractive, inelastic.
   - Inclusive: extract events generated by PYTHIA with at least one b or c hadron in 400 mrad with respect to the LHCb z axis. If all of these hadrons have $p_z < 0$, flip the whole event.
   - Signal: extract events generated by PYTHIA containing at least one specific particle in 400 mrad. Again, if the candidate has $p_z < 0$, flip the whole event. In the case of b hadrons and to speed up the generation, if the interaction contains the b, repeat the hadronisation process of PYTHIA until the interaction contains the correct particle.

4.2.8.1 Turbo Stream

The Turbo Stream was introduced in 2015 and applied to several physics analysis. The Turbo candidates selected by HLT2 (see Section 4.2.5.4) are saved to disk and used directly for analysis. Therefore, no offline reconstruction using Brunel [110] is applied. The Turbo stream data is prepared for physics analysis using an application called Tesla [119, 120]. Events saved to such stream contain only the candidates that were reconstructed in the trigger [121]. In this way, it allows for increased output rates, that translate into higher average efficiencies and smaller selection biases [122].

Chapter 5

Kaon Physics

5.1 Introduction

Kaons play a major role in particle physics, both for Standard Model (SM) measurements and for New Physics (NP) searches. Rare kaon decays proceed mainly via flavour-changing neutral currents (FCNC), thus forbidden at tree level within the SM. This makes their branching fraction highly suppressed in the SM. Therefore, they constitute an excellent probe for New Physics manifesting in new particles entering the process.

Even though the LHCb experiment was initially designed for measurements of particles with a b or a c quark, studies of strange particles are also possible since they are produced in large numbers at the LHC. Indeed, LHCb has demonstrated very good performance in the search for rare leptonic K^0_S decays [123]. In the following sections, the potential sensitivity of LHCb to $\mathcal{B}(K^0_S \to \pi^0\mu^+\mu^-)$ considering the data to be collected with the LHCb detector before and after its upgrade starting in 2019 is evaluated, as well as supersymmetric contributions to the decay $K^0_S \to \mu^+\mu^-$ in light of current experimental data.

In section 5.2, the theoretical MSSM effects for $K^0_S \to \mu^+\mu^-$ are reviewed. In section 5.3 a sensitivity study of $K^0_S \to \pi^0\mu^+\mu^-$ is described.

5.2 Probing SUSY effects in $K^0_S \to \mu^+\mu^-$

Leptonic decays of pseudoscalar mesons with down-type quarks are known to be very sensitive to the Higgs sector of the Minimal Supersymmetric Standard Model (MSSM), due to, among others, enhancement factors proportional to $(\tan^6\beta/M_A^4)$.[1] This factor comes from the so-called non-holomorphic Yukawa terms at large $\tan\beta$ [124–129],[2] which are triggered by the supersymmetric (SUSY) μ term, and hence the non-SUSY two-Higgs-doublet model cannot produce this enhancement [128]. The best known example is $B^0_s \to \mu^+\mu^-$ [124–129, 133–141].

[1] Note that this enhancement factor is not present in the up-type quark case.

[2] The higher-order contributions have been derived up to two-loop level in refs. [130–132].

If Minimal Flavour Violation (MFV) is imposed, then $B_s^0 \to \mu^+\mu^-$ is the dominant constraint in $P \to \mu^+\mu^-$ decays. This is due to the stronger Yukawa coupling of the b–quark compared to the s–quark, and to the better experimental precision in $B_s^0 \to \mu^+\mu^-$ compared to $B_d^0 \to \mu^+\mu^-$. However, in the presence of new sources of flavour violation, the sensitivity of each mode depends on the flavour and CP structures of the corresponding terms.

Hence, a priori, $B_s^0 \to \mu^+\mu^-$, $B_d^0 \to \mu^+\mu^-$, $K_S^0 \to \mu^+\mu^-$, and $K_L^0 \to \mu^+\mu^-$ are all separate constraints that carry complementary information in the general MSSM. The observables related to these decay modes are typically branching fractions and CP asymmetries. Even though the muon polarization could carry interesting information, it cannot be observed by current experiments. Note that the decay $K_S^0 \to \mu^+\mu^-$ can also constrain other NP models, such as *leptoquarks* [142].

In this section, the MSSM effects in the $K_S^0 \to \mu^+\mu^-$ decay are explored. The Standard Model expectation for the branching fraction is $(5.18 \pm 1.50_{\rm LD} \pm 0.02_{\rm SD}) \times 10^{-12}$ [143–145], where the first uncertainty comes from the long-distance (LD) contribution and the second one comes from the short-distance (SD) contribution. The current experimental upper bound is 8×10^{-10} at 90% C.L., using 3 fb^{-1} of LHCb data [146]. The LHCb upgrade could reach sensitivities at the level of about 1×10^{-11} or even below, approaching the SM prediction [147]. The expected limit in $\mathcal{B}(K_S^0 \to \mu^+\mu^-)$ from LHCb and upgrades, as a function of integrated luminosity times trigger efficiency [148] is shown in Figure 5.1.

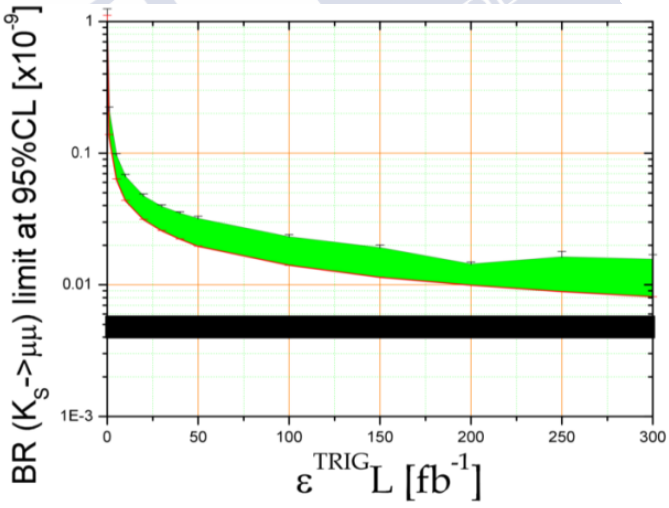

Figure 5.1: Expected limit in $\mathcal{B}(K_S^0 \to \mu^+\mu^-)$ from LHCb and upgrades, as a function of integrated luminosity times trigger efficiency [148].

The branching ratio $\mathcal{B}(K_S^0 \to \mu^+\mu^-)$ is predicted taking into account the relevant experimental constraints on the branching fractions $\mathcal{B}(K_L^0 \to \mu^+\mu^-)$, $\mathcal{B}(B^+ \to \tau^+\nu_\tau)$ and $\mathcal{B}(K^+ \to \mu^+\nu_\mu)$, the CP violation parameters $\varepsilon'_K/\varepsilon_K$ and ε_K, the K_L^0–K_S^0 mass difference, $\Delta M_K \equiv M_{K_L^0} - M_{K_S^0} > 0$, and the Wilson coefficient C_7 from $b \to s\gamma$.

For this, the Mass Insertion Approximation (hereafter MIA) method [149] is used,

treating the corresponding terms as phenomenological parameters at the SUSY scale. The details of the formalism are given in section 5.2.2. The SM and MSSM contributions to $\mathcal{B}(K_S^0 \to \mu^+\mu^-)$ are analyzed in section 5.2.1. The subsets of the MSSM parameter space are studied in scans performed on Graphics Processing Units (GPU), as detailed in section 5.2.3. The results are shown in section 5.2.4 and conclusions are drawn in section 5.2.5.

5.2.1 $\mathcal{B}(K_S^0 \to \mu^+\mu^-)$

The $|\Delta S| = 1$ effective Hamiltonian relevant for the $K^0 \to \ell\bar{\ell}$ transition at the Z boson mass scale is

$$\mathcal{H}_{\text{eff}} = -C_A Q_A - \tilde{C}_A \tilde{Q}_A - C_S Q_S - \tilde{C}_S \tilde{Q}_S - C_P Q_P - \tilde{C}_P \tilde{Q}_P + \text{h.c.}, \tag{5.1}$$

where C_A, C_S and C_P are the axial, scalar and pseudoscalar Wilson coefficients. The right-handed and left-handed axial ($\tilde{Q}_A$, Q_A), scalar (Q_S, $\tilde{Q}_S$) and pseudoscalar (Q_P, $\tilde{Q}_P$) operators are given by:

$$\begin{aligned} Q_A &= (\bar{s}\gamma^\mu P_L d)(\bar{\ell}\gamma_\mu\gamma_5\ell), \quad \tilde{Q}_A = (\bar{s}\gamma^\mu P_R d)(\bar{\ell}\gamma_\mu\gamma_5\ell), \\ Q_S &= m_s(\bar{s}P_R d)(\bar{\ell}\ell), \qquad \tilde{Q}_S = m_s(\bar{s}P_L d)(\bar{\ell}\ell), \\ Q_P &= m_s(\bar{s}P_R d)(\bar{\ell}\gamma_5\ell), \quad \tilde{Q}_P = m_s(\bar{s}P_L d)(\bar{\ell}\gamma_5\ell), \end{aligned} \tag{5.2}$$

where $P_{L,R}$ are the left and right-handed projection operators. For $\mathcal{B}(K^0_{S,L} \to \mu^+\mu^-)$ [3], there are two contributions from S-wave ($A_{S,L}$) and P-wave transitions ($B_{S,L}$), resulting in:

$$\mathcal{B}(K^0_{S,L} \to \mu^+\mu^-) = \tau_{S,L}\Gamma(K^0_{S,L} \to \mu^+\mu^-) = \tau_{S,L}\frac{f_K^2 M_K^3 \beta_\mu}{16\pi}\left(|A_{S,L}|^2 + \beta_\mu^2 |B_{S,L}|^2\right), \tag{5.3}$$

with

$$A_S = \frac{m_s M_K}{m_s + m_d}\text{Im}(C_P - \tilde{C}_P) + \frac{2m_\mu}{M_K}\text{Im}(C_A - \tilde{C}_A), \tag{5.4}$$

$$B_S = \frac{2G_F^2 M_W^2 m_\mu}{\pi^2 M_K} B^\mu_{S\gamma\gamma} - \frac{m_s M_K}{m_s + m_d}\text{Re}(C_S - \tilde{C}_S), \tag{5.5}$$

and

$$A_L = \frac{2G_F^2 M_W^2 m_\mu}{\pi^2 M_K} A^\mu_{L\gamma\gamma} - \frac{m_s M_K}{m_s + m_d}\text{Re}(C_P - \tilde{C}_P) - \frac{2m_\mu}{M_K}\text{Re}(C_A - \tilde{C}_A), \tag{5.6}$$

$$B_L = \frac{m_s M_K}{m_s + m_d}\text{Im}(C_S - \tilde{C}_S), \tag{5.7}$$

[3] The electron modes are suppressed by m_e^2/m_μ^2, and they are not considered in this work.

where

$$\beta_\mu = \sqrt{1 - \frac{4m_\mu^2}{M_K^2}}. \tag{5.8}$$

The long-distance contributions are [143–145, 150]:

$$\frac{2G_F^2 M_W^2 m_\mu}{\pi^2 M_K} B^\mu_{S\gamma\gamma} = (-2.65 + 1.14i) \times 10^{-11}\,(\text{GeV})^{-2}, \tag{5.9}$$

$$\frac{2G_F^2 M_W^2 m_\mu}{\pi^2 M_K} A^\mu_{L\gamma\gamma} = \pm(0.54 - 3.96i) \times 10^{-11}\,(\text{GeV})^{-2}, \tag{5.10}$$

with[4]

$$B^\mu_{S\gamma\gamma} = \frac{\pi\alpha_0}{G_F^2 M_W^2 f_K M_K |H(0)|} \mathcal{I}\left(\frac{m_\mu^2}{M_K^2}, \frac{m_{\pi^\pm}^2}{M_K^2}\right) \sqrt{\frac{2\pi}{M_K} \frac{\mathcal{B}(K_S^0 \to \gamma\gamma)^{\text{EXP}}}{\tau_S}}, \tag{5.11}$$

$$A^\mu_{L\gamma\gamma} = \frac{\pm 2\pi\alpha_0}{G_F^2 M_W^2 f_K M_K} \mathcal{A}\left(M_K^2\right) \sqrt{\frac{2\pi}{M_K} \frac{\mathcal{B}(K_L^0 \to \gamma\gamma)^{\text{EXP}}}{\tau_L}}, \tag{5.12}$$

where a two-loop function $\mathcal{I}(a, b)$ from the $2\pi^\pm 2\gamma$ intermediate state is given in refs. [143, 151], a pion one-loop contribution with two external on-shell photons is represented as $H(0) = 0.331 + i0.583$ [143], and a one-loop function $\mathcal{A}(s)$ from the 2γ intermediate state is given in refs. [152, 153]. A detailed computation of $\mathcal{B}(P \to l^+ l^-)$ is described in appendix A.

Here, $\alpha_0 = 1/137.04$, $f_K = (155.9 \pm 0.4)$ MeV [154], and $\tau_{S,L}$ are the $K^0_{S,L}$ lifetimes. Note that there is a theoretically and experimentally unknown sign in $A^\mu_{L\gamma\gamma}$, which is determined by higher chiral orders than $\mathcal{O}(p^4)$ contributions [155,156], and they provide two different constraints on $\mathcal{B}(K_L^0 \to \mu^+\mu^-)^{\text{EXP/SM}}$ in table 5.1. This sign can be determined by a precise measurement of the interference between $K_L^0 \to \mu^+\mu^-$ and $K_S^0 \to \mu^+\mu^-$ [145].

5.2.1.1 $\mathcal{B}(K_S^0 \to \mu^+\mu^-)$ in the MSSM

So as to determine the regions of the parameter space where each chirality dominates, pure left-handed and right-handed scenarios are studied. In the case in which new physics enters only in $\tilde{C}_S$ and $\tilde{C}_P = \tilde{C}_S$ (pure left-handed MSSM scenario), the following relations between the branching fractions of K_S^0 and K_L^0 decaying into $\mu^+\mu^-$ can be established:

$$\begin{aligned}\mathcal{B}\left(K_S^0 \to \mu^+\mu^-\right) \propto\ & \beta_\mu^2 \left|N_S^{\text{LD}}\right|^2 + \left(A_{S,\text{SM}}^{\text{SD}}\right)^2 - 2M_K \left[A_{S,\text{SM}}^{\text{SD}} \text{Im}(\tilde{C}_S) - \beta_\mu^2 \text{Re}\left(N_S^{\text{LD}}\right) \text{Re}(\tilde{C}_S)\right] \\ & + M_K^2 \left\{\left[\text{Im}(\tilde{C}_S)\right]^2 + \beta_\mu^2 \left[\text{Re}(\tilde{C}_S)\right]^2\right\}, \end{aligned} \tag{5.13}$$

$$\begin{aligned}\mathcal{B}\left(K_L^0 \to \mu^+\mu^-\right) \propto\ & \left|N_L^{\text{LD}}\right|^2 + \left(A_{L,\text{SM}}^{\text{SD}}\right)^2 - 2M_K \text{Re}(\tilde{C}_S) \left[A_{L,\text{SM}}^{\text{SD}} - \text{Re}\left(N_L^{\text{LD}}\right)\right] \\ & + M_K^2 \left\{\left[\text{Re}(\tilde{C}_S)\right]^2 + \beta_\mu^2 \left[\text{Im}(\tilde{C}_S)\right]^2\right\} - 2A_{L,\text{SM}}^{\text{SD}} \text{Re}\left(N_L^{\text{LD}}\right), \end{aligned} \tag{5.14}$$

[4] Note that $B^\mu_{S\gamma\gamma}$ is denoted by $A^\mu_{S\gamma\gamma}$ in refs. [145, 150].

with

$$A_{S,\mathrm{SM}}^{\mathrm{SD}} = \frac{2m_\mu}{M_K}\mathrm{Im}(C_{A,\mathrm{SM}}), \quad A_{L,\mathrm{SM}}^{\mathrm{SD}} = \frac{2m_\mu}{M_K}\mathrm{Re}(C_{A,\mathrm{SM}}), \tag{5.15}$$

and

$$N_S^{\mathrm{LD}} = \frac{2G_F^2 M_W^2 m_\mu}{\pi^2 M_K} B_{S\gamma\gamma}^\mu, \quad N_L^{\mathrm{LD}} = \frac{2G_F^2 M_W^2 m_\mu}{\pi^2 M_K} A_{L\gamma\gamma}^\mu, \tag{5.16}$$

where m_d terms are discarded for simplicity. Note that in the MSSM, the correlation between $\mathcal{B}(K_S^0 \to \mu^+\mu^-)$ and $\mathcal{B}(K_L^0 \to \mu^+\mu^-)$ depends on the unknown sign of $A_{L\gamma\gamma}^\mu$.

On the other hand, if new physics produces only C_S and $C_P = -C_S$ (pure right-handed MSSM), the two branching fractions are

$$\begin{aligned}\mathcal{B}\left(K_S^0 \to \mu^+\mu^-\right) \propto\ & \beta_\mu^2 \left|N_S^{\mathrm{LD}}\right|^2 + \left(A_{S,\mathrm{SM}}^{\mathrm{SD}}\right)^2 - 2M_K\left[A_{S,\mathrm{SM}}^{\mathrm{SD}}\mathrm{Im}(C_S) + \beta_\mu^2 \mathrm{Re}\left(N_S^{\mathrm{LD}}\right)\mathrm{Re}(C_S)\right] \\ & + M_K^2\left\{\left[\mathrm{Im}(C_S)\right]^2 + \beta_\mu^2\left[\mathrm{Re}(C_S)\right]^2\right\}, \end{aligned} \tag{5.17}$$

$$\begin{aligned}\mathcal{B}\left(K_L^0 \to \mu^+\mu^-\right) \propto\ & \left|N_L^{\mathrm{LD}}\right|^2 + \left(A_{L,\mathrm{SM}}^{\mathrm{SD}}\right)^2 - 2M_K\mathrm{Re}(C_S)\left[A_{L,\mathrm{SM}}^{\mathrm{SD}} - \mathrm{Re}\left(N_L^{\mathrm{LD}}\right)\right] \\ & + M_K^2\left\{\left[\mathrm{Re}(C_S)\right]^2 + \beta_\mu^2\left[\mathrm{Im}(C_S)\right]^2\right\} - 2A_{L,\mathrm{SM}}^{\mathrm{SD}}\mathrm{Re}\left(N_L^{\mathrm{LD}}\right). \end{aligned} \tag{5.18}$$

It is shown that $\mathcal{B}\left(K_L^0 \to \mu^+\mu^-\right)$ is the same as the pure left-handed one by a replacement of $C_S \to \tilde{C}_S$, while $\mathcal{B}\left(K_S^0 \to \mu^+\mu^-\right)$ is not; the final terms of the first line have opposite sign. Hence, the relations between the two branching fractions are different for left-handed and right-handed new physics scenarios.

For those cases, the experimental measurement of $\mathcal{B}(K_L^0 \to \mu^+\mu^-)$ [154],

$$\mathcal{B}(K_L^0 \to \mu^+\mu^-)^{\mathrm{EXP}} = (6.84 \pm 0.11) \times 10^{-9}, \tag{5.19}$$

imposes an upper bound on $\mathcal{B}(K_S^0 \to \mu^+\mu^-)$. This bound can be alleviated if $|C_S| \neq |C_P|$ or if new physics is present simultaneously in the left-handed and right-handed Wilson coefficients.

5.2.1.2 $\mathcal{B}(K_S^0 \to \mu^+\mu^-)_{\mathrm{eff}}$ and direct CP asymmetry

Experimentally, an *effective* branching ratio of $K_S^0 \to \mu^+\mu^-$ [145] can also be accessed. This includes an interference contribution with $K_L^0 \to \mu^+\mu^-$ in the neutral kaon sample,

$$\begin{aligned}\mathcal{B}(K_S^0 \to \mu^+\mu^-)_{\mathrm{eff}} = \tau_S \left(\int_{t_{\min}}^{t_{\max}} dt e^{-\Gamma_S t}\varepsilon(t)\right)^{-1} \Bigg[\int_{t_{\min}}^{t_{\max}} dt \Bigg\{ & \Gamma(K_S^0 \to \mu^+\mu^-)e^{-\Gamma_S t} \\ & + \frac{D f_K^2 M_K^3 \beta_\mu}{8\pi}\mathrm{Re}\left[i\left(A_S A_L - \beta_\mu^2 B_S^* B_L\right)e^{-i\Delta M_K t}\right] e^{-\frac{\Gamma_S+\Gamma_L}{2}t}\Bigg\}\varepsilon(t)\Bigg], \end{aligned} \tag{5.20}$$

where the dilution factor D is a measure of the initial ($t = 0$) K^0–$\overline{K}^0$ asymmetry,

$$D = \frac{K^0 - \overline{K}^0}{K^0 + \overline{K}^0}, \tag{5.21}$$

and $\varepsilon(t)$ is the decay-time acceptance of the detector. The second line of eq. (5.20) corresponds to an interference effect between K_L^0 and K_S^0, and for $D = 0$, $\mathcal{B}(K_S^0 \to \mu^+\mu^-)_{\text{eff}}$ corresponds to $\mathcal{B}(K_S^0 \to \mu^+\mu^-)$. The current experimental bound [146],

$$\mathcal{B}(K_S^0 \to \mu^+\mu^-)^{\text{EXP}} < 8 \times 10^{-10} \text{ [90\% C.L.]}, \tag{5.22}$$

uses untagged K^0 and $\bar{K}^0$ mesons produced in almost equal amounts, and hence $D = 0$ is assumed. A pure $K_L^0 \to \mu^+\mu^-$ background can be subtracted by a combination of simultaneous measurement of $K_S^0 \to \pi^+\pi^-$ events and knowledge of the observed value of $\mathcal{B}(K_L^0 \to \mu^+\mu^-)$ in eq. (5.19) [145]. The decay-time acceptance of the LHCb detector is parametrized by $\varepsilon(t) = \exp(-\beta t)$ with $\beta \simeq 86\,\text{ns}^{-1}$, and the range of the detector for selecting $K^0 \to \mu^+\mu^-$ is $t_{\text{min}} = 8.95\,\text{ps} = 0.1\tau_S$ and $t_{\text{max}} = 130\,\text{ps} = 1.45\tau_S$.

Given the potential measurement of an effective branching ratio by different dilution factors $D > 0$ and $D' < 0$ using K^- tagging and K^+ tagging [145], respectively, the direct CP asymmetry can be measured using the difference $\mathcal{B}(K_S^0 \to \mu^+\mu^-)_{\text{eff}}(D) - \mathcal{B}(K_S^0 \to \mu^+\mu^-)_{\text{eff}}(D')$, which is a theoretically clean quantity that emerges from a genuine direct CP violation. Here, the charged kaon is accompanied by the neutral kaon beam as, for instance, $pp \to K^0K^-X$ or $pp \to \overline{K}^0K^+X$. Note that a definition of D' is the same as D in eq. (5.21) but charged kaons of opposite sign are required in the event selection. Therefore, following direct CP asymmetry in $K_S^0 \to \mu^+\mu^-$ can be defined:

$$A_{CP}(K_S^0 \to \mu^+\mu^-)_{D,D'} = \frac{\mathcal{B}(K_S^0 \to \mu^+\mu^-)_{\text{eff}}(D) - \mathcal{B}(K_S^0 \to \mu^+\mu^-)_{\text{eff}}(D')}{\mathcal{B}(K_S^0 \to \mu^+\mu^-)_{\text{eff}}(D) + \mathcal{B}(K_S^0 \to \mu^+\mu^-)_{\text{eff}}(D')}. \tag{5.23}$$

The indirect CP-violating contributions, numerically negligible when compared to the CP-conserving and the direct CP-violating contributions [145], were discarded.

5.2.1.3 SM contributions

Within the SM, the Wilson coefficients are,

$$C_{A,\text{SM}} = -\frac{[\alpha_2(M_Z)]^2}{2M_W^2}\left(V_{ts}^* V_{td} Y_t + V_{cs}^* V_{cd} Y_c\right), \tag{5.24}$$

$$\tilde{C}_{A,\text{SM}} = C_{S,\text{SM}} = \tilde{C}_{S,\text{SM}} = C_{P,\text{SM}} = \tilde{C}_{P,\text{SM}} \simeq 0, \tag{5.25}$$

where $Y_t = 0.950 \pm 0.049$ and $Y_c = (2.95 \pm 0.46) \times 10^{-4}$ [157]. Using the CKM matrix tailored for probing the MSSM contributions, the SM prediction of A_{CP} is obtained,

$$A_{CP}(K_S^0 \to \mu^+\mu^-)_{D,D'}^{\text{SM}} = \begin{cases} -\frac{3.71(D-D')}{(10.53\pm3.01)-3.71(D+D')}, & (+) \\ \frac{3.98(D-D')}{(10.53\pm3.01)+3.98(D+D')}, & (-) \end{cases} \tag{5.26}$$

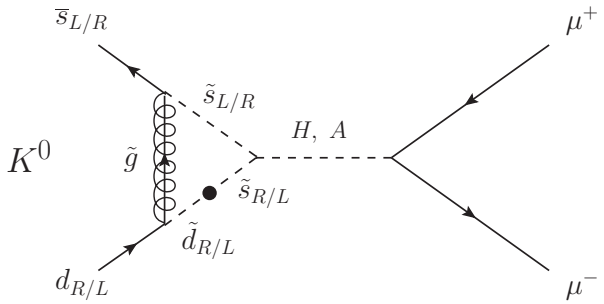

Figure 5.2: Feynman diagram of the leading (pseudo-)scalar MSSM contributions to $K_S^0 \to \mu^+\mu^-$ and $K_L^0 \to \mu^+\mu^-$, which include a gluino and a heavy Higgs boson. The black dot is the corresponding mass insertion term.

where (+) and (−) correspond to the unknown sign of $A^{\mu}_{L\gamma\gamma}$ in eq. (5.10). The uncertainty is totally dominated by $B^{\mu}_{S\gamma\gamma}$ [145] and it will be sharpened by the dispersive treatment of $K_S^0 \to \gamma^{(*)}\gamma^{(*)}$ [158].

In the case where $D' = -D$, achieved by the accompanying opposite-charged-kaon tagging, the SM prediction of A_{CP} is simplified:

$$A_{CP}(K_S^0 \to \mu^+\mu^-)^{\rm SM}_{D,-D} = \begin{cases} \left(-0.704^{+0.156}_{-0.281}\right) \times D, & (+) \\ \left(+0.756^{+0.302}_{-0.168}\right) \times D. & (-) \end{cases} \tag{5.27}$$

5.2.1.4 MSSM contributions

In the MSSM, the leading contribution to C_A, induced by terms of second order in the expansion of the squark mass matrix of the chargino Z-penguin, is [129, 159],

$$C_A = -\frac{(\alpha_2)^2}{16 M_W^2} \frac{[(\mathcal{M}_U^2)_{LR}]^*_{23}\,[(\mathcal{M}_U^2)_{LR}]_{13}}{M_2^4}\, l\left(x_2^Q, x_2^u\right), \tag{5.28}$$

$$\tilde{C}_A = 0, \tag{5.29}$$

where $x_2^Q = \tilde{m}_Q^2/M_2^2$ and $x_2^u = \tilde{m}_u^2/M_2^2$. The loop function $l(x,y)$ [159] is defined in appendix B.2.1. Here, contributions from the Wino-Higgsino mixing are omitted, since they are considered to be small. Setting $\tilde{m}_Q^2 = \tilde{m}_u^2$ gives the MIA result of refs. [160, 161].

The leading MSSM contributions to $C_{S(P)}$ and $\tilde{C}_{S(P)}$ in $K_S^0 \to \mu^+\mu^-$ and $K_L^0 \to \mu^+\mu^-$ are shown in Figure 5.2.

For C_S and $\tilde{C}_S$, it is obtained

$$\begin{aligned}
C_S =& -\frac{2}{3}\frac{\alpha_s\alpha_2 m_\mu}{M_W^2}\frac{\mu M_3}{M_A^2\tilde{m}_d^2}\left(\delta_d^{RR}\right)_{12}\frac{\tan^3\beta}{(1+\epsilon_g\tan\beta)^2(1+\epsilon_\ell\tan\beta)}G\left(x_d^3,x_d^Q\right)\\
&-\frac{2}{3}\frac{\alpha_s\alpha_2 m_\mu}{M_W^2}\frac{m_b}{m_s}\frac{\mu M_3\tilde{m}_Q^2}{M_A^2\tilde{m}_d^4}\left(\delta_d^{RR}\right)_{13}\left(\delta_d^{LL}\right)_{32}\\
&\quad\times\frac{\tan^3\beta}{(1+\epsilon_g\tan\beta)[1+(\epsilon_g+\epsilon_Y y_t^2)\tan\beta](1+\epsilon_\ell\tan\beta)}H\left(x_d^3,x_d^Q\right), \qquad (5.30)\\
\tilde{C}_S =& -\frac{2}{3}\frac{\alpha_s\alpha_2 m_\mu}{M_W^2}\frac{\mu M_3}{M_A^2\tilde{m}_Q^2}\left(\delta_d^{LL}\right)_{12}\frac{\tan^3\beta}{(1+\epsilon_g\tan\beta)^2(1+\epsilon_\ell\tan\beta)}G\left(x_Q^3,x_Q^d\right)\\
&-\frac{2}{3}\frac{\alpha_s\alpha_2 m_\mu}{M_W^2}\frac{m_b}{m_s}\frac{\mu M_3\tilde{m}_d^2}{M_A^2\tilde{m}_Q^4}\left(\delta_d^{LL}\right)_{13}\left(\delta_d^{RR}\right)_{32}\\
&\quad\times\frac{\tan^3\beta}{(1+\epsilon_g\tan\beta)[1+(\epsilon_g+\epsilon_Y y_t^2)\tan\beta](1+\epsilon_\ell\tan\beta)}H\left(x_Q^3,x_Q^d\right)\\
&+\frac{(\alpha_2)^2 m_\mu m_t^2}{8M_W^4}\frac{\mu A_t}{M_A^2\tilde{m}_Q^2}V_{ts}^*V_{td}\frac{\tan^3\beta[1+(\epsilon_g+\epsilon_Y y_t^2)\tan\beta]^2}{(1+\epsilon_g\tan\beta)^4(1+\epsilon_\ell\tan\beta)}F\left(x_Q^\mu,x_Q^u\right)\\
&+\frac{(\alpha_2)^2 m_\mu}{4M_W^2}\frac{\mu M_2}{M_A^2\tilde{m}_Q^2}\left(\delta_u^{LL}\right)_{12}\frac{\tan^3\beta}{(1+\epsilon_g\tan\beta)^2(1+\epsilon_\ell\tan\beta)}G\left(x_Q^2,x_Q^\mu\right), \qquad (5.31)
\end{aligned}$$

with

$$\epsilon_g = \frac{2\alpha_s}{3\pi}\frac{\mu M_3}{\tilde{m}_Q^2}F\left(x_Q^3,x_Q^d\right), \qquad (5.32)$$

$$\epsilon_Y = \frac{1}{16\pi}\frac{\mu A_t}{\tilde{m}_Q^2}F\left(x_Q^\mu,x_Q^u\right), \qquad (5.33)$$

$$\epsilon_\ell \simeq -\frac{3\alpha_2}{16\pi}, \qquad (5.34)$$

where $x_d^3 = M_3^2/\tilde{m}_d^2$, $x_d^Q = \tilde{m}_Q^2/\tilde{m}_d^2$, $x_Q^3 = M_3^2/\tilde{m}_Q^2$, $x_Q^d = \tilde{m}_d^2/\tilde{m}_Q^2$, $x_Q^\mu = \mu^2/\tilde{m}_Q^2$, $x_Q^u = \tilde{m}_u^2/\tilde{m}_Q^2$, $x_Q^2 = M_2^2/\tilde{m}_Q^2$, and $x_Q^\mu = \mu^2/\tilde{m}_Q^2$. The loop functions $F(x,y)$, $G(x,y)$, and $H(x,y)$ are defined in appendix B.2.1. These results are consistent with ref. [162] in the universal squark mass limit after changing the flavour and its chirality for B_s^0 decay. Here, the following approximation is used

$$\alpha \simeq \beta - \frac{\pi}{2}, \quad M_H \simeq M_A, \qquad (5.35)$$

where α is an angle of the orthogonal rotation matrix for the CP-even Higgs mass, and M_H (M_A) is a CP-even (odd) heavy Higgs mass. The contributions to C_P and $\tilde{C}_P$ are

$$C_P = -C_S, \quad \tilde{C}_P = \tilde{C}_S. \qquad (5.36)$$

Note that the Wilson coefficients in the MSSM are given at the $\mu^{\rm SUSY}$ scale, and there is no QCD correction from the renormalization-group (RG) evolution at the leading order.

5.2.2 Formalism

The followed notation is the one of refs. [162,163]. The right-handed down and up squarks are denoted as D and U, respectively. Because of the $\mathrm{SU}(2)_L$ doublet, the two left-handed squarks are nearly degenerate, and are denoted as Q. The average of the Q, D, and U-squark masses squared are denoted by $\tilde{m}_Q^2$, $\tilde{m}_d^2$, $\tilde{m}_u^2$, respectively.

5.2.2.1 Mass Insertion Approximation (MIA)

The off-diagonal terms of the squarks mass matrices can be parametrized in terms of the so-called Mass Insertions, MIs, provided these terms are small enough, similarly to what happens in perturbation theory. These MIs are defined as:

$$\tilde{m}_Q^2 \delta_d^{LL} + \mathrm{diag}(\tilde{\mathrm{m}}_{\mathrm{Q}}^2) = \left(\mathcal{M}_{\mathrm{D}}^2\right)_{\mathrm{LL}} \tag{5.37}$$

$$\tilde{m}_Q^2 \delta_u^{LL} + \mathrm{diag}(\tilde{\mathrm{m}}_{\mathrm{Q}}^2) = \left(\mathcal{M}_{\mathrm{U}}^2\right)_{\mathrm{LL}} \tag{5.38}$$

$$\tilde{m}_d^2 \delta_d^{RR} + \mathrm{diag}(\tilde{\mathrm{m}}_{\mathrm{d}}^2) = \left(\mathcal{M}_{\mathrm{D}}^2\right)_{\mathrm{RR}} \tag{5.39}$$

Hence:

$$\left(\delta_d^{LL}\right)_{ij} = \frac{\left[(\mathcal{M}_D^2)_{LL}\right]_{ij}}{\tilde{m}_Q^2} = \frac{(m_Q^2)_{ji}}{\tilde{m}_Q^2}, \tag{5.40}$$

$$\left(\delta_u^{LL}\right)_{ij} = \frac{\left[(\mathcal{M}_U^2)_{LL}\right]_{ij}}{\tilde{m}_Q^2} = \frac{(V m_Q^2 V^\dagger)_{ji}}{\tilde{m}_Q^2}, \tag{5.41}$$

$$\left(\delta_d^{RR}\right)_{ij} = \frac{\left[(\mathcal{M}_D^2)_{RR}\right]_{ij}}{\tilde{m}_d^2} = \frac{(m_D^2)_{ij}}{\tilde{m}_d^2}, \tag{5.42}$$

where $i \neq j$, V is the Cabibbo–Kobayashi–Maskawa (CKM) matrix and $\mathcal{M}_{D,U}^2$ are the 6×6 squark mass matrices. Note that the indices ij are inverted for LL. Comparison with the SUSY Les Houches Accord 2 convention [164] is given in the appendix of ref. [162].

5.2.2.2 Coupling constants

The running coupling constants α_1, α_2, and α_3 are defined as

$$\alpha_1 = \frac{g_1^2}{4\pi} = \frac{5}{3}\frac{g'^2}{4\pi}, \tag{5.43}$$

$$\alpha_2 = \frac{g_2^2}{4\pi} = \frac{g^2}{4\pi}, \tag{5.44}$$

$$\alpha_3 = \frac{g_3^2}{4\pi} = \frac{g_s^2}{4\pi}, \tag{5.45}$$

where g', g, and g_s are the $\mathrm{U}(1)_Y$, $\mathrm{SU}(2)_L$, and $\mathrm{SU}(3)_C$ group coupling constants, respectively. In the following, these couplings are evaluated at the μ^{SUSY} scale, defined as $\mu^{\mathrm{SUSY}} = \sqrt{\tilde{m}_Q M_3}$.

5.2.2.3 Observables

As will be shown in the next subsections, the main MSSM contribution to $\mathcal{B}(K_S^0 \to \mu^+\mu^-)$ is proportional to $\left[\left(\delta_d^{LL(RR)}\right)_{12} \mu \tan^3\beta M_3/M_A^2\right]^2$, where μ is the Higgs mixing parameter, M_3 is the gluino mass, $\tan\beta$ is the ratio of Higgs VEV and M_A is the heavy Higgs mass, considered to be almost degenerate with M_H in this scenario. In order to constrain those parameters, the following observables are calculated in addition to $\mathcal{B}(K_S^0 \to \mu^+\mu^-)$:

- Observables sensitive, among others, to the off-diagonal mass insertion terms $\left(\delta_d^{LL(RR)}\right)_{12}$:
  $\mathcal{B}(K_L^0 \to \mu^+\mu^-)$, $\varepsilon'_K/\varepsilon_K$, ε_K, and ΔM_K.[5]
- Observables sensitive to $\tan\beta$ and the heavy Higgs mass: $\mathcal{R}(B^+ \to \tau^+\nu_\tau)$, $\mathcal{R}(K^+ \to \mu^+\nu_\mu)$, ΔC_7.

The definitions of $\mathcal{R}(B^+ \to \tau^+\nu_\tau)$, $\mathcal{R}(K^+ \to \mu^+\nu_\mu)$, and C_7 are [162]:

$$\epsilon = \frac{2\alpha_s \mu M_{\tilde{g}} F(x_Q^3, x_Q^d)}{3\pi \tilde{m}_Q^2} \tag{5.46}$$

$$\epsilon_l = -3\frac{\alpha_2}{16\pi} \tag{5.47}$$

where

$$x_Q^3 = \frac{M_{\tilde{g}}^2}{\tilde{m}_Q^2},\ x_Q^d = \frac{\tilde{m}_d^2}{\tilde{m}_d^2} \tag{5.48}$$

$$\mathcal{R}(B^+ \to \tau^+\nu_\tau) = 1 - \frac{m_{B^+}^2 \tan\beta^2}{M_{H^+}^2(1+\epsilon\tan\beta)(1+\epsilon_l\tan\beta)} \tag{5.49}$$

$$\mathcal{R}(K^+ \to \mu^+\nu_\mu) = 1 - \frac{m_{K^+}^2 \tan\beta^2}{M_{H^+}^2(1+\epsilon\tan\beta)(1+\epsilon_l\tan\beta)} \tag{5.50}$$

$$\Delta C_7 = C_7^{\mathrm{NP}} - C_7^{\mathrm{SM}},\ C_7^{\mathrm{SM}} = -0.29 \tag{5.51}$$

$$C_7^{\mathrm{NP}} = C_7^{H^\pm} + C_7^{\chi^\pm} + C_7^{\tilde{g}} \tag{5.52}$$

$$C_7^{H^\pm} \simeq \left(\frac{1-\epsilon\tan\beta}{1+\epsilon\tan\beta}\frac{1}{2}h_7(y_t)\right),\ y_t = m_t^2/M_{H^\pm}^2 \tag{5.53}$$

$$\frac{4G_F}{\sqrt{2}}C_7^{\chi^\pm} \simeq \frac{g_2^2}{\tilde{m}^2}\left[\frac{(\delta_u^{LL})_{32}}{V_{tb}V_{ts}^*}\frac{\mu M_2}{\tilde{m}^2}f_7^{(1)}(x_2,x_\mu) + \frac{m_t^2}{M_W^2}\frac{A_t\mu}{\tilde{m}^2}f_7^{(2)}(x_\mu)\right]\frac{\tan\beta}{(1+\epsilon\tan\beta)}\ x_2 = \frac{|M_2|}{\tilde{m}^2},\ x_\mu = \frac{|\mu|}{\tilde{m}^2} \tag{5.54}$$

[5] The contributions to $\mathcal{B}(K \to \pi\nu\overline{\nu})$ are controlled by an additional free parameter, the slepton mass, and $\mathcal{O}(1)$ effects are possible in this scenario [165].

Table 5.1: Physics observables constraints imposed in this study. The two different constraints on $\mathcal{B}(K_L^0 \to \mu^+\mu^-)^{\rm EXP/SM}$ arise from an unknown sign of $A^{\mu}_{L\gamma\gamma}$ in eq. (5.10) (see refs. [145, 173]).

Observable	Constraint
$\mathcal{B}(K_S^0 \to \mu^+\mu^-)^{\rm EXP/SM}$	unconstrained
$\mathcal{B}(K_L^0 \to \mu^+\mu^-)^{\rm EXP/SM}$	1.00 ± 0.12 (+) [145, 154, 173] 0.84 ± 0.16 (−) [145, 154, 173]
$\Delta M_K^{\rm EXP/SM}$	1 ± 1
$\varepsilon_K^{\rm EXP/SM}$	1.05 ± 0.10 [154, 174, 175]
$\Delta(\varepsilon'_K/\varepsilon_K)^{\rm EXP-SM}$	$[15.5 \pm 2.3(\text{EXP}) \pm 5.07(\text{TH})] \times 10^{-4}$ [154, 176]
$\mathcal{B}(B^+ \to \tau^+\nu_\tau)^{\rm EXP/SM}$	0.91 ± 0.22 [154]
$\mathcal{B}(K^+ \to \mu^+\nu_\mu)^{\rm EXP/SM}$	1.0004 ± 0.0095 [154]
ΔC_7	-0.02 ± 0.02 [177]
$\tan\beta$:M_A plane	ATLAS limits for hMSSM scenario [178]
LSP	Lightest neutralino
B_G	$1 \pm 3(\text{TH})$ [160, 179]

$$\frac{4G_F}{\sqrt{2}} C_7^{\tilde{g}} \simeq \frac{g_s^2}{\tilde{m}^2}\left[\frac{M_{\tilde{g}}}{m_b}\frac{(\delta_d^{RL})_{32}}{V_{tb}V_{ts}^*} g_7^{(1)}(x_g) + \frac{M_{\tilde{g}}\mu}{\tilde{m}^2}\frac{\tan\beta}{(1+\epsilon\tan\beta)}\frac{(\delta_d^{LL})_{32}}{V_{tb}V_{ts}^*} g_7^{(2)}(x_g)\right],\ x_g = \frac{M_{\tilde{g}}^2}{\tilde{m}^2}. \tag{5.55}$$

The loop functions are defined in B.2.2, and the remaining observables are defined in the following subsections. The CKM matrix is fitted excluding measurements with potential sensitivity to MSSM contributions.

The constraints that are imposed on physics observables sensitive to the MSSM same parameters as $\mathcal{B}(K_S^0 \to \mu^+\mu^-)$ are listed in table 5.1, where the EXP/SM represents the measured value over the SM prediction with their uncertainties. Due to the poor theoretical knowledge of ΔM_K, it is assigned a 100% theoretical uncertainty; thus, the constraint imposed on this observable penalizes only $\mathcal{O}(1)$ effects. It is not counted as a degree of freedom in the χ^2 tests, so that the ΔM_K constraint can only make the bounds tighter, but never looser.

Remaining constraints can in principle be satisfied by adjusting the other parameters of the model. In particular, B physics constraints not included in the list can be satisfied by parameters unspecified in the scan (e.g. setting $\delta_{13} \approx \delta_{23} \approx 0$ and small A_t). The relation of eq. (5.41) may induce non-zero up-type MIs in the B sector and hence modify $B^0_{s(d)} \to \mu^+\mu^-$. These effects were checked and found to be negligible in the considered scenarios. The large SUSY masses in our scan are typically beyond the reach of LHC.

The lattice values for $(\varepsilon'_K/\varepsilon_K)^{\rm SM}$ used are from refs. [166–169], although the conclusions extracted from this study remain largely unchanged if the χ_{PT} value from refs. [170–172] is used instead. Both $\varepsilon_K^{\rm EXP/SM}$ and $\Delta(\varepsilon'_K/\varepsilon_K)^{\rm EXP-SM}$ are discussed in more detail in the following subsections.

5.2.2.4 $\varepsilon'_K/\varepsilon_K$

New physics models affecting $\varepsilon'_K/\varepsilon_K$ have recently attracted some attention, since lattice results from the RBC and UKQCD collaborations [166–169] have been reporting 2–3σ below [176, 180] the experimental world average of $\mathrm{Re}(\varepsilon'_K/\varepsilon_K)$ [154]. This is consistent with the recent calculations in the large-N_c analyses [181, 182]. Although the lattice simulation [169] includes final-state interactions partially along the line of ref. [183], final-state interactions have to be still fully included in the calculations in light of a discrepancy of a strong phase shift δ_0 [184–186]. Conversely, combining large-N_c methods with chiral loop corrections can bring the value of $\varepsilon'_K/\varepsilon_K$ in agreement with the experiment [170–172].

The hadronic matrix elements used in this work come from lattice simulations. For the χ^2 test, the following constraint is used,

$$\Delta\left(\frac{\varepsilon'_K}{\varepsilon_K}\right)^{\mathrm{EXP-SM}} \equiv \mathrm{Re}\left(\frac{\varepsilon'_K}{\varepsilon_K}\right)^{\mathrm{EXP}} - \left(\frac{\varepsilon'_K}{\varepsilon_K}\right)^{\mathrm{SM}} = [15.5 \pm 2.3(\mathrm{EXP}) \pm 5.07(\mathrm{TH})] \times 10^{-4}, \tag{5.56}$$

with

$$\left(\frac{\varepsilon'_K}{\varepsilon_K}\right)^{\mathrm{SM}} \to \left(\frac{\varepsilon'_K}{\varepsilon_K}\right)^{\mathrm{SM}} + \left(\frac{\varepsilon'_K}{\varepsilon_K}\right)^{\mathrm{SUSY}}, \tag{5.57}$$

where the SM prediction at the next-to-leading order in ref. [176] is used. The experimental value of ε_K is used in the calculation of the ratio.

Within the MSSM, the SUSY contributions to $\varepsilon'_K/\varepsilon_K$ are dominated by gluino box, chargino-mediated Z-penguin, and chromomagnetic dipole contributions. The first two contributions are represented by the same $|\Delta S| = 1$ four-quark effective Hamiltonian at the μ^{SUSY} scale, which is:

$$\mathcal{H}_{\mathrm{eff}} = \frac{G_F}{\sqrt{2}} \sum_q \sum_{i=1}^{4} \left[C_i^q Q_i^q + \tilde{C}_i^q \tilde{Q}_i^q \right] + \mathrm{h.c.}, \tag{5.58}$$

with

$$\begin{aligned}
Q_1^q &= (\bar{s}d)_{V-A}\,(\bar{q}q)_{V+A}\,, & \tilde{Q}_1^q &= (\bar{s}d)_{V+A}\,(\bar{q}q)_{V-A}\,,\\
Q_2^q &= (\bar{s}_\alpha d_\beta)_{V-A}\,(\bar{q}_\beta q_\alpha)_{V+A}\,, & \tilde{Q}_2^q &= (\bar{s}_\alpha d_\beta)_{V+A}\,(\bar{q}_\beta q_\alpha)_{V-A}\,,\\
Q_3^q &= (\bar{s}d)_{V-A}\,(\bar{q}q)_{V-A}\,, & \tilde{Q}_3^q &= (\bar{s}d)_{V+A}\,(\bar{q}q)_{V+A}\,,\\
Q_4^q &= (\bar{s}_\alpha d_\beta)_{V-A}\,(\bar{q}_\beta q_\alpha)_{V-A}\,, & \tilde{Q}_4^q &= (\bar{s}_\alpha d_\beta)_{V+A}\,(\bar{q}_\beta q_\alpha)_{V+A}\,,
\end{aligned} \tag{5.59}$$

where $(V \mp A)$ refers to $\gamma_\mu(1 \mp \gamma_5)$, and α and β are color indices.

The Wilson coefficients from the gluino box contributions are leading contributions when the mass difference between right-handed squarks exists [187, 188]. They are shown in appendix B.1.1 with their corresponding loop functions defined in appendix B.2.3.1. Here, $(\delta_d)_{13}(\delta_d)_{32}$ terms are discarded for simplicity.

The Wilson coefficients of the chargino-mediated Z-penguin are induced by terms of second order in the expansion of MIA. These ones are shown in appendix B.1.2, where the loop function $l(x,y)$ is given by eq. (B.15).

The matching conditions to the standard four-quark Wilson coefficients [176] are

$$\begin{aligned}
s_1 &= 0, & s_2 &= 0, \\
s_3 &= \tfrac{1}{3}\left(C_3^u + 2C_3^d\right), & s_4 &= \tfrac{1}{3}\left(C_4^u + 2C_4^d\right), \\
s_5 &= \tfrac{1}{3}\left(C_1^u + 2C_1^d\right), & s_6 &= \tfrac{1}{3}\left(C_2^u + 2C_2^d\right), \\
s_7 &= \tfrac{2}{3}\left(C_1^u - C_1^d\right), & s_8 &= \tfrac{2}{3}\left(C_2^u - C_2^d\right), \\
s_9 &= \tfrac{2}{3}\left(C_3^u - C_3^d\right), & s_{10} &= \tfrac{2}{3}\left(C_4^u - C_4^d\right).
\end{aligned} \tag{5.60}$$

The coefficients for the opposite-chirality operators, $\tilde{s}_{1,\ldots,10}$, are trivially found from the previous ones by replacing $C^q_{1,2,3,4} \to \tilde{C}^q_{1,2,3,4}$. Using the Wilson coefficients $\vec{s} = (s_1, s_2, \ldots, s_{10})^T$ and $\vec{\tilde{s}} = (\tilde{s}_1, \tilde{s}_2, \ldots, \tilde{s}_{10})^T$ at the $\mu^{\rm SUSY}$ scale, the dominant box and penguin contributions to $\varepsilon'_K/\varepsilon_K$ are given by [176]

$$\left.\frac{\varepsilon'_K}{\varepsilon_K}\right|_{\rm box+pen} = \frac{G_F \omega_+}{2|\varepsilon_K^{\rm EXP}|{\rm Re}A_0^{\rm EXP}} \langle \vec{Q}_{\varepsilon'}(\mu)^T\rangle \hat{U}(\mu, \mu^{\rm SUSY}) {\rm Im}\left[\vec{s} - \vec{\tilde{s}}\right], \tag{5.61}$$

with

$$\omega_+ = (4.53 \pm 0.02) \times 10^{-2}, \tag{5.62}$$

$$|\varepsilon_K^{\rm EXP}| = (2.228 \pm 0.011) \times 10^{-3}, \tag{5.63}$$

$${\rm Re}A_0^{\rm EXP} = (3.3201 \pm 0.0018) \times 10^{-7}\ {\rm GeV}. \tag{5.64}$$

The hadronic matrix elements at $\mu = 1.3$ GeV, including $I = 0$ and $I = 2$ parts, are [176]

$$\langle \vec{Q}_{\varepsilon'}(\mu)^T\rangle = \Big(0.345, 0.133, 0.034, -0.179, 0.152, 0.288, 2.653, 17.305, 0.526, 0.281\Big)\ ({\rm GeV})^3, \tag{5.65}$$

and the approximate function of the RG evolution matrix $\hat{U}(\mu, \mu^{\rm SUSY})$ is given in ref. [176].

Next, the $|\Delta S| = 1$ chromomagnetic-dipole operator that contributes to $\varepsilon'_K/\varepsilon_K$ is

$$\mathcal{H}_{\rm eff} = C_g^- Q_g^- + {\rm h.c.}, \tag{5.66}$$

with

$$Q_g^- = -\frac{g_s}{(4\pi)^2}\left(\bar{s}\sigma^{\mu\nu} T^A \gamma_5 d\right) G^A_{\mu\nu}. \tag{5.67}$$

The complete expression for the Wilson coefficient C_g^- at the $\mu^{\rm SUSY}$ scale is shown in appendix B.1.3, where $(\delta_d)_{13}(\delta_d)_{32}$ terms are discarded for simplicity. The corresponding loop functions $I(x,y)$, $J(x,y)$, $K(x,y)$, $L(x,y)$, $M_3(x)$, and $M_4(x)$ are defined in appendix B.2.3.2.

The chromomagnetic-dipole contribution to $\varepsilon'_K/\varepsilon_K$ is [160]

$$\left.\frac{\varepsilon'_K}{\varepsilon_K}\right|_{\rm chromo} = \frac{\omega_+}{|\varepsilon_K^{\rm EXP}|{\rm Re}A_0^{\rm EXP}}\left(1-\hat{\Omega}_{\rm eff}\right)\frac{11\sqrt{3}}{64\pi^2}\frac{M_\pi^2 M_K^2}{f_\pi(m_s+m_d)}\eta_s B_G {\rm Im}C_g^-, \tag{5.68}$$

where $f_\pi = (130.2 \pm 1.7)$ MeV [154], and [180, 189, 190]

$$\hat{\Omega}_{\rm eff} = 0.148 \pm 0.080, \tag{5.69}$$

$$\eta_s = \left[\frac{\alpha_s(m_b)}{\alpha_s(1.3\,{\rm GeV})}\right]^{\frac{2}{25}}\left[\frac{\alpha_s(m_t)}{\alpha_s(m_b)}\right]^{\frac{2}{23}}\left[\frac{\alpha_s(\mu^{\rm SUSY})}{\alpha_s(m_t)}\right]^{\frac{2}{21}}. \tag{5.70}$$

According to refs. [160, 179], the hadronic matrix element for the chromomagnetic-dipole operator into two pions, B_G, is enhanced by $1/N_c \cdot M_K^2/M_\pi^2$ from the large next-to-leading-order corrections that it receives. Therefore, the leading order in the chiral quark model, $B_G = 1$, is implausible. In the following analyses, it is considered $B_G = 1 \pm 3$.

The other contributions are negligible [187]. The sub-leading contributions which come from the gluino-mediated photon-penguin and the chargino-mediated Z-penguins induced by terms of first order in the expansion of the squark mass matrix, have opposite sign and practically cancel each other [187].

Finally, the SUSY contributions to $\varepsilon'_K/\varepsilon_K$ are given as

$$\left(\frac{\varepsilon'_K}{\varepsilon_K}\right)^{\rm SUSY} \simeq \left.\frac{\varepsilon'_K}{\varepsilon_K}\right|_{\rm box+pen} + \left.\frac{\varepsilon'_K}{\varepsilon_K}\right|_{\rm chromo}. \tag{5.71}$$

Note that the contributions to $\varepsilon'_K/\varepsilon_K$ from the heavy Higgs exchanges were discarded, although they give the strong isospin-violating contribution naturally: the contribution is enhanced by $\tan^3\beta$ for only down-type four-fermion scalar operators. These contributions must be proportional to $m_d m_s$ which cannot be compensated by $\tan^3\beta$, so that they should be the higher-order contributions for $\varepsilon'_K/\varepsilon_K$.

5.2.2.5 ε_K and ΔM_K

Although ε_K is one of the most sensitive quantities to new physics, the SM prediction is still controversial. Especially, the leading short-distance contribution to ε_K in the SM is proportional to $|V_{cb}|^4$ (cf., ref. [191]), whose measured values from inclusive semileptonic B decays ($\overline{B} \to X_c \ell^- \overline{\nu}$) and from exclusive decays ($\overline{B} \to D^{(*)}\ell^-\overline{\nu}$ and $\Lambda_b \to \Lambda_c \ell^- \overline{\nu}$) are inconsistent at a 4.1σ level [174,192]. A recent discussion about the exclusive $|V_{cb}|$ is given in refs. [193–195].

In this paper, for the SM prediction, it is used [175]

$$\varepsilon_K^{\rm SM} = (2.12 \pm 0.18) \times 10^{-3}, \tag{5.72}$$

with

$$\varepsilon_K = e^{i\varphi_\varepsilon}\varepsilon_K^{\rm SM}, \tag{5.73}$$

where $\varphi_\varepsilon = \arctan\left(2\Delta M_K/\Delta\Gamma_K\right) = (43.51 \pm 0.05)^\circ$ [154]. This value and the uncertainty are based on the inclusive $|V_{cb}|$ [174], the Wolfenstein parameters in the angle-only-fit method [196], and the long-distance contribution obtained by the lattice simulation [169]. Combining the measured value in eq. (5.63)

$$\varepsilon_K^{\rm EXP/SM} = 1.05 \pm 0.10({\rm TH}), \tag{5.74}$$

on the χ^2 test, with

$$\varepsilon_K^{\rm SM} \to \varepsilon_K^{\rm SM} + \varepsilon_K^{\rm SUSY}. \tag{5.75}$$

Note that it is also imposed that ${\rm Re}(\varepsilon_K) > 0$ from ${\rm Re}(\varepsilon_K) = (1.596 \pm 0.013) \times 10^{-3}$ [197].

Within the MSSM, the SUSY contributions to ε_K are dominated by gluino box diagrams. In this work, however, their suppressed region will be studied in detail. The crossed and uncrossed gluino-box diagrams give opposite-sign contributions and there is a certain cancellation region [187, 198], and/or simultaneous mixings of (δ_d^{LL}) and (δ_d^{RR}) can also produce the cancellation. Therefore, the sub-dominant contributions which come from Wino and Higgsino boxes are also considered. The $|\Delta S| = 2$ four-quark effective Hamiltonian at the $\mu^{\rm SUSY}$ scale is [199]

$$\mathcal{H}_{\rm eff} = \sum_{i=1}^{5} C_i Q_i + \sum_{i=1}^{3} \tilde{C}_i \tilde{Q}_i + {\rm h.c.}, \tag{5.76}$$

with

$$\begin{aligned}
&Q_1 = \left(\bar{d}\gamma_\mu P_L s\right)\left(\bar{d}\gamma^\mu P_L s\right), \quad Q_2 = \left(\bar{d}P_L s\right)\left(\bar{d}P_L s\right), \quad Q_3 = \left(\bar{d}_\alpha P_L s_\beta\right)\left(\bar{d}_\beta P_L s_\alpha\right), \\
&Q_4 = \left(\bar{d}P_L s\right)\left(\bar{d}P_R s\right), \qquad Q_5 = \left(\bar{d}_\alpha P_L s_\beta\right)\left(\bar{d}_\beta P_R s_\alpha\right), \\
&\tilde{Q}_1 = \left(\bar{d}\gamma_\mu P_R s\right)\left(\bar{d}\gamma^\mu P_R s\right), \quad \tilde{Q}_2 = \left(\bar{d}P_R s\right)\left(\bar{d}P_R s\right), \quad \tilde{Q}_3 = \left(\bar{d}_\alpha P_R s_\beta\right)\left(\bar{d}_\beta P_R s_\alpha\right).
\end{aligned} \tag{5.77}$$

The kaon mixing amplitude $M_{12}^{(K)}$, ΔM_K and ε_K are given by

$$M_{12}^{(K)} = \frac{\langle K^0|\mathcal{H}_{\rm eff}|\overline{K}^0\rangle}{2M_K}, \tag{5.78}$$

$$\Delta M_K = 2{\rm Re}[M_{12}^{(K)}], \tag{5.79}$$

$$\varepsilon_K = \kappa_\varepsilon \frac{e^{i\varphi_\varepsilon}}{\sqrt{2}} \frac{{\rm Im}[M_{12}^{(K)}]}{\Delta M_K^{\rm EXP}} = e^{i\varphi_\varepsilon}\varepsilon_K^{\rm SUSY}, \tag{5.80}$$

where $\kappa_\varepsilon = 0.94 \pm 0.02$ [200]. Using the latest lattice result [201], for the hadronic matrix elements

$$\langle K^0|\vec{Q}(\mu)|\overline{K}^0\rangle = \Big(0.00211, -0.04231, 0.01288, 0.09571, 0.02452\Big)\ ({\rm GeV})^4, \tag{5.81}$$

with $\langle K^0|\tilde{Q}_{1,2,3}(\mu)|\overline{K}^0\rangle = \langle K^0|Q_{1,2,3}(\mu)|\overline{K}^0\rangle$, where $\mu = 3$ GeV and using $m_s(\mu) = (81.64 \pm 1.17)$ MeV and $m_d(\mu) = (2.997 \pm 0.049)$ MeV [201].

The leading-order QCD RG corrections are given by [202]

$$C_1(\mu) = \eta_1^K C_1(\mu^{\text{SUSY}}), \tag{5.82}$$

$$\begin{pmatrix} C_2(\mu) \\ C_3(\mu) \end{pmatrix} = X_{23}\eta_{23}^K X_{23}^{-1} \begin{pmatrix} C_2(\mu^{\text{SUSY}}) \\ C_3(\mu^{\text{SUSY}}) \end{pmatrix}, \tag{5.83}$$

$$\begin{pmatrix} C_4(\mu) \\ C_5(\mu) \end{pmatrix} = \begin{pmatrix} (\eta_1^K)^{-4} & \frac{1}{3}\left[(\eta_1^K)^{-4} - (\eta_1^K)^{\frac{1}{2}}\right] \\ 0 & (\eta_1^K)^{\frac{1}{2}} \end{pmatrix} \begin{pmatrix} C_4(\mu^{\text{SUSY}}) \\ C_5(\mu^{\text{SUSY}}) \end{pmatrix}, \tag{5.84}$$

with

$$\eta_1^K = \left[\frac{\alpha_s(m_b)}{\alpha_s(\mu)}\right]^{\frac{6}{25}} \left[\frac{\alpha_s(m_t)}{\alpha_s(m_b)}\right]^{\frac{6}{23}} \left[\frac{\alpha_s(\mu^{\text{SUSY}})}{\alpha_s(m_t)}\right]^{\frac{6}{21}}, \tag{5.85}$$

$$\eta_{23}^K = \begin{pmatrix} (\eta_1^K)^{\frac{1}{6}\left(1-\sqrt{241}\right)} & 0 \\ 0 & (\eta_1^K)^{\frac{1}{6}\left(1+\sqrt{241}\right)} \end{pmatrix}, \tag{5.86}$$

$$X_{23} = \begin{pmatrix} \frac{1}{2}\left(-15-\sqrt{241}\right) & \frac{1}{2}\left(-15+\sqrt{241}\right) \\ 1 & 1 \end{pmatrix}. \tag{5.87}$$

The QCD corrections to $\tilde{C}_{1,2,3}$ are the same as $C_{1,2,3}$.

The Wilson coefficients from the $|\Delta S| = 2$ gluino boxes are shown in appendix B.1.4 with their corresponding loop functions defined in appendix B.2.4.1. In the universal squark mass limit, these results are consistent with ref. [162]. Here, the terms proportional to $[(\mathcal{M}_D^2)_{LR}]_{12}$ or $(\delta_d)_{13}(\delta_d)_{32}$ are discarded for simplicity. As for the sub-leading contributions to ε_K, the Wilson coefficients and their corresponding loop functions are given in appendix B.1.5 and B.2.4.2, respectively.

5.2.3 Parameter scan

The MSSM parameter scan is performed with the framework `Ipanema-`β [203] using a GPU of the model GeForce GTX 1080. The samples are a combination of flat scans plus scans based on genetic algorithms [204]. The cost function used by the genetic algorithm is the likelihood function with the observable constrains. In addition, aiming to get a dense population in regions with $\mathcal{B}(K_S^0 \to \mu^+\mu^-)$ significantly different from the SM prediction, specific penalty contributions are added to the total cost function. Specific scans at $\tan\beta \approx 50$ and $M_A \approx 1.6$ TeV are performed, as for those values the chances to get sizable MSSM effects are larger. Three different scenarios are studied (for the ranges of the scanned parameters see table 5.2):

- **Scenario A**: A generic scan with universal gaugino masses. No constraint on the Dark Matter relic density is applied in this case, other than the requirement of neutralino Lightest Supersymmetric Particle (LSP). The LSP is Bino-like in most cases, although some points with Higgsino LSP are also found.

Table 5.2: Scan ranges for scenario A, B (motivated by Higgsino Dark Matter) and C (motivated by Wino Dark Matter). All masses are in TeV. The nuisance parameter B_G appears in the chromomagnetic-dipole contribution to $\varepsilon'_K/\varepsilon_K$.

Parameter	Scenario A	Scenario B	Scenario C
$\tilde{m}_Q$	[2, 10]	[2, 10]	[4, 10]
$\tilde{m}_Q^2/\tilde{m}_d^2$	[0.25, 4]	[0.25, 4]	[0.25, 4]
M_3	[2, 10]	[4.5, 15]	[4, 15]
$\tan\beta$	[10, 50]	[10, 50]	[10, 50]
M_A	[1, 2]	[1, 2]	[1, 2]
$\lvert\mu\rvert$	[1, 10]	1	[5, 20]
M_1	$\frac{\alpha_1(\mu^{SUSY})}{\alpha_3(\mu^{SUSY})}M_3$	$\frac{\alpha_1(\mu^{SUSY})}{\alpha_3(\mu^{SUSY})}M_3$	5
M_2	$\frac{\alpha_2(\mu^{SUSY})}{\alpha_3(\mu^{SUSY})}M_3$	$\frac{\alpha_2(\mu^{SUSY})}{\alpha_3(\mu^{SUSY})}M_3$	3
B_G	[-2, 4]	[-2, 4]	[-2, 4]
Re $\left[(\delta_d^{LL(RR)})_{12}\right]$	[-0.2, 0.2]	[-0.2, 0.2]	[-0.2, 0.2]
Im $\left[(\delta_d^{LL(RR)})_{12}\right]$	[-0.2, 0.2]	[-0.2, 0.2]	[-0.2, 0.2]

- **Scenario B**: A scan motivated by scenarios with Higgsino Dark Matter. In this scenario, the relic density is mostly function of the LSP mass, which fulfills the measured density [205] at $m_{\chi_1^0} \approx 1$ TeV [50–52,206]. Thus, a scan is performed with $|\mu| = 1$ TeV $< M_1$. Universal gaugino masses are assumed in this scenario, which then implies that $M_3 > 4.5$ TeV.

- **Scenario C**: A scan motivated by scenarios with Wino Dark Matter, which is possible in mAMSB or pMSSM, although it is under pressure by γ-rays and antiprotons data [207]. In those scenarios, the relic density is mostly function of the LSP mass, which fulfills the experimental value [205] at $m_{\chi_1^0} \approx 3$ TeV [50,208]. Thus, a scan is made with $M_2 = 3$ TeV $< |\mu|, M_{1,3}$. The Bino mass M_1 is set to 5 TeV for simplicity. Since it is only necessary in order to ensure that the LSP is Wino-like, any other value above 3 TeV (such as, e.g., an mAMSB-like relation $M_1 \approx 9.7$ TeV) could also be used without changing the obtained results. The lightest neutralino and the lightest chargino are nearly degenerate, and radiative corrections are expected to bring the chargino mass to be ≈ 160 MeV heavier than the lightest neutralino [209].

For simplicity, in all cases the trilinear couplings and the mass insertions (other than $\left(\delta_d^{LL(RR)}\right)_{12}$ and $\left(\delta_u^{LL}\right)_{12}$) are set to zero, and μ is treated as a real parameter, with both signs allowed a priori.

Further studies were also performed at the MFV limit, using RG equations induced MIs in CMSSM. As expected, no significant effect is found in this case.

For the squark masses, it is considered that $\tilde{m}_Q = \tilde{m}_u \neq \tilde{m}_d$. This set up is motivated by the SUSY SU(5) grand unified theory, where Q and U-squark are contained in **10**

representation matter multiplet while D-squark is in $\overline{\mathbf{5}}$ representation one. In general, their soft-SUSY breaking masses are different and depend on couplings between the matter multiplets and the SUSY breaking spurion field.

5.2.4 Results

5.2.4.1 χ^2 computation

The total χ^2 for each scan is computed as a sum over the contributions from the different observables (x), as follows:

$$\chi^2 = \sum_x \chi_x^2 \tag{5.88}$$

$$\chi_x^2 = \frac{(x - x^{\text{meas}})^2}{(s_x^{\text{TH}})^2 + (s_x^{\text{EXP}})^2} \tag{5.89}$$

where x is the computed observable, x^{meas} is the value of the corresponding constraint (specified in table 5.1, and s_x^{EXP}, s_x^{TH} are the experimental and theoretical uncertainties of said constraint. The number of degrees of freedom has been calculated as the number of observables, not counting the nuisance parameter B_G, the rigid bound on the $\tan\beta$:M_A plane, and ΔM_K, which are not Gaussian distributed.

In this subsection, the main results of the performed scans are shown. The points with $\chi^2 < 12.5$, corresponding to 95% C.L. for six degrees of freedom (computed as described above), are considered experimentally viable. Therefore, the χ^2 requirement corresponds to a 95% C.L. or tighter.

Similar plots are obtained applying a looser bound on the absolute χ^2 accompanied with a $\Delta\chi^2 < 5.99$ across the plane being plotted. Due to the large theory uncertainty, $\mathcal{B}(K_L^0 \to \mu^+\mu^-)$ can go up to $\approx 1 \times 10^{-8}$ at 2σ level. Values slightly above that limit can still be allowed if they reduce the χ^2 contribution in other observables. The allowed regions are separated by the sign of $A_{L\gamma\gamma}^{\mu}$ in eq. (5.10). Results for A_{CP} are also shown, which could be experimentally accessed by means of a tagged analysis.

5.2.4.2 Effects from $\left(\boldsymbol{\delta}_{\boldsymbol{d}}^{\boldsymbol{LL(RR)}}\right)_{\mathbf{12}}$ separately

In this subsection, the effects with only left-handed(right-handed) MIs are shown, to determine the regions of the MSSM parameter space in which either LL MIs or RR MIs dominate[6].

The obtained scatter plots for $\mathcal{B}(K_L^0 \to \mu^+\mu^-)$ vs $\mathcal{B}(K_S^0 \to \mu^+\mu^-)$ and $\mathcal{B}(K_S^0 \to \mu^+\mu^-)$ vs $\varepsilon'_K/\varepsilon_K$ are shown in Figure 5.3 and Figure 5.4 for Scenario A, Figure 5.5 and Figure 5.6 for Scenario B, and Figure 5.7 and Figure 5.8 for Scenario C. The points in the planes correspond to predictions from different values of the input parameters. It should be

[6] As an example, MFV models the LL MIs can become non-zero after RGE, which does not happen for RR MIs [162].

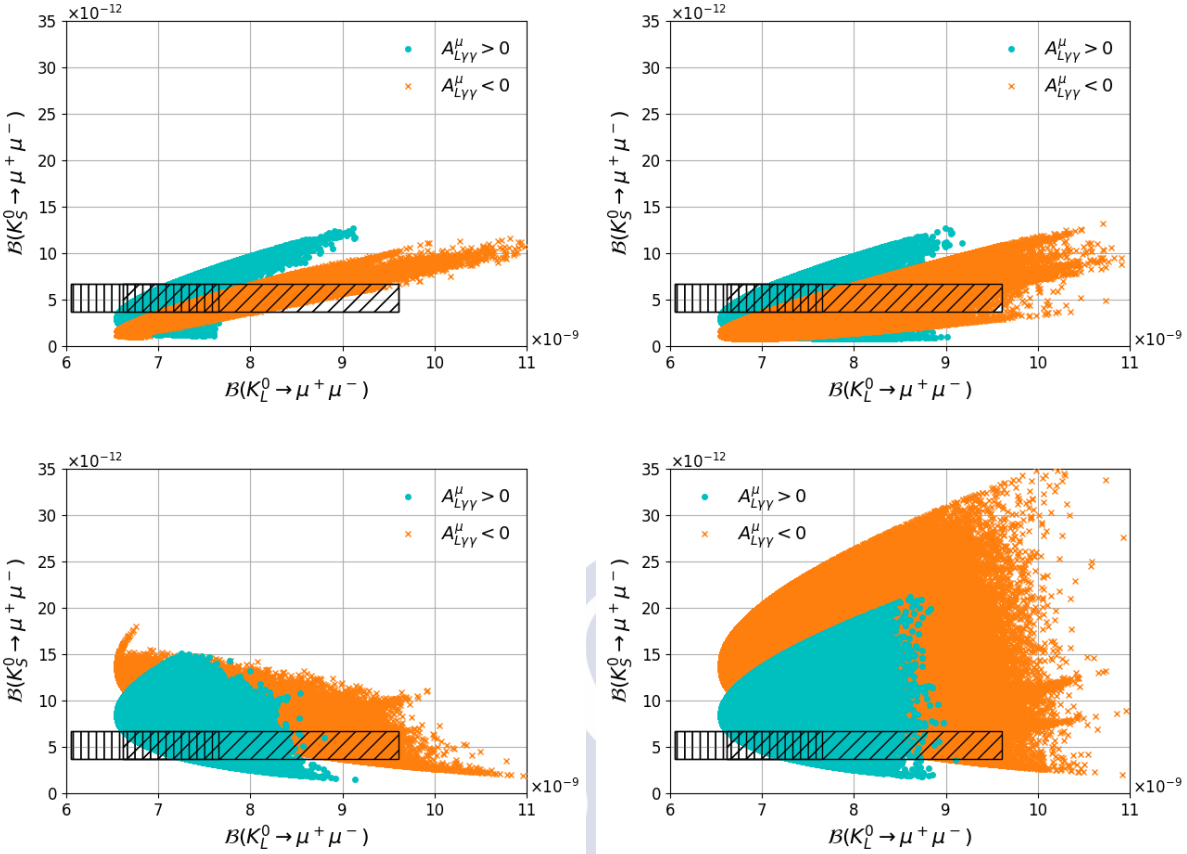

Figure 5.3: Scenario A: $\mathcal{B}(K_S^0 \to \mu^+\mu^-)$ vs $\mathcal{B}(K_L^0 \to \mu^+\mu^-)$ for $\left(\delta_d^{LL}\right)_{12} \neq 0$ and $(M_3 \cdot \mu) > 0$ (upper left), $\left(\delta_d^{LL}\right)_{12} \neq 0$ and $(M_3 \cdot \mu) < 0$ (upper right), $\left(\delta_d^{RR}\right)_{12} \neq 0$ and $(M_3 \cdot \mu) > 0$ (lower left), and $\left(\delta_d^{RR}\right)_{12} \neq 0$ and $(M_3 \cdot \mu) < 0$ (lower right). The cyan dots correspond to $A^{\mu}_{L\gamma\gamma} > 0$ and the orange crosses to $A^{\mu}_{L\gamma\gamma} < 0$. The vertically hatched area corresponds to the SM prediction for $A^{\mu}_{L\gamma\gamma} > 0$ and the inclined hatched area corresponds to the SM prediction for $A^{\mu}_{L\gamma\gamma} < 0$.

noted that in such cases, the SUSY contributions to ε_K can be suppressed naturally in a heavy gluino region ($M_3 \gtrsim 1.5\tilde{m}_Q$) [187, 198].

In Scenario A (see Figure 5.3) and Scenario C (see Figure 5.7), it can be seen that the 95% C.L. allowed regions for $\mathcal{B}(K_S^0 \to \mu^+\mu^-)$ in light of the constraints listed in table 5.1 are approximately $[0.78, 14] \times 10^{-12}$ for LL-only contributions, and $[1.5, 35] \times 10^{-12}$ for RR-only contributions, without any need of fine-tuning the parameters to avoid constraints from $\mathcal{B}(K_L^0 \to \mu^+\mu^-)$. The MSSM contributions are similar for RR and LL, and the differences on the allowed ranges for $\mathcal{B}(K_S^0 \to \mu^+\mu^-)$ arise from the interference with the SM amplitudes in $K^0_{S(L)} \to \mu^+\mu^-$, which are shown in section 5.2.1.

The allowed regions for scenarios A and C are very similar to each other, although marginally larger on A. It can also be seen that, in Scenario B (see Figure 5.5) the

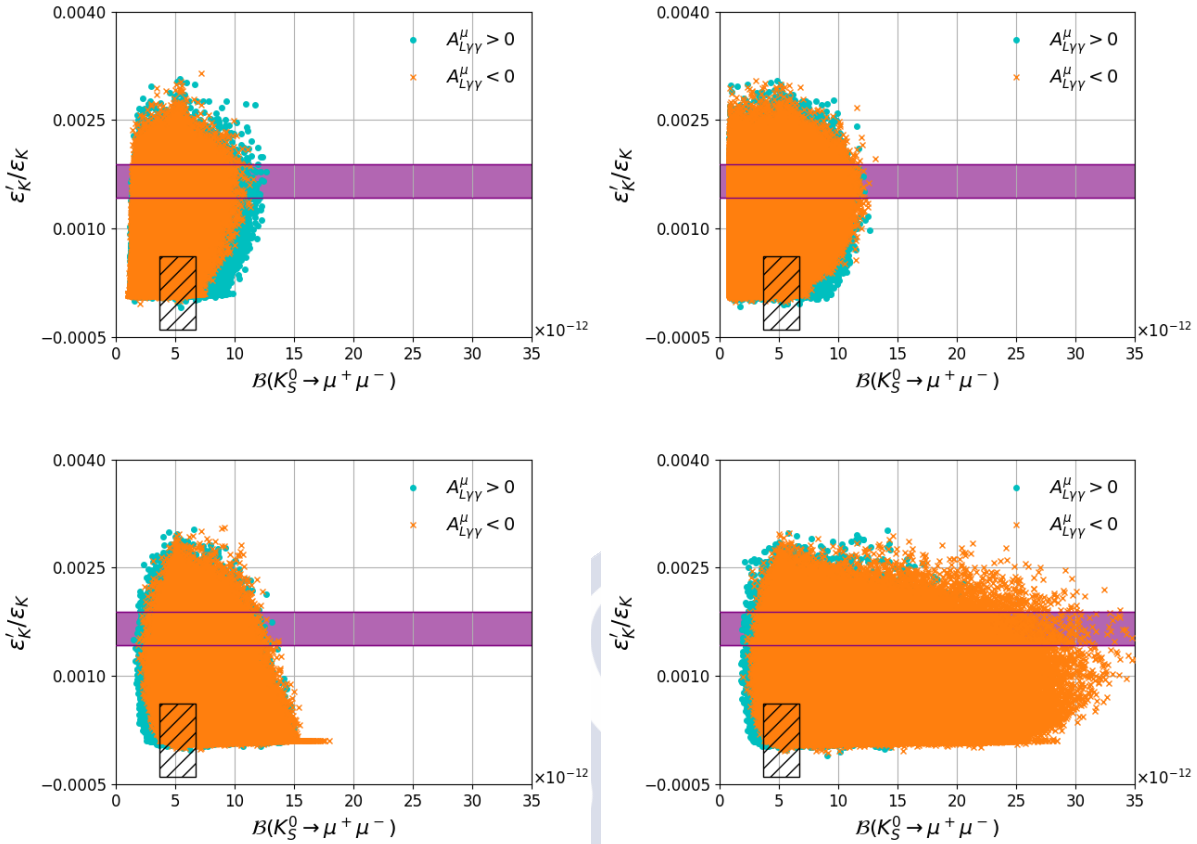

Figure 5.4: Scenario A: $\frac{\varepsilon'_K}{\varepsilon_K}$ vs $\mathcal{B}(K^0_S \to \mu^+\mu^-)$ for $\left(\delta_d^{LL}\right)_{12} \neq 0$ and $(M_3 \cdot \mu) > 0$ (upper left), $\left(\delta_d^{LL}\right)_{12} \neq 0$ and $(M_3 \cdot \mu) < 0$ (upper right), $\left(\delta_d^{RR}\right)_{12} \neq 0$ and $(M_3 \cdot \mu) > 0$ (lower left), and $\left(\delta_d^{RR}\right)_{12} \neq 0$ and $(M_3 \cdot \mu) < 0$ (lower right). The cyan dots correspond to $A^{\mu}_{L\gamma\gamma} > 0$ and the orange crosses to $A^{\mu}_{L\gamma\gamma} < 0$. The deep purple band corresponds to the experimental results and the hatched area to the SM prediction.

maximum departure of $\mathcal{B}(K^0_S \to \mu^+\mu^-)$ from the SM is smaller than in the other scenarios, since $C_{S,P} \propto \mu$ and μ is small relative to squark and gluino masses. In the contributions to $(\varepsilon'_K/\varepsilon_K)^{\text{SUSY}}$, the chromomagnetic-dipole contribution can be significant in both LL-only and RR-only cases when $\mu \tan\beta$ and B_G have large values, while the box contributions can be significant only via LL MIs [187]. Note that the penguin contributions to $(\varepsilon'_K/\varepsilon_K)^{\text{SUSY}}$ are neglected in the parameter scan. This is because, as shown in Section 5.2.2.4, the sub-leading penguin contributions induced by terms of first order in the MIA practically cancel each other. As for the terms of second order, they are considered very small (since the MIs are small), thus being neglected.

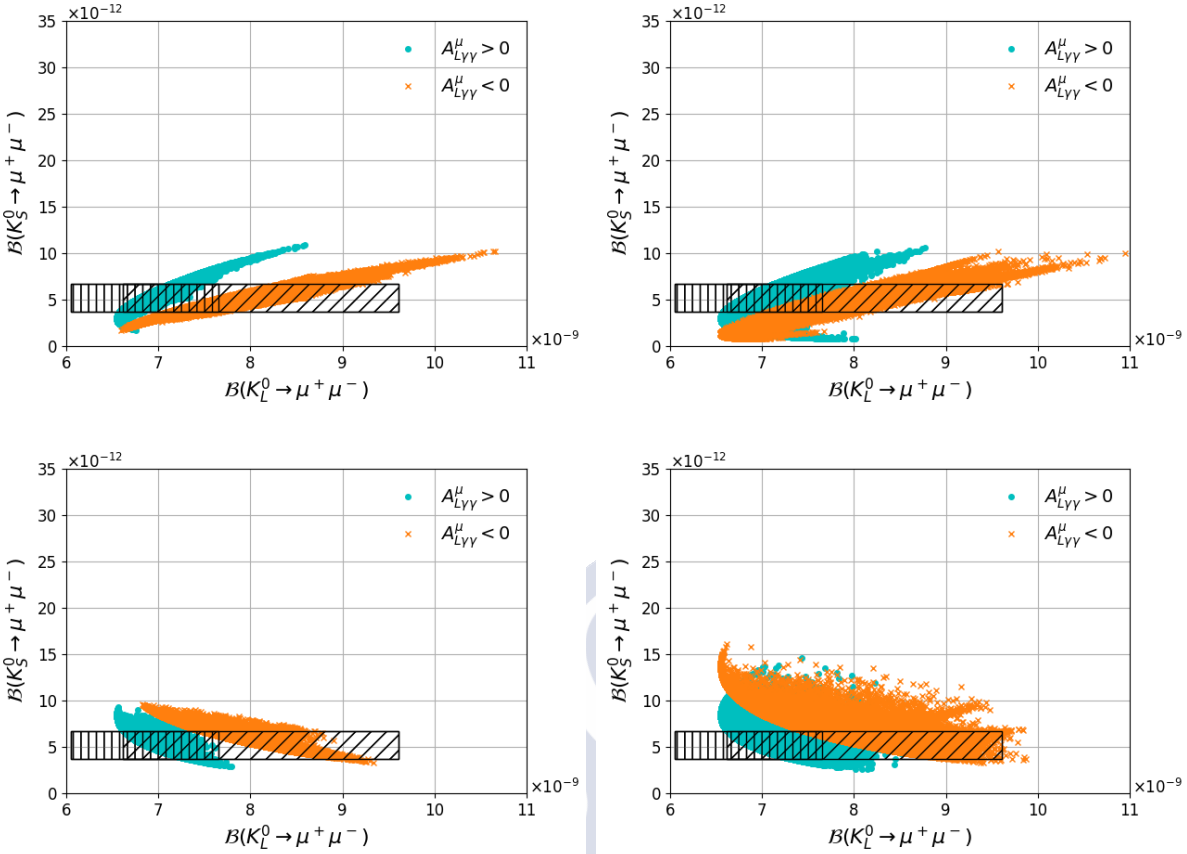

Figure 5.5: Scenario B, motivated by Higgsino Dark Matter with universal gaugino masses: $\mathcal{B}(K_S^0 \to \mu^+\mu^-)$ vs $\mathcal{B}(K_L^0 \to \mu^+\mu^-)$ for $\left(\delta_d^{LL}\right)_{12} \neq 0$ and $(M_3 \cdot \mu) > 0$ (upper left), $\left(\delta_d^{LL}\right)_{12} \neq 0$ and $(M_3 \cdot \mu) < 0$ (upper right), $\left(\delta_d^{RR}\right)_{12} \neq 0$ and $(M_3 \cdot \mu) > 0$ (lower left), and $\left(\delta_d^{RR}\right)_{12} \neq 0$ and $(M_3 \cdot \mu) < 0$ (lower right). The cyan dots correspond to $A^{\mu}_{L\gamma\gamma} > 0$ and the orange crosses to $A^{\mu}_{L\gamma\gamma} < 0$. The vertically hatched area corresponds to the SM prediction for $A^{\mu}_{L\gamma\gamma} > 0$ and the inclined hatched area corresponds to the SM prediction for $A^{\mu}_{L\gamma\gamma} < 0$.

The effective branching fraction and CP asymmetry are shown in Figure 5.9 for Scenario A. The negative value of $\mathcal{B}(K_S^0 \to \mu^+\mu^-)_{\text{eff}}$ is compensated in data by inclusion of the background events from $K_L^0 \to \mu^+\mu^-$, so that the overall $K^0 \to \mu^+\mu^-$ is always positive. Correlation patterns of A_{CP} with other observables can be seen in Figure 5.10, where $D' = -D$ and $D = 0.5$ are chosen for simplicity. It is found that CP asymmetries can be up to ≈ 6 (at $D = 1$), approximately eight times bigger than in the SM. The largest effects are found in left-handed scenarios.

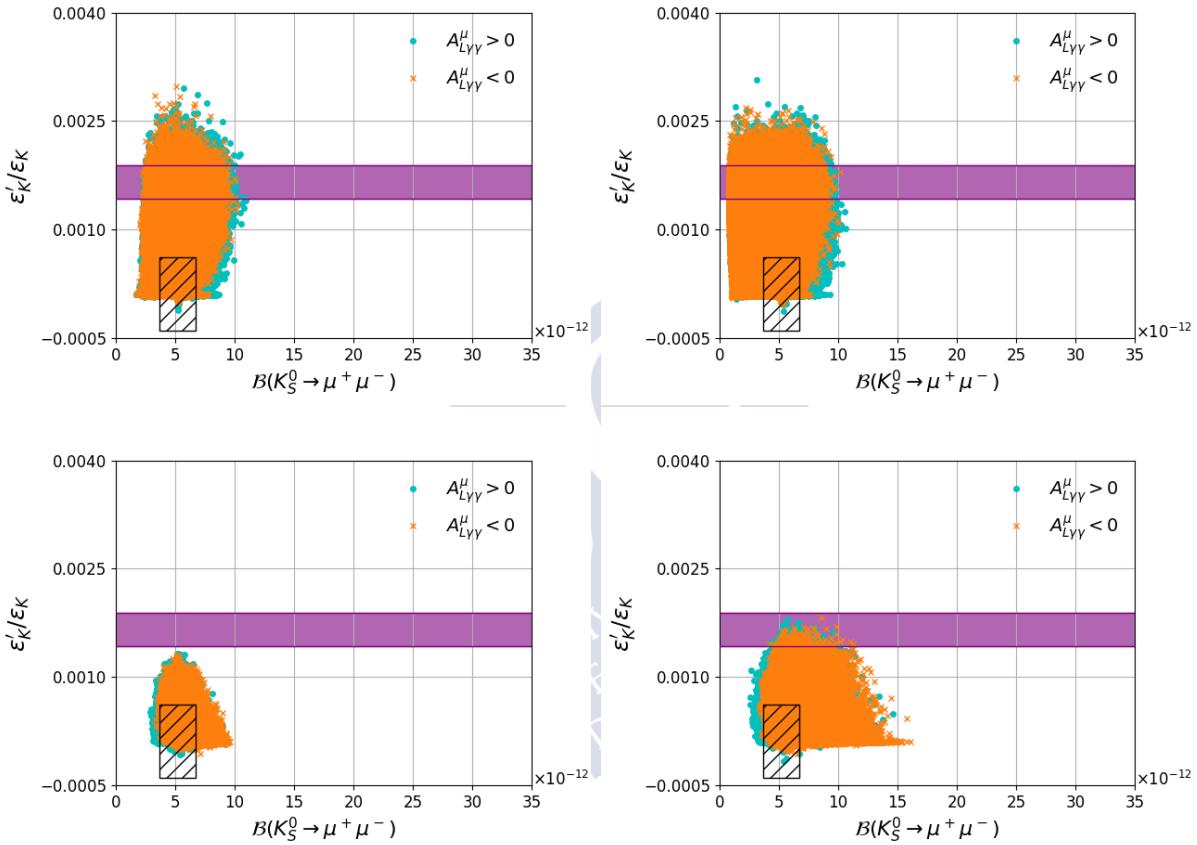

Figure 5.6: Scenario B, motivated by Higgsino Dark Matter and universal gaugino masses: $\frac{\varepsilon'_K}{\varepsilon_K}$ vs $\mathcal{B}(K_S^0 \to \mu^+\mu^-)$ for $\left(\delta_d^{LL}\right)_{12} \neq 0$ and $(M_3 \cdot \mu) > 0$ (upper left), $\left(\delta_d^{LL}\right)_{12} \neq 0$ and $(M_3 \cdot \mu) < 0$ (upper right), $\left(\delta_d^{RR}\right)_{12} \neq 0$ and $(M_3 \cdot \mu) > 0$ (lower left), and $\left(\delta_d^{RR}\right)_{12} \neq 0$ and $(M_3 \cdot \mu) < 0$ (lower right). The cyan dots correspond to $A^{\mu}_{L\gamma\gamma} < 0$ and the orange crosses to $A^{\mu}_{L\gamma\gamma} > 0$. The deep purple band corresponds to the experimental results and the hatched area to the SM prediction.

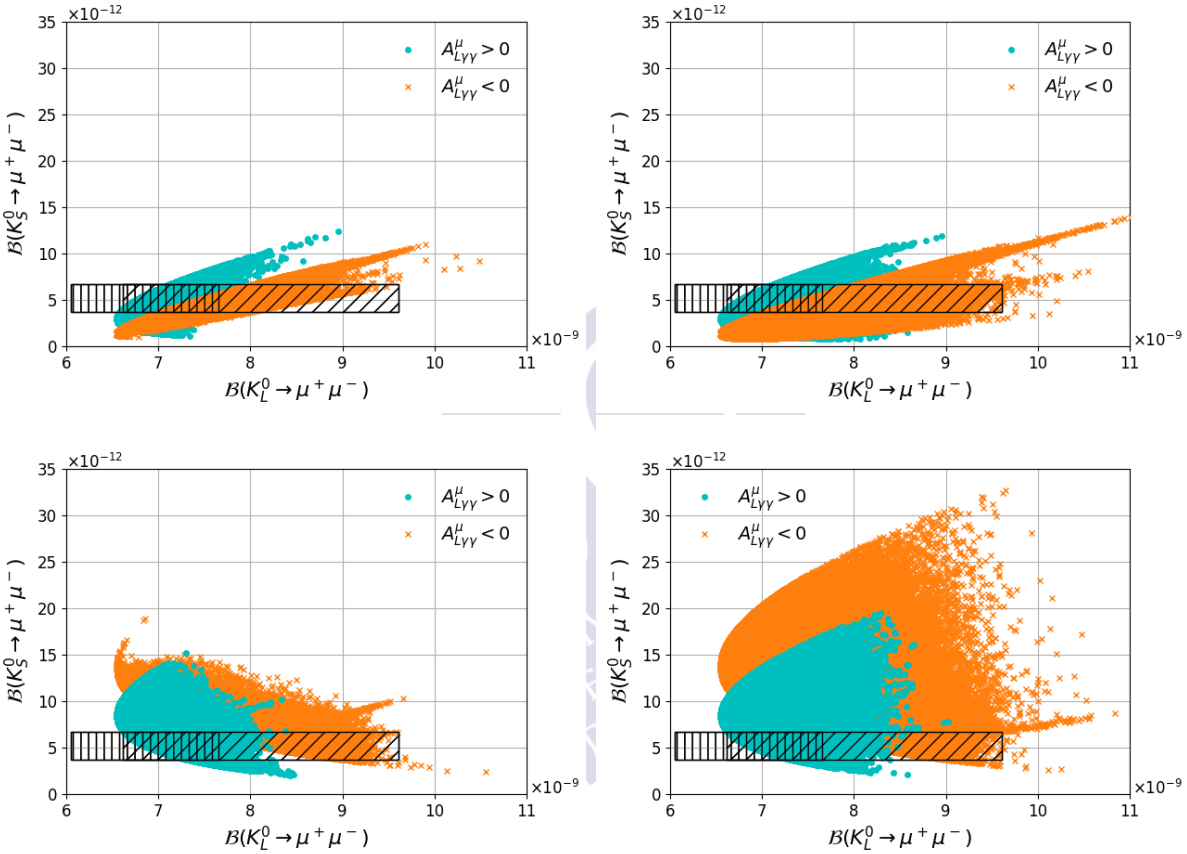

Figure 5.7: Scenario C (motivated by Wino Dark Matter): $\mathcal{B}(K_S^0 \to \mu^+\mu^-)$ vs $\mathcal{B}(K_L^0 \to \mu^+\mu^-)$ for $\left(\delta_d^{LL}\right)_{12} \neq 0$ and $(M_3 \cdot \mu) > 0$ (upper left), $\left(\delta_d^{LL}\right)_{12} \neq 0$ and $(M_3 \cdot \mu) < 0$ (upper right), $\left(\delta_d^{RR}\right)_{12} \neq 0$ and $(M_3 \cdot \mu) > 0$ (lower left), and $\left(\delta_d^{RR}\right)_{12} \neq 0$ and $(M_3 \cdot \mu) < 0$ (lower right). The cyan dots correspond to $A^{\mu}_{L\gamma\gamma} > 0$ and the orange crosses to $A^{\mu}_{L\gamma\gamma} < 0$. The vertically hatched area corresponds to the SM prediction for $A^{\mu}_{L\gamma\gamma} > 0$ and the inclined hatched area corresponds to the SM prediction for $A^{\mu}_{L\gamma\gamma} < 0$.

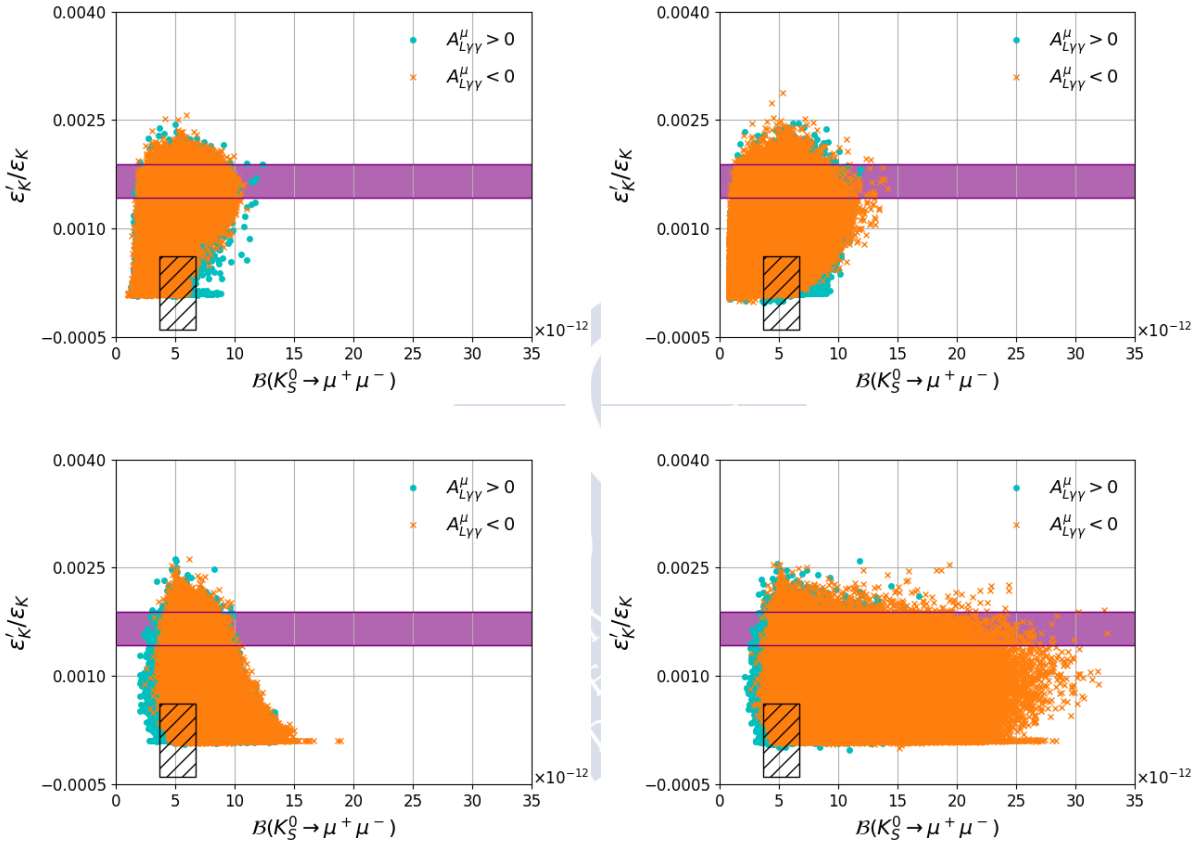

Figure 5.8: Scenario C, motivated by Wino Dark Matter: $\frac{\varepsilon'_K}{\varepsilon_K}$ vs $\mathcal{B}(K_S^0 \to \mu^+\mu^-)$ for $\left(\delta_d^{LL}\right)_{12} \neq 0$ and $(M_3 \cdot \mu) > 0$ (upper left), $\left(\delta_d^{LL}\right)_{12} \neq 0$ and $(M_3 \cdot \mu) < 0$ (upper right), $\left(\delta_d^{RR}\right)_{12} \neq 0$ and $(M_3 \cdot \mu) > 0$ (lower left), and $\left(\delta_d^{RR}\right)_{12} \neq 0$ and $(M_3 \cdot \mu) < 0$ (lower right). The cyan dots correspond to $A^{\mu}_{L\gamma\gamma} > 0$ and the orange crosses to $A^{\mu}_{L\gamma\gamma} < 0$. The deep purple band corresponds to the experimental results and the hatched area to the SM prediction.

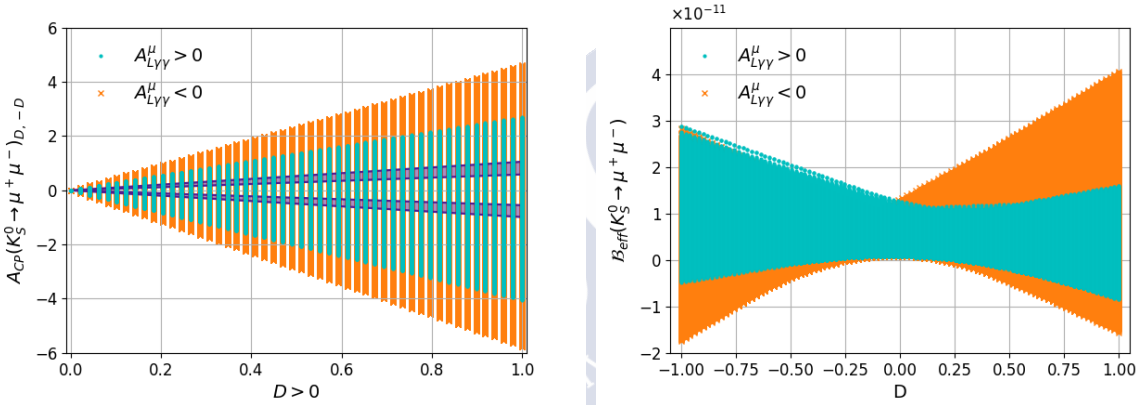

Figure 5.9: Scenario A, $\left(\delta_d^{LL}\right)_{12} \neq 0$ and $(M_3 \cdot \mu) < 0$. Plots of $A_{CP}(K_S^0 \to \mu^+\mu^-)$ vs D (left) for the case $D = -D'$ ($D > 0$) where the cyan dots correspond to $A^{\mu}_{L\gamma\gamma} > 0$, the orange crosses to $A^{\mu}_{L\gamma\gamma} < 0$, and the deep purple bands correspond to the SM predictions in eq. (5.27). $\mathcal{B}(K_S^0 \to \mu^+\mu^-)_{\text{eff}}$ vs D (right).

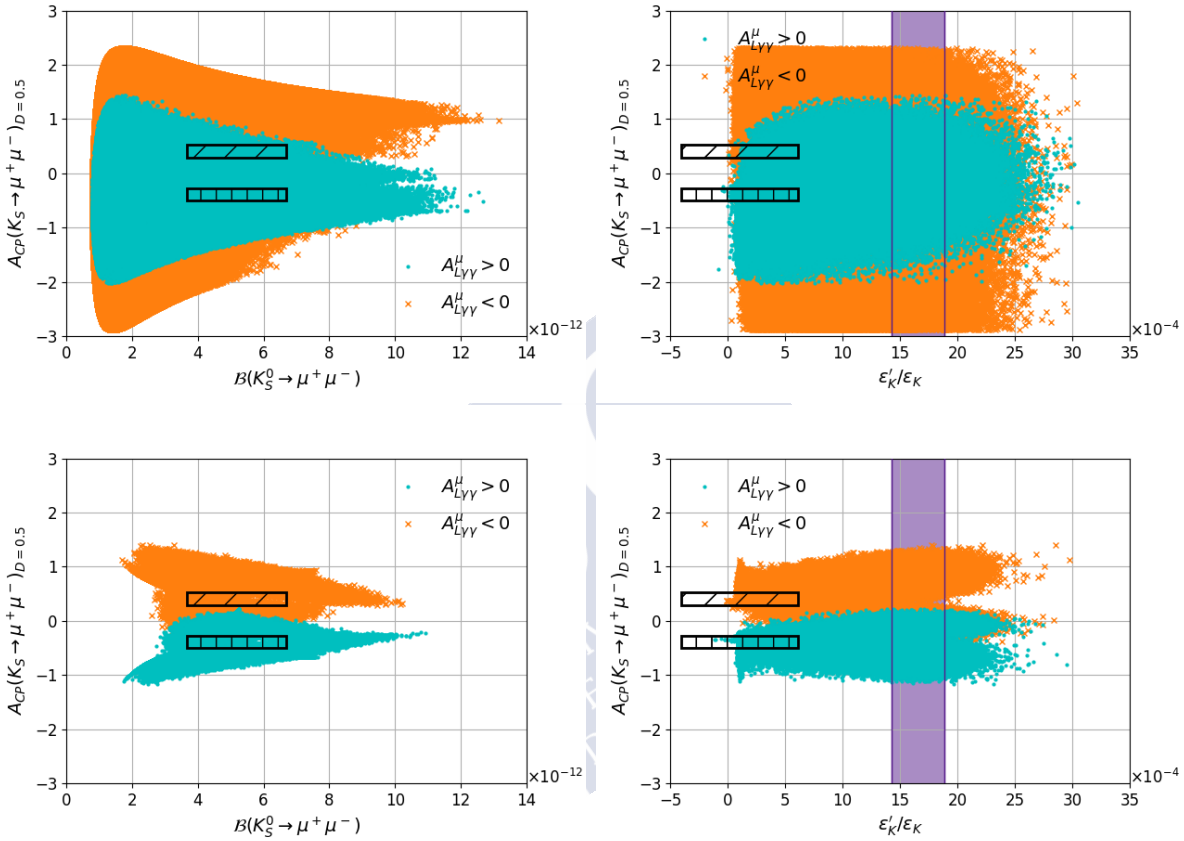

Figure 5.10: A_{CP} vs $\mathcal{B}(K_S^0 \to \mu^+\mu^-)$ (left) and vs $\varepsilon'_K/\varepsilon_K$ (right). The top panels correspond to Scenario A, $\left(\delta_d^{LL}\right)_{12} \neq 0$ and $(M_3 \cdot \mu) < 0$. The bottom panels correspond to Scenario B, $\left(\delta_d^{LL}\right)_{12} \neq 0$ and $(M_3 \cdot \mu) > 0$. The plots are done for $D = -D' = 0.5$. The cyan dots correspond to $A^{\mu}_{L\gamma\gamma} > 0$ and the orange crosses to $A^{\mu}_{L\gamma\gamma} < 0$. The deep purple bands correspond to the experimental value of $\varepsilon'_K/\varepsilon_K$, the vertically hatched areas correspond to the SM prediction for $A^{\mu}_{L\gamma\gamma} > 0$ and the inclined hatched areas to the SM prediction for $A^{\mu}_{L\gamma\gamma} < 0$.

5.2.4.3 Floating *LL* and *RR* MIs simultaneously

A priori, one possibility to avoid the constraint from $\mathcal{B}(K_L^0 \to \mu^+\mu^-)$ is to allow simultaneously for non-zero LL and RR mass insertions. This way both $C_{S(P)}$ and $\tilde{C}_{S(P)}$ are non-zero and eqs. (5.13)–(5.18) do not hold. Tuning the values of the MIs, regions in which the MSSM contributions to $\mathcal{B}(K_S^0 \to \mu^+\mu^-)$ do not alter $\mathcal{B}(K_L^0 \to \mu^+\mu^-)$ significantly (thus satisfying the experimental bound) can be found. Choosing for example

$$\mathrm{Re}\left[\left(\delta_d^{LL}\right)_{12}\right] = -\mathrm{Re}\left[\left(\delta_d^{RR}\right)_{12}\right], \quad \mathrm{Im}\left[\left(\delta_d^{LL}\right)_{12}\right] = \mathrm{Im}\left[\left(\delta_d^{RR}\right)_{12}\right], \tag{5.90}$$

then the SUSY contributions to $\mathcal{B}(K_L^0 \to \mu^+\mu^-)$ are cancelled, while the SUSY contributions to $\mathcal{B}(K_S^0 \to \mu^+\mu^-)$ are maximized (see eqs. (5.3)–(5.7)). However, it is known that in those cases the bounds from ΔM_K and ε_K are very stringent. Fine-tuned regions with $\mathcal{B}(K_S^0 \to \mu^+\mu^-) > 10^{-10}$, or even at the level of the current experimental bound of 8×10^{-10} at 90% C.L. [146] (consistent with all the listed constraints) while targetting large values of $\mathcal{B}(K_S^0 \to \mu^+\mu^-)$, can be found using genetic algorithms with cost functions.

These points are located along very narrow strips in the $\left(\delta_d^{LL}\right)_{12}$ vs $\left(\delta_d^{RR}\right)_{12}$ planes, as shown in Figure 5.11. The figure corresponds to Scenario C as it is the one with higher density of points at large values of $\mathcal{B}(K_S^0 \to \mu^+\mu^-)$ and the pattern observed in Scenario A is nearly identical. A particularly favorable region corresponds to $|(\delta_d^{LL})_{12}| \approx 2|(\delta_d^{RR})_{12}| \sim 0.03$ and $arg\left[(\delta_d^{LL})_{12}\right] \approx -arg\left[(\delta_d^{RR})_{12}\right] + \pi$, which is in the vicinity of eq. (5.90), and with δ_u^{LL} given by the symmetry relation of eq. (5.41). They also favor narrow regions in the squark vs gluino masses planes as shown in Figure 5.12. The values close to the experimental upper bound can still be obtained even if the constraint on ΔM_K is significantly tightened.

Using the SM prediction for ε_K provided in ref. [174]:

$$\varepsilon_K^{\mathrm{EXP/SM}} = 1.41 \pm 0.16(\mathrm{TH}), \tag{5.91}$$

it is found that it is easier to accommodate LL and RR MIs of similar sizes, and fine-tuned regions with $\mathcal{B}(K_S^0 \to \mu^+\mu^-) > 10^{-10}$ are found with higher chances. The shapes of the strips in the mass insertion planes do not change substantially. Notice however that this prediction, that is obtained using $|V_{cb}|$ from exclusive decays, is less consistent with data than the one that was used previously.

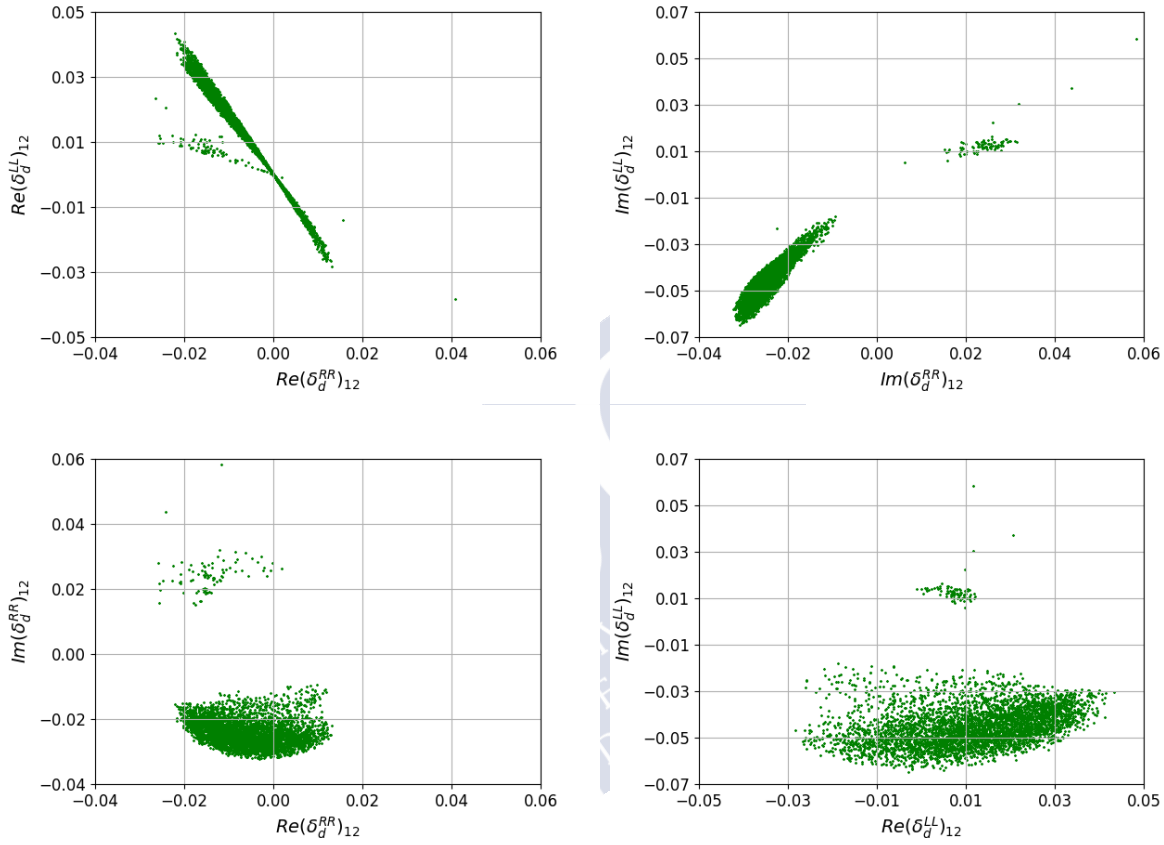

Figure 5.11: Scatter plots of the real (upper left) and the imaginary (upper right) parts of the mass insertions $\left(\delta_d^{RR}\right)_{12}$ and $\left(\delta_d^{LL}\right)_{12}$ for $\mathcal{B}(K_S^0 \to \mu^+\mu^-) > 2 \times 10^{-10}$, of the real vs imaginary $\left(\delta_d^{RR}\right)_{12}$ (lower left) and of the real vs imaginary $\left(\delta_d^{LL}\right)_{12}$ (lower right). All points in the plane pass the experimental constraints defined in section 5.2.2. The up-type MI $(\delta_u^{LL})_{12}$ is given by eq. (5.41). The plots correspond to Scenario C, with a sample of 4378 points with $\mathcal{B}(K_S^0 \to \mu^+\mu^-) > 2 \times 10^{-10}$ and $\chi^2 < 12.5$, produced after 6M generations of $200k$ points each. The pattern observed in Scenario A is very similar.

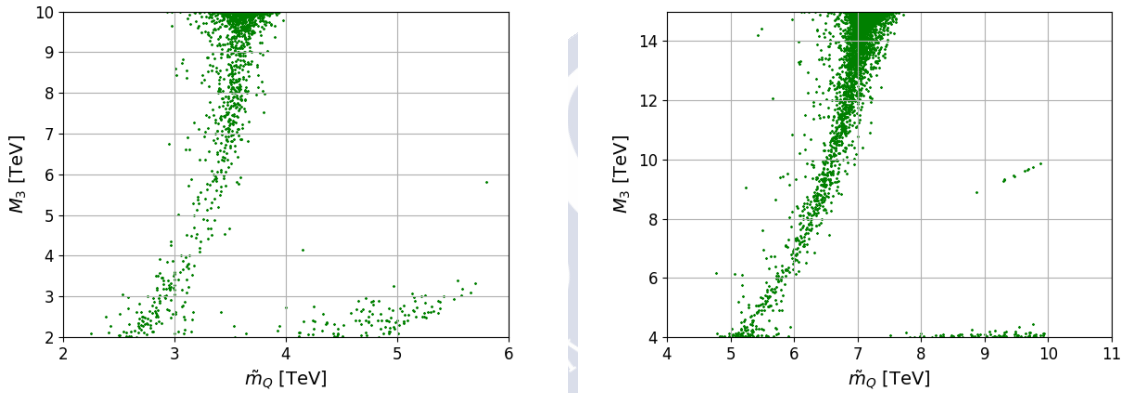

Figure 5.12: Scatter plot of the squark and gluino masses for $\mathcal{B}(K_S^0 \to \mu^+\mu^-) > 2 \times 10^{-10}$ taking into account the constraints defined in section 5.2.2. Left: Scenario A, Right: Scenario C. The χ^2 cut in Scenario A has been relaxed to 14 to increase the density of points.

5.2.4.4 Non-degenerate Higgs masses

The results so far have been obtained in the MSSM framework, in which $|C_S| \approx |C_P|$, due to the mass degeneracy $M_H \approx M_A$. In models in which such degeneracy can be broken, the constraint that $\mathcal{B}(K_L^0 \to \mu^+\mu^-)$ imposes to $\mathcal{B}(K_S^0 \to \mu^+\mu^-)$ becomes looser the more those two masses differ. This happens for example at low values of M_A in the MSSM, and requiring $\tan\beta$ to be small to avoid constraints from $\tan\beta : M_A$ planes from LHC. Those regions are more difficult to study, since it would require a detailed specification of the MSSM and test it against bounds of the Higgs sector. The mass degeneracy is also broken in extensions such as NMSSM. According to the scans performed, on those cases values of $\mathcal{B}(K_S^0 \to \mu^+\mu^-) > 10^{-10}$ could be reached for mass differences of $\mathcal{O}(33\%)$ or larger without fine-tuning the MIs.

5.2.5 Conclusions

The MSSM contribution to $\mathcal{B}(K_S^0 \to \mu^+\mu^-)$ for non-zero $(\delta_d^{LL})_{12}$ and $(\delta_d^{RR})_{12}$ mass insertions has been studied, motivated by the experimental value of $\varepsilon'_K/\varepsilon_K$, and in the large $\tan\beta$ regime. It is found that MSSM contributions to $\mathcal{B}(K_S^0 \to \mu^+\mu^-)$ can surpass the SM contributions $[\mathcal{B}(K_S^0 \to \mu^+\mu^-)^{\rm SM} = 5.18 \times 10^{-12}]$ by up to a factor of seven (see Figure 5.3), reaching the level of 3.5×10^{-11} even for large SUSY masses, with no conflict with existing experimental data, and are detectable by LHCb. This is also the case even if $\varepsilon'_K/\varepsilon_K$ turns out to be SM-like as predicted by refs. [170–172]. Figures of correlations between $\mathcal{B}(K_S^0 \to \mu^+\mu^-)$ and other observables have been provided for different regions of the MSSM parameter space, and can be used to understand which scenarios are more or less favoured, depending on the experimental outcomes. The 3.5×10^{-11} bound is due to the combined effect of $\Delta M_K, \varepsilon_K$, and $K_L^0 \to \mu^+\mu^-$ constraints. Such bound is not rigid, and fine-tuned regions can bring the branching fraction above the 10^{-10} level, even up to the current experimental bound; the largest deviations from SM are found at $|(\delta_d^{LL})_{12}| \approx 2|(\delta_d^{RR})_{12}| \sim 0.03$ and $arg\left[(\delta_d^{LL})_{12}\right] \approx -arg\left[(\delta_d^{RR})_{12}\right] + \pi$ for large squark and gluino masses. The the CP asymmetry of $K^0 \to \mu^+\mu^-$ can be significantly modified by MSSM contributions, being up to eight times bigger than the SM prediction in the pure LL case. It should be noted that, for simplicity, only the main contributions in the large $\tan\beta$ regime have been considered. Discarded terms could, in principle, provide even more flexibility to the allowed regions.

5.3 $K^0_S \to \pi^0\mu^+\mu^-$ Sensitivity study

The decay $K^0_L \to \pi^0\mu^+\mu^-$ has been shown to be sensitive to, for example, models with extra dimensions [210]. However, the potential for this decay to constrain scenarios beyond the Standard Model is limited by the large SM uncertainty on its branching fraction prediction [210],

$$\mathcal{B}(K^0_L \to \pi^0\mu^+\mu^-)_{\rm SM} = \{1.4 \pm 0.3; 0.9 \pm 0.2\} \times 10^{-11}. \tag{5.92}$$

The two numbers in the brackets correspond to two theoretical solutions, depending on whether constructive or destructive interference between the contributing waves (long-distance and short-distance) is present. The reason for the large theoretical uncertainty on $\mathcal{B}(K^0_L \to \pi^0\mu^+\mu^-)_{\rm SM}$ is the limited precision on the chiral-perturbation-theory parameter $|a_S|$ [210]:

$$\mathcal{B}(K^0_L \to \pi^0 l^+ l^-)_{\rm SM} = \left(C^l_{\rm dir} \pm C^l_{\rm int}|a_S| + C^l_{\rm mix}|a_S|^2 + C^l_{\gamma\gamma} + C^l_S\right) \times 10^{-12} \tag{5.93}$$

where the coefficients in Eq. 5.93 describe the short-distance direct CP-violating contribution ($C^l_{\rm dir}$), the long-distance indirect CP-violating term ($C^l_{\rm mix}$), a long-distance CP-conserving correction ($C^l_{\gamma\gamma}$), the interference between direct and indirect CP-violating amplitudes ($C^l_{\rm int}$) and additional contributions due to scalar operators (C^l_S) [210].

An improved measurement of $\mathcal{B}(K^0_S \to \pi^0\mu^+\mu^-)$ will reduce this uncertainty, since it can be calculated from the following expression [211]:

$$\mathcal{B}(K^0_S \to \pi^0\mu^+\mu^-) = [0.07 - 4.52a_S - 1.50b_S + 98.7a_S^2 + 57.7a_Sb_S + 8.95b_S^2] \times 10^{-11}. \tag{5.94}$$

Assuming vector-meson dominance, $b_S = 0.4a_S$ [211]. Hence [212]:

$$\mathcal{B}(K^0_S \to \pi^0\mu^+\mu^-) \simeq 1.2 \times 10^{-9} a_S^2. \tag{5.95}$$

The most precise measurement of $\mathcal{B}(K^0_S \to \pi^0\mu^+\mu^-)$ was performed by the NA48 experiment at CERN [213], which obtained

$$\mathcal{B}(K^0_S \to \pi^0\mu^+\mu^-) = (2.9^{+1.5}_{-1.2}(\text{stat}) \pm 0.2(\text{syst})) \times 10^{-9}. \tag{5.96}$$

5.3.1 Analysis strategy

Decays of the K^0_S in LHCb are characterized by decay vertices separated from the interaction point[7], and with tracks having an average transverse momentum significantly lower than those from b and c decays.

Muon candidates are combined into $\mu^+\mu^-$ pairs. Then a π^0 can be added to the dimuon pair to make a fully reconstructed K^0_S decay. However, since the reconstruction efficiency of the π^0 is limited, events in which no π^0 is found are also considered, based only on the

[7] The K^0_S at LHC typically decays after traversing tens of centimeters to even several meters.

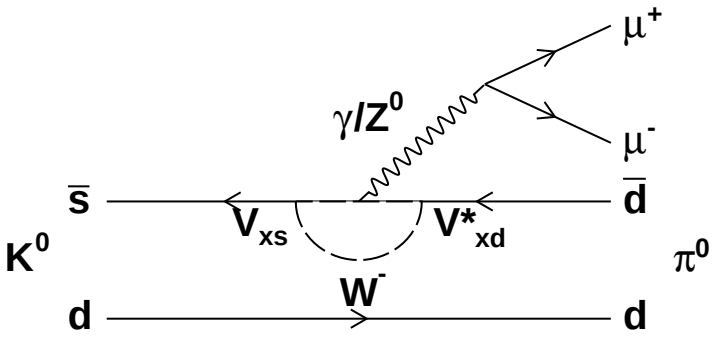

Figure 5.13: Feynman diagram of the process $K^0 \to \pi^0\mu^+\mu^-$.

dimuon information. This leads to two independent analyses: one for the events in which all decay products are considered (hereafter FULL) and one in which only the dimuon pair is used (hereafter PARTIAL). The reconstructed candidates are then passed through a selection algorithm followed by a *Boosted Decision Tree* (BDT) classification, to reduce the high level of background. These *decision trees* (see for example Refs. [214,215]) contain a set of cuts. The decisions about the cuts are made are called *nodes* and the return values, *leaves*. The *boosting* terms refers to the combination of weak learners (algorithms that provide a separation only slightly correlated with the samples) into a common strong learner. This is done assigning different weights to the events from one learner to the other, depending on whether they were misclassified or not.

The properties of the $K^0_S \to \pi^0\mu^+\mu^-$ decays are studied using simulated samples with a differential decay rate modeled according to the SM prediction in Ref. [211]:

$$A(K(k) \to \pi(p) l^+(p_+) l^-(p_-)) = -\frac{e^2}{M_K^2 (4\pi)^2} W(z)(k+p)^\mu \bar{u}_l(p_-)\gamma_\mu \bar{\nu}_l(p_+) \qquad (5.97)$$

where:

- $W(z)$ is a form factor, $W(z) = G_F M_K^2 W^{\rm pol}(z) + W^{\pi\pi}(z)$, $z = (k-p)^2/M_K^2$, with $W^{\rm pol}(z) = a_S + b_S z$ basically a constant and $W^{\pi\pi}(z)$ a dipion term, as shown in Figure 5.14.

- $\bar{u}_l(p_-)\gamma_\mu \bar{\nu}_l(p_+)$ is a spinor-gamma-spinor product.

The model was implemented in `EvtGen` [216] and cross-cheked using `qft++` [217] and a custom `python` code.

The corresponding $\mu\mu$ mass distribution, $m_{\mu\mu}$, as well as the dependence of the (cosine of the) dimuon helicity angle, $\cos\theta_\mu$ (see the angle definitions in Figure 5.15), on $m_{\mu\mu}$ are shown in Figure 5.16.

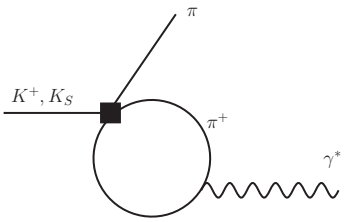

Figure 5.14: Feynman diagram of the process $K \to \pi^0 \mu^+ \mu^-$.

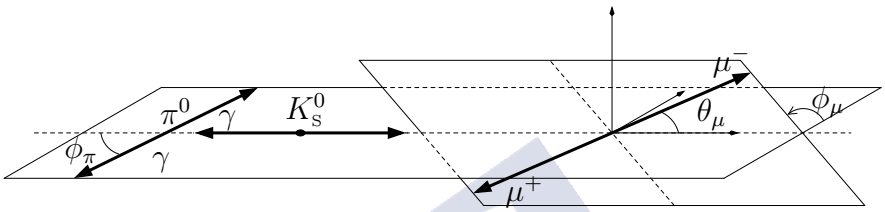

Figure 5.15: Definition of the helicity angles in the K^0_S rest frame.

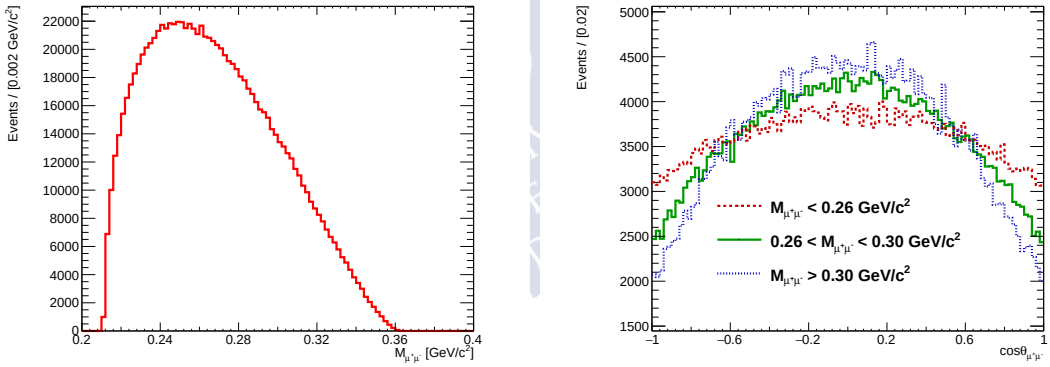

Figure 5.16: $m_{\mu\mu}$ distribution (left), and the dimuon helicity angle depending on $m_{\mu\mu}$ (right).

The BDT is trained with simulated signal events and combinatorial background events from the existing LHCb data. Details on the variables used in the BDT are given in Section 5.3.2.3. Since the main goal of this study is to evaluate the sensitivity for the LHCb upgrade, where the trigger efficiency is expected to be very high, trigger unbiased data samples are preferred. Therefore, the events are obtained from the *Trigger Independent of Signal* (TIS) [218] category of the LHCb trigger. This means that the tracks and clusters of the reconstructed candidate are not needed to fire the trigger at any level, because another object in the underlying event already fired it. This ensures an almost

trigger unbiased data set, while still providing a sample much larger than random selection triggers.

The expected signal yield is obtained assuming the NA48 central value for $\mathcal{B}(K^0_{\rm S} \to \pi^0\mu^+\mu^-)$, normalizing the signal yield with respect to $K^0_{\rm S} \to \pi^+\pi^-$ as

$$\frac{N(K^0_{\rm S} \to \pi^0\mu^+\mu^-)}{N(K^0_S \to \pi^+\pi^-)} = \frac{\mathcal{B}(K^0_{\rm S} \to \pi^0\mu^+\mu^-)\epsilon_{K^0_{\rm S}\to\pi^0\mu^+\mu^-}}{\mathcal{B}(K^0_S \to \pi^+\pi^-)\epsilon_{K^0_S\to\pi^+\pi^-}}, \tag{5.98}$$

where the observed $K^0_{\rm S} \to \pi^+\pi^-$ yield is extracted from data and the efficiency ratio, $\frac{\epsilon_{K^0_{\rm S}\to\pi^0\mu^+\mu^-}}{\epsilon_{K^0_S\to\pi^+\pi^-}}$, is obtained from simulation.

The $\mathcal{B}(K^0_{\rm S} \to \pi^0\mu^+\mu^-)$ sensitivity is measured in a pseudo-experiment study. First, the signal and background yields are extrapolated for a desired expected luminosity and trigger efficiency, then pseudo-experiments are generated according to those yields. The $\mathcal{B}(K^0_{\rm S} \to \pi^0\mu^+\mu^-)$ uncertainty is obtained from a fit to the $K^0_{\rm S}$ candidate mass distribution of the pseudo-experiments, using the signal and background models obtained from MC and the fit to the available LHCb data, respectively. The mass fit range is $[420, 580]\,\text{MeV}/c^2$.

5.3.2 Reconstruction and selection

Pairs of muon candidates are reconstructed combining opposite-charged tracks with hits in the vertex locator (VELO), trigger tracker, tracker stations, and muon chambers. In addition, the tracks are required to be separated by at least 6σ from any $p-p$ collision point in the event. Tracks with transverse momentum lower than $80\,\text{MeV}/c$ are rejected. A dimuon candidate pair can be combined with a π^0 candidate to build a $K^0_{\rm S}$ candidate. The events in which the entire decay chain is used are classified as FULL.

Requiring a well-reconstructed π^0 implies an inefficiency penalty of a factor ten. Thus, a complementary strategy in which only the dimuon information is used, PARTIAL, is also investigated. Indeed, the constraints on the π^0 mass and the $K^0_{\rm S}$ momentum are sufficient to create a peaking distribution if there is an estimate of the typical value of the π^0 longitudinal momentum, p_z, $(8.9\,\text{GeV}/c)$, as shown in Figure 5.17. This value is the one that provides the best kaon candidate mass resolution in the p_z range between 0 and $30\,\text{GeV}/c$. A comparison of the reconstructed mass resolution between FULL and PARTIAL is difficult due to the asymmetric and non-Gaussian distribution of the PARTIAL case. To get an estimate, the corresponding FWHM values are calculated. In the FULL case, it is 23.3 MeV/c^2 and in the PARTIAL 40.6 MeV/c^2.

Details on the trigger (Section 5.3.2.1), stripping (Section 5.3.2.2) and offline selections (Section 5.3.2.3) applied to data and simulation are given in this section.

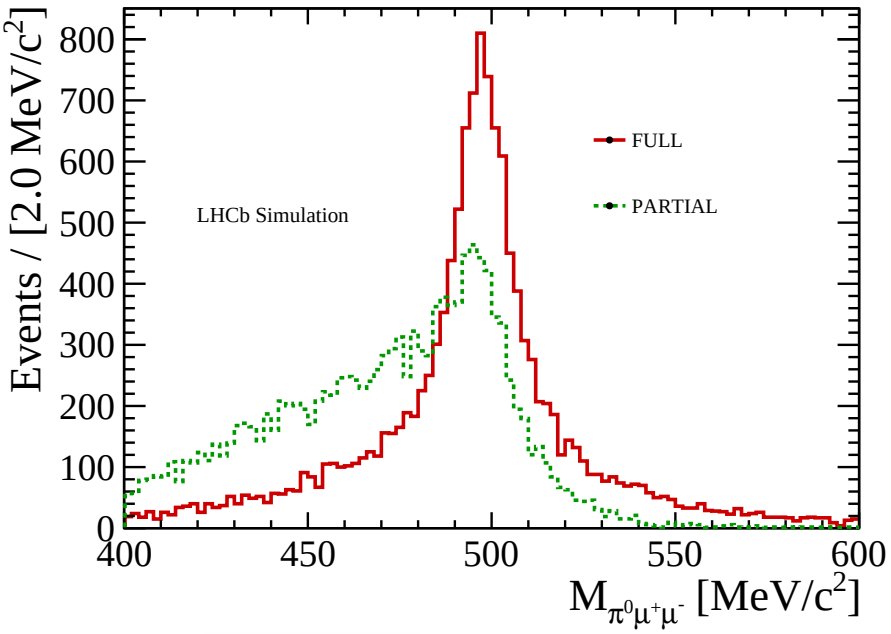

Figure 5.17: Comparison between the FULL (solid red) and PARTIAL (dashed green) kaon candidate mass distributions.

5.3.2.1 Trigger selection

In order to emulate the behavior of a 100% trigger efficiency, only TIS events, as defined in Section 5.3.1, are retained. These come from all the physical trigger-lines required to be `TIS` at L0, Hlt1 and Hlt2 stages. Examples of such lines are `Hlt1TrackMuonDecision`, `Hlt1DiMuonLowMassDecision`, `Hlt2DiMuonSoftDecision`, `Hlt2DiMuonDetachedDecision`.

5.3.2.2 Stripping selection

The stripping selection lines for the $K^0_S \to \pi^0\mu^+\mu^-$and $K^0_S \to \pi^+\pi^-$ candidates are

- StrippingK0s2Pi0MuMuLines: used for the FULL $K^0_S \to \pi^0\mu^+\mu^-$category
- TriggerTestLine (in StrippingRareNStrange): used for the PARTIAL $K^0_S \to \pi^0\mu^+\mu^-$category.

Both stripping lines use the same selection criteria for $K^0_S \to \pi^+\pi^-$. The PARTIAL selection does not require any information about a reconstructed π^0. Some requirements had to be tightened in order to keep the background at a manageable level. These include a lower distance of closest approach between the two muon tracks; a minimum requirement on the K^0_S vertex quality, $\chi^2 < 9$; a higher minimum requirement on the K^0_S vertex detachment from the interaction point; and minimum radial, z- and absolute distance requirements between the K^0_S vertex and the interaction point. The PARTIAL analysis is tested in Stp26, while the FULL is tested in Stp21. The stripping criteria for all lines are summarized in Table 5.3. They are as follows:

- The $K^0_S \to \pi^+\pi^-$ sample is prescaled by a factor of 0.001 due to its large size.
- The charged-particle containers StdAllLooseMuons (all charged tracks compatible with being a muon) and StdNoPidsPions (with standard selection, not including cuts on the PID variables) are used.
- Only resolved (the two photon candidates are distinct) π^0 candidates are used, as the merged (where the two photon candidates overlap forming a "merged cluster" in the calorimeter) contribute only with additional 2.9%. These are reconstructed from γ candidate pairs that correspond to two independent clusters in the calorimeter. Each photon candidate is required to have a transverse momentum of at least 200 MeV/c and the pion candidate a mass within 30 MeV/c^2 of the world average π^0 mass.
- $M(K^0_S)$: K^0_S candidate mass is required to be in the range [400, 600] MeV/c^2 for the FULL and $K^0_S \to \pi^+\pi^-$ samples.
- $M(\mu^+\mu^-)$: The dimuon candidate mass for the PARTIAL sample is required to be smaller than 450 MeV/c^2 to reduce the contribution from misidentified $K^0_S \to \pi^+\pi^-$. This is a loose requirement, given that the maximum dimuon mass, without considering the detector response, is $m_{K^0_S} - m_{\pi^0} = 362$ MeV/c^2.

- K^0_S TOF: Proper decay time of the K^0_S candidate given in a fraction of the K^0_S lifetime. This variable is computed using the reconstructed momentum of the K^0_S candidate and the distance between the reconstructed secondary (SV) and primary (PV) vertices.
- K^0_S IP: The K^0_S candidate must be compatible with the PV, asking for a low impact parameter with respect to PV.
- $\mu^+\mu^-$ DIRA: Forward K^0_S decay, requiring a positive cosine of the polar direction angle (DIRA).
- $\mu^+\mu^-$ DOCA: Good reconstruction quality of the SV required asking for a low distance of closest approach (DOCA) of the two daughter tracks.
- Daug. Track $\chi^2/ndof$: Good reconstruction quality of the muon/pion tracks is required using the $\chi^2/ndof$ of the track fit. This is the standard cut of long tracks in LHCb.
- Daug. IP_{χ^2} : Daughters must not be compatible with coming directly from the PV, by requiring a high impact parameter χ^2, which is defined as the difference of the χ^2 of the PV fit obtained with and without the considered track.
- Daug. Track ghost prob.: accounts for the probability that a track does not correspond to a track from a single charged particle.
- Daug. PID: The DLL $\mu - \pi$ ($log(P_\mu/P_{pi})$) is used to increase the muon purity at stripping level.
- Vertex ρ: The radial distance between the dimuon vertex in LHCb coordinates.
- Vertex z: The distance in z (LHCb coordinates).
- Vertex $\chi^2/ndof$: A good-quality vertex is assured by placing a requirement on its fit quality.
- δ_z: Distance from the end vertex of the particle and the related primary vertex.
- $\cos\alpha$: Cosine of the angle between the K^0_S momentum and the direction fo flight from the best PV to the decay vertex.
- $\text{IP}_{\text{max}}/\delta_z$.

The candidates were selected using three Strippings:

- Stripping 21: used for 2011/2012 data
- Stripping 26: used for 2016 data.

Table 5.3: The $K^0_S \to \pi^0\mu^+\mu^-$ and $K^0_S \to \pi^+\pi^-$ selection cuts performed in the stripping phase. The definitions of the variables is given in the text.

Variables	$\boldsymbol{K^0_S \to \pi^0\mu^+\mu^-}$ **FULL**	$\boldsymbol{K^0_S \to \pi^0\mu^+\mu^-}$ **PARTIAL**	$\boldsymbol{K^0_S \to \pi^+\pi^-}$
Stripping line	K0s2Pi0MuMuLines	TriggerTestLine	K0s2Pi0MuMuLines RareNStrange
Prescale	1	1	0.001
Input Particles	StdAllLooseMuons StdLooseResolvedPi0	StdAllLooseMuons	StdNoPidsPions
$M(K^0_S)$	[400, 600] MeV/c^2	-	[400, 600] MeV/c^2
$M(\mu^+\mu^-)$	-	< 450 MeV/c^2	
K^0_S TOF	$> 0.06\tau$	$> 0.06\tau$	$> 0.1\tau$
K^0_S IP	< 0.9 mm	-	< 0.4 mm
$\mu^+\mu^-$ DIRA	> 0 s	> 0 s	> 0 s
$\mu^+\mu^-$ DOCA	< 0.3 mm	< 0.1 mm	< 0.3 mm
Daug. Track $\chi^2/ndof$	< 5	<5	< 5
Daug. IP_{χ^2}	> 36	> 60	> 100
Daug. Track ghost prob.	-	< 0.1	-
Daug. PID	-	> 0	-
Vertex ρ	-	> 4 mm	-
Vertex z	-	> 650 mm	-
Vertex $\chi^2/ndof$	-	< 9	-
δ_z	-	> 0 mm	-
$\cos\alpha$	-	> 0	-
$\text{IP}_{\text{max}}/\delta_z$	-	$< 1/60$ s^{-1}	-

Additional constraints are applied to the sample after the stripping and trigger selections. The mass resolution is improved by constraining the π^0 candidate mass to the world average π^0 mass, and by constraining the three-momentum vector of the K^0_S to point back to the production vertex. For the PARTIAL candidates, a momentum vector with an absolute value of 8.9 GeV/c is used as a representative of the π^0 momentum when calculating the invariant mass. As a consequence of these kinematic constraints, the K^0_S candidate mass resolution depends only weakly on the π^0 momentum.

Further selection requirements are applied to reduce the amount of data to analyze, fulfill the rate requirements for LHCb offline processing and reduce the amount of background. These include a K^0_S candidate lifetime of at least 1 ps, and removing events in the kinematic region of $\Lambda \to p\pi$ and $K^0_S \to \pi^+\pi^-$ in the Armenteros-Podolanski plane [219]. The total reconstruction and selection efficiency for the FULL channel is 5.47×10^{-4}. The total reconstruction and selection efficiency for the PARTIAL analysis is 3.0×10^{-3}, well above that of the FULL, but at a cost of an increased background yield.

5.3.2.3 BDT Training

A BDT is used to separate signal from combinatorial background. It is trained with MC events (signal class) and a part of the data that is not used in the fit (combinatorial background class, outside the fit range, $[420, 580]\,\mathrm{MeV}/c^2$). The BDT uses information about the geometrical properties of the events, kinematics, track quality, and muon identification quality. The BDT response for signal and background for both FULL and PARTIAL is shown in Figure 5.18.

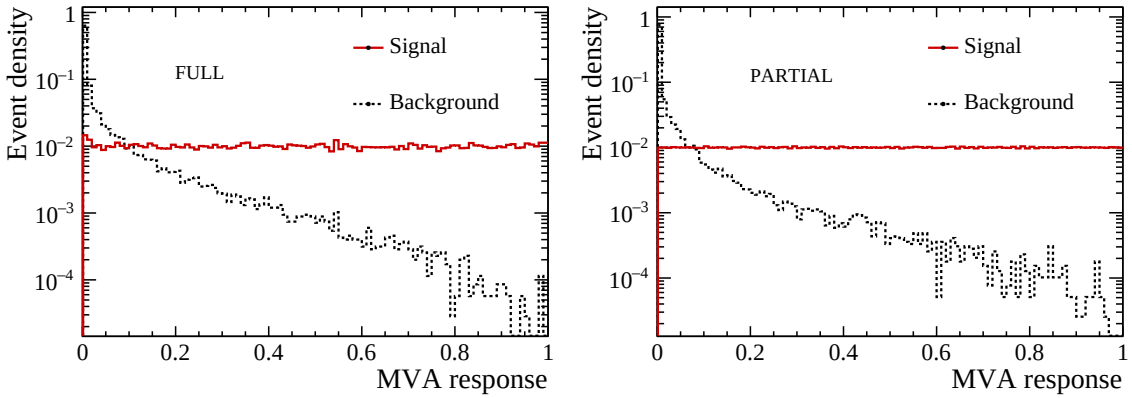

Figure 5.18: BDT response both for signal (solid red) and background (dashed black). Right: FULL channel. Left: PARTIAL channel. Signal and background are normalized to the same area.

Before the BDT training, the following cuts are applied to the data to reduce the amount of background while keeping most of the signal:

- Number of hits in the Trigger Tracker greater than 0.1 for both muons
- ProbNN (standard Multivariate Analysis used for PID at LHCb) for the muons greater than 0.05
- Lifetime of the K^0_S greater than 1 ps
- Invariant mass of the decay result smaller than 490 MeV
- Kinematic cut in the Armenteros-Podolanski plane, removing $\Lambda \to p\pi$ and $K^0_S \to \pi^+\pi^-$

The input MVA variables used are divided into continuous variables and discrete variables. The continuous variables are gaussianized, decorrelated, and gaussianized again [220]. Then the gaussianized and the discrete variables are inputs for the BDT training. The set of variables common to the FULL and PARTIAL cases consists of:

- Distance of closest approach (DOCA)

- K^0_S flight distance significance.
- χ^2 of μ track fit
- Vertex χ^2
- K^0_S p_T
- K^0_S impact parameter significance (difference in the χ^2 of the fit of the vertex obtained with and without the introduction of the track in the fit)
- Impact parameter significance of the muons with respect to any PV in the event
- PID variables for muons
- Hits in VELO
- Hits in Inner Tracker
- Hits in Trigger Tracker
- Hits in Outer Tracker
- Secondary Vertex coordinates

Apart from these, there are inputs that are specifically used for FULL.

FULL:

- Angle between $\mu\mu$ and $\gamma\gamma$ planes
- π^0mass
- Helicity angles (as defined in Figure 5.15).

The ROC (Receiver Operating Characteristic) curves obtained for both cases are represented in Figure 5.19. Finally, in Figures 5.20, 5.21, 5.22 and 5.23, the histograms for signal and background of the BDT input variable distributions are shown for the FULL and PARTIAL categories, respectively. The fraction of MC signal K^0_S coming from b or c decays is found to be less than a per mil.

Applying a cut on the BDT, BDT > 0.6, a 40% of signall efficiency is obtained, while rejecting 99.3% (99.8%) of the background for the FULL (PARTIAL) strategy. The events are thus classified in the four equally populated bins of the BDT response that pass the cut. The binning is done to improve the sensitivity. The signal yields are obtained in a simultaneous fit of the mass distribution in each BDT bin, as described in the following sections.

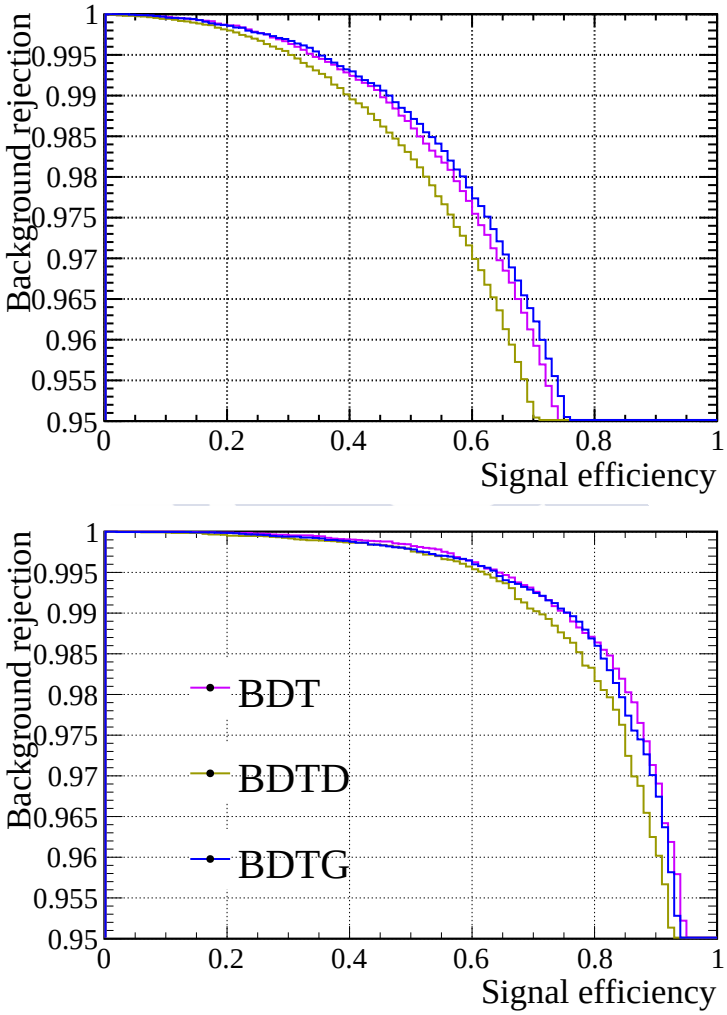

Figure 5.19: ROC curves for the FULL (top) and PARTIAL (bottom) categories.

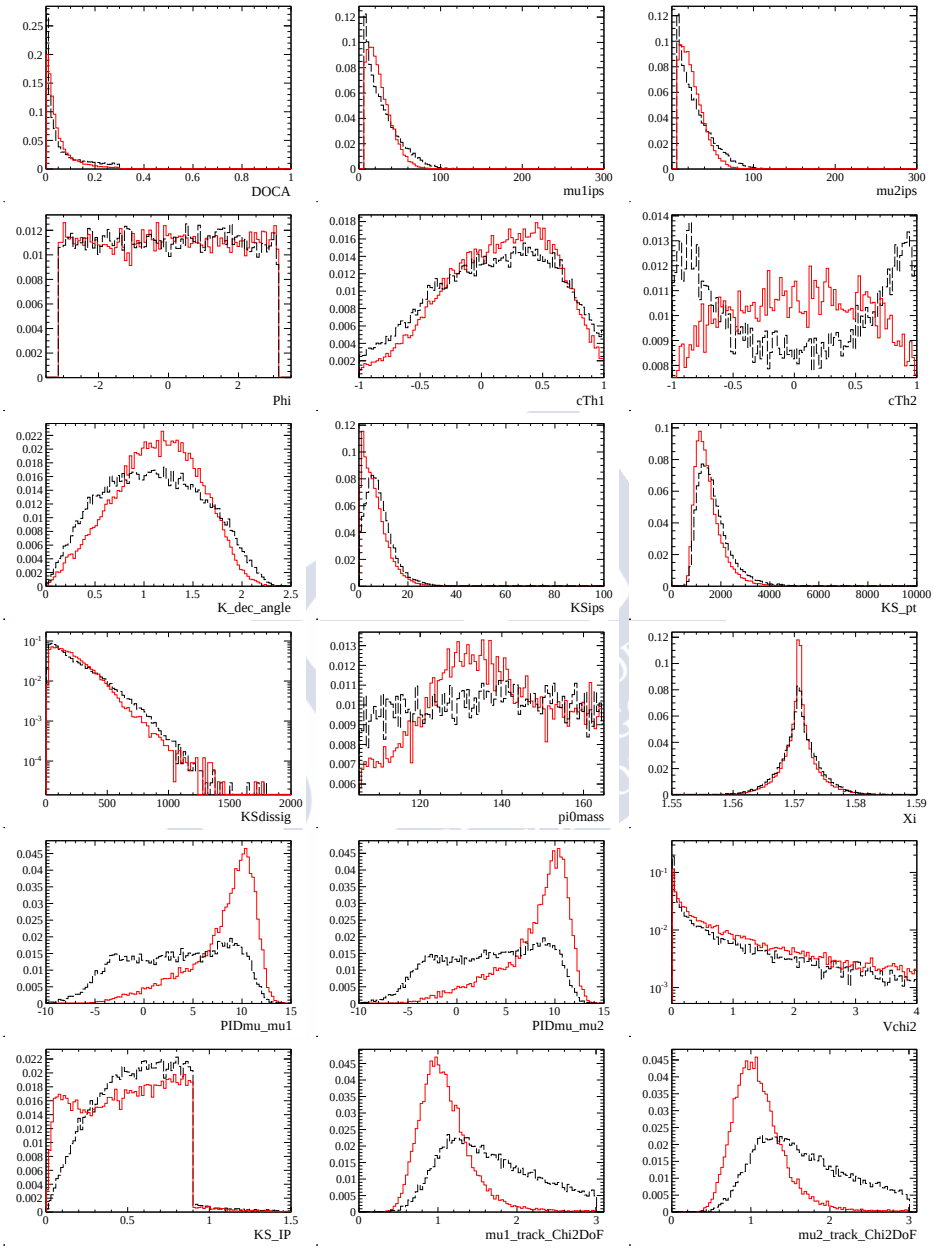

Figure 5.20: BDT input variable distributions for signal (red) and background (black) for the FULL case.

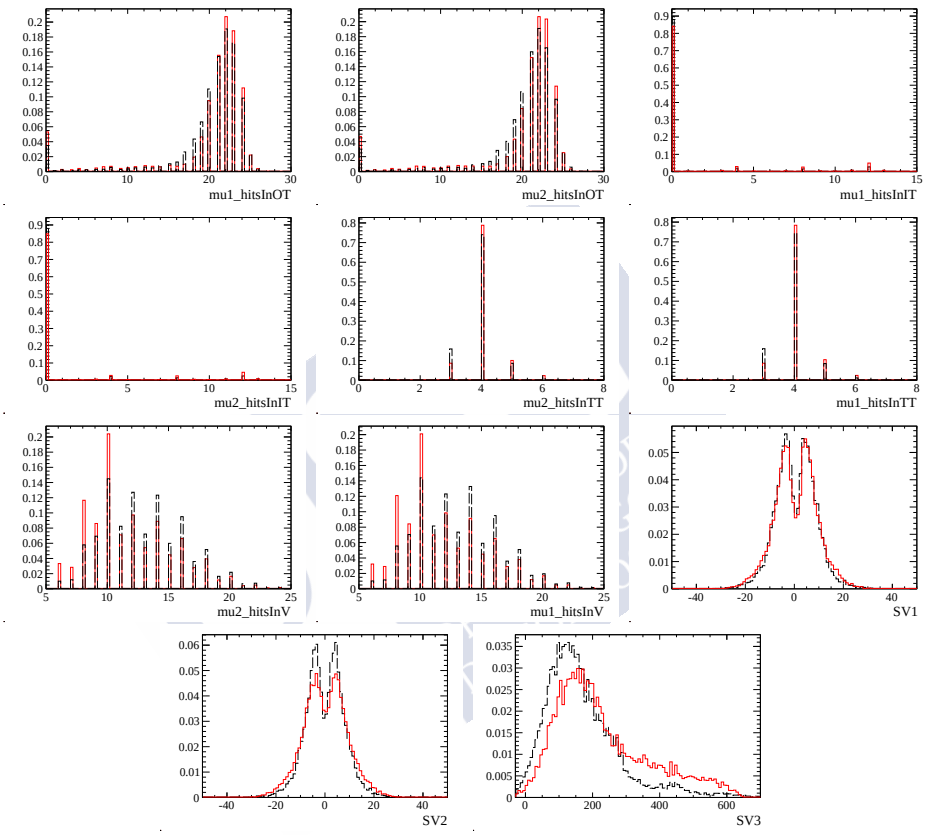

Figure 5.21: BDT input variable distributions for signal (red) and background (black) for the FULL case.

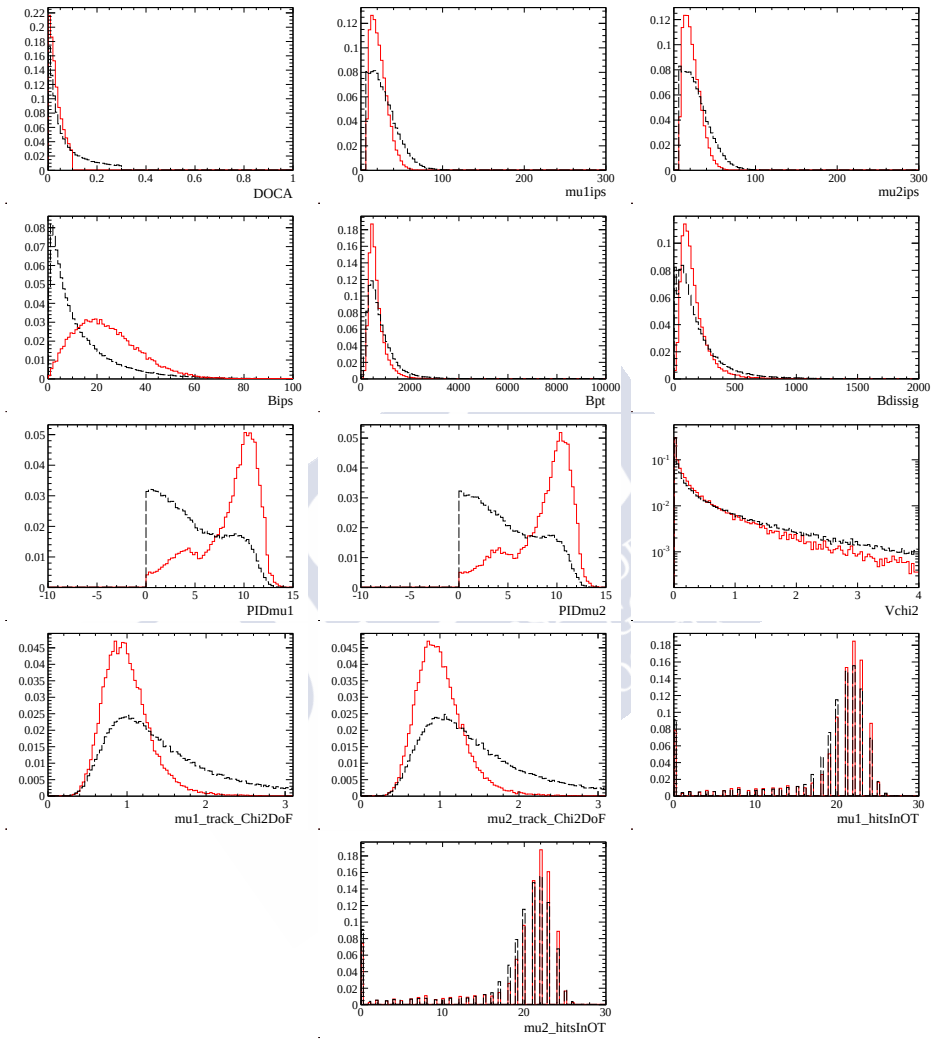

Figure 5.22: BDT input variable distributions for signal (red) and background (black) for the PARTIAL case.

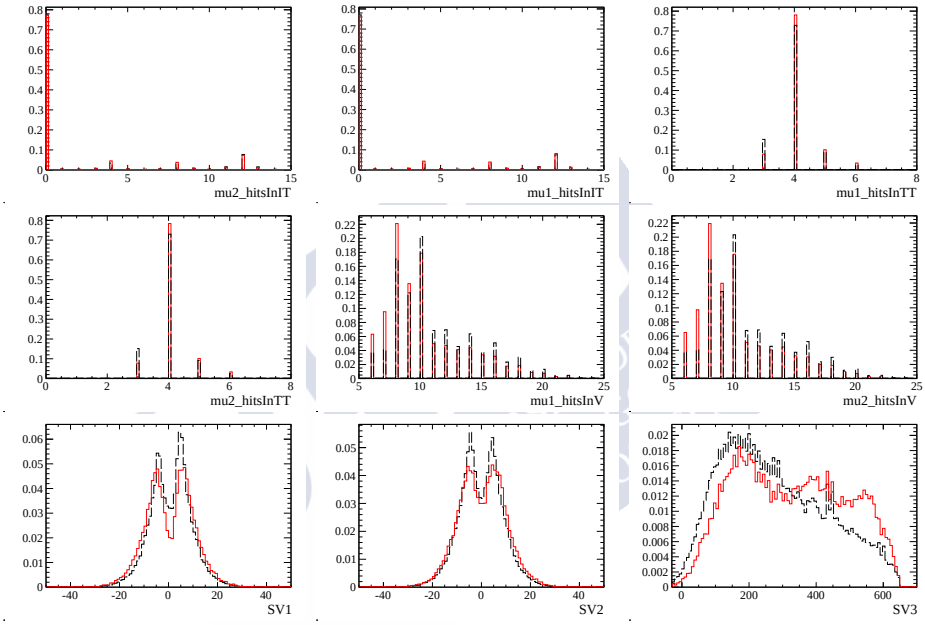

Figure 5.23: BDT input variable distributions for signal (red) and background (black) for the PARTIAL case.

5.3.3 Background sources

Several sources of background are investigated to assess their relevance for a measurement of $\mathcal{B}(K^0_S \to \pi^0\mu^+\mu^-)$:

- $K^0_S \to \pi^+\pi^-$ decays, where both pions are misidentified as muons, and in the case of the FULL category, combined with a random π^0 from the underlying event. These decays have a mass larger than that of the K^0_S and do not enter the fit region, except for potential residual tails that effectively add up to the combinatorial background. No evidence for $K^0_S \to \pi^+\pi^-$ background is seen for the BDT region being fitted.

- $K^0 \to \mu^+\mu^-\gamma\gamma$ decays. This background was considered in the NA48 analysis [213]. Nevertheless, its contribution at LHCb is found to be negligible: in the case of the K^0_L decay (with a branching fraction of $1.0^{+0.8}_{-0.6} \times 10^{-8}$ [1]) the upper decay time acceptance introduces an effective 10^{-3} reduction with respect to K^0_S and hence the effective $\mathcal{B}(K^0_L \to \mu^+\mu^-\gamma\gamma)$ becomes as low as 10^{-11}. There is no experimental measurement of $\mathcal{B}(K^0_S \to \mu^+\mu^-\gamma\gamma)$, however, since the process is dominated by the two-photon exchange[8], it can be estimated as:

$$\mathcal{B}(K^0_S \to \mu^+\mu^-\gamma\gamma) = \frac{\mathcal{B}(K^0_S \to \gamma\gamma)}{\mathcal{B}(K^0_L \to \gamma\gamma)}\mathcal{B}(K^0_L \to \mu^+\mu^-\gamma\gamma) \sim 4.8 \times 10^{-11} \tag{5.99}$$

  and is thus negligible.

- $K^0_L \to \pi^0\pi^+\pi^-$ decays. The mass distribution of these decays is shown in Figure 5.27 as obtained in simulation. Since there is no evidence of this background in the data, it is neglected. Including a $K^0_L \to \pi^0\pi^+\pi^-$ component to the observed background, modeled using a Landau function with parameters fixed to those obtained from simulation at the stripping filtered level (see Figures 5.25, 5.24), does not change significantly the sensitivity estimates (see Figure 5.26). The K^0_S counterpart has a branching fraction of 3.5×10^{-7} and thus is about four orders of magnitude smaller than $K^0_L \to \pi^0\pi^+\pi^-$. In general, no sign of a resonant structure in the $\pi^+\pi^-\pi^0$ is seen on data.

- $K^0 \to \pi^\pm\mu^\mp\nu$ decays, where $\pi^\pm \to \mu^\mp\nu$, and in the case of the FULL category, combined with a random π^0 from the underlying event. The branching fraction for this decay is of the order of 10^{-4} for K^0_S and 10^{-1} for K^0_L [29], several orders of magnitude above the one for $K^0_S \to \pi^0\mu^+\mu^-$. Therefore, it constitutes an important source of background for $K^0_S \to \pi^0\mu^+\mu^-$, especially for high values of the BDT. Nevertheless, the sensitivity is obtained from data, thus meaning that this background is already accounted for. The full analysis will contain a more detailed study of this background source using simulation samples.

[8] Isidori and D'Ambrosio, private communication.

- Combinatorial background. Combinatorial background is considered to be composed by random combination of tracks, including those generated by pseudo-random combinations of hits during the pattern recognition. It has a monotonic shape across the studied invariant mass range.

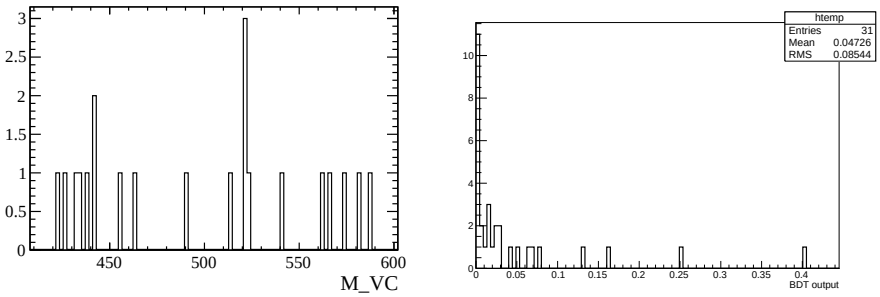

Figure 5.24: Mass and BDT distribution of the $K^0_S \to \pi^0\pi^+\pi^-$ simulated FULL candidates.

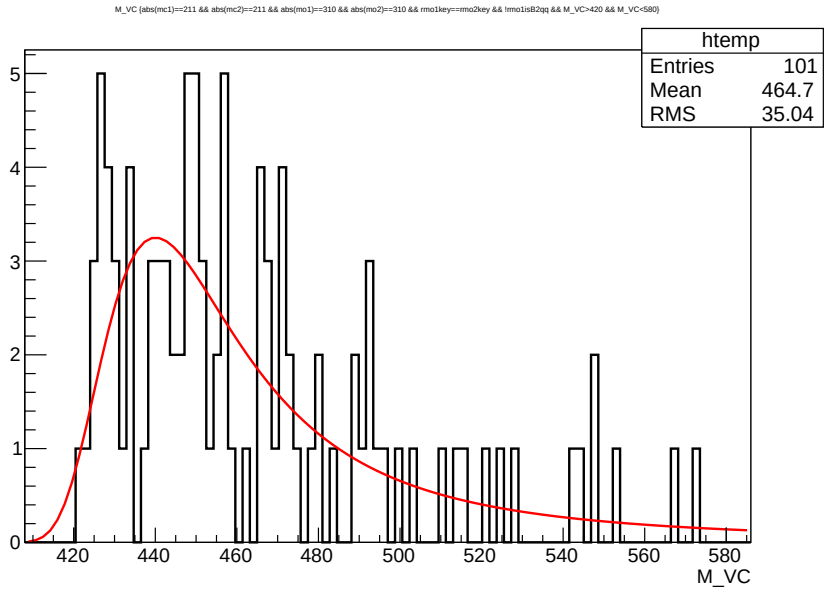

Figure 5.25: Mass of $K^0_S \to \pi^0\pi^+\pi^-$ after stripping FULL, and fit to a Landau PDF.

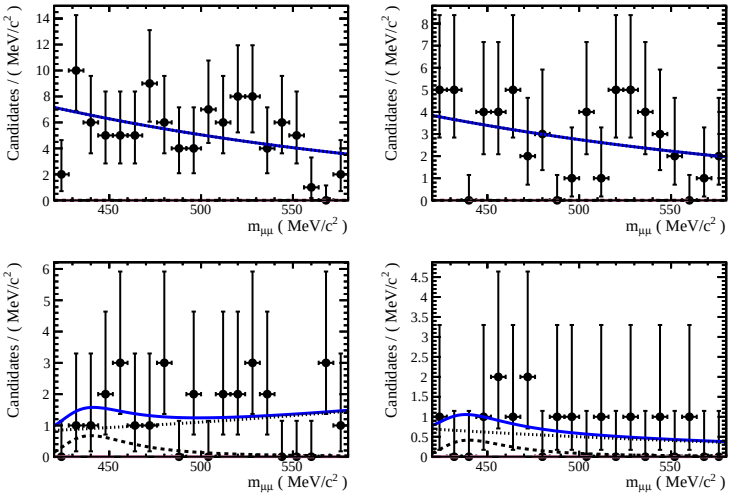

Figure 5.26: Fit to the dataset FULL (in four BDT bins) including a Landau component for $K^0_L \to \pi^0\pi^+\pi^-$. The size of the Landau component is consistent with zero at one sigma in all BDT bins.

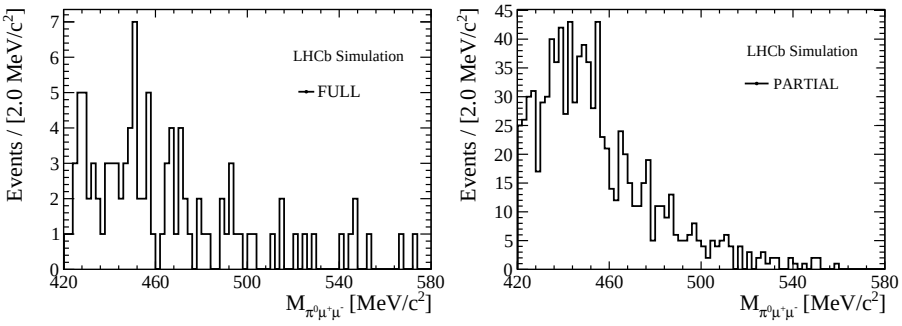

Figure 5.27: Invariant mass distribution of simulated $K^0 \to \pi^+\pi^-\pi^0$ decays selected in the FULL (left) and PARTIAL (right) categories.

5.3.4 Fit model

Only events in the BDT range [0.6,1] are considered in the fit to the data. A simultaneous fit to the mass distribution across four equally-sized independent bins of the BDT response is performed, in order to maximize the sensitivity. The combinatorial background is described with an exponential PDF for both FULL and PARTIAL analysis, with independent floating yields and decay constants in each BDT bin. The signal model is an Hypathia distribution [221] with different configurations for FULL and PARTIAL (see Figure 5.28). The signal model parameters are independent in each BDT bin and are obtained from simulation. The fractions of signal events allotted to each BDT bin are also fixed from values obtained from simulation, with a total signal yield remaining as the sole free parameter describing signal in the simultaneous fit. The signal yield is floated in the fit to the data. It is measured to be compatible with zero within one to two sigma: $N_{\rm sig}^{\rm FULL} = 0 \pm 19$, $N_{\rm sig}^{\rm PARTIAL} = 24^{+15}_{-14}$. The fit projections to the FULL and PARTIAL data are shown in Figure 5.29.

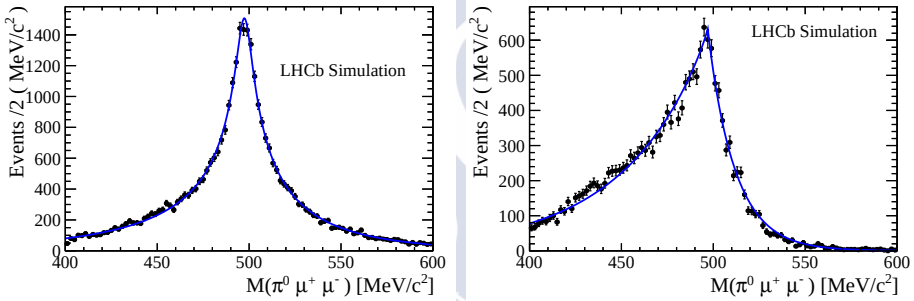

Figure 5.28: Signal fit using the Hypathia function for FULL (left) and PARTIAL (right) categories.

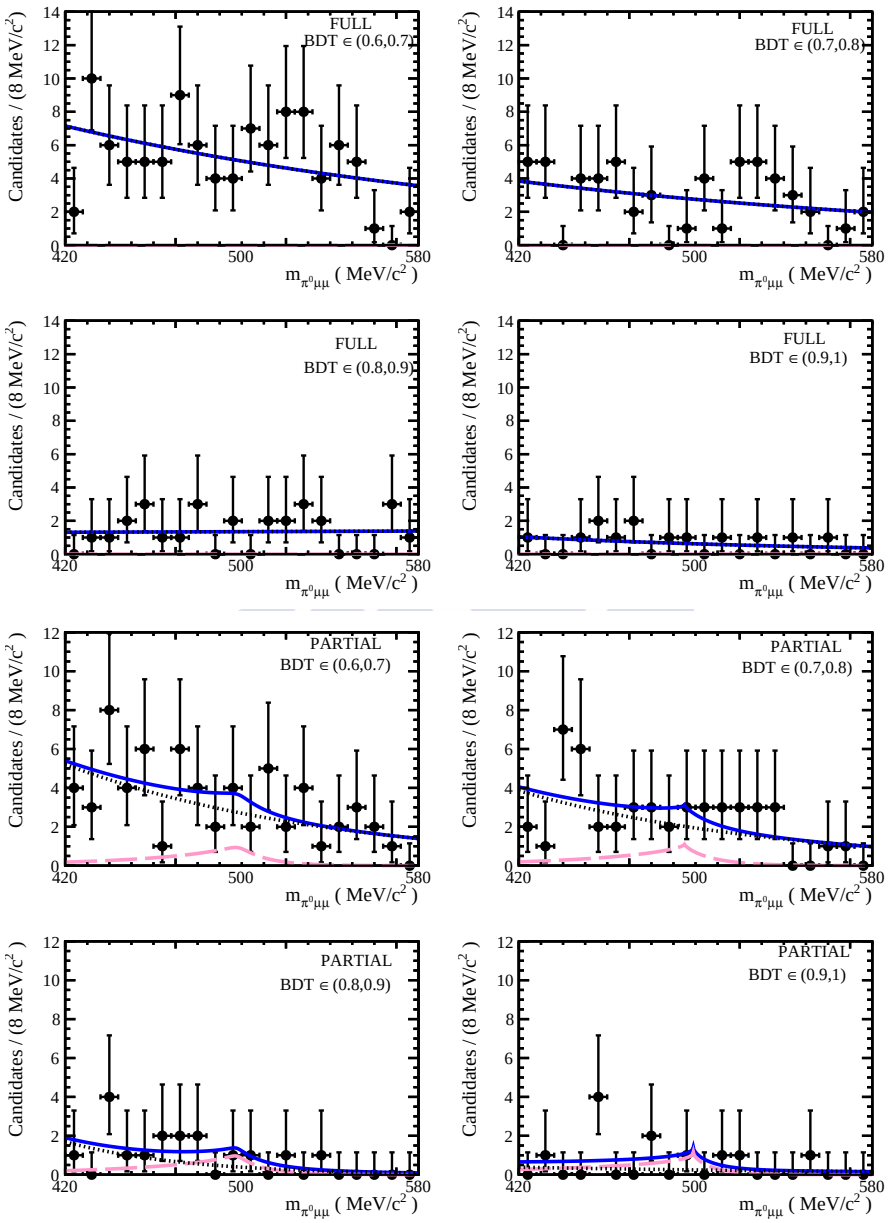

Figure 5.29: Fit to data for FULL (top) and PARTIAL (bottom) categories. The magenta dashed line shows the signal contribution, the dotted black line the background, and the solid blue line the prediction from the total fit model.

5.3.5 Expected sensitivity

The expected statistical precision on $\mathcal{B}(K^0_S \to \pi^0\mu^+\mu^-)$ for multiple values of the integrated luminosity up to 100 fb^{-1} is estimated in this section. The TIS samples used are equivalent to a 100% trigger efficiency sample with an integrated luminosity of 4.9 and 0.77 pb^{-1} for the FULL and PARTIAL samples, respectively. The expected background yield is extrapolated from the current data fit result, where the signal yield is consitent with zero, as expected given the branching fraction measured by NA48 [213]. The background yield is scaled linearly for larger integrated luminosities.

For each integrated luminosity in the studied range, sets of pseudo-experiments are generated with the above background expectations, and with a signal yield expectation of

$$N(K^0_S \to \pi^0\mu^+\mu^-) = \sigma(K^0_S)\mathcal{B}(K^0_S \to \pi^0\mu^+\mu^-)\epsilon_{K^0_S\to\pi^0\mu^+\mu^-}L, \tag{5.100}$$

where $\sigma(K^0_S)$ is the K^0_S production cross section (≈ 0.6 barn at 14 TeV), $\epsilon_{K^0_S\to\pi^0\mu^+\mu^-}$ the absolute efficiency and L the integrated luminosity. Taking the ratio of $\mathrm{N}(K^0_S \to \pi^0\mu^+\mu^-)$ with respect to $\mathrm{N}(K^0_S \to \pi^+\pi^-)$, both the cross section and the luminosity get cancelled out, leading to the formula:

$$\frac{N(K^0_S \to \pi^0\mu^+\mu^-)}{N(K^0_S \to \pi^+\pi^-)} = \frac{\mathcal{B}(K^0_S \to \pi^0\mu^+\mu^-)}{\mathcal{B}(K^0_S \to \pi^+\pi^-)}\frac{\epsilon_{K^0_S\to\pi^0\mu^+\mu^-}}{\epsilon_{K^0_S\to\pi^+\pi^-}}. \tag{5.101}$$

yielding

$$N_{sig} = \frac{\mathcal{B}(K^0_S \to \pi^0\mu^+\mu^-)}{\mathcal{B}(K^0_S \to \pi^+\pi^-)}\frac{\epsilon_{K^0_S\to\pi^0\mu^+\mu^-}}{\epsilon_{K^0_S\to\pi^+\pi^-}}N(K^0_S \to \pi^+\pi^-) \times \frac{L_{fut}}{L_{curr}}, \tag{5.102}$$

where L_{fut} and L_{curr} are the future and current luminosities, respectively. The effective current luminosity, L_{curr}, is calculated according to

$$L_{curr} = \epsilon^{TIS}_{K^0_S\to\pi^+\pi^-}L^{dat}, \tag{5.103}$$

where $\epsilon_{TIS}(K^0_S \to \pi^+\pi^-)$ is the TIS efficiency calulated using $K^0_S \to \pi^+\pi^-$ events and L^{dat} is the luminosity used for the fit to the data.

$$L^{FULL,2011}_{curr} = 0.0016 \cdot 992 \text{ pb}^{-1} = 1.59 \text{ pb}^{-1}, \tag{5.104}$$
$$L^{FULL,2012}_{curr} = 0.0016 \cdot 2037 \text{ pb}^{-1} = 3.26 \text{ pb}^{-1}, \tag{5.105}$$
$$L^{PARTIAL}_{curr} = 0.0025 \cdot 306 \text{ pb}^{-1} = 0.77 \text{ pb}^{-1}. \tag{5.106}$$

The offline signal efficiency or, equivalently, the total efficiency for a 100% efficient trigger for the FULL channel is calculated as follows:

- The generator level efficiency is estimated to be 0.361.

- The efficiency of the FULL stripping on generated events is 1.84 per mil according to the statistics produced by the DaVinci [112] filtering script, that retains the events passing the required stripping lines. This number has to be corrected by the fact that 3.3% of the events did not actually contain a signal candidate at all [9]. It also has to be corrected by the fact that some of the selected candidates are not matched to the signal. After this corrections, it becomes 1.79 per mil.

- The efficiency of the fiducial cuts and mass fit window are 0.931 and 0.922. These are applied prior to BDT training.

The offline signal efficiency (or, equivalently, the total efficiency for a 100% efficient trigger) for the PARTIAL channel is calculated as follows:

- The generator level efficiency is estimated to be 0.361.

- The efficiency of the PARTIAL stripping on generated events, calculated in the same way as above is 1.23%.

- The efficiency of the fiducial cuts and mass fit window are 0.734 and 0.917 respectively. These are applied prior to BDT training.

The models described in section 5.3.4 are fit to each pseudo-experiment with a floating $\mathcal{B}(K^0_S \to \pi^0\mu^+\mu^-)$. The background model parameters used are the ones obtained from the fit to the data section 5.3.4. The statistical uncertainties are obtained as the variations of $\mathcal{B}(K^0_S \to \pi^0\mu^+\mu^-)$ that deviate from the minimum of the log-likelihood profile by half a unit. Finally, the uncertainties are averaged across the set of pseudo-experiments for a given integrated luminosity. The uncertainties on the background extrapolation are large and translate into large uncertainties on the luminosity needed for achieving a given sensitivity.

The resulting sensitivity curves are shown in Figure 5.30. It can be seen that the analyses of both PARTIAL and FULL categories can lead to a precision better than NA48 for the LHCb upgrade if a trigger efficiency above $\approx 50\%$ can be maintained. The K^0_S production cross section increases by $\approx 20\%$ at 14 TeV compared to 8 TeV, but this increase is cancelled by a larger fraction of K^0_S decaying outside of the VELO volume. For this reason, no cross section correction has been applied to the sensitivity estimate. Studies of $K^0_S \to \pi^0\mu^+\mu^-$ and minimum bias samples simulated with the LHCb upgrade detector and conditions show that the High Level Trigger rate can be kept low enough for a 100 % efficiency.

[9] In a fraction of events, the information on how the K^0_S should decay is lost as the particle is passed to GEANT4.

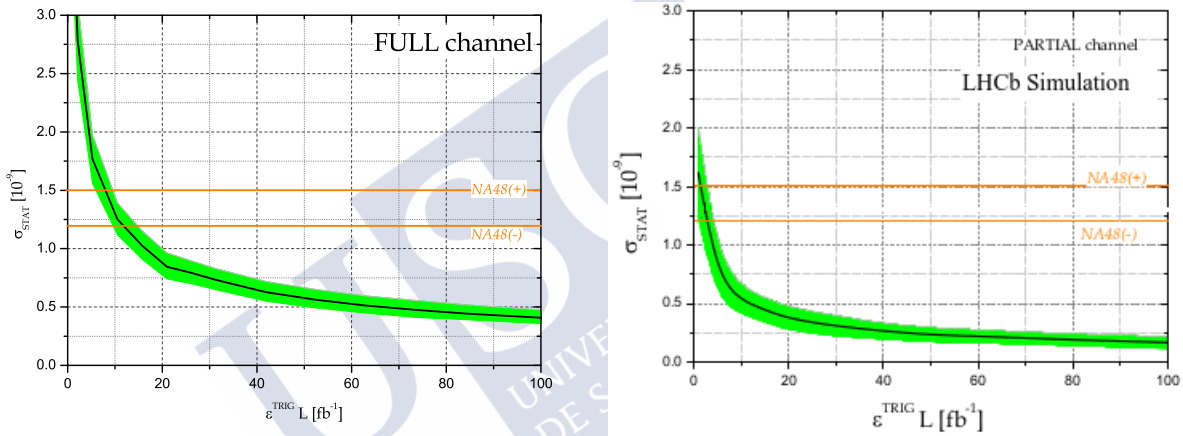

Figure 5.30: Expected precision on $\mathcal{B}(K^0_S \to \pi^0\mu^+\mu^-)$ for the FULL (top) and PARTIAL (bottom) channels, as a function of the integrated luminosity times trigger efficiency, $L \times \varepsilon^{TRIG/SEL}$.

5.3.6 Conclusions

A precise measurement of the $K^0_S \to \pi^0\mu^+\mu^-$ branching fraction is crucial for a precise $\mathcal{B}(K^0_L \to \pi^0\mu^+\mu^-)$ SM theoretical prediction and the search for physics beyond the SM in $K^0_L \to \pi^0\mu^+\mu^-$. The sensitivity of the LHCb experiment to $\mathcal{B}(K^0_S \to \pi^0\mu^+\mu^-)$ was studied based on 3 fb^{-1} of data recorded at 7 and 8 TeV center-of-mass energy during 2011 and 2012, and on 0.3 fb^{-1} of data recorded at 13 TeV center-of-mass energy during 2016. Full and partial decay reconstruction algorithms were considered, aiming at a high reconstruction efficiency. The sensitivity study was performed using pseudo-experiments by extrapolating signal yield results based on the currently available data to expected future integrated luminosities. If a trigger efficiency of at least 50% can be assured in the future, LHCb can determine $\mathcal{B}(K^0_S \to \pi^0\mu^+\mu^-)$ with a precision significantly better than that of NA48.

Chapter 6

Measurement and phenomenological studies of the CP violating phase ϕ_s

6.1 Introduction

In the SM, CP-violation originates from a single-phase in the Cabibbo-Kobayashi-Maskawa (CKM) quark-mixing matrix [222], as explained in Section 1.3. There are 3 different kinds of CP-violation for neutral mesons:

1. Direct CP-violation: originated by a difference in the magnitude of the amplitudes associated to the direct decay of the B_s^0 and $\bar{B}_s^0$ mesons into the same final state.

2. CP-violation in the $B_s^0 - \bar{B}_s^0$ oscillation, that arises when the oscillation rate from B_s^0 to $\bar{B}_s^0$ is different from the oscillation rate from $\bar{B}_s^0$ to B_s^0.

3. CP-violation in the interference between the amplitudes associated to the direct decay of a B_s^0 meson into a CP-eigenstate final state and those associated to the decay after a $B_s^0 - \bar{B}_s^0$ oscillation.

In the case of B_s^0 mesons, the third type of CP-violation is characterized by the CP-violating phase, ϕ_s, defined as:

$$\phi_s^f = -\arg(\lambda_{\rm f}),\ \lambda_{\rm f} = \eta_{\rm f}\frac{\rm q}{\rm p}\frac{\bar{\mathcal{A}}_{\rm f}}{\mathcal{A}_{\rm f}}, \tag{6.1}$$

where f is the final state, η_f is 1(-1) for CP-even(CP-odd) states, $\left|\frac{q}{p}\right|$ determines the amount of CP-violation in mixing, and $\mathcal{A}_f(\bar{\mathcal{A}}_f)$ is the amplitude of the $B_s^0(\bar{B}_s^0)$ meson decaying into the final state.

In the SM, for $b \to c\bar{c}s$ transitions and ignoring subleading penguin contributions, this phase is predicted to be $-2\beta_s$, where $\beta_s = \arg\left[-(V_{ts}V_{tb}^*)/(V_{cs}V_{cb}^*)\right]$ and V_{ij} are elements of the CKM quark flavour mixing matrix [223, 224]. The indirect determination via global fits to experimental data gives $-2\beta_s = -0.0364 \pm 0.0016$ rad [222]. This precise value

within the SM allows for NP searches in ϕ_s. In particular, new particles could contribute to the $B_s^0 - \bar{B}_s^0$ mixing diagrams [225, 226]. The Feynman diagrams for the mixing and the decay of the B_s^0 mesons are shown in Figure 6.1.

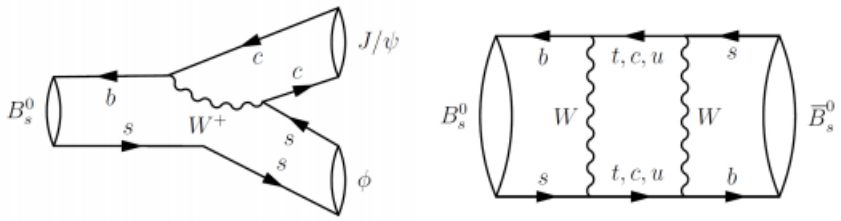

Figure 6.1: Feynman for the for the decay (left) and the $B_s^0 - \bar{B}_s^0$ mixing (right).

The experimental measurement of the weak mixing angle ϕ_s is discussed in detail in Section 6.2. A `MultiNest` scan [227] is presented in Section 6.2.12, and theoretical interpretations of this observable are reviewed in Section 6.3.

6.2 ϕ_s experimental

Various experiments have measured ϕ_s. The status after including all Run 1 results from LHCb, and all results from ATLAS, CMS, CDF and D0 is shown in Figure 6.2. Current preliminary world averages (and their correlations) for the CP violating phase ϕ_s and the decay width difference in the B_s^0 system, $\Delta\Gamma_s$, are:

$$\begin{aligned} \phi_s &= -0.021 \pm 0.031\,\text{rad} \\ \Delta\Gamma_s &= 0.085 \pm 0.006\,\text{ps}^{-1} \\ \rho(\phi_s, \Delta\Gamma_s) &= -0.0095. \end{aligned}$$

The aim of this analysis is to perform the measurement of ϕ_s in the $B_s^0 \to J/\psi K^+K^-$ channel by adding a further 2 fb^{-1} of integrated luminosity collected at 13 TeV in Run 2 of LHC in 2015 and 2016. In addition, updated measurements of the decay width difference of the light (L) and heavy (H) B_s^0 mass eigenstates, $\Delta\Gamma_s \equiv \Gamma_\text{L} - \Gamma_\text{H}$, and the ratio between the average widths in the B_s^0 and in the B_d^0 systems, Γ_s/Γ_d are presented.

6.2.1 Phenomenology

There are 4 amplitudes entering this decay, three of which come from the P-wave (dominant, corresponding to the ϕ resonance) contribution to the K^+K^- pair ($\mathcal{A}_0$, $\mathcal{A}_\perp$, $\mathcal{A}_\parallel$), and one minor contribution that comes from the S-wave ($\mathcal{A}_S$). The baseline fit is obtained assuming that direct CP violation caused by penguin diagrams is the same for all polarization states, therefore λ_f is considered to be independent of the polarization state, f. Checks were made to check this ansatz.

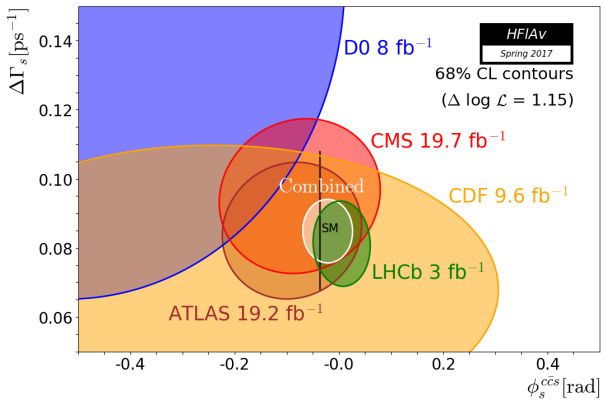

Figure 6.2: Individual 68% confidence-level contours of ATLAS, CMS, CDF, D0 and LHCb in the $(\phi_s^{c\bar{c}s}, \Delta\Gamma_s)$, their combined contour (solid line and shaded area), as well as the SM predictions (thick black rectangle) as performed by HFLAV [228].

The theoretical differential decay rate for an initial B_s^0 as a function of decay time and angles using polarization dependent $\lambda_f = |\lambda_f| e^{-i\phi_s^f} \equiv |\lambda_f| e^{-i\phi_f}$ ($f = 0, ||, \perp, \mathrm{S}$) is given by [229]

$$\frac{d^4\Gamma(t)}{dm_{KK}^2 d\cos\theta_K d\cos\theta_l d\phi} = \sum_{k=1}^{10} N_k h_k(t) f_k(\theta_K, \theta_l, \phi), \tag{6.2}$$

where N_k are normalization factors, $f_k(\theta_K, \theta_l, \phi)$ are the helicity angle-dependent functions, given in [229] and the decay-time-dependent functions $h_k(t)$ are given as

$$h_k(t) = \frac{3}{4\pi} e^{-\Gamma t} \left\{ a_k \cosh\frac{\Delta\Gamma t}{2} + b_k \sinh\frac{\Delta\Gamma t}{2} + c_k \cos(\Delta m t) + d_k \sin(\Delta m t) \right\}. \tag{6.3}$$

For an initial $\bar{B}_s^0$ at production, the signs of c_k and d_k should be reversed. The coefficients are specified in Table C.2 (Appendix C). For the purpose of reducing correlation between fit parameters, it can be chosen to fit $|\lambda_0|$, ϕ_0 and $|\frac{\lambda_f}{\lambda_0}|$, $\phi_f - \phi_0$, for $f \neq 0$.

6.2.2 Samples and event selection

In this section, the data and simulated samples used in this analysis are introduced, together with the trigger, stripping and offline selections applied to them.

6.2.2.1 Data sample

The analysis presented here uses a data sample collected at the LHCb experiment at the LHC. The dataset corresponded to a total integrated luminosity of 1.9 fb^{-1} recorded at a center-of-mass energy ($\sqrt{s}$) of 13 TeV. Of these, 0.3 fb^{-1} were taken in 2015 and 1.6 fb^{-1} were taken in 2016.

6.2.2.2 Simulation samples

In the LHCb simulation, pp collisions are generated using `Pythia` [116] with a specific LHCb configuration [230].

In order to simulate the events, the decays of hadronic particles are described by `EvtGen` [231], in which final state radiation is generated using `Photos` [232]. The `Geant4` toolkit simulates the interaction of the generated particles with the detector, and the detector response [233, 234]. Further details of the simulation process can be found in Ref. [235]. The simulated data is processed in a very similar way to the real data, with the stripping ran in flagging mode, such that the decisions are only recorded for later inspection, instead of throwing away the events that do not pass the requirements provided by the stripping line. No prescales are applied for the trigger, meaning that all the events are accepted. Sim09b was used for the simulated samples. The samples used are listed in Table C.1 (Appendix C).

Simulated signal samples are used to determine the angular acceptance. As will be discussed in Sec. 6.2.6, the samples are reweighted to match various distributions observed in data before obtaining the final acceptance. Similarly, the Λ_b^0 and the B^0 samples are used for background studies and decay time acceptance studies, respectively. This is discussed in Sec. 6.2.3 and Sec. 6.2.7, respectively. As for $B_s^0 \to J/\psi K^{*0}$ and the prompt J/ψ samples (produced in the interaction point), they are used for time resolution studies (see Sec. 6.2.5). The B^+ sample is used for tagging studies, as described in Sec. 6.2.8.

The main physics parameters used in the main simulation used in this analysis, `Eventtype = 13144011, Bs_Jpsiphi,mm=CPV,update2016,DecProdCut`, are summarized in Table 6.1. For simulated samples a momentum smearing is applied in order to reproduce better the distributions in data.

Table 6.1: Decay model parameters for the Sim09b MC sample used in this analysis, `Eventtype = 13144011, Bs_Jpsiphi,mm=CPV,update2016,DecProdCut`.

Parameter	Value
Δm_s	17.8 ps^{-1}
$\Delta\Gamma_s$	0.08543 ps^{-1}
Γ_s	0.6614 ps^{-1}
ϕ_s	-0.03 rad
$\lvert A_0(0)\rvert^2$	0.5242
$\lvert A_\parallel(0)\rvert^2$	0.2256
$\lvert A_\perp(0)\rvert^2$	0.2500
$\delta_\parallel - \delta_0$	3.26 rad
$\delta_\perp - \delta_0$	3.08 rad

6.2.2.3 Stripping selection

In this case, Stripping version 28r1 was used for 2016 data and stripping version 24r1 was used for 2015 data. All stripping versions use exactly the same selection, based on the `StrippingBetaSBs2JpsiPhiDetached` `StrippingBetaSBd2JpsiKstarDetached` and `StrippingBetaSBu2JpsiKDetached` lines in the DIMUON stream. The first line corresponds to the signal and the other two lines to control samples. The selection of particles for these lines can be found in Tables 6.2, 6.3 and 6.4 respectively. The data samples were processed using `DaVinci` version v44r4. Given that the precision on the track momentum scale is 0.03%, the momentum components of the tracks are scaled by 1.0003 (the so-called *momentum scaling*).

Table 6.2: Selection criteria used to identify $B_s^0 \to J/\psi\,\phi$ candidates.

	Variable	Stripping
all tracks	$\chi^2_{\text{track}}/\text{nDoF}$	< 3
$J/\psi \to \mu^+\mu^-$	$\Delta\ln\mathcal{L}_{\mu\pi}$ $(\mu^\pm)$	> 0
	p_T $(\mu^\pm)$	> 500 MeV/c
	χ^2_{DOCA}	< 20
	$\chi^2_{\text{vtx}}/\text{nDoF}$	< 16
	$m(\mu^+\mu^-)$	$\in [3020, 3170]\,\text{MeV}/c^2$
$\phi \to K^+K^-$	χ^2_{DOCA}	< 30
	p_T (ϕ)	> 500 MeV/c
	$m(K^+K^-)$	$\in [980, 1050]\,\text{MeV}/c^2$
	$\chi^2_{\text{vtx}}/\text{nDoF}$	< 25
	$\Delta\ln\mathcal{L}_{K\pi}$ (K^+)	> 0
$B_s^0 \to J/\psi\,\phi$	$m(J/\psi\,K^+K^-)$	$\in [5150, 5550]\text{MeV}/\text{c}^2$
	$\chi^2_{\text{vtx}}/\text{nDoF}$	< 20
	t	> 0.2 ps

For the signal, a cut on the χ^2 of all tracks is made, to ensure a good quality. Cuts on the PID variables for the muons that come from the J/ψ are also imposed, to increase the muon purity. Moreover, their reconstructed invariant mass is constrained to be within 80 MeV/c^2 from the J/ψ PDG mass. Their individual transverse momentum is required to be higher than 500 MeV/c, and a good reconstruction quality of the secondary vertex (SV) and of the muon tracks is ensured with cuts on χ^2_{DOCA} (where DOCA is the distance of closest approach) and $\chi^2_{\text{vtx}}/\text{nDoF}$, respectively. Similar cuts on the track and SV quality (even though more relaxed in this case), as well as the transverse momentum and the PID variables are applied to the kaons coming from the ϕ meson. Their reconstructed invariant mass is required to be within 40 MeV/c^2 from the ϕ PDG mas. Regarding the final combination of these particles to form a B_s^0, good reconstruction quality of the decay vertex is imposed, together with a lower cut on the decay time and a loose mass window.

For time resolution studies the stripping line `BetaSBs2JpsiPhiPrescaledLine` is used, which has the same selection as shown in Table 6.2 apart from the cut on the decay time

Table 6.3: Selection criteria used to identify $B^0 \to J/\psi\, K^*(892)^0$ candidates.

	Variable	Stripping
all tracks	$\chi^2_{\text{track}}/\text{nDoF}$	< 3
$J/\psi \to \mu^+\mu^-$	$\Delta\ln\mathcal{L}_{\mu\pi}$ $(\mu^\pm)$	> 0
	p_T $(\mu^\pm)$	> 500 MeV/c
	χ^2_{DOCA}	< 20
	$\chi^2_{\text{vtx}}/\text{nDoF}$	< 16
	$m(\mu^+\mu^-)$	$\in [3020, 3170]\,\text{MeV}/c^2$
$K^{*0} \to K^+\pi^-$	χ^2_{DOCA}	< 30
	p_T (K^*)	> 1300 MeV/c
	$m(K^+\pi^-)$	$\in [826, 966]\,\text{MeV}/c^2$
	$\chi^2_{\text{vtx}}/\text{nDoF}$	< 25
	$\Delta\ln\mathcal{L}_{K\pi}$ (K^+)	> 0
	$\Delta\ln\mathcal{L}_{K\pi}$ (π^-)	< 0
$B^0 \to J/\psi\, K^*(892)^0$	$m(J/\psi\, K^+\pi^-)$	$\in [5150, 5450]\text{MeV}/\text{c}^2$
	$\chi^2_{\text{vtx}}/\text{nDoF}$	< 20
	t	> 0.2 ps

Table 6.4: Selection criteria used to identify $B^+ \to J/\psi\, K^+$ candidates.

	Variable	Stripping
all tracks	$\chi^2_{\text{track}}/\text{nDoF}$	< 3
$J/\psi \to \mu^+\mu^-$	$\Delta\ln\mathcal{L}_{\mu\pi}$ $(\mu^\pm)$	> 0
	p_T $(\mu^\pm)$	> 500 MeV/c
	χ^2_{DOCA}	< 20
	$\chi^2_{\text{vtx}}/\text{nDoF}$	< 16
	$m(\mu^+\mu^-)$	$\in [3020, 3170]\,\text{MeV}/c^2$
K^+	p_T (K^+)	> 500 MeV/c
	$\chi^2_{\text{vtx}}/\text{nDoF}$	< 25
	$\Delta\ln\mathcal{L}_{K\pi}$ (K^+)	> 0
$B^+ \to J/\psi\, K^+$	$m(J/\psi\, K^+)$	$\in [5150, 5450]\text{MeV}/\text{c}^2$
	$\chi^2_{\text{vtx}}/\text{nDoF}$	< 10
	t	> 0.2 ps

of the B^0_s candidate.

6.2.2.4 Trigger selection

The following trigger strategy has been identified in order to retain the largest number of signal events while keeping a small number of trigger lines.

- No L0 requirements

- HLT1 selection: `Jpsi_Hlt1DiMuonHighMassDecision_TOS` or `B_Hlt1TrackMuonDecision_TOS` or `B_Hlt1TwoTrackMVADecision_TOS`. In these lines a lower limit is required on the reconstructed mass of the muons, a cut is made on the track and a MVA is trained to associate the tracks to the corresponding dimuon system.

- HLT2 selection: `Jpsi_Hlt2DiMuonDetachedJPsiDecision_TOS`, where the two muons reconstructed in the previous stage are required to be detached from the J/ψ vertex.

6.2.2.5 Corrections and additional selection requirements

Corrections are applied to the simulated samples to match the distributions obtained from data:

1. The stripped and triggered $B_s^0 \to J/\psi K^+K^-$ candidates are taken, with the B_s^0 decay time restricted to the range [0.3,15] ps.

2. The data invariant mass distribution of stripped and triggered $B_s^0 \to J/\psi K^+K^-$ candidates is fitted to obtain an sWeighted sample of data that is used in the following steps.

3. For MC, in addition to the selection mentioned before only background categories 0 (signal) and 50 (corresponding to low-mass background, mainly radiative events) with true decay time different from 0 are included

4. The simulation PID variable distributions are corrected using the `PIDCalib` package [236], a LHCb software package that is used to reweight PID variables in simulation using data control samples. Using `MCResampling`, the PID response is replaced by the one generated from calibration PDFs. Standard calibration samples for kaons and muons are used. For protons the Λ and Λ_c^+ samples are combined to cover a wider kinematic range.

5. Using the above data sample, the B_s^0 production kinematics, nTracks distribution and the muon/kaon track ghost probability variables are reweighted.

A BDT is trained with 2016 samples to further improve the signal to background ratio. Namely, the 2016 corrected simulated sample for the signal sample while 2016 data candidates in the B_s^0 mass candidate sideband region of 5450 MeV/c^2 < m(J/ψK$^+$K$^-$) < 555 0MeV/c^2 are used for the background sample. Special care was taken to avoid variables that could introduce angular or decay time efficiencies, like impact parameter χ^2 of final state particles, the direction angle of the B_s^0 (DIRA) or transverse momentum of final state particles. The figure of merit used to optimise the BDT response is given by

$$\text{FOM} = \frac{(\sum_i w_i)^2}{\sum_i w_i^2}, \tag{6.4}$$

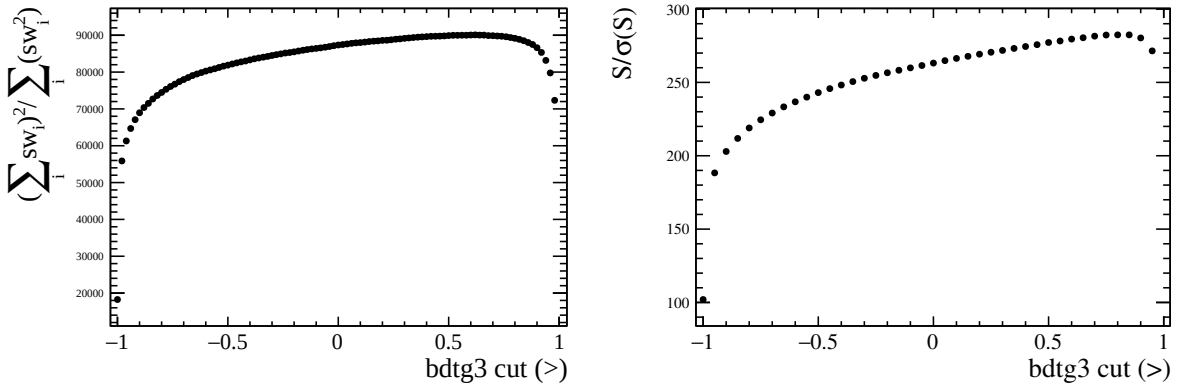

Figure 6.3: Distribution of the figure of merit used to optimise the cut on the BDT response (left) and distribution of signal yield divided by its uncertainty (right).

where the index i runs over all candidates in the sample and w_i are per-candidate weights that are determined from the invariant mass fit that is performed at each point in the scan over the BDT response. Figure 6.3 shows on the left how the figure of merit performs and on the right the number of signal events divided by its uncertainty, both as a function of the BDT response. A similar distribution is observed. The optimal value is found to be at > 0.58. After the BDT requirement has been applied there are approximately 102 000 signal candidates and 26 000 background candidates in the mass window of the fit, $[5320,\ 5420]$ MeV/c^2, in 2016 data. The signal to background ratio is ~ 3.9. The mass fit used to determine sweights to statistically remove this background and also the removal of peaking backgrounds for both 2015 and 2016 data samples is described in detail in the next subsection.

6.2.3 Mass fit and computation of signal sWeights

The physics parameters of interest are extracted via a log-likelihood fit of the signal PDF to the unbinned decay time and angular distributions. The events are first weighted to statistically subtract the background components using the *sPlot* method [237] with $m(J/\psi K^+K^-)$ as the discriminating variable.

In order to have an improved resolution, the $m(J/\psi K^+K^-)$ is determined using both the J/ψ mass and PV constraints. The background sources that are considered consist in:

- $B^0 \to J/\psi K^{*0}$ peaking background, vetoed using PID cuts.
- $\Lambda_b^0 \to J/\psi p K^-$ peaking background, vetoed using PID cuts. The remaining events (1190 ± 83(stat.) $\pm$ 68(syst.) in 2016 and 242 ± 37(stat.) $\pm$ 33(syst.) in 2015, $\sim 1.2\%$ of the signal) are statistically subtracted by injecting simulated events into the data tuple with a negative sum of weights equal to the expected number of events.

- $B^0 \to J/\psi K^+K^-$ peaking background, modelled with a Gaussian in the nominal mass fit.

The combinatorial background is modelled with an exponential function and the signal distribution with a double-sided *Crystal Ball* (CB) function. The double-sided CB function uses the per-event mass error as conditional observable, so that the correlation between $\cos\theta_\mu$ and mass resolution is taken into account. The full *p.d.f* is the following:

$$p(m(J/\psi K^+K^-)|\sigma_i) = N_{sig}CB(m(J/\psi K^+K^-); \mu, \alpha_1, \alpha_2, n_1, n_2, s_1, s_2|\sigma_i) \\ + N_{bkg}((1 - f_{B_d})e^{-\gamma_b m(J/\psi K^+K^-)} + f_{B_d}Gauss(m(J/\psi K^+K^-); \mu_{B_d}, \sigma_{B_d})),$$

where N_{sig} and N_{bkg} are the number of signal and background events correspondingly, μ is the mean of the distribution, s_1 and s_2 are the scale factors, which accounts for underestimation of the per-event mass error, $\alpha_1, \alpha_2, n_1, n_2$ are the tail parameters and γ_b is the coefficient in the exponential to describe the background.

For the fit to the $m(J/\psi K^+K^-)$ distribution, the sample is divided into twenty-four subsamples, each with an independent signal fraction and different signal mass shapes. The subsamples correspond to six bins in the K^+K^- mass, namely [990, 1008, 1016, 1020, 1024, 1032, 1050] MeV/c^2, two trigger categories:

- **"Biased"**: `B_Hlt1TrackMuonDecision_TOS` or `B_Hlt1TwoTrackMVADecision_TOS` and not `Jpsi_Hlt1DiMuonHighMassDecision_TOS`
- **"Unbiased"**: `Jpsi_Hlt1DiMuonHighMassDecision_TOS`

and two years of the data-taking (2015 and 2016). The fit results for 2016 are shown in Figures 6.5 and 6.4.

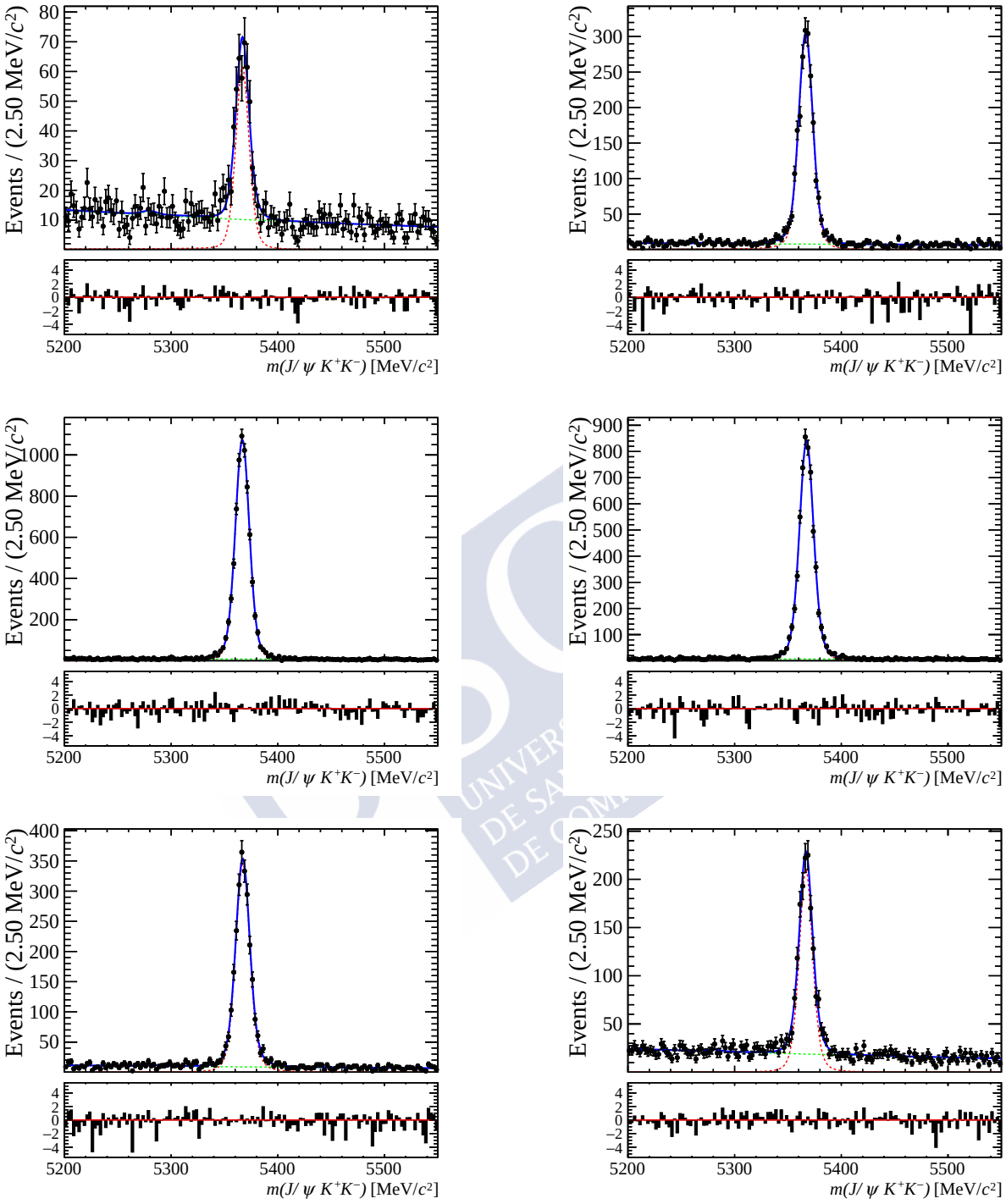

Figure 6.4: Fit to the $m(J/\psi K^+K^-)$ distribution in biased 2016 sample (solid blue line) and pull plot using a Crystal Ball shape for the signal (dashed blue line) and an exponential distribution for the background (dashed green line). The $m(J/\psi K^+K^-)$ distribution is divided into six bins in m_{KK}, from upper left to lower right: [990, 1008, 1016, 1020, 1024, 1032, 1050] MeV/c^2.

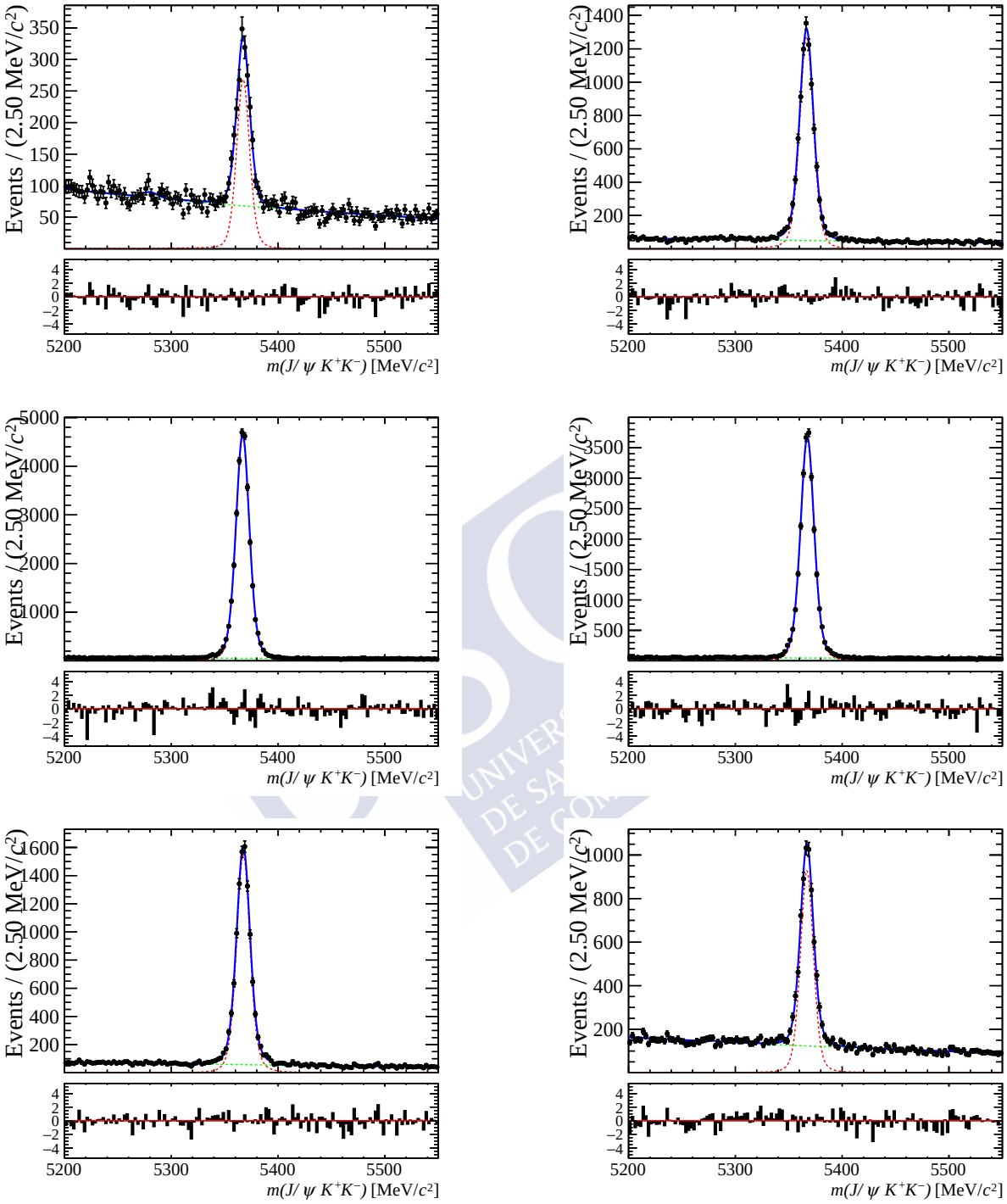

Figure 6.5: Fit to the $m(J/\psi K^+K^-)$ distribution in unbiased 2016 sample (solid blue line) and pull plot using a Crystal Ball shape for the signal (dashed blue line) and an exponential distribution for the background (dashed green line). The $m(J/\psi K^+K^-)$ distribution is divided into six bins in m_{KK}, from upper left to lower right: [990, 1008, 1016, 1020, 1024, 1032, 1050] MeV/c^2.

The event multipliciy, defined as ratio between the number of events containing more than one candidate and the total number of events is found to be 1.2% in the full B_s^0 mass region, but only 0.2% for candidates in the signal region. Most of these candidates are due to cases where the J/ψ is shared and one or two different kaons are added, making these events truly combinatorial in character. Since the fraction of multiple events is quite small we will evaluate a systematic contribution removing them randomly if they fulfill a certain "clone" criteria, that is, if their final state tracks are at most separated by an angle of 5 mrad.

6.2.4 $C_{\rm SP}$ factors

The relative change of the S-wave m_{KK} line shape with respect to that of the P-wave has to be considered in the interference terms of the angular expressions, as the analysis is being performed in finite m_{KK} bins (see Ref. [238] for a detailed discussion). This is taken into account by adding a multiplicative correction factor, $C_{\rm SP}$, to the signal PDF, namely to the S-P-wave interference terms with $k = 8, 9, 10$ in Eq. 6.2, i.e. $N_k \to C_{{\rm SP},i} N_k$. There are in total six $C_{\rm SP}$ factors, one for each m_{KK} bin.

The line shapes of the P and S wave are denoted as $p(m_{KK})$ and $s(m_{KK})$, respectively, where both are normalised to unity over a range $[m^L_{KK}, m^U_{KK}]$. It has to be accounted for the fact that $\langle p \times s^* \rangle \neq \langle p \rangle \times \langle s^* \rangle$ in each m_{KK} bin. Therefore, the product $p \times s^*$ is integrated, as it appears in the interference terms between the P and S wave. This yields

$$\frac{\int_{m^L_{KK}}^{m^H_{KK}} p \times s^* \; dm_{KK}}{\sqrt{\int_{m^L_{KK}}^{m^H_{KK}} |p|^2 \; dm_{KK} \int_{m^L_{KK}}^{m^H_{KK}} |s|^2 \; dm_{KK}}} = C_{\rm SP} e^{-i\theta_{\rm SP}}, \tag{6.5}$$

where $C_{\rm SP}$ is the correction factor and the phase $\theta_{\rm SP}$ is absorbed in the measurement of the S-wave strong phase. The P-wave and S-wave are assumed to be a ϕ and an f_0 resonances. Their lineshapes, $L(m_{KK})$, are constructed following the approach of [239], and are given by:

$$L(m_{KK}) = \sqrt{P_B P_R} F^{(L_B)} F^{(L_R)} A_R(m_{KK}) \left(\frac{P_B}{m_B}\right)^{L_B} \left(\frac{P_R}{m_{KK}}\right)^{L_R} \tag{6.6}$$

where

- P_B is the J/ψ momentum in the B_s^0 rest frame
- P_R is the momentum of either of the two kaons in the dikaon rest frame
- m_B is the PDG mass of the B_s^0
- m_{KK} is the pole mass of the dikaon resonance, with $m_{KK} = 0.9499$ GeV/c^2 for the f_0 as measured in the the $B_s^0 \to J/\psi \pi^+ \pi^-$ measurement [240], and $m_{KK} = 1.0195$ GeV/c^2 for the ϕ [59]

- L_B is the orbital angular momentm between the J/ψ and the dikaon system, such tat $L_B = 1$ for f_0 and $L_B = 0$ for ϕ
- L_R is the orbital momentum of the dikaon resonance (its spin): $L_R = 0$ for f_0 and $L_R = 1$ for ϕ
- $F^{(L_B)}$ and $F^{(L_R)}$ are the Blatt-Weisskopf barrier factors of the B_s^0 and dikaon resonances
- $A_R(m_{KK})$ is the mass-squared shape of the dikaon resonance - a Flatté distribution [241] for the f_0 and a Breit-Wigner [242] for the ϕ.

The phase space factor $\sqrt{P_B P_R}$ results from converting the phase space of the natural Dalitz plot variables $m^2(KK)$ and $m^2(J/\psi K)$ to that of $m(KK)$ and $\cos\theta_K$. The factors $\left(\frac{P_B}{m_B}\right)^{L_B}$ and $\left(\frac{P_R}{m_{KK}}\right)^{L_R}$ are the B_s^0 decay momentum and KK birth momentum.

The detector resolution effect on the $C_{\rm SP}$ factors needs to be taken into account. While Eq. 6.5 is defined in dependence on the true m_{KK}, the mass bins are defined in dependence on the measured m_{KK}. The resolution effect can be incorporated as an efficiency correction, $\epsilon_i(m_{KK})$, of the $C_{\rm SP}$ factors according to

$$C_{SP}e^{-i\theta_{SP}} = \frac{\int_{2m_K}^{m_{B_s^0}-m_{J/\psi}} p \times s^* \times \epsilon(m_{KK})\ dm_{KK}}{\sqrt{\int_{2m_K}^{m_{B_s^0}-m_{J/\psi}} |p|^2 \times \epsilon(m_{KK})\ dm_{KK} \int_{2m_K}^{m_{B_s^0}-m_{J/\psi}} |s|^2 \times \epsilon(m_{KK})\ dm_{KK}}}, \quad (6.7)$$

where $\epsilon(m_{KK})$ is

$$\epsilon(m_{KK}) = \begin{cases} 1, \text{ if } m_L < m_{KK} < m_H \\ 0 \text{ otherwise.} \end{cases}, \quad (6.8)$$

in the case where the bins are made in the true m_{KK} mass (or equivalently, have perfect resolution). Since the cut is applied on a measured mass that has a finite resolution, and hence $\epsilon_i(m_{KK})$ will have a non-trivial structure. Note that in this definition events in the true m_{KK} spectrum up to 2.27 GeV/c^2 should be considered, which is the value of $m_{B_s^0} - m_{J/\psi}$. However, the ϕ contribution after a certain point in m_{KK} is too small to be modelled well in MC, so an upper limit cut at 1.06 GeV/c^2 is applied. Simulated events from the 2016 MC sample are used with and without S wave (see Table C.1) to determine $\epsilon_i(m_{KK})$, as well as events produced with a standalone version of `EvtGen` with the same parameter inputs as the models used for LHCb MC. The reason to use it is the enhanced statistics, especially in the tails of the m_{KK} distribution.

In each KK bin the ratio is built dividing the entries from the full LHCb MC by the entries from the standalone MC. The full LHCb MC contains truth-matched B_s^0 candidates, and the reconstructed mass is required to be within the limits of the corresponding bin. Figure 6.6 shows the corresponding distributions. The $C_{\rm SP}$ obtained from the MC without S wave are used with exception of the first bin, where the MC with S wave is used. The reason for this is that in the region of m_{KK}, the contribution of the S wave is the largest and the MC with S wave has more events. With this, the $C_{\rm SP}$ factors shown in Table 6.5 are obtained.

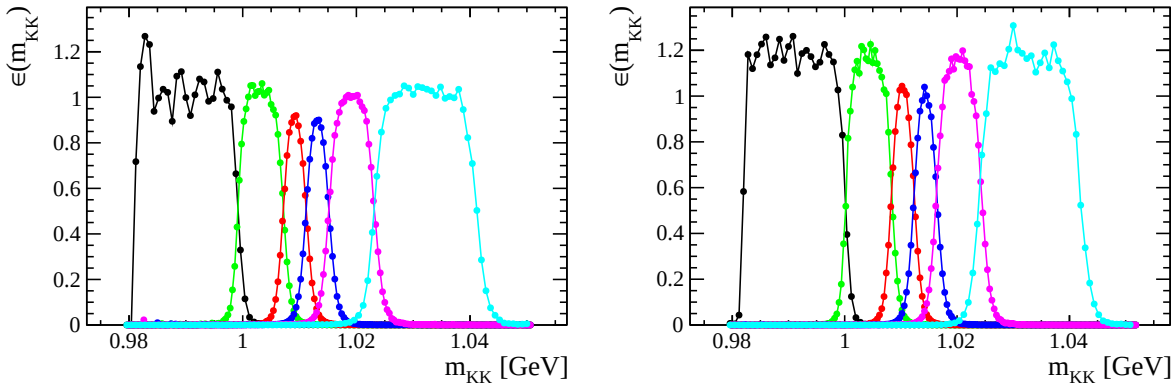

Figure 6.6: Efficiency of each m_{KK} bin selection as a function of MC true m_{KK} using MC without (left) and with (right) S wave.

Table 6.5: C_{SP} factors obtained using Eq. (6.7). The ϕ resonance is parametrized with a relativistic Breit-Wigner.

	S-wave line shape
m_{KK} bin	f_0
1	0.8463
2	0.8756
3	0.8478
4	0.8833
5	0.9415
6	0.9756

6.2.5 Decay time resolution

An effective single-Gaussian model is used to parametrize the decay time resolution. This is sufficient to describe the damping effect of the time resolution. It is defined as follows,

$$\mathcal{P}(t) = \mathcal{R}(t) \otimes \left[f_{\mathrm{prompt}} \delta(t) + f_{\mathrm{ll}} \left(f_{\mathrm{sl}} e^{-t/\tau_s} + (1 - f_{\mathrm{sl}}) e^{-t/\tau_l} \right) \right] + f_{\mathrm{wpv}} W(t), \tag{6.9}$$

where t is the decay time, δ_t the decay time uncertainty, f, f_{ll}, f_{sl} and f_{wpv} the fraction of events that are prompt J/ψ candidates, long-lived candidates, long-lived background with the smaller lifetime, and candidates which have been incorrectly associated to a PV, respectively, and τ_s, τ_l the corresponding short-lived, long-lived lifetimes. This model is fitted to t in ten bins of δ_t, and consists of a Dirac-delta function and two exponential

functions convolved with

$$\mathcal{R}(t) \propto \sum_{i=1}^{3} f_i \frac{1}{\sqrt{2\pi}\sigma_i} e^{-\frac{1}{2}\left(\frac{t-\mu}{\sigma_i}\right)^2}, \tag{6.10}$$

where $\sum_i f_i = 1$. The three Gaussians have a common mean, different widths and two relative fractions, which are allowed to vary in the fit, as are the lifetime and relative fractions of the exponential functions. Another component corresponding to events with a wrongly-associated PV is added, the fraction of which is allowed to float in the fit. In each bin of δ_t, the dilution of the triple Gaussian model is computed as,

$$D = \sum_{i=1}^{3} f_i e^{-\sigma_i^2 \Delta m_s^2/2}, \tag{6.11}$$

and the effective single Gaussian width as,

$$\sigma_{\text{eff}} = \sqrt{(-2/\Delta m_s^2) \ln D}, \tag{6.12}$$

where $\Delta m_s = 17.77\text{ps}^{-1}$. This converts the resolution into a single-Gaussian function with an effective resolution that causes the same damping effect on the magnitude of the B_s^0 oscillation.

In order to perform the calibration for the time resolution, three calibrations are determined from signal, prompt MC and prompt data. Afterwards, the same correction as in MC is applied from prompt data to signal data. For each case, a linear or quadratic calibration curve is fitted to the variation of the effective resolution as a function of $\langle \delta_t \rangle$ to determine the calibration parameters.

Simulated $B_s^0 \to J/\psi\phi$ events are first used, fitting the difference between the reconstructed and true decay time, $t_{\text{reco}} - t_{\text{true}}$ in bins of δ_t. The resolution model is a sum of three Gaussian functions, and the effective single Gaussian width is assumed to vary quadratically with δ_t:

$$\sigma_{\text{eff}}(\delta_t) = p_0 + p_1 \langle \delta_t \rangle + p_2 \left\langle \delta_t^2 \right\rangle \tag{6.13}$$

where $p_0 = 0.00797 \pm 0.00015$ ps, $p_1 = 0.7468 \pm 0.0082$ and $p_2 = 2.988 \pm 0.11$ ps^{-1}, corresponding to $\sigma_{\text{eff}} = 41.62 \pm 0.04 \pm 0.02$, where first uncertainty is statistical from the size of the sample and the second from the uncertainties on the calibration parameters. No wrong-PV component is included.

A simulated sample of inclusive J/ψ events is used to measure the resolution calibration parameters. As before, no wrong-PV component is incuded in the fit (to ensure proper behaviour for the fit) and a quadratic dependence of σ_{eff} with δ_t is considered. The calibration parameters in this case are $p_0 = 0.00540 \pm 0.00094$ ps, $p_1 = 0.885 \pm 0.04$ and $p_2 = 0.56 \pm 0.43$ ps^{-1}, corresponding to $\sigma_{\text{eff}} = 40.46 \pm 0.04 \pm 0.09$. The difference with respect to the results from the simulated $B_s^0 \to J/\psi\phi$ sample (2.8%) is taken as the systematic uncertainty from translating the resolution from the prompt sample to the signal sample.

A third calibration is made using the prompt J/ψ data sample, selected in the same way as the signal data sample, but without any requirement on the decay time of the $J/\psi K^+K^-$ candidates. Assuming a linear dependence, $\sigma_{\rm eff}(\delta_t) = p_0 + p_1 \langle\delta_t\rangle$, the calibration parameters for $B_s^0 \to J/\psi\phi$ are obtained, $p_0 = 0.01297 \pm 0.00022$ ps, $p_1 = 0.8446 \pm 0.0057$, corresponding to:

$$\sigma_{\rm eff} = 45.54 \pm 0.04 \pm 0.05 \text{ fs}. \tag{6.14}$$

Again, the first uncertainty is statistical from the size of the $B_s^0 \to J/\psi\phi$ data sample and the second from the uncertainties on the calibration parameters. The main source of systematic uncertainty in the calibration of the decay time resolution model is the translation from the prompt background sample to the signal sample. This is computed as the difference between the resuls obtained using the simulated inclusive J/ψ sample and those using the simulated signal sample. In addition, there are three other systematic sources, due to the choice to include or not the wrong-PV component, setting the mean of the Gaussian to zero and varying the parameters within their uncertainties, taking into account the correlation between them.

6.2.6 Angular acceptance

The angular acceptance is modelled using *normalization weights* (see Ref. [243], Sec. 3.3) obtained from fully simulated signal events from the Sim09b production. This simulation sample is iteratively weighted to match the distributions of final-state particle kinematics in the real data, as well as to match the physics parameters obtained from data, in order to correct for imperfections in the detector simulation. In order to do this, a GB reweighting is first applied in $p(B_s^0)$, $p_T(B_s^0)$ and $m(K^+K^-)$, together with a reweighting in $p(K^\pm)$, $p_T(K^\pm)$ so as to correct for a mismodeled acceptance in MC. The angular normalizations are computed, and the process is repeated until convergence is achieved after 4 iterations.

A total of 10 normalization weights are computed for each year and trigger category, as indicated in table 6.6, where the combined weights are shown. The factorization of angular acceptance and decay time acceptance is assumed. A systematic effect is assigned to this assumption, comparing the final acceptance normalization weights obtained in six equal populated decay time bins. A cross-check has been performed using a sample of $B^+ \to J/\psi K^+$ decays in 2016 data, yielding a good consistency in the method.

6.2.7 Decay time acceptance

The reconstruction efficiency is not constant as a function of the B_s^0 decay time due to displacement requirements made on signal tracks in the trigger and event selection and to a decay-time-dependent efficiency to reconstruct the tracks in the VELO [244]. The overall decay-time acceptance is determined using the control channel $B^0 \to J/\psi K^*(892)^0$, with $K^*(892)^0 \to K^+\pi^-$, which is kinematically very similar to the signal decay and it is assumed to have a purely exponential decay-time distribution with a well-known lifetime (i.e. the width difference $\Delta\Gamma_d$ is ignored), namely 1.520 ± 0.004 ps [245]. The strategy

Table 6.6: Angular acceptance weights determined from all available Monte Carlo samples. The f_k are the normalizations of the angular functions (see Equation 6.2) including the acceptance. They are used in the normalization of the *p.d.f.*

k		f_k/f_1			
		2015		2016	
		"Unbiased trigger"	"Biased" trigger	"Unbiased trigger"	"Biased trigger"
1	(00)	1 ± 0	1 ± 0	1 ± 0	1 ± 0
2	($\parallel\parallel$)	1.0435 ± 0.0020	1.0452 ± 0.0039	1.03800 ± 0.00070	1.0370 ± 0.0015
3	($\perp\perp$)	1.0439 ± 0.0020	1.0451 ± 0.0038	1.03776 ± 0.00069	1.0371 ± 0.0015
4	($\parallel\perp$)	-0.0024 ± 0.0016	-0.0100 ± 0.0032	-0.00082 ± 0.00055	0.0027 ± 0.0012
5	(0 $\parallel$)	-0.00132 ± 0.00096	0.0035 ± 0.0018	0.00023 ± 0.00033	0.00307 ± 0.00072
6	(0 $\perp$)	0.00121 ± 0.00094	0.0020 ± 0.0019	0.00025 ± 0.00033	-0.00022 ± 0.00072
7	(SS)	1.0155 ± 0.0014	1.0259 ± 0.0027	1.01034 ± 0.00047	1.0220 ± 0.0011
8	(S$\parallel$)	-0.0018 ± 0.0012	-0.0040 ± 0.0024	0.00009 ± 0.00042	0.00029 ± 0.00093
9	(S$\perp$)	0.0013 ± 0.0012	-0.0010 ± 0.0025	0.00008 ± 0.00043	0.00005 ± 0.00094
10	(S0)	-0.0189 ± 0.0026	-0.0375 ± 0.0050	-0.00240 ± 0.00089	0.0026 ± 0.0019

to select $B^0 \to J/\psi K^*(892)^0$ events and compute the sWeights is similar to the one used for $B_s^0 \to J/\psi K^+K^-$ events. The $K^+\pi^-$ system in the $B^0 \to J/\psi K^+\pi^-$ decay can be in a relative S-wave or P-wave configuration. About 6% S-wave presence has been observed in data, as described in [246]. However, the simulated $B^0 \to J/\psi K^*(892)^0$ sample only includes the P-wave component. To account for this, an iterative procedure similar to the one described in Section 6.2.6 is applied, reweigthing the simulation to match the B^0 p and p_T, as well as $m(K^+\pi^-)$ distributions in data.

The decay time acceptance is defined as

$$\varepsilon_{\text{data}}^{B_s^0}(t) = \varepsilon_{\text{data}}^{B^0}(t) \times \frac{\varepsilon_{\text{sim}}^{B_s^0}(t)}{\varepsilon_{\text{sim}}^{B^0}(t)}, \tag{6.15}$$

where $\varepsilon_{\text{data}}^{B^0}(t)$ is the efficiency in data of the fully triggered, selected and sweighted events in the B^0 control channel and $\varepsilon_{\text{sim}}^{B_s^0}(t)/\varepsilon_{\text{sim}}^{B^0}(t)$ is the ratio of efficiencies of the simulated signal and control modes after the full trigger, selection and MC-data correction chain has been applied. This second term in the acceptance accounts for the small differences in the lifetime and kinematics between the signal and control modes. The MC events are reweighted to match the *p.d.f.* of the respective data.

To derive $\varepsilon_{\text{data}}^{B_s^0}(t)$ a simultaneous fit is performed to both the simulation samples and the data control channel. This allows to have the overall uncertainties on the B_s^0 data spline coefficients, thus providing an easier control on the associated systematic uncertainty. The decay time acceptance $\varepsilon_{\text{data}}^{B_s^0}(t)$ is then used in the fit to the B_s^0 data signal sample to determine the physics parameters.

For the B^0 and B_s^0 the model used for the fit is composed of the product of a single exponential, convolved with a single Gaussian resolution, and the respective acceptance

function. The latter is modelled using cubic splines with knots at [0.3, 0.58, 0.91, 1.35, 1.96, 3.01,7.00] ps and the first coefficient is fixed to unity. The knot positions have been chosen according to an exponential distribution between [0.3,15] ps in order to have six equally populated bins considering $\Gamma = 0.66$ ps. The last knot position is moved from 15 ps to 7 ps in order to have stable fits also for the trigger-year categories which have no decay candidates at these large decay times. The acceptance in the last bin is modelled using a linear extrapolation.

In order to obtain a single spline, $s^{B^0_s}_{data}$, that represents $\varepsilon^{B^0_s}_{\text{data}}(t)$, combinations of the following three splines are used to describe the acceptance of the three datasets:

- One spline representing the acceptance in B^0_s MC: $s^{B^0_s}_{sim}$
- One spline representing the ratio of acceptances in B^0 and B^0_s MC: $s^{B^0/B^0_s}_{sim}$
- One spline representing the final acceptance in B^0_s data: $s^{B^0_s}_{data}$.

These splines are used in the following combinations to describe the acceptances for the three datasets:

- B^0_s MC: $s^{B^0_s}_{sim}$
- B^0 MC: $s^{B^0/B^0_s}_{sim} \times s^{B^0_s}_{sim}$
- B^0 data: $s^{B^0_s}_{data} \times s^{B^0/B^0_s}_{sim}$

A single Gaussian models the resolution, and has a mean of 0ps and a width of 42fs/39fs/42fs for B^0_s MC/B^0 MC/B^0 data, motivated by the studies in Section 6.2.5 and the difference of the resolution between B^0_s and B^0 seen in truth matched MC. The lifetime in the fit is fixed to the World average value for data $\tau^{\text{data}}_{B^0} = 1.520\,\text{ps}$ [245], and to the value used in the generation of the MC for the simulated samples, namely $\tau^{\text{MC}}_{B^0} = 1.519\,\text{ps}$ and $\tau^{\text{MC}}_{B^0_s} = 1.512\,\text{ps}$.

The decay time acceptance is obtained separately for the data taking periods 2015 and 2016 and two different trigger paths ("unbiased" and "exclusively biased"). Figure 6.7 shows the corresponding acceptance for both data-taking years and trigger categories.

The lifetimes $\tau(B^0)$ and $\tau(B^+)$ in $B^0 \to J/\psi K^{*0}$ and $B^+ \to J/\psi K^+$ decays are measured as a crosscheck of the time acceptance procedure. Samples of 2016 data and simulation for both validation channels are used. The same procedure as for $B^0_s \to J/\psi\phi$ is used, including the spline knot positions and time resolution.

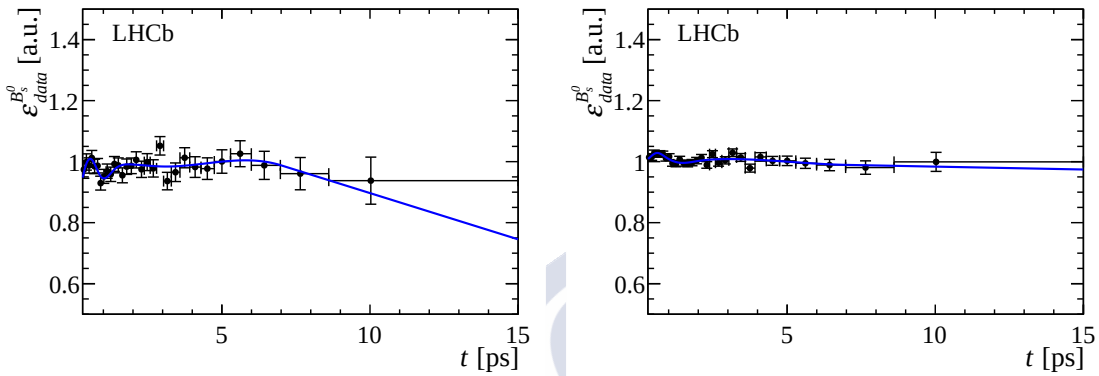

(a) Final B_s^0 acceptance 2015

(b) Final B_s^0 acceptance 2016

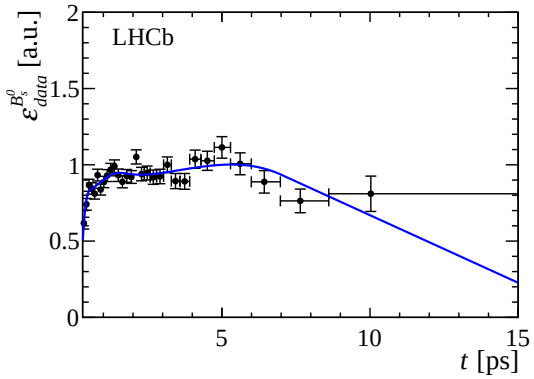

(c) Final B_s^0 acceptance 2015

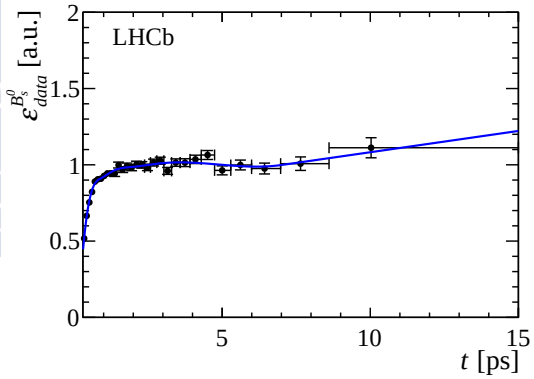

(d) Final B_s^0 acceptance 2016

Figure 6.7: The blue lines show the respective efficiency (combinations) modelled using either a single cubic spline or products of cubic splines. In black, the according histogram acceptances are shown. Data with the "unbiased" ("biased") trigger is used in the top (bottom).

6.2.7.1 Measurement of $\tau(B^0)$

The procedure to determine the decay time efficiency (Section 6.2.7) is validated by splitting the $B^0 \to J/\psi K^{*0}$ control sample, both data and simulation, into two independent sets. One half of the sample is then used as a control while the other is used to measure $\tau(B^0)$. Three different criteria are considered for this, namely:

- Splitting according to odd/even eventNumber in the original sample. This sets a baseline and validates the general implementation.
- A *random* splitting, according to odd/even eventNumber in the original sample, where the sample that is used instead of B_s^0 has a cut on $\sigma_t < 0.04$ ps to better mimic the $B_s^0 \to J/\psi\phi$ sample.
- Splitting according to odd/even eventNumber in the original sample, where the sample that is used for fitting has a cut on the opening angle between the kaon and the pion that come from the K^{*0}, angle < 0.025 rad. The position of the cut is chosen such that the average of the opening angle distribution is close to the corresponding one for the $B_s^0 \to J/\psi\phi$ sample.
- A splitting on the K^{*0} mass, to see if there is a dependence on its value: events with $m(K^{*0}) < 890$ GeV/c^2 are used for fitting, events with $m(K^{*0}) > 890$ GeV/c^2 are used as control sample.

For the control samples, the B^0 lifetime is fixed to its input for simulation (1.519 ps) and to the world average value for data (1.520 ps) [245]. The values that are obtained are listed in the first column of Table 6.7, where the deviation from the input value of the control sample is also shown. The spline coefficients of the time acceptance are constrained to the values obtained from the control samples using the respective covariance matrix. To further improve these results, the same corrections that are applied to the baseline are applied to the control samples. The corresponding values for the lifetime (second column of Table 6.7) show a better agreement with the input value. The fits to the decay time distributions with all corrections for the different splittings are shown in Figure 6.8.

Table 6.7: Values of $\tau(B^0)$ obtained for validation of the time acceptance method for the different considered splittings, with (first column) and without corrections (second column).

Splitting	No corrections	With corrections
Only by event number	1.513 ± 0.006 ps (1.2σ,0.44%)	-
$\delta_t < 0.04$ ps	1.489 ± 0.006 ps (4.9σ,2.1%)	1.507 ± 0.007 ps (2.0σ,0.90%)
angle < 0.025 rad	1.507 ± 0.007 ps (1.8σ,0.84%)	1.511 ± 0.008 ps (1.3σ,0.63%)
$m(K^{*0})$	1.522 ± 0.006 ps (0.32σ,0.01%)	1.523 ± 0.006 ps (0.54σ,0.02%)

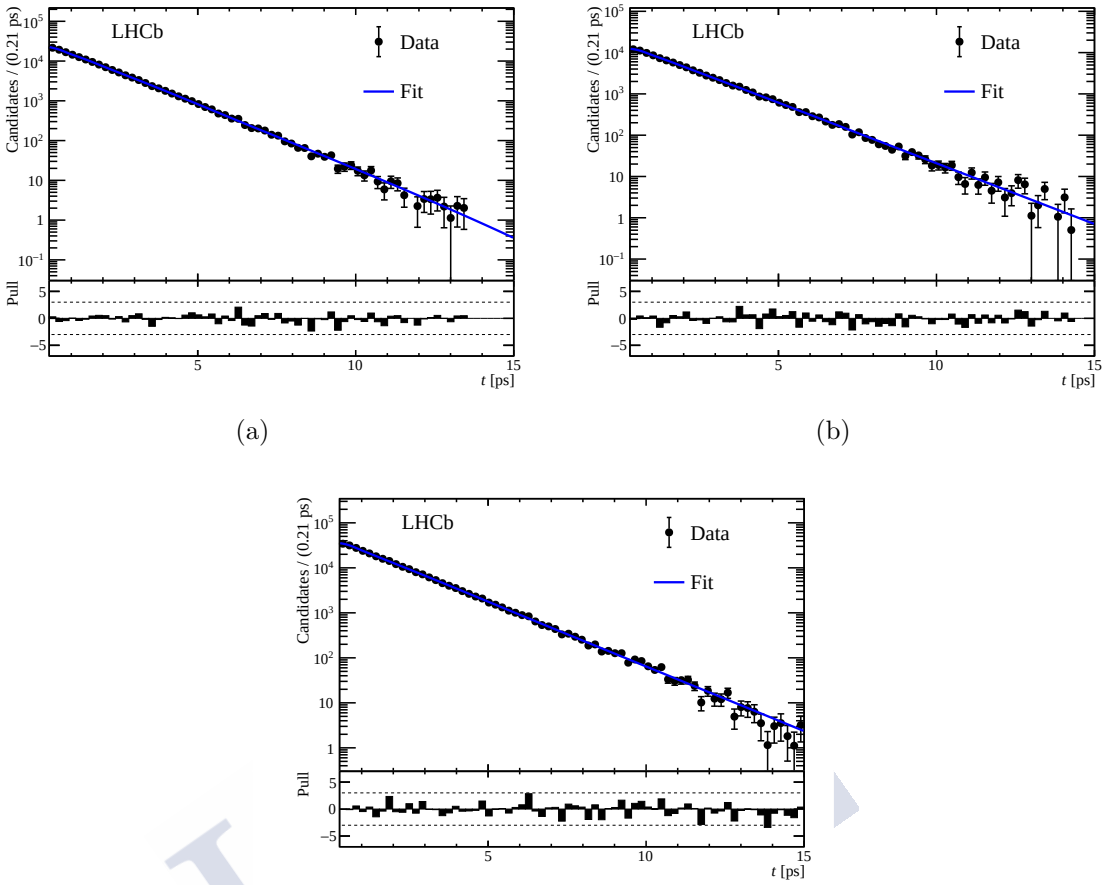

Figure 6.8: Decay time distribution of $B^0 \to J/\psi K^{*0}$ decays and the corresponding likelihood fit result, splitting according to eventNumber with $\sigma_t < 0.04$ ps (a) and angle < 0.025 rad (b), and splitting according to $m(K^{*0})$ (c). All corrections in analogy to the baseline time acceptance are applied.

6.2.7.2 Measurement of $\tau(B^+)$

In this case the decay time acceptance for $B^+ \to J/\psi K^+$ is calculated using $B^0 \to J/\psi K^{*0}$ as control channel. For each sample ((B^0,B^+) $\times$ (data, simulation)), the decay time distribution is fitted using a exponential with a resolution of 44 fs. The respective acceptance function is modelled using a spline with knots fixed to the same values as the ones used for $B_s^0 \to J/\psi\phi$, but whose coefficients are determined from the fit. The B^0 and B^+ lifetimes are fixed to their MC inputs, 1.519 ps and 1.638 ps, respectively, for simulation, and to the world average for B^0 data, 1.520 ps [245].

It is obtained $\tau(B^+)/\tau(B^0) = 1.0783 \pm 0.0024$, which deviates from the world average [245], $\tau(B^+)/\tau(B^0)_{\rm PDG}) = 1.076 \pm 0.004$, by less than 0.5σ (0.2%). Note that the fit uncertainty on the lifetime does include the uncertainty from the spline coefficients that

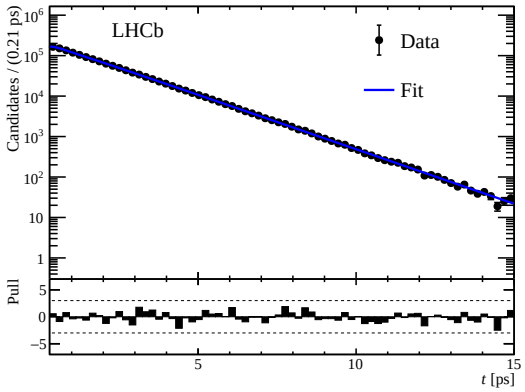

Figure 6.9: Fit to the B^+ decay time distribution in data.

are determined from the other data/MC control samples and subsequently constrained in the fit to the B^+ data sample. When applying the same corrections to the control samples as in the baseline analysis, except for the weighting in $m(KK)$, it is obtained $\tau(B^+)/\tau(B^0) = 1.0780 \pm 0.0025$, which again agrees with the PDG value within below 0.5σ (0.2%). The corresponding decay time distribution is shown in Figure 6.9.

Finally, a check is performed on whether the time distribution is really exponential or whether the procedure introduces a second exponencial component. For this, intead of fitting the lifetime with $\exp(-t\Gamma)$, $f\exp(-t(\Gamma+\Delta\Gamma/2)) + (1-f)\exp(t(\Gamma-\Delta\Gamma/2))$ is used. The parameter $\Delta\Gamma$ that quantifies the shift is found to be consistent with zero.

6.2.8 Flavour tagging

For time-dependent studies the ability of properly identifying the initial flavour of the meson (known as *flavour tagging*) is fundamental. To this end, two flavour tagging algorithms are used: the opposite-side (OS) taggers and the same-side kaon (SSK) taggers, which exploit specific features of the incoherent production of $b\bar{b}$ quark pairs in pp collisions. For the OS taggers, these features entail determining the flavour of the B_s^0 meson from the charge of the kaon originating from the PV. For the SSK, the flavour of the B_s^0 meson is deduced from the charge of the kaon, muon or electron originating from a SV.

Each tagging algorithm gives a tag decision and a mistag probability, the fraction of events with the wrong tag decision, $\eta \in [0, 0.5]$. The tag decision takes values ± 1, or 0, if the signal meson is tagged as B_s^0, $\bar{B}_s^0$ or untagged, respectively. The fraction of events in the sample with a non-zero tagging decision gives the efficiency of the tagger, ε. The mistag probability is then calibrated to obtain the corrected per-event mistag probability, ω. This is used to determine the dilution factor, $\mathcal{D} = (1-2\omega)$, that rescales the efficiency of the tagger to quantify the fraction of the sample equivalent to perfectly tagged events. This effective efficiency is called tagging power, given by the product of the efficiency and the square dilution, $\varepsilon\mathcal{D}^2$.

In this analysis the taggers have been optimised and calibrated using Run 2 data. A

linear dependence of ω with η is assumed,

$$\omega = p_0 + p_1(\eta - \langle\eta\rangle) \tag{6.16}$$

where p_0, p_1 are calibration parameters and $\langle\eta\rangle$ is the average predicted mistag probability for each calibration sample. When using OS and SSK algorithms, the calibration model become:

$$\omega^{\text{alg}} = \left(p_0^{\text{alg}} + \frac{\Delta p_0^{\text{alg}}}{2}\right) + \left(p_1^{\text{alg}} + \frac{\Delta p_1^{\text{alg}}}{2}\right)\left(\eta^{\text{alg}} - \left\langle\eta^{\text{alg}}\right\rangle\right) \text{ for an initial } B_s^0 \text{ event}$$

$$\omega^{\text{alg}} = \left(p_0^{\text{alg}} - \frac{\Delta p_0^{\text{alg}}}{2}\right) + \left(p_1^{\text{alg}} - \frac{\Delta p_1^{\text{alg}}}{2}\right)\left(\eta^{\text{alg}} - \left\langle\eta^{\text{alg}}\right\rangle\right) \text{ for an initial } \bar{B}_s^0 \text{ event}$$

where alg = OS, SSK and Δp_i^{alg} are mistag asymmetries.

The calibration of the opposite-side tagger is made using $B^+ \to J/\psi K^+$ decays, while for the same-side kaon tagger $B_s^0 \to D_s^- \pi^+$ decays are used. The overall tagging performance is summarised in table 6.8.

Table 6.8: Tagging performance

Category	Fraction(%)	$\varepsilon(\%)$	$\mathcal{D}^2$	$\varepsilon\mathcal{D}^2(\%)$
OS-only	14.595	11.349	0.078	0.88±0.04
SSK-only	54.751	42.574	0.032	1.38±0.30
OS&SSK	30.654	23.837	0.104	2.47±0.15
Total	100	77.760	0.061	4.73±0.34

6.2.9 Data fitting

The fitting procedure uses the sFit technique for background subtraction, as described in Section 6.2.3. The full PDF for each year y (2015 and 2016), trigger category g (biased and unbiased) and m_{KK} bin i ($i \in [1;6]$), based on Eq. 6.2 and taking into account all detector response effects, is given by

$$\mathcal{P}_{y,g}^i\left(t, \Omega | q^{\text{OS}}, q^{\text{SSK}}, \eta^{\text{OS}}, \eta^{\text{SSK}}, \sigma_t\right) = \sum_{k=1}^{10} \frac{1}{\mathcal{N}_{y,g}} \mathcal{P}_k^i\left(t, \Omega | q^{\text{OS}}, q^{\text{SSK}}, \eta^{\text{OS}}, \eta^{\text{SSK}}, \sigma_t\right) \tag{6.17}$$

$$= \sum_{k=1}^{10} \frac{1}{\mathcal{N}_{y,g}} \tilde{N}_k^i f_{g,y,k}(\Omega) \varepsilon_{g,y}(t)$$
$$\cdot \left\{ \left[\left(1 + q^{\text{OS}}\left(1 - 2\omega^{\text{OS}}\left(\eta^{\text{OS}}\right)\right)\right)\left(1 + q^{\text{SSK}}\left(1 - 2\omega^{\text{SSK}}\left(\eta^{\text{SSK}}\right)\right)\right) \cdot h_k\left(t | B_s^0\right) \right.\right.$$
$$\left.\left. + \left(1 - q^{\text{OS}}\left(1 - 2\bar{\omega}^{\text{OS}}\left(\eta^{\text{OS}}\right)\right)\right)\left(1 - q^{\text{SSK}}\left(1 - 2\bar{\omega}^{\text{SSK}}\left(\eta^{\text{SSK}}\right)\right)\right) \cdot h_k\left(t | \overline{B}_s^0\right) \right] \otimes G\left(t | \sigma_t\right) \right\},$$

where q^{OS} and q^{SSK} are the OS and SSK tag decisions, η^{OS} and η^{SSK} the measured mistag probabilities, ω and $\bar{\omega}$ the mistag probability calibration for B_s^0 and $\overline{B}_s^0$ (see Section 6.2.8); $\varepsilon(t)$

is the decay time acceptance (see Section 6.2.7); $G\left(t|\sigma_t\right)$ is the decay time resolution with decay time uncertainty σ_t (see Section 6.2.5); $\tilde{N}_{i,k} = N_k$ for $k < 8$ and $\tilde{N}_{i,k} = C_{\mathrm{SP},i} N_k$ for $k = 8, 9, 10$ (see Section 6.2.4); $\mathcal{N}_{y,g}$ is the normalisation given by

$$\mathcal{N}_{y,g}\left(t, \Omega | q^{\mathrm{OS}}, q^{\mathrm{SSK}}, \eta^{\mathrm{OS}}, \eta^{\mathrm{SSK}}, \sigma_t\right) = \int_{t=0.3\mathrm{ps}}^{15\mathrm{ps}} \int_{\Omega} \sum_{i=1}^{6} \sum_{k=1}^{10} w_k \mathcal{P}_{i,k}\left(t, \Omega | q^{\mathrm{OS}}, q^{\mathrm{SSK}}, \eta^{\mathrm{OS}}, \eta^{\mathrm{SSK}}, \sigma_t\right) dt d\Omega, \tag{6.18}$$

where w_k are the angular acceptance weights (see Section 6.2.6).

The values of ϕ_s and $\Delta\Gamma_s$ were kept blinded during the full analysis.

6.2.10 Baseline fit

The difference between the lifetimes, $\Delta\Gamma_d^s = \Gamma_s - \Gamma_d$, is fitted instead of Γ_s, given that it can be measured with a higher precision, independently of the value of Γ_d used in the determination of the time acceptance.

The decay time acceptance can be parametrized as a fuction of Γ_d as follows (see Section 6.2.7:

$$\varepsilon_{\mathrm{data}}^{B_s^0}(t) \propto \frac{N(t)}{e^{-\Gamma_d t} \bigotimes G(t, \sigma_t)} \tag{6.19}$$

Where $N(t)$ represents the background subtracted B^0 data sample, and $G(t, \sigma_t)$ the Gaussian resolution function. Expressing Γ_d around the used value, $\Gamma_d^0 = 1.0/1.520$ ps^{-1}:

$$\begin{aligned}
\varepsilon_{\mathrm{data}}^{B_s^0}(t; \Gamma_d) &\propto \frac{N(t)}{e^{-(\Gamma_d^0 + \delta\Gamma_d)t} \bigotimes G(t, \sigma_t)} \\
&\approx \frac{N(t)}{e^{-\Gamma_d^0 t} \bigotimes G(t, \sigma_t)} \times e^{\delta\Gamma_d t} \\
&= \varepsilon_{\mathrm{data}}^{B_s^0}(t; \Gamma_d^0) \times e^{\delta\Gamma_d t}
\end{aligned}$$

where $\delta\Gamma_d$ accounts for the deviation from the chosen value and it is assumed that t is much larger than the decay time resolution (which is fulfilled, given that $t_{min}/\sigma_t \approx 0.3/0.05$). Constraining $\delta\Gamma_d$ to the uncertainty on Γ_d, and using Eq. 6.20, the systematic uncertainty of the physics parameters due to the chosen value of Γ_d is directly obtained in the fit. The parameter Γ_s can be also expressed in terms of Γ_d^0 and $\delta\Gamma_d$ as follows:

$$\Gamma_s = \Delta\Gamma_d^s + \Gamma_d = \Delta\Gamma_d^s + \Gamma_d^0 + \delta\Gamma_d \tag{6.20}$$

Inserting Eq. 6.20 into the term of the pdf (see Eq. 6.18) that is decay time dependent:

$$\begin{aligned}
pdf(t) &\approx \varepsilon_{\mathrm{data}}^{B_s^0}(t; \Gamma_d^0) \times e^{\delta\Gamma_d t} \times [e^{-(\Delta\Gamma_d^s + \Gamma_d^0 + \delta\Gamma_d)} \bigotimes G(t, \sigma_t)] \\
&\approx \varepsilon_{\mathrm{data}}^{B_s^0}(t; \Gamma_d^0) \times e^{\delta\Gamma_d t} \times e^{-\delta\Gamma_d t} \times [e^{-(\Gamma_d^0 + \delta\Gamma_d)} \bigotimes G(t, \sigma_t)] \\
&= \varepsilon_{\mathrm{data}}^{B_s^0}(t; \Gamma_d^0) \times [e^{-(\Gamma_d^0 + \delta\Gamma_d)} \bigotimes G(t, \sigma_t)].
\end{aligned}$$

Notice that Eq. 6.21 does not depend on $\delta\Gamma_d$. Hence, $\Delta\Gamma_d^s$ will be independent of the chosen Γ_d. For this reason, $\delta\Gamma_d$ can be set to 0. Toy studies have been carried on to check this independence.

Events with negative mistag probability are manually assigned $\omega = 0$. As said before, $|\lambda|$ and ϕ_s are assumed to be common to all polarisation states. Checks of this assumption are made, where polarisation dependence is instead considered. These are in agreement with the baseline fit. Several fitters were independently developed, including the baseline one, which is based on the usage of graphics processing units (GPUs). These are optimized for parallel calculations that allow a faster computation. Given the high complexity of the fit, that translates into a long time until the algorithm reaches convergence, a fit speed up is crucial especially when dealing with large data sets, e.g. when estimating some systematic uncertainties. The algorithm is based on the `Ipanema` framework [203]. It has a CPU component, written in `python` that constitutes a front-end to control the fit inputs. These inputs are then passed to the GPU component, based on `CUDA` (a parallel computing platform created by `Nvidia`), that takes care of the pdf computation. Both parts interact via `pycuda`, that acts as a wrapper around the `CUDA` code. Timing tests can be found in Table 6.9.

Table 6.9: Fit convergence times on two different graphics cards for the nominal data set and a sample ten times its size.

Graphics card	146798 events 2170 calls	10x146798 events 1868 calls
GeForce GTX 1080	0.5 min	3.8 min
Tesla M2090	0.97 min	7.5 min

A good agreement is found between the fit results provided by the different fitters. The *preliminary* fit result is given in Table 6.11 and the corresponding *preliminary* correlation matrix in Table 6.12. The statisitical uncertainties reported are the symmetric uncertainties from either `MINOS` (when asymmetric) or `HESSE`. The *preliminary* background subtracted projection plots are shown in Figures 6.10 and 6.11. A *preliminary* summary of the systematic uncertainties is shown in Table 6.10. They can be further classified in several blocks, depending on their source, as follows:

- The strategy followed with the fraction of multiple candidates found in the data sample (*multiple candidates*). A systematic is taking computing the difference between the baseline result and the result obtained when recalculating the acceptances and redoing the fit with the samples without clones.

- The correlation of the mass with the decay time and the helicity angles (*mass factorisation*). The only non-negligible systematic due to this is the one concerning the decay time, since the shape of the combinatorial background varies with time.

- The parametrisation of the mass error in the computation of the sWeights (*mass shape*). The systematics is studied using a linear parametrisation instead of a quadratic one.

- The intrinsic fit bias (*fit bias*). A systematic is assigned using toy MC. with pseudo-experiments.

- The C_{SP} factors (C_{SP} *factors*). In this case, the parameters that are used are varied within their uncertainties. Furthermore, a different solution for f_0 [239] and an alternative,

data-driven shape for the S-wave are tested. The value for this systematics is assigned accordingly.

- The systematics arising when studying the time resolution. These were explained in Section 6.2.5 and correspond to *Time res.: prompt*, *Time res.: statistical*, *Time res.: $\mu(\delta t)$* and *Time res.: Wrong PV*.

- The tagging parameters (*Quadratic OS tagging*). A systematic effect is evaluated concerning the usage of a second order polynomial instead of a first order polynomial for the OS tagging calibration.

- The angular acceptance studies. There are 4 systematics originating from these studies:

  - *Ang. acc.: statistical*: computed coherently varying the weights within their errors, taking into account the correlations between them, and repeating the fit.
  - *Ang. acc.: correction*: this uncertainty assess the choice of the variables as well as the method used in the iterative procedure to correct for differences between the simulation sample that is used to calculate the normalisation weights.
  - *Ang. acc.: t & σ_t dependence*, that accounts for the correlation between the decay time and the angular acceptance, as well as the correlation between the angular acceptance and the decay time uncertainty. These dependencies are not included in the fit to data. Therefore, they are addressed as systematics.

- The determination of the time acceptance. In this case the systematic sources are:

  - *Dec. time acc.: knot pos.*: the position of the knots is varied for systematic studies.
  - *Dec. time acc.: p.d.f reweighting* and *Dec. time acc.: kinematic reweighting*: these systematic values concern the reweighting of the pdf and the corrections in kinematic variables made in order to account for the differences between data and simulation.
  - *Dec. time acc.: statistical*, that assesses the impact of the statistical uncertainties of the spline coefficients on the decay time acceptance computation.
  - *Dec. time acc.: Other MC sample*, that studies the changes observed when using simulated events with $\Delta\Gamma_s \neq 0$ instead of $\Delta\Gamma_s = 0$.

- The precision on the length (0.022%) and track momentum (0.03%) scales, that are 0.022% and 0.03% respectively (*Length scale*). To study this, a momentum scaling is used.

- The treatment of `BKGCAT == 60` events in simulation (*`BKGCAT == 60`*). These are events that are not truth-matched but partially peak at the correct B_s^0 mass. Different strategies are analysed to reduce the residual events (non-peaking background) of this type after applying sWeights to the full simulation samples.

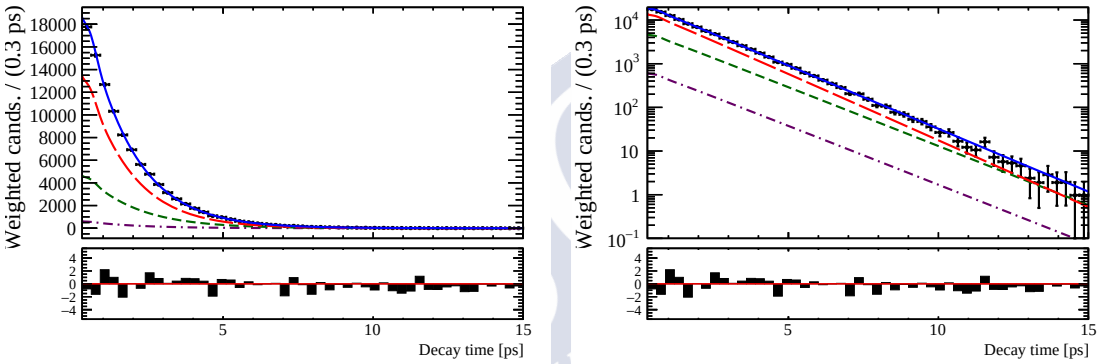

(a) (b)

Figure 6.10: Decay-time distributions for background subtracted $B_s^0 \to J/\psi K^+K^-$ decays (data points) with the one-dimensional projections of the PDF at the maximal likelihood point. The solid blue line shows the total signal contribution, which contains CP-even (long-dashed red), CP-odd (short-dashed green) and S-wave (dotted-dashed purple) contributions. Data and fit projections for 2015 and 2016 and both trigger categories are combined.

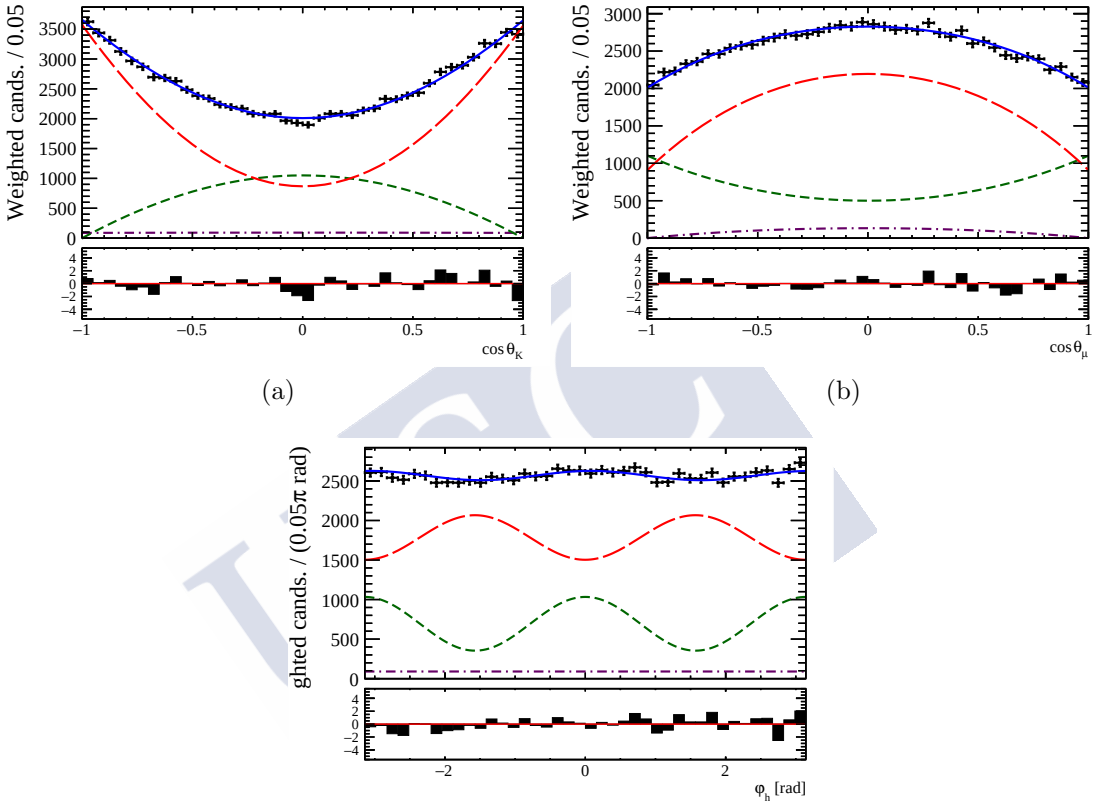

Figure 6.11: Helicity-angle distributions for background subtracted $B_s^0 \to J/\psi K^+K^-$ decays (data points) with the one-dimensional projections of the PDF at the maximal likelihood point. The solid blue line shows the total signal contribution, which contains CP-even (long-dashed red), CP-odd (short-dashed green) and S-wave (dotted-dashed purple) contributions. Data and fit projections for 2015 and 2016 and both trigger categories are combined.

Table 6.10: Summary of the systematic uncertainties for the polarisation-independent fit.

Source	$\lvert A_0\rvert^2$	$\lvert A_\perp\rvert^2$	ϕ_s [rad]	$\lvert\lambda\rvert$	$\delta_\perp - \delta_0$ [rad]	$\delta_\parallel - \delta_0$ [rad]	$-\Gamma_d$ [ps^{-1}]
Central value	0.5191	0.2454	-0.081	1.006	2.65	3.059	-0.0041
Stat. error	$^{+0.0029}_{-0.0029}$	$^{+0.0040}_{-0.0040}$	$^{+0.041}_{-0.041}$	$^{+0.016}_{-0.016}$	$^{+0.13}_{-0.13}$	$^{+0.084}_{-0.073}$	$^{+0.0024}_{-0.0023}$
Multiple candidates	0.00060	0.00012	0.0011	0.0011	0.0073	0.0021	0.00033
Mass factorisation	0.0004	0.0004	0.001	0.0008	0.0099	0.004	0.0006
Mass shape	0.0006	0.0004	-	-	0.0005	0.003	-
Fit bias	0.0001	0.0006	0.001	-	0.022	0.033	-
$C_{\rm SP}$ factors	-	0.0001	0.001	0.001	0.013	0.005	-
Time res.: prompt	-	-	-	-	0.001	0.001	-
Time res.: statistical	-	-	-	-	-	-	-
Time res.: $\mu(\delta t)$	-	-	0.0032	0.001	0.080	0.001	0.0002
Time res.: Wrong PV	-	-	-	-	0.001	0.001	-
Quadratic OS tagging	-	-	-	-	-	-	-
Ang. acc.: statistical	0.00030	0.00036	0.0011	0.0018	0.0025	0.0044	0.00003
Ang. acc.: correction	0.00070	0.00029	0.0016	0.0021	0.0016	0.0016	-
Ang. acc.: t & σ_t dependence	0.00084	0.00120	0.0012	0.0007	0.029	0.0055	0.00021
Dec. time acc.: knot pos.	-	-	-	-	-	-	0.00019
Dec. time acc.: p.d.f. reweighting	-	-	-	-	-	-	0.00007
Dec. time acc.: kinematic reweighting	-	-	-	-	-	-	0.00021
Dec. time acc.: statistical	0.00020	0.00030	-	-	-	-	0.00120
Dec. time acc.: Other MC sample	0.00012	0.00018	-	-	-	-	0.00031
Length scale	-	-	-	-	-	-	-
`BKGCAT==60`	0.00019	0.00013	0.0005	0.0014	-	0.0017	0.00020
Quadratic sum of syst.	0.0015	0.0016	0.0045	0.0037	0.090	0.035	0.0015

Source	$\Delta\Gamma_s$ [ps^{-1}]	Δm_s [ps^{-1}]	$\delta_S^1 - \delta_\perp$ [rad]	$\delta_S^2 - \delta_\perp$ [rad]	$\delta_S^3 - \delta_\perp$ [rad]	$\delta_S^4 - \delta_\perp$ [rad]	$\delta_S^5 - \delta_\perp$ [rad]
Central value	0.0772	17.706	2.21	1.57	1.11	-0.29	-0.541
Stat. error	$^{+0.0076}_{-0.0077}$	$^{+0.057}_{-0.059}$	$^{+0.17}_{-0.20}$	$^{+0.29}_{-0.29}$	$^{+0.49}_{-0.37}$	$^{+0.16}_{-0.27}$	$^{+0.091}_{-0.102}$
Multiple candidates	0.00011	0.0014	0.011	-	0.024	0.007	0.0041
Mass factorisation	0.0004	0.0028	0.0229	0.0093	0.0136	0.0074	0.0124
Mass shape	0.0002	0.001	0.005	0.001	0.01	0.01	0.0097
Fit bias	0.0003	0.001	0.05	0.02	0.08	0.11	0.01
$C_{\rm SP}$ factors	0.0001	0.002	0.18	0.02	0.03	0.01	0.01
Time res.: prompt	-	0.001	-	-	-	0.003	0.002
Time res.: statistical	-	-	-	-	-	-	-
Time res.: $\mu(\delta t)$	0.0003	0.005	-	0.003	0.002	0.003	0.0056
Time res.: Wrong PV	-	0.001	-	0.001	0.001	0.001	0.001
Quadratic OS tagging	-	-	-	0.003	0.001	0.001	-
Ang. acc.: statistical	-	0.0011	0.003	0.006	0.013	0.012	0.0044
Ang. acc.: correction	0.00021	-	-	0.009	-	0.011	0.0046
Ang. acc.: t & σ_t dependence	0.00095	0.0028	0.013	0.022	0.027	0.032	0.010
Dec. time acc.: knot pos.	-	-	-	-	-	-	-
Dec. time acc.: p.d.f. reweighting	0.00009	-	-	-	-	-	-
Dec. time acc.: kinematic reweighting	-	-	-	-	-	-	-
Dec. time acc.: statistical	0.00083	-	-	-	-	-	-
Dec. time acc.: Other MC sample	0.00050	-	-	-	-	-	-
Length scale	-	0.004	-	-	-	-	-
`BKGCAT==60`	0.00012	-	-	-	-	0.004	0.0018
Quadratic sum of syst.	0.0015	0.008	0.19	0.039	0.095	0.117	0.025

Source	$\delta_S^6 - \delta_\perp$ [rad]	F_S^1	F_S^2	F_S^3	F_S^4	F_S^5	F_S^6
Central value	-1.11	0.490	0.0401	0.0041	0.0069	0.073	0.151
Stat. error	$^{+0.14}_{-0.16}$	$^{+0.043}_{-0.043}$	$^{+0.0081}_{-0.0075}$	$^{+0.0029}_{-0.0016}$	$^{+0.0061}_{-0.0045}$	$^{+0.014}_{-0.013}$	$^{+0.019}_{-0.018}$
Multiple candidates	0.007	0.0017	0.00120	0.00015	0.00067	0.0014	0.0006
Mass factorisation	0.0349	0.0184	0.0006	0.0001	0.0005	0.0032	0.0065
Mass shape.	0.0117	0.0049	0.0006	0.0001	0.0008	0.0031	0.005
Fit bias	0.04	0.0008	0.0042	0.0013	0.0007	0.0002	0.0007
$C_{\rm SP}$ factors	0.10	0.001	0.0031	0.0004	0.0004	0.001	0.007
Time res.: prompt	0.002	0.0001	0.0001	-	0.0002	0.0004	-
Time res.: statistical	-	-	-	-	-	-	-
Time res.: $\mu(\delta t)$	0.002	0.0001	-	-	0.0001	0.0001	-
Time res.: Wrong PV	0.001	0.0001	0.0001	-	0.0001	0.0002	-
Quadratic OS tagging	0.001	-	-	-	0.0002	-	-
Ang. acc.: statistical	0.004	0.0007	0.00032	0.00011	0.00026	0.0006	0.0006
Ang. acc.: correction	0.003	0.0014	0.00031	0.00006	0.00059	0.0013	0.0011
Ang. acc.: t & σ_t dependence	0.010	0.0063	0.00069	0.00024	0.00015	0.0010	0.0016
Dec. time acc.: knot pos.	-	-	-	-	-	-	-
Dec. time acc.: pd.f. reweighting	-	-	-	-	-	-	-
Dec. time acc.: kinematic reweighting	-	-	-	-	-	-	-
Dec. time acc.: statistical	-	-	-	-	-	-	-
Dec. time acc.: Other MC sample	-	-	-	-	-	-	-
Length scale	-	-	-	-	-	-	-
`BKGCAT==60`	0.002	-	0.00022	0.00009	0.00020	0.0006	0.0005
Quadratic sum of syst.	0.115	0.020	0.0055	0.0014	0.0016	0.0051	0.011

Table 6.11: Parameter estimates for the baseline (Santiago) polarisation-independent fit compared to the Run 1 result [247].

Par	baseline	$\|\lambda\| = 1$	Fixed tag	Run I
ϕ_s[rad]	$-0.081^{+0.041}_{-0.041}$	-0.083 ± 0.040	-0.081 ± 0.038	-0.058 ± 0.049
$\|\lambda^0\|$	$1.006^{+0.016}_{-0.016}$	1	1.008 ± 0.015	0.964 ± 0.019
$\Delta\Gamma^s_d$[ps^{-1}]	$-0.0041^{+0.0024}_{-0.0023}$	-0.0041 ± 0.0023	-0.0041 ± 0.0023	0.0024 ± 0.0027
$\Delta\Gamma_s$[ps^{-1}]	$0.0772^{+0.0076}_{-0.0077}$	0.0773 ± 0.0076	0.0770 ± 0.0076	0.0805 ± 0.0091
Δm_s[ps^{-1}]	$17.706^{+0.057}_{-0.059}$	17.707 ± 0.058	17.698 ± 0.057	$17.711^{+0.055}_{-0.057}$
$\|A_\perp\|^2$	$0.2454^{+0.0040}_{-0.0040}$	0.2454 ± 0.0040	0.2455 ± 0.0040	0.2504 ± 0.0049
$\|A_0\|^2$	$0.5191^{+0.0029}_{-0.0029}$	0.5191 ± 0.0029	0.5190 ± 0.0029	0.5241 ± 0.0034
F_{S1}	$0.490^{+0.043}_{-0.043}$	0.490 ± 0.043	0.491 ± 0.043	0.426 ± 0.054
F_{S2}	$0.0401^{+0.0081}_{-0.0075}$	0.0400 ± 0.0079	0.0395 ± 0.0077	0.059 ± 0.017
F_{S3}	$0.0041^{+0.0029}_{-0.0016}$	0.0040 ± 0.0020	0.0041 ± 0.0022	0.0101 ± 0.0067
F_{S4}	$0.0069^{+0.0061}_{-0.0045}$	0.0070 ± 0.0052	0.0063 ± 0.0047	0.0103 ± 0.0061
F_{S5}	$0.073^{+0.014}_{-0.013}$	0.073 ± 0.013	0.071 ± 0.013	0.049 ± 0.015
F_{S6}	$0.151^{+0.019}_{-0.018}$	0.151 ± 0.018	0.147 ± 0.018	0.193 ± 0.025
$\delta_\parallel - \delta_0$[rad]	$3.059^{+0.084}_{-0.073}$	3.059 ± 0.078	3.049 ± 0.076	$3.258^{+0.099}_{-0.181}$
$\delta_\perp - \delta_0$[rad]	$2.65^{+0.13}_{-0.13}$	2.65 ± 0.13	2.65 ± 0.13	$3.08^{+0.14}_{-0.15}$
$\delta_{S1} - \delta_\perp$[rad]	$2.21^{+0.17}_{-0.20}$	2.20 ± 0.19	2.21 ± 0.18	0.84 ± 0.20
$\delta_{S2} - \delta_\perp$[rad]	$1.57^{+0.29}_{-0.29}$	1.60 ± 0.30	1.57 ± 0.29	2.15 ± 0.28
$\delta_{S3} - \delta_\perp$[rad]	$1.11^{+0.49}_{-0.37}$	1.14 ± 0.45	1.07 ± 0.42	0.47 ± 0.21
$\delta_{S4} - \delta_\perp$[rad]	$-0.29^{+0.16}_{-0.27}$	-0.28 ± 0.18	-0.32 ± 0.19	-0.34 ± 0.17
$\delta_{S5} - \delta_\perp$[rad]	$-0.541^{+0.091}_{-0.102}$	-0.540 ± 0.095	-0.537 ± 0.095	-0.59 ± 0.15
$\delta_{S6} - \delta_\perp$[rad]	$-1.11^{+0.14}_{-0.16}$	-1.11 ± 0.15	-1.12 ± 0.15	-0.90 ± 0.14
p_0^{os}	$0.3892^{+0.0028}_{-0.0028}$	0.3892 ± 0.0028	0.39	-
Δp_0^{os}	$0.0090^{+0.0014}_{-0.0014}$	0.0090 ± 0.0014	0.009	-
p_1^{os}	$0.846^{+0.027}_{-0.027}$	0.846 ± 0.027	0.85	-
Δp_1^{os}	$0.015^{+0.012}_{-0.012}$	0.015 ± 0.012	0.014	-
p_0^{ss}	$0.4432^{+0.0072}_{-0.0072}$	0.4433 ± 0.0072	0.43	-
Δp_0^{ss}	$0.003^{+0.029}_{-0.029}$	0.003 ± 0.029	0.000	-
p_1^{ss}	$0.608^{+0.088}_{-0.088}$	0.607 ± 0.088	0.92	-
Δp_1^{ss}	$-0.000^{+0.030}_{-0.030}$	-0.000 ± 0.030	0.000	-

Table 6.12: Fit correlation matrix.

	ϕ_s [rad]	$\lvert\lambda^0\rvert$	$\Delta\Gamma_d^s$ [ps^{-1}]	$\Delta\Gamma_s$ [ps^{-1}]	Δm_s [ps^{-1}]	$\lvert A_\perp\rvert^2$	$\lvert A_0\rvert^2$	F_{S1}	F_{S2}	F_{S3}	F_{S4}	F_{S5}	F_{S6}	$\delta_\parallel - \delta_0$ [rad]	$\delta_\perp - \delta_0$ [rad]	$\delta_{S1} - \delta_\perp$ [rad]	$\delta_{S2} - \delta_\perp$ [rad]	$\delta_{S3} - \delta_\perp$ [rad]	$\delta_{S4} - \delta_\perp$ [rad]	$\delta_{S5} - \delta_\perp$ [rad]	$\delta_{S6} - \delta_\perp$ [rad]	p_0^{os}	Δp_0^{os}	p_1^{os}	Δp_1^{os}	p_0^{ss}	Δp_0^{ss}	p_1^{ss}	Δp_1^{ss}
ϕ_s [rad]	1.00	0.19	-0.03	-0.00	0.04	-0.03	0.02	-0.00	0.00	0.04	-0.03	-0.00	-0.02	0.01	0.03	0.00	-0.05	-0.04	-0.01	0.00	-0.01	-0.00	-0.00	0.03	-0.00	-0.01	0.03	-0.02	-0.00
$\lvert\lambda^0\rvert$	0.19	1.00	0.01	-0.04	0.00	0.02	-0.02	0.01	0.01	0.14	-0.08	-0.00	0.01	-0.00	0.07	0.06	-0.19	-0.15	-0.06	-0.02	0.02	0.01	0.00	-0.00	-0.00	-0.03	0.01	0.03	-0.00
$\Delta\Gamma_d^s$ [ps^{-1}]	-0.03	0.01	1.00	-0.47	-0.00	0.39	-0.32	0.05	0.04	0.03	0.03	0.07	0.06	0.03	-0.00	0.01	-0.00	-0.02	0.02	0.02	0.01	0.00	0.00	-0.00	0.00	0.00	-0.00	-0.00	0.00
$\Delta\Gamma_s$ [ps^{-1}]	-0.00	-0.04	-0.47	1.00	0.01	-0.69	0.63	-0.07	-0.05	-0.02	0.02	-0.06	-0.06	-0.01	0.00	-0.00	0.01	0.01	0.01	0.00	0.00	0.00	-0.00	-0.00	0.00	0.00	0.00	-0.00	-0.00
Δm_s [ps^{-1}]	0.04	0.00	-0.00	0.01	1.00	-0.03	0.01	-0.01	-0.01	-0.06	0.10	0.07	-0.03	-0.04	0.75	-0.02	-0.08	0.10	0.06	0.07	-0.04	0.02	0.00	0.03	-0.00	0.01	-0.02	-0.06	0.00
$\lvert A_\perp\rvert^2$	-0.03	0.02	0.39	-0.69	-0.03	1.00	-0.60	0.04	-0.02	-0.02	-0.05	0.01	0.03	0.13	0.01	0.02	-0.01	0.01	-0.02	0.00	0.02	-0.00	-0.00	-0.00	0.00	0.00	-0.00	0.00	0.00
$\lvert A_0\rvert^2$	0.02	-0.02	-0.32	0.63	0.01	-0.60	1.00	-0.05	-0.01	0.01	0.05	-0.01	-0.03	0.00	0.00	-0.00	0.01	-0.01	0.03	0.01	0.01	0.00	-0.00	-0.00	0.00	0.01	0.00	-0.00	-0.00
F_{S1}	-0.00	0.01	0.05	-0.07	-0.01	0.04	-0.05	1.00	0.00	0.00	-0.00	0.00	0.01	0.01	-0.01	0.08	-0.00	-0.00	-0.00	-0.00	0.00	0.00	0.00	-0.00	0.00	-0.00	-0.00	0.00	0.00
F_{S2}	0.00	0.01	0.04	-0.05	-0.01	-0.02	-0.01	0.00	1.00	0.01	0.00	0.01	0.01	-0.01	-0.02	0.00	0.12	-0.00	0.00	0.00	0.00	0.01	-0.00	-0.01	0.00	-0.02	-0.00	-0.02	0.00
F_{S3}	0.04	0.14	0.03	-0.02	-0.06	-0.02	0.01	0.00	0.01	1.00	-0.02	0.00	0.00	0.03	0.01	0.00	-0.03	-0.69	-0.01	-0.01	-0.01	0.00	-0.00	-0.01	0.00	-0.01	-0.01	-0.01	0.00
F_{S4}	-0.03	-0.08	0.03	0.02	0.10	-0.05	0.05	-0.00	0.00	-0.02	1.00	0.01	0.00	0.02	0.04	-0.00	0.01	0.03	0.48	0.01	0.00	0.03	-0.00	0.01	0.00	0.06	0.01	-0.01	-0.00
F_{S5}	-0.00	-0.00	0.07	-0.06	0.07	0.01	-0.01	0.00	0.01	0.00	0.01	1.00	0.01	0.03	0.04	-0.00	-0.00	0.01	0.01	0.46	0.00	0.02	0.00	-0.02	-0.00	0.02	0.00	-0.03	-0.00
F_{S6}	-0.02	0.01	0.06	-0.06	-0.03	0.03	-0.03	0.01	0.01	0.00	0.00	0.01	1.00	0.00	-0.07	0.01	0.01	0.00	0.01	0.00	0.44	0.00	0.00	-0.01	0.00	0.03	-0.00	-0.04	0.00
$\delta_\parallel - \delta_0$ [rad]	0.01	-0.00	0.03	-0.01	-0.04	0.13	0.00	0.01	-0.01	0.03	0.02	0.03	0.00	1.00	0.20	-0.02	-0.03	-0.04	0.01	-0.01	-0.03	0.01	0.00	-0.00	0.00	0.05	0.01	-0.02	0.00
$\delta_\perp - \delta_0$ [rad]	0.03	0.07	-0.00	0.00	0.75	0.01	0.00	-0.01	-0.02	0.01	0.04	0.04	-0.07	0.20	1.00	-0.06	-0.18	-0.01	-0.01	0.00	-0.16	0.01	0.00	-0.00	-0.00	0.00	-0.00	-0.00	0.00
$\delta_{S1} - \delta_\perp$ [rad]	0.00	0.06	0.01	-0.00	-0.02	0.02	-0.00	0.08	0.00	0.00	-0.00	-0.00	0.01	-0.02	-0.06	1.00	0.00	-0.00	0.00	0.00	0.02	0.00	0.00	0.01	-0.00	0.01	0.00	0.01	0.00
$\delta_{S2} - \delta_\perp$ [rad]	-0.05	-0.19	-0.00	0.01	-0.08	-0.01	0.01	-0.00	0.12	-0.03	0.01	-0.00	0.01	-0.03	-0.18	0.00	1.00	0.04	0.02	0.01	0.03	0.00	-0.00	0.01	0.00	0.02	-0.01	-0.01	0.00
$\delta_{S3} - \delta_\perp$ [rad]	-0.04	-0.15	-0.02	0.01	0.10	0.01	-0.01	-0.00	-0.00	-0.69	0.03	0.01	0.00	-0.04	-0.01	-0.00	0.04	1.00	0.02	0.02	0.01	0.00	0.00	0.02	-0.00	0.03	0.01	-0.02	-0.00
$\delta_{S4} - \delta_\perp$ [rad]	-0.01	-0.06	0.02	0.01	0.06	-0.02	0.03	-0.00	0.00	-0.01	0.48	0.01	0.01	0.01	-0.01	0.00	0.02	0.02	1.00	0.01	0.01	0.01	-0.00	0.01	0.00	0.05	0.01	-0.03	-0.00
$\delta_{S5} - \delta_\perp$ [rad]	0.00	-0.02	0.02	0.00	0.07	0.00	0.01	-0.00	0.00	-0.01	0.01	0.46	0.00	-0.01	0.00	0.00	0.01	0.02	0.01	1.00	0.01	0.01	0.00	-0.01	-0.00	-0.00	-0.00	0.01	-0.00
$\delta_{S6} - \delta_\perp$ [rad]	-0.01	0.02	0.01	0.00	-0.04	0.02	0.01	0.00	0.00	-0.01	0.00	0.00	0.44	-0.03	-0.16	0.02	0.03	0.01	0.01	0.01	1.00	-0.01	-0.00	-0.00	0.00	0.03	-0.01	-0.02	0.00
p_0^{os}	-0.00	0.01	0.00	0.00	0.02	-0.00	0.00	0.00	0.01	0.00	0.03	0.02	0.00	0.01	0.01	0.00	0.00	0.00	0.01	0.01	-0.01	1.00	0.00	0.01	-0.00	0.01	-0.00	-0.01	-0.00
Δp_0^{os}	-0.00	0.00	0.00	-0.00	0.00	-0.00	-0.00	0.00	-0.00	-0.00	-0.00	0.00	0.00	0.00	0.00	0.00	-0.00	0.00	-0.00	0.00	-0.00	0.00	1.00	-0.00	0.00	0.00	-0.00	0.00	0.00
p_1^{os}	0.03	-0.00	-0.00	-0.00	0.03	-0.00	-0.00	-0.00	-0.01	-0.01	0.01	-0.02	-0.01	-0.00	-0.00	0.01	0.02	0.01	-0.01	-0.00	0.01	-0.00	0.00	1.00	0.00	-0.00	-0.00	0.00	-0.00
Δp_1^{os}	-0.00	-0.00	0.00	0.00	-0.00	0.00	0.00	0.00	0.00	0.00	0.00	-0.00	0.00	0.00	-0.00	-0.00	0.00	-0.00	0.00	-0.00	0.00	-0.00	0.00	0.00	1.00	-0.00	0.00	-0.00	-0.00
p_0^{ss}	-0.01	-0.03	0.00	0.00	0.01	0.00	0.01	-0.00	-0.02	-0.01	0.06	0.02	0.03	0.05	0.00	0.01	0.02	0.03	0.05	-0.00	0.03	0.01	0.00	-0.00	-0.00	1.00	0.01	-0.17	0.00
Δp_0^{ss}	0.03	0.01	-0.00	0.00	-0.02	-0.00	0.00	-0.00	-0.00	-0.01	0.01	0.00	-0.00	0.01	-0.00	0.00	-0.01	0.01	0.01	-0.00	-0.01	-0.00	-0.00	-0.00	0.00	0.01	1.00	0.01	0.01
p_1^{ss}	-0.02	0.03	-0.00	-0.00	-0.06	0.00	-0.00	0.00	-0.02	-0.01	-0.01	-0.03	-0.04	-0.02	-0.00	0.01	-0.01	-0.02	-0.03	0.01	-0.02	-0.01	0.00	0.00	-0.00	-0.17	0.01	1.00	-0.00
Δp_1^{ss}	-0.00	-0.00	0.00	-0.00	0.00	0.00	-0.00	0.00	0.00	0.00	-0.00	-0.00	0.00	0.00	0.00	0.00	0.00	-0.00	-0.00	-0.00	0.00	-0.00	0.00	0.00	-0.00	0.00	0.01	-0.00	1.00

6.2.11 Coverage of the uncertainty with the sFit

To check the reliability of the uncertainties on the physics parameters in the data fit to the time and helicity angles, the method of bootstrapping [248] is applied to both data and simulation. For this, a set of pseudo-samples is created by randomly selecting events from the simulation or data sample. The number of events in each pseudo-sample is the same as the number of events of the original one. After creating the samples, they are fitted, and the central value and pull distributions for each fit parameter are plotted (see Figures in Appendix D). The corresponding bootstrapping uncertainty (and the uncertainty on the uncertainty) for each parameter is obtained from the RMS of the distribution of its central values.

6.2.11.1 Simulation

The results for bootstrapping using simulation are shown in Table 6.13. For this study a simulation sample from 2016 has been used, with `S26` applied. Good agreement is found between the errors provided by the fit and the ones computed using bootstrapping.

Table 6.13: Variation in the statistical uncertainties for the fit parameters using the errors provided by the fit and the ones obtained with bootstrapping for simulation.

Parameter	Fit	Bootstrapping
f_L	0.0006	0.0005819 ± 0.000002
$f_\perp$	0.0008	0.000796 ± 0.0000126
ϕ_s [rad] *	0.0016	0.0016091 ± 0.0000256
$\delta_\perp$ [rad]	0.006	0.0063273 ± 0.0001005
$\delta_\parallel$ [rad]	0.007	0.006711 ± 0.0001066
$\lvert\lambda\rvert$	0.001	0.0010967 ± 0.0000174
$\Delta\Gamma_d^s$ [ps^{-1}]	0.0005	0.00057 ± 0.0000091
$\Delta\Gamma_s$ [ps^{-1}]*	0.0016	0.0015527 ± 0.0000247
Δms [ps^{-1}]	0.0021	0.0021915 ± 0.0000348

6.2.11.2 Data

The results for bootstrapping using 2015 and 2016 data can be seen in Table 6.14. In this case, sWeighted data has been used, with Stripping version 28. Contrary to simulation, discrepancies are found between bootstrapping and fit errors, especially in the strong phases and the S-wave fit fractions. A few effects contribute to this. First, the sWeights used for the fit are not recalculated for each randomly drawn sample, which can lead to differences in the uncertainties. However, this does not seem to affect the MC and so is probably only a secondary effect. Second, some of the S-wave phases have a second, less pronounced minimum. In this case, a reliable error estimation for the lower minimum is impossible because it merges with the higher minimum before the likelihood changes by a significance of 1σ. In addition, the likelihoods of some parameters show an asymmetric and non-Gaussian behaviour. This is especially true for the S-wave parameters,

where the S-wave fit fractions are consistent with zero within 2σ an the S-wave and phase uncertainties cannot be determined precisely. In these cases, the `MIGRAD/HESSE` errors are not a correct estimate of the uncertainties. Instead, for the final result the uncertainties are taken from `MINOS`.

Table 6.14: Variation in the statistical uncertainties for the fit parameters using the errors provided by the fit and the ones obtained with bootstrapping for 2015 and 2016 data.

Parameter	Fit	Bootstrapping
f_L	0.0029	0.0029 ± 0.0002
$f_\perp$	0.0040	0.0040 ± 0.0003
ϕ_s [rad] *	0.041	0.043 ± 0.004
$\delta_\perp$ [rad]	0.13	0.16 ± 0.02
$\delta_\parallel$ [rad]	$^{+0.083}_{-0.074}$	0.055 ± 0.017
$\lvert\lambda\rvert$	0.016	0.019 ± 0.006
$\Gamma_s - \Gamma_d$ [ps^{-1}]	$^{+0.0024}_{-0.0023}$	0.0023 ± 0.0001
$\Delta\Gamma_s$ [ps^{-1}]*	$^{+0.0076}_{-0.0077}$	0.0074 ± 0.0005
Δm_s [ps^{-1}]	$^{+0.057}_{-0.060}$	0.081 ± 0.015
$\delta_S^1 - \delta_\perp$	$^{+0.17}_{-0.20}$	0.62 ± 0.77
$\delta_S^2 - \delta_\perp$	$^{+0.29}_{-0.30}$	0.25 ± 0.19
$\delta_S^3 - \delta_\perp$	$^{+0.49}_{-0.37}$	0.38 ± 0.17
$\delta_S^4 - \delta_\perp$	$^{+0.16}_{-0.26}$	0.72± 1.82
$\delta_S^5 - \delta_\perp$	$^{+0.091}_{-0.103}$	0.17 ± 0.08
$\delta_S^6 - \delta_\perp$	$^{+0.14}_{-0.16}$	0.16 ± 0.04
F_S^1	0.043	0.045 ± 0.004
F_S^2	$^{+0.0081}_{-0.0074}$	0.0083 ± 0.0026
F_S^3	$^{+0.0029}_{-0.0016}$	0.0024 ± 0.0017
F_S^4	$^{+0.0062}_{-0.0045}$	0.0053 ± 0.025
F_S^5	0.013	0.014 ± 0.002
F_S^6	$^{+0.019}_{-0.018}$	0.018 ± 0.002

6.2.12 ϕ_s MultiNest

In order to further corroborate the previous result, and see the behaviour of the probability with each of the fit parameters, a scan is performed using the MultiNest Bayesian inference tool [227] with 2016 LHCb data. The lower and upper bins are removed from the scan, as they represent a high computational cost and they do not have much statistics. Therefore, only 4 m_{KK} bins are used. To this same end, $\Gamma_s - \Gamma_d$ is fixed to its PDG value, -0.002678 ps^{-1} [59]. The tagging parameters also remain fixed. As in the previous section, the CP-violating parameter $|\lambda|$ is assumed to be common to all polarization states. A total of 16 parameters are scanned, with 10000 live points set in the MultiNest algorithm. The tolerance paramter, that defines the termination criterion based on the accuracy of the evidence, is set to the default one, 0.5. Enough accuracy should be provided with this value. MultiNest will terminate if either has reached the maximum number of iterations or convergence criterion has been satisfied [249]. The results are shown in Figures 6.12, 6.13 and appendix E. As it can be seen from these, the scan results (first column in Table 6.15) are in good agreement (within uncertainties) with the fit results (second column in Table 6.15).

The discrepancies found for ϕ_s^0 and $\Delta\Gamma_s$ are due to the existence of two minima. These come from the invariance of the time dependent differential decay rate under the transformation $(\phi_s^0, \Delta\Gamma_s) \leftrightarrow (\pi - \phi_s^0, -\Delta\Gamma_s)$ [250]. Because of this, the results provided by MultiNest are an average of the two solutions. From Figure 6.12 it can be seen that the values corresponding to $(\phi_s^0, \Delta\Gamma_s)$ are close to the fit result. Moreover, the strong phases, as well as $\delta_\perp$, $\delta_\parallel$, are also affected, which translates into two minima for all of them (almost merged together in some cases), where one minimum is in agreement with the second column of Table 6.15. To resolve the ambiguity, the strong interaction phase shift is required [250]. From the experimental analysis it can be seen that the preferred solution is the one corresponding to $(\phi_s^0, \Delta\Gamma_s)$, as expected.

Table 6.15: Scan results obtained with MultiNest, as compared to the fit results.

Parameter	Scan results	Fit results
ϕ_s^0 [rad]	-1.580 ± 1.464	-0.116 ± 0.043
$\lvert\lambda^0\rvert$	1.030 ± 0.016	1.030 ± 0.016
$\Delta\Gamma_s$ [ps^{-1}]	-0.00094±0.08058	0.0805 ± 0.0077
Δm [ps^{-1}]	17.706 ± 0.061	17.700 ± 0.059
f_L	0.5174 ± 0.0031	0.5175 ± 0.0031
$f_\perp$	0.2468 ± 0.0042	0.2649 ± 0.0042
F_S^2	0.0422 ± 0.0092	0.0394 ± 0.0090
F_S^3	0.0056 ± 0.0026	0.0047 ± 0.0027
F_S^4	0.0117 ± 0.0062	0.0120 ± 0.0065
F_S^5	0.065 ± 0.014	0.065 ± 0.014
$\delta_\perp$ [rad]	1.56 ± 0.98	2.53 ± 0.13
$\delta_\parallel$ [rad]	3.142 ± 0.110	3.053 ± 0.083
$\delta_S^2 - \delta_\perp$	1.57 ± 0.30	1.69 ± 0.33
$\delta_S^3 - \delta_\perp$	1.58 ± 0.60	1.05 ± 0.45
$\delta_S^4 - \delta_\perp$	-1.58 ± 1.31	-0.23 ± 0.14
$\delta_S^5 - \delta_\perp$	-1.58 ± 1.08	-0.47 ± 0.10

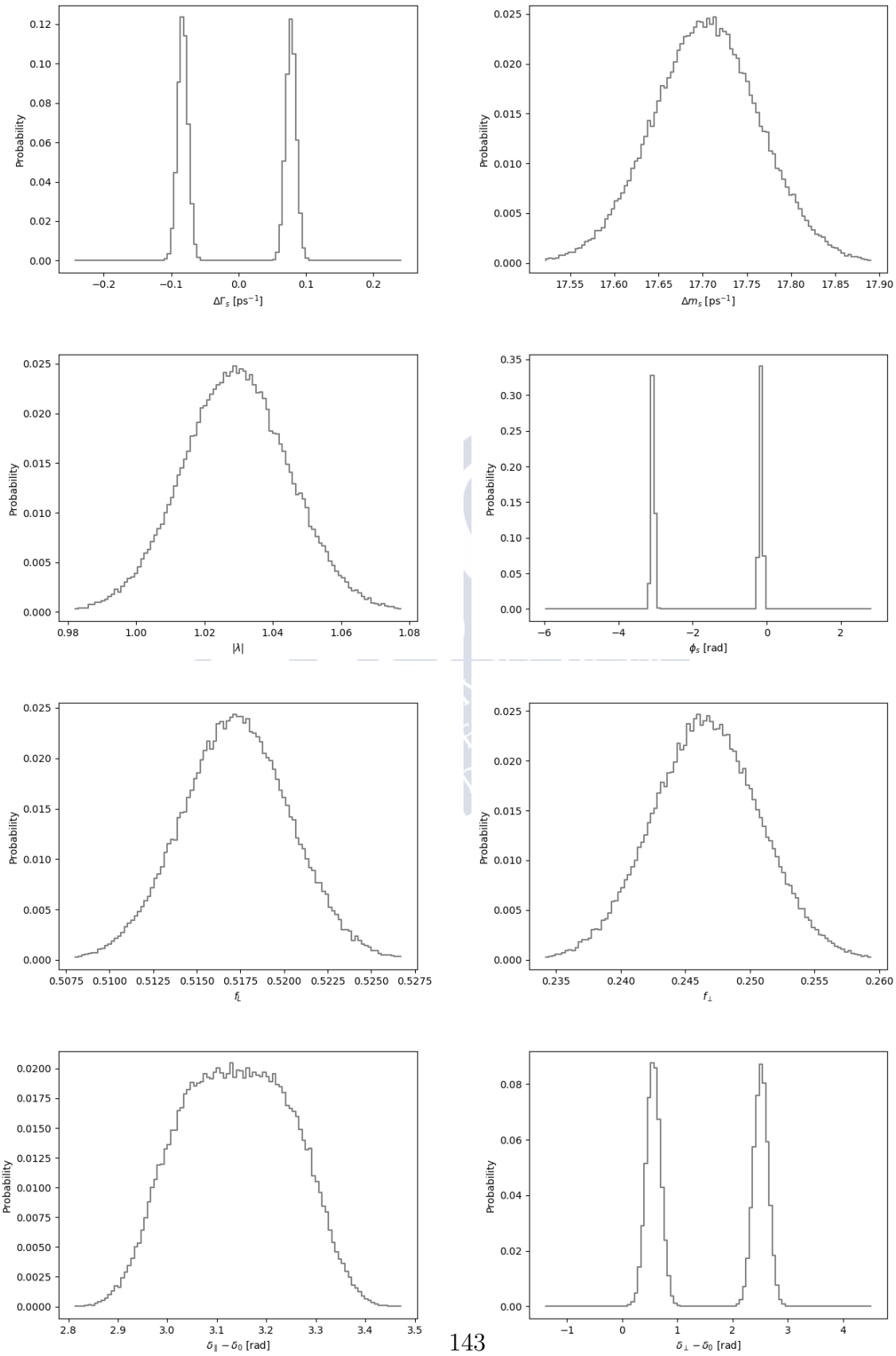

Figure 6.12: Results obtained from the `MultiNest` scan.

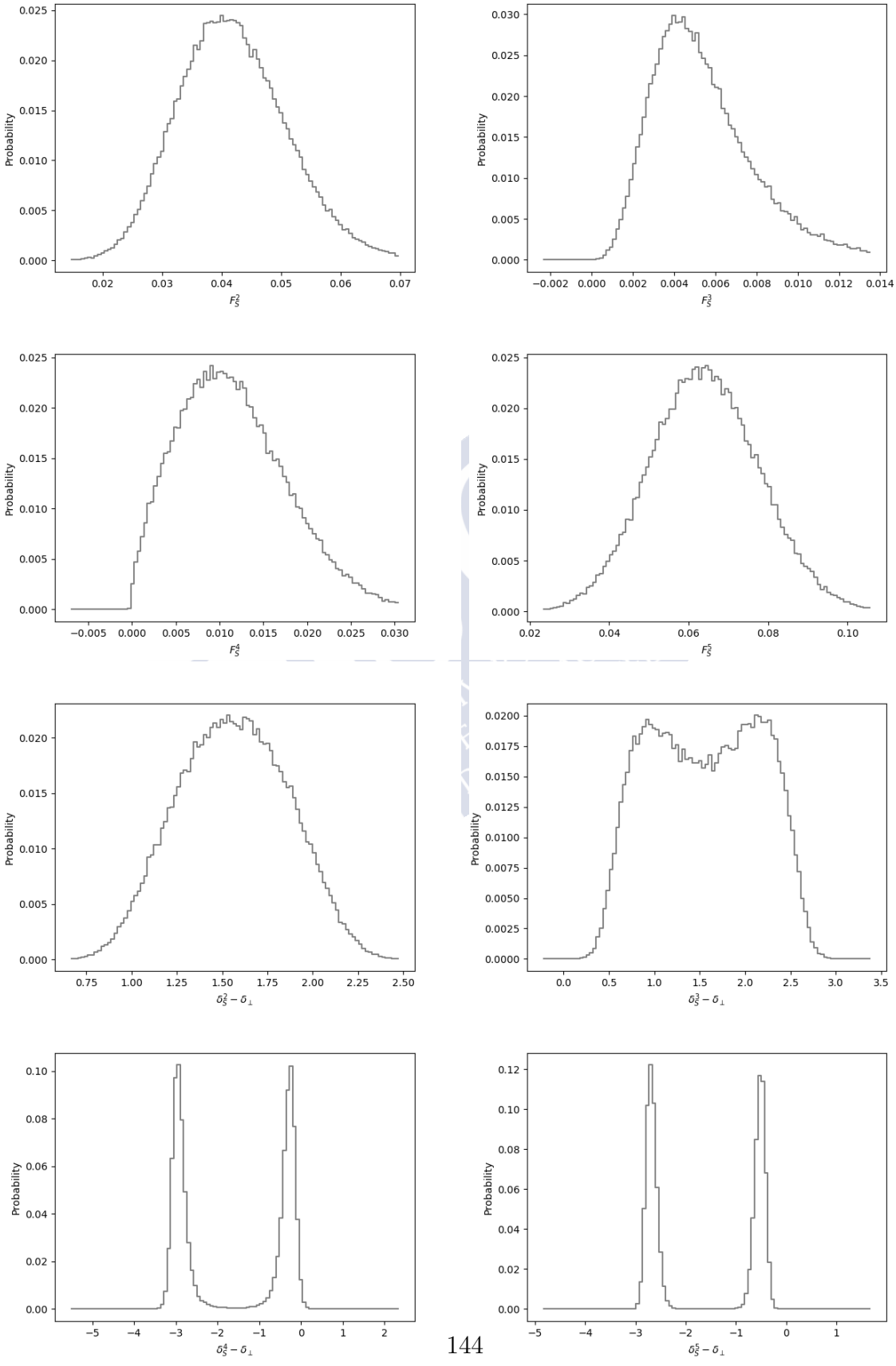

Figure 6.13: Results obtained from the `MultiNest` scan.

6.2.13 Conclusions

The tagged, time dependent angular analysis of approximately 100k $B_s^0 \to J/\psi K^+K^-$ has been performed at LHCb using 1.9 fb^{-1} of pp collision data collected by the experiment in 2015 and 2016. Such study has yielded the most precise measurement of CP violation parameters in the interference between mixing and decay for the B_s^0 system so far. The *preliminary* results, still to be approved by the LHCb collaboration, are:

$$\begin{aligned} \phi_s &= -0.081 \pm 0.041 \pm 0.005\text{rad} \\ |\lambda| &= 1.006 \pm 0.016 \pm 0.004 \\ \Delta\Gamma_s &= 0.0772^{+0.0076}_{-0.0077} \pm 0.0015\text{ps}^{-1} \\ \Gamma_s - \Gamma_d &= -0.0041^{+0.0024}_{-0.0023} \pm 0.0015\text{ps}^{-1} \end{aligned} \tag{6.21}$$

where the first uncertainties are statistical and the second sytematic. This result is in agreement with the Run 1 measurement of LHCb [247] within 1.7σ, considering statistical uncertainties only. The value of ϕ_s is 1.2σ away from the SM prediction [222]. Combining this result with the Run 1 result [247] taking into account correlations between the systematic uncertainties, and making the weighted average of this with the ϕ_s value in the high m_{KK} mass analysis [239] yields an *unapproved* average:

$$\phi_s = -0.081 \pm 0.030 \text{ rad} \tag{6.22}$$

As for future runs, the expected sensitivity for ϕ_s as a function of the luminosity can be seen in Figure 6.14.

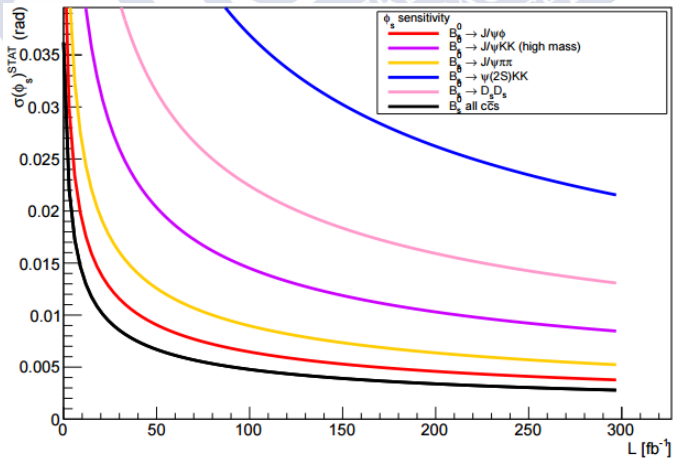

Figure 6.14: Expected sensitivity for ϕ_s as a function of the luminosity. The current central value is $\phi_s^{c\bar{c}s} = -0.021 \pm 0.031$ [245], and the SM prediction: $-2\beta_s = -0.0364 \pm 0.0016$ rad [222].

Complementarily to the analysis described in 6.2, a `MultiNest` scan has also been performed using Run 2 (2016) data, finding good agreement between this and the former. Two minima for $\Delta\Gamma_s$ and ϕ_s are found, in agreement with what is stated in Ref. [250].

6.3 Phenomenological studies

The meson-antimeson ocillations are described by the mixing amplitudes [162]

$$M_{12}^{(M)} \equiv \langle M|\mathcal{H}_{\rm eff}^{\Delta F=2}|\bar{M}\rangle \quad M = K^0, B_{d,s}, \tag{6.23}$$

where $\mathcal{H}_{\rm eff}^{\Delta F=2}$ is the *effective* Hamiltonian. Within the MSSM, it has the form:

$$\mathcal{H}_{\rm eff}^{\Delta F=2} = \sum_{i=1}^{5} C_i Q_i + \sum_{i=1}^{3} \tilde{C}_i \tilde{Q}_i + \text{h.c.} \tag{6.24}$$

with the operators Q_i given, in the case of B_s mixing, by:

$$\begin{aligned} Q_1 &= (\bar{s}^\alpha \gamma_\mu P_L b^\alpha)(\bar{s}^\beta \gamma^\mu P_L b^\beta) \\ Q_2 &= (\bar{s}^\alpha P_L b^\alpha)(\bar{s}^\beta P_L b^\beta) \\ Q_3 &= (\bar{s}^\alpha P_L b^\beta)(\bar{s}^\beta P_L b^\alpha) \\ Q_4 &= (\bar{s}^\alpha P_L b^\alpha)(\bar{s}^\beta P_R b^\beta) \\ Q_5 &= (\bar{s}^\alpha P_L b^\beta)(\bar{s}^\beta P_R b^\alpha) \end{aligned} \tag{6.25}$$

where $P_{R,L} = \frac{1}{2}(1 \pm \gamma_5)$ and α, β are colour indices. The operators $\tilde{Q}_{1,2,3}$ are obtained from $Q_{1,2,3}$ by the replacement $L \leftrightarrow R$ [162]. In the case of B_d, the replacement $s \to d$ needs to be done in equation 6.25. Several representative observables can be extracted from these amplitudes, such as the mixing phase, the oscillation frequency or the semileptonic asymmetry:

$$\phi_s = \arg(M_{12}), \;\; \Delta m_s = |M_{12}|, \;\; A_{SL} = -\frac{\Delta\Gamma_s}{\Delta M_s}\tan\phi_s \tag{6.26}$$

Note that their value strongly depends on NP contributions:

$$M_{12} = M_{12}^{SM} + M_{12}^{NP} \tag{6.27}$$

For NP searches the observables related to the $B_s^0 - \bar{B}_s^0$ oscillation (a $\Delta F = 2$ process), such as ϕ_s and Δm_s play a major role, as they are very sensitive to these NP effects. For example, new particles entering the diagrams and therefore modifying the value of the measured observables. Indeed, there are many well motivated scenarios such as Supersymmetry [54, 162] where a big difference with respect to the SM value can be achieved.

In this section, the MSSM effects in $\Delta F = 2$ processes involving B-mesons, as well as in the Electric Dipole Moments (hereafter, EDMs) of the proton and the neutron, and processes related to $\Delta F = 0$ and $\Delta F = 1$ transitions are analysed. Such observables are predicted under consideration of MSSM contributions, accounting for the relevant experimental and theoretical constraints.

Table 6.16: Scan ranges for scenario A, B (motivated by Higgsino Dark Matter) C (motivated by Wino Dark Matter), D and E. All masses are in TeV.

Parameter	Scenario A	Scenario B	Scenario C	Scenario D	Scenario E
$\tilde{m}_Q$	[2, 10]	[2, 10]	[4, 10]	[2, 5]	[2,10]
$\tilde{m}_Q^2/\tilde{m}_d^2$	[0.25, 4]	[0.25, 4]	[0.25, 4]	[0.25, 4]	[0.25, 4]
$\tilde{m}_u^2/\tilde{m}_Q^2$	1	1	1	$10/\tilde{m}_Q^2$	1
M_3	[2, 10]	[4.5, 15]	[4, 15]	[2, 10]	[2, 10]
$\tan\beta$	[2, 50]	[10, 50]	[10, 50]	[2, 50]	[2, 50]
A_t	0	0	0	0	[-3, 3]
M_A	[2, 10]	[2, 10]	[5, 20]	[2, 10]	[2, 10]
$\lvert\mu\rvert$	[2, 10]	1	[5, 20]	[2, 10]	[2, 10]
M_1	$\frac{\alpha_1(\mu^{SUSY})}{\alpha_3(\mu^{SUSY})}M_3$	$\frac{\alpha_1(\mu^{SUSY})}{\alpha_3(\mu^{SUSY})}M_3$	5	$\frac{\alpha_1(\mu^{SUSY})}{\alpha_3(\mu^{SUSY})}M_3$	$\frac{\alpha_1(\mu^{SUSY})}{\alpha_3(\mu^{SUSY})}M_3$
M_2	$\frac{\alpha_2(\mu^{SUSY})}{\alpha_3(\mu^{SUSY})}M_3$	$\frac{\alpha_2(\mu^{SUSY})}{\alpha_3(\mu^{SUSY})}M_3$	3	$\frac{\alpha_2(\mu^{SUSY})}{\alpha_3(\mu^{SUSY})}M_3$	$\frac{\alpha_2(\mu^{SUSY})}{\alpha_3(\mu^{SUSY})}M_3$
$\mathrm{Re}\left[(\delta_d^{LL})_{23}\right]$	[-0.4, 0.4]	[-0.4, 0.4]	[-0.4, 0.4]	[-0.4, 0.4]	[-0.4, 0.4]
$\mathrm{Im}\left[(\delta_d^{LL})_{23}\right]$	[-0.4, 0.4]	[-0.4, 0.4]	[-0.4, 0.4]	[-0.4, 0.4]	[-0.4, 0.4]
$\mathrm{Re}\left[(\delta_d^{LL})_{23}\times(\delta_d^{RR})_{23}\right]$	[-0.01, 0.01]	[-0.01, 0.01]	[-0.01, 0.01]	[-0.01, 0.01]	[-0.01, 0.01]
$\mathrm{Im}\left[(\delta_d^{LL})_{23}\times(\delta_d^{RR})_{32}\right]$	[-0.01, 0.01]	[-0.01, 0.01]	[-0.01, 0.01]	[-0.01, 0.01]	[-0.01, 0.01]

6.3.1 Formalism and parameter scan

The formalism, as well as the first three scenarios, are the same as the ones used in Section 5.2. Apart from these scenarios, two additional ones are also explored:

- Scenario D: a scenario with trilinear couplings set to zero, $A_t = 0$ and a very heavy right-handed stop, motivated by scenarios with conservative predictions for EDMs.
- Scenario E: a scenario with $A_t \neq 0$, $\tilde{m}_Q = \tilde{m}_t$, motivated by sccenarios with more aggressive predictions for EDMs.

A summary of the corresponding ranges for the different parameters can be found in Table 6.16.

6.3.2 Observables

The following observables are calculated:

- Observables sensitive to $\tan\beta$ and the heavy Higgs mass: $\mathcal{B}(B^+ \to \tau^+\nu_\tau)$, ΔC_7.
- $\mathcal{B}(B_s^0 \to \mu^+\mu^-)$, $\mathcal{B}(B_d^0 \to \mu^+\mu^-)$

The definitions of $\mathcal{B}(B^+ \to \tau^+\nu_\tau)$ and ΔC_7 are given in ref. [162] and in Section 5.2.2.3. The branching fractions $\mathcal{B}(B_s^0 \to \mu^+\mu^-)$ and $\mathcal{B}(B_d^0 \to \mu^+\mu^-)$ are computed following the expressions in Appendix G.1. The CKM matrix is fitted excluding measurements with potential sensitivity to MSSM contributions. The following observables are calculated from the mixing amplitudes for B_s and B_d:

- The mixing phase of the $B_{s,d}$ meson system with respect to its SM prediction, $\Delta\phi_{s,d} = \arg\left(M_{12}/M_{12}^{\mathrm{SM}}\right)$

- The mass difference of the $B_{s,d}$ meson system with respect to its SM prediction, $\Delta m_s/\Delta m_s^{SM} = |M_{12}|/|M_{12}^{\rm SM}|$
- The semileptonic asymmetry, computed as $-\frac{\Delta\Gamma_s}{\Delta M_s}\tan\phi_s$ The value for $\Delta\Gamma_s$ is taken as 0.085 ± 0.015 [251]. In order to use a quantity easier to construct from the theoretical point of view, the quantity $\Delta M_s A_{SL}/\Delta\Gamma_s$ is used.

The Electric Dipole Moments for each scenario are also computed, as they have been shown to be very good probes for New Physics contributions, given that they are predicted to be very small in the SM and can be accurately measured. Therefore, they can be used as complementary NP serches. These are CP-violating but flavour conserving observables. Proton and neutron represent complementary information, as they have different sensitivities to the EDMs, in addition to different up and down distributions. The formulae used are specified in appendix G.2.3. The neutron, proton and mercury EDMs (the element that provides the strongest experimental limit [252]) are computed as follows:

$$d_n = 1.4 * (d_d/e - 0.25 * d_u/e) + 0.83 * (d_u^c + d_d^c) - 0.27 * (d_u^c - d_d^c) \tag{6.28}$$

$$d_p = 1.4 * (d_u/e - 0.25 * d_d/e) + 0.83 * (d_u^c + d_d^c) + 0.27 * (d_u^c - d_d^c) \tag{6.29}$$

$$d_{Hg} = -2.4 \times 10^{-4} * (1.9 * d_n + 0.2 * d_p); \tag{6.30}$$

Finally, the difference of the CP asymmetries in $B^- \to X_s^-\gamma$ and $\bar{B}^- \to X_s^0\gamma$ is computed, as it is sensitive to the contributions to C_7, C_8, C_7' and C_8' in these type of studies. The formula is taken from Ref. [175]

$$\Delta A_{CP}(b\to s\gamma) = A_{\rm CP}(B^-\to X_s^-\gamma) - A_{\rm CP}(\bar{B}^-\to X_s^0\gamma) = 4\pi^2\alpha_s(\mu_b)\frac{\tilde{\Lambda}_{78}}{m_b}{\rm Im}\left[\frac{{\rm C}_{7\gamma}^*{\rm C}_{8g} + {\rm C}_{7\gamma}'^*{\rm C}_{8g}'}{|{\rm C}_{7\gamma}|^2 + |{\rm C}_{7\gamma}'|^2}\right] \tag{6.31}$$

where the hadronic parameter is assumed to be $\tilde{\Lambda}_{78} = 89$ MeV. The constraints imposed on physics observables are listed in table 6.17 where the EXP/SM represents the measured value over the SM prediction with their uncertainties. The expressions used for the Wilson coefficients are specified in Appendix G.2.1.

6.3.3 Results

Scatter plots are shown for each scenario, corresponding to the 95% CL, given the number of degrees of freedom. The black points are computed without including the ϕ_s constraint, while the pink asterisks are made including the ϕ_s constraint. It can be seen that this constraint greatly affects the allowed range of ϕ_s- ϕ_s^{SM} , as well as the range of the other observables. The experimental results from Table 6.17 are indicated with variations of $\pm 1\sigma$ with respect to their uncertainties with green shaded areas. For points satisfying the imposed cut on χ^2 ($\chi^2 < 21.0$ when applying the $\phi_s - \phi_s^{SM}$ constraint and $\chi^2 < 19.7$ otherwise), it is found that the most stringent constraints are those coming from $\Delta A_{CP}(b\to s\gamma)$ and $\mathcal{B}(B_s^0\to\mu^+\mu^-)^{\rm EXP/SM}$. Because of the smaller value of μ as compared to the other scenarios, the allowed range for the different observables is generally more limited in scenario B.

For each scenario, $\Delta\phi_{s,d}$ is shown versus the phase of the product of the MIs (in Figures 6.15 and 6.16. Any deviation from the 0 in the Y axis implies a discrepancy with the SM prediction.

Table 6.17: Physics observables constraints imposed in this study.

Observable	Constraint
$\Delta m_s/\Delta m_s^{SM}$	0.948 ± 0.062 [29, 253]
$\phi_s - \phi_s^{SM}$	-0.0447 ± 0.0301 [222, 245]
$\phi_d - \phi_d^{SM}$	-0.1796 ± 0.0535 [245]
$\mathcal{B}(B_s^0 \to \mu^+\mu^-)^{\mathrm{EXP/SM}}$	0.71 ± 0.12 [29, 254]
$\mathcal{B}(B_d^0 \to \mu^+\mu^-)^{\mathrm{EXP/SM}}$	9.71 ± 6.41 [29, 254]
$\Delta m_s A_{SL}/\Delta\Gamma_s - (\Delta m_s A_{SL}/\Delta\Gamma_s)^{\mathrm{SM}}$	-0.1257 ± 0.5651 [245]
$\mathcal{B}(B^+ \to \tau^+\nu_\tau)^{\mathrm{EXP/SM}}$	0.87 ± 0.21 [29, 254]
ΔC_7	-0.02 ± 0.02 [177]
$\Delta A_{CP}(b \to s\gamma)$	$5.0 \pm 3.9_{\mathrm{stat}} \pm 1.5_{\mathrm{syst}}$ [255]
$\lvert d_n \rvert$	2.9×10^{-26} e cm (90% CL) [256]
$\lvert d_{Hg} \rvert$	7.4×10^{-30} e cm (90% CL) [252]
m_H	125.18 ± 20 [GeV] [29]
$\tan\beta$:M_A plane	ATLAS limits for hMSSM scenario [178]
LSP	Lightest neutralino

As it can be seen, in most cases the majority of the points stand further than 1σ away from the experimental result. Nevertheless, points with the same prediction as in the SM are also observed.

Figure 6.17 shows the values of $\mathrm{Re}(C_4)$ vs $\mathrm{Im}(C_4)$ from B_s^0 oscillation for the different scenarios, again with and without the constraint on ϕ_s. Given that in the SM there is no contribution to C_4, any deviation would be a sign of NP. As it can be seen, large values can be obtained within the different cases considered.

As for the EDMs, they are shown for the different scenarios in Figure 6.18. For these, only points where the constraint on ϕ_s is applied are shown. As expected, the allowed range for the scenario E is much wider than for scenario D, given that it is tailor made for aggressive EDM predictions. Big deviations from the SM are foreseen, some of these entering the experimental upper limits [252, 256], indicated by shaded yellow areas.

The ratios of the EDMs over CEDMs for the down-quark and strange-quark are also shown as a function of the mass ratio $x_{\tilde{g}} = M_3/\tilde{m}^2$ (Figures 6.19, 6.20). A clear dependence can be seen, as this ratio of EDMs only depends on loop functions that have x_g as an argument. Therefore, they can be used to set limits on the corresponding masses.

The difference $\left|\phi_d - \phi_d^{SM}\right|$ is represented as a function of the neutron EDM in Figure 6.21, showing a clear dependence. Again, the yellow shaded area indicates the upper limit on the neutron EDM [256], where some of the predicted points enter. As before, large departures from the SM in both variables can be seen.

Finally, in Figure 6.22, ϕ_s-ϕ_s^{SM} is shown as a function of the semileptonic asymmetry (taking the ratio of this over the SM prediction). A manifest dependence can be seen for the latter, that acquires values very different from 1. Moreover, the effect imposed by the constraint on ϕ_s can be clearly appreciated in this result.

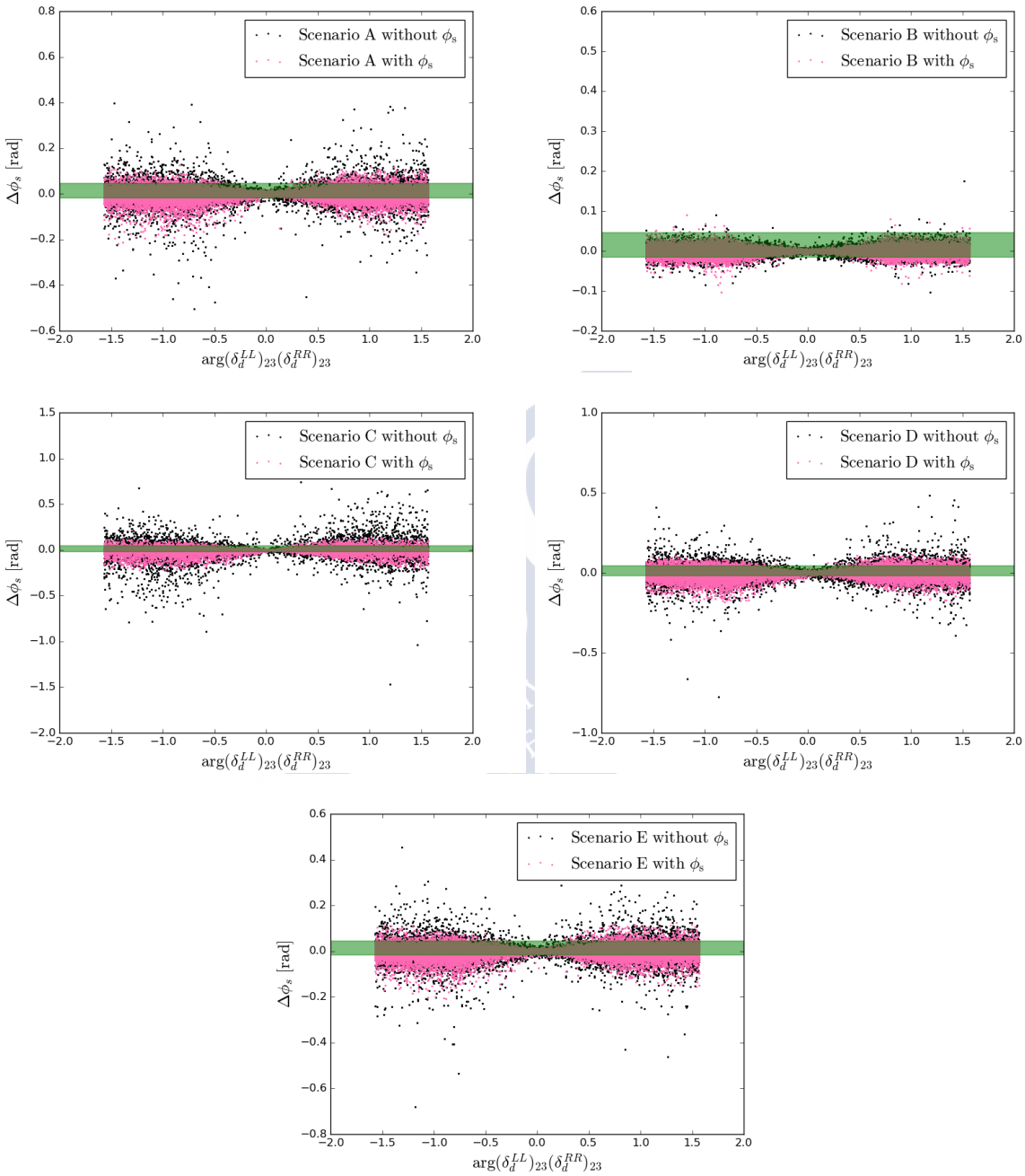

Figure 6.15: ϕ_s- ϕ_s^{SM} vs the the argument of the 23 $\delta_d^{LL}\delta_d^{RR}$ for scenarios A (upper left), B (upper right), C (middle left), D (middle right) and E (bottom).

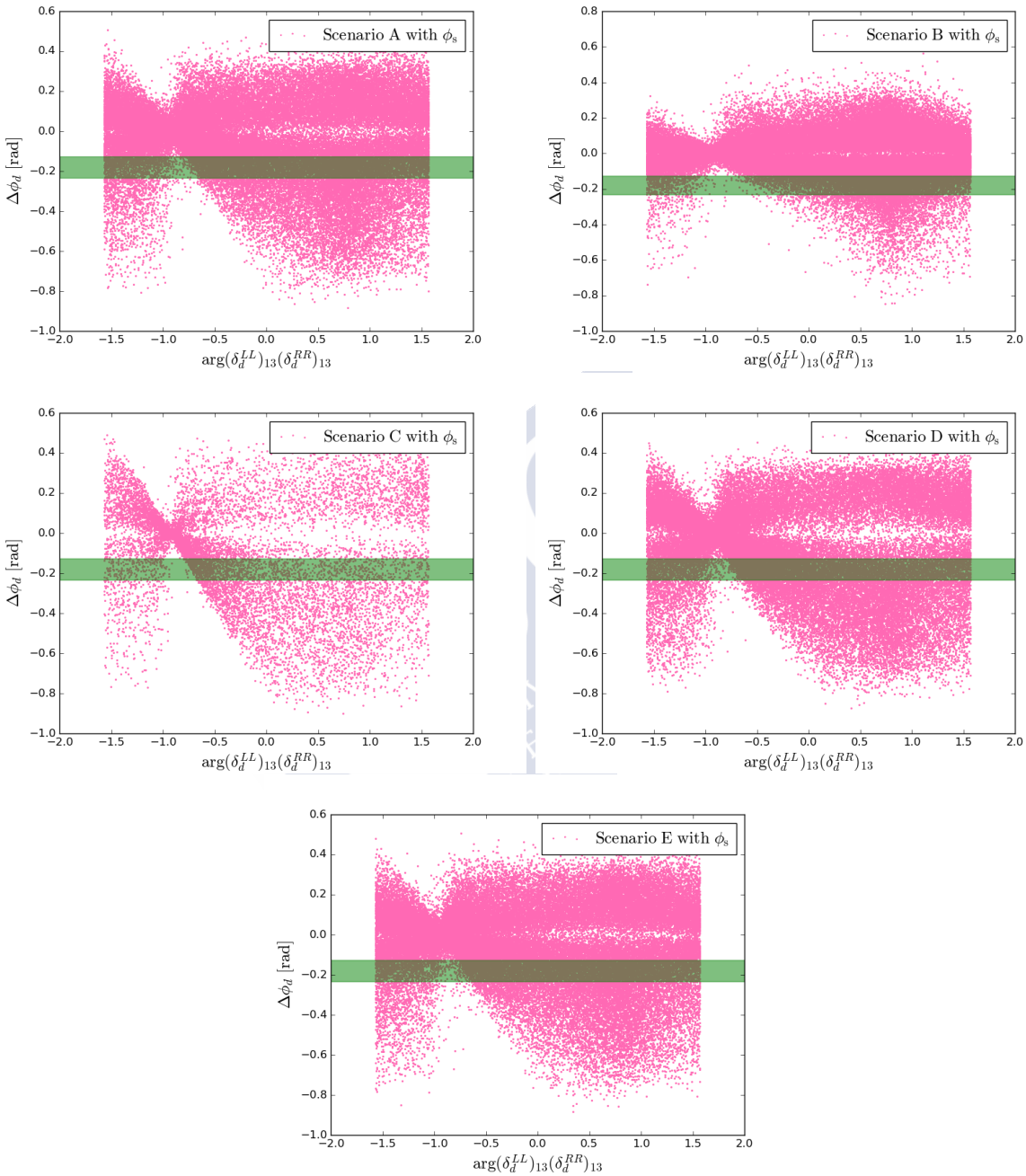

Figure 6.16: ϕ_d - ϕ_d^{SM} vs the the argument of the $\delta_d^{LL}\delta_d^{RR}$ MIs for scenarios A (upper left), B (upper right), C (middle left), D (middle right) and E (bottom).

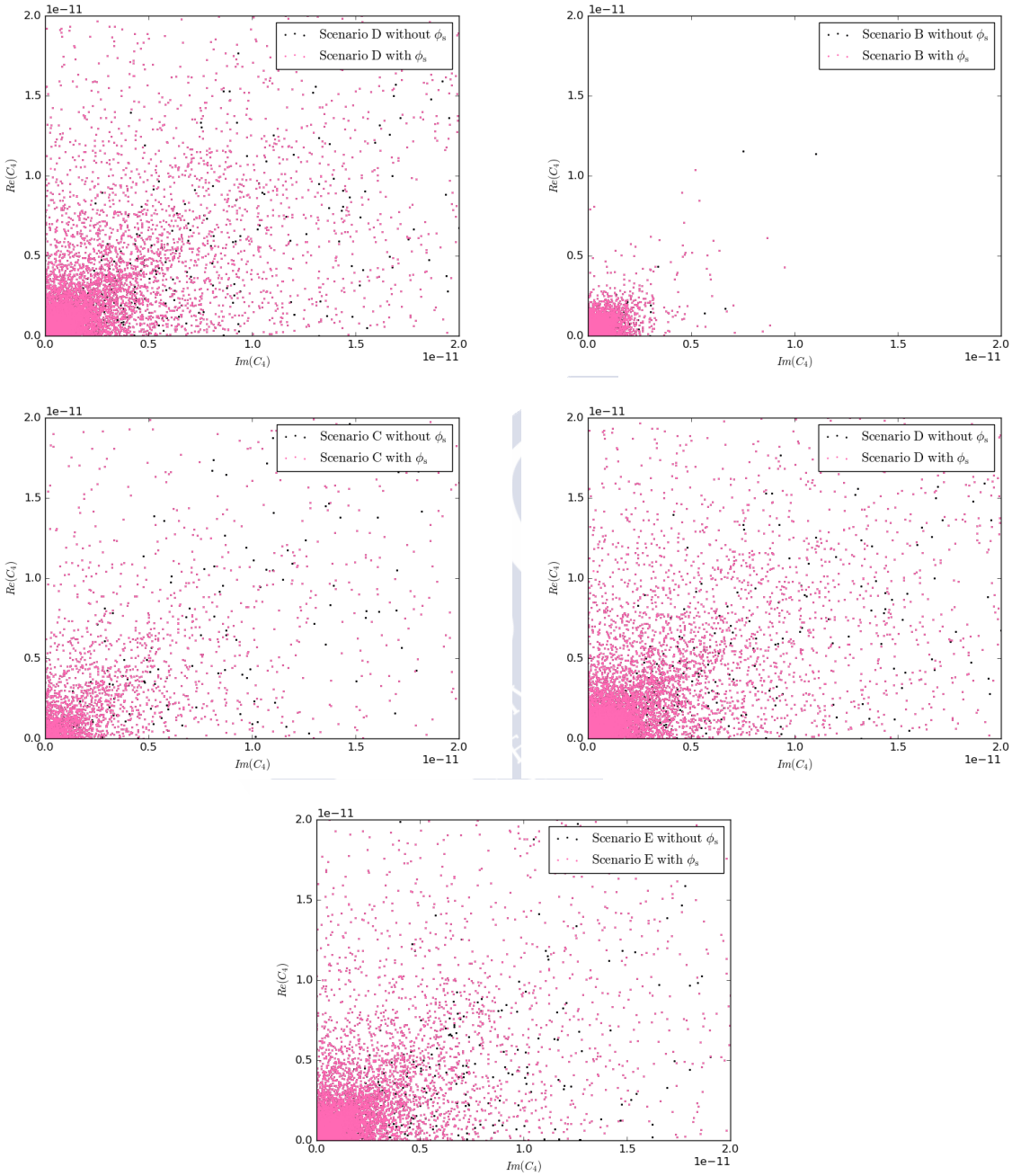

Figure 6.17: Re(C_4) vs Im(C_4) from B_s^0 oscillation, for scenarios A (upper left), B (upper right), C (middle left), D (middle right) and E (bottom).

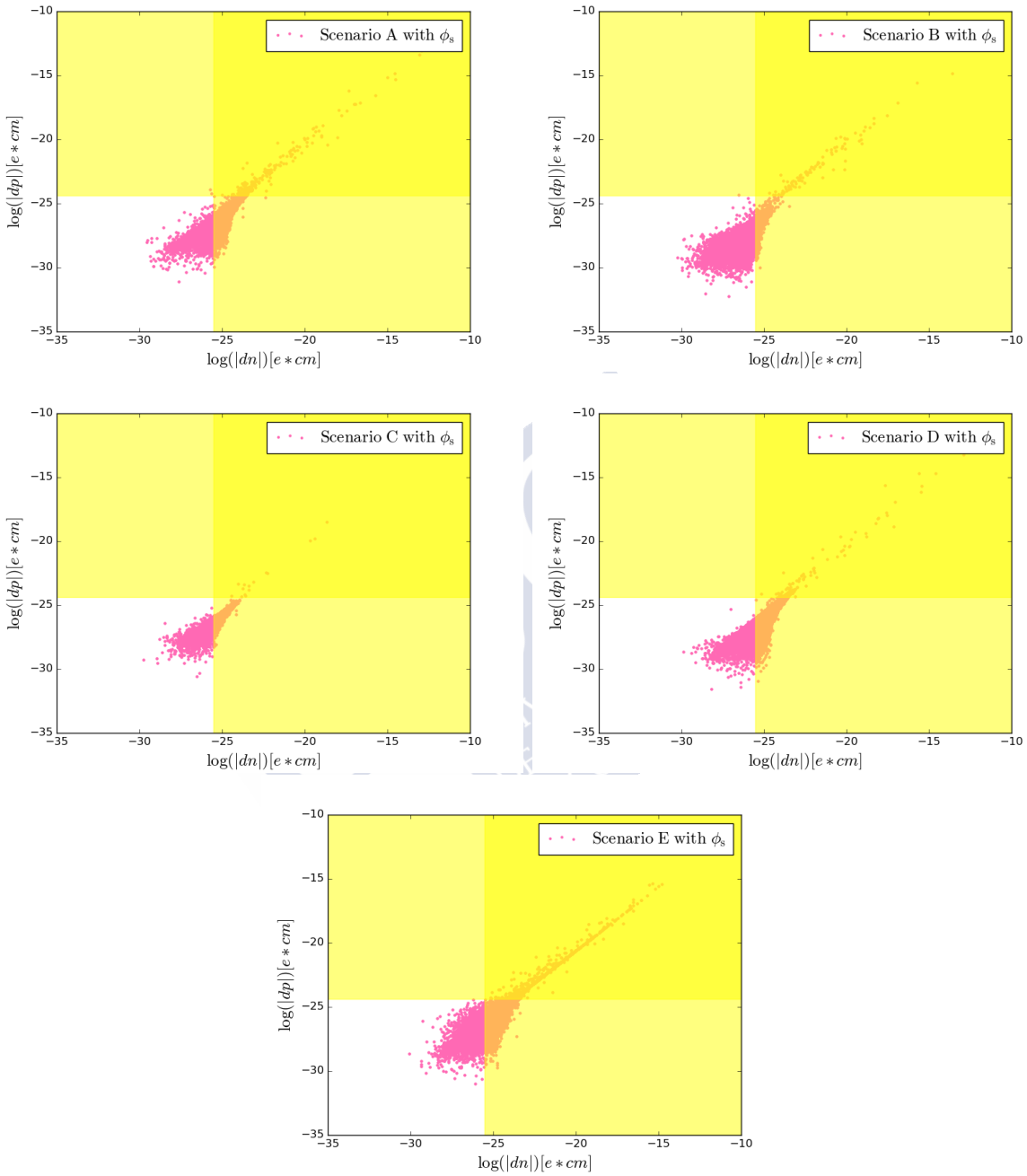

Figure 6.18: Neutron EDM vs proton EDM for scenarios A (upper left), B (upper right), C (middle left), D (middle right) and E (bottom). The yellow shaded area corresponds to the region excluded by the present limit on neutron EDM at 90% CL [256].

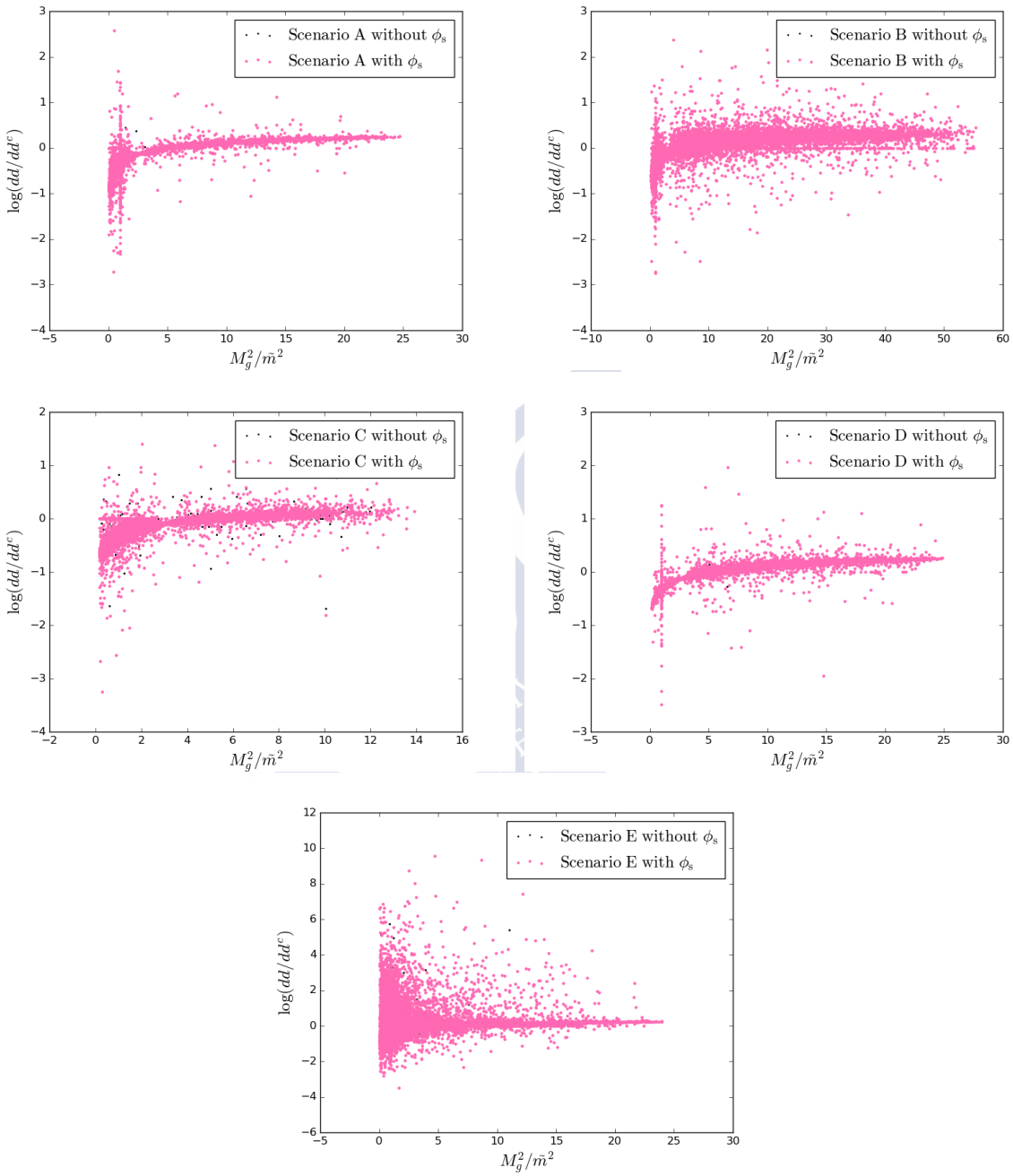

Figure 6.19: Ratio of the down-quark (C)EDMs vs $x_{\tilde{g}} = M_3/\tilde{m}^2$ for scenarios A (upper left), B (upper right), C (middle left), D (middle right) and E (bottom).

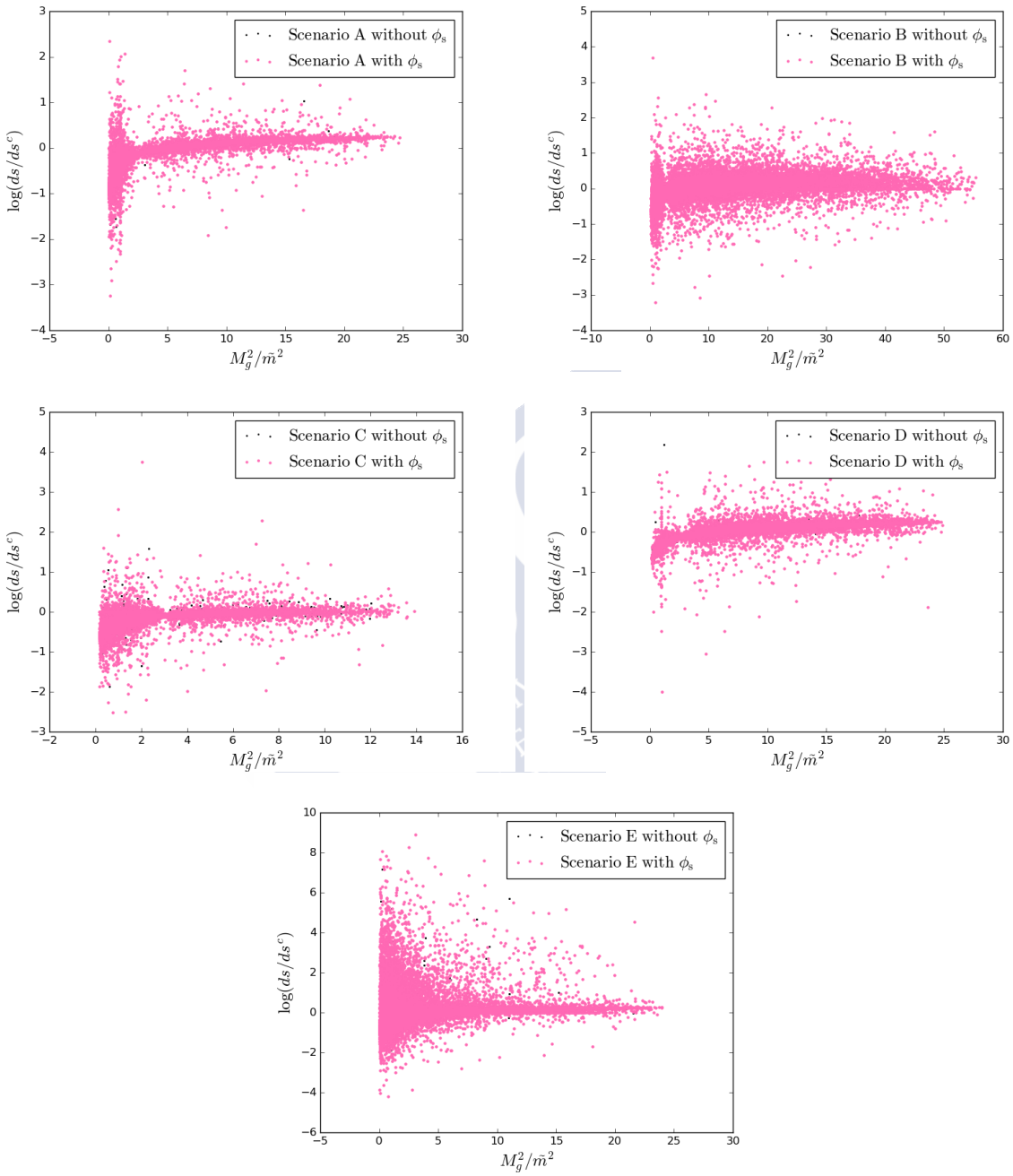

Figure 6.20: Ratio of the strange-quark (C)EDMs vs $x_g = M_3/\tilde{m}^2$ for scenarios A (upper left), B (upper right), C (middle left), D (middle right) and E (bottom).

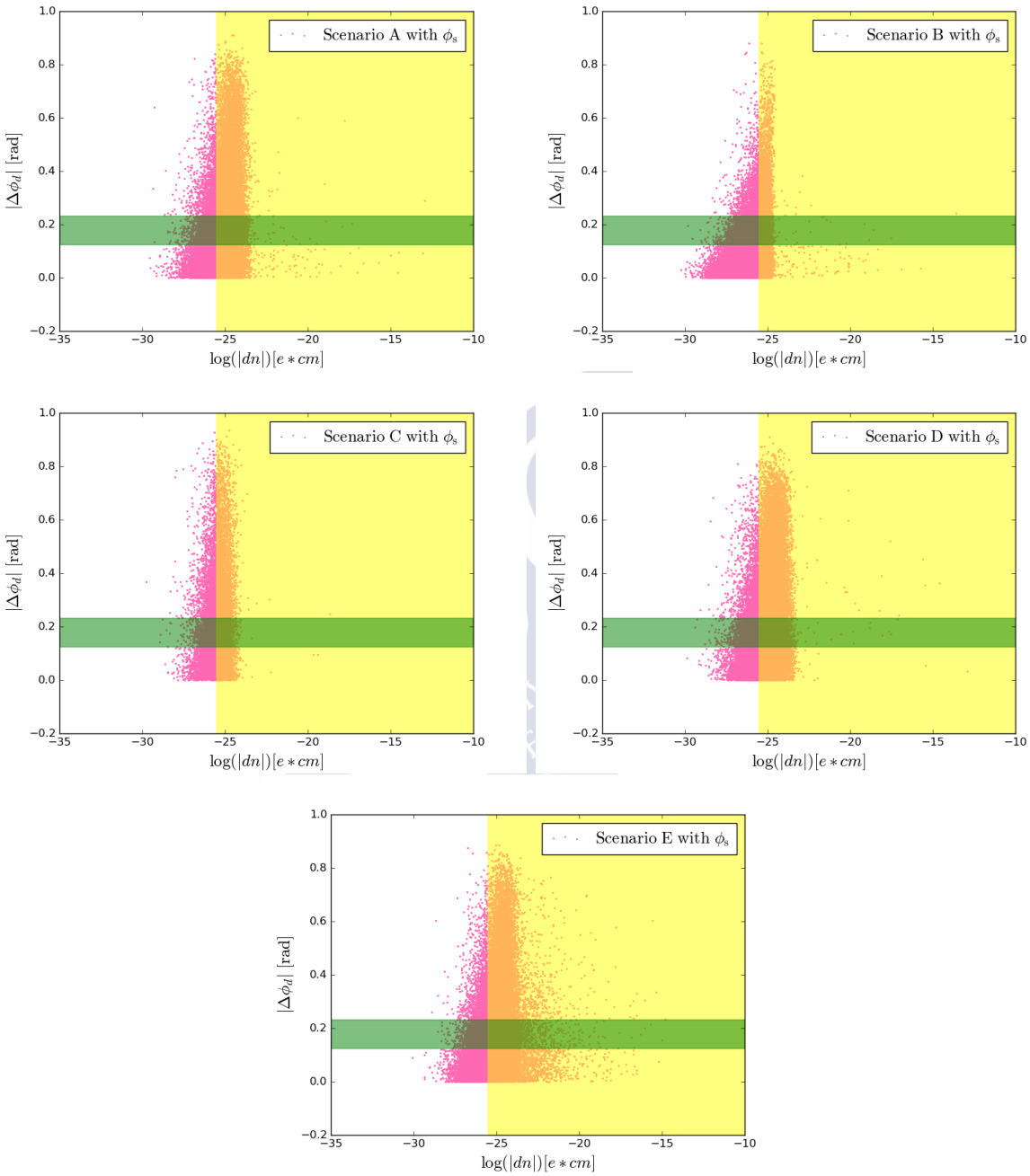

Figure 6.21: $|\phi_c - \phi_d^{SM}|$ vs the EDM of the neutron for scenarios A (upper left), B (upper right), C (middle left), D (middle right) and E (bottom).

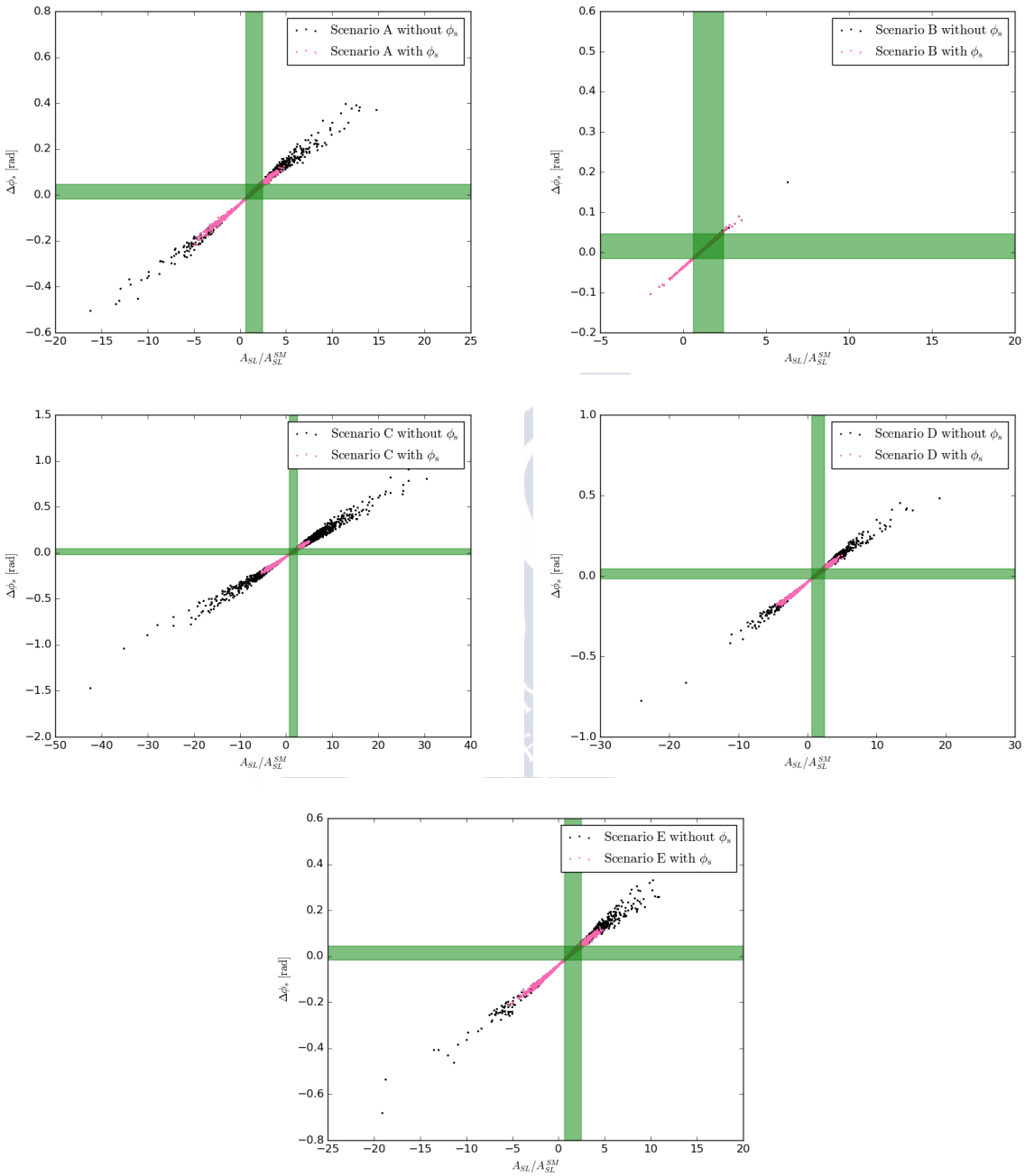

Figure 6.22: ϕ_s- ϕ_s^{SM} vs A_{sl}/A_{sl}^{SM} for scenarios A (upper left), B (upper right), C (middle left), D (middle right) and E (bottom).

6.3.4 Conclusions

Phenomenological studies for the B_s, B_d system and the EDMs have been performed under a MSSM scenario, similarly to what has been done in Section 5. Regions where large variations from the respective SM values have been found to fulfill the relevant constraints. Moreover, the ϕ_s result imposes a very important constraint on the available parameter space. Furthermore, correlations among the different studied observables have been seen, such as the neutron EDM with respect to $|\phi_d - \phi_d^{SM}|$ or $\phi_s - \phi_s^{SM}$ with respect to the semileptonic asymmetry.

Chapter 7

MasterCode

7.1 MasterCode framework

The MasterCode framework performs global fits following a frequentist approach. Its core consists of tools to compute the different the SUSY observables, tools to calculate the χ^2 (that will be discussed in more details in Section 7.4) and the interface to an appropiate sampling algorithm, MultiNest [227]. So as to compute the SUSY observables, the full MSSM spectrum for electroweak observables (including masses, mixing matrices and couplings) is computed by SoftSUSY 3.7.2 [257]. The Higgs sector of this spectrum is further refined using calculations from FeynHiggs 2.12.1β [258–262]. This spectrum (in a format compliant with SUSY Les Houches Accord [263, 264]) is then used as input for other codes to compute more observables and constraints, summarised in Table 7.1. Moreover, SuperIso v3.5 [265–267] and Susy_Flavor v2.54 [268] are used to check the evaluations of flavour observables, and Matplotlib [269] and PySLHA [270] for plotting purposes. From this, a global likelihood function is constructed, including contributions from electroweak precision observables, flavour measurements, the cosmological dark matter density and direct searches for dark matter, as well as the LHC Higgs mass measurement and missing transverse energy (net momentum in the transverse direction indicating non-interacting particles) searches.

Table 7.1: Codes used to calculate SUSY observables in the MasterCode framework.

Code	Reference	Observables
SoftSUSY 3.7.2	[257]	SUSY spectrum
FeynHiggs-2.12.1β	[258–262]	Higgs sector, $(g-2)_\mu$
micrOMEGAs-3.2	[271]	$\Omega_{\rm CDM}h^2$
SSARD	[272]	$\sigma_p^{\rm SI}$, $\Delta\sigma_p^{\rm SI}$
SuFla, SuperIso v3.5	[273, 274], [265–267]	Flavour physics
FeynWZ	[275, 276]	M_W, Z-pole
HiggsSignals-1.4.0	[277, 278]	Constraints Higgs signal-strengths
HiggsBounds-4.3.1	[279–282]	Constraints $H/A \to \tau^+\tau^-$ decay
SDECAY-1.3b	[283]	Decay tables

7.2 Sampling algorithm

The main goal of the `MasterCode` framework is establishing confidence intervals for parameters and observables. In order to do this, the desired region is sampled and the likelihood function is inspected by means of the `MultiNest` algorithm [227]. Even though it was designed as a Bayesian inference tool, it has proven to be very sucessful in computing profile likelihood functions [284].

The likelihood is computed iteratively based on the so-called ellipsoidal nested sample. In this mechanism, ellipsoidal bounds are constructed in the unit cube based on clustering of N *active* points. For each iteration, the point with the lowest likelihood amongst a set of points (*live* or active) is discarded, and another one with higher likelihood is searched. When found, it replaces the former, that turns into an *inactive* point. This is done until the Bayesian evidence has reaches a value controlled by the *tolerance*.

Apart from its robustness and efficiency, this algorithm was specifically designed to deal with multiple local maxima and elongated curving degeneracies, thus fulfilling `MasterCode`'s requirements. A special feature of `MultiNest` is that once a point becomes active, it forms a basin of attraction, so that proximal points will be sampled. This ensures the coverage of small volumes, provided one of their points becomes active.

In order to ensure a good coverage of the parameter space, it is divided into segments. The "cross-produc" of these segments constitute *boxes*. For each of these boxes, the number of active points is $N = 1000$. Priors are defined in order to convert the input parameters into physical quantities computable by the likelihood. Usually soft flat priors are used (an example of this distribution can be seen in Figure 7.1). With this, 80% of the distribution lies within the nominal segment range, with the oher 20 % outside these bounds. This allows for some overlap between boxes, hence avoiding edge effects between neighbouring parameter segments.

7.3 Scan Ranges

The scan ranges are chosen such that they include a full coverage of parameter space, focusing on the mass scales relevant for LHC, while maintaining the Yukawa couplings perturbatively small. The input parameters and the nuisance parameters are sampled using soft flat and Gaussian priors, respectively.

7.4 Method

So as to explore the different models within the `MasterCode` framework, frequentist confidence intervals and regions for the model parameters and corresponding predictions for physical observables are established. In order to do this, a χ^2 function is constructed from the likelihood function using Wilks' theorem, $\chi^2 \approx -2\ln(\theta) + \text{const.}$, where the normalisation constant is irrelevant. The χ^2 function is given by

$$\chi^2(\theta) \equiv \sum_i \left(\frac{O_{i,\text{meas.}} - O_{i,\text{pred.}}}{\sigma(O_i)} \right)^2 + \sum_j \left(\frac{\theta^{\text{SM}}_{j,\text{meas.}} - \theta^{\text{SM}}_{j,\text{nuis.}}}{\sigma(\theta^{\text{SM}}_{j,\text{meas.}})} \right)^2 + \sum_k \chi^2_{k,\text{non-Gaussian}} \qquad (7.1)$$

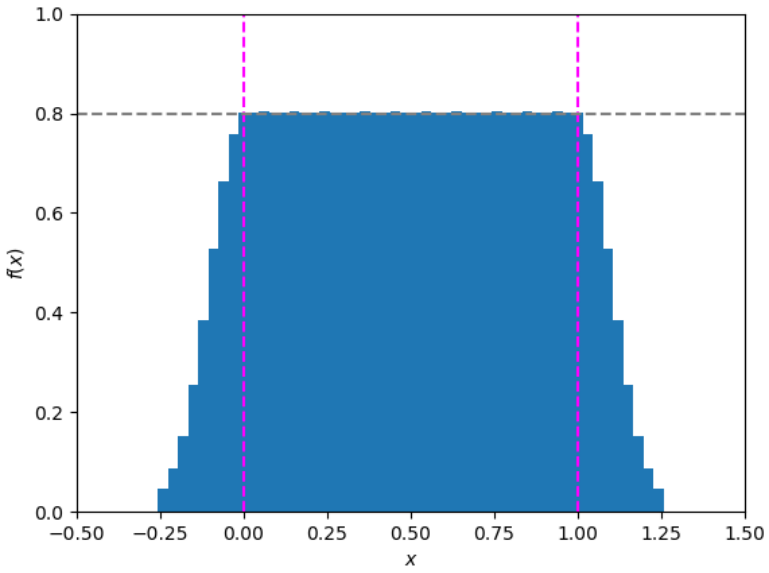

Figure 7.1: Illustration of soft flat prior, for which 80% is flat and lies within the nominal range of the segment ([0,1]), while 20% of the distribution lies outside the nominal range, and is normally distributed.

where $O_{i,\text{pred.}}(\theta)$ ($O_{i,\text{meas.}}(\theta)$) are the predicted (measured) values for the observables, $\theta(O_i)$ is the total uncertainty, obtained adding the experimental and theoretical uncertainties in quadrature, and $\theta_{k,\text{nuis.}}$ are the SM nuisance parameters m_t, $\Delta\alpha^{(5)}_{\text{had}}(M_Z)$, M_Z that are allowed to vary in the fit while being constrained according to their measured values and uncertainties. The first two terms in Eq. 7.1 correspond to a normal distribution of the likelihood, thus being "Gaussian" constraints, while the third term is "non-Gaussian" and a more refined treatment is needed. The confidence intervals for n parameters and/or physical observables of interest at a confidence level α are thus given by the condition $\Delta\chi^2 \leq \Delta\chi^2(\alpha, n)$. Some typical values are given in Table 7.2.

Table 7.2: Values for $\Delta\chi^2(\alpha, n)$ that define the acceptance region $\Delta\chi^2 \leq \Delta\chi^2(\alpha, n)$ for a confidence level of α assuming a χ^2-distribution for n degrees of freedom.

$\alpha(\%)$	$\Delta\chi^2(\alpha, 1)$	$\Delta\chi^2(\alpha, 2)$
68	0.99	2.27
68.3	1	2.30
95	3.84	5.99
95.4	4	6.18
99	6.63	9.21
99.7	9	11.82

Therefore, 68% CL intervals (regions) correspond to $\Delta\chi^2 < 1 (\Delta\chi^2 < 2.30)$, while 95% CL intervals (regions) correspond to $\Delta\chi^2 < 4 (\Delta\chi^2 < 5.99)$ for one-(two-)dimensional profile likelihood functions.

7.4.1 Gaussian Constraints

The following Gaussian Constraints are used in the study (references are given with the corresponding value):

- 95% CL lower limits on the masses of SUSY particles from ALEPH, DELPHI, L3, OPAL experiments [285].
- Top mass, a SM input parameter to the MSSM spectrum calculaton, therefore treated as a nuisance parameter.
- The mass of the light Higgs boson, which is one of the most accurately and constraining properties of this particle. The assumed theoretical uncertainty for the lightest Higgs mass within MSSM (computed using `FeynHiggs-2.12.1`β) is a conservative but accurate estimate of the point-by-point uncertainty that can be calculated with such code. Further constraints on the Higgs decays are incorporated using `HiggsSignals-1.3.1`.
- Dark matter relic density, determined from anisotropies in the Cosmic Microwave Background and satellite measurements. The origin of its value remains unanswered by the SM (see Section 1.4.3), therefore being a crucial input for any NP scenario. The SUSY prediction is taken from `micrOMEGAs-3.2`. Given the high sensitivity of such prediction to the given spectrum, a theoretical uncertainty of $\sim 10\%$ is assumed.
- Electroweak precision observables (EWPOs), M_W and the Z-pole observables. Being very accurately measured and predicted in the SM, they are valuable probes to disentangle NP contributions from SM ones. These are computed using `FeynWZ`. Its inputs, $\Delta\alpha^{(5)}_{\text{had}}(M_Z)$ and M_Z, are treated as nuisance parameters in the fit.
- Flavour physics observables, such as branching fractions from rare B decays, rare K decays, $B - \bar{B}$ mixing and ϵ_K. As shown in Chapter 6, their values are very sensitive to NP effects. Moreover, most of these observables are strongly suppressed within the SM. The SUSY predictions for flavour physics observables are calculated using `SuFla` and `SuperIso`.

7.4.2 Non-Gaussian Constraints

Contributions from non-Gaussian constraints include:

- Searches for squarks and gluinos by ATLAS and CMS, that strongly constrain the parameter space of the models. A χ^2 is estrapolated from the provided contour plots.
- Production of heavy neutral Higgs bosons decaying into taus, $H/A \to \tau^+\tau^-$. The experimental result [286] constitutes a search for NP particles (A), as well as a test of the Higgs properties. As before, a χ^2 is constructed from the exclusion contours from ATLAS and CMS using `HiggsBounds-4.3.1`.

- Spin-independent cross section of neutralino-nucleus elastic scattering. If measured different from zero, it would constitute a striking evidence of the existence of the LSP within a Supersymmetric scenario. Results from LUX, XENON, Panda and PICO and experimental uncertainties in the theoretical calculation [287] are considered.

7.5 CMSSM Results

The ranges, the number of segments and the resulting number of boxes that are used in the scan are given in table 7.3 (column labelled as "Total range"). A dedicated supplementary scan of the low-mass region (for m_0 and $m_{1/2}$) is performed, with the same number of segments (column named "Low-mass range"). A total of $\sim 35(50) \times 10^6$ points have been sampled with $\mu > 0$ ($\mu < 0$), being μ is the Higgs mixing parameter.

Table 7.3: Sampling ranges and segment definitions in the CMSSM model.

Parameter	Total range	Low-mass range	Segments
m_0	(0, 10) TeV	(0,4) TeV	2
$m_{1/2}$	(0, 10) TeV	(0,4) TeV	2
A_0	(-10,10) TeV	(-10,10) TeV	4
$\tan\beta$	(2 , 70)	(2,70)	2
Total number of boxes			32

7.5.1 Constraints

The constraints considered in this study are summarized in table 7.4. Note that, in order to be able to appreciate the effect of the LHC 13 constraints, only LHC 8 constraints have been included so far in the study. Moreover, future plans include imposing the dark matter relic density constraint as an upper limit, so that the neutralino does not account for the whole CDM, but only for a fraction. In addition, the $(g-2)_\mu$ constraint is not applied, since it would just represent a constant shift throughout the points and cannot be accommodated within the CMSSM.

Apart from the constraints listed in 7.4, constraints including 95% CL lower limits on the masses of SUSY particles supersymmetric searches and universal limits have been also included, as described in sections 7.4.1 and 7.4.2, together with constraints from `HiggsSignals` and `HiggsBounds`. Moreover, the LSP is required to be a neutralino.

Table 7.4: List of experimental constraints used in this work, including experimental and (where applicable) theoretical errors: supersymmetric theory uncertainties are indicated separately.

m_t [GeV]	[288]	173.34 ± 0.76
$\Delta\alpha^{(5)}_{\rm had}(M_Z)$	[1]	0.02771 ± 0.00011
M_Z [GeV]	[289, 290]	91.1876 ± 0.0021
Γ_Z [GeV]	[275, 276, 289, 291]	$2.4952 \pm 0.0023 \pm 0.001_{\rm SUSY}$
$\sigma^0_{\rm had}$ [nb]	[275, 276, 289, 291]	41.540 ± 0.037
R_l	[275, 276, 289, 291]	20.767 ± 0.025
$A_{\rm FB}(l)$	[275, 276, 289, 291]	0.01714 ± 0.00095
$A_l(P_\tau)$	[275, 276, 289, 291]	0.1465 ± 0.0032
R_b	[275, 276, 289, 291]	0.21629 ± 0.00066
R_c	[275, 276, 289, 291]	0.1721 ± 0.0030
$A_{\rm FB}(b)$	[275, 276, 289, 291]	0.0992 ± 0.0016
$A_{\rm FB}(c)$	[275, 276, 289, 291]	0.0707 ± 0.0035
A_b	[275, 276, 289, 291]	0.923 ± 0.020
A_c	[275, 276, 289, 291]	0.670 ± 0.027
A^e_{LR}	[275, 276, 289, 291]	0.1513 ± 0.0021
$\sin\theta^l_W{}^2(Q_{fb})$	[275, 276, 289, 291]	0.2324 ± 0.0012
M_W [GeV]	[275, 276, 289, 290]	80.379 ± 0.012
M_h [GeV]	[258–262, 292]	$125.09 \pm 0.24 \pm 0.15_{\rm SUSY}$
$BR^{\rm EXP/SM}_{b\to s\gamma}$	[228, 293]	$0.988 \pm 0.045_{\rm EXP} \pm 0.068_{\rm TH,SM} \pm 0.050_{\rm TH,SUSY}$
$R_{\mu\mu}$	[254, 294, 295]	2D likelihood, MFV
$BR^{\rm EXP/SM}_{B\to\tau\nu}$	[59, 254]	$0.883 \pm 0.158_{\rm EXP} \pm 0.096_{\rm SM}$
$BR^{\rm EXP/SM}_{B\to X_s ll}$	[254, 296]	$0.966 \pm 0.278_{\rm EXP} \pm 0.037_{\rm SM}$
$BR^{\rm EXP/SM}_{K\to\mu\nu}$	[59, 297]	1.0004 ± 0.0095
$BR^{\rm EXP/SM}_{K\to\pi\nu\bar{\nu}}$	[59, 298]	2.01 ± 1.31
$\Delta M^{\rm EXP/SM}_{B_s}$	[59, 299]	$0.968 \pm 0.001_{\rm EXP} \pm 0.078_{\rm SM}$
$\frac{\Delta M^{\rm EXP/SM}_{B_s}}{\Delta M^{\rm EXP/SM}_{B_d}}$	[59, 299]	0.84 ± 0.12
$\Delta\epsilon^{\rm EXP/SM}_K$	[273, 274, 300]	$1.14 \pm 0.10_{\rm EXP+TH}$
$\Omega_{\rm CDM}h^2$	[271, 272, 301]	$0.1186 \pm 0.0022_{\rm EXP} \pm 0.0024_{\rm TH}$
$\sigma^{\rm SI}_p$	[302, 303]	Combined likelihood in the $(m_{\tilde{g}}, m_{\tilde{\chi}^0_1})$ plane
$H/A \to \tau^+\tau^-$	[282, 304]	Likelihood in the $(M_A, \tan\beta)$ plane

7.5.2 2D Plots

The 2D projections of the scan results over the parameter space defined by the input parameters can be seen in Figures 7.2, 7.3, 7.4, 7.5, 7.5, 7.6 and 7.7, obtained using `micrOMEGAs`. The coloured contours bound regions of parameter space with 68% (red) and 95% (dark blue) CL regions, as explained before. The best-fit point is indicated by a green star. The different colours correspond to the dominant DM mechanism, indicated in the legend. As it can be seen, the preferred mechanism is chargino coannihilation, and regions where the rapid annihilation via A/H-funnel, stau coannihilation as well as stop coannihilation dominate can also be found.

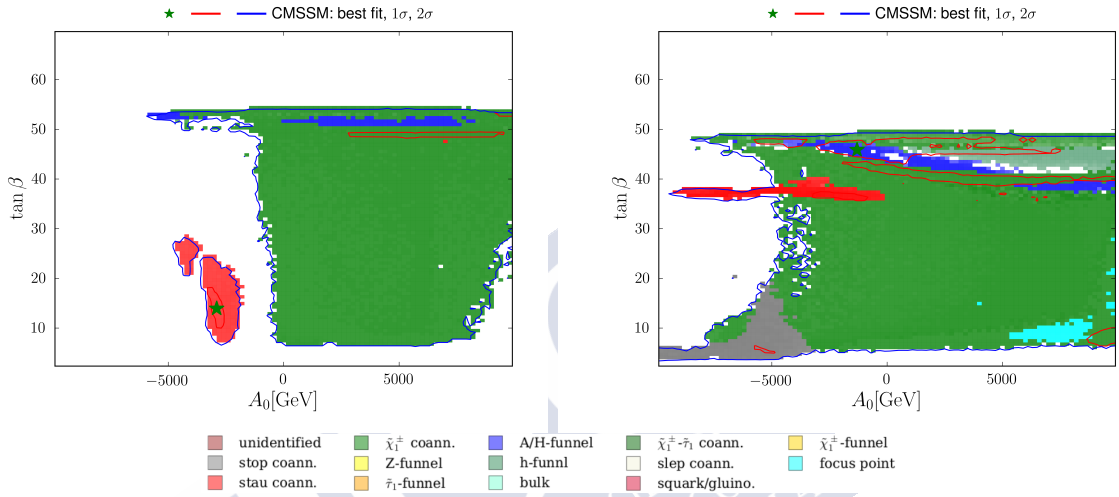

Figure 7.2: The $(A_0, \tan\beta)$ planes for $\mu > 0$ (left panel) and $\mu < 0$ (right panel). The red and blue coloured contours surround regions that are allowed at the 68 and 95% confidence levels (CL_s), corresponding approximately to one and two standard deviations, respectively, assuming that all the CDM is provided by the $\tilde{\chi}_0^1$. The best-fit points are indicated by green stars.

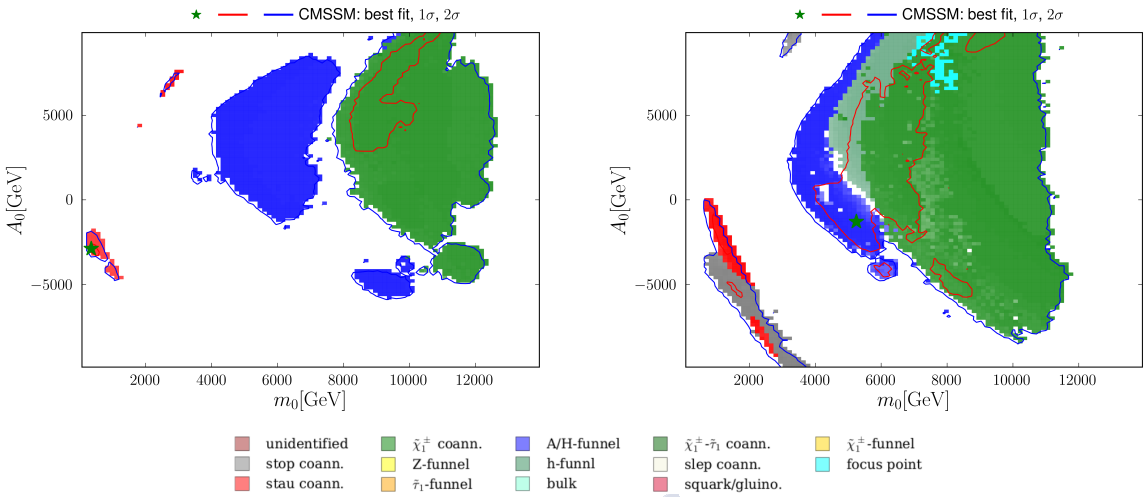

Figure 7.3: The (m_0, A_0) planes for $\mu > 0$ (left panel) and $\mu < 0$ (right panel). The red and blue coloured contours surround regions that are allowed at the 68 and 95% confidence levels (CL_s), corresponding approximately to one and two standard deviations, respectively, assuming that all the CDM is provided by the $\tilde{\chi}_0^1$. The best-fit points are indicated by green stars.

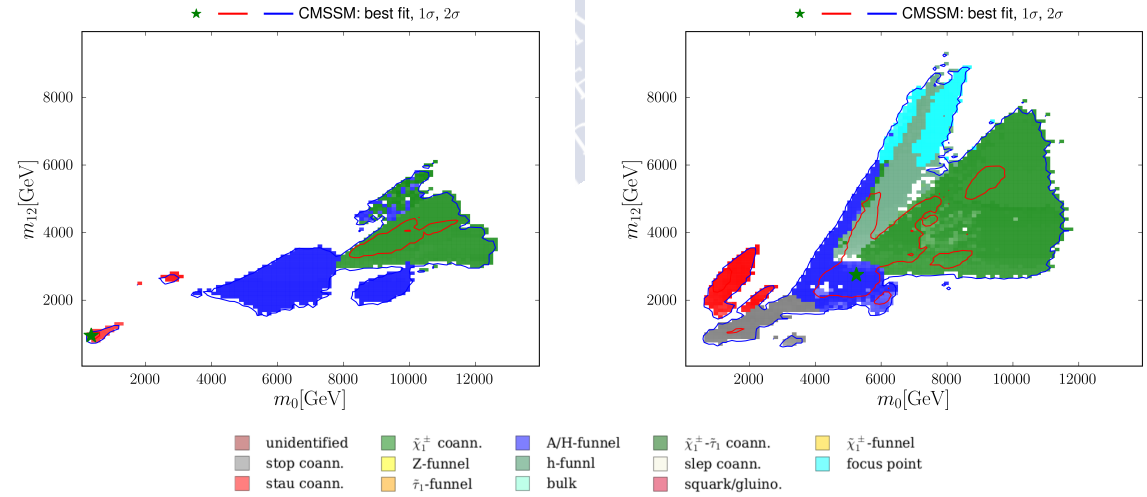

Figure 7.4: The $(m_0, m_{1/2})$ planes for $\mu > 0$ (left panel) and $\mu < 0$ (right panel). The red and blue coloured contours surround regions that are allowed at the 68 and 95% confidence levels (CL_s), corresponding approximately to one and two standard deviations, respectively, assuming that all the CDM is provided by the $\tilde{\chi}_0^1$. The best-fit points are indicated by green stars.

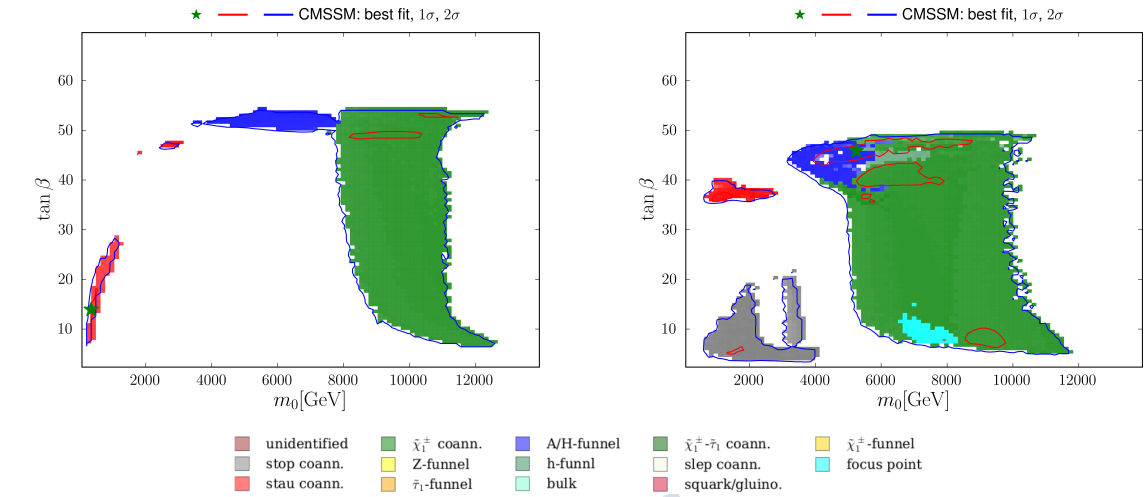

Figure 7.5: The $(m_0, \tan\beta)$ planes for $\mu > 0$ (left panel) and $\mu < 0$ (right panel). The red and blue coloured contours surround regions that are allowed at the 68 and 95% confidence levels (CL_s), corresponding approximately to one and two standard deviations, respectively, assuming that all the CDM is provided by the $\tilde{\chi}_0^1$. The best-fit points are indicated by green stars.

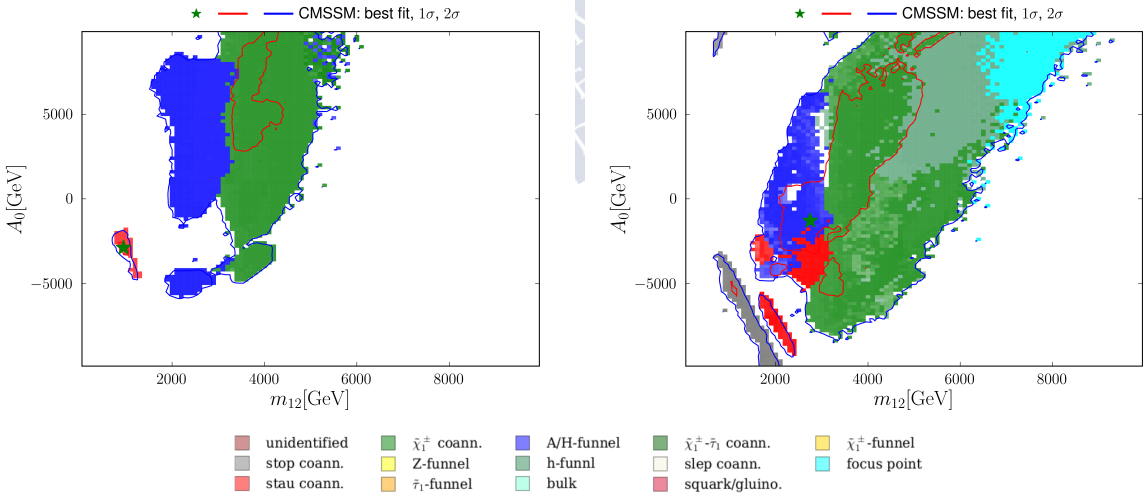

Figure 7.6: The (m_{12}, A_0) planes for $\mu > 0$ (left panel) and $\mu < 0$ (right panel). The red and blue coloured contours surround regions that are allowed at the 68 and 95% confidence levels (CL_s), corresponding approximately to one and two standard deviations, respectively, assuming that all the CDM is provided by the $\tilde{\chi}_0^1$. The best-fit points are indicated by green stars.

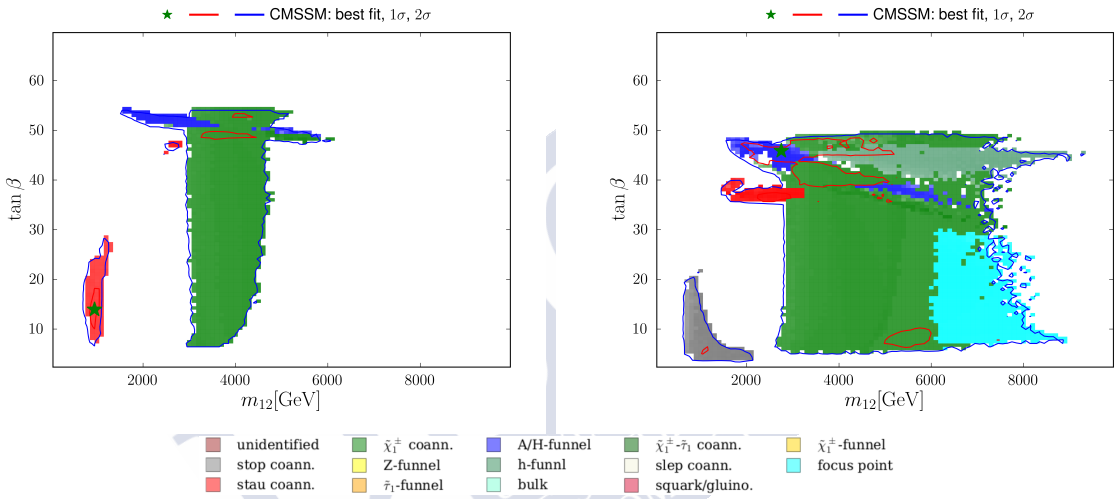

Figure 7.7: The $(m_{12}, \tan\beta)$ planes for $\mu > 0$ (left panel) and $\mu < 0$ (right panel). The red and blue coloured contours surround regions that are allowed at the 68 and 95% confidence levels (CL_s), corresponding approximately to one and two standard deviations, respectively, assuming that all the CDM is provided by the $\tilde{\chi}_0^1$. The best-fit points are indicated by green stars.

7.5.3 1D Plots

The profile likelihood for the Higgs mass and $BR^{MSSM/SM}_{B_{s,d}\to\mu^+\mu^-}$ are displayed in Figure 7.8. Notice that the preference for the latter to be above or below 1 depends on the sign of μ. Indeed, it is the case in which $\mu < 0$ the one that seems to provide a better fit to present data.

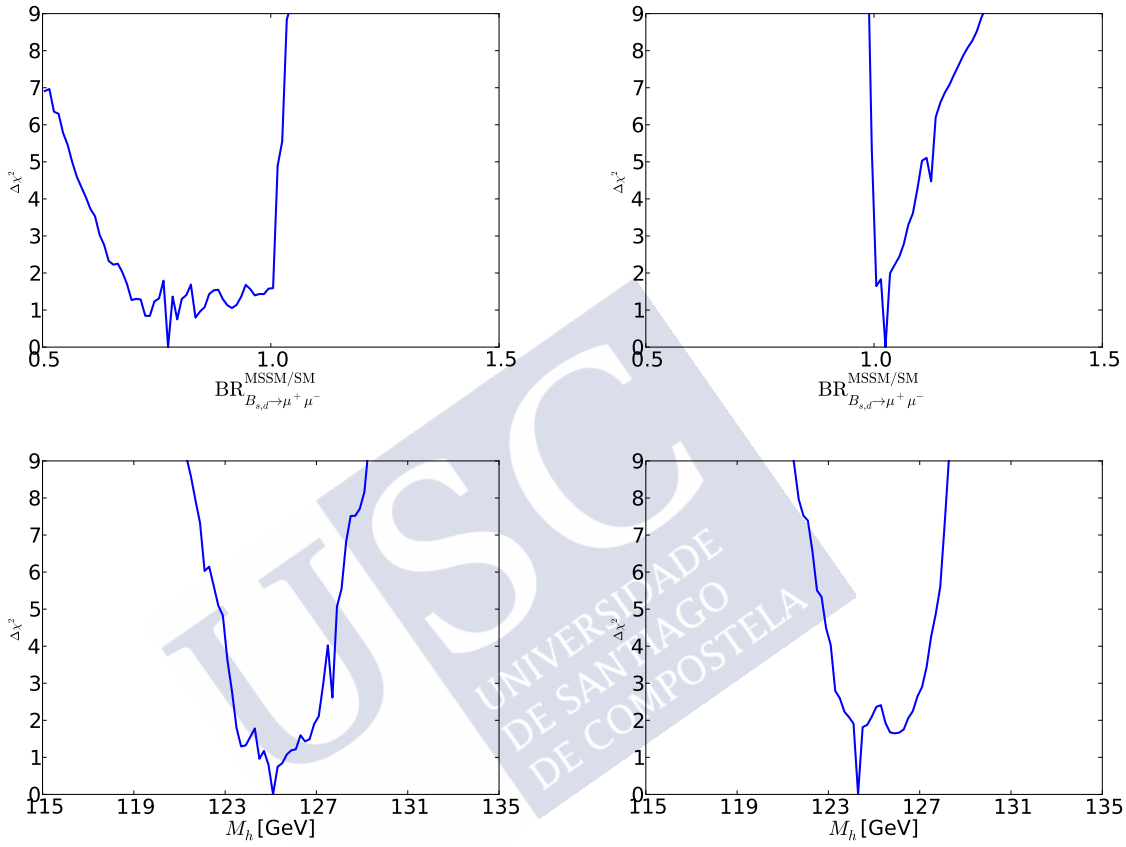

Figure 7.8: Top: one-dimensional profile likelihood function for $BR^{MSSM/SM}_{B_{s,d}\to\mu^+\mu^-}$ for $\mu < 0$ (upper left panel) and for $\mu > 0$ (upper right panel); bottom: one-dimensional profile likelihood function for M_h for $\mu < 0$ (bottom left panel) and for $\mu > 0$ (bottom right panel).

7.5.4 Prospects for Direct Detection of Dark Matter

Figure 7.9 shows the LSP mass versus the spin independent dark matter proton scattering cross section, $(m_{\tilde{\chi}^0_1}, \sigma_p^{\mathrm{SI}})$, planes for both signs of μ, together with the experimental limits and projections. As it can be seen, for the negative case part of the 2σ region lies close to the neutrino floor, where background coming from neutrinos becomes indistinguishable from the interaction with dark matter particles. The other part lies somewhat below the experimental limit. On

the other hand, for $\mu > 0$ the contour is much more restricted, being below the experimental limit and in the border of the projected sensitivity for future experiments. It should be noted that there are considerable uncertainties in the calculation of $\sigma_p^{\rm SI}$, that are taken into account in the global fit. Hence, points with nominal values of $\sigma_p^{\rm SI}$ above the experimental limit may nevertheless lie within the 95% CL range for the global fit.

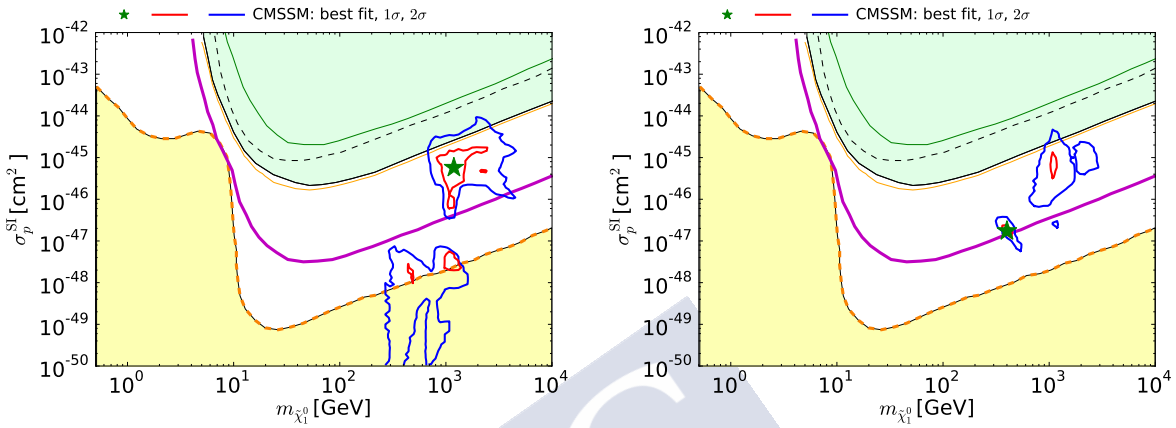

Figure 7.9: Two-dimensional profile likelihood function for the nominal value of $\sigma_p^{\rm SI}$ clculated using the `SSARD` code [272] in the $(m_{\tilde{\chi}_1^0}, \sigma_p^{\rm SI})$ plane for $\mu < 0$ (left) and $\mu > 0$ (right), displaying also the upper limits established by the LUX and XENON100 [305,306] Collaborations shown as solid (dashed) black and green contours respectively. The combination from LUX and Panda [306, 307] is shown in orange. The projected future 90% CL sensitivities of the LUX-Zeplin (LZ) [308] experiment is shown as magenta, and the neutrino background 'floor' is shown as a dashed orange line with yellow shading below [305, 308].

7.5.5 Best-fit point

Figures 7.10 and 7.11 show the different contributions to the χ^2 of the best-fit points for both signs of μ. As it can be seen, the greatest contributions come from the electroweak observables for both signs of μ, setting aside the contributions from `HiggsSignals` so as to avoid biasing the analysis by giving too much importance to the Higgs signal rates. The flavour contribution to χ^2 is bigger in the case $\mu > 0$, that can be explained by the behaviour of $BR^{\rm MSSM/SM}_{B_{s,d}\to\mu^+\mu^-}$ seen in the previous section. Moreover, there is a mild preference for $\mu < 0$, in agreement with what was found in [309], where a global fit of the CMSSM was performed by the GAMBIT collaboration [310]. Further studies are needed to assess the impact of both LHC 13 TeV constraints.

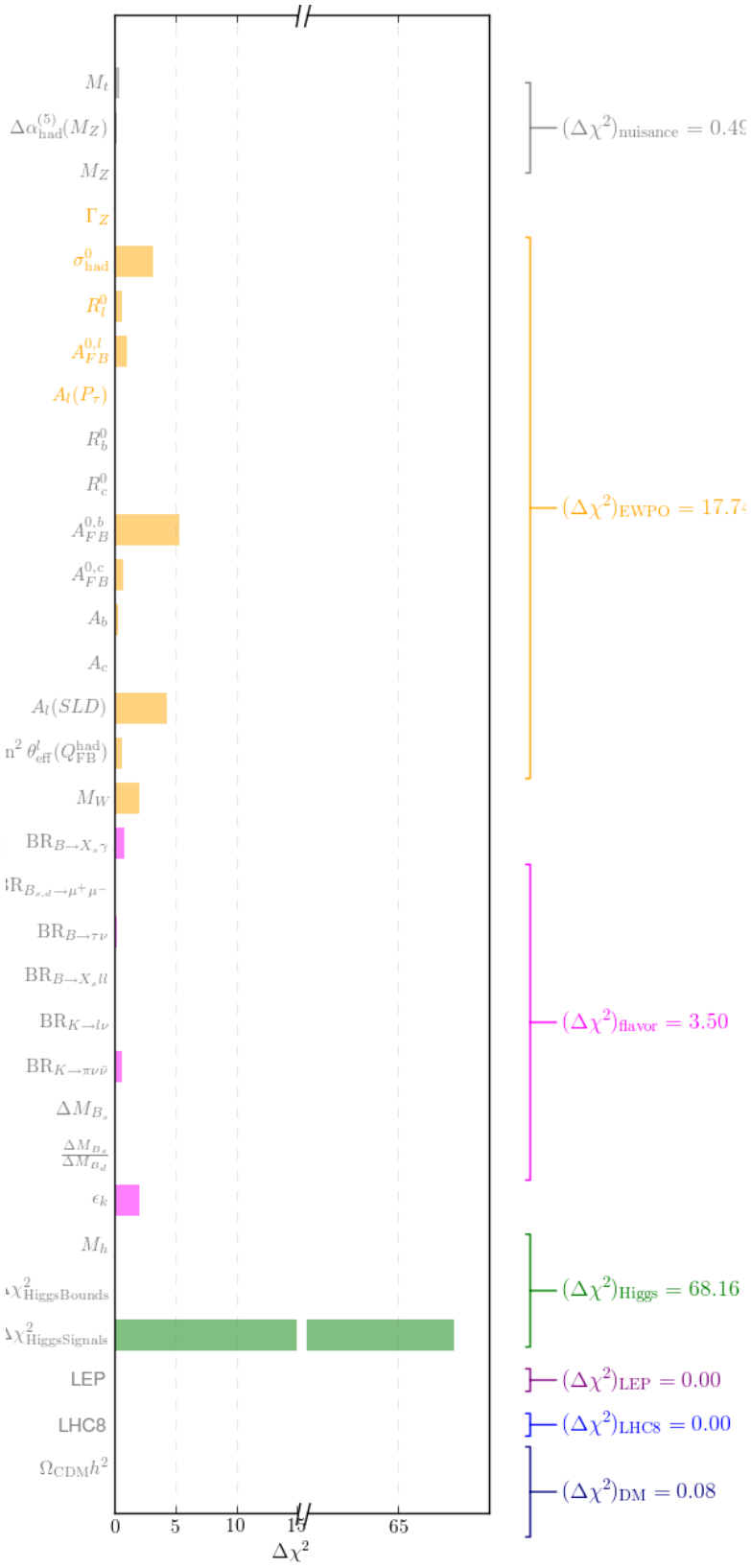

Figure 7.10: The χ^2 pulls at the best-fit points in the CMSSM for $\mu < 0$.

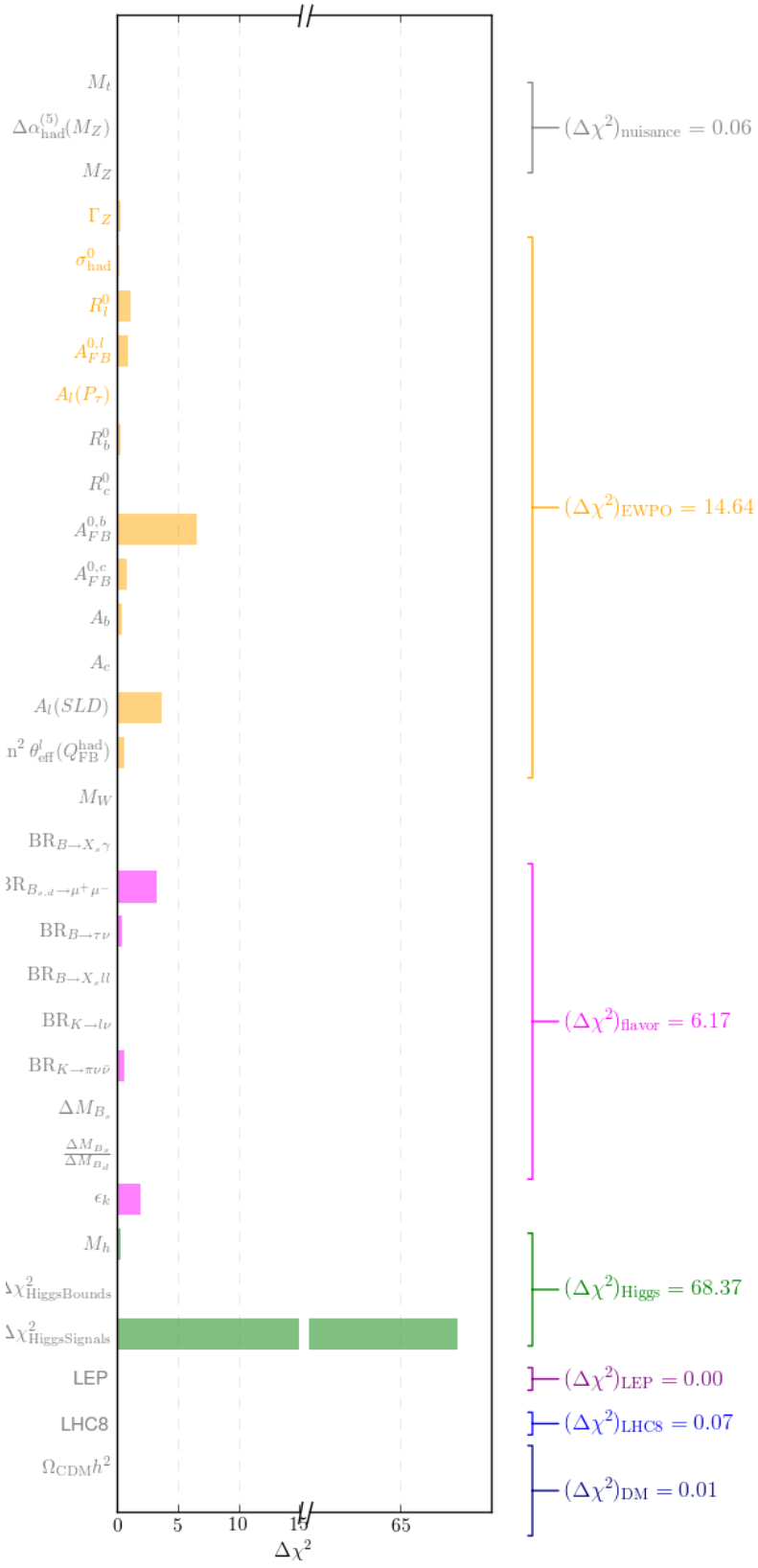

Figure 7.11: The χ^2 pulls at the best-fit points in the CMSSM for $\mu > 0$.

The spectra for the two best-fit points can be seen in Figure 7.12. Notice that for $\mu > 0$ it is considerably heavier than for $\mu < 0$. Moreover, for this case the lighter chargino and the LSP are nearly degenerate. This does not hold for the negative case.

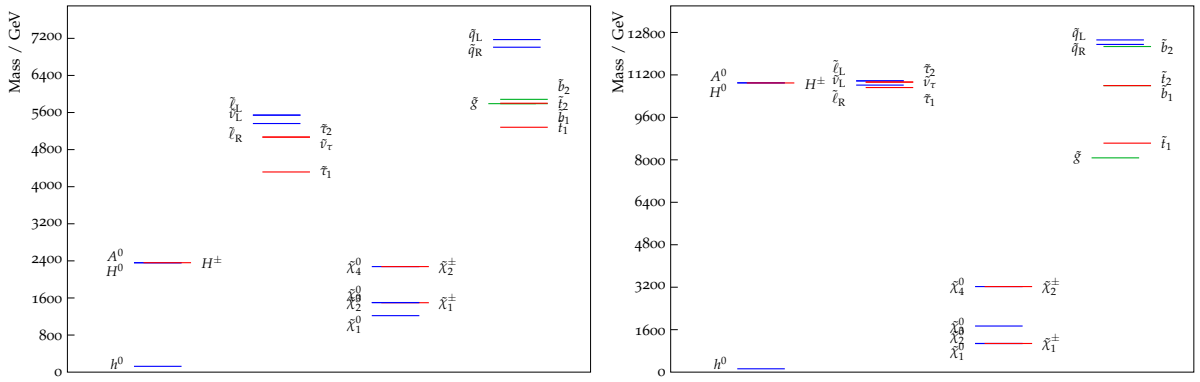

Figure 7.12: The spectra of Higgs bosons and sparticles at the best-fit points in the CMSSM for $\mu < 0$ (left) and $\mu > 0$ (right). These plots were made using `PySLHA` [270].

7.5.6 Outlook

Extensions of this work comprise the inclusion of 13 TeV constraints and the latest DM results from direct (and indirect) detection experiment, together with an update on the flavour constraints. Furthermore, an issue was found related to the usage of the `SoftSUSY` version. As a matter of fact, relative differences in the stop mass higher than 50% were found between this version and updated versions of `SoftSUSY` as well as `FlexibleSUSY`. With this, the stop mass coannihilation area is smaller with respect to [309]. This difference is due to the different threshold corrections in the running m_t determination. For this work, approximate 2-loop expressions are used, which have been disabled in newer versions of `SoftSUSY` in favor of the complete expressions. Therefore, a study with the latest version of `SoftSUSY` as well as `HiggsSignals`, `HiggsBounds` and `FeynHiggs` is foreseen. Including the vacuum stability as an afterburner is also planned, together with the DM relic density as an upper bound, as it was mentioned before.

7.5.7 Conclusions

A study within the CMSSM scenario have been performed. The preferred DM mechanism is chargino coannihilation. Nevertheless other mechanisms, such as stop coannihilation, are also found to have non-negligible contributions. As for the 1D profile likelihood, $\mu < 0$ is the case which seems to better accommodate present data, in agreement with other recent results present in the literature [309]. Regarding the prospects for direct detection of dark matter, the contour for $\mu > 0$ is much more restricted than for the negative case, being close to the experimental sensitivity. Future extensions of this work are foreseen, including an update on the used experimental constraints.

7.6 mAMSB Results

The spectrum of this model is quite different from those in other GUT-based models, with a different composition of the LSP. Within this scenario, either a wino-like or a Higgsino-like neutralino LSP may provide the CDM, both with similar likelihoods. In both cases the $\tilde{\chi}_1^0$ is almost degenerate with the lighter chargino, $\tilde{\chi}_1^0$. In the case in which the wino-like (Higgsino-like) neutralino is forced to be the dominant source of the CDM density indicated by Planck measurements of the cosmic microwave background radiation ($\Omega_{\rm CDM}h^2 = 0.1186 \pm 0.0020$), $m_{\tilde{\chi}_1^0} \simeq 3$TeV ($m_{\tilde{\chi}_1^0} \simeq 1.1$TeV) after inclusion of Sommerfeld enhancement effects [311]. In both cases, the mass of the sparticles is beyond the LHC reach, and supersymmetric contributions to EWPOs, flavour observables and $(g-2)_\mu$ are small. On the other hand, if this condition is alleviated by setting the CDM as an upper limit, so that the LSP does not account for the full CDM density, therefore existing some other external contribution to the CDM, $m_{3/2}$ and $m_{\tilde{\chi}_1^0}$ can be reduced, although M_h still imposes a significant lower limit. In this case, some direct searches for sparticles at the LHC also become relevant.

7.6.1 Constraints

7.6.1.1 Flavour, Electroweak and Higgs Constraints

The ATLAS result for $BR(B_{s,d} \to \mu^+\mu^-)$ is included [312], as well as the combination of ATLAS and CMS measurements for the mass of the Higgs boson: $M_h = 125.09 \pm 0.24$GeV [313]. Its impact on the parameter space is evaluated using `FeynHiggs`. The constraints from EWPOs are not evaluated independently (except for M_W), since they have been checked to be indistinguishable from the SM values within the current experimental uncertainties. The χ^2 contributions of 85 Higgs search channels from LHC and Tevatron are evaluated using `HiggsSignals` and `HiggsBounds`, as done in [314].

7.6.1.2 LHC Constraints

In this scenario, only gluinos and winos can be light enough at the 2σ level to be within the reach of the LHC experiments. Hence, constraints from these searches are considered in detail, as they are expected to have an impact for future LHC runs.

7.6.1.3 Dark Matter Constraints

For a wino-like dark matter particle, the non-perturbative Sommerfeld effect [311] needs to be accounted for. Due to the high computational cost of doing so point by point, a phenomenological fit applicable near 3.1 TeV is performed. More details can be found in [38].

As for direct constraints on the spin-independent dark matter proton scattering cross section, $\sigma_p^{\rm SI}$, these are implemented using the `SSARD` code.

All the constraints are treated as gaussian, except for $BR(B_{s,d} \to \mu^+\mu^-)$ and $\sigma_p^{\rm SI}$, for which a likelihood function is constructed. For a more detailed description of the constraints used, see [314].

7.6.2 Scan Ranges

The ranges, the number of segments and the resulting number of boxes that are used in the scan are given in Table 7.5. A dedicated supplementary scan of the Higgsino-LSP region is performed. A total of $\sim 11(13) \times 10^6$ points have been sampled with $\mu > 0$ ($\mu < 0$).

Table 7.5: Sampling ranges and segment definitions in the mAMSB model.

Parameter	Range	Generic Segments	Higgsino Segments
m_0	(0.1, 50) TeV	4	6
$m_{3/2}$	(10, 1500) TeV	3	3
$\tan\beta$	(1 , 50)	4	2
Total number of boxes		48	36

7.6.3 Results I. CDM is mainly the lightest neutralino (all-CDM)

Figure 7.13 shows the $(m_0, m_{3/2})$ planes for both signs of μ in this study. The colour coding for the CL contours is similar to the former case, with a full green star indicating the best-fit point (bfp) for wino-like DM, and an open green star denoting the bfp for Higgsino-like DM. The regions with a Higgsino fraction exceeding 90% are coloured as yellow; those with a wino fraction bigger than 90% are shaded as blue, and the mixing regions as orange.

As it can be seen, for a wino-like LSP the regions favoured at the 2σ level are bands where 900 TeV $\leq m_{3/2} \leq$ 1000 TeV. The lower limit $m_0 \geq 5$ TeV corresponds to the region where the $\tilde{\tau}_1$ becomes the LSP.

Figures 7.14, 7.15 display the $(\tan\beta, m_0)$, $(\tan\beta, m_{3/2})$ planes, which are shown to be qualitatively similar for both signs of μ. Larger m_0 and $m_{3/2}$ values are allowed in the Higgsino-LSP case, provided that $\tan\beta$ is small.

It is worth noticing that the precise location of the Higgsino-LSP region depends on the spectrum calculator employed, and also on the version used. These variation can be as large as tens of TeV for m_0 or a couple of units for $\tan\beta$, and can change the χ^2 penalty coming from the Higgs mass. This variability is related to the uncertainty in the exact location of the electroweak symmetry-breaking boundary, which is very sensitive to numerous corrections, in particular those related to the top quark Yukawa coupling [38].

For all cases considered (Higgsino-like DM, wino-like DM, $\mu > 0$, $\mu < 0$), the obtained χ^2 probabilities are similar. The contributions to the total χ^2 of the bfp for these scenarios are shown in Figure 7.16. Note that the main penalties come from the EWPOs defined in Appendix F (hadronic pole cross section $\sigma^0_{\rm had}$, the ratio of hadronic to leptonic decay R_l, the forward backward asymmetry $A^b_{\rm FB}$, the asymmetry parameter $A^e_{\rm LR}$), together with M_W, $(g-2)_\mu$, $BR(B_s \to \mu^+\mu^-)$, $\frac{\Delta M_{B_s}}{\Delta M_{B_d}}$, ϵ_K and `HiggsSignals`.

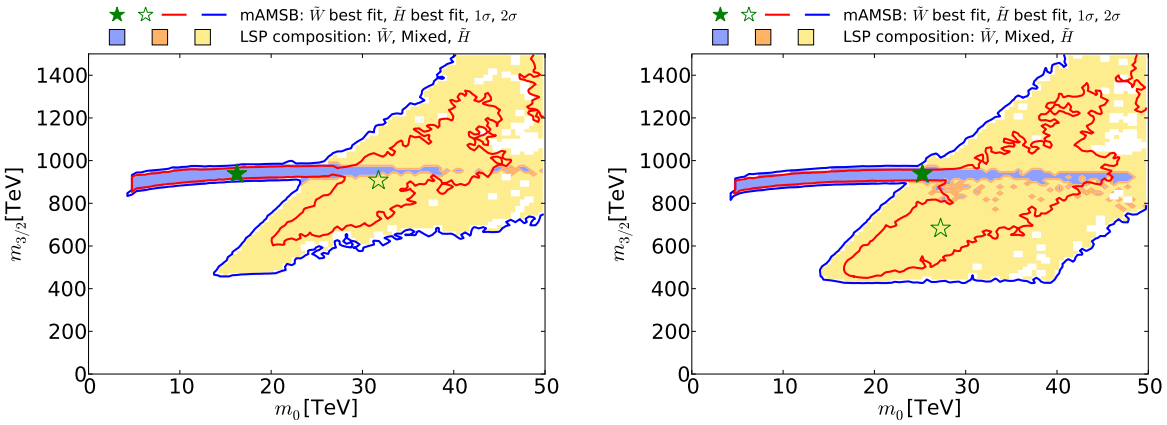

Figure 7.13: The $(m_0, m_{3/2})$ planes for $\mu > 0$ (left panel) and $\mu < 0$ (right panel). The red and blue coloured contours surround regions that are allowed at the 68 and 95% confidence levels, corresponding approximately to one and two standard deviations, respectively, assuming that all the CDM is provided by the $\tilde{\chi}_1^0$. The wino-(Higgsino-)like DM regions are shaded blue (yellow), and mixed wino-Higgsino regions are shaded orange. The best-fit points for the two signs of μ are indicated by green stars, closed in the wino-like region and open in the Higgsino-like region.

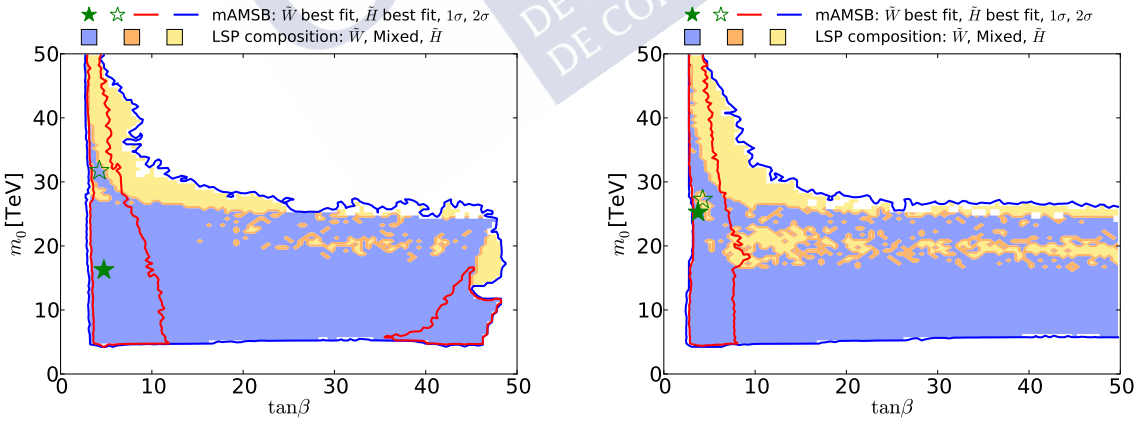

Figure 7.14: The $(\tan\beta, m_0)$ planes for $\mu > 0$ (left panel) and for $\mu < 0$ (right panel), assuming that the $\tilde{\chi}_1^0$ provides all the CDM density. The colouring convention for the shadings and contours is the same as in Figure 7.13, and the best-fit points for the two signs of μ are again indicated by green stars.

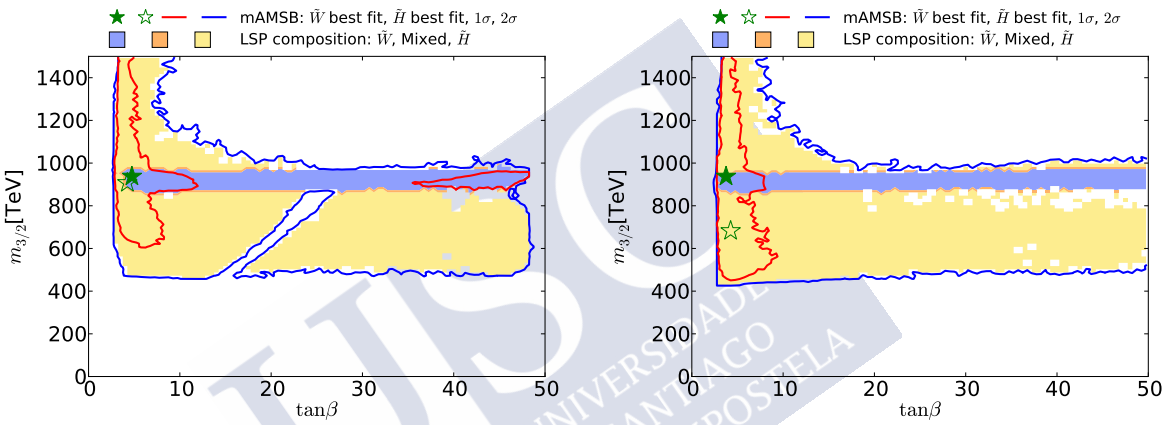

Figure 7.15: The $(\tan\beta, m_{3/2})$ planes for $\mu > 0$ (left panel) and $\mu < 0$ (right panel), assuming that the $\tilde{\chi}_1^0$ provides all the CDM density. The shadings and colouring convention for the contours are the same as in 7.13, and the best-fit points for the two signs of μ are again indicated by green stars.

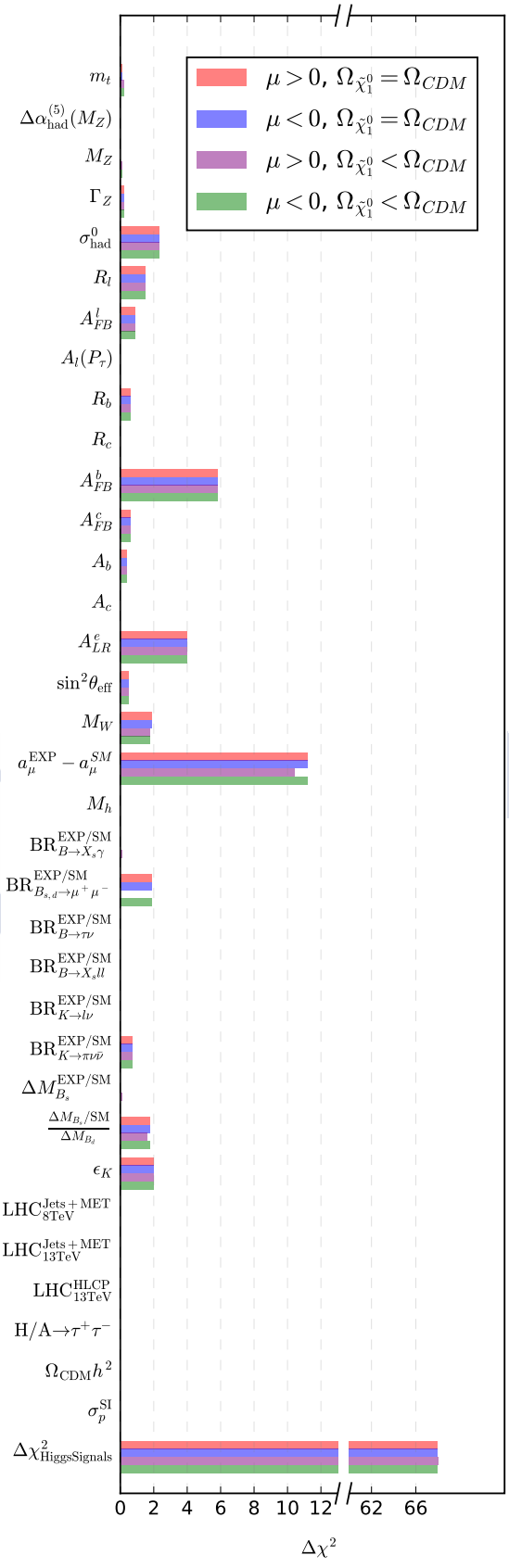

Figure 7.16: All the contributions to the total χ^2 for the best-fit points for mAMSB assuming different hypotheses on the composition of the dark matter relic density and on the sign of μ as indicated in the legend.

Figure 7.17 shows the spectra for both the wino and Higgsino scans (for both signs of μ), in the case in which the neutralino is considered to account for most of the cold dark matter relic density. Branching fractions exceeding 20% are indicated by dashed lines. As it can be seen, relatively heavy spectra are obtained, as expected. The spectra for the Higgsino case are heavier than ones for the wino case, except for the gauginos, that are lighter. These high masses imply a non significant departure from the SM prediction in the flavor sector and $(g-2)_\mu$. It can also be noticed that the wino-LSP is almost degenerate with the lightest chargino, with a difference of approximately 170 MeV due to radiative corrections. This translates into a long-lived chargino, that could be decay inside the ATLAS tracker. Nevertheless, its mass is too large to be within the LHC reach.

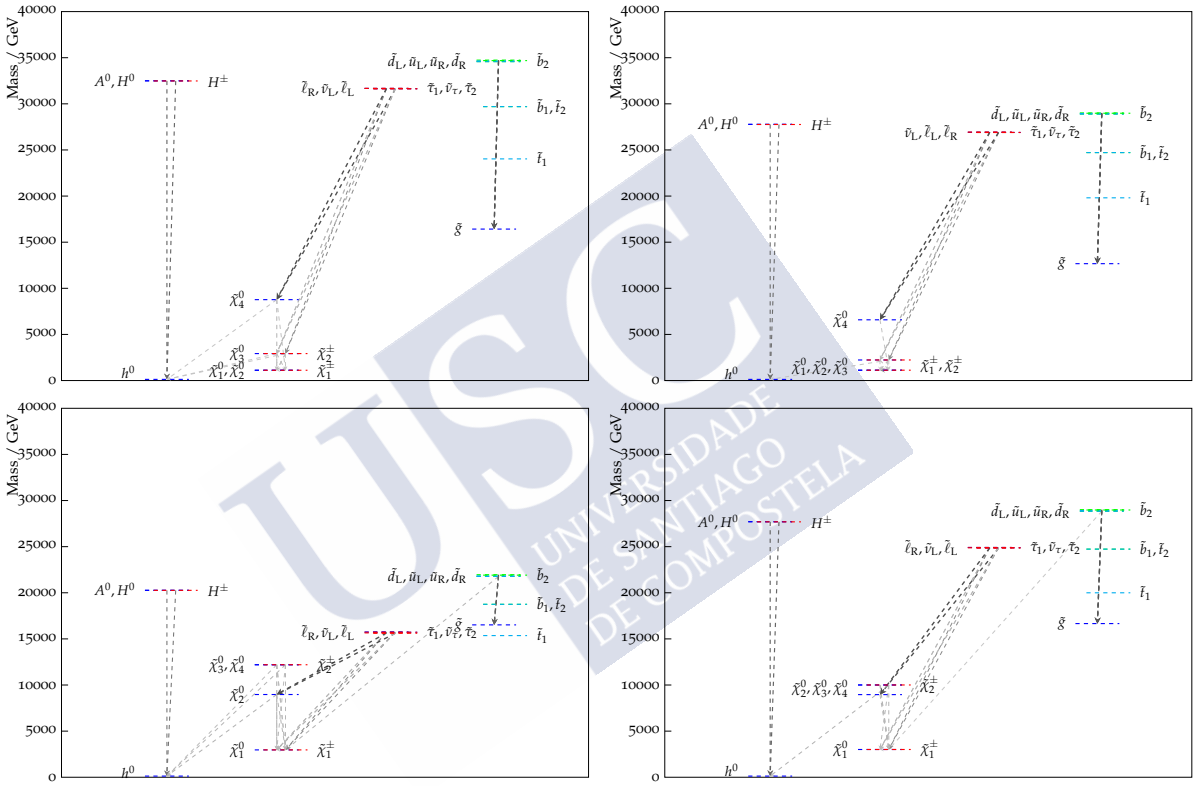

Figure 7.17: The spectra of the best-fit points for $\mu > 0$ (left panel) and $\mu < 0$ (right panel), assuming that the LSP makes the dominant contribution to the cold dark matter density. Both the wino- (upper) and the Higgsino-like LSP (lower) best-fit points are shown. In each case, all the decay modes with branching ratios (BRs) above 20%, with darker shading for larger BRs, are also indicated, and the colours of the horizontal bars reflect particles electric charges.

7.6.4 Results II. The LSP does not provide all the cold dark matter (part-CDM)

In this case, the LSP mass as well as $m_{3/2}$ can become substantially lower. Therefore, some particles can be within the LHC reach, in contrast to the results shown in section 7.6.3.

The $(m_0, m_{3/2})$ are shown in Figure 7.18. As it can be seen, the wino 95% CL region extends to smaller $m_{3/2}$ for both signs of μ, and to larger m_0 for $m_{3/2} \gtrapprox 300$ for negative μ. The 68% CL contour is considerably larger in this case as compared to the positive case. The best-fit point also moves to larger masses than for $\mu > 0$, though with smaller $\tan\beta$.

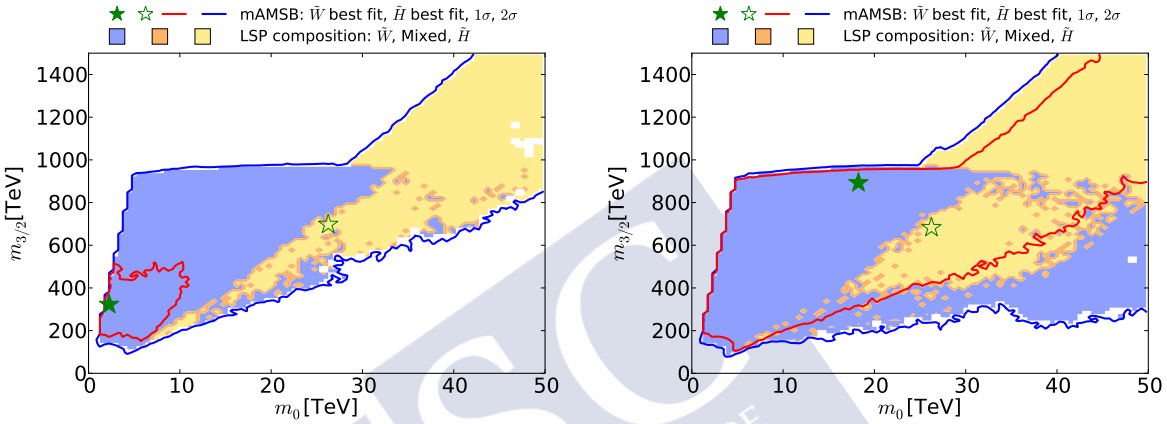

Figure 7.18: The $(m_0, m_{3/2})$ planes for $\mu > 0$ (left panel) and for $\mu < 0$ (right panels), allowing the $\tilde{\chi}_1^0$ to contribute only part of the CDM density. The shadings are the same as in Figure 7.13.

Concerning the χ^2 value for the best fit point, the positive case with a higher value of $\tan\beta$ is slightly more favoured, given that a negative interference between the mAMSB and SM contributions to the decay amplitude in this parameter space region provides a better fit for the $BR(B_{s,d} \to \mu^+\mu^-)$ result. This interference is constructive for $\mu < 0$, thus giving a worst result for $BR(B_{s,d} \to \mu^+\mu^-)$.

The panels of Figure 7.19 show the $(\tan\beta, m_{3/2})$, planes for positive (left) and negative (right) μ. Comparing with the former case, a large expansion of the wino-like region can be seen.

As in section 7.6.3, Figure 7.20 shows the spectra for both the wino and Higgsino scans (for both signs of μ,) in the case in which the neutralino is considered to account for only a part of the cold dark matter relic density. Branching fractions exceeding 20% are indicated by dashed lines. Comparing the spectra, it can be deduced that, while in the all-CDM case the sparticles in the mAMSB are too heavy to be produced at the LHC, in the part-CDM case the sparticle masses may be much lighter, and hence some of them accessible at the LHC.

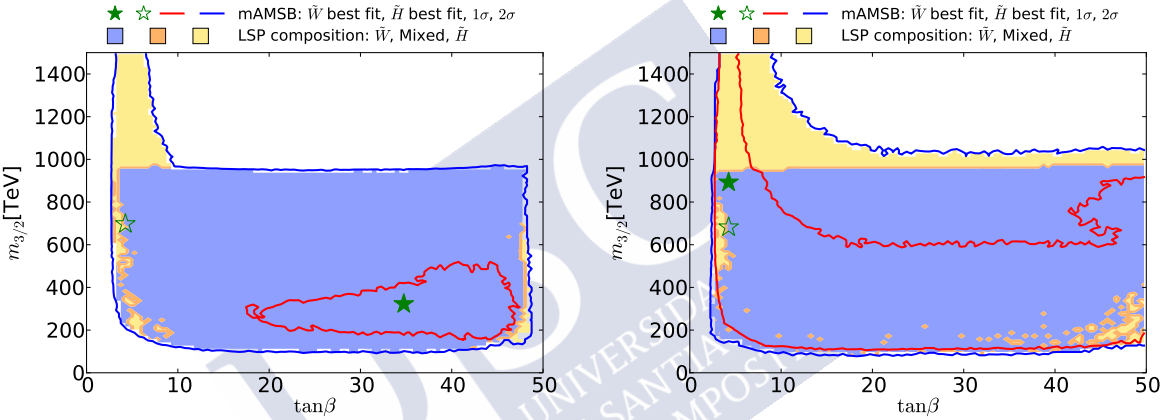

Figure 7.19: The $(\tan\beta, m_{3/2})$ planes for $\mu > 0$ (left panel) and for $\mu < 0$ (right panels), allowing the $\tilde{\chi}_1^0$ to contribute only part of the CDM density. The shadings are the same as in Figure 7.13.

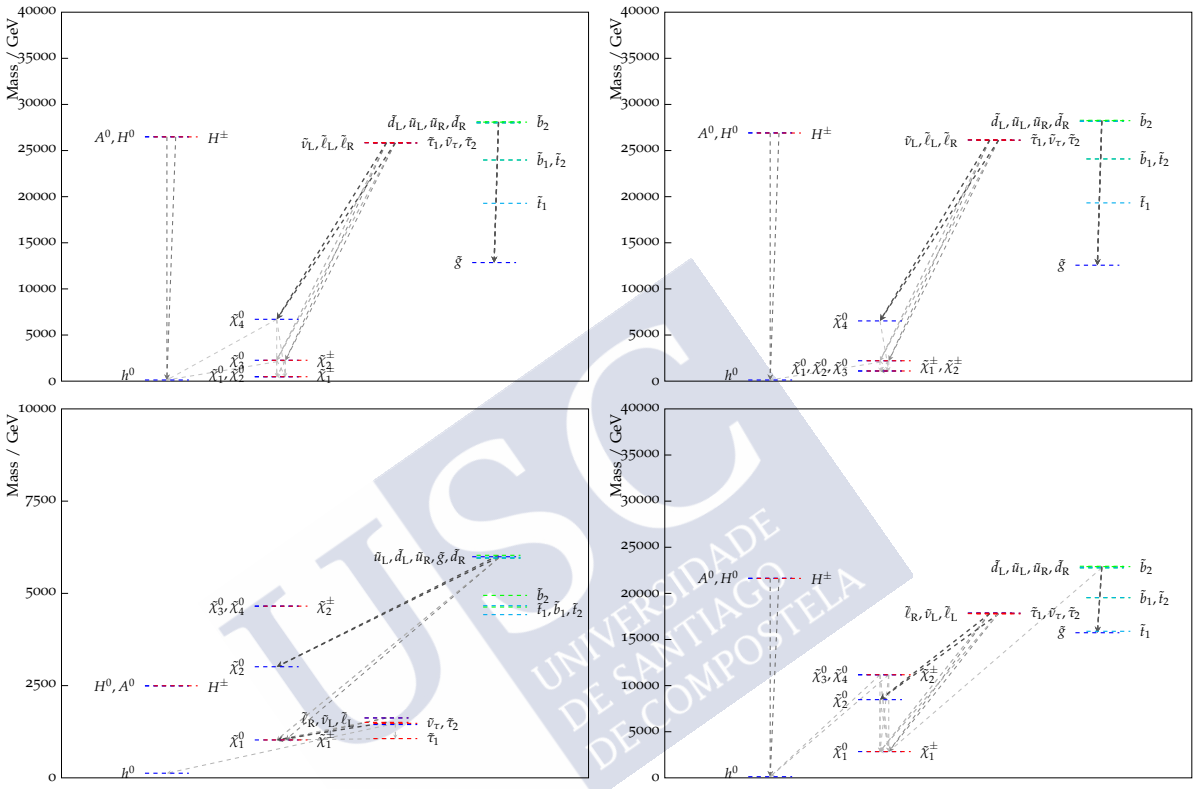

Figure 7.20: The spectra of the best-fit points for $\mu > 0$ (left panel) and $\mu < 0$ (right panel), allowing the LSP to contribute only part of the cold dark matter density. Both the wino- (upper) and the Higgsino-like LSP (lower) best-fit points are shown. In each case, all the decay modes with branching ratios (BRs) above 20%, with darker shading for larger BRs are also indicated, and the colours of the horizontal bars reflect particles electric charges. The range of masses shown for the $\tilde{W}$-LSP $\mu > 0$ best fit point (top-left panel) is smaller than the others, since its mass spectrum is considerably lighter.

7.6.5 1D Plots

The profile likelihoods for $BR^{MSSM/SM}_{B_{s,d}\to\mu^+\mu^-}$ and $(g-2)_\mu$ are displayed in Figure 7.21. Small departures from the SM if the LSP accounts for all of the CDM can be seen. As the CDM constraint is relaxed, these effects become more significant. In particular, for $\mu > 0$, the aforementioned destructive interference causes a sizeable decrease of $BR(B_{s,d} \to \mu^+\mu^-)$. This destructive interference is accompanied by a constructive interference in $BR(b \to s\gamma)$. As for $(g-2)_\mu$, small effects can appear for both signs of μ.

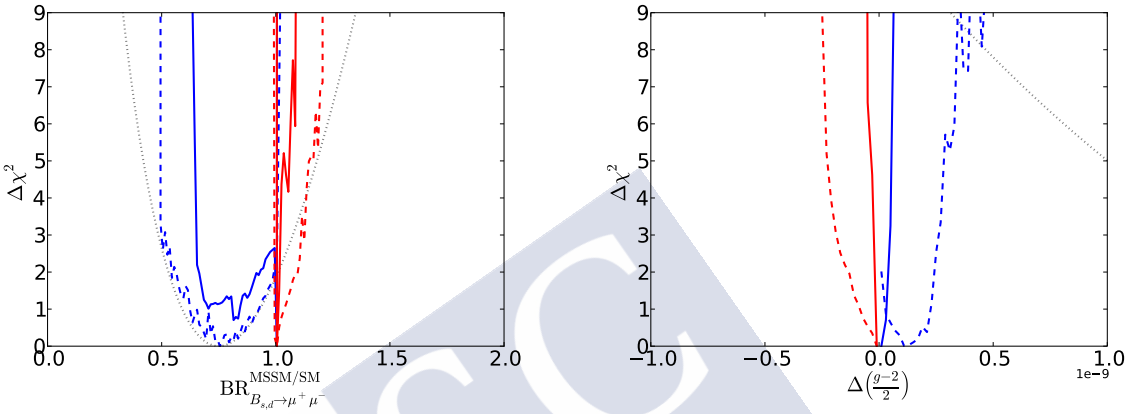

Figure 7.21: The spectra of the best-fit points for $\mu > 0$ (left panel) and $\mu < 0$ (right panel), allowing the LSP to contribute only part of the cold dark matter density. Both the wino- (upper) and the Higgsino-like LSP (lower) best-fit points are shown. In each case, all the decay modes with branching ratios (BRs) above 20%, with darker shading for larger BRs, are also indicated, and the colours of the horizontal bars reflect particles electric charges. The range of masses shown for the $\tilde{W}$ -LSP $\mu > 0$ best fit point (top-left panel) is smaller than the others, since its mass spectrum is considerably lighter.

7.6.6 Prospects for Direct Detection of Dark Matter

Future direct DM search experiments may be capable of detecting the interaction of a mAMSB neutralino, even if it does not provide all the CDM density [315–317]. Figure 7.22 shows the $(m_{\tilde{\chi}^0_1}, \sigma_p^{\mathrm{SI}})$ exclusion regions for both signs of μ ($\mu > 0$ on the left panel and $\mu < 0$ on the right panel), together with the experimental limits and projections. The pale-green-shaded region represents the range of σ_p^{SI} excluded at the 95% CL by the combination of PandaX [302] and LUX [303] results. The purple and blue lines show the prospective sensitivities of the LUX-Zeplin (LZ), XENON1T and XENONnT experiments [318, 319]. Also shown, as a dashed orange line, is the neutrino "floor", below which astrophysical neutrino backgrounds would dominate any DM signal [305] (grey region).

As for the CMSSM case, the large theoretical uncertainties that arise when computing σ_p^{SI} need to be considered, as points otherwise excluded by present experimental limits can become

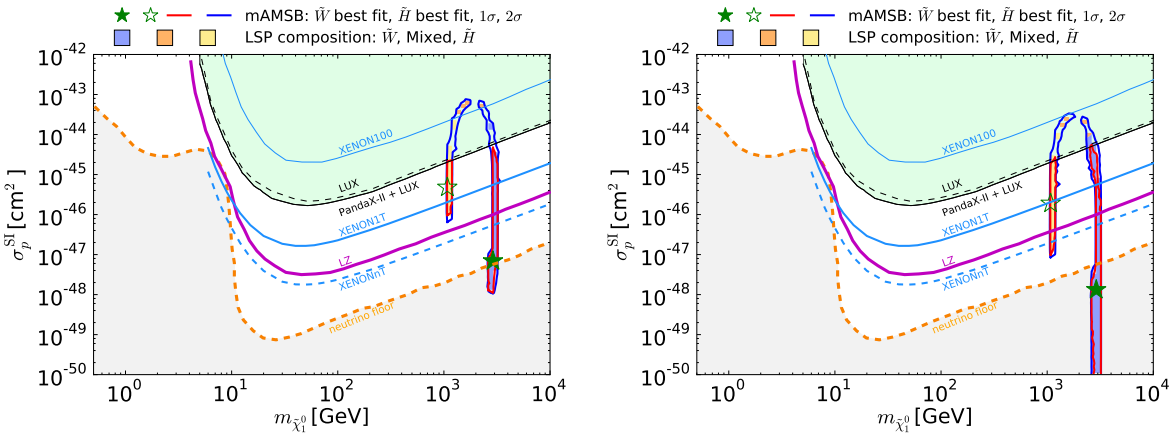

Figure 7.22: The $(m_{\tilde{\chi}_1^0}, \sigma_p^{\rm SI})$ planes in the mAMSB for $\mu > 0$ (left) and $\mu < 0$ (right) in the case when the LSP accounts for the whole DM density. The red and blue solid lines are the 1 and 2 CL contours, and the solid purple and blue lines show the projected 95% exclusion sensitivities of the LUX-Zeplin (LZ) [319] and XENON1T/nT experiments [318], respectively. The green line and shaded region show the combined limit from the LUX and PandaX experiments [302, 303], and the dashed orange line shows the astrophysical neutrino 'floor' [305], below which astrophysical neutrino backgrounds dominate (grey region). The blue, orange and yellow shadings are the same as in Figure 7.13.

allowed when doing so. Nevertheless, in the the left and right vertical strips that appear in the left panel of Figure 7.22, it can be seen that the current data already put pressure on the mAMSB for the case of positive μ, for both the wino and Higgsino-like LSP cases. In this case, the Higgsino-like LSP could be explored with the expected LZ sensitivity, while for a wino-like LSP experiments like Darwin [320] could be used. For $\mu < 0$, the values for $\sigma_p^{\rm SI}$ become lower, lying below the LZ sensitivity in the Higgsino case and well below the neutrino "floor" in the wino case [38].

Figure 7.23 shows the situation in which the LSP does not provide all the CDM. In this case $\sigma_p^{\rm SI}$ needs to be weighted by $\Omega_{\tilde{\chi}_1^0}/\Omega_{\rm CDM}$, since this would be the fraction of the galactic halo provided by the LSP in this case. An increase in the allowed region with respect to the former case can be appreciated, with a bigger percentage of this region below the neutrino "floor" for the negative case.

7.6.7 Conclusions

Similarly to what has been done in Section 7.5, a study within the mAMSB scenario has been performed. Different signs on μ have been considered, as well as two different cases depending on the amount of CDM density provided by the mAMSB dark matter candidate. The preferred spectra for this model has been found to be quite different from those in other GUT-based models, with a different composition of the LSP. Within this scenario, either a wino-like or a Higgsino-like neutralino LSP may provide the CDM, both with similar likelihoods. In both cases the $\tilde{\chi}_1^0$ is almost degenerate with the lighter chargino, $\tilde{\chi}_1^0$, and the mass of the sparticles is beyond

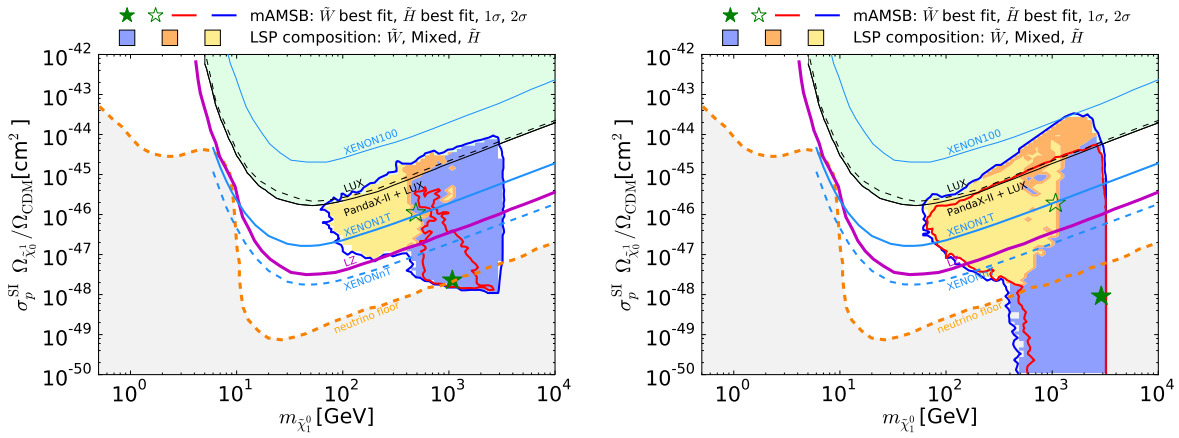

Figure 7.23: The $(m_{\tilde{\chi}_1^0}, \sigma_p^{\rm SI})$ planes in the mAMSB for $\mu > 0$ (left) and $\mu < 0$ (right) in the case when the LSP accounts for a fraction of the CDM density. The legends, line styles and shadings are the same as in Figure 7.22.

the LHC reach. These high masses imply a non significant departure from the SM prediction in the flavor sector and $(g-2)_\mu$. Nonetheless, if the neutralino is not required to account for the full CDM density, the bounds are alleviated and some direct searches for sparticles at the LHC become relevant. Moreover, some effects in the flavor sector as well as in $(g-2)_\mu$ are seen. In all cases considered, the main penalties in terms of χ^2 come from the EWPOs. Concerning the prospects for Direct Detection of Dark Matter, there is a big difference in the allowed parameter space depending on whether or not the LSP accounts for the full CDM. In the former case, the allowed contours are very narrow, becoming much wider in the latter case. Present data already put pressure on the mAMSB for some of the scenarios considered.

USC
UNIVERSIDADE
DE SANTIAGO
DE COMPOSTELA

Chapter 8

Conclusions

This thesis represents a comprehensive study of New Physics searches, both regarding the flavour sector at LHCb, with studies of its implications in kaon physics and in processes involving the CP violating phase ϕ_s, as well as in the more general sector, with frequentist studies of two supersymmetric models performed using the `MasterCode` framework.

In chapter 5 a sensitivity study of $K_s^0 \to \pi^0\mu^+\mu^-$ has been presented, using a newly developed *PARTIAL* strategy in which only the dimuon system is reconstructed. This study has been performed using 3 fb^{-1} from Run 1 and 0.3 fb^{-1} from Run 2 data recorded at the LHCb experiment. It predicts a measurement of $\mathcal{B}(K_s^0 \to \pi^0\mu^+\mu^-)$ with a precision significantly better than that of NA48 at the LHCb Upgrade, provided a trigger efficiency of at least 50%. The precise knowledge of $\mathcal{B}(K_S^0 \to \pi^0\mu^+\mu^-)$ will allow for improvement of the theoretical prediction of $\mathcal{B}(K_L^0 \to \pi^0\mu^+\mu^-)$, that is sensitivite to New Physics in several models, such as Extra Dimensions.

Moreover, a phenomenological study of $K_s^0 \to \mu^+\mu^-$ has been carried out under a MSSM scenario, in the large $\tan\beta$ regime. Contributions to $\mathcal{B}(K_s^0 \to \mu^+\mu^-)$ surpassing those of the SM by up to a factor of seven have been found, in agreement with present experimental constraints. Correlations between this and other observables have also been provided for different regions of the parameter space, as well as fine-tuned regions where such branching fraction is even at the level of current experimental bounds.

As for the CP violating phase ϕ_s, a tagged, time-dependent angular analysis of $B_s^0 \to J/\psi K^+K^-$ in the $m(K^+K^-)$ region around the $\phi(1020)$ meson mass has been shown in chapter 6, using data from LHCb recorded during 2015 and 2016. This *preliminary* result is the most precise measurement of the CP violating phase ϕ_s so far. Complementarily, a `MultiNest` scan has also been performed using Run 2 (2016) data, finding good agreement between this and the fit result with `Minuit`.

Phenomenological studies have been performed for ϕ_s and ϕ_d, as well as for other physics observables such as the Electric Dipole Moments (EDMs) or the CP semileptonic asymmetry, under a MSSM scenario, followed the approach presented in chapter 5. Regions with large variations from the respective SM values have been found to be in agreement with the relevant constraints, even though the ϕ_s result imposes a stringent contraint on the available parameter space.

Finally, Chapter 7 reviews the results from exploring the constraints imposed by the available data on flavor, electroweak and Higgs observables, as well as LHC searches, in two supersym-

metric scenarios: the constrained MSSM (CMSSM) and the minimal AMSB (mAMSB). Both of them have been investigated by means of the `MasterCode` framework.

Regarding the CMSSM model, a large area allowed by the included constraints has been found, where several DM mechanisms play an important role, of which the chargino coannihilation is the dominant one. The case in which $\mu < 0$ shows a better fit to $BR^{\mathrm{MSSM/SM}}_{B_{s,d}\to\mu^+\mu^-}$ than the case in which $\mu > 0$, which translates into a lower χ^2. The spectrum for the best fit point is heavier for the positive case than for the negative case, as it was predicted by GAMBIT. With regard to the prospects for direct detection of dark matter, the contour for $\mu > 0$ is much more restricted than for $\mu < 0$, being below the experimental limit and at the border of the projected sensitivity for future experiments. Further studies are needed, including the DM relic density as un upper limit rather than a constraint itself, as well as LHC 13 TeV constraints.

For mAMSB, when considering that the neutralino provides all the CDM density (all-CDM case), the spectrum is found to be heavy, but smaller masses are possible if the LSP contributes only to a fraction of the overall CDM density (part-CDM case). In the all-CDM case, the LSP may be either a wino (of approximately 3 TeV) or a Higgsino (of approximately 1 TeV) with similar likelihood, while in the part-CDM much lighter LSP masses are allowed. This generally lighter spectrum makes it possible to be within the LHC reach, as opposed to the all-CDM case. In both cases, wide ranges of σ_p^{SI} are allowed.

Chapter 9

Resumen

9.1 Introducción Teórica

El Modelo Estándar (SM) de la Física de Partículas es una teoría cuántica de campos que describe las interacciones fuerte y electrodébil. Aunque ha demostrado ser una teoría muy exitosa, no proporciona explicación para varios de los fenómenos encontrados en la naturaleza. Por ejemplo, no incluye la gravedad como una de las interacciones, ni explica el origen de la asimetría materia-antimateria o de la energía y de la materia oscura. En el SM tampoco se unifican las interacciones a altas energías.

Por lo tanto, un nuevo modelo más allá del SM es necesario. Ésto es conocido como Nueva Física (NP). Entre las alternativas más reseñables se incluye la Supersymetría (SUSY), estudiada en esta tesis. Este marco establece una invariancia bajo las transformaciones de fermiones (partículas con momento angular intrínseco, *spin*, semientero) a bosones (partículas con spin entero). La atención recibida por SUSY se debe a que, si se encontrase, podría resolver varios de los problemas del SM, como el valor de la masa del bosón de Higgs, la unificación de las fuerzas a la *escala de Planck* o la asimetría materia-antimateria. Además de SUSY, hay más modelos NP dignos de mención, como aquellos con dimensiones extra. Esta tesis representa un estudio exhaustivo de búsquedas e implicaciones de NP, tanto en el experimento LHCb como en un sector más general.

9.2 LHCb

El detector LHCb (Figura 9.1) es uno de los cuatro grandes detectores del *Large Hadron Collider*, LHC, el acelerador de partículas más grande y potente del mundo, situado en el CERN (*Centro Europeo para la Investigación Nuclear*). Mide colisiones de haces de protones que viajan en direcciones opuestas, aunque también se realizan colisiones con iones pesados de forma periódica.

El LHC ha proporcionado datos a diferentes energías del centro de masas ($\sqrt{s}$), correspondientes a dos períodos de toma de datos: Run 1 (2009 - 2013, $\sqrt{s} = 7$, 8 TeV) y Run 2 (2015 - 2018, $\sqrt{s} = 13$, 14 TeV). Tras el Run 2 se está realizando un *upgrade* de este detector.

El LHCb cubre un rango de pseudorapidez $2 < \eta < 5$. Contiene un imán que deflecta partículas cargadas para medir su momento. Incluye un sistema de trazas que proporciona

una medida de dicho momento, p, con una incertidumbre relativa que varía de 0.5% para bajo momento a 1.0% a 200GeV/c. Este sistema de trazas está compuesto por dos partes:

- *VErtex LOcator*, VELO: detector de silicio en el entorno del punto de interacción, responsable de la elevada precisión a la hora de reconstruir los vértices.
- Cuatro *tracking stations*: el *Tracker Turicensis* (TT) y T1-T3, compuestas por un *Inner Tracker* (IT) y un *Outer Tracker* (OT). Ambos pertenecen al proyecto del *Silicon Tracker*, ST.

La distancia mínima de una traza a un vértice primario (PV), el *parámetro de impacto* (IP), es medido con una resolución de $(15 + 29/p_T)\mu$m, donde p_T es el componente del momento transverso al haz, en GeV/c.

Los diferentes tipos de hadrones cargados se distinguen usando información procedente de 2 detectores de Cherenkov (RICH). Los fotones, electrones y hadrones son identificados por un sistema de calorímetros que consisten en paneles centelleadores y detectores *preshower*, un calorímetro electromagético y un calorímetro hadrónico. Los muones son identificados por un sistema compuesto por detectores de gas intercalados con filtros muónicos.

La selección *online* es realizada por un trigger, que consiste en un primer estadio de hardware (que hace uso de información de los calorímetros y las cámaras de muones), seguido de una etapa de software, donde se aplica una reconstrucción total del evento.

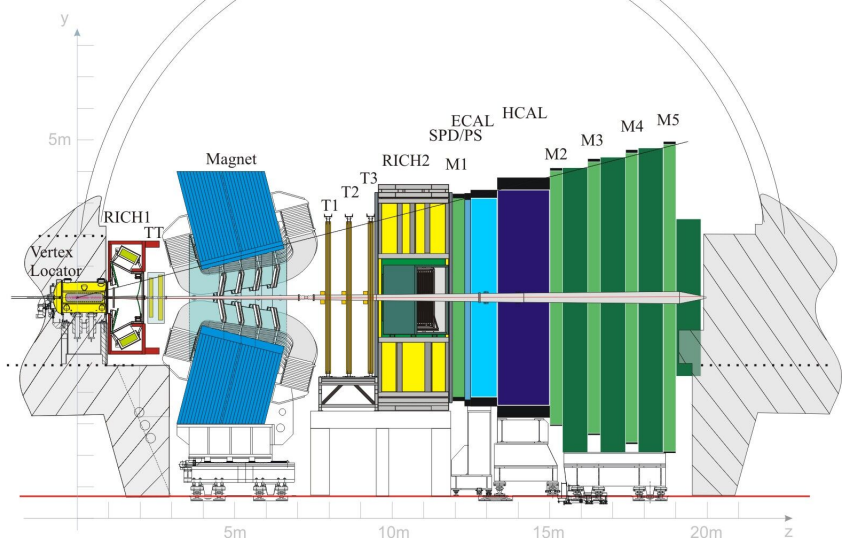

Figure 9.1: El detector LHCb [81].

9.3 Física de kaones

Los kaones ejercen un papel muy importante en la física de partículas, tanto en NP como en el SM. Los decaimientos raros de kaones tienen lugar a través de corrientes neutras que cambian de sabor (FCNC), prohibidas a *tree level* en el SM, lo que hace que su tasa de decaimiento esté altamente suprimida en este escenario. En consecuencia, consitutyen un excelente lugar donde buscar NP a través de partículas que intervengan en un determinado proceso.

Además, $K_S^0 \to \mu^+\mu^-$ aporta información complementaria a $B_s^0 \to \mu^+\mu^-$, $B_d^0 \to \mu^+\mu^-$, y $K_L^0 \to \mu^+\mu^-$ en el MSSM, especialmente en presencia de nuevas fuentes de violación de sabor (non-MFV), que no tengan su origen en la matriz CKM.

9.3.1 Estudio de la sensibilidad de $K_S^0 \to \pi^0\mu^+\mu^-$

El proceso $K_L^0 \to \pi^0\mu^+\mu^-$ es de particular importancia en modelos de NP como las dimensiones extra. Sin embargo, su potencial para restringir escenarios más allá del SM es limitado, debido a su gran incertidumbre en el SM:

$$\mathcal{B}(K_L^0 \to \pi^0\mu^+\mu^-)_{\rm SM} = \{1.4 \pm 0.3; 0.9 \pm 0.2\} \times 10^{-11}. \tag{9.1}$$

Dicha incertidumbre procede de la medida del parámetro de teoría de perturbación quiral, $|a_S|$, presente en la predicción teórica y que procede de la medida de $\mathcal{B}(K_S^0 \to \pi^0\mu^+\mu^-)$, realizada por NA48 con un error relativo del 50%. Así, una mejora en la medida de $\mathcal{B}(K_S^0 \to \pi^0\mu^+\mu^-)$ se traduce en una mejora en la predicción en el SM de $\mathcal{B}(K_L^0 \to \pi^0\mu^+\mu^-)$. Los experimentos de kaones actuales no esperan realizar dicha mejora. En esta tesis se presenta un estudio de la sensibilidad de LHCb a dicho canal, para evaluar si es posible mejorar el resultado obtenido por NA48.

Para ello, se hace uso del hecho de que la resolución en masa del K_S^0 no depende en gran medida de la información del π^0 reconstruido. Por lo tanto, y dado que la eficiencia de reconstrucción del π^0 es limitada, eventos en los que se emplea solamente información del dimuón son también considerados. Tal y como se ve en la Figura 9.2, los cortes en la masa del π^0 y el momento del K_S^0 son suficientes para crear una distribución resonante, siempre y cuando se emplee una estimación del momento típico del momento del π^0 (8.9 GeV/c). Ésto lleva a dos análisis independientes, uno en el cual todos los productos de la desintegración son considerados (*FULL*) y uno en el cual solamente se usa el par dimuónico (*PARTIAL*).

Los candidatos reconstruidos se pasan a continuación a un algoritmo de selección, seguido de un análisis multivariable, empleando una *Boosted Decision Tree* (BDT), para reducir el alto nivel de fondo. Este análisis se realiza en tres pasos: primero las variables continuas se gaussianizan, decorrelacionan y vuelven a gaussianizar. El resultado de dicho paso es añadido en una BDT común con las variables discretas. Finalmente, la respuesta de la BDT se *aplana*. El corte en la BDT asegura una eficiencia de señal del 40% para ambas estrategias, eliminando un 99.3% y un 99.8% de fondo para FULL y PARTIAL, respectivamente. De todas las fuentes de fondo consideradas, la más importante es el fondo combinatorial. Para modelar dicho fondo se usa una exponencial, mientras que una función de Hypathia [221] se emplea para describir la señal, con diferentes parámetros para FULL y PARTIAL. Empleando las anteriores parametrizaciones, se realiza un ajuste en 4 bines de la BDT. Los resultados de dicho ajuste son compatibles con 0 a 1 y 2σ en ambos casos.

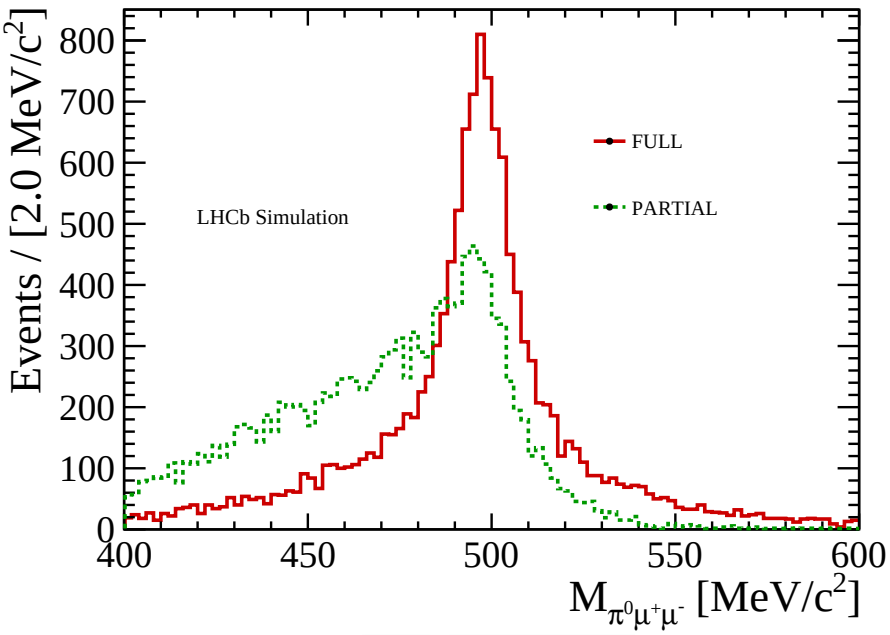

Figure 9.2: Comparación entre las distribuciones del candidato K_S^0 entre *FULL* (línea sólida roja) y *PARTIAL* (línea discontinua verde).

Para extrapolar de la luminosidad actual a la luminosidad del *LHCb Upgrade* (50 fb^{-1}) se emplea como canal de normalización $K_S^0 \to \pi^+\pi^-$. Se generan conjuntos de pseudo-experimentos, para los que el número de eventos de fondo se extrapola usando el resultado obtenido, mientras que el número de eventos de señal se extrapola conforme a la fórmula:

$$N_{sig} = \frac{\mathcal{B}(K_S^0 \to \pi^0\mu^+\mu^-)}{\mathcal{B}(K_S^0 \to \pi^+\pi^-)} \frac{\epsilon_{K_S^0 \to \pi^0\mu^+\mu^-}}{\epsilon_{K_S^0 \to \pi^+\pi^-}} N(K_S^0 \to \pi^+\pi^-) \times \frac{L_{fut}}{L_{curr}}, \tag{9.2}$$

donde L_{fut} y L_{curr} son los valores de la luminosidad futura y presente, respectivamente.

Así, los modelos descritos anteriormente se ajustan a cada pseudo-experimento dejando $\mathcal{B}(K_S^0 \to \pi^0\mu^+\mu^-)$ variar. Las incertidumbres estadísticas se obtienen como las variaciones de $\mathcal{B}(K_S^0 \to \pi^0\mu^+\mu^-)$ que se desvían del mínimo del logaritmo del perfil de la verosimilitud en media unidad. Finalmente, las incertidumbres se promedian sobre el conjunto de pseudo-experimentos para un determinado valor de la luminosidad. Las curvas de sensibilidad resultantes son las mostradas en la Figura 9.3. Como se puede ver, ambos análisis conllevan una precisión mejor que la de NA48 para el *upgrade*, si se puede mantener una eficiencia de triger del 50%.

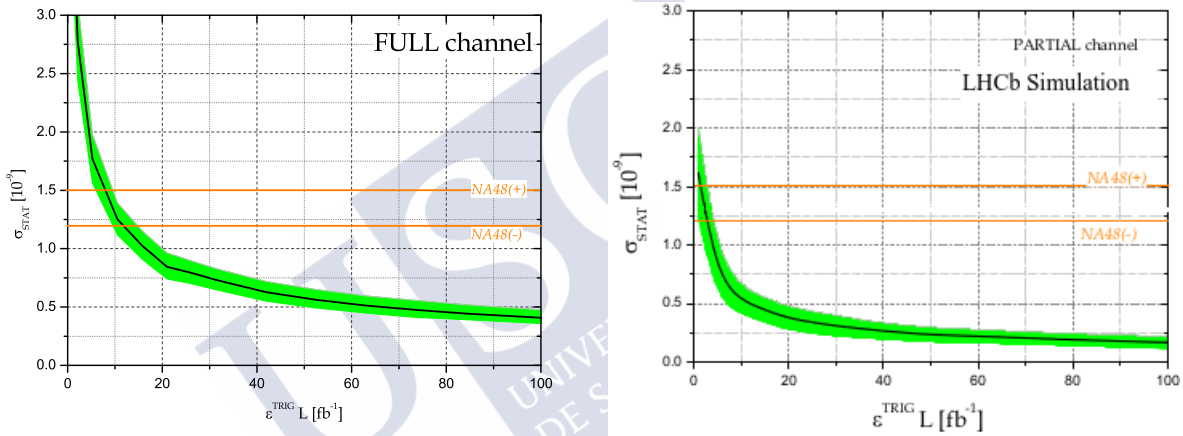

Figure 9.3: Precision esperada para $\mathcal{B}(K^0_S \to \pi^0\mu^+\mu^-)$ para los canales *FULL* (parte superior) y *PARTIAL* (parte inferior), en función de la luminosidad integrada multiplicada por la eficiencia del trigger, $L \times \varepsilon^{TRIG/SEL}$.

9.3.2 Sondeando los efectos de SUSY en $K_S^0 \to \mu^+\mu^-$

La predicción del SM para la tasa de desintegración de este canal es $(5.18 \pm 1.50_{\rm LD} \pm 0.02_{\rm SD}) \times 10^{-12}$ [143–145], donde la primera incertidumbre proviene de la contribución de larga distancia (LD) y la segunda procede de la contribución de corta distancia (SD). El límite experimental actual es 8×10^{-10} at 90% C.L., usando 3 fb^{-1} de datos del LHCb [146]. El LHCb *upgrade* podría alcanzar sensibilidades del nivel de aproximadamente 1×10^{-11} o incluso inferiores, acercándose así a la predicción del SM [147].

En esta sección el valor de $\mathcal{B}(K_S^0 \to \mu^+\mu^-)$ es predicho considerando las medidas experimentales más relevantes. Para ello, se usa la *Mass Insertion Approximation* (MIA), en la que los términos de fuera de la diagonal de las matrices de masa de los squarks se parametrizan en función de unas variables, conocidas como *Mass Insertions* (MIs). Se considera que dichas variables tienen un valor pequeño. Así:

$$\tilde{m}_Q^2 \delta_d^{LL} + \mathrm{diag}(\tilde{\mathrm{m}}_{\mathrm{Q}}^2) = \left(\mathcal{M}_{\mathrm{D}}^2\right)_{\mathrm{LL}} \tag{9.3}$$

$$\tilde{m}_Q^2 \delta_u^{LL} + \mathrm{diag}(\tilde{\mathrm{m}}_{\mathrm{Q}}^2) = \left(\mathcal{M}_{\mathrm{U}}^2\right)_{\mathrm{LL}} \tag{9.4}$$

$$\tilde{m}_d^2 \delta_d^{RR} + \mathrm{diag}(\tilde{\mathrm{m}}_{\mathrm{d}}^2) = \left(\mathcal{M}_{\mathrm{D}}^2\right)_{\mathrm{RR}} \tag{9.5}$$

Los observables que se emplean en este estudio se dividen, según su dependencia, en dos bloques:

- Observables sensibles, entre otros, a las MIs $\left(\delta_d^{LL(RR)}\right)_{12}$: $\mathcal{B}(K_L^0 \to \mu^+\mu^-)$, $\varepsilon'_K/\varepsilon_K$, ε_K, and ΔM_K.
- Observables sensibles a $\tan\beta$ (el cociente de los valores esperados en el vacío de los 2 dobletes del Higgs en el MSSM) y a la masa del Higgs pesado: $\mathcal{R}(B^+ \to \tau^+\nu_\tau)$, $\mathcal{R}(K^+ \to \mu^+\nu_\mu)$, ΔC_7.

La matriz CKM se ajusta excluyendo medidas con potencial sensibilidad a contribuciones de naturaleza MSSM. Los cortes aplicados se resumen en la Tabla 9.1, donde EXP/SM representa el valor medido sobre la predicción en el SM con sus respectivas incertidumbres.

El scan se realiza con la herramienta `Ipanema-`β [203], usando una GPU modelo GeForce GTX 1080. Los resultados obtenidos son una combinación de scans planos y scans basados en algoritmos genéticos [204]. Se han considerado tres escenarios diferentes:

- **Escenario A**: un scan genérico, sin corte en la densidad de la Materia Oscura, aparte del requerimiento de que el candidato de Materia Oscura sea un neutralino.
- **Escenario B**: un scan motivado por escenarios con un Higgsino (partícula supercompañera del Higgs) como candidato a materia oscura.
- **Escenario C**: un scan motivado por escenarios con un Wino (partícula supercompañera del bosón W) como candidato a materia oscura.

Table 9.1: Observables físicos aplicados como cortes en este estudio.

Observable	Constraint
$\mathcal{B}(K_S^0 \to \mu^+\mu^-)^{\mathrm{EXP/SM}}$	unconstrained
$\mathcal{B}(K_L^0 \to \mu^+\mu^-)^{\mathrm{EXP/SM}}$	1.00 ± 0.12 (+) [145, 154, 173] 0.84 ± 0.16 (−) [145, 154, 173]
$\Delta M_K^{\mathrm{EXP/SM}}$	1 ± 1
$\varepsilon_K^{\mathrm{EXP/SM}}$	1.05 ± 0.10 [154, 174, 175]
$\Delta(\varepsilon'_K/\varepsilon_K)^{\mathrm{EXP-SM}}$	$[15.5 \pm 2.3(\mathrm{EXP}) \pm 5.07(\mathrm{TH})] \times 10^{-4}$ [154, 176]
$\mathcal{B}(B^+ \to \tau^+\nu_\tau)^{\mathrm{EXP/SM}}$	0.91 ± 0.22 [154]
$\mathcal{B}(K^+ \to \mu^+\nu_\mu)^{\mathrm{EXP/SM}}$	1.0004 ± 0.0095 [154]
ΔC_7	-0.02 ± 0.02 [177]
$\tan\beta$:M_A plane	ATLAS limits for hMSSM scenario [178]
LSP	Lightest neutralino
B_G	$1 \pm 3(\mathrm{TH})$ [160, 179]

9.3.2.1 Resultados

El χ^2 total para cada scan se calcula como sigue:

$$\chi^2 = \sum_x \chi_x^2 \tag{9.6}$$

$$\chi_x^2 = \frac{(x - x^{\mathrm{meas}})^2}{(s_x^{\mathrm{TH}})^2 + (s_x^{\mathrm{EXP}})^2} \tag{9.7}$$

donde x es el observable, x^{meas} es su correspondiente valor en la Tabla 9.1, y s_x^{EXP} , s_x^{TH} son las incertidumbres experimental y teórica de dicho corte. Los puntos de las siguientes gráficas corresponden a un 95% C.L (o superior). Debido a su elevada incertidumbre teórica, $\mathcal{B}(K_L^0 \to \mu^+\mu^-)$ puede alcanzar hasta $\approx 1 \times 10^{-8}$ a 2σ. Valores ligeramente superiores a este límite pueden estar permitidos si reducen la contribución al χ^2 en otros observables.

En primer lugar los efectos con MIs de una única quiralidad (levógira o dextrógira) se muestran con el fin de determinar las regiones del espacio de parámetros donde cada MI domina. Las gráficas obtenidas para $\mathcal{B}(K_L^0 \to \mu^+\mu^-)$ vs $\mathcal{B}(K_S^0 \to \mu^+\mu^-)$ se muestran en la Figura 9.4 para el escenario A, la Figura 9.5 para el escenario B, y la Figura 9.6 para el escenario C. Los puntos en los planos se corresponden con predicciones procedentes de diferentes valores en los parámetros de entrada.

En el escenario A y el escenario C se puede ver que las regiones permitidas a un 95% C.L. para $\mathcal{B}(K_S^0 \to \mu^+\mu^-)$ en presencia de restricciones experimentales son aproximadamente $[0.78, 14] \times 10^{-12}$ para contribuciones LL, y $[1.5, 35] \times 10^{-12}$ para contribuciones RR. Dichas regiones son muy similares en ambos escenarios, y mucho mayores que para el escenario B, ya que en este último el parámetro de autoacoplo del Higgs μ es pequeño en comparación con masas de partículas supersimétricas.

En segundo lugar se dejan variar MIs LL y RR a la vez. Ésto permite evitar la restricción

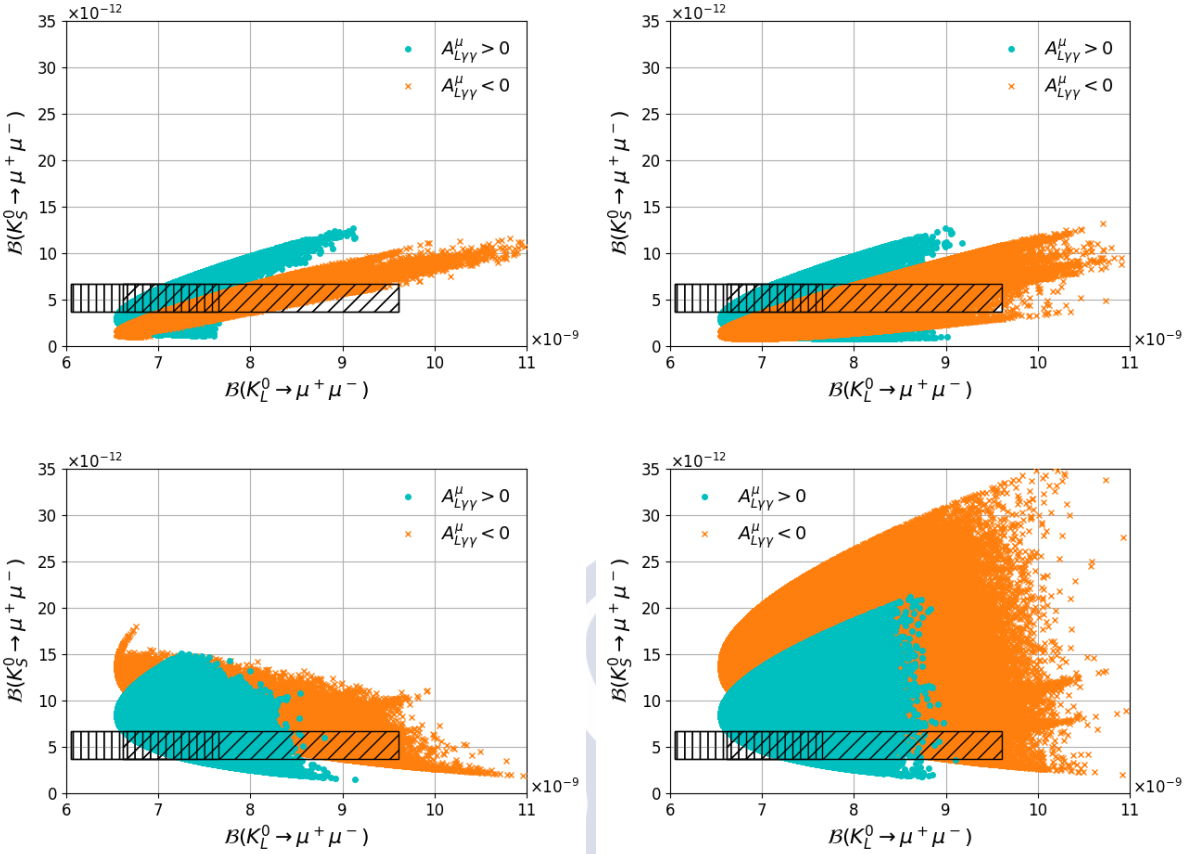

Figure 9.4: Escenario A: $\mathcal{B}(K_S^0 \to \mu^+\mu^-)$ vs $\mathcal{B}(K_L^0 \to \mu^+\mu^-)$ para $\left(\delta_d^{LL}\right)_{12} \neq 0$ y $(M_3 \cdot \mu) > 0$ (panel superior izquierdo), $\left(\delta_d^{LL}\right)_{12} \neq 0$ y $(M_3 \cdot \mu) < 0$ (panel superior derecho), $\left(\delta_d^{RR}\right)_{12} \neq 0$ y $(M_3 \cdot \mu) > 0$ (panel inferior izquierdo), y $\left(\delta_d^{RR}\right)_{12} \neq 0$ y $(M_3 \cdot \mu) < 0$ (panel inferior derecho). Los puntos de color cian se corresponden con $A^{\mu}_{L\gamma\gamma} > 0$ y las cruces naranjas con $A^{\mu}_{L\gamma\gamma} < 0$. El área rayada verticalmente se corresponde con la predicción del SM para $A^{\mu}_{L\gamma\gamma} > 0$ y el área rayada inclinada se corresponde con la predicción del SM para $A^{\mu}_{L\gamma\gamma} < 0$.

impuesta por $\mathcal{B}(K_L^0 \to \mu^+\mu^-)$. Eligiendo por ejemplo:

$$\mathrm{Re}\left[\left(\delta_d^{LL}\right)_{12}\right] = -\mathrm{Re}\left[\left(\delta_d^{RR}\right)_{12}\right], \quad \mathrm{Im}\left[\left(\delta_d^{LL}\right)_{12}\right] = \mathrm{Im}\left[\left(\delta_d^{RR}\right)_{12}\right], \tag{9.8}$$

las contribuciones supersimétricas a $\mathcal{B}(K_L^0 \to \mu^+\mu^-)$ se cancelan, mientras que las que contribuciones supersimétricas a $\mathcal{B}(K_S^0 \to \mu^+\mu^-)$ se maximizan. En esos casos, sin embargo, los límites procedentes de ΔM_K y ε_K son muy severos. Regiones donde $\mathcal{B}(K_S^0 \to \mu^+\mu^-) > 10^{-10}$, o incluso a nivel del actual límite experimental, satisfaciendo todas las restricciones experimentales, se pueden encontrar empleando algoritmos genéticos.

Hasta ahora se ha tratado el caso en el que los Higgs del MSSM tenían prácticamente la misma masa, $M_H \approx M_A$. En modelos donde dicha aproximación puede no ser válida, la restricción que $\mathcal{B}(K_L^0 \to \mu^+\mu^-)$ impone sobre $\mathcal{B}(K_S^0 \to \mu^+\mu^-)$ se hace más relajada cuanto más

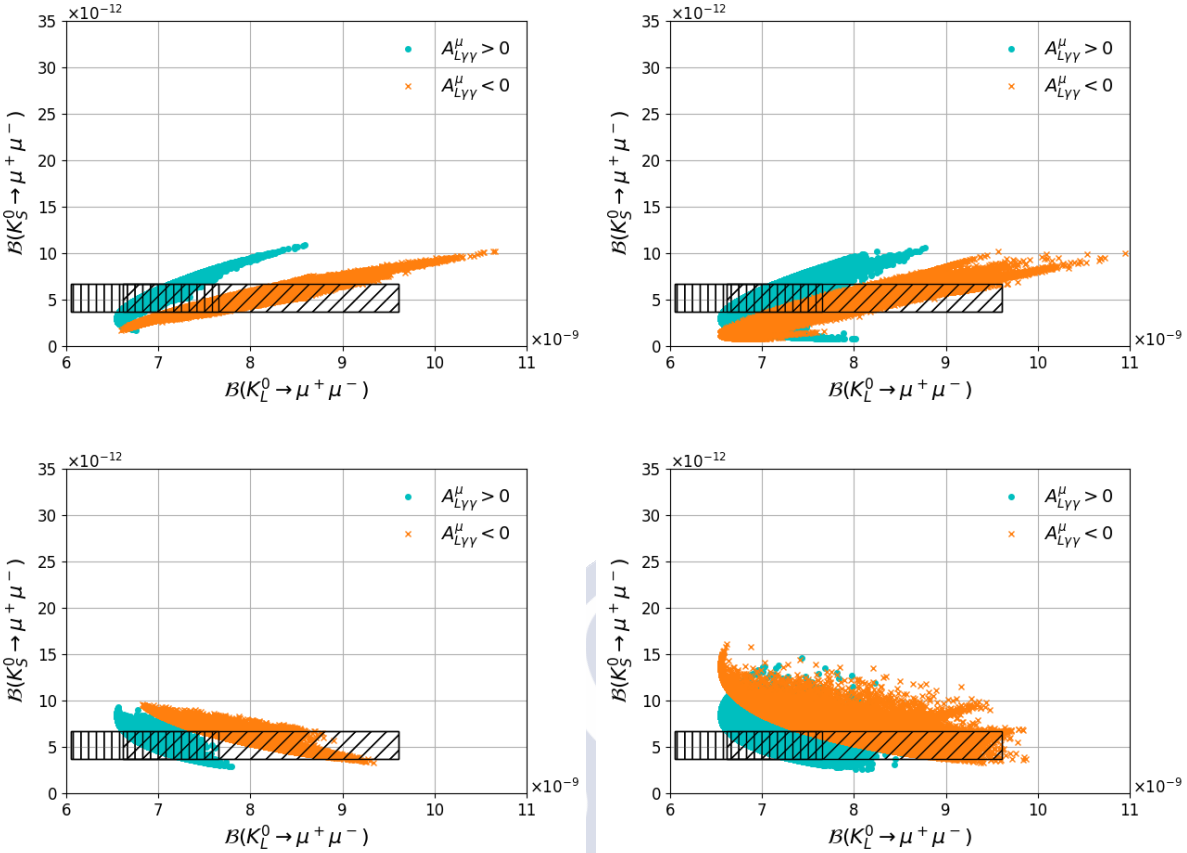

Figure 9.5: Escenario B: $\mathcal{B}(K_S^0 \to \mu^+\mu^-)$ vs $\mathcal{B}(K_L^0 \to \mu^+\mu^-)$ para $\left(\delta_d^{LL}\right)_{12} \neq 0$ y $(M_3 \cdot \mu) > 0$ (panel superior izquierdo), $\left(\delta_d^{LL}\right)_{12} \neq 0$ y $(M_3 \cdot \mu) < 0$ (panel superior derecho), $\left(\delta_d^{RR}\right)_{12} \neq 0$ y $(M_3 \cdot \mu) > 0$ (panel inferior izquierdo), y $\left(\delta_d^{RR}\right)_{12} \neq 0$ y $(M_3 \cdot \mu) < 0$ (panel inferior derecho). Los puntos de color cian se corresponden con $A^{\mu}_{L\gamma\gamma} > 0$ y las cruces naranjas con $A^{\mu}_{L\gamma\gamma} < 0$. El área rayada verticalmente se corresponde con la predicción del SM para $A^{\mu}_{L\gamma\gamma} > 0$ y el área rayada inclinada se corresponde con la predicción del SM para $A^{\mu}_{L\gamma\gamma} < 0$.

difieran las masas. Ésto sucede por ejemplo para valores bajos de M_A en el MSSM, requiriendo que tan β sea pequeño para evitar restricciones de los planos tan $\beta : M_A$ del LHC, o en extensiones como el NMSSM. Estas regiones son más dificiles de estudiar.

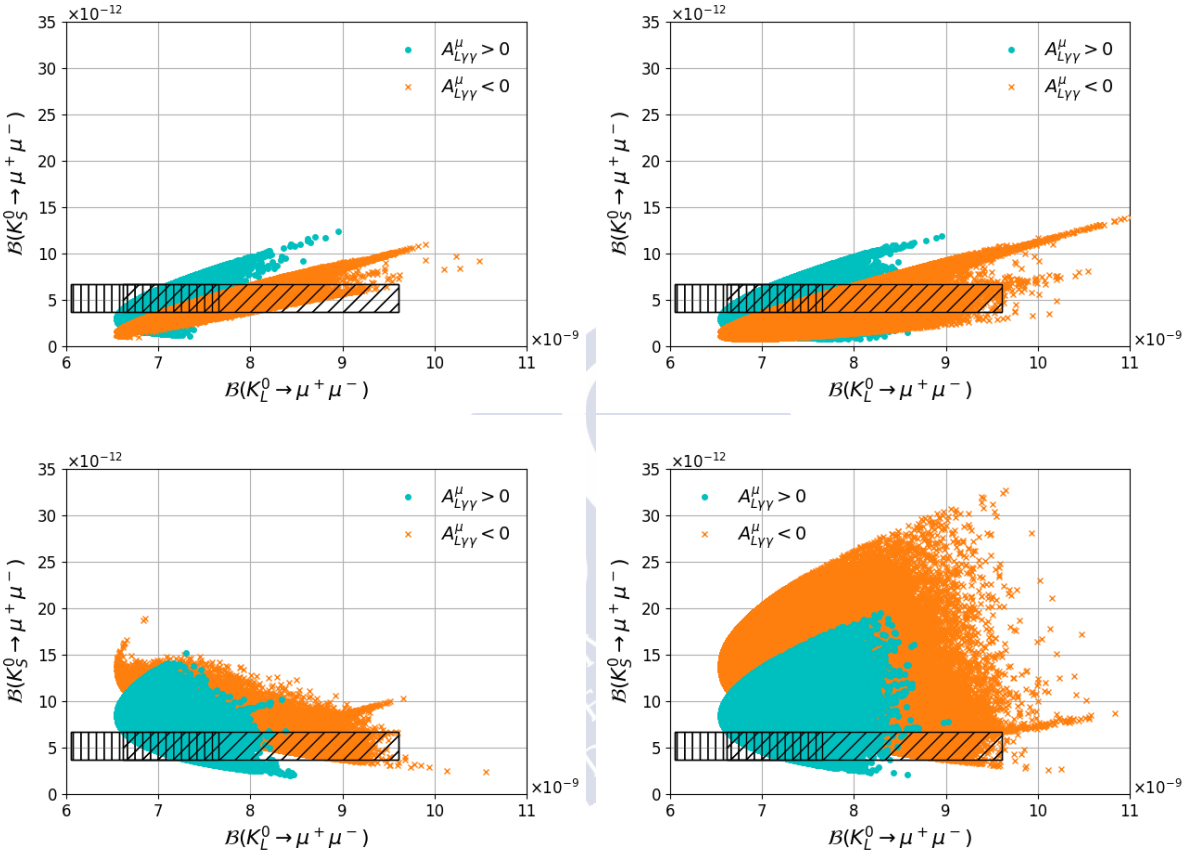

Figure 9.6: Escenario C: $\mathcal{B}(K_S^0 \to \mu^+\mu^-)$ vs $\mathcal{B}(K_L^0 \to \mu^+\mu^-)$ para $\left(\delta_d^{LL}\right)_{12} \neq 0$ y $(M_3 \cdot \mu) > 0$ (panel superior izquierdo), $\left(\delta_d^{LL}\right)_{12} \neq 0$ y $(M_3 \cdot \mu) < 0$ (panel superior derecho), $\left(\delta_d^{RR}\right)_{12} \neq 0$ y $(M_3 \cdot \mu) > 0$ (panel inferior izquierdo), y $\left(\delta_d^{RR}\right)_{12} \neq 0$ y $(M_3 \cdot \mu) < 0$ (panel inferior derecho). Los puntos de color cian se corresponden con $A^{\mu}_{L\gamma\gamma} > 0$ y las cruces naranjas con $A^{\mu}_{L\gamma\gamma} < 0$. El área rayada verticalmente se corresponde con la predicción del SM para $A^{\mu}_{L\gamma\gamma} > 0$ y el área rayada inclinada se corresponde con la predicción del SM para $A^{\mu}_{L\gamma\gamma} < 0$.

9.4 Medida y estudios fenomenológicos de la fase de violación CP ϕ_s

Las oscilaciones mesón-antimesón vienen descritas por las amplitudes de mezcla [162]

$$M_{12}^{(M)} \equiv \langle M|\mathcal{H}_{\text{eff}}^{\Delta F=2}|\bar{M}\rangle \quad M = K^0, B_{d,s} \tag{9.9}$$

donde $\mathcal{H}_{\text{eff}}^{\Delta F=2}$ es el Hamiltoniano efectivo que, en el marco del MSSM, tiene la forma:

$$\mathcal{H}_{\text{eff}}^{\Delta F=2} = \sum_{i=1}^{5} C_i Q_i + \sum_{i=1}^{3} \tilde{C}_i \tilde{Q}_i + \text{h.c.} \tag{9.10}$$

siendo Q_i los operadores y C_i los coeficientes de Wilson. De dichas amplitudes se pueden extraer varios observables representativos cuyo valor depende fuertemente de las contribuciones de NP. Ejemplos de ellos son la fase de mezcla, la frecuencia de oscilación o la asimetría semileptónica:

$$\phi_s = \arg\left(M_{12}\right),\ \Delta m_s = |M_{12}|,\ A_{SL} = -\frac{\Delta\Gamma_s}{\Delta M_s}\tan\phi_s \tag{9.11}$$

En el SM la violación CP tiene su origen en la matriz de Cabibbo-Kobayashi-Maskawa (CKM), que describe la mezcla entre los quarks [222]. La violación CP que tiene lugar en la interferecia entre amplitudes asociadas a la desintegración directa del mesón B_s^0 a un estado final autovalor de CP y aquellas asociadas al decaimiento tras las oscilación $B_s^0 - \bar{B}_s^0$ viene caracterizada por la fase de violación CP, ϕ_s^f, definida como:

$$\phi_s^f = -\text{arg}(\lambda_\text{f}),\ \lambda_\text{f} = \eta_\text{f}\frac{\text{q}}{\text{p}}\frac{\bar{\mathcal{A}}_\text{f}}{\mathcal{A}_\text{f}}, \tag{9.12}$$

donde f es el estado final, η_f es 1(-1) para estados finales $CP-even$ ($CP-odd$), $\left|\frac{q}{p}\right|$ determina la cantidad de violación CP en la mezcla, y $\mathcal{A}_f(\bar{\mathcal{A}}_f)$ es la amplitud del mesón $B_s^0(\bar{B}_s^0)$ meson decayendo al estado final. Se necesitan medidas de precisión de esta fase para diferenciar contribuciones de SM y NP.

En el SM, para transiciones $b \to c\bar{c}s$, la determinación indirecta via ajustes globales a datos experimentales resulta en $\phi_s^{c\bar{c}s} = 0.0364 \pm 0.0016$ rad [222]. La NP podría modificar la fase si nuevas partículas contribuyeran a los diagramas de caja de B_s^0–$\bar{B}_s^0$ [225, 226].

9.4.1 ϕ_s experimental

El objetivo de este análisis es de realizar la medida de ϕ_s en el canal $B_s^0 \to J/\psi K^+K^-$ empleando datos recogidos por LHCb en 2015 y 2016. Además, se realizan medidas actualizadas de la diferencia en anchura de decaimiento para los autoestados pesado y ligero, $\Delta\Gamma_s$, y el cociente entre las anchuras promedio para los sistemas B_s^0 y B_d^0, Γ_s/Γ_d.

9.4.1.1 Fenomenología

Hay 4 amplitudes que contribuyen a esta desintegración: 3 procedentes de la contribución de la onda P (dominante) al par K^+K^- y una contribución menor de la onda S. El ajuste nominal

se realiza asumiendo que la violación CP directa causada por diagramas *penguin* es la misma para todos los estados de polarización. Se han realizado checks para corroborar dicho *ansatz*.

La tasa diferencial de decaimiento para un B_s^0 inicial en función del tiempo de decaimiento y ángulos usando $\lambda_f = |\lambda_f| e^{-i\phi_s^f} \equiv |\lambda_f| e^{-i\phi_f}$ ($f = 0, ||, \perp$, S) viene dada por [229]

$$\frac{d^4\Gamma(t)}{dm^2_{KK} d\cos\theta_K d\cos\theta_l d\phi} = \sum_{k=1}^{10} N_k h_k(t) f_k(\theta_K, \theta_l, \phi), \tag{9.13}$$

donde N_k son factores de normalización, $f_k(\theta_K, \theta_l, \phi)$ son las funciones dependientes de los ángulos de helicidad, dadas en [229], y las funciones dependientes del tiempo de decaimiento $h_k(t)$ vienen dadas por

$$h_k(t) = \frac{3}{4\pi} e^{-\Gamma t} \left\{ a_k \cosh\frac{\Delta\Gamma t}{2} + b_k \sinh\frac{\Delta\Gamma t}{2} + c_k \cos(\Delta m t) + d_k \sin(\Delta m t) \right\}. \tag{9.14}$$

Para una producción inicial de $\bar{B}_s^0$, los signos de c_k y d_k son los contrarios. Los coeficientes se especifican en la Tabla C.2 (Apéndice C). Para reducir la correlación entre los parámetros del ajuste, se puede decidir ajustar $|\lambda_0|$, ϕ_0 and $|\frac{\lambda_f}{\lambda_0}|$, $\phi_f - \phi_0$, para $f \neq 0$.

9.4.1.2 Correcciones a las muestras utilizadas

Tras unos cortes iniciales aplicados a las muestras de datos y la simulación, detallados en la sección 6.2.2, se entrena una BDT para mejorar la proporción entre señal y fondo. Para ello se usan datos y simulación del 2016. Tras aplicar dicha BDT, dicha proporción es ~ 3.9.

9.4.1.3 Ajuste a masa y cálculo de los sWeights

Los parámetros de interés físico se extran mediante un ajuste de la PDF de la señal a las distribuciones angulares y de tiempo de desintegración. Éstos eventos se *pesan* primero para sustraer estadísticamente componentes de fondo usando el método *sPlot* [237] empleando $m(J/\psi K^+K^-)$ como la variable discriminatoria.

Para mejorar la resolución, $m(J/\psi K^+K^-)$ se determina usando la masa del J/ψ y restricciones al vértice primario. Las fuentes de fondo consideradas son sustraídas usando vetos en variables de identificación ($B^0 \to J/\psi K^{*0}$, $\Lambda_b^0 \to J/\psi p K^-$), así como *inyectando* pesos negativos en la muestra ($\Lambda_b^0 \to J/\psi p K^-$). Finalmente, la desintegración $B^0 \to J/\psi K^+K^-$ es modelada en la pdf. El fondo combinatorial se modela usando una función exponencial, y la distribución de señal con una función *Crystal Ball* (CB) usando el error en masa por evento como observable condicional. De esta forma, la correlación entre $\cos\theta_\mu$ y la resolución en masa se tiene en cuenta. La $p.d.f$ viene dada por:

$$\begin{aligned} p(m(J/\psi K^+K^-)|\sigma_i) = {} & N_{sig} CB(m(J/\psi K^+K^-); \mu, \alpha_1, \alpha_2, n_1, n_2, s_1, s_2|\sigma_i) \\ & + N_{bkg}((1 - f_{B_d}) e^{-\gamma_b m(J/\psi K^+K^-)} + f_{B_d} Gauss(m(J/\psi K^+K^-); \mu_{B_d}, \sigma_{B_d})), \end{aligned}$$

donde N_{sig} y N_{bkg} son el número de eventos de señal y fondo, respectivamente, μ es la media de la distribución, s_1 y s_2 los factores de escala (para tener en cuenta la subestimación del error en masa por evento), $\alpha_1, \alpha_2, n_1, n_2$ son parámetros de cola y γ_b el coeficiente en la exponencial para describir el fondo.

El ajuste a la distribución de $m(J/\psi K^+K^-)$ se realiza a la muestra dividida en 24 submuestras, correpondiéndose con seis bines en la masa del par K^+K^-, [990, 1008, 1016, 1020, 1024, 1032, 1050] MeV/c^2, dos categorías de trigger (*biased* y *unbiased*) y dos años de tom de datos (2015 y 2016).

9.4.1.4 Factores C_{SP}

El cambio relativo de la curva para la onda S con respecto a la correspondiente a la onda P debe tenerse en cuenta a través de términos de interferencia en las expresiones angulares, dado que el análisis se realiza en bines de m_{KK} finitos. Ésto se hace añadiendo un factor de corrección multiplicativo a la pdf de la señal, C_{SP}. Hay en total seis factores C_{SP}, uno por cada bin de m_{KK}.

Las formas de las curvas para las ondas S y P se denotan como $p(m_{KK})$ y $s(m_{KK})$, respectivamente, donde ambas están normalizadas a la unidad en el rango $[m^L_{KK}, m^U_{KK}]$. Debido a que en cada bin de m_{KK}, $\langle p \times s^* \rangle \neq \langle p \rangle \times \langle s^* \rangle$, el producto $p \times s^*$ debe ser integrado (al dar cuenta de la interferencia entre las ondas P y S). Ésto lleva a

$$\frac{\int_{m^L_{KK}}^{m^H_{KK}} p \times s^* \; dm_{KK}}{\sqrt{\int_{m^L_{KK}}^{m^H_{KK}} |p|^2 \; dm_{KK} \int_{m^L_{KK}}^{m^H_{KK}} |s|^2 \; dm_{KK}}} = C_{\mathrm{SP}} e^{-i\theta_{\mathrm{SP}}}, \tag{9.15}$$

donde C_{SP} es el factor de corrección y la fase θ_{SP} se absorbe en la medida de la fase fuerte de la onda S. Se considera que las ondas P y S se corresponden con las resonancias ϕ y f_0, respectivamente.

La resolución del detector causa un efecto en los factores C_{SP} que debe de ser tenido en cuenta. La ecuación 9.15 se define en función de la *verdadera* m_{KK}, pero los bines de masa se definen en función de la m_{KK} *medida*. Dicho efecto se incorpora como una corrección en la eficiencia, $\epsilon_i(m_{KK})$, de los factores C_{SP}, de acuerdo con

$$C_{SP} e^{-i\theta_{SP}} = \frac{\int_{2m_K}^{m_{B^0_s} - m_{J/\psi}} p \times s^* \times \epsilon(m_{KK}) \; dm_{KK}}{\sqrt{\int_{2m_K}^{m_{B^0_s} - m_{J/\psi}} |p|^2 \times \epsilon(m_{KK}) \; dm_{KK} \int_{2m_K}^{m_{B^0_s} - m_{J/\psi}} |s|^2 \times \epsilon(m_{KK}) \; dm_{KK}}}, \tag{9.16}$$

Las distributciones de $\epsilon_i(m_{KK})$ se muestran en la Figura 9.7. Los factores C_{SP} obtenidos son los que aparecen en la Tabla 9.2.

9.4.1.5 Resolución temporal

Para parametrizar la resolución del tiempo de desintegración se emplea un modelo efectivo de una única Gaussiana. Dicho modelo se ajusta al tiempo de desintegración, t en diez bines de la incertidumbre de t, δ_t. Consiste en una delta de Dirac y dos funciones exponenciales convolucionadas con:

$$\mathcal{R}(t) \propto \sum_{i=1}^{3} f_i \frac{1}{\sqrt{2\pi}\sigma_i} e^{-\frac{1}{2}\left(\frac{t-\mu}{\sigma_i}\right)^2}, \tag{9.17}$$

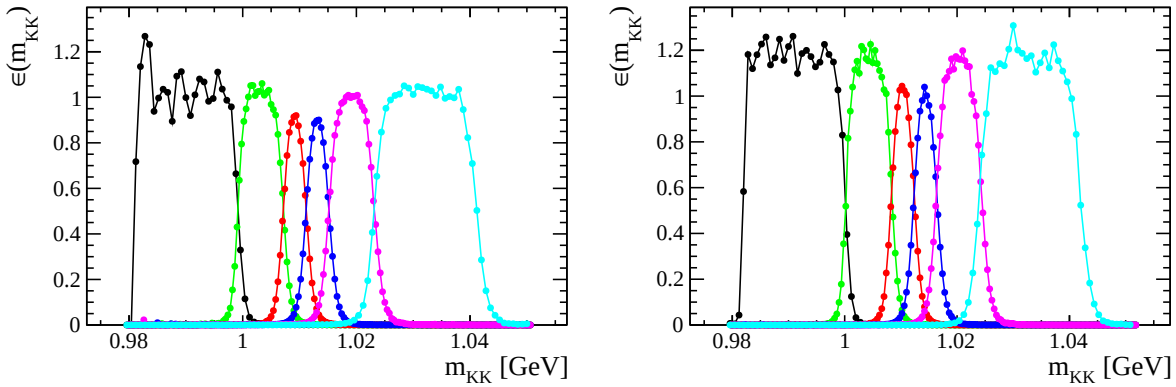

Figure 9.7: Eficiencia de cada selección de bin en m_{KK} en función de la m_{KK} *verdadera* simulada usando simuación sin (izquierda) y con (derecha) onda S.

Table 9.2: Factores $C_{\rm SP}$ obtenidos usando Eq. (9.16).

	S-wave line shape
m_{KK} bin	f_0
1	0.8463
2	0.8756
3	0.8478
4	0.8833
5	0.9415
6	0.9756

donde $\sum_i f_i = 1$. Se añade un componente extra para dar cuenta de eventos donde el vértice primario se asigna de forma incorrecta. La anchura efectiva de la Gaussiana se computa como:

$$\sigma_{\rm eff} = \sqrt{(-2/\Delta m_s^2)\ln D}, \tag{9.18}$$

donde

$$D = \sum_{i=1}^{3} f_i e^{-\sigma_i^2 \Delta m_s^2/2}, \tag{9.19}$$

y $\Delta m_s = 17.77 \text{ps}^{-1}$. Para determinar los parámetros de calibración, se considera una dependencia lineal o cuadrática de $\sigma_{\rm eff}$ con $\langle \delta_t \rangle$. Con este fin se emplean diferentes muestras, entre las que se encuentran eventos simulados de $B_s^0 \to J/\psi\phi$, J/ψ *prompt* (producidas en el vértice de interacción) y datos correspondientes a J/ψ *prompt*. Con ello se obtiene:

$$\sigma_{\rm eff} = 45.54 \pm 0.04 \pm 0.05 \text{ fs} \tag{9.20}$$

Donde la primera incertidumbre es estadística debido al tamaño finito de la muestra de datos de $B_s^0 \to J/\psi\phi$ y la segunda procede de incertidumbres en los parámetros de calibración.

9.4.1.6 Aceptancia angular

La aceptancia angular se modela utilizando *pesos de normalización* (véase Ref. [243], Sec. 3.3), obtenidos de eventos simulados. Dicha muestra de simulación se somete a un proceso iterativo de pesado en variables cinemáticas ($p(K^{\pm})$, $p_T(K^{\pm})$, $p(B_s^0)$, $p_T(B_s^0)$ y $m(K^+K^-)$) para corregir las diferencias entre datos y simulación. Se calculan un total de 10 pesos de normalización para cada año y categoría de trigger, tal y como se indica en la Tabla 9.3.

Table 9.3: Pesos de la aceptancia angular determinados con simulación. Los factores f_k son de normlización de las funciones angulares. Se emplean en la normalizacion de la pdf.

k		f_k/f_1			
		2015		2016	
		"Unbiased trigger"	"Biased" trigger	"Unbiased trigger"	"Biased trigger"
1	(00)	1 ± 0	1 ± 0	1 ± 0	1 ± 0
2	($\parallel\parallel$)	1.0435 ± 0.0020	1.0452 ± 0.0039	1.03800 ± 0.00070	1.0370 ± 0.0015
3	($\perp\perp$)	1.0439 ± 0.0020	1.0451 ± 0.0038	1.03776 ± 0.00069	1.0371 ± 0.0015
4	($\parallel\perp$)	-0.0024 ± 0.0016	-0.0100 ± 0.0032	-0.00082 ± 0.00055	0.0027 ± 0.0012
5	(0 $\parallel$)	-0.00132 ± 0.00096	0.0035 ± 0.0018	0.00023 ± 0.00033	0.00307 ± 0.00072
6	(0 $\perp$)	0.00121 ± 0.00094	0.0020 ± 0.0019	0.00025 ± 0.00033	-0.00022 ± 0.00072
7	(SS)	1.0155 ± 0.0014	1.0259 ± 0.0027	1.01034 ± 0.00047	1.0220 ± 0.0011
8	(S$\parallel$)	-0.0018 ± 0.0012	-0.0040 ± 0.0024	0.00009 ± 0.00042	0.00029 ± 0.00093
9	(S$\perp$)	0.0013 ± 0.0012	-0.0010 ± 0.0025	0.00008 ± 0.00043	0.00005 ± 0.00094
10	(S0)	-0.0189 ± 0.0026	-0.0375 ± 0.0050	-0.00240 ± 0.00089	0.0026 ± 0.0019

9.4.1.7 Aceptancia temporal

La eficiencia de reconstrucción no es constante en función del tiempo de desintegración del B_s^0. La aceptancia temporal general se determina usando como canal de control $B^0 \to J/\psi K^*(892)^0$, cinemáticamente muy similar al de la señal y con un tiempo de vida media muy bien conocido. La aceptancia temporal se define como

$$\varepsilon^{B_s^0}_{\text{data}}(t) = \varepsilon^{B^0}_{\text{data}}(t) \times \frac{\varepsilon^{B_s^0}_{\text{sim}}(t)}{\varepsilon^{B^0}_{\text{sim}}(t)}, \tag{9.21}$$

donde $\varepsilon^{B^0}_{\text{data}}(t)$ es la eficiencia de los eventos del canal de control que han pasado el proceso de selección y de pesado con sWeights y $\varepsilon^{B_s^0}_{\text{sim}}(t)/\varepsilon^{B^0}_{\text{sim}}(t)$ el cociente de las eficiencias de eventos simulados de los canales de señal y control tras haber pasado toda la cadena de selección y las correcciones pertinentes. Este segundo término da cuenta de las pequeñas diferencias en el tiempo de vida medio y la cinemática existentes entre el canal de control y el de señal.

Para derivar $\varepsilon^{B_s^0}_{\text{data}}(t)$ se realiza un ajuste simultáneo a todas las muestras. La aceptancia temporal $\varepsilon^{B_s^0}_{\text{data}}(t)$ obtenida se usa para ajustar a la muestra de señal y determinar los parámetros físicos. El modelo usado en el ajuste en todos los casos es el producto de una exponencial, convolucionada con una resolución Gaussiana y la respectiva aceptancia temporal. Esta función

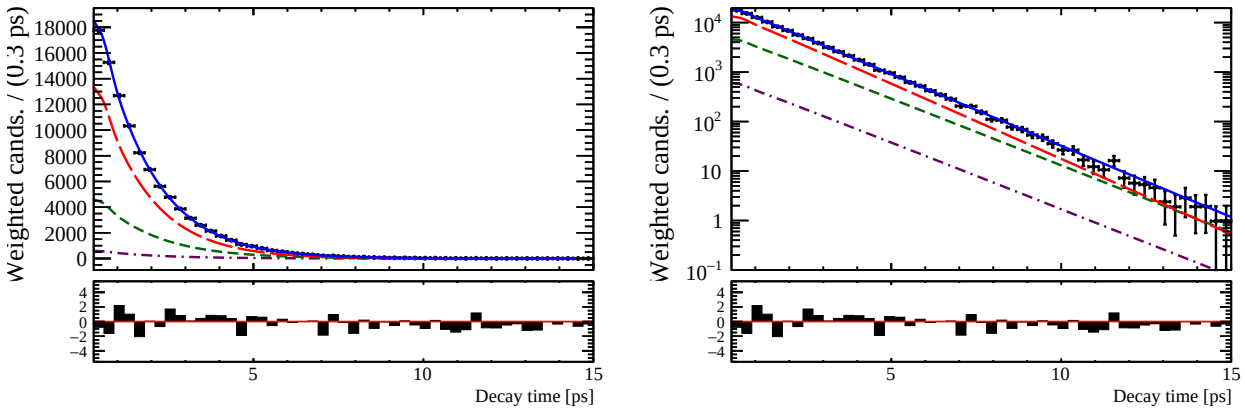

(a) (b)

Figure 9.8: Distribuciones del tiempo de desintegración para decaimientos de $B_s^0 \to J/\psi K^+ K^-$ con el fondo sustraído (puntos de datos), con las proyecciones unidimensionales de la pdf en el punto de máxima verosimilitud. La línea sólida azul muestra la distribución total, mientras que sus componentes $CP-even$, $CP-odd$ y onda S se indican con líneas discontinuas roja, verde y líneas discontinuas y punteadas violetas, respectivamente. Se muestran resultados combinados para los dos años de toma de datos y las dos categorías de trigger.

se modela empleando *splines* cúbicas. La aceptancia temporal se obtiene de forma separada para los dos años de toma de datos y dos categorías de trigger.

Los tiempos de vida media $\tau(B^0)$ y $\tau(B^+)$ en las desintegraciones $B^0 \to J/\psi K^{*0}$ y $B^+ \to J/\psi K^+$ se miden como forma de comprobar el procedimiento seguido para determinar la aceptancia temporal. Para ello, se emplean muestras de datos y simulación del 2016. Se encuentra un buen acuerdo entre los resultados obtenidos y los esperados.

9.4.1.8 Identificación de sabor

Para estudios dependientes del tiempo es necesario identificar correctamente el sabor inicial del mesón. Para ello se usan dos algoritmos separados que explotan características diferentes de la producción incoherente de $b\bar{b}$ en colisiones pp. En este análisis se han optimizado y calibrado (usando las desintegraciones $B^+ \to J/\psi K^+$ y $B_s^0 \to D_s^- \pi^+$) empleando datos del Run 2.

9.4.1.9 Ajuste a los datos

El procedimiento de ajuste emplea la técnica de sFit para sustraer el fondo, tal y como se describe en la Sección 6.2.3. Se han desarrollado varios programas de ajustes, incluyendo el nominal, que emplea tarjetas gráficas (GPUs). Todos los programas proporcionan un buen acuerdo entre ellos. Las gráficas con el fondo sustraido se muestran en las Figuras 9.8 y 9.9.

Este estudio resulta en la medida más precisa hasta la fecha de los parámetros de violación

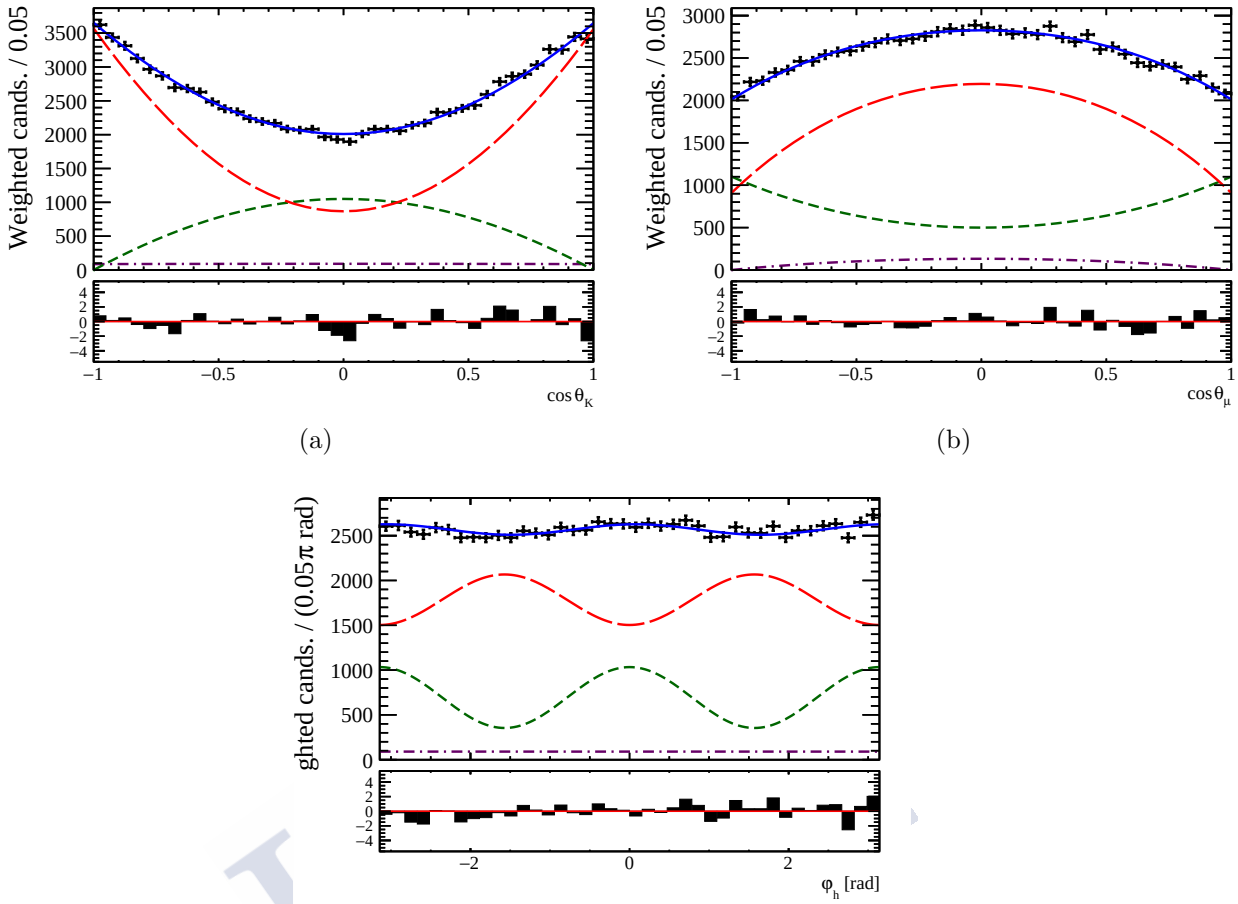

Figure 9.9: Distribuciones de los ángulos de helicidad para decaimientos de $B_s^0 \to J/\psi K^+K^-$ con el fondo sustraído (puntos de datos), con las proyecciones unidimensionales de la pdf en el punto de máxima verosimilitud. La línea sólida azul muestra la distribución total, mientras que sus componentes $CP-even$, $CP-odd$ y onda S se indican con líneas discontinuas roja, verde y líneas discontinuas y punteadas violetas, respectivamente. Se muestran resultados combinados para los dos años de toma de datos y las dos categorías de trigger.

CP en la interferencia entre mezcla y desintegración. Se ha obtenido:

$$\begin{aligned} \phi_s &= -0.080 \pm 0.041 \pm 0.005\text{rad} \\ |\lambda| &= 1.006 \pm 0.016 \pm 0.004 \\ \Delta\Gamma_s &= 0.0772^{+0.0076}_{-0.0077} \pm 0.0015\text{ps}^{-1} \\ \Gamma_s - \Gamma_d &= -0.0041^{+0.0024}_{-0.0023} \pm 0.0015\text{ps}^{-1} \end{aligned} \tag{9.22}$$

donde las primeras incertidumbres son estadísticas y las segundas sistemáticas. Este resultado está de acuerdo a nivel de 1.7σ con la medida del Run 1 realizada por LHCb [247], y de 1.2σ con respecto a la medida del SM [222]

9.4.2 Estudios fenomenológicos

Para búsquedas de NP los observables relativos a la transición $B_s^0 - \bar{B}_s^0$, como ϕ_s y Δm_s juegan un papel muy importante, al ser muy sensibles a los efectos de NP. En esta sección se estudian los efectos del MSSM en dichos procesos, así como para los Momentos Dipolares Eléctricos (EDMs) del protón y del neutron, y procesos relacionados con transiciones $\Delta F = 0$ y $\Delta F = 1$.

9.4.2.1 Formalismo y scan

El formalismo es el mismo que el empleado en la Sección 9.3.2. A los escenarios allí considerados se añaden dos adicionales:

- **Escenario D**: motivado por escenarios con predicciones conservadoras para los EDMs.
- **Escenario E**: motivado por escenarios con predicciones más agresivas para los EDMs

9.4.2.2 Observables

Se calculan los siguientes observables:

- Observables sensibles a $\tan\beta$ y a la masa del Higgs pesado: $\mathcal{B}(B^+ \to \tau^+\nu_\tau)$, ΔC_7.
- $\mathcal{B}(B_s^0 \to \mu^+\mu^-)$, $\mathcal{B}(B_d^0 \to \mu^+\mu^-)$

Adicionalmente se computan observables relacionados con las oscilaciones mesón-antimesón en los sectores B_s, B_d, tomando el cociente con respecto a la predicción del SM:

- La fase de mezcla, $\Delta\phi_{s,d} = \arg\left(M_{12}/M_{12}^{\rm SM}\right)$
- La diferencia de masa, $\Delta m_s/\Delta m_s^{SM} = |M_{12}|/|M_{12}^{\rm SM}|$.
- La asimetría semileptónica, calculada como $-\frac{\Delta\Gamma_s}{\Delta M_s}\tan\phi_s$. Con el fin de construir una cantidad más fácil de manejar teóricamente, se usa $\Delta M_s A_{SL}/\Delta\Gamma_s$.

Finalmente, la diferencia de asimetrías CP en $B^- \to X_s^-\gamma$ and $\bar{B}^- \to X_s^0\gamma$ se calcula, tomando la fórmula de la Referecia [175]. Todas las restricciones aplicadas se resumen en la Tabla 9.4.

9.4.2.3 Resultados

Se muestran las gráficas para cada escenario, correspondiéndose con el 95% CL. Los puntos negros se calculan incluyendo el corte en ϕ_s, mientras que los asteriscos rosas se calculan sin él. Como se puede observar, este resultado afecta en gran medida el rango de ϕ_s- ϕ_s^{SM} , así como el de otros observables. Los resultados experimentales de la Tabla 9.4 se indican con variaciones de $\pm 1\sigma$ con respecto a sus incertidumbres con áreas sombreadas en verde. Para los EDMs, se indican las cotas superiores con áreas sombreadas en amarillo.

Para los EDMs, se muestran puntos con el corte en ϕ_s aplicado en diferentes escenarios en la Figura 9.10. Tal y como se esperaba, el rango permitido para el escenario E es mucho más amplio que el permitido en el escenario D. Se observan grandes desviaciones con respecto al SM, algunas de ellas introduciéndose en las cotas superiores experimentales [252, 256].

La Figura 9.11 muestra ϕ_s-ϕ_s^{SM} en función de la asimetría semileptónica. Una dependencia manifiesta se observa entre ambas. También se observa cómo dicha asimetría puede adquirir valores muy diferentes de los predichos por el SM.

Table 9.4: Resultados físicos en los observables aplicados en este estudio.

Observable	Constraint
$\Delta m_s/\Delta m_s^{SM}$	0.948 ± 0.062
$\phi_s - \phi_s^{SM}$	-0.0447 ± 0.0301 [245]
$\phi_d - \phi_d^{SM}$	-0.1796 ± 0.0535 [245]
$\mathcal{B}(B_s^0 \to \mu^+\mu^-)^{\mathrm{EXP/SM}}$	0.71 ± 0.12
$\mathcal{B}(B_d^0 \to \mu^+\mu^-)^{\mathrm{EXP/SM}}$	9.71 ± 6.41
$\Delta m_s A_{SL}/\Delta\Gamma_s - (\Delta m_s A_{SL}/\Delta\Gamma_s)^{\mathrm{SM}}$	-0.1257 ± 0.5651
$\mathcal{B}(B^+ \to \tau^+\nu_\tau)^{\mathrm{EXP/SM}}$	0.87 ± 0.21 [29]
ΔC_7	-0.02 ± 0.02 [177]
$\Delta A_{CP}(b \to s\gamma)$	$5.0 \pm 3.9_{\mathrm{stat}} \pm 1.5_{\mathrm{syst}}$ [255]
$\lvert d_n \rvert$	2.9×10^{-26} e cm (90% CL) [256]
$\lvert d_{Hg} \rvert$	7.4×10^{-30} e cm (90% CL) [252]
m_H	125.18 ± 20 [GeV] [29]
$\tan\beta$:M_A plane	ATLAS limits for hMSSM scenario [178]
LSP	Lightest neutralino

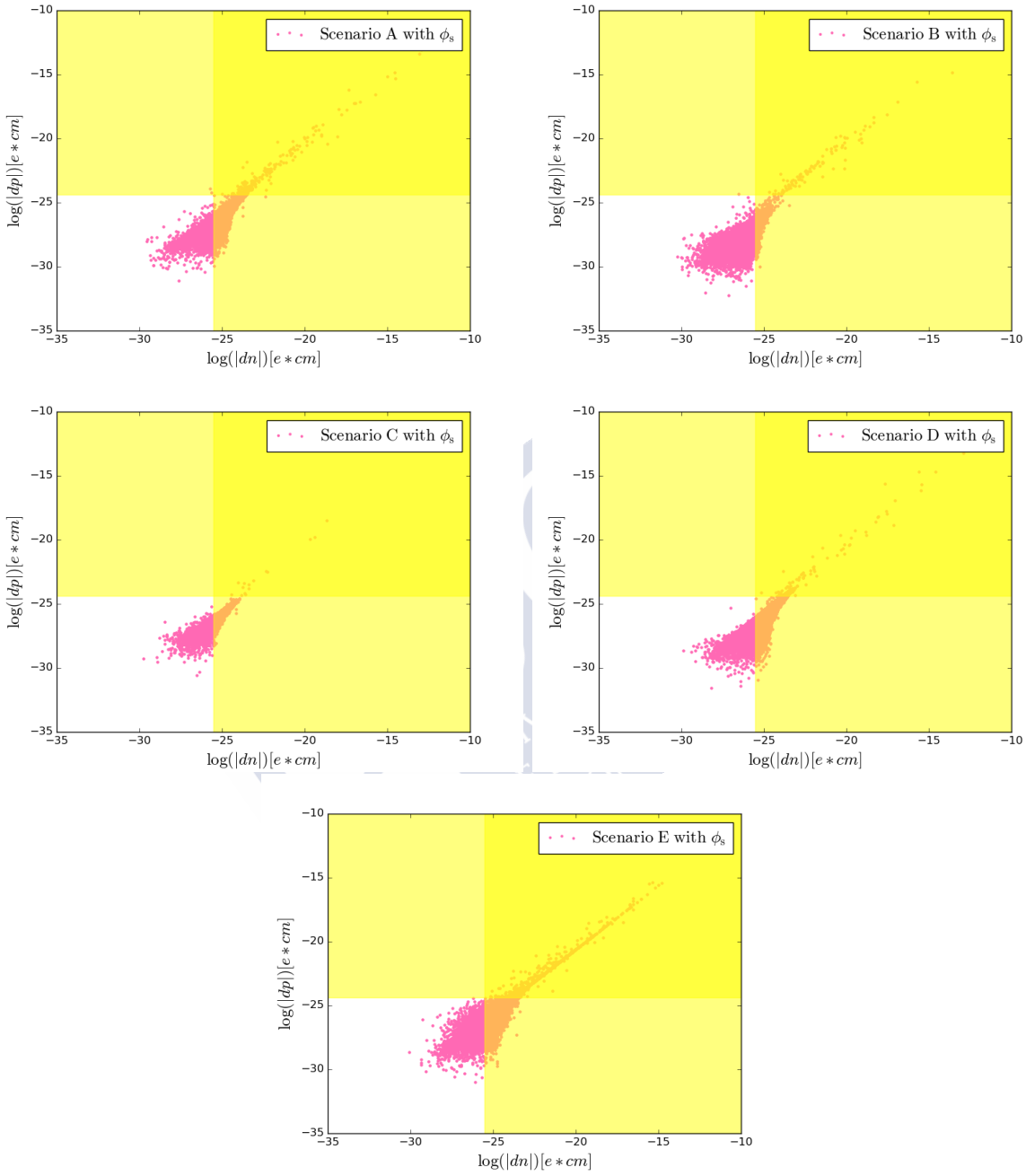

Figure 9.10: EDM del neutrón vs EDM del neutrón para los escenarios A (parte superior izquierda), B (parte superior derecha), C (parte intermedia izquierda), D (parte intermedia derecha) y E (parte inferior). La parte sombreada amarilla se corresponde con la región excluida por el actual límite en los EDM del neutrón [256] y del mercurio [252].

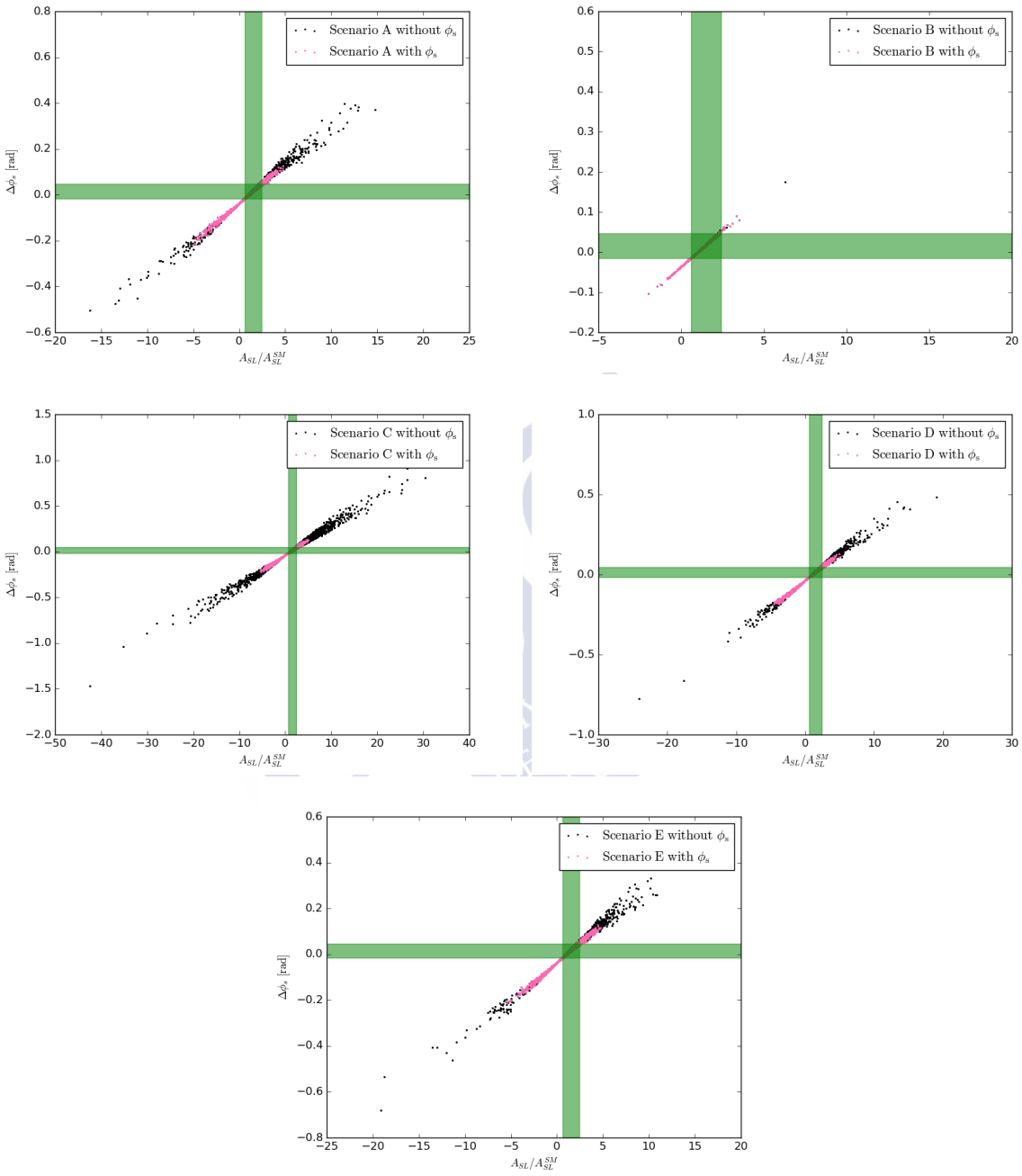

Figure 9.11: ϕ_s- ϕ_s^{SM} vs A_{sl}/A_{sl}^{SM} para los escenarios A (parte superior izquierda), B (parte superior derecha), C (parte intermedia izquierda), D (parte intermedia derecha) y E (parte inferior).

Table 9.5: Rangos de los parámetros empleados en el scan del CMSSM.

Parámetro	Rango total	Rango de baja masa
m_0	(0, 10) TeV	(0,4) TeV
$m_{1/2}$	(0, 10) TeV	(0,4) TeV
A_0	(-10,10) TeV	(-10,10) TeV
$\tan\beta$	(2,70)	(2,70)

9.5 MasterCode

El marco analítico de `MasterCode` realiza ajustes globales desde un punto de vista frecuentista. Contiene herramientas para calcular, dado un modelo de NP, diferentes observables y su correspondiente χ^2, así como la interfaz con un algoritmo (`MultiNest` [227]) para samplear dicho modelo. A partir de éstos se construye una función de probabilidad global, incluyendo las medidas experimentales. Dichas medidas se clasifican según la naturaleza del χ^2 que proporcionan en:

- Gaussianas. Ejemplos de ello son la masa del top, la masa del bosón de Higgs ligero, observables electrodébiles de precisión, observables de la física del sabor, etc.
- No Gaussianas, entre las que se incluyen la búsquedas de partículas supersimétricas realizadas por ATLAS y CMS.

9.5.1 CMSSM

El *constrained* MSSM (CMSSM) impone universalidad de las masas para una escala de gran unificación, $\Lambda \sim 2\times10^{16}$GeV. Consta de 5 parámetros libres: la masa de las partículas escalares, m_0, la masa de los gauginos (compañeros supersimétricos de los bosones gauge) $m_{1/2}$, el acoplo trilineal A_0, $\tan\beta$ y sign(μ).

Los rangos empleados en el scan se especifican en la Tabla 9.5. Como se puede ver, se ha realizado un scan específico para valores bajos de masa.

9.5.1.1 Resultados

Las proyecciones 2D de los resultados del scan se muestran en las Figuras 9.12 y 9.13 (realizadas usando `micrOMEGAs` [271]). Los contornos coloreados restringen regiones del espacio de parámetros correspondientes al 68% (rojo) y 95% (azul oscuro) CL. El punto con mejor valor del χ^2 (*best-fit point*, bfp) se indica con una estrella verde. Los diferentes colores en el interior de los contornos se corresponden con los mecanismos dominantes (indicados en la leyenda) para traer la densidad de materia oscura dentro del rango permitido por medidas experimentales. Tal y como se puede ver, el mecanismo preferido es la coaniquilación de charginos (partículas supersimétricas cargadas).

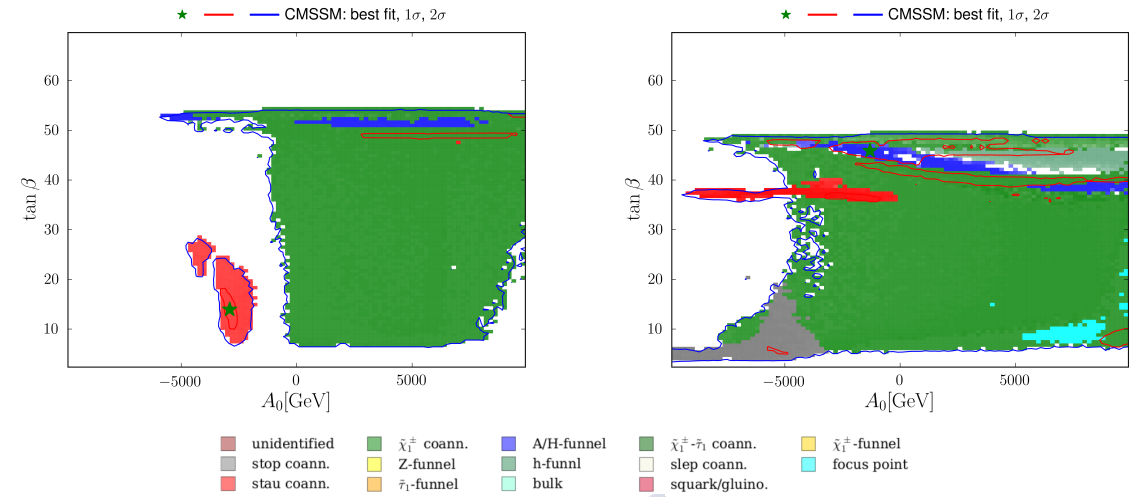

Figure 9.12: Los planos $(A_0, \tan\beta)$ para $\mu > 0$ (izquierda) y $\mu < 0$ (derecha). Los contornos rodean regiones permitidas a 68 y 95% CL, correspondiéndose aproximadamente con 1 y 2σ, respectivamente. Se considera que el neutralino es el responsable de toda la densidad de materia oscura fría. Los puntos con máxima verosimilitud se indican con estrellas verdes.

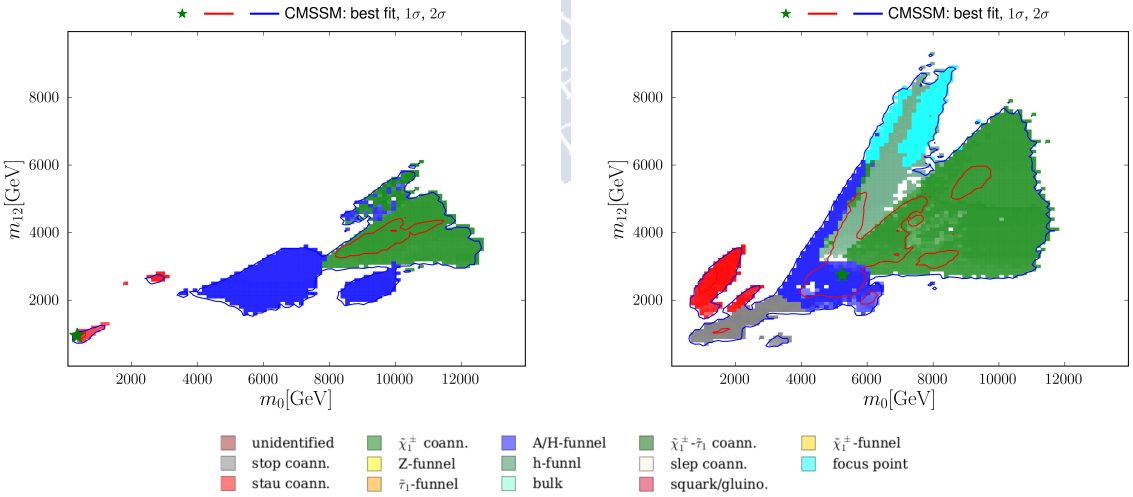

Figure 9.13: Los planos $(m_0, m_{1/2})$ para $\mu > 0$ (izquierda) y $\mu < 0$ (derecha). Los contornos rodean regiones permitidas a 68 y 95% CL, correspondiéndose aproximadamente con 1 y 2σ, respectivamente. Se considera que el neutralino es el responsable de toda la densidad de materia oscura fría. Los puntos con máxima verosimilitud se indican con estrellas verdes.

El perfil de la probabilidad para la masa del Higgs y $BR^{MSSM/SM}_{B_{s,d}\to\mu^+\mu^-}$ se muestran en la Figura 9.14. La preferencia de esta última de estar por encima o por debajo de 1 depende de signo de μ. Es el caso $\mu < 0$ el que parece proporcionar un mejor ajuste a los datos existentes. Ésto se muestra de acuerdo con otros resultados presentes en la literatura (véase Ref. [309]).

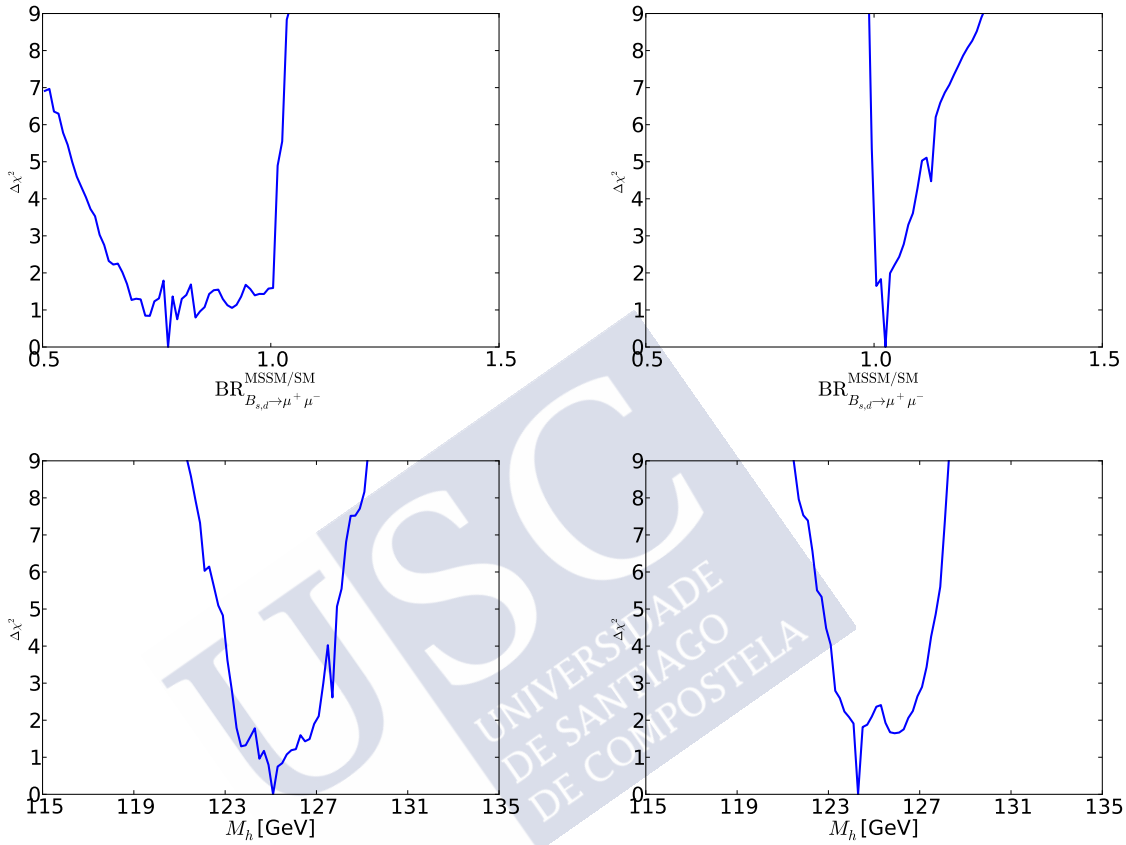

Figure 9.14: Parte superior: perfil unidimensional de la función de probabilidad para $BR^{MSSM/SM}_{B_{s,d}\to\mu^+\mu^-}$ para $\mu < 0$ (panel superior izquierda) and for $\mu > 0$ (panel superior derecha); parte inferior: perfil unidimensional de la función de probabilidad para M_h para $\mu < 0$ (panel inferior izquierda) y para $\mu > 0$ (panel inferior derecha).

Los espectros para los dos bfp se muestra en la Figura 9.15. En el caso $\mu > 0$ es mucho más pesado que en el caso $\mu < 0$. Extensiones de este trabajo abarcan la inclusión de nuevas medidas experimentales, así como la nueva versión de `SoftSUSY` [257] para obtener mejora en la predicción de las masas de las partículas supersimétricas.

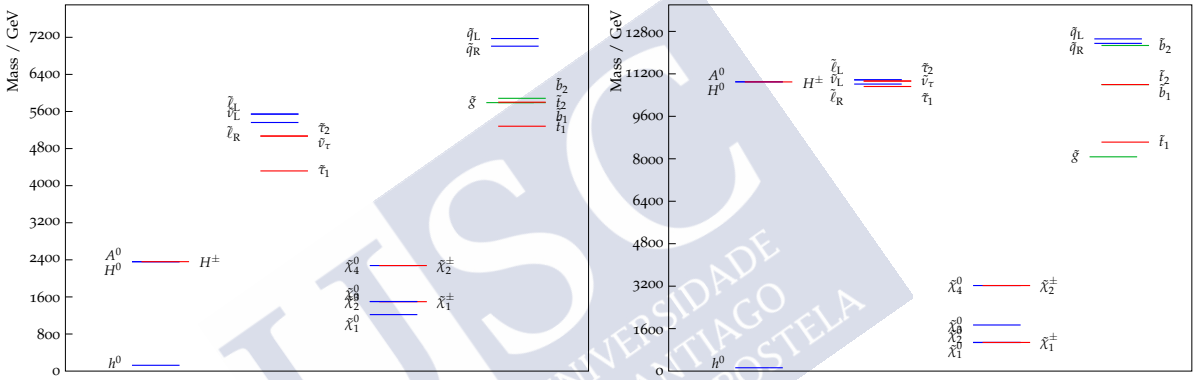

Figure 9.15: Espectros de los bosones de Higgs y las partículas supersimétricas en los bfp en CMSSM para $\mu < 0$ (izquierda) y $\mu > 0$ (derecha). Estos gráficos han sido realizados usando `PySLHA` [270].

9.5.2 mAMSB

En la *Minimal Anomaly Mediated SUSY Breaking* (mAMSB), la ruptura de supersimetría ocurre principalmente mediante una anomalía de súper-Weyl. Contiene 4 parámetros libres: un término que se añade como contribución de las masas escalares, m_0, $m_{3/2}$, $\tan\beta$ y sign(μ). El espectro de este modelo es muy diferente de otros modelos supersimétricos, con una composición diferente de la partícula supersimétrica candidata a Materia Oscura (LSP). En este escenario dicha partícula puede ser un wino o un Higgsino, ambos con una probabilidad similar.

Se consideran dos escenarios: uno en el que la LSP da cuenta de la mayor parte de la densidad de materia oscura fría, y otro en el que no. En el primero, la masa de las partículas supersimétricas se encuentra más allá del alcance del LHC, y sus contribuciones a otros observables son pequeñas. En el segundo caso, aunque la masa del Higgs aún representa una importante cota inferior, algunas búsquedas directas de partículas supersimétricas en el LHC pueden ser relevantes.

Los rangos empleados en el scan se especifican en la Tabla 9.6 Se ha realizado un scan específico para una Higgsino-LSP.

Table 9.6: Rangos de los parámetros empleados en el scan del modelo mAMSB.

Parameter	Rango
m_0	(0.1, 50) TeV
$m_{3/2}$	(10, 1500) TeV
$\tan\beta$	(1 , 50)

9.5.2.1 Resultados I. La LSP proporciona la mayor parte de la CDM (all-CDM)

La Figura 9.16 muestra los planos $(m_0, m_{3/2})$ para ambos signos de μ en este estudio. El código de colores para los contores de CL es similar al caso anterior, con una estrella verde indicando el bfp para un DM wino, y una estrella abierta vacía para indicar el bfp para un DM Higgsino. Las regiones donde la fracción de Higgsino excede el 90% aparecen coloreadas en amarillo. Aquellas donde la fracción de wino es superior al 90% aparecen coloreadas en azul, y las regiones mixtas en naranja. Tal y como se aprecia en la Figura, para una LSP wino las regiones favorecidas a nivel de 2σ son bandas donde 900 TeV $\leq$ m$_{3/2}$ $\leq$ 1000 TeV.

La Figura 9.17 muestra el espectro para los scans con wino y Higgsino (para ambos signos de μ). Tasas de desintegración superiores al 20% se indican con líneas discontinuas. Como se dijo al principio, se obtienen espectros relativamente pesados. Los espectros para el caso del Higgsino son en general más pesados que para el caso del wino.

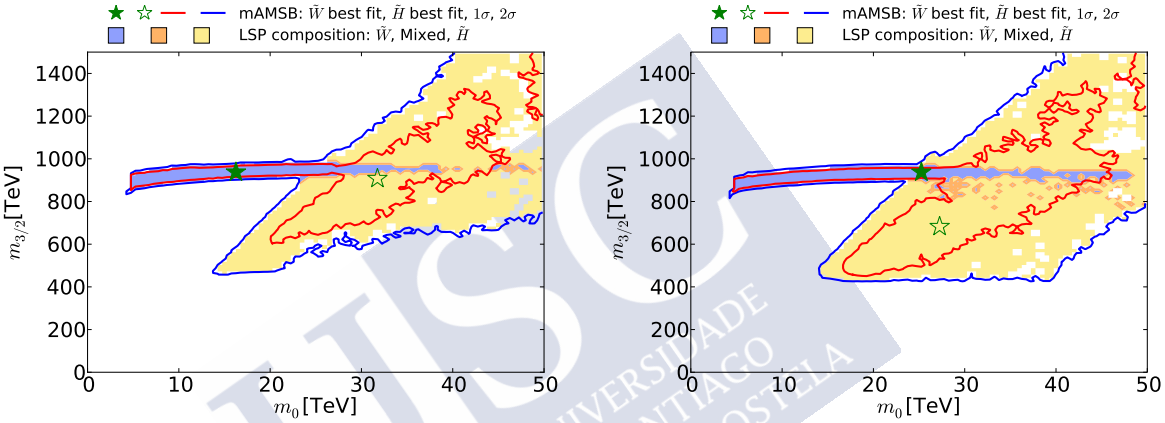

Figure 9.16: Planos $(m_0, m_{3/2})$ para $\mu > 0$ (panel izquierdo) y $\mu < 0$ (panel derecho). Los contornos azul y rojo rodean regiones que están permitidas a 68 y 95% CL, respectivamente. Las zonas de DM Higgsino (wino) están coloreadas en amarillo (azul), y las mixtas en naranja. Los bfp para los dos signos de μ etán indicados por estrellas verdes, rellenas en el caso wino y abiertas en el caso Higgsino.

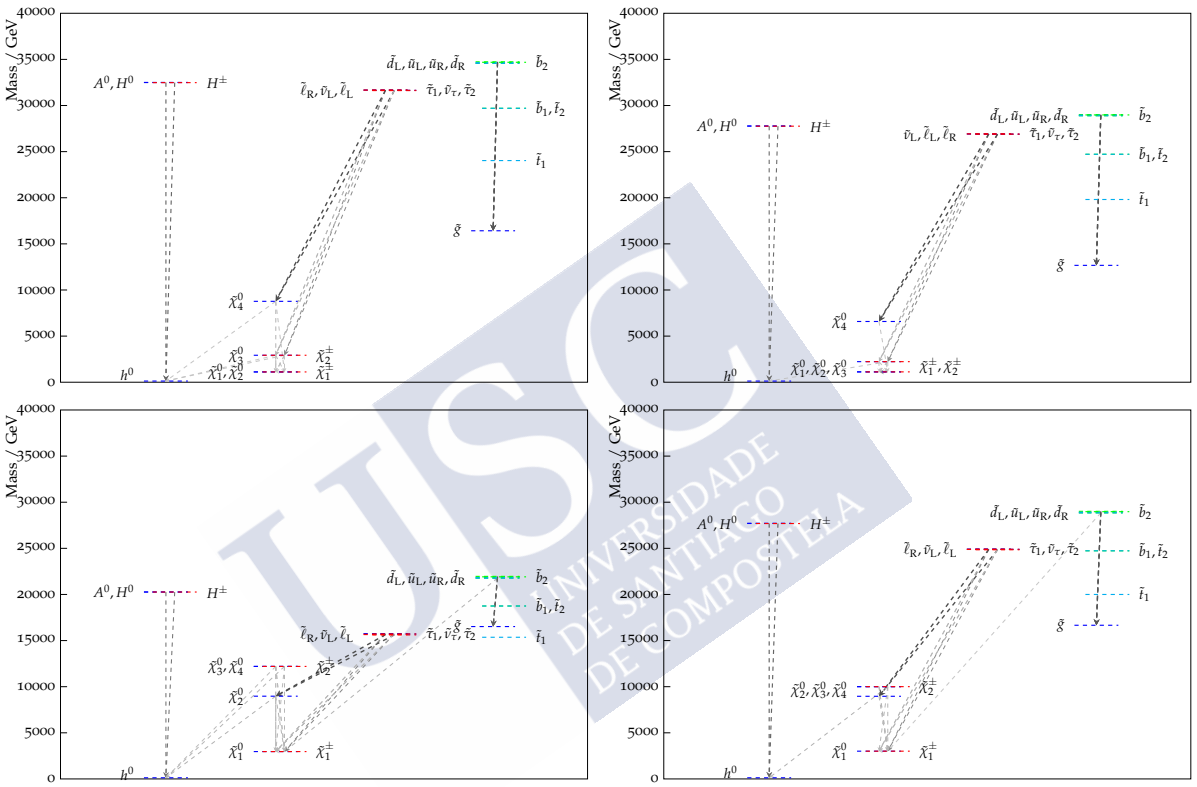

Figure 9.17: Espectros de los bfp para $\mu > 0$ (panel izquierdo) y $\mu < 0$ (panel derecho), asumiendo que la LSP realiza la contribución dominante a la CDM. Los colores de las barras horizontales indican las cargas eléctricas de las partículas.

9.5.3 Resultados II. La LSP no proporciona toda la CDM (part-CDM)

En este caso, tanto la masa de la LSP como $m_{3/2}$ pueden ser sustancialmente inferiores al caso anterior. Por lo tanto, algunas de las partículas supersimétricas pueden estar dentro del alcance del LHC, a diferencia de lo que ocurría en la sección 9.5.2.1.

Los planos correspondientes a $(m_0, m_{3/2})$ se muestran en la Figura 9.18. Tal y como se puede apreciar, la región del 95% CL para el wino se extiende a valores más bajos de $m_{3/2}$ para ambos signos de μ y para valores más altos de m_0 para $m_{3/2} \gtrsim 300$ para $\mu < 0$.

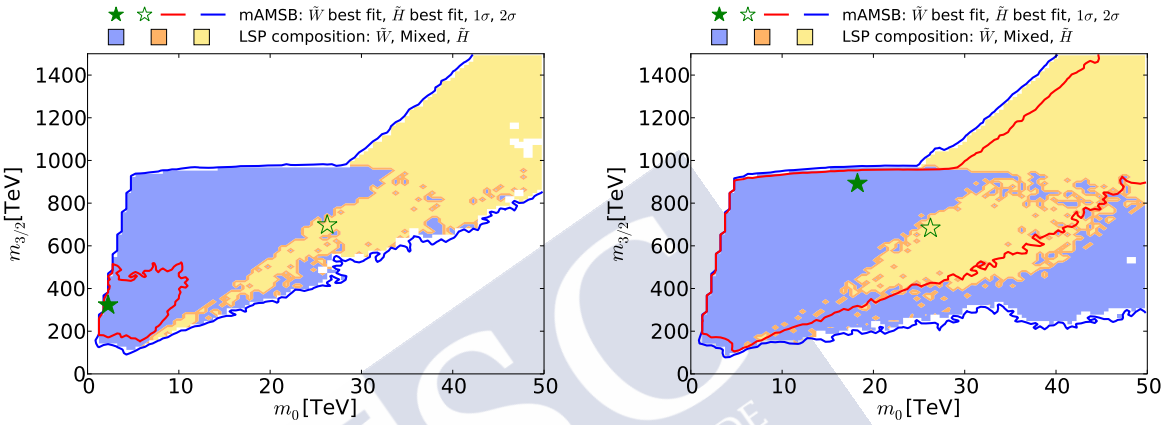

Figure 9.18: Los planos $(m_0, m_{3/2})$ para $\mu > 0$ (panel izquierdo) y para $\mu < 0$ (panel derecho). Los sombreados son los mismos que en la Figura 9.16.

La Figura 9.19 muestra el espectro para los scans con wino y Higgsino, con los dos signos de μ. Comparando los espectros se puede deducir que, mientras en el caso all-CDM las superpartículas eran demasiado pesadas para ser producidas en el LHC, en el caso part-CDM pueden ser mucho más ligeras, y por lo tanto accesibles al LHC.

El perfil de probabilidad para $BR^{MSSM/SM}_{B_{s,d}\to\mu^+\mu^-}$ y $(g-2)_\mu$ se muestra en la Figura 9.20. Se pueden observar pequeñas desviaciones con respecto al SM. En el caso part-CDM, dichas desviaciones se hacen más importantes, en particular para $\mu < 0$ en el caso de $BR(B_{s,d} \to \mu^+\mu^-)$.

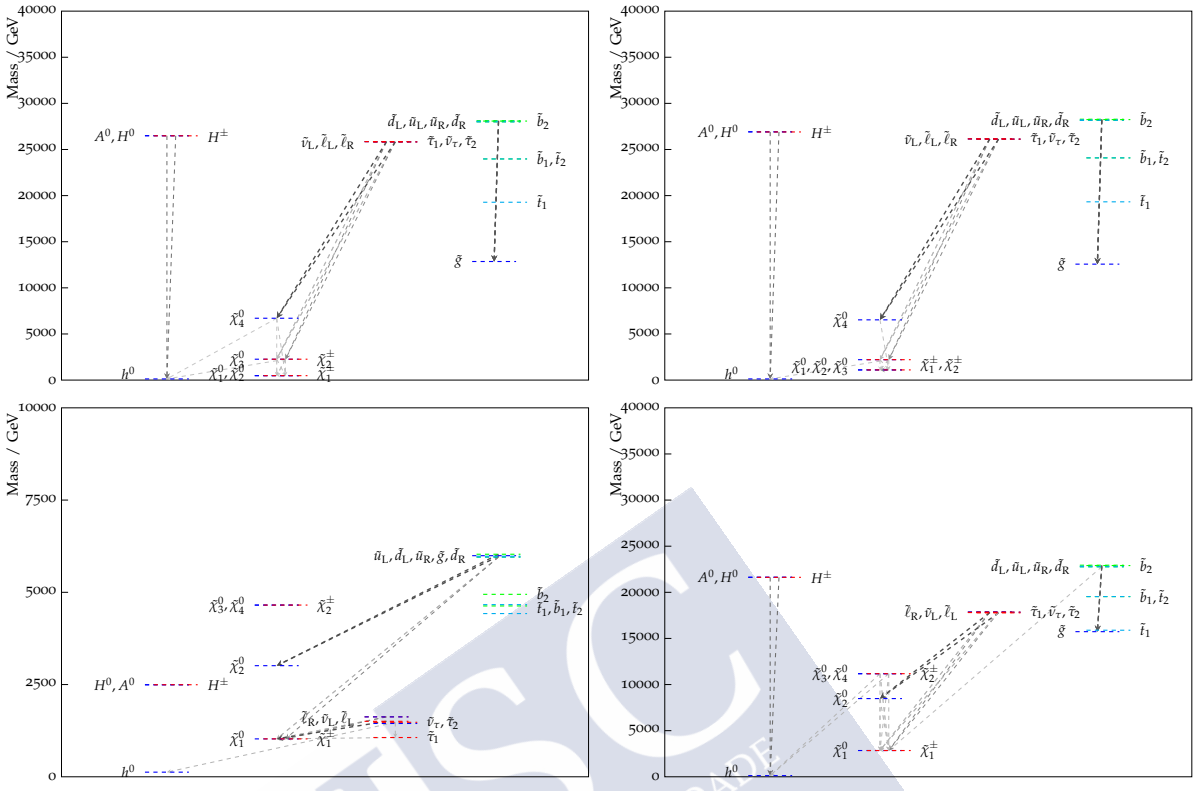

Figure 9.19: Espectros de los bfp para $\mu > 0$ (panel izquierdo) y $\mu < 0$ (panel derecho).

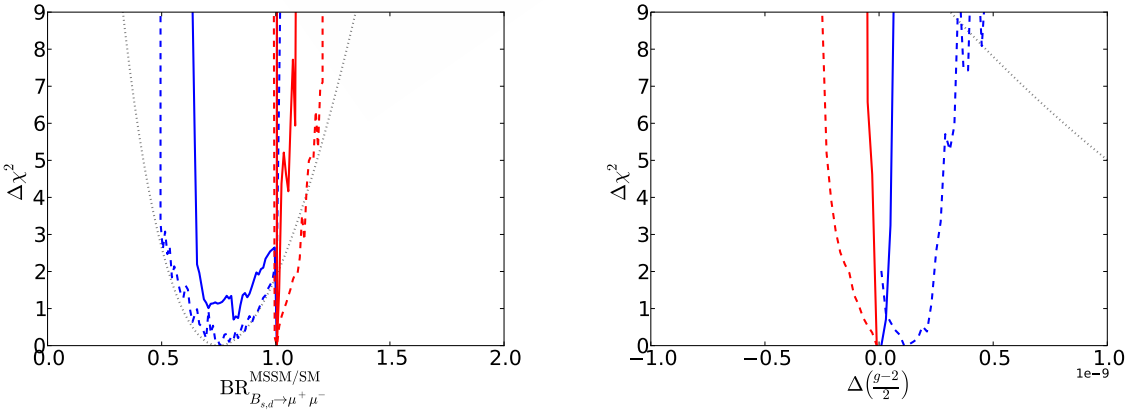

Figure 9.20: Espectros para los bfp para $\mu > 0$ (panel izquierdo) y $\mu < 0$ (panel derecho).

9.6 Conclusiones

Esta tesis representa un estudio exhaustivo de búsquedas de Nueva Física, tanto en el sector del sabor en LHCb, con estudios de sus implicaciones en física de kaones y en procesos involucrando la fase de violación CP ϕ_s, como en un ámbito más general, con estudios frecuentistas de dos modelos supersimétricos, realizados dentro del marco analítico `MasterCode`.

En el capítulo 5 se ha presentado un estudio de la sensibilidad de LHCb a $K_s^0 \to \pi^0\mu^+\mu^-$, usando una nueva estrategia, *PARTIAL*, donde tan sólo los muones se reconstruyen. Dicho estudio ha sido realizado usando 3 fb^{-1} de datos del Run 1 y 0.3 fb^{-1} de datos del Run 2. Predice una medida para el *Upgrade* con una precisión considerablemente mejor que la obtenida por el experimento NA48. El conocimiento preciso de $\mathcal{B}(K_S^0 \to \pi^0\mu^+\mu^-)$ permitirá una mejora en la predicción teórica de $\mathcal{B}(K_L^0 \to \pi^0\mu^+\mu^-)$, importante en modelos de Nueva Física como Dimensiones Extra.

Por otra parte, se ha llevado a cabo un estudio fenomenológico de $K_s^0 \to \mu^+\mu^-$, en un escenario MSSM, para valores elevados de tan β. Se han encontrado contribuciones a $\mathcal{B}(K_s^0 \to \mu^+\mu^-)$ que sobrepasan en un factor 7 las correspondientes al SM de acuerdo con las actuales limitaciones experimentales. También se ha mostrado la correlación entre éste y otros observables, así como regiones donde dicha tasa de desintegración se encuentra incluso a nivel de los existentes límites experimentales.

En cuanto a $\Delta F = 2$ se ha mostrado en el capítulo 6 un análisis de $B_s^0 \to J/\psi K^+K^-$ en la región de $m(K^+K^-)$ alrededor de la masa del mesón $\phi(1020)$, usando datos de LHCb recogidos en 2015 y 2016. De forma complementaria se han realizado estudios fenomenológicos para ϕ_s y ϕ_d, así como para otros observables tales como los Momentos Dipolares Electricos o la asimetría semileptónica, también en un escenario conforme al MSSM. El enfoque es análogo al seguido en el capítulo 5. Se han encontrado regiones con amplias variaciones con respecto a los valores del SM, de acuerdo con los cortes aplicados. También se ha apreciado el gran impacto que supone incluir el resultado de ϕ_s.

Finalmente, en el capítulo 7 se han expuesto los resultados de explorar las restricciones impuestas por los datos disponibles en el sector del sabor, electrodébil y del Higgs, así como búsquedas del LHC, en dos escenarios supersimétricos: el CMSSM y el mAMSB. Ambos han sido investigados empleando el marco analítico `MasterCode`. Para el CMSSM, se ha encontrado una gran área permitida por las restricciones experimentales. El caso con $\mu < 0$ representa un mejor ajuste a $BR^{\mathrm{MSSM/SM}}_{B_{s,d}\to\mu^+\mu^-}$ que $\mu > 0$. En cuanto a mAMSB, considerando que el neutralino proporciona toda la densidad CDM, el espectro que se obtiene es pesado. Masas más pequeñas son posibles si la LSP contribuye sólo a una fracción de la densidad CDM.

USC
UNIVERSIDADE
DE SANTIAGO
DE COMPOSTELA

Appendices

USC
UNIVERSIDADE
DE SANTIAGO
DE COMPOSTELA

Appendix A

$P \to l^+ l^-$

The effective Hamiltonian can be expressed as:

$$\mathcal{H}_{eff} = -\frac{G_F^2}{M_W^2}\pi^2[C_A Q_A + C'_A Q'_A + C_S Q_S + C'_S Q'_S + C_P Q_P + C'_P Q'_P] \tag{A.1}$$

where

$$\begin{aligned} Q_A &= \bar{d}^i_L \gamma^\mu d^j_L \bar{l}\gamma_\mu\gamma_5 l,\ Q'_A = \bar{d}^i_R \gamma^\mu d^j_R \bar{l}\gamma_\mu\gamma_5 l \\ Q_S &= \bar{d}^i_R d^j_L \bar{l}l,\ Q'_S = \bar{d}^i_L d^j_R \bar{l}l \\ Q_P &= \bar{d}^i_R d^j_L \bar{l}\gamma_5 l,\ Q'_P = \bar{d}^i_L d^j_R \bar{l}\gamma_5 l \end{aligned} \tag{A.2}$$

Being the axial and pseudoscalar currents:

$$\langle 0|\bar{q}^i \gamma_\mu\gamma_5 q^j|P\rangle = ip_\mu f_P \tag{A.3}$$

$$\langle 0|\bar{q}^i \gamma_5 q^j|P(p)\rangle = -if_P \frac{M_P^2}{(m_i + m_j)} \tag{A.4}$$

Computing the conjugate:

$$(\langle 0|\bar{q}^i \gamma_\mu\gamma_5 q^j|P\rangle)^\dagger = (ip_\mu f_P)^\dagger = -ip_\mu f_P \tag{A.5}$$

$$\begin{aligned} &\left\langle P|q^{\dagger j}\gamma_5\gamma^0\gamma_\mu\gamma_0\gamma_0 q^i|0\right\rangle = -\langle P|\bar{q}^j\gamma_5\gamma_\mu q^i|0\rangle \\ &= \langle p|\bar{q}^j\gamma_\mu\gamma_5 q^i|0\rangle = -ip_\mu f_P \end{aligned} \tag{A.6}$$

$$(\langle 0|\bar{q}^i \gamma_5 q^j|P(p)\rangle)^\dagger = if_P \frac{M_P^2}{(m_i + m_j)} \tag{A.7}$$

$$\begin{aligned} &\left\langle P|q^{\dagger j}\gamma_5\gamma^0 q^i|0\right\rangle = -\langle P|\bar{q}^j\gamma_5 q^i|0\rangle \\ &\langle P|\bar{q}^j\gamma_5 q^i|0\rangle = -if_P \frac{M_P^2}{(m_i + m_j)} \end{aligned} \tag{A.8}$$

To compute $\mathcal{B}(P \to l^+l^-)$:

$$\mathcal{B}(P \to l^+l^-) = \frac{\Gamma_{fi}}{\Gamma} = \tau_P \Gamma_{fi} \tag{A.9}$$

using the expression for a two-particle decay:

$$d\Gamma_{fi} = \frac{|A|^2}{32\pi^2}\frac{|p|}{M_P^2}d\Omega \tag{A.10}$$

where p is the l^{pm} momentum:

$$|p| = \sqrt{E_l^2 - m_l^2} = \sqrt{\frac{M_P^2}{4} - m_l^2} = \frac{M_P}{2}\sqrt{1 - \frac{4m_l^2}{M_P^2}} \tag{A.11}$$

and A is the amplitude of the process. Then:

$$d\Gamma_{fi} = \frac{|A|^2}{64\pi^2 M_P}\sqrt{1 - \frac{4m_l^2}{M_P^2}}d\Omega \tag{A.12}$$

$$\Gamma_{fi} = \frac{|A|^2}{16\pi M_P}\sqrt{1 - \frac{4m_l^2}{M_P^2}} \tag{A.13}$$

Therefore:

$$\mathcal{B}(P \to l^+l^-) = \frac{\tau_P}{16\pi M_P}\sqrt{1 - \frac{4m_l^2}{M_P^2}}|A|^2 \tag{A.14}$$

The amplitude:

$$\begin{aligned} &|A|^2 = |\left\langle l^+l^-|\mathcal{H}_{eff}|P\right\rangle|^2 = AA^\dagger \\ &A = \left\langle l^+l^-|\mathcal{H}_{eff}|P\right\rangle \\ &A^\dagger = (\left\langle l^+l^-|\mathcal{H}_{eff}|P\right\rangle)^\dagger = \left\langle P|\mathcal{H}_{e}ff^\dagger|l^+l^-\right\rangle = \left\langle P|\mathcal{H}_{e}ff|l^+l^-\right\rangle \end{aligned} \tag{A.15}$$

Where it has been used the fact that the effective Hamiltonian is hermitic ($\mathcal{H}_{eff} = \mathcal{H}_{eff}^\dagger$) and l is the lepton field, hence a solution of the Dirac equation. Decomposing the Hamiltonian into the different terms:

$$A = [\left\langle l^+l^-|C_AQ_A|P\right\rangle + \left\langle l^+l^-|C'_AQ'_A|P\right\rangle + ...]\left(-\frac{G_F^2M_W^2}{\pi^2}\right) \tag{A.16}$$

$$A^\dagger = -\left(\frac{G_F^2M_W^2}{\pi^2}\right)[\left\langle P|C_A^\dagger Q_A^\dagger|l^+l^-\right\rangle + \left\langle P|C_A'^\dagger Q_A'^\dagger|l^+l^-\right\rangle + ...] \tag{A.17}$$

Using again the hermiticity of the Hamiltonian:

$$C_AQ_A + C'_AQ'_A + ... = C_A^\dagger Q_A^\dagger + C_A'^\dagger Q_A'^\dagger ... \tag{A.18}$$

Then:

$$\left\langle P|C_A^\dagger Q_A^\dagger|l^+l^-\right\rangle + ... = \left\langle l^+l^-|C_AQ_A|P\right\rangle + ... \tag{A.19}$$

$$A^\dagger = -\frac{G_F^2 M_W^2}{\pi^2}[\langle P|C_A Q_A|l^+l^-\rangle + \langle P|C'_A Q'_A|l^+l^-\rangle + ...] \tag{A.20}$$

Being the projection operators:

$$\begin{aligned} p_\pm &= \frac{1}{2}(1 \pm \gamma_5),\ p_\pm^2 = p_\pm \\ d_R &= \frac{1}{2}(1+\gamma_5)d,\ d_L = \frac{1}{2}(1-\gamma_5)d \\ \bar{d}_R &= \bar{d}\frac{1}{2}(1-\gamma_5),\ \bar{d}_L = \bar{d}\frac{1}{2}(1+\gamma_5) \end{aligned} \tag{A.21}$$

and the properties of the gamma matrices:

$$\begin{aligned} &(\gamma^0)^\dagger = \gamma^0,\ \{\gamma_5, \gamma^\mu\} = 0,\ (\gamma_5)^\dagger = \gamma_5 \\ &(\gamma^\mu)^\dagger = \gamma^0\gamma^\mu\gamma^0,\ \{\gamma^\mu, \gamma^\nu\} = 2g^{\mu\nu},\ (\gamma_5)^2 = 1 \end{aligned} \tag{A.22}$$

Computing now the different components of $A^\dagger$:

$$\begin{aligned} &\langle P|C_A Q_A|l^+l^-\rangle = C_A \left\langle P|(\bar{d}^i\gamma^\mu d^j \frac{1}{2} - \frac{1}{2}\bar{d}^i\gamma^\mu\gamma_5 d^j)(l\gamma_\mu\gamma_5 l)|l^+l^-\right\rangle \\ &= C_A \left\langle P|(-\frac{1}{2}\bar{d}^i\gamma^\mu\gamma_5 d^j)|0\right\rangle \langle 0|\bar{l}\gamma_\mu\gamma_5 l|\rangle \\ &= \frac{C_A}{2} i f_P p^\mu \langle 0|\bar{l}\gamma_\mu\gamma_5 l|l^+l^-\rangle \\ &= -C_A i f_P m_l \langle 0|\bar{l}\gamma_5 l|l^+l^-\rangle \end{aligned} \tag{A.23}$$

$$\begin{aligned} \langle P|C_P Q_P|l^+l^-\rangle &= \left\langle P|\bar{d}_R^i d_L^j \bar{l}\gamma_5 l|l^+l^-\right\rangle \\ &= \left\langle P|\bar{d}^i \frac{1}{2}(1-\gamma_5)d^j|0\right\rangle \langle 0|\bar{l}\gamma_5 l|l^+l^-\rangle \\ &= \left\langle P|\bar{d}^i \frac{1}{2}(1-\gamma_5)d^j|0\right\rangle \langle 0|\bar{l}\gamma_5 l|l^+l^-\rangle \\ &= -\frac{1}{2}\langle P|\bar{d}^i\gamma_5 d^j|0\rangle \langle 0|\bar{l}\gamma_5 l|l^+l^-\rangle \\ &= -\frac{1}{2}\left(-i f_P \frac{M_P^2}{m_i + m_j}\right)\langle 0|\bar{l}\gamma_5 l|l^+l^-\rangle \\ &= \frac{i}{2} f_P \frac{M_P^2}{m_i + m_j}\langle 0|\bar{l}\gamma_5 l|l^+l^-\rangle \end{aligned} \tag{A.24}$$

Then:

$$\langle P|C_A Q_A + C_P Q_P|l^+l^-\rangle = i f_P \langle 0|\bar{l}\gamma_5 l|l^+l^-\rangle \left[\frac{M_P^2}{2(m_i+m_j)}C_P - m_l C_A\right] \tag{A.25}$$

$$\begin{aligned}
&\left\langle P|Q'_A C'_A|l^+l^-\right\rangle = C'_A \left\langle p|\bar{d}^i_R \gamma^\mu d^j_R \bar{l}\gamma_\mu\gamma_5 l|l^+l^-\right\rangle \\
&= C'_A \left\langle P|\bar{d}^i \frac{1}{2}(1-\gamma_5)\gamma^\mu \frac{1}{2}(1+\gamma_5) d^j|0\right\rangle \left\langle 0|\bar{l}\gamma_\mu\gamma_5 l|l^+l^-\right\rangle \\
&= C'_A \left\langle P|\bar{d}^i \gamma^\mu \frac{1}{2}(1+\gamma_5) d^j|0\right\rangle \left\langle 0|\bar{l}\gamma_\mu\gamma_5 l|l^+l^-\right\rangle \\
&= \frac{C'_A}{2} \left\langle P|\bar{d}^i \gamma^\mu\gamma_5 d^j|0\right\rangle \left\langle 0|\bar{l}\gamma_\mu\gamma_5 l|l^+l^-\right\rangle \\
&= -\frac{C'_A}{2} i p^\mu f_P \left\langle 0|\bar{l}\gamma_\mu\gamma_5 l|l^+l^-\right\rangle
\end{aligned} \tag{A.26}$$

where:

$$p^\mu = p^\mu_l + p^\mu_{\bar{l}} \tag{A.27}$$

taking into account the incoming leptons ($\bar{l} = \bar{v}, l = u$), then:

$$(p^\mu_l + p^\mu_{\bar{l}})\bar{v}\gamma_\mu\gamma_5 u = -\bar{v}\gamma_5 \not{p}^\mu_l + \bar{v} \not{p}_{\bar{l}}\gamma_5 u = -2m_l \bar{v}\gamma_5 u = -2m_l \bar{l}\gamma_5 l \tag{A.28}$$

hence:

$$\left\langle P|Q'_A C'_A|l^+l^-\right\rangle = C'_A i f_P m_l \left\langle 0|\bar{l}\gamma_5 l|P\right\rangle \tag{A.29}$$

$$\begin{aligned}
&\left\langle P|Q'_P C'_P|l^+l^-\right\rangle = \left\langle P|\bar{d}^i \frac{1}{2}(1+\gamma_5)\frac{1}{2} d^j|0\right\rangle \left\langle 0|\bar{l}\gamma_5 l\right\rangle \\
&= \frac{C'_P}{2} \left\langle P|\bar{d}^i \gamma_5 d^j|0\right\rangle \left\langle 0|\bar{l}\gamma_5 l|l^+l^-\right\rangle \\
&= -C'_P i f_P \frac{M_P^2}{2(m_i+m_j)} \left\langle 0|\bar{l}\gamma_5 l|l^+l^-\right\rangle
\end{aligned} \tag{A.30}$$

$$\left\langle P|Q'_P C'_P|l^+l^-\right\rangle = -C'_P i f_P \frac{M_P^2}{2(m_i+m_j)} \left\langle 0|\bar{l}\gamma_5 l|l^+l^-\right\rangle \tag{A.31}$$

The calculation for $C_S Q_S$ and $C'_S Q'_S$ is the same as for $C_P Q_P$ and $C'_P Q'_P$ but with $\left\langle 0|\bar{l}l|l^+l^-\right\rangle$, therefore:

$$\left\langle P|Q_S C_S|l^+l^-\right\rangle = C_S i f_P \frac{M_P^2}{2(m_i+m_j)} \left\langle 0|\bar{l}l|l^+l^-\right\rangle \tag{A.32}$$

$$\left\langle P|Q'_S C'_S|l^+l^-\right\rangle = -C'_S i f_P \frac{M_P^2}{2(m_i+m_j)} \left\langle 0|\bar{l}l|l^+l^-\right\rangle \tag{A.33}$$

Putting everything together:

$$\begin{aligned}
&\left\langle P|\mathcal{H}_{eff}|l^+l^-\right\rangle = -\frac{G_F^2 M_W^2}{\pi^2}[i f_P m_l \left\langle 0|\bar{l}\gamma_5 l|l^+l^-\right\rangle (C'_A - C_A) \\
&+ i f_P \frac{M_P^2}{2(m_i+m_j)} \left\langle 0|\bar{l}\gamma_5 l|l^+l^-\right\rangle (C'_P - C_P) \\
&+ i f_P \frac{M_P^2}{2(m_i+m_j)} \left\langle 0|\bar{l}l|l^+l^-\right\rangle (C'_S - C_S)]
\end{aligned} \tag{A.34}$$

Note that $\langle 0|\bar{l}l|l^+l^-\rangle$ is actually $\langle 0|\bar{l}|l^+\rangle \langle 0|l|l^-\rangle$, where $|l^-\rangle = |p,s\rangle$ $|l^+\rangle = |q,r\rangle$. The creation and anihilation operators are, for fermions:

$$\sqrt{2E_p}a_p^\dagger |0\rangle = |p,s\rangle \tag{A.35}$$

and for antifermions:

$$\sqrt{2E_p}b_q^\dagger |0\rangle = |q,r\rangle \tag{A.36}$$

where $\left\{a_p, a_{p'}^\dagger\right\} = (2\pi)^3\delta^{(3)}(\overrightarrow{p} - \overrightarrow{p'})$ and the leptonic fields:

$$l(x) = \int \frac{d^3p}{(2\pi)^3}\frac{1}{\sqrt{2E_p}}\sum_s (a_p^s u^s(p)e^{-ipx} + (b_p^s)^\dagger v^s(p)e^{ipx}) \tag{A.37}$$

$$\bar{l}(x) = \int \frac{d^3q}{(2\pi)^3}\frac{1}{\sqrt{2E_q}}\sum_s (b_q^r \bar{v}^r(q)e^{iqx} + (a_q^r)^\dagger \bar{u}^r(q)e^{iqx}) \tag{A.38}$$

Considering that:

$$\begin{aligned} a_q^\dagger b_q^\dagger |0\rangle = a_q^\dagger |l^+\rangle = 0 \\ b_p^\dagger a_p^\dagger |0\rangle = b_p^\dagger |l^-\rangle = 0 \end{aligned} \tag{A.39}$$

then:

$$\begin{aligned} \langle 0|l|l^-\rangle &= \left\langle 0| \int \frac{d^3p'}{(2\pi)^3}\sum_s (a_{p'}^{s'}u^{s'}(p')e^{-ip'x}\sqrt{2E_p}a_p^{s\dagger})|0 \right\rangle \\ &= \sum_s \langle 0|e^{-ipx}u^s(p)\rangle \end{aligned} \tag{A.40}$$

and

$$\langle 0|\bar{l}|l^+\rangle = \sum_r \langle 0|e^{-iqx}\bar{v}^r(q)|0\rangle \tag{A.41}$$

Due to momentum conservation $q = -p$:

$$\langle 0|\bar{l}l|l^+l^-\rangle = \langle 0|e^{ipx}e^{-ipx}\bar{v}^r u^s|0\rangle = \sum_{r,s}\bar{v}^r(q)u^s(p) \tag{A.42}$$

$$\langle 0|\bar{l}l|l^+l^-\rangle = \sum_{r,s}\bar{v}^r(q)u^s(p) \tag{A.43}$$

With γ_5:

$$\langle 0|\bar{l}\gamma_2 l|l^+l^-\rangle = \sum_{s,r}\bar{v}^r(q)\gamma_5 u^s(p) \tag{A.44}$$

In order to compute the amplitude squared, terms like $|\langle 0|\bar{l}l|l^+l^-\rangle|^2$, $|\langle 0|\bar{l}\gamma_5 l|l^+l^-\rangle|^2$, $\langle 0|\bar{l}l|l^+l^-\rangle(\langle 0|\bar{l}\gamma_5 l|l^+l^-\rangle)^\dagger$ and $\langle 0|\bar{l}\gamma - 5l|l^+l^-\rangle(\langle 0|\bar{l}l|l^+l^-\rangle)^\dagger$ are bound to appear. Therefore, the trace formalism will have to be used:

$$|\langle 0|\bar{l}l|l^+l^-\rangle|^2 = \sum_{r,s}\bar{v}_a^r(q)u_a^s(p)\bar{u}_b^s(p)v_b^r(q) \tag{A.45}$$

where the following completeness relations hold:

$$\sum_s u_a^s(p)\bar{u}_b^s(p) = (\not{p} + m)_{ab} \tag{A.46}$$

$$\sum_r v_b^r(q)\bar{v}_a^r(q) = (\not{q} - m)_{ba} \tag{A.47}$$

Therefore:

$$\begin{aligned} |\left\langle 0|\bar{l}l|l^+l^-\right\rangle|^2 &= (\not{p} + m)_{ab}(\not{q} - m)_{ba} = tr[(\not{p} + m)(\not{q} - m)] \\ &= tr[(\gamma^\mu p_\mu + m)(\gamma^\nu q_\nu - m)] = tr[\gamma^\mu p_\mu \gamma^\nu q_\nu - \gamma^\mu p_\mu m + \\ & m\gamma^\nu q_\nu - m^2] = p_\mu q_\nu tr(\gamma^\mu\gamma^\nu) - m p_\mu tr(\gamma^\mu) + m q_\nu tr(\gamma^\nu) \\ & - m^2 tr(\mathbb{I}) \end{aligned} \tag{A.48}$$

Considering the properties of the traces:

$$tr(\mathbb{I}) = 4 \tag{A.49}$$

$$tr(\gamma^\mu) = 0 \tag{A.50}$$

where the former applies for any odd combination of gamma matrices

$$tr(\gamma^\mu\gamma^\nu) = 4g^{\mu\nu} \tag{A.51}$$

$$tr(\gamma_5) = 0 \tag{A.52}$$

Then:

$$|\left\langle 0|\bar{l}l|l^+l^-\right\rangle|^2 = p_\mu q_\nu 4g^{\mu\nu} - 4m^2 = 4(p_\mu q^\mu - m^2) \tag{A.53}$$

using:

$$p_\mu = (E_p, \overrightarrow{p}),\ q_\mu = (E_q, \overrightarrow{q} = (E_p, -\overrightarrow{p}) \tag{A.54}$$

and the used metric:

$$g^{\mu\nu} = \text{diag}(1, -1, -1, -1) \tag{A.55}$$

$$p_\mu q^\mu = E_p^2 + |\overrightarrow{p}|^2 = E_p^2 + (\sqrt{E_p^2 - m_l^2})^2 = 2E_p^2 - m_l^2 \tag{A.56}$$

Therefore:

$$|\left\langle 0|\bar{l}l|l^+l^-\right\rangle|^2 = 8(E_p^2 - m_l^2) \tag{A.57}$$

where

$$E_p = \frac{M_P}{2} \tag{A.58}$$

hence

$$|\left\langle 0|\bar{l}l|l^+l^-\right\rangle|^2 = 2M_P\left(1 - \frac{4m_l^2}{M_P^2}\right) \tag{A.59}$$

$$
\begin{aligned}
&|\left\langle 0|\bar{l}\gamma_5 l|l^+l^-\right\rangle|^2 = \sum_{r,s}[\bar{v}_a(q)\gamma_{5,ab}u_b^s(p)][\bar{u}_c^s(p)\gamma_{5,cd}v_d^r(q)](-1)\\
&= -\sum_r \bar{v}_a^r(q)\gamma_{5,ab}(\not{p}+m)_{bc}\gamma_{5,cd}v_d^r = -\gamma_{5,ab}(\not{p}+m)_{bc}\gamma_{5,cd}(\not{q}-m)_{da}\\
&= -tr[\gamma_5(\gamma^\mu p_\mu + m\gamma_5(\gamma^\nu q_\nu - m)] = -tr[(\gamma_5\gamma^\mu p_\mu + \gamma_5 m)\\
&(\gamma_5\gamma^\nu q_\nu - \gamma_5 m)] = -tr[\gamma_5\gamma^\mu p_\mu\gamma_5\gamma^\nu q_\nu\\
&- \gamma_5\gamma^\mu p_\mu\gamma_5 m + \gamma_5 m\gamma_5\gamma^\nu q_\nu - \gamma_5 m\gamma_5 m]\\
&= p_\mu q_\nu 4g^{\mu\nu} + 4m^2 = 4(p_\mu q^\nu + m^2) = 8\frac{M_P^2}{4} = 2M_P^2
\end{aligned}
\tag{A.60}
$$

$$
\begin{aligned}
&\left\langle 0|\bar{l}l|l^+l^-\right\rangle\left(\left\langle 0|\bar{l}\gamma_5 l|l^+l^-\right\rangle\right)^\dagger\\
&= \sum_{s,r}[\bar{v}_a^r(q)u_a^s(p)](-1)[\bar{u}_b^s(p)\gamma_{5,bc}v_c^r(q)] = -(\not{p}+m)_{ab}\gamma_{5,bc}(\not{q}-m)_{ca}\\
&= -tr[(\gamma^\mu p_\mu + m)\gamma_5(\gamma^\nu q_\nu - m)] = -tr[\gamma^\mu p_\mu\gamma^5\gamma^\nu q_\nu\\
&- \gamma^\mu p_\mu\gamma_m + m\gamma_5\gamma^\nu q_\nu - m^2\gamma_5]
\end{aligned}
\tag{A.61}
$$

where

$$tr(\gamma^\mu\gamma^5) = itr(\gamma^\mu\gamma^0\gamma^1\gamma^2\gamma^3) = 0 \tag{A.62}$$

$$tr(\gamma^\mu\gamma^\nu\gamma_5) = 0 \tag{A.63}$$

therefore:

$$\left\langle 0|\bar{l}l|l^+l^-\right\rangle\left(\left\langle 0|\bar{l}\gamma_5 l|l^+l^-\right\rangle\right)^\dagger = 0 \tag{A.64}$$

Similarly:

$$
\begin{aligned}
&\left\langle 0|\bar{l}\gamma_5 l|l^+l^-\right\rangle\left(\left\langle 0|\bar{l}l|l^+l^-\right\rangle\right)^\dagger\\
&\sum_{s,r}[\bar{v}_a^r(q)\gamma_{5,ab}u_b^s(p)][\bar{u}_c^s(p)v_c^r(q)] = \gamma_{5,ab}(\not{p}+m)_{bc}(\not{q}-m)_{ca}
\end{aligned}
\tag{A.65}
$$

where:

$$tr[\gamma_5(\gamma^\mu p_\mu + m)(\gamma^\nu q_\nu - m)] = 0 \tag{A.66}$$

obtaining:

$$\left\langle 0|\bar{l}\gamma_5 l|l^+l^-\right\rangle\left(\left\langle 0|\bar{l}l|l^+l^-\right\rangle\right)^\dagger = 0 \tag{A.67}$$

Computing the amplitude squared $|A|^2$:

$$|A|^2 = \frac{G_F^4 M_W^4}{\pi^4} f_P^4 m_l \left[2M_P^2(1 - \frac{4m_l^2}{M_P^2}\left|\frac{M_P^2(C_S - C_S')}{2m_l(m_i+m_j)}\right|^2 + 2M_P^2\left|\frac{M_P^2(C_P - C_P')}{2m_l(m_i+m_j)} - C_A + C_A'\right|^2\right] \tag{A.68}$$

Substituting inside the branching fraction:

$$
\begin{aligned}
&\mathcal{B}(P\to l^+l^-) = \frac{G_F^4 M_W^4}{8\pi^5} f_P^2 M_P \tau_P m_l^2\sqrt{1-\frac{4m_l^2}{M_P^2}}\times\\
&\left[\left(1-\frac{4m_l^2}{M_P^2}\right)\left|\frac{M_P^2(C_S - C_S')}{2m_l(m_i+m_j)}\right|^2 + \left|\frac{M_P^2(C_P - C_P')}{2m_l(m_i+m_j)}\right|^2\right]
\end{aligned}
\tag{A.69}
$$

USC
UNIVERSIDADE
DE SANTIAGO
DE COMPOSTELA

Appendix B

$K_S^0 \to \mu^+\mu^-$

B.1 Wilson coefficients ($K_S^0 \to \mu^+\mu^-$)

B.1.1 $|\Delta S| = 1$ gluino box contribution

The Wilson coefficients of the gluino box contributions to $\varepsilon'_K/\varepsilon_K$ are

$$
\begin{aligned}
C_1^q &= \frac{(\alpha_s)^2}{2\sqrt{2}G_F M_3^2}\left(\delta_d^{LL}\right)_{12}\left[\frac{1}{18}f\left(x_3^Q, x_3^q\right) - \frac{5}{18}g\left(x_3^Q, x_3^q\right)\right], \\
C_2^q &= \frac{(\alpha_s)^2}{2\sqrt{2}G_F M_3^2}\left(\delta_d^{LL}\right)_{12}\left[\frac{7}{6}f\left(x_3^Q, x_3^q\right) + \frac{1}{6}g\left(x_3^Q, x_3^q\right)\right], \\
C_3^q &= \frac{(\alpha_s)^2}{2\sqrt{2}G_F M_3^2}\left(\delta_d^{LL}\right)_{12}\left[-\frac{5}{9}f\left(x_3^Q, x_3^Q\right) + \frac{1}{36}g\left(x_3^Q, x_3^Q\right)\right], \\
C_4^q &= \frac{(\alpha_s)^2}{2\sqrt{2}G_F M_3^2}\left(\delta_d^{LL}\right)_{12}\left[\frac{1}{3}f\left(x_3^Q, x_3^Q\right) + \frac{7}{12}g\left(x_3^Q, x_3^Q\right)\right], \\
\tilde{C}_1^q &= \frac{(\alpha_s)^2}{2\sqrt{2}G_F M_3^2}\left(\delta_d^{RR}\right)_{12}\left[\frac{1}{18}f\left(x_3^d, x_3^Q\right) - \frac{5}{18}g\left(x_3^d, x_3^Q\right)\right], \\
\tilde{C}_2^q &= \frac{(\alpha_s)^2}{2\sqrt{2}G_F M_3^2}\left(\delta_d^{RR}\right)_{12}\left[\frac{7}{6}f\left(x_3^d, x_3^Q\right) + \frac{1}{6}g\left(x_3^d, x_3^Q\right)\right], \\
\tilde{C}_3^q &= \frac{(\alpha_s)^2}{2\sqrt{2}G_F M_3^2}\left(\delta_d^{RR}\right)_{12}\left[-\frac{5}{9}f\left(x_3^d, x_3^q\right) + \frac{1}{36}g\left(x_3^d, x_3^q\right)\right], \\
\tilde{C}_4^q &= \frac{(\alpha_s)^2}{2\sqrt{2}G_F M_3^2}\left(\delta_d^{RR}\right)_{12}\left[\frac{1}{3}f\left(x_3^d, x_3^q\right) + \frac{7}{12}g\left(x_3^d, x_3^q\right)\right],
\end{aligned}
\tag{B.1}
$$

where q runs u and d, and $x_3^Q = \tilde{m}_Q^2/M_3^2$ and $x_3^q = \tilde{m}_q^2/M_3^2$.

B.1.2 $|\Delta S| = 1$ chargino-mediated Z-penguin contribution

The Wilson coefficients of the chargino-mediated Z-penguin are

$$
\begin{aligned}
C_1^u &= -\frac{(\alpha_2)^2 \sin^2\theta_W}{12\sqrt{2}G_F M_W^2} \frac{\left[(\mathcal{M}_U^2)_{LR}\right]_{23}^* \left[(\mathcal{M}_U^2)_{LR}\right]_{13}}{M_2^4} l\left(x_2^Q, x_2^u\right), \\
C_1^d &= \frac{(\alpha_2)^2 \sin^2\theta_W}{24\sqrt{2}G_F M_W^2} \frac{\left[(\mathcal{M}_U^2)_{LR}\right]_{23}^* \left[(\mathcal{M}_U^2)_{LR}\right]_{13}}{M_2^4} l\left(x_2^Q, x_2^u\right), \\
C_3^u &= \frac{(\alpha_2)^2}{16\sqrt{2}G_F M_W^2}\left(1 - \frac{4}{3}\sin^2\theta_W\right) \frac{\left[(\mathcal{M}_U^2)_{LR}\right]_{23}^* \left[(\mathcal{M}_U^2)_{LR}\right]_{13}}{M_2^4} l\left(x_2^Q, x_2^u\right), \\
C_3^d &= -\frac{(\alpha_2)^2}{16\sqrt{2}G_F M_W^2}\left(1 - \frac{2}{3}\sin^2\theta_W\right) \frac{\left[(\mathcal{M}_U^2)_{LR}\right]_{23}^* \left[(\mathcal{M}_U^2)_{LR}\right]_{13}}{M_2^4} l\left(x_2^Q, x_2^u\right), \\
C_{2,4}^q &= \tilde{C}_{1,2,3,4}^q = 0.
\end{aligned} \tag{B.2}
$$

B.1.3 $|\Delta S| = 1$ chromomagnetic dipole contribution

The Wilson coefficients of the chromomagnetic dipole contributions to $\varepsilon'_K/\varepsilon_K$ are

$$
\begin{aligned}
C_g^- = &\frac{\alpha_s \pi}{3} \frac{\tilde{m}_Q^2 \mu m_s}{M_3^5} \left(\delta_d^{LL}\right)_{12} \frac{\tan\beta}{1+\epsilon_g \tan\beta}\left[I\left(x_3^Q, x_3^d\right) + 9J\left(x_3^Q, x_3^d\right)\right] \\
&- \frac{\alpha_s \pi}{3} \frac{\tilde{m}_d^2 \mu m_s}{M_3^5} \left(\delta_d^{RR}\right)_{12} \frac{\tan\beta}{1+\epsilon_g \tan\beta}\left[I\left(x_3^d, x_3^Q\right) + 9J\left(x_3^d, x_3^Q\right)\right] \\
&+ \frac{\alpha_s \pi}{3} \frac{\left[(\mathcal{M}_D^2)_{LR}\right]_{12} - \left[(\mathcal{M}_D^2)_{LR}\right]_{21}^*}{M_3^3}\left[K\left(x_3^Q, x_3^d\right) + 9L\left(x_3^Q, x_3^d\right)\right] \\
&- \frac{\alpha_s \pi}{3} \frac{m_s}{\tilde{m}_Q^2} \left(\delta_d^{LL}\right)_{12}\left[M_3\left(x_Q^3\right) + 9M_4\left(x_Q^3\right)\right] \\
&+ \frac{\alpha_s \pi}{3} \frac{m_s}{\tilde{m}_d^2} \left(\delta_d^{RR}\right)_{12}\left[M_3\left(x_d^3\right) + 9M_4\left(x_d^3\right)\right].
\end{aligned} \tag{B.3}
$$

B.1.4 $|\Delta S| = 2$ gluino box contribution

The Wilson coefficients of the gluino box contributions to ε_K are

$$
C_1 = -\frac{(\alpha_s)^2}{\tilde{m}_Q^2}\left[\left(\delta_d^{LL}\right)_{21}\right]^2 g_1^{(1)}\left(x_Q^3\right), \tag{B.4}
$$

$$
C_4 = -\frac{(\alpha_s)^2}{M_3^2}\left[\left(\delta_d^{LL}\right)_{21}\left(\delta_d^{RR}\right)_{21}\right] g_4^{(1)}\left(x_Q^3, x_d^3\right), \tag{B.5}
$$

$$
C_5 \simeq -\frac{(\alpha_s)^2}{M_3^2}\left[\left(\delta_d^{LL}\right)_{21}\left(\delta_d^{RR}\right)_{21}\right] g_5^{(1)}\left(x_Q^3, x_d^3\right), \tag{B.6}
$$

$$
\tilde{C}_1 = -\frac{(\alpha_s)^2}{\tilde{m}_d^2}\left[\left(\delta_d^{RR}\right)_{21}\right]^2 g_1^{(1)}\left(x_d^3\right), \tag{B.7}
$$

$$
C_2 = C_3 = \tilde{C}_2 = \tilde{C}_3 = 0. \tag{B.8}
$$

B.1.5 Sub-leading contributions to ε_K

The Wilson coefficients of the Wino and Higgsino contributions are

$$C_1 = -\frac{\alpha_s \alpha_2}{6\tilde{m}_Q^2}\left[\left(\delta_d^{LL}\right)_{21}\right]^2 g_{\tilde{g}\tilde{w}}^{(1)}\left(x_Q^3, x_Q^2\right) - \frac{(\alpha_2)^2}{8\tilde{m}_Q^2}\left[\left(\delta_d^{LL}\right)_{21}\right]^2 g_{\tilde{w}}^{(1)}\left(x_Q^2\right) - \frac{(\alpha_2)^2}{8\tilde{m}_u^2}\left(V_{ts}V_{td}^*\right)^2 \frac{m_t^4}{M_W^4} f_1\left(x_u^\mu\right), \tag{B.9}$$

$$\tilde{C}_3 = -\frac{(\alpha_2)^2}{8}\left(V_{ts}V_{td}^*\right)^2 \frac{m_s^2 \tan^2\beta}{(1+\epsilon_g \tan\beta)^2}\frac{m_t^4}{M_W^4}\frac{\mu^2 A_t^2}{\tilde{m}_Q^4 \tilde{m}_u^4} f_3\left(x_Q^\mu, x_u^\mu\right), \tag{B.10}$$

$$C_2 = C_3 = C_4 = C_5 = \tilde{C}_1 = \tilde{C}_2 = 0. \tag{B.11}$$

Note that a $\tan^4\beta$ enhanced contribution to ε_K comes from the exchange of neutral Higgses, which is discarded because of $(\delta_d)_{23}(\delta_d)_{31} = 0$ in our analyses. For the Wilson coefficient,

$$C_2 \simeq \tilde{C}_2 \simeq 0, \tag{B.12}$$

$$C_4 \simeq -\frac{8(\alpha_s)^2\alpha_2}{9\pi}\frac{m_b^2}{M_W^2}\frac{\tan^4\beta}{(1+\epsilon_g\tan\beta)^2[1+(\epsilon_g+\epsilon_Y y_t^2)\tan\beta]^2}\frac{\mu^2 M_3^2}{M_A^2 \tilde{m}_Q^2 \tilde{m}_d^2} \times\left[\left(\delta_d^{LL}\right)_{23}\left(\delta_d^{LL}\right)_{31}\left(\delta_d^{RR}\right)_{23}\left(\delta_d^{RR}\right)_{31}\right] H\left(x_Q^3, x_d^d\right) H\left(x_d^3, x_d^Q\right), \tag{B.13}$$

$$C_1 = C_3 = C_5 = \tilde{C}_1 = \tilde{C}_3 = 0, \tag{B.14}$$

where the approximation in eq. (5.35) is used, and the loop function $H(x,y)$ is given in eq. (B.18). Note that the CP-even and CP-odd Higgs contributions to C_2 ($\tilde{C}_2$) are canceled out by each other.

B.2 Loop functions

B.2.1 $K^0 \to \mu^+\mu^-$

The loop functions $l(x,y)$, $F(x,y)$, $G(x,y)$, and $H(x,y)$ are given by

$$l(x,y) = -\frac{\left[x^2+(x-2)y\right]x\ln x}{(x-1)^2(x-y)^3} + \frac{\left[y^2+(y-2)x\right]y\ln y}{(y-1)^2(x-y)^3} - \frac{x+y-2xy}{(x-1)(y-1)(x-y)^2}, \tag{B.15}$$

$$F(x,y) = \frac{x\ln x}{(x-1)(x-y)} + \frac{y\ln y}{(y-1)(y-x)}, \tag{B.16}$$

$$G(x,y) = \frac{x\ln x}{(x-1)^2(x-y)} + \frac{y\ln y}{(y-1)^2(y-x)} + \frac{1}{(x-1)(y-1)}, \tag{B.17}$$

$$H(x,y) = \frac{x\ln x}{(x-1)^2(x-y)^2} + \frac{(x+xy-2y^2)\ln y}{(y-1)^3(x-y)^2} - \frac{2x-y-1}{(x-1)(y-1)^2(x-y)}, \tag{B.18}$$

where $l(1,1) = -1/12$, $F(1,1) = 1/2$, $G(1,1) = -1/6$, and $H(1,1) = 1/12$.

B.2.2 $\Delta F = 1$ Processes

$$h_7(x) = -\frac{5x^2-3x}{12(1-x)^2} - \frac{3x^2-2x}{6(1-x)^3}\log x \tag{B.19}$$

$$f_7^{(2)}(x) = -\frac{13-7x}{24(1-x)^3} - \frac{3+2x-2x^2}{12(1-x)^4}\log x \tag{B.20}$$

$$f_7^{(1)}(x,y) = \frac{2}{x-y}(f_7^2(x) - f_7^2(y)) \tag{B.21}$$

$$g_7^{(1)}(x) = -\frac{2(1+5x)}{9(1-x)^3} - \frac{4x(2+x)}{9(1-x)^4}\log x \tag{B.22}$$

$$g_7^{(2)}(x) = -\frac{2(1+10x+x^2)}{9(1-x)^4} - \frac{4x(1+x)}{3(1-x)^5}\log x \tag{B.23}$$

B.2.3 $\varepsilon'_K/\varepsilon_K$

B.2.3.1 $|\Delta S| = 1$ gluino box contributions

The loop functions $f(x,y)$ and $g(x,y)$ [188] are

$$f(x,y) = \frac{x[2x^2-(x+1)y]\ln x}{(x-1)^3(x-y)^2} - \frac{xy\ln y}{(y-1)^2(x-y)^2} + \frac{x(x+1-2y)}{(x-1)^2(y-1)(x-y)}, \tag{B.24}$$

$$g(x,y) = -\frac{x^2[x(x+1)-2y]\ln x}{(x-1)^3(x-y)^2} + \frac{xy^2\ln y}{(y-1)^2(x-y)^2} + \frac{x[-2x+(x+1)y]}{(x-1)^2(y-1)(x-y)}, \tag{B.25}$$

which lead to

$$f(x,x) = -\frac{1+4x-5x^2+2x(2+x)\ln x}{2(x-1)^4} = \frac{1}{x}B_2\left(\frac{1}{x}\right), \tag{B.26}$$

$$g(x,x) = \frac{x\left[5-4x-x^2+2(1+2x)\ln x\right]}{2(x-1)^4} = -\frac{4}{x}B_1\left(\frac{1}{x}\right). \tag{B.27}$$

The loop functions $B_{1,2}(x)$ are consistent with ref. [199] for the universal squark masses case.

B.2.3.2 Chromomagnetic-dipole operator

The loop functions $I(x,y)$, $J(x,y)$, $K(x,y)$, $L(x,y)$, $M_3(x)$, and $M_4(x)$ are given by

$$I(x,y) = \frac{(3x^2-y-2xy)\ln x}{(x-1)^4(x-y)^2} - \frac{y\ln y}{(y-1)^3(x-y)^2} + \frac{-2+(-5+x)x+9y+(2+x)xy-(5+x)y^2}{2(x-y)(x-1)^3(y-1)^2}, \tag{B.28}$$

$$J(x,y) = -\frac{x[(1+2x)x-(2+x)y]\ln x}{(x-1)^4(x-y)^2} + \frac{y^2\ln y}{(y-1)^3(x-y)^2} + \frac{(5+x)x-3y(1+x)^2+(1+5x)y^2}{2(x-1)^3(y-1)^2(x-y)}, \tag{B.29}$$

$$K(x,y) = \frac{x\ln x}{(x-y)(x-1)^3} + \frac{y\ln y}{(y-x)(y-1)^3} + \frac{xy+x+y-3}{2(x-1)^2(y-1)^2}, \tag{B.30}$$

$$L(x,y) = -\frac{x^2\ln x}{(x-y)(x-1)^3} - \frac{y^2\ln y}{(y-x)(y-1)^3} + \frac{1+x+y-3xy}{2(x-1)^2(y-1)^2}, \tag{B.31}$$

$$M_3(x) = \frac{-1+9x+9x^2-17x^3+6x^2(3+x)\ln x}{12(x-1)^5}, \tag{B.32}$$

$$M_4(x) = \frac{-1-9x+9x^2+x^3-6x(1+x)\ln x}{6(x-1)^5}, \tag{B.33}$$

which lead to

$$K(x,x) = \frac{-5+4x+x^2-2(1+2x)\ln x}{2(x-1)^4} = \frac{1}{x^2}M_1\left(\frac{1}{x}\right), \tag{B.34}$$

$$L(x,x) = \frac{1+4x-5x^2+2x(2+x)\ln x}{2(x-1)^4} = -\frac{1}{x}B_2\left(\frac{1}{x}\right). \tag{B.35}$$

The above $M_{1,3,4}(x)$ are consistent with ref. [199] in the universal squark masses case.[1]

[1] It was found that in eq. (14) of ref. [199], $M_2(x) = -xB_2(x)$ should be replaced by $M_2(x) = -B_2(x)/x$, which has been pointed out in ref. [321].

B.2.4 ε_K

B.2.4.1 $|\Delta S| = 2$ gluino box contributions

The loop functions $g_1^{(1)}(x)$, $g_4^{(1)}(x,y)$, and $g_5^{(1)}(x,y)$ are given by

$$g_1^{(1)}(x) = -\frac{11+144x+27x^2-2x^3}{108(1-x)^4} - \frac{x(13+17x)}{18(1-x)^5}\ln x, \tag{B.36}$$

$$\begin{aligned} g_4^{(1)}(x,y) = &-\frac{x^2 y \ln x}{3(x-y)^3(1-x)^3}\left\{x^2(5+7x)+y\left[2+7(x-3)x\right]\right\} \\ &-\frac{y^2 x \ln y}{3(y-x)^3(1-y)^3}\left\{y^2(5+7y)+x\left[2+7(y-3)y\right]\right\} \\ &+\frac{xy}{3(1-x)^2(1-y)^2(x-y)^2}\left(x+y-13x^2-13y^2+8xy+15x^2y+15xy^2-14x^2y^2\right), \end{aligned} \tag{B.37}$$

$$\begin{aligned} g_5^{(1)}(x,y) = &-\frac{x^2 y \ln x}{9(x-y)^3(1-x)^3}\left[x^2(11+x)+(x-5)(x+2)y\right] \\ &-\frac{y^2 x \ln y}{9(y-x)^3(1-y)^3}\left[y^2(11+y)+(y-5)(y+2)x\right] \\ &-\frac{xy}{9(1-x)^2(1-y)^2(x-y)^2}\left(5x+5y+7x^2+7y^2-32xy+3x^2y+3xy^2+2x^2y^2\right). \end{aligned} \tag{B.38}$$

B.2.4.2 Wino and Higgsino contributions

The loop functions $g^{(1)}_{\tilde{g}\tilde{w}}$, $g^{(1)}_{\tilde{w}}(x)$, $f_1(x)$ and $f_3(x,y)$ are given by

$$\begin{aligned} g^{(1)}_{\tilde{g}\tilde{w}}(x,y) = &-\sqrt{xy}\Bigg[\frac{x\ln x}{(x-y)(1-x)^4} + \frac{y\ln y}{(y-x)(1-y)^4} \\ &+ \frac{11-7(x+y)+2(x^2+y^2)-10xy+5xy(x+y)-x^2y^2}{6(1-x)^3(1-y)^3}\Bigg] \\ &- \frac{x^2\ln x}{2(x-y)(1-x)^4} - \frac{y^2\ln y}{2(y-x)(1-y)^4} \\ &- \frac{2+5(x+y)-(x^2+y^2)-22xy+5xy(x+y)+2x^2y^2}{12(1-x)^3(1-y)^3}, \end{aligned} \tag{B.39}$$

$$g^{(1)}_{\tilde{w}}(x) = \frac{-5-67x-13x^2+x^3}{12(1-x)^4} - \frac{x(3+4x)}{(1-x)^5}\ln x, \tag{B.40}$$

$$f_1(x) = -\frac{x+1}{4(1-x)^2} - \frac{x}{2(1-x)^3}\ln x, \tag{B.41}$$

$$\begin{aligned} f_3(x,y) = &-\frac{x^2[x(1+x+y)-3y]}{(x-y)^3(1-x)^3}\ln x - \frac{y^2[y(1+x+y)-3x]}{(y-x)^3(1-y)^3}\ln y \\ &- 2\frac{x^2+y^2-xy-x^2y-xy^2+x^2y^2}{(1-x)^2(1-y)^2(x-y)^2}, \end{aligned} \tag{B.42}$$

$$f_3(x) = \frac{x^2-8x-17}{6(1-x)^4} - \frac{3x+1}{(1-x)^5}\ln x, \tag{B.43}$$

where $\lim_{y\to x} f_3(x,y) = f_3(x)$.[2]

[2] It was found that in eq. (A.15) in ref. [162], $f_3(x) = (x^2-6x-17)/[6(1-x)^4] - (3x+1)\ln x/(1-x)^5$ should be replaced by eq. (B.43).

USC
UNIVERSIDADE
DE SANTIAGO
DE COMPOSTELA

Appendix C

ϕ_s experimental

Table C.1: MC samples used in the analysis. SXX indicates the stripping version that is used to flag the events. DecProdCut means that all the daughters are required to be within LHCb acceptance. BcVegPy means that the generator was configured for the hadronic production of B_c^+ ($gg \to B_c^{+[*]} + b + \overline{c}$).

Event type	Decay mode	Options	Year	Events
		Signal modes		
13144004	$B_s^0 \to J/\psi\,\phi$	`Update2012,dG=0,DecProdCut,S24`	2015	4M
13144004	$B_s^0 \to J/\psi\,\phi$	`Update2012,dG=0,DecProdCut,S26`	2016	25M
13144011	$B_s^0 \to J/\psi\,\phi$	`Update2016,DecProdCut,S24`	2015	4M
13144011	$B_s^0 \to J/\psi\,\phi$	`Update2016,DecProdCut,S26`	2016	20M
13144011	$B_s^0 \to J/\psi\,\phi$	`Update2012,DecProdCut,S28`	2016	10M
13144041	$B_s^0 \to J/\psi\,K^+K^-$	`DecProdCut,S26`	2016	7M
13100004	$B_s^0 \to J/\psi\,K^+K^-$	`DecProdCut,S28`	2016	20M
		Backgrounds		
15144001	$\Lambda_b^0 \to J/\psi\,pK^-$	`PHSP,DecProdCut,S24`	2015	15M
15144001	$\Lambda_b^0 \to J/\psi\,pK^-$	`PHSP,DecProdCut,S26`	2016	10M
24142001	Inclusive Jpsi	`DecProdCut,S24`	2015	2M
24142001	Inclusive Jpsi	`DecProdCut,S26`	2016	43M
		Control samples		
11144001	$B^0 \to J/\psi K^{*0}$	`Update2016,DecProdCut,S24`	2015	10M
11144001	$B^0 \to J/\psi K^{*0}$	`Update2016,DecProdCut,S26`	2016	15M
12143001	$B^+ \to J/\psi K^+$	`Update2016,DecProdCut,S24`	2015	10M
12143001	$B^+ \to J/\psi K^+$	`Update2016,DecProdCut,S26`	2016	14M
14135000	$B_c^+ \to B_s^0(\to J/\psi\phi)\pi^+$	`BcVegPy,DecProdCut,S20`	2012	2M
24142001	Inclusive Jpsi	`DecProdCut,S24`	2015	2M
24142001	Inclusive Jpsi	`DecProdCut,S26`	2016	43M
		Generator Level		

Table C.2: The angular and time-dependent functions used in Eqs. (6.2) and (6.3) , as discussed in the text. Some abbreviations have been used for cosine and sine functions: $c_K = \cos\theta_K$, $s_K = \sin\theta_K$, $c_l = \cos\theta_l$, $s_l = \sin\theta_l$.

f_k	N_k	a_k	b_k	c_k	d_k
$c_K^2 s_l^2$	$\lvert A_0\rvert^2$	$\frac{1}{2}(1+\lvert\lambda_0\rvert^2)$	$-\lvert\lambda_0\rvert\cos(\phi_0)$	$\frac{1}{2}(1-\lvert\lambda_0\rvert^2)$	$\lvert\lambda_0\rvert\sin(\phi_0)$
$\frac{1}{2}s_K^2(1-c_\phi^2 s_l^2)$	$\lvert A_\parallel\rvert^2$	$\frac{1}{2}(1+\lvert\lambda_\parallel\rvert^2)$	$-\lvert\lambda_\parallel\rvert\cos(\phi_\parallel)$	$\frac{1}{2}(1-\lvert\lambda_\parallel\rvert^2)$	$\lvert\lambda_\parallel\rvert\sin(\phi_\parallel)$
$\frac{1}{2}s_K^2(1-s_\phi^2 s_l^2)$	$\lvert A_\perp\rvert^2$	$\frac{1}{2}(1+\lvert\lambda_\perp\rvert^2)$	$\lvert\lambda_\perp\rvert\cos(\phi_\perp)$	$\frac{1}{2}(1-\lvert\lambda_\perp\rvert^2)$	$-\lvert\lambda_\perp\rvert\sin(\phi_\perp)$
$s_K^2 s_l^2 s_\phi c_\phi$	$\lvert A_\perp A_\parallel\rvert$	$\frac{1}{2}\Big[\sin(\delta_\perp-\delta_\parallel)-\lvert\lambda_\perp\lambda_\parallel\rvert$ $\sin(\delta_\perp-\delta_\parallel-\phi_\perp+\phi_\parallel)\Big]$	$\frac{1}{2}\Big[\lvert\lambda_\perp\rvert\sin(\delta_\perp-\delta_\parallel-\phi_\perp)$ $+\lvert\lambda_\parallel\rvert\sin(\delta_\parallel-\delta_\perp-\phi_\parallel)\Big]$	$\frac{1}{2}\Big[\sin(\delta_\perp-\delta_\parallel)+\lvert\lambda_\perp\lambda_\parallel\rvert$ $\sin(\delta_\perp-\delta_\parallel-\phi_\perp+\phi_\parallel)\Big]$	$-\frac{1}{2}\Big[\lvert\lambda_\perp\rvert\cos(\delta_\perp-\delta_\parallel-\phi_\perp)$ $+\lvert\lambda_\parallel\rvert\cos(\delta_\parallel-\delta_\perp-\phi_\parallel)\Big]$
$\sqrt{2}s_K c_K s_l c_l c_\phi$	$\lvert A_0 A_\parallel\rvert$	$\frac{1}{2}\Big[\cos(\delta_0-\delta_\parallel)+\lvert\lambda_0\lambda_\parallel\rvert$ $\cos(\delta_0-\delta_\parallel-\phi_0+\phi_\parallel)\Big]$	$-\frac{1}{2}\Big[\lvert\lambda_0\rvert\cos(\delta_0-\delta_\parallel-\phi_0)$ $+\lvert\lambda_\parallel\rvert\cos(\delta_\parallel-\delta_0-\phi_\parallel)\Big]$	$\frac{1}{2}\Big[\cos(\delta_0-\delta_\parallel)-\lvert\lambda_0\lambda_\parallel\rvert$ $\cos(\delta_0-\delta_\parallel-\phi_0+\phi_\parallel)\Big]$	$-\frac{1}{2}\Big[\lvert\lambda_0\rvert\sin(\delta_0-\delta_\parallel-\phi_0)$ $+\lvert\lambda_\parallel\rvert\sin(\delta_\parallel-\delta_0-\phi_\parallel)\Big]$
$-\sqrt{2}s_K c_K s_l c_l s_\phi$	$\lvert A_0 A_\perp\rvert$	$-\frac{1}{2}\Big[\sin(\delta_0-\delta_\perp)-\lvert\lambda_0\lambda_\perp\rvert$ $\sin(\delta_0-\delta_\perp-\phi_0+\phi_\perp)\Big]$	$\frac{1}{2}\Big[\lvert\lambda_0\rvert\sin(\delta_0-\delta_\perp-\phi_0)$ $+\lvert\lambda_\perp\rvert\sin(\delta_\perp-\delta_0-\phi_\perp)\Big]$	$-\frac{1}{2}\Big[\sin(\delta_0-\delta_\perp)+\lvert\lambda_0\lambda_\perp\rvert$ $\sin(\delta_0-\delta_\perp-\phi_0+\phi_\perp)\Big]$	$-\frac{1}{2}\Big[\lvert\lambda_0\rvert\cos(\delta_0-\delta_\perp-\phi_0)$ $+\lvert\lambda_\perp\rvert\cos(\delta_\perp-\delta_0-\phi_\perp)\Big]$
$\frac{1}{3}s_l^2$	$\lvert A_S\rvert^2$	$\frac{1}{2}(1+\lvert\lambda_S\rvert^2)$	$\lvert\lambda_S\rvert\cos(\phi_S)$	$\frac{1}{2}(1-\lvert\lambda_S\rvert^2)$	$-\lvert\lambda_S\rvert\sin(\phi_S)$
$\frac{2}{\sqrt{6}}s_K s_l c_l c_\phi$	$\lvert A_S A_\parallel\rvert$	$\frac{1}{2}\Big[\cos(\delta_S-\delta_\parallel)-\lvert\lambda_S\lambda_\parallel\rvert$ $\cos(\delta_S-\delta_\parallel-\phi_S+\phi_\parallel)\Big]$	$\frac{1}{2}\Big[\lvert\lambda_S\rvert\cos(\delta_S-\delta_\parallel-\phi_S)$ $-\lvert\lambda_\parallel\rvert\cos(\delta_\parallel-\delta_S-\phi_\parallel)\Big]$	$\frac{1}{2}\Big[\cos(\delta_S-\delta_\parallel)+\lvert\lambda_S\lambda_\parallel\rvert$ $\cos(\delta_S-\delta_\parallel-\phi_S+\phi_\parallel)\Big]$	$\frac{1}{2}\Big[\lvert\lambda_S\rvert\sin(\delta_S-\delta_\parallel-\phi_S)$ $-\lvert\lambda_\parallel\rvert\sin(\delta_\parallel-\delta_S-\phi_\parallel)\Big]$
$-\frac{2}{\sqrt{6}}s_K s_l c_l s_\phi$	$\lvert A_S A_\perp\rvert$	$-\frac{1}{2}\Big[\sin(\delta_S-\delta_\perp)+\lvert\lambda_S\lambda_\perp\rvert$ $\sin(\delta_S-\delta_\perp-\phi_S+\phi_\perp)\Big]$	$-\frac{1}{2}\Big[\lvert\lambda_S\rvert\sin(\delta_S-\delta_\perp-\phi_S)$ $-\lvert\lambda_\perp\rvert\sin(\delta_\perp-\delta_S-\phi_\perp)\Big]$	$-\frac{1}{2}\Big[\sin(\delta_S-\delta_\perp)-\lvert\lambda_S\lambda_\perp\rvert$ $\sin(\delta_S-\delta_\perp-\phi_S+\phi_\perp)\Big]$	$-\frac{1}{2}\Big[-\lvert\lambda_S\rvert\cos(\delta_S-\delta_\perp-\phi_S)$ $+\lvert\lambda_\perp\rvert\cos(\delta_\perp-\delta_S-\phi_\perp)\Big]$
$\frac{2}{\sqrt{3}}c_K s_l^2$	$\lvert A_S A_0\rvert$	$\frac{1}{2}\Big[\cos(\delta_S-\delta_0)-\lvert\lambda_S\lambda_0\rvert$ $\cos(\delta_S-\delta_0-\phi_S+\phi_0)\Big]$	$\frac{1}{2}\Big[\lvert\lambda_S\rvert\cos(\delta_S-\delta_0-\phi_S)$ $-\lvert\lambda_0\rvert\cos(\delta_0-\delta_S-\phi_0)\Big]$	$\frac{1}{2}\Big[\cos(\delta_S-\delta_0)+\lvert\lambda_S\lambda_0\rvert$ $\cos(\delta_S-\delta_0-\phi_S+\phi_0)\Big]$	$\frac{1}{2}\Big[\lvert\lambda_S\rvert\sin(\delta_S-\delta_0-\phi_S)$ $-\lvert\lambda_0\rvert\sin(\delta_0-\delta_S-\phi_0)\Big]$

Appendix D

Coverage of the uncertainty with the sFit

Figures below show the distributions of the parameters from the fit together with their corresponding pull distributions, obtained when performing the bootstrapping test, for both simulation (Figures D.2 and D.1) and data (Figures D.5, D.6, D.3 and D.4).

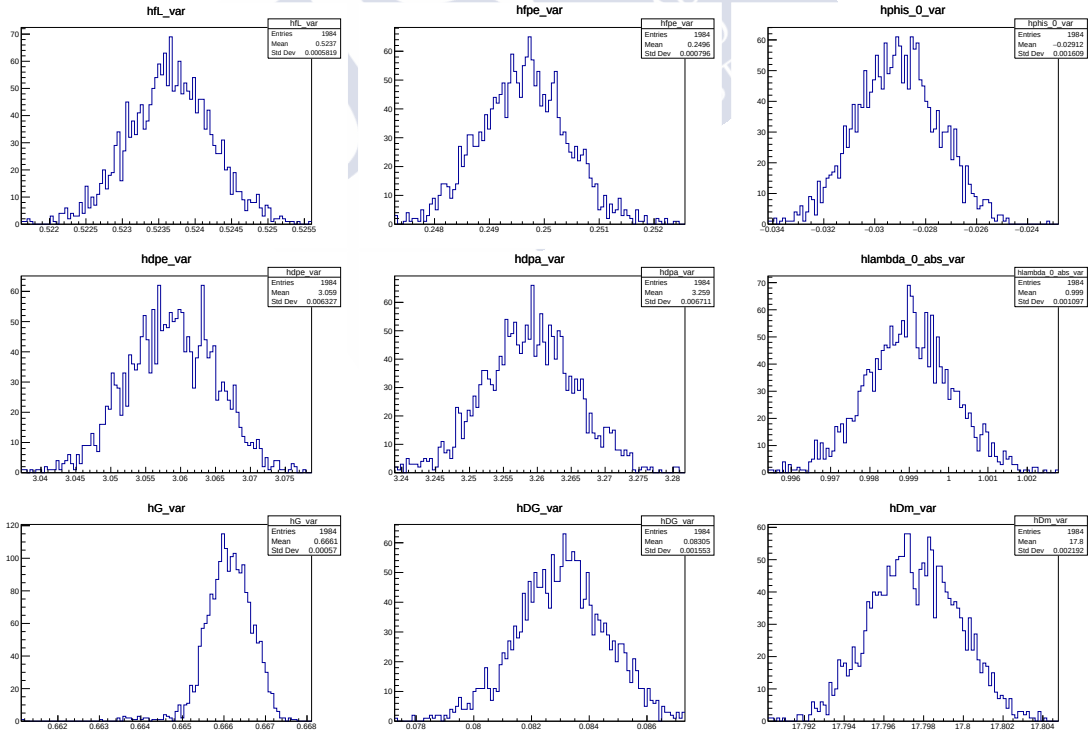

Figure D.1: Distributions of the fit parameters using bootstrapping (MC).

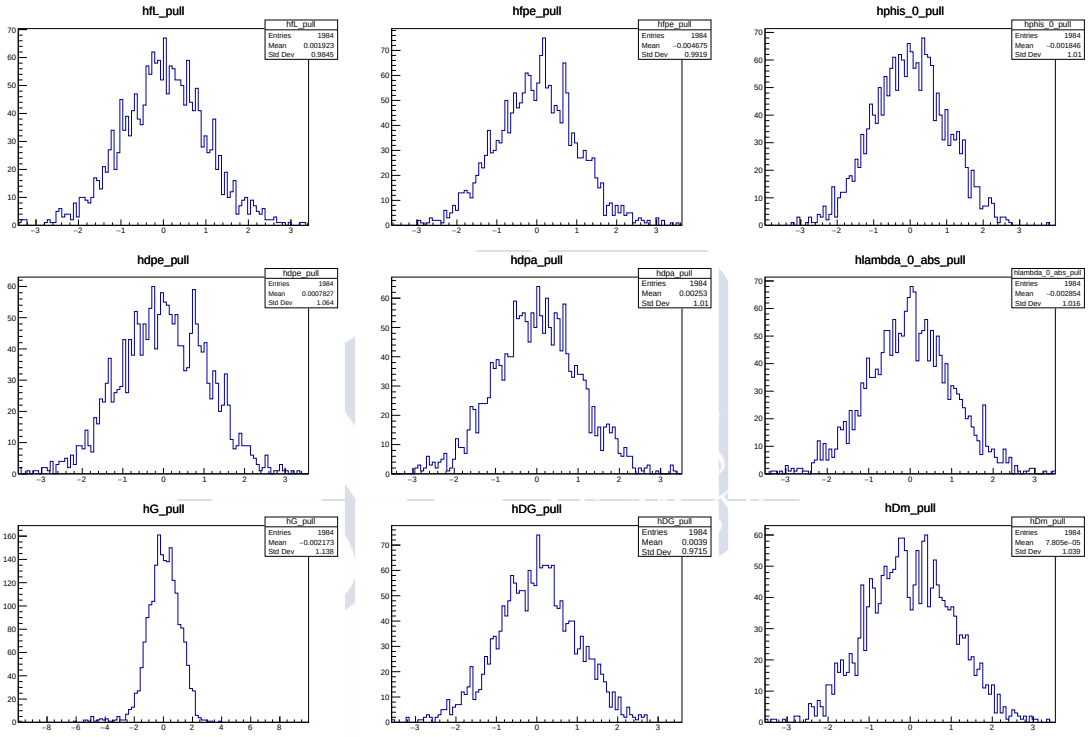

Figure D.2: Pull distributions of the fit parameters using bootstrapping (MC). Pulls are computed relative to MC generation values.

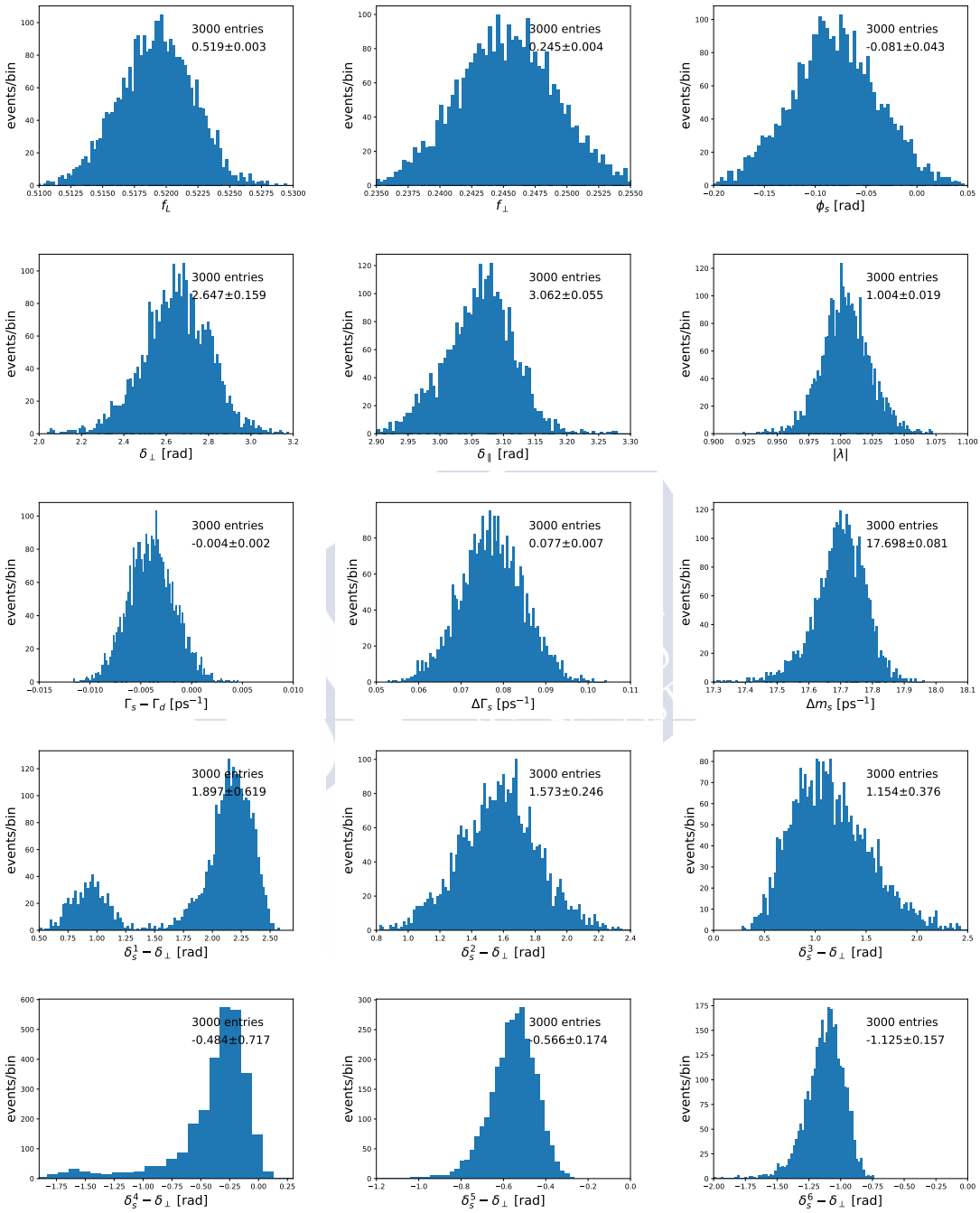

Figure D.3: Distributions of the fit parameters using bootstrapping (data).

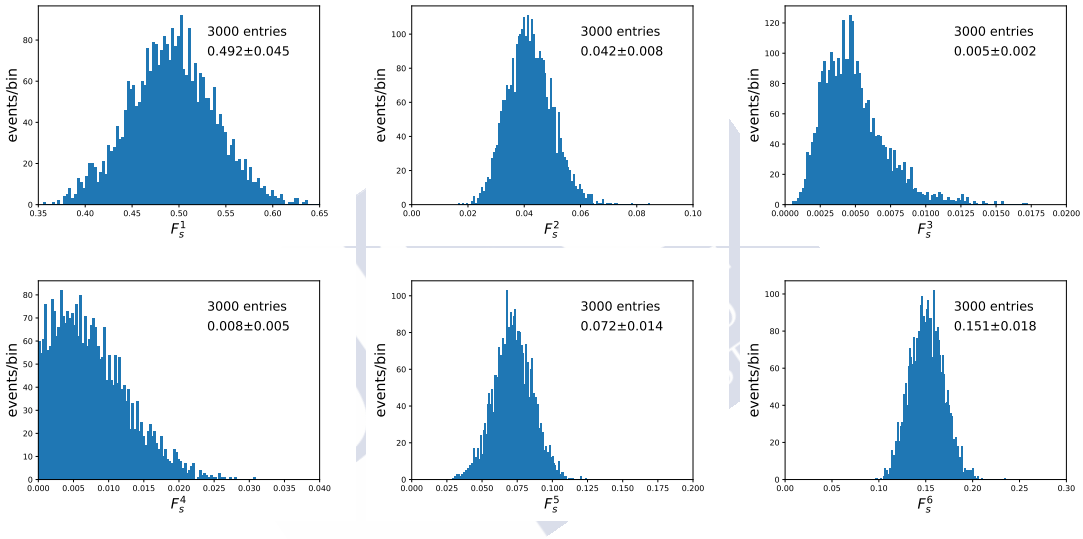

Figure D.4: Distributions of the fit parameters using bootstrapping (data).

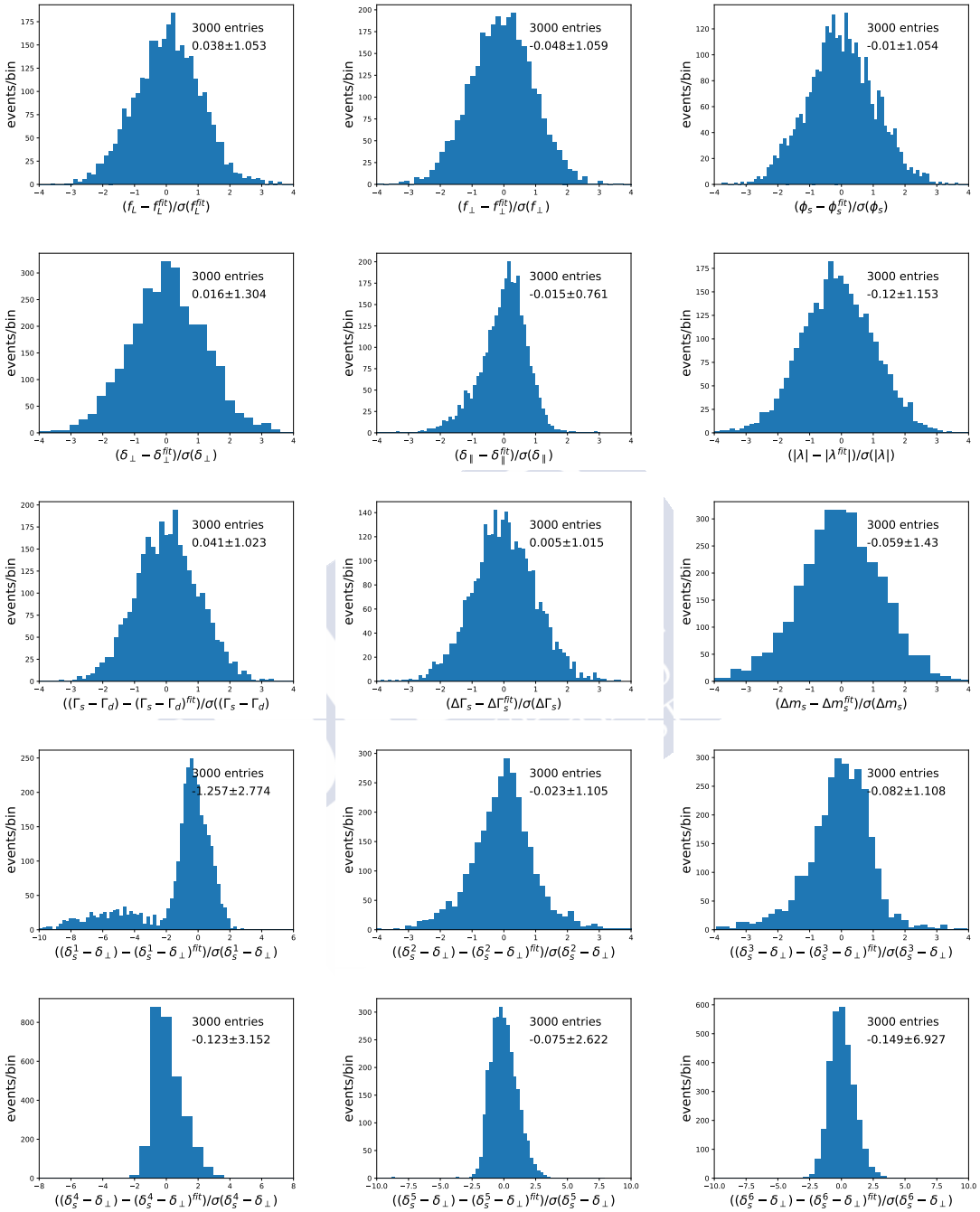

Figure D.5: Pull distributions of the fit parameters using bootstrapping (data). Pulls are computed relative to data central values.

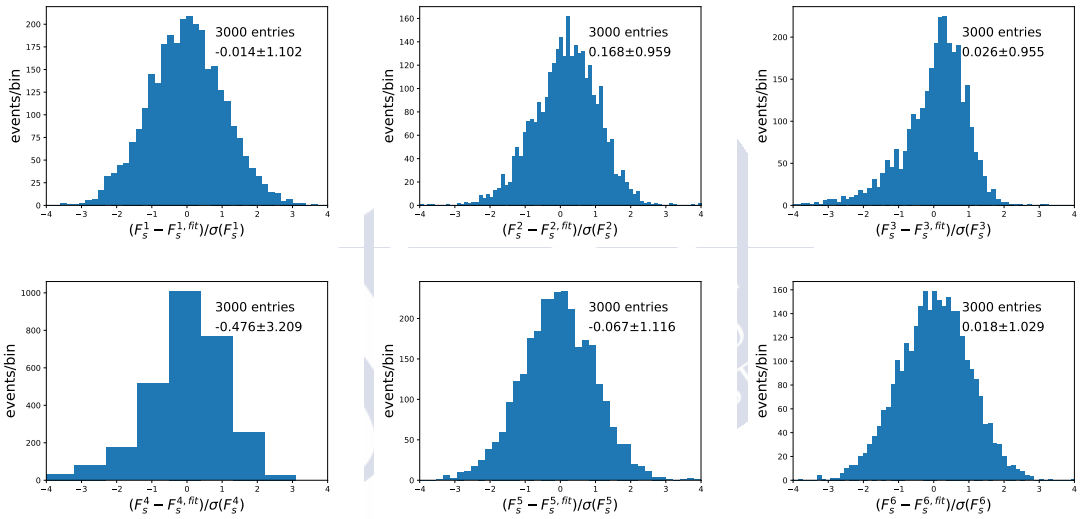

Figure D.6: Pull distributions of the fit parameters using bootstrapping (data). Pulls are computed relative to data central values.

Appendix E

2D Projections (ϕ_s MultiNest)

Figures below show the 2D projections of the scan values obtained with MultiNest.

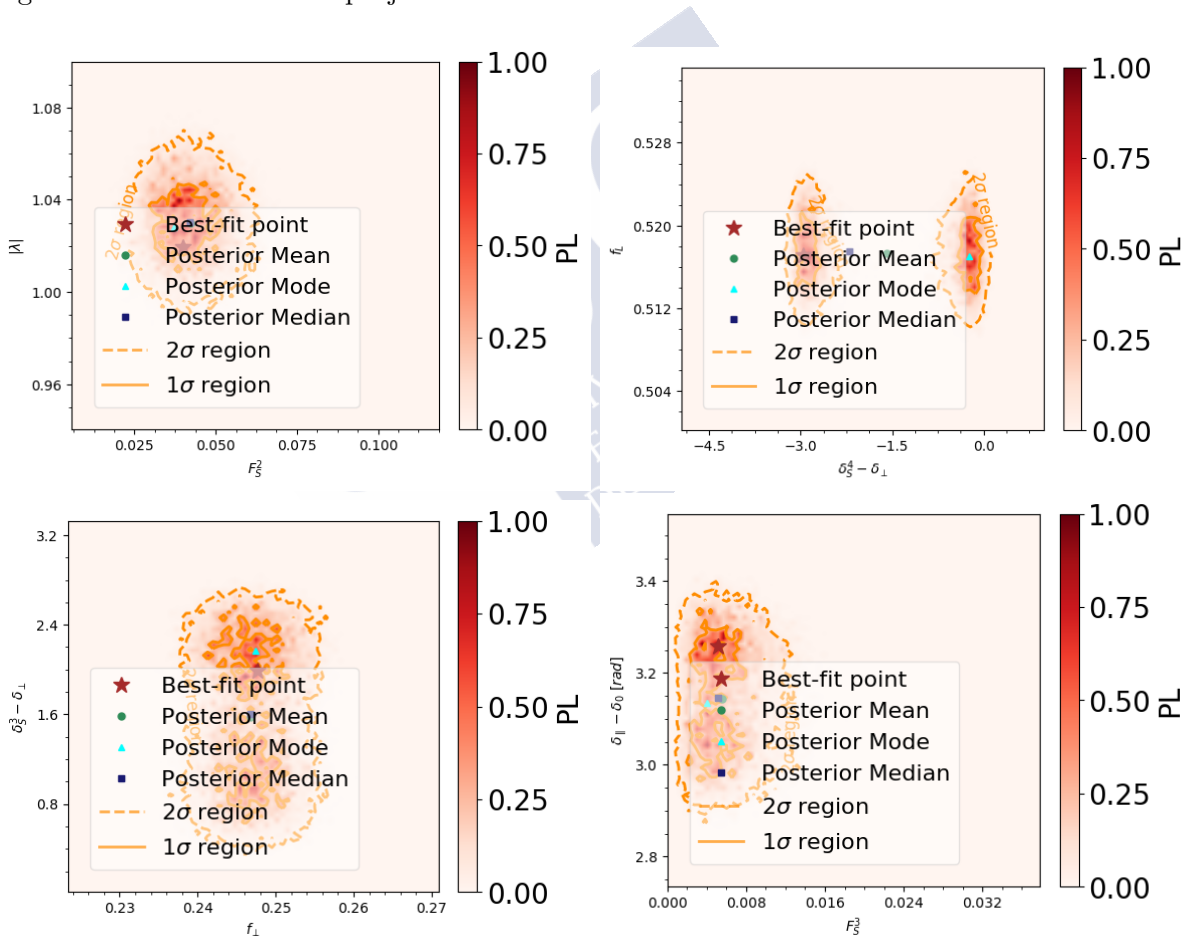

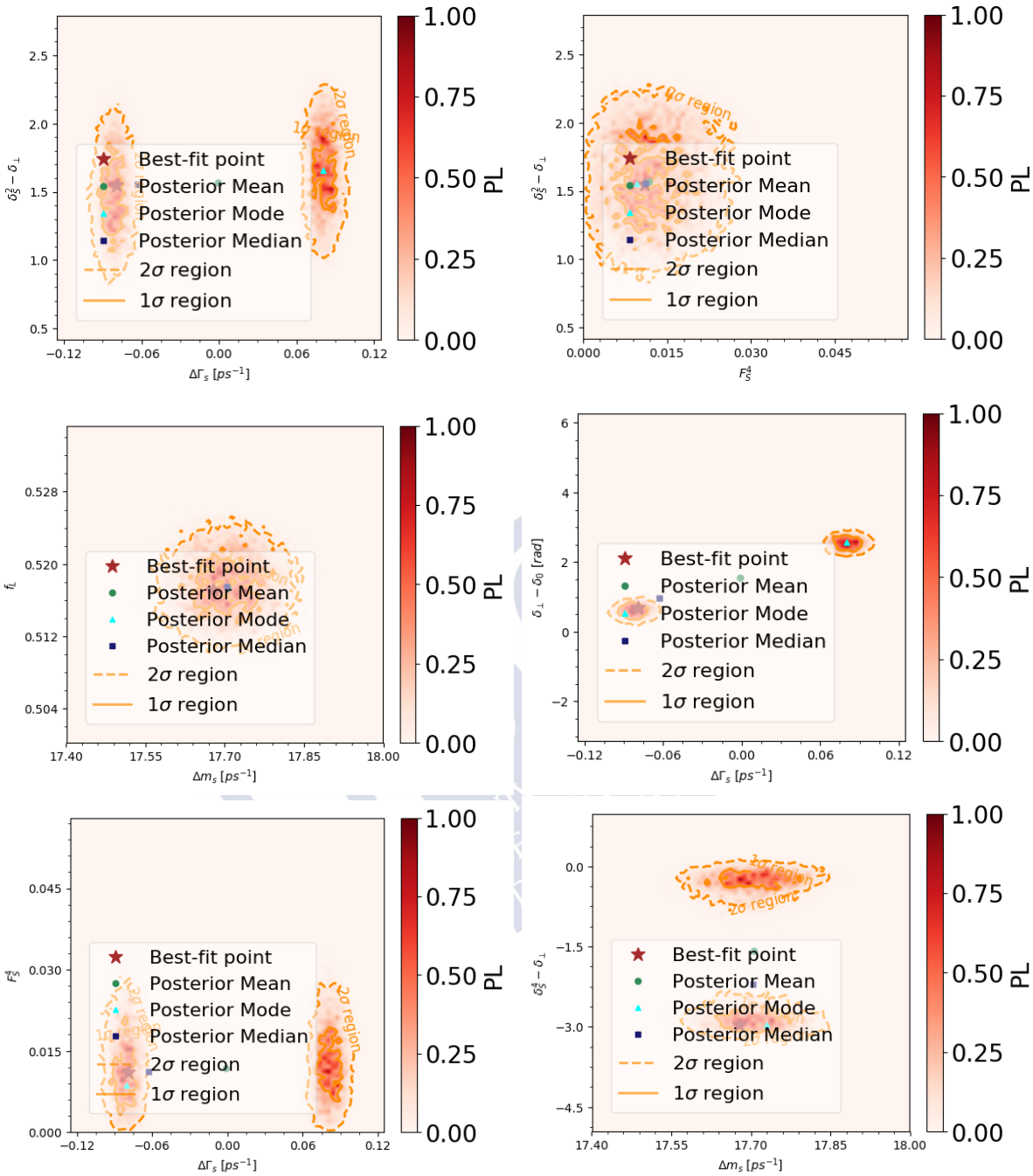
Best-fit point
Posterior Mean
Posterior Mode
Posterior Median
2σ region
1σ region
PL
1.00
0.75
0.50
0.25
0.00
$\Delta\Gamma_s\ [ps^{-1}]$
$\Delta m_s\ [ps^{-1}]$
f_L
F_S^4
$\delta_\perp - \delta_0\ [rad]$
$\delta_S^4 - \delta_\perp$

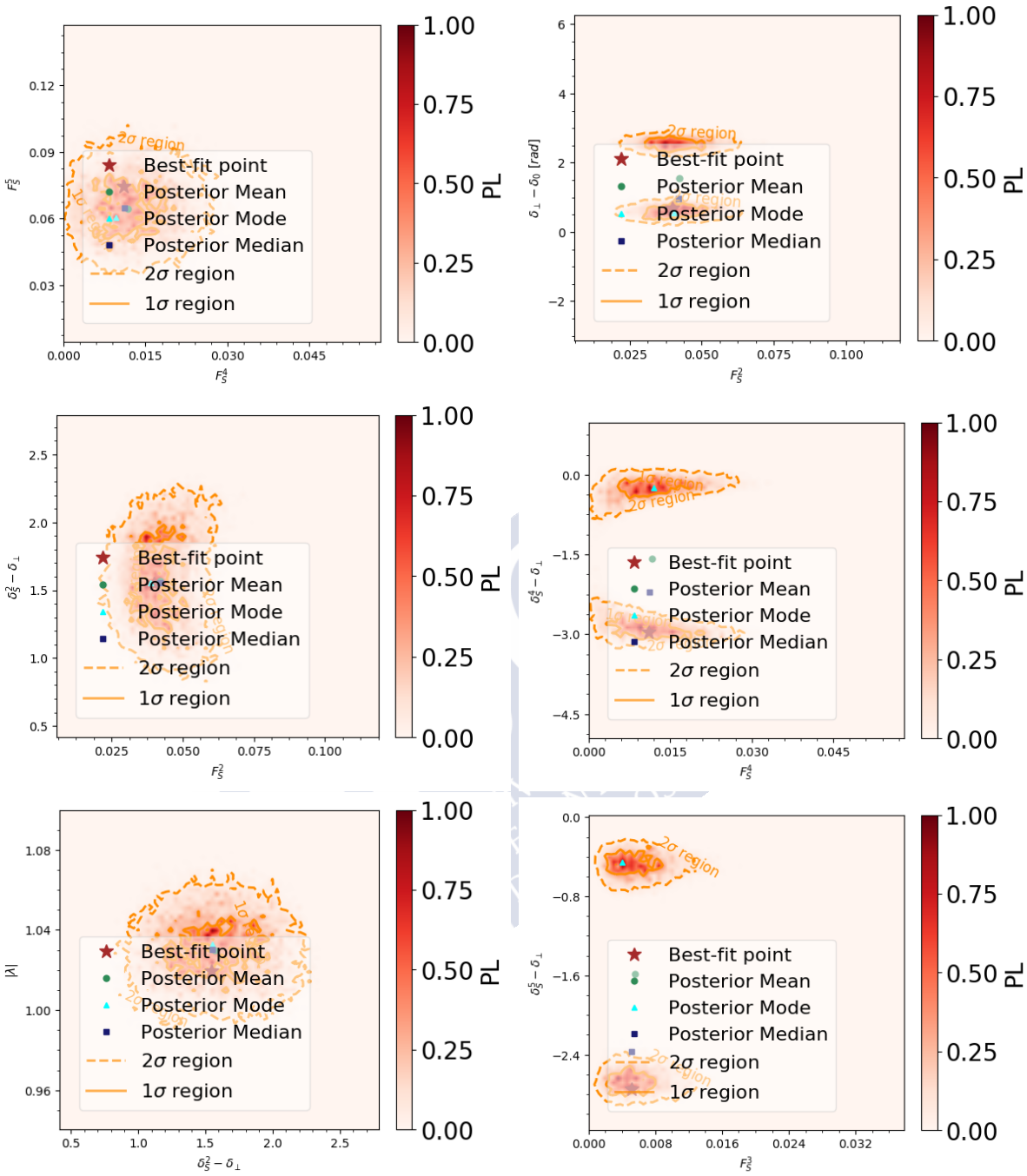
Best-fit point
Posterior Mean
Posterior Mode
Posterior Median
2σ region
1σ region
PL
1.00
0.75
0.50
0.25
0.00
F_S^5
F_S^4
$\delta_\perp - \delta_0$ [rad]
F_S^2
$\delta_S^2 - \delta_\perp$
$\delta_S^4 - \delta_\perp$
$|\lambda|$
$\delta_S^5 - \delta_\perp$
F_S^3

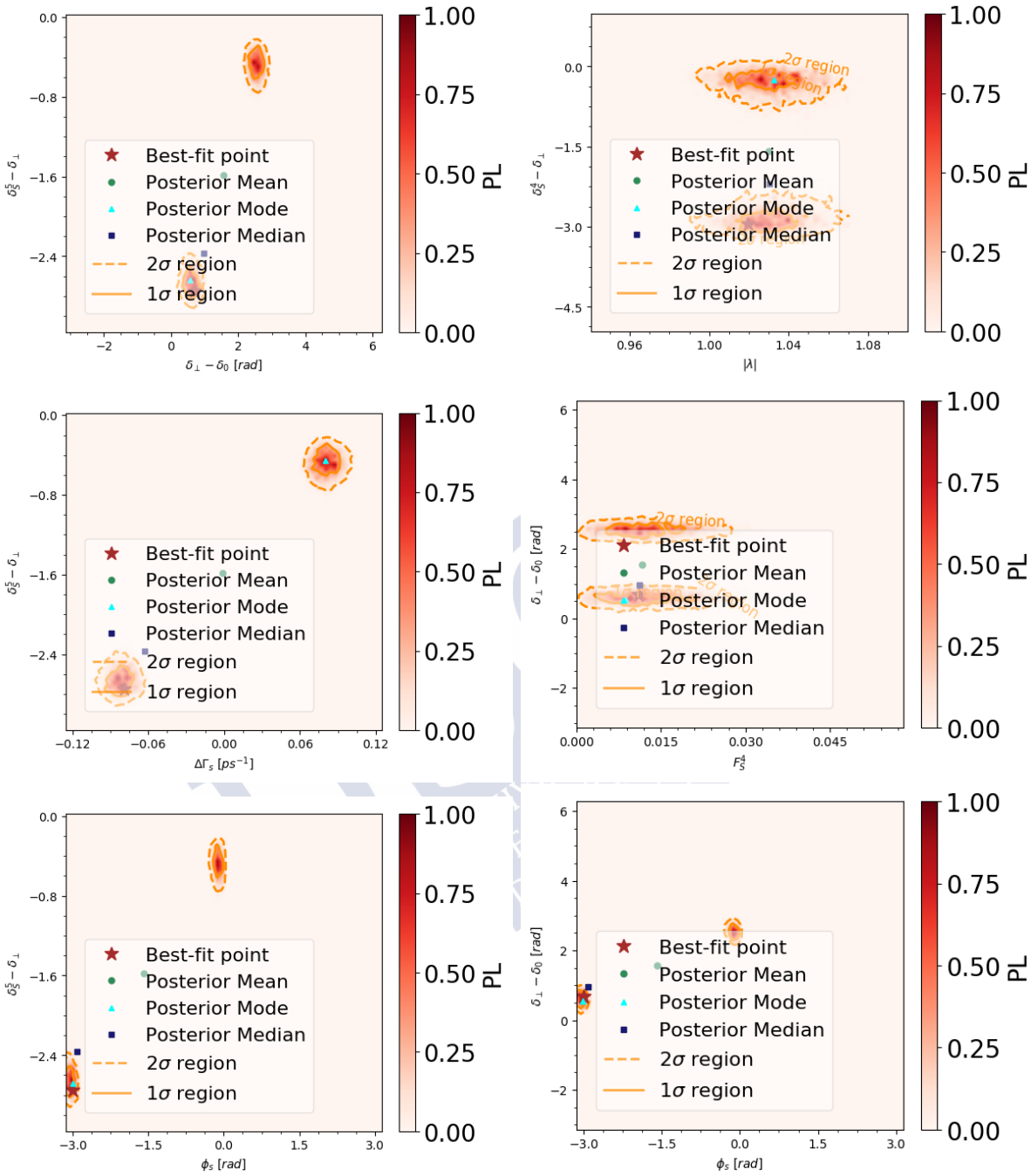
Best-fit point
Posterior Mean
Posterior Mode
Posterior Median
2σ region
1σ region
PL
1.00
0.75
0.50
0.25
0.00
$\delta_\perp - \delta_0$ [rad]
$|\lambda|$
$\Delta\Gamma_s$ [ps^{-1}]
F_S^4
ϕ_s [rad]

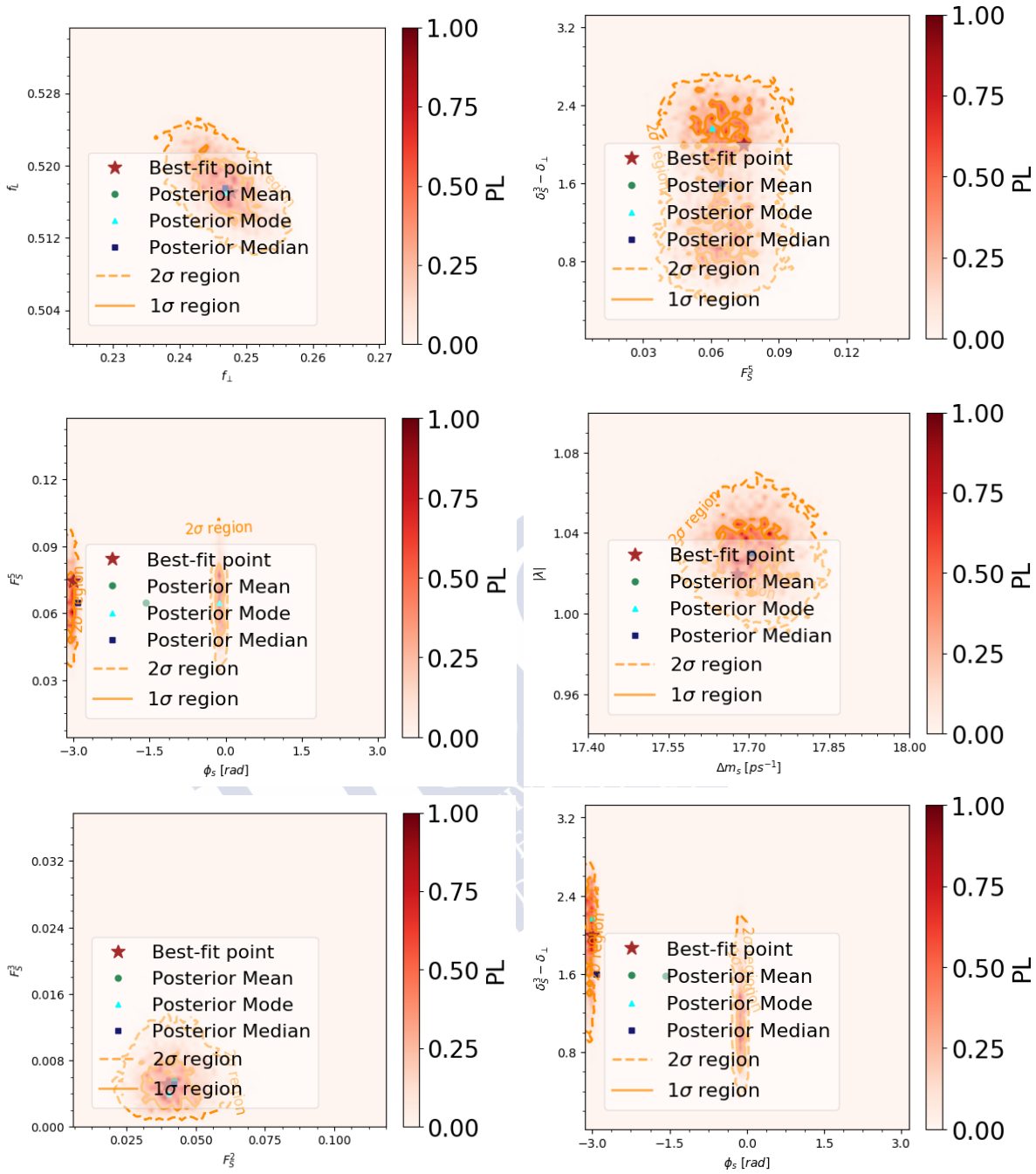
Best-fit point
Posterior Mean
Posterior Mode
Posterior Median
2σ region
1σ region
PL
1.00
0.75
0.50
0.25
0.00
$f_\perp$
$f_\parallel$
F_S^5
$\delta_S^3 - \delta_\perp$
ϕ_s [rad]
$|\lambda|$
Δm_s [ps^{-1}]
F_S^3
F_S^2

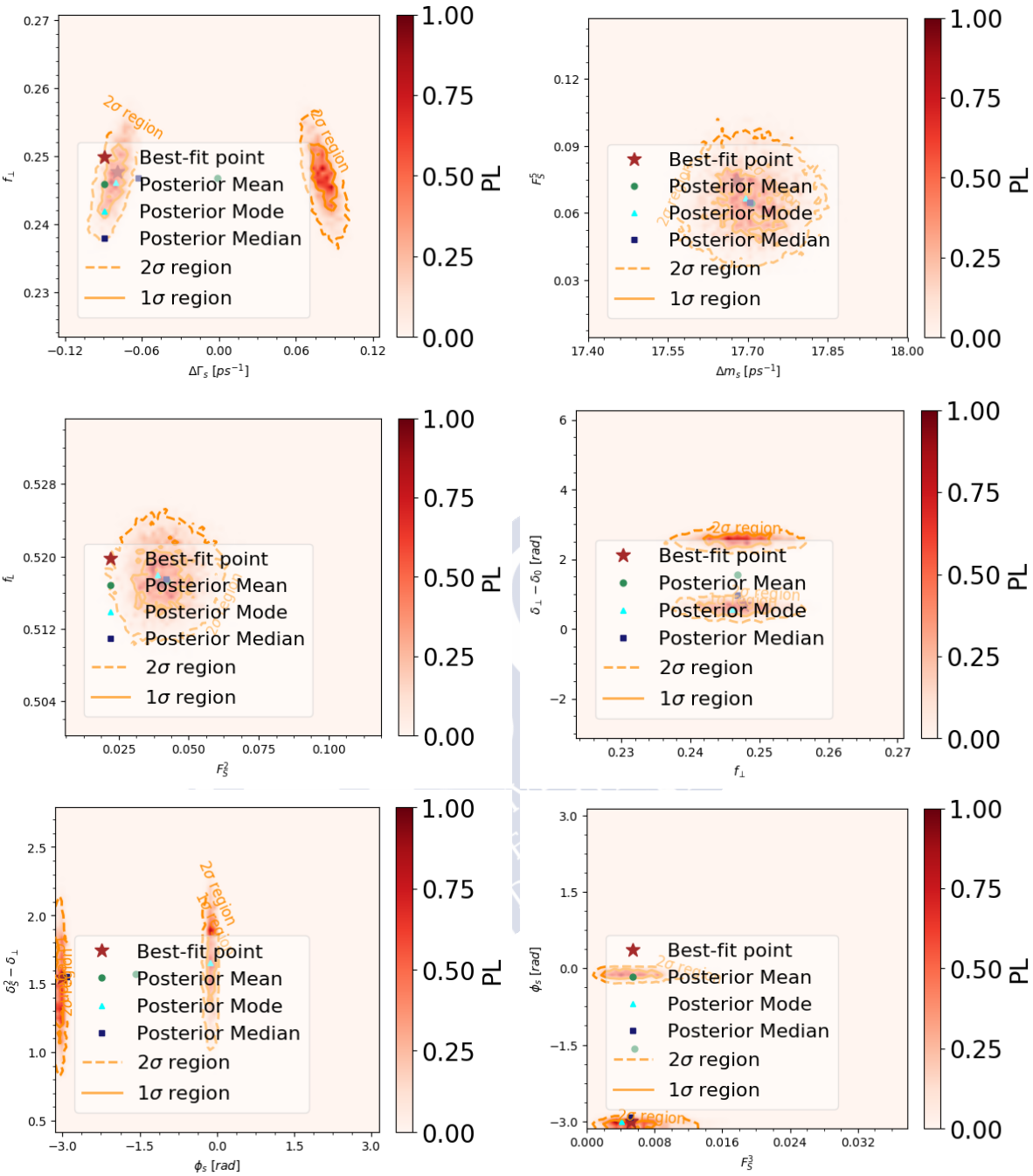
Best-fit point
Posterior Mean
Posterior Mode
Posterior Median
2σ region
1σ region
PL
1.00
0.75
0.50
0.25
0.00
$\Delta\Gamma_s\ [ps^{-1}]$
$\Delta m_s\ [ps^{-1}]$
$f_\perp$
F_S^5
F_S^2
$\delta_\perp - \delta_0\ [rad]$
$\delta_S^2 - \delta_\perp$
$\phi_s\ [rad]$
F_S^3

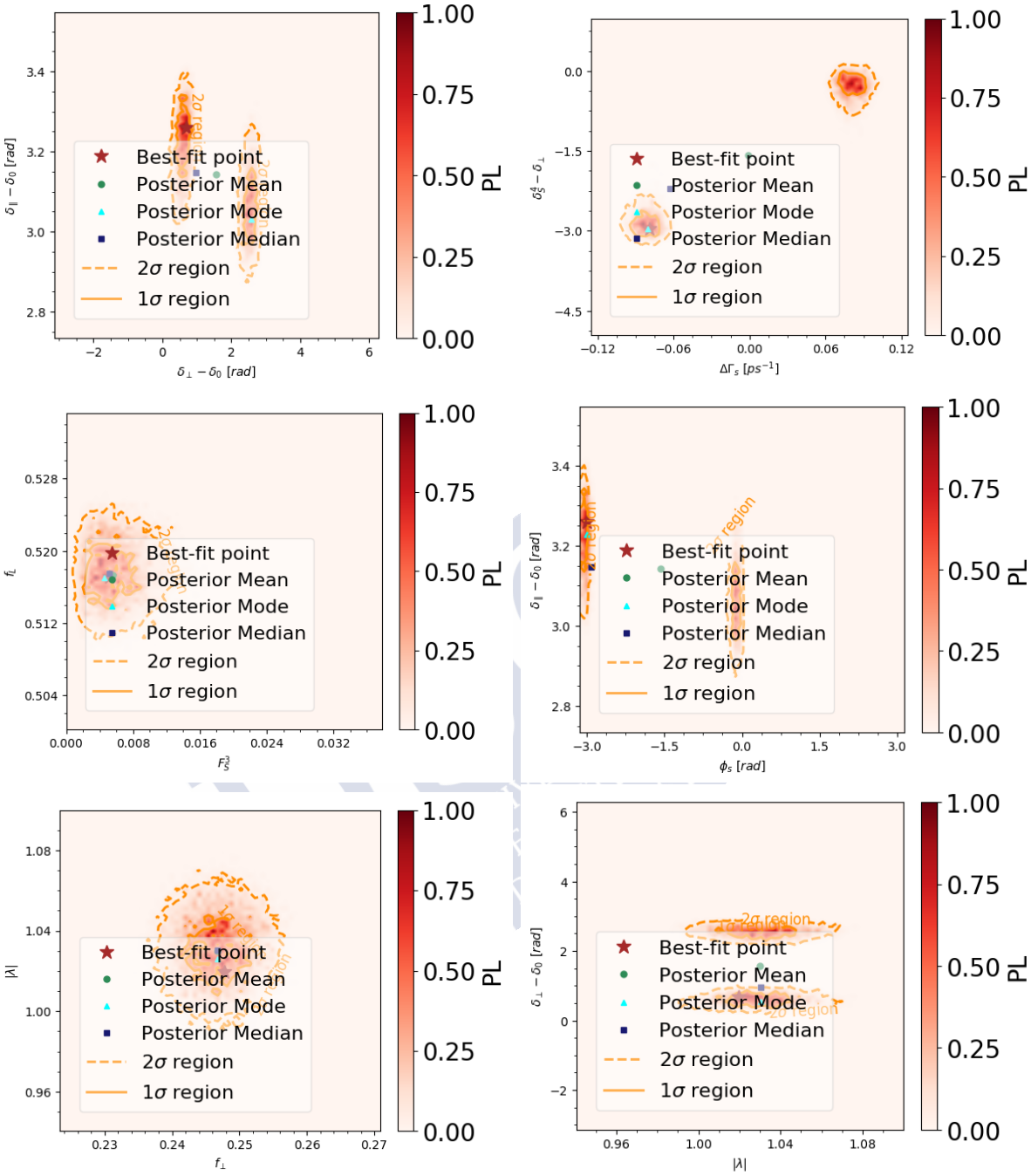
Best-fit point
Posterior Mean
Posterior Mode
Posterior Median
2σ region
1σ region
PL
1.00
0.75
0.50
0.25
0.00
$\delta_\perp - \delta_0$ [rad]
$\delta_\parallel - \delta_0$ [rad]
$\Delta\Gamma_s$ [ps^{-1}]
$\delta_s^4 - \delta_\perp$
$f_\perp$
$f_\parallel$
F_S^3
ϕ_s [rad]
$|\lambda|$

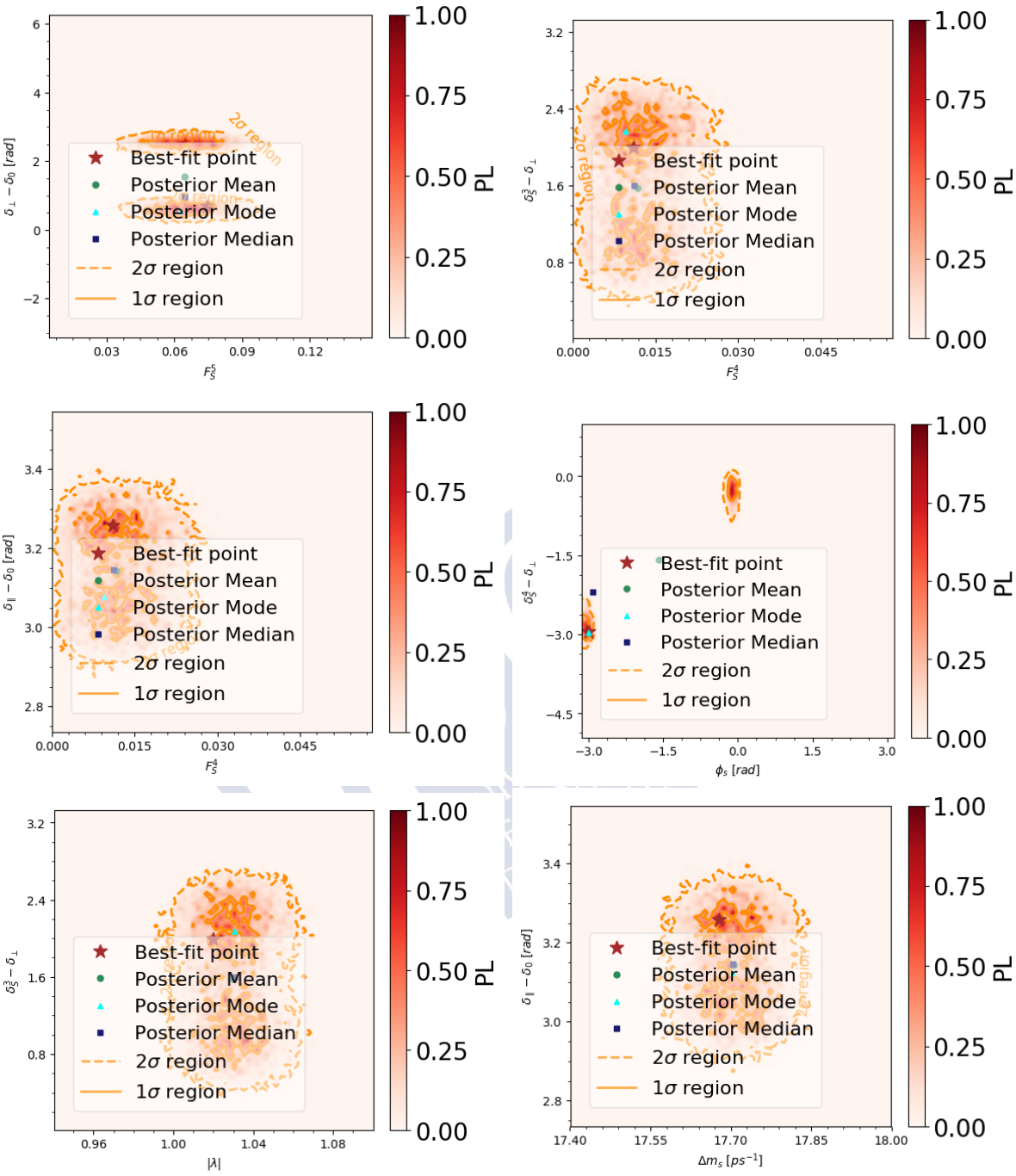
Best-fit point
Posterior Mean
Posterior Mode
Posterior Median
2σ region
1σ region
PL
1.00
0.75
0.50
0.25
0.00
$\delta_\perp - \delta_0$ [rad]
F_S^5
$\delta_S^3 - \delta_\perp$
F_S^4
$\delta_\parallel - \delta_0$ [rad]
$\delta_S^4 - \delta_\perp$
ϕ_s [rad]
$\delta_S^3 - \delta_\perp$
$|\lambda|$
$\delta_\parallel - \delta_0$ [rad]
Δm_s [ps^{-1}]

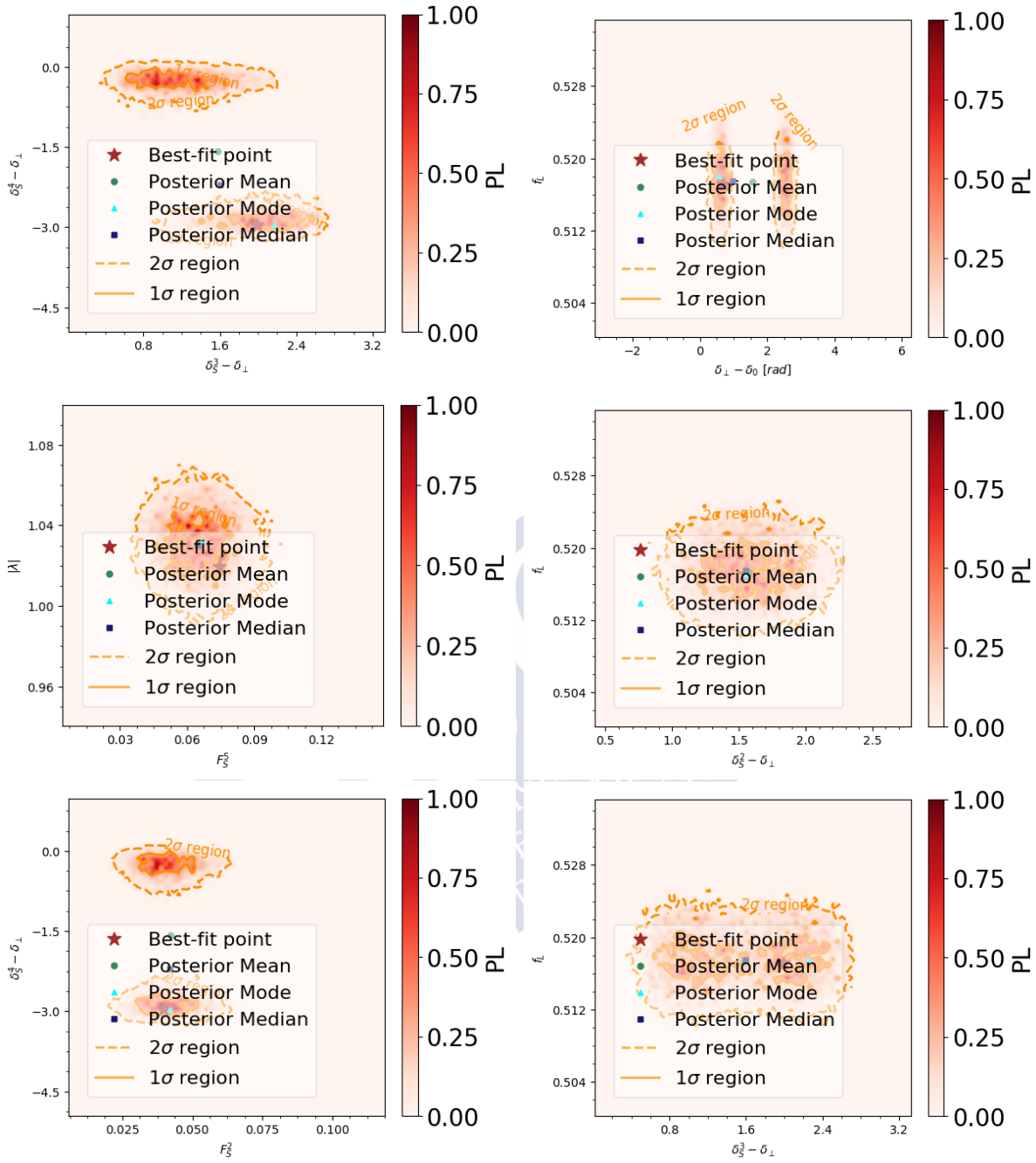
Best-fit point
Posterior Mean
Posterior Mode
Posterior Median
2σ region
1σ region
PL
1.00
0.75
0.50
0.25
0.00
$\delta_S^3 - \delta_\perp$
$\delta_\perp - \delta_0$ [rad]
f_L
$|\lambda|$
F_S^5
$\delta_S^2 - \delta_\perp$
F_S^2
$\delta_S^4 - \delta_\perp$

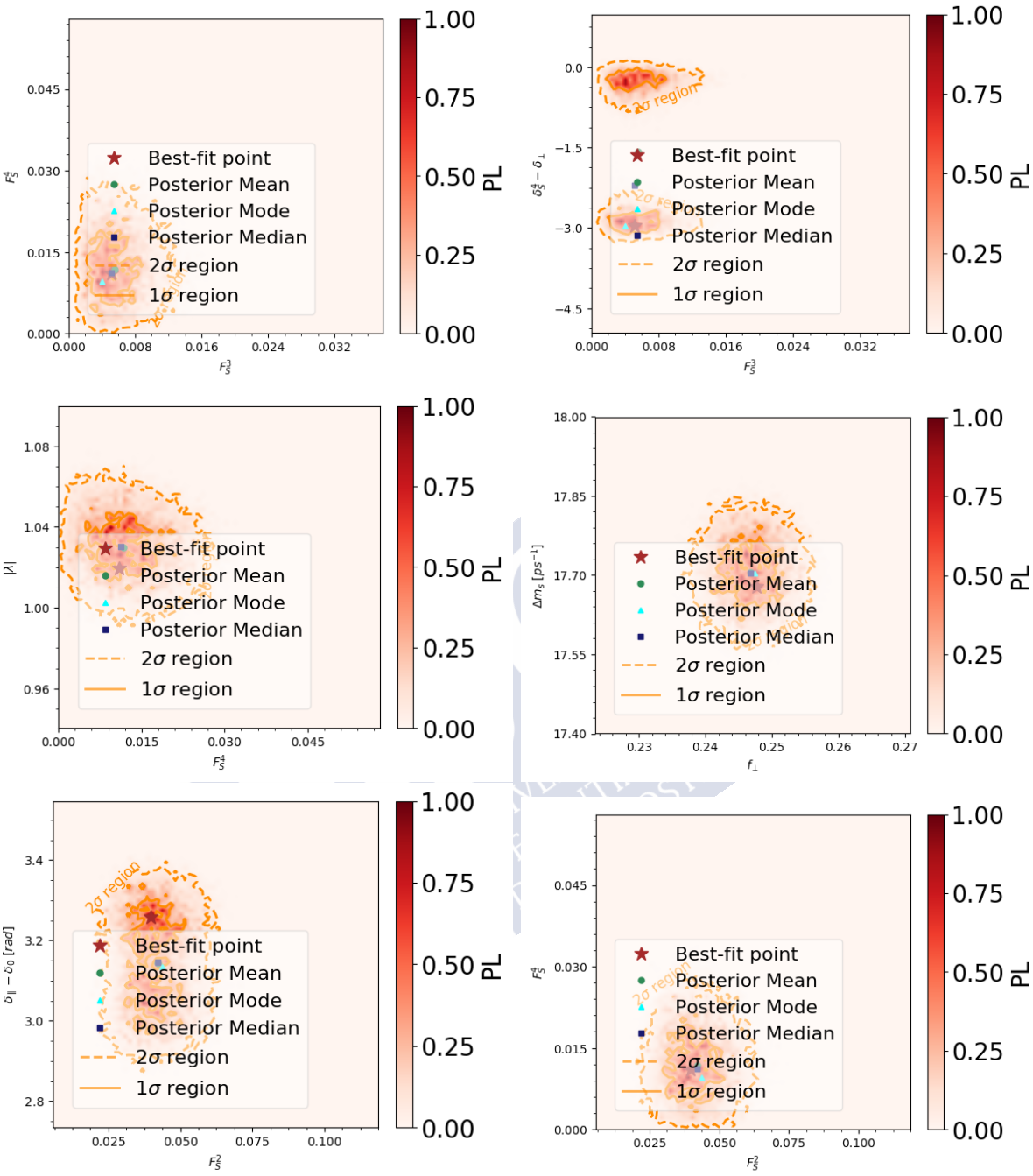
Best-fit point
Posterior Mean
Posterior Mode
Posterior Median
2σ region
1σ region
PL
1.00
0.75
0.50
0.25
0.00
F_S^3
F_S^4
$|\lambda|$
$\delta_S^4 - \delta_\perp$
$\Delta m_s\ [ps^{-1}]$
$f_\perp$
$\delta_\parallel - \delta_0\ [rad]$
F_S^2

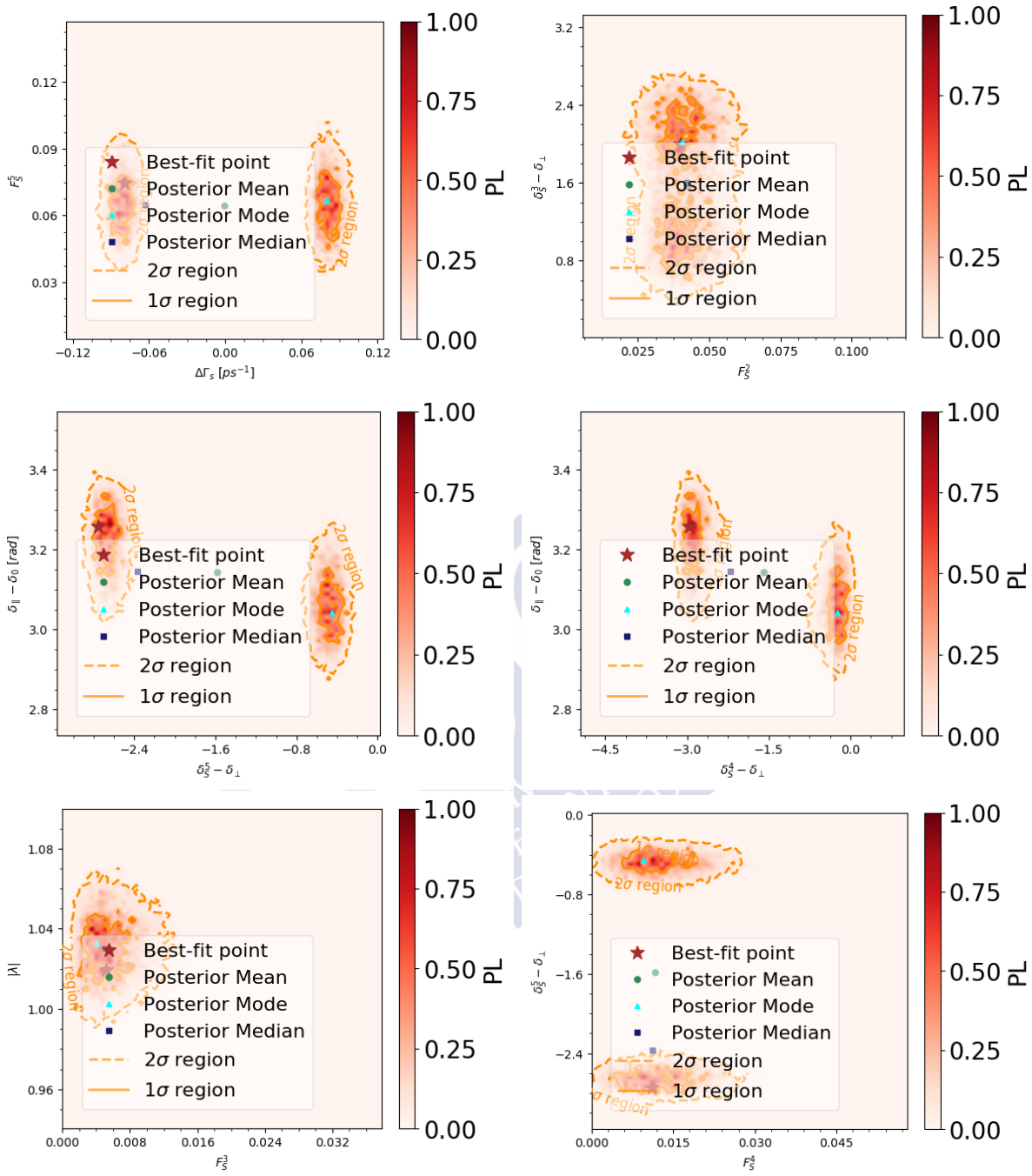
Best-fit point
Posterior Mean
Posterior Mode
Posterior Median
2σ region
1σ region
PL
1.00
0.75
0.50
0.25
0.00
$\Delta\Gamma_s\ [ps^{-1}]$
F_S^5
F_S^2
$\delta_S^3 - \delta_\perp$
$\delta_\parallel - \delta_0\ [rad]$
$\delta_S^5 - \delta_\perp$
$\delta_S^4 - \delta_\perp$
$|\lambda|$
F_S^3
F_S^4

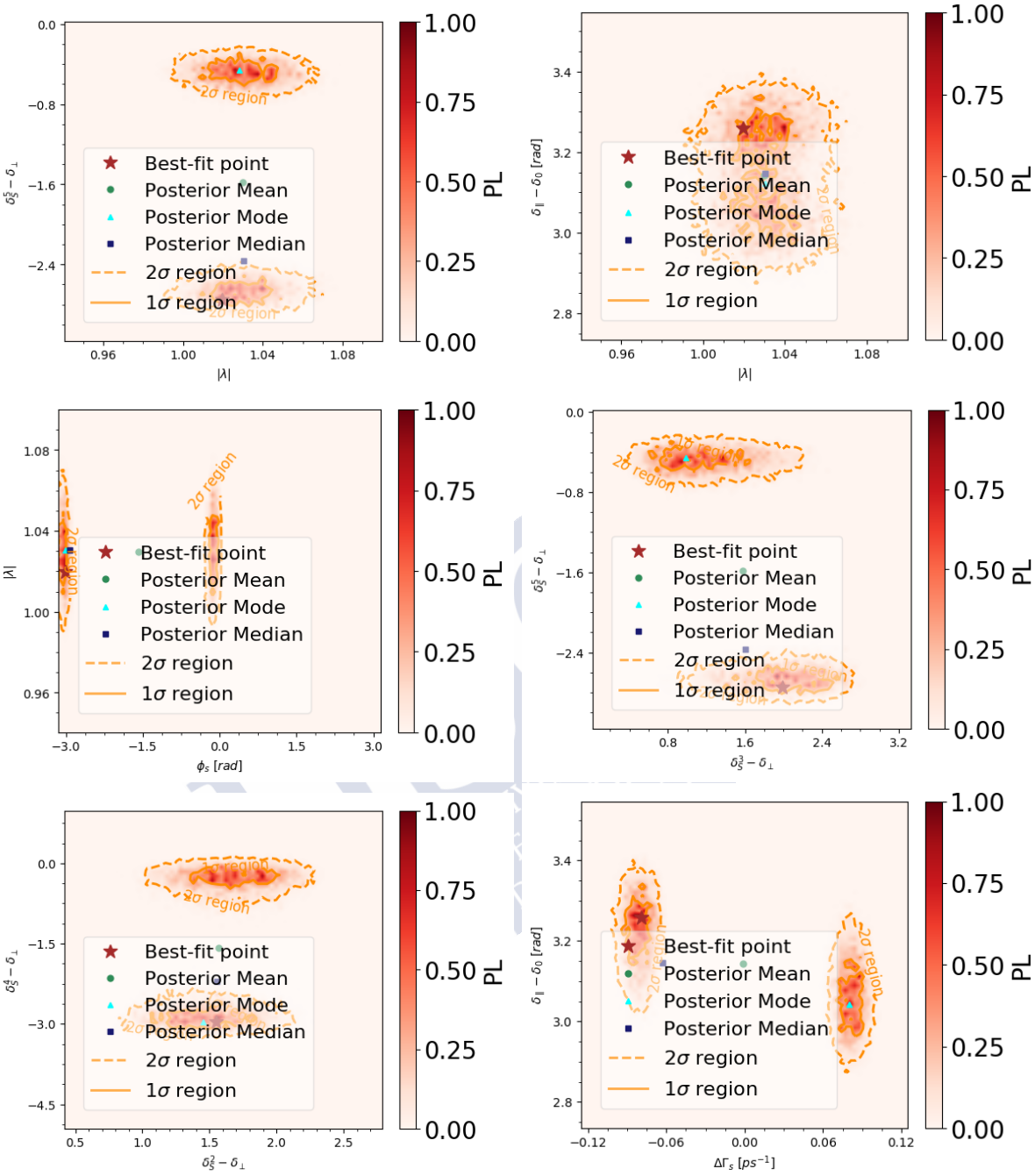
Best-fit point
Posterior Mean
Posterior Mode
Posterior Median
2σ region
1σ region
PL
1.00
0.75
0.50
0.25
0.00
|λ|
$\delta_S^5 - \delta_\perp$
$\delta_\parallel - \delta_0$ [rad]
ϕ_s [rad]
$\delta_S^3 - \delta_\perp$
$\delta_S^4 - \delta_\perp$
$\Delta\Gamma_s$ [ps^{-1}]

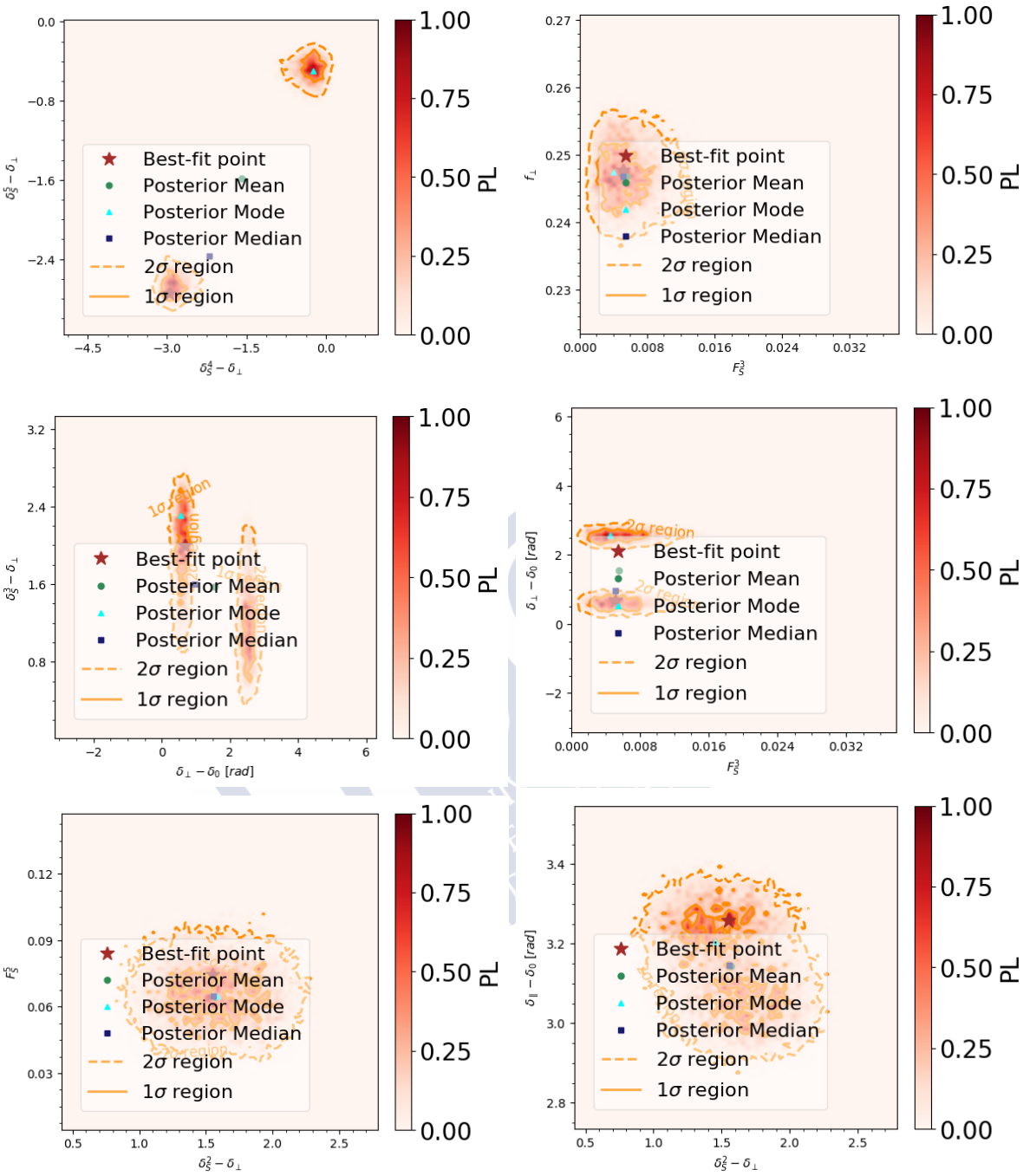
Best-fit point
Posterior Mean
Posterior Mode
Posterior Median
2σ region
1σ region
PL
1.00
0.75
0.50
0.25
0.00
$\delta_S^4 - \delta_\perp$
$\delta_S^5 - \delta_\perp$
$f_\perp$
F_S^3
$\delta_\perp - \delta_0$ [rad]
$\delta_S^3 - \delta_\perp$
$\delta_\parallel - \delta_0$ [rad]
$\delta_S^2 - \delta_\perp$
F_S^5

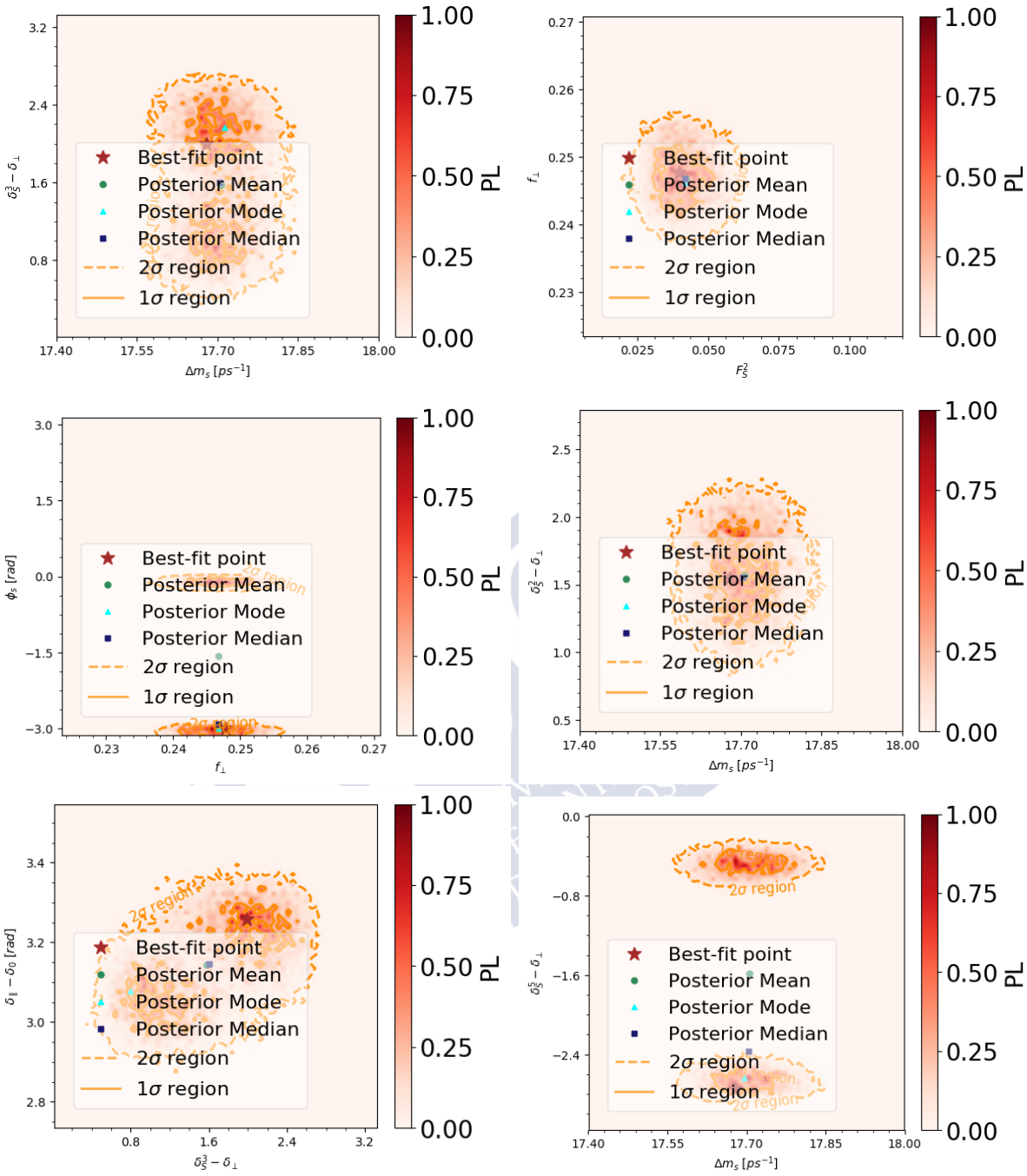
Best-fit point
Posterior Mean
Posterior Mode
Posterior Median
2σ region
1σ region
PL
1.00
0.75
0.50
0.25
0.00
$\Delta m_s\,[ps^{-1}]$
F_S^2
$f_\perp$
$\phi_s\,[rad]$
$\delta_S^3-\delta_\perp$
$\delta_S^2-\delta_\perp$
$\delta_S^5-\delta_\perp$
$\delta_\parallel-\delta_0\,[rad]$

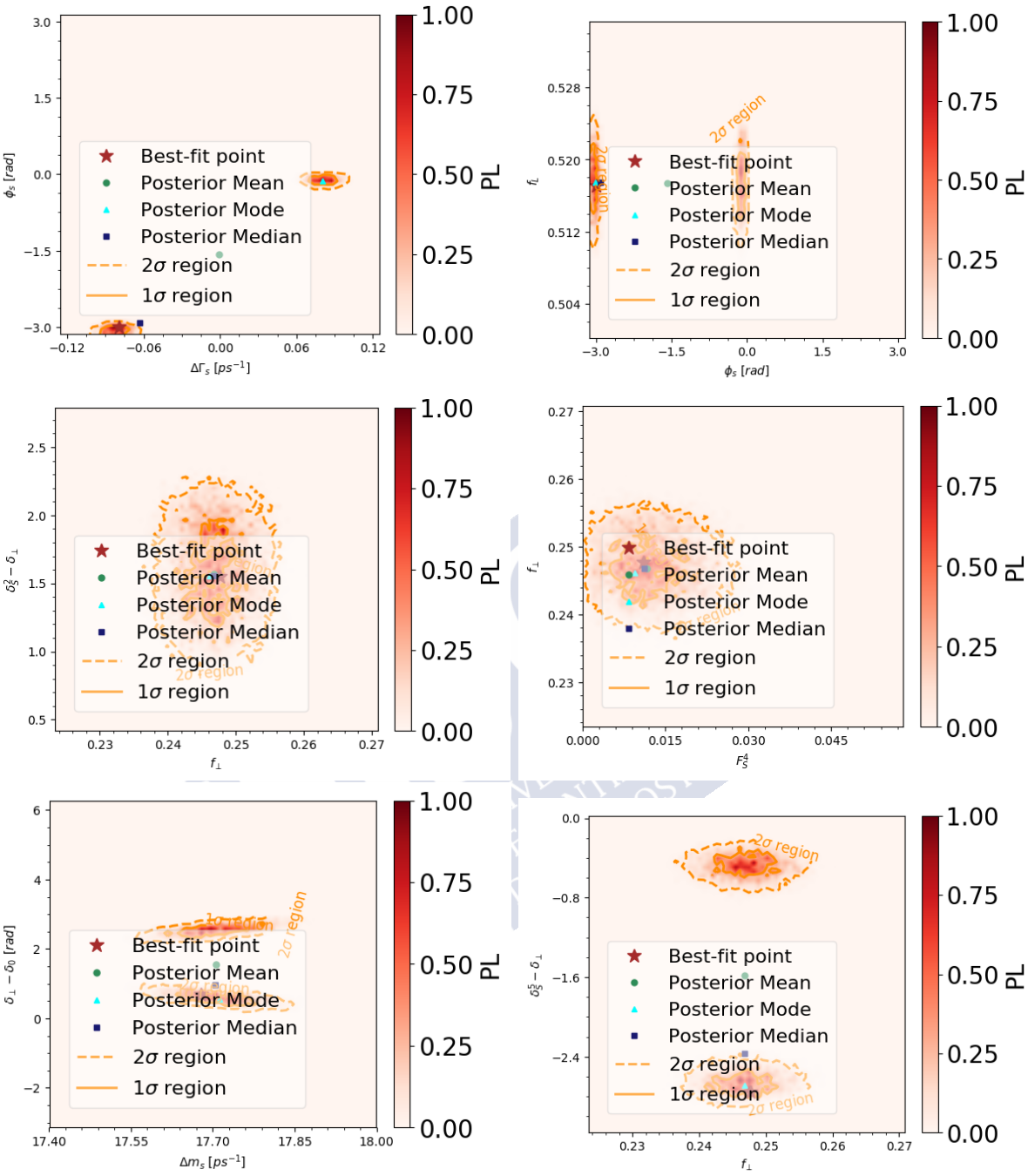
Best-fit point
Posterior Mean
Posterior Mode
Posterior Median
2σ region
1σ region
PL
$\Delta\Gamma_s\ [ps^{-1}]$
$\phi_s\ [rad]$
$f_\perp$
F_S^4
$\delta_S^2 - \delta_\perp$
$\delta_S^5 - \delta_\perp$
$\delta_\perp - \delta_0\ [rad]$
$\Delta m_s\ [ps^{-1}]$

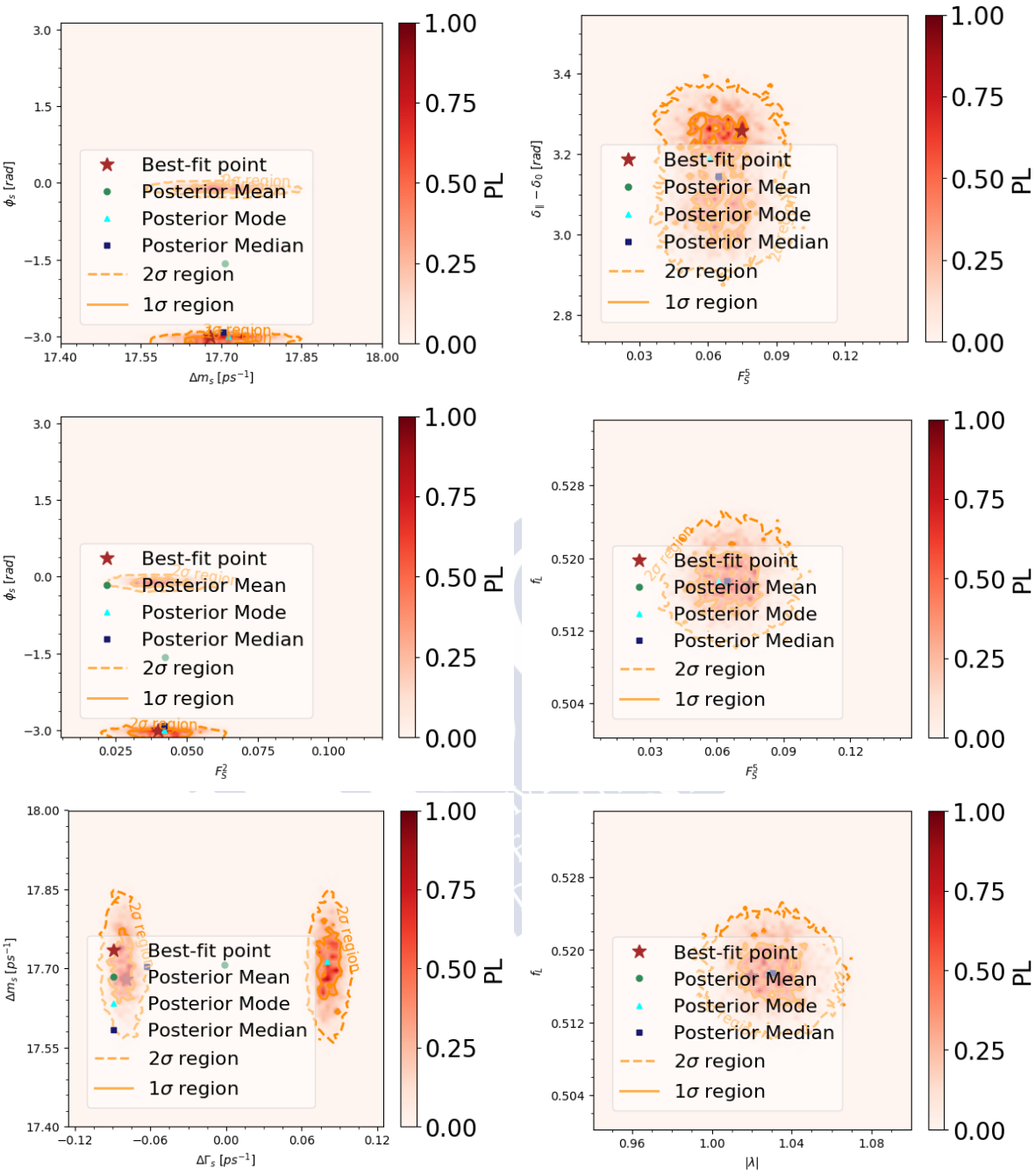
Best-fit point
Posterior Mean
Posterior Mode
Posterior Median
2σ region
1σ region
PL
ϕ_s [rad]
Δm_s [ps^{-1}]
$\delta_\parallel - \delta_0$ [rad]
F_S^5
F_S^2
f_L
$\Delta\Gamma_s$ [ps^{-1}]
$|\lambda|$

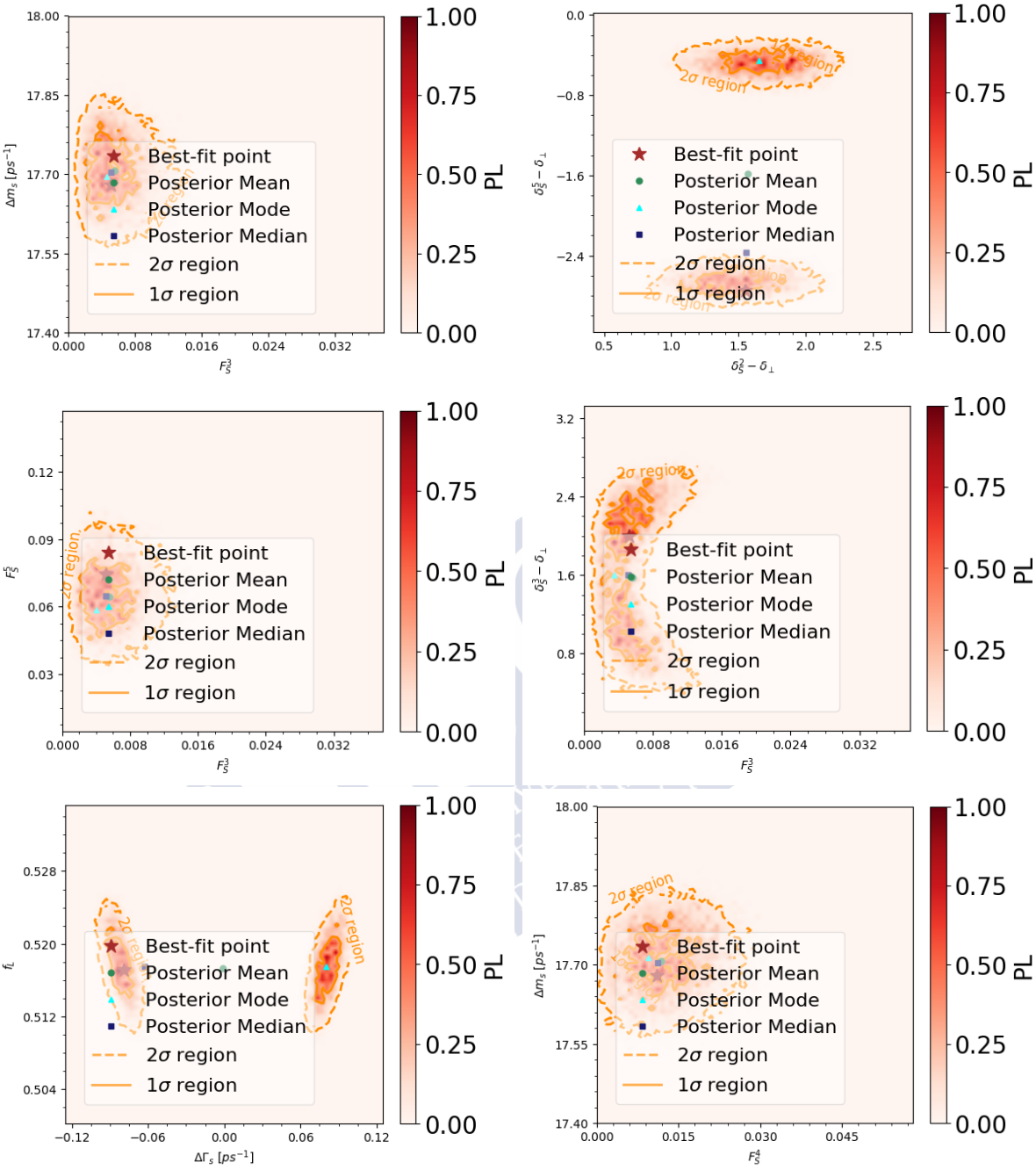
Best-fit point
Posterior Mean
Posterior Mode
Posterior Median
2σ region
1σ region
PL
1.00
0.75
0.50
0.25
0.00
$\Delta m_s\ [ps^{-1}]$
F_S^3
$\delta_S^5 - \delta_\perp$
$\delta_S^2 - \delta_\perp$
F_S^5
$\delta_S^3 - \delta_\perp$
f_L
$\Delta\Gamma_s\ [ps^{-1}]$
F_S^4

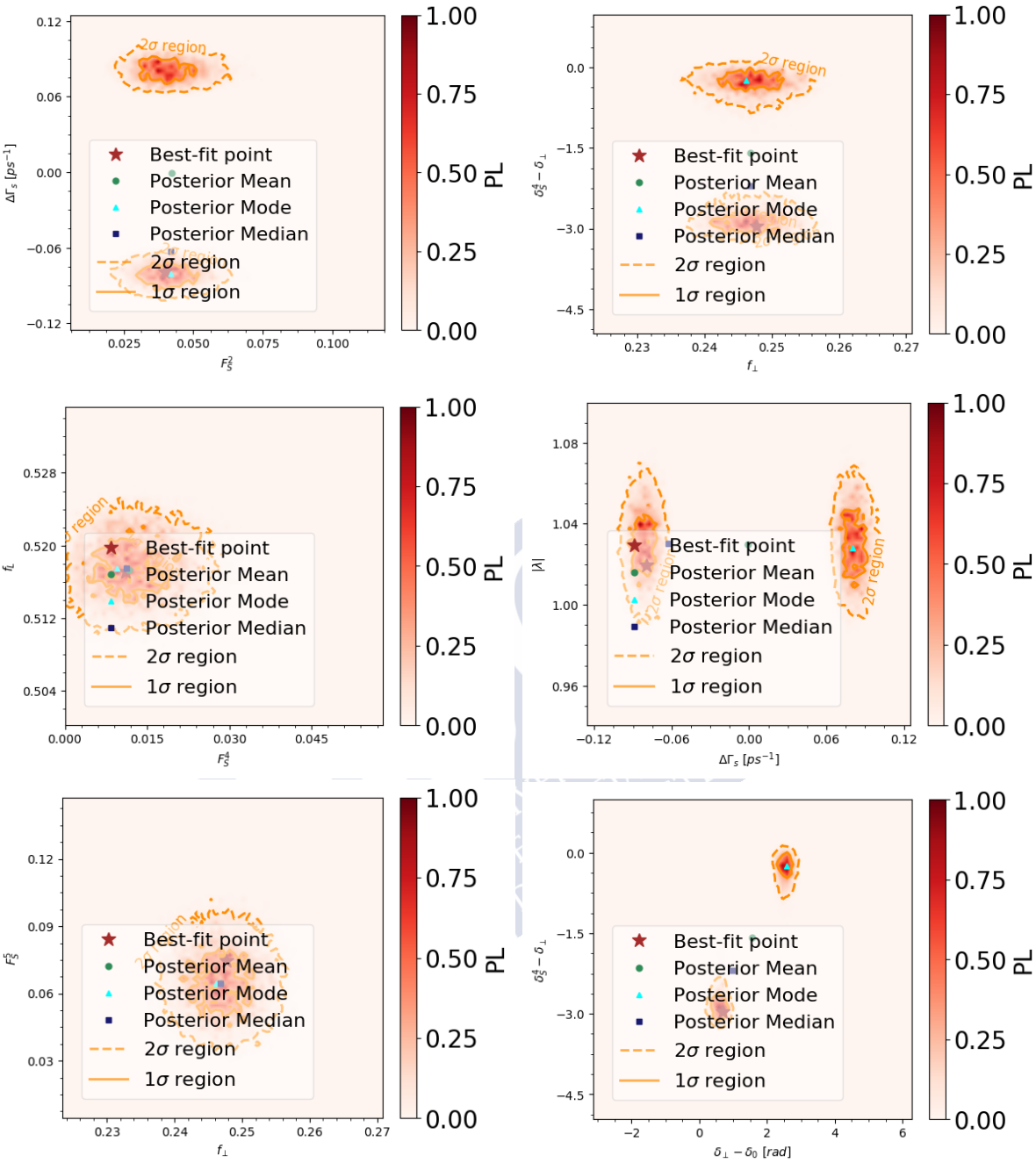
Best-fit point
Posterior Mean
Posterior Mode
Posterior Median
2σ region
1σ region
PL
1.00
0.75
0.50
0.25
0.00
$\Delta\Gamma_s\ [ps^{-1}]$
F_S^2
$\delta_S^4 - \delta_\perp$
$f_\perp$
f_L
F_S^4
$|\lambda|$
$\Delta\Gamma_s\ [ps^{-1}]$
F_S^5
$f_\perp$
$\delta_S^4 - \delta_\perp$
$\delta_\perp - \delta_0\ [rad]$

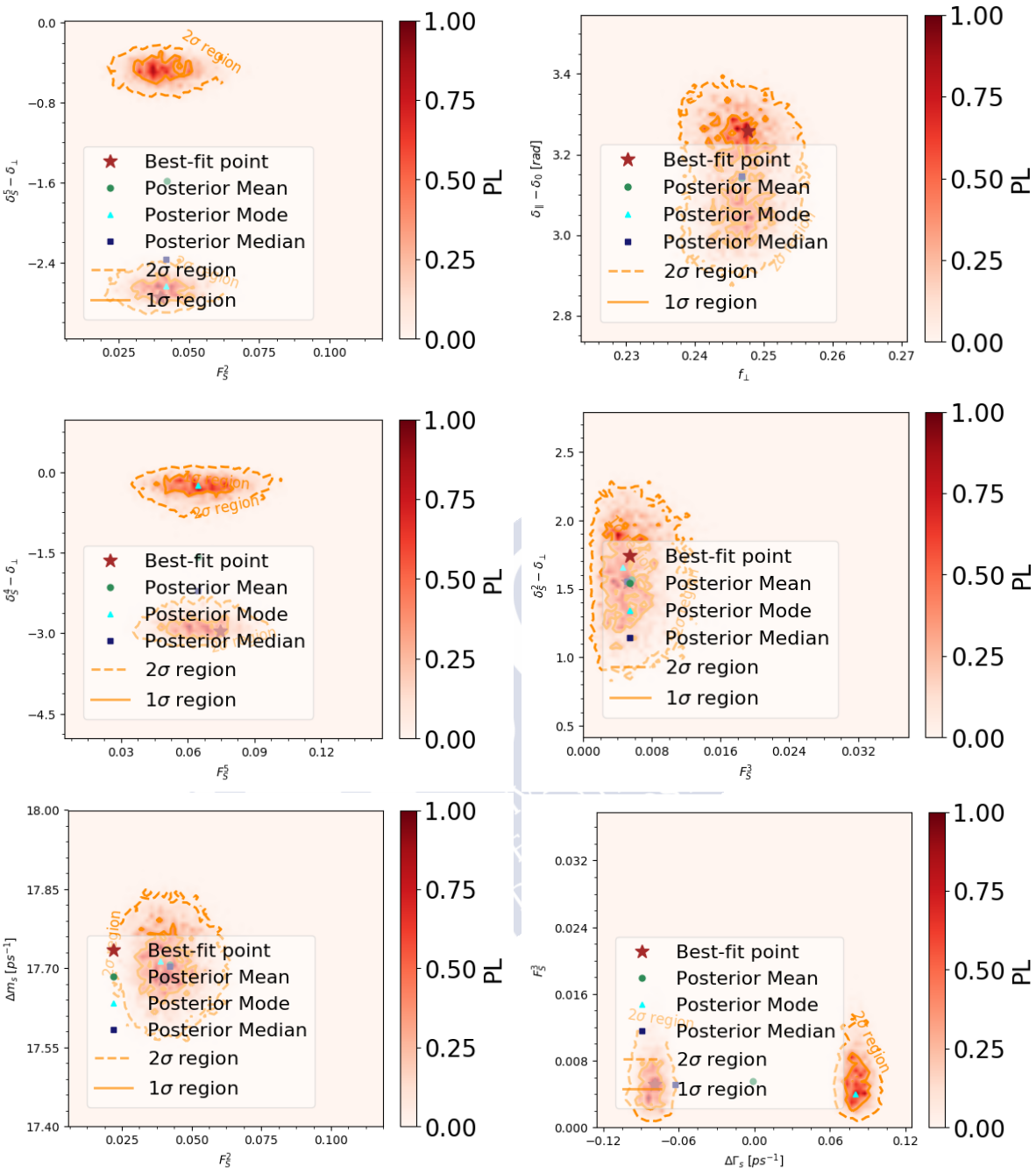
Best-fit point
Posterior Mean
Posterior Mode
Posterior Median
2σ region
1σ region
PL
1.00
0.75
0.50
0.25
0.00
$\delta_S^5 - \delta_\perp$
F_S^2
$\delta_\parallel - \delta_0$ [rad]
$f_\perp$
$\delta_S^4 - \delta_\perp$
F_S^5
$\delta_S^2 - \delta_\perp$
F_S^3
Δm_s [ps^{-1}]
$\Delta\Gamma_s$ [ps^{-1}]

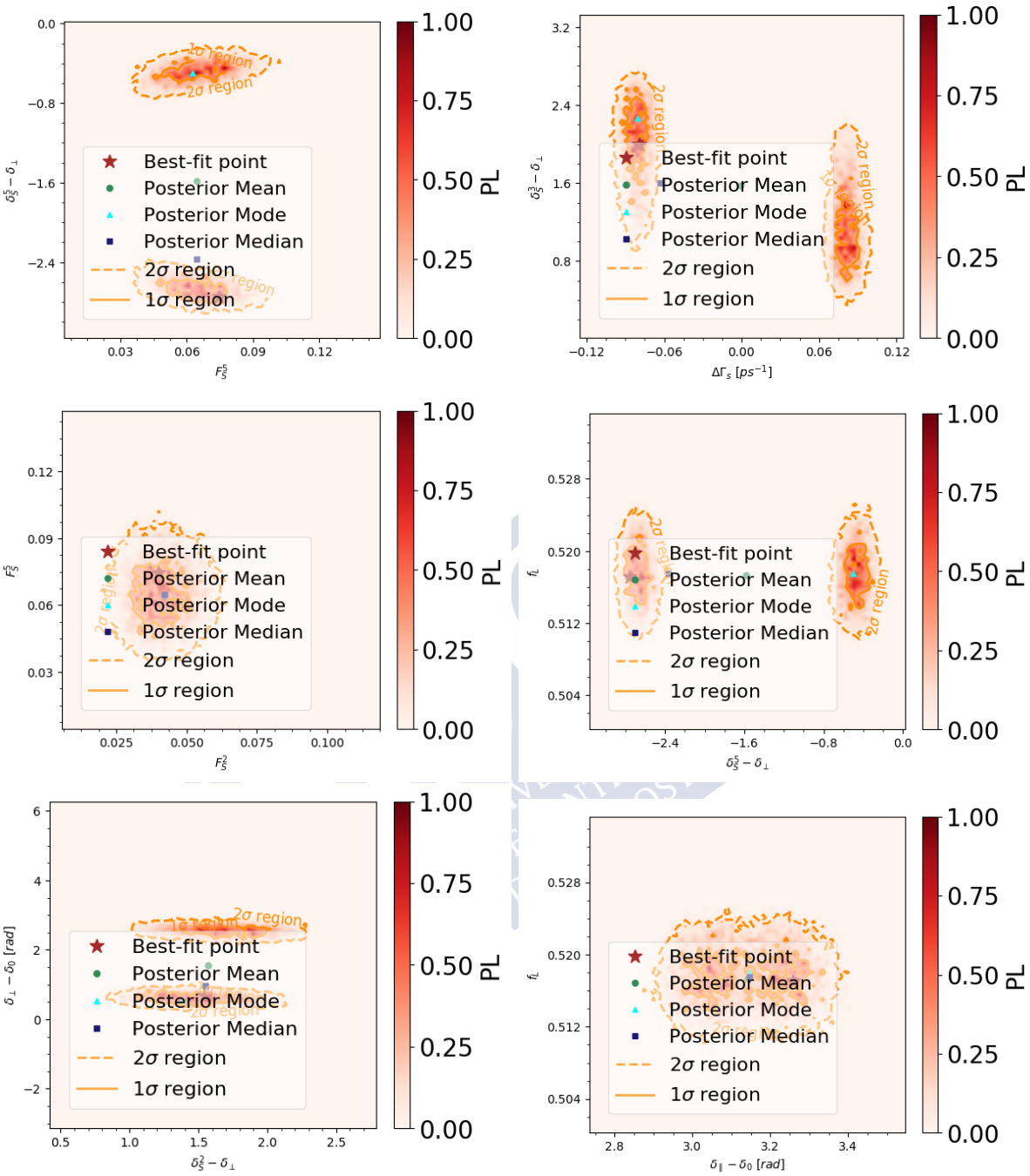
Best-fit point
Posterior Mean
Posterior Mode
Posterior Median
2σ region
1σ region
PL
1.00
0.75
0.50
0.25
0.00
F_S^5
$\delta_S^5 - \delta_\perp$
$\Delta\Gamma_s\ [ps^{-1}]$
$\delta_S^3 - \delta_\perp$
F_S^3
$f_\parallel$
$\delta_\perp - \delta_0\ [rad]$
$\delta_S^2 - \delta_\perp$
$\delta_\parallel - \delta_0\ [rad]$

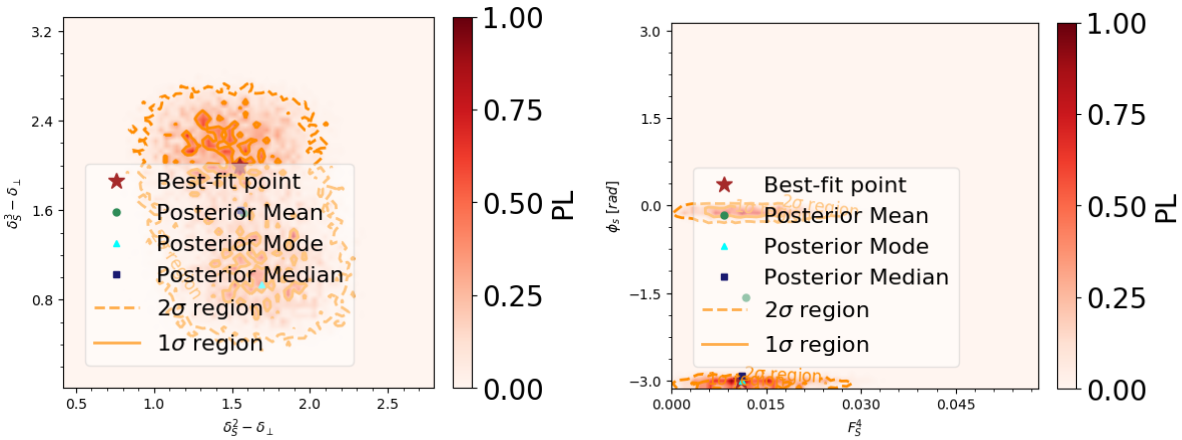

USC
UNIVERSIDADE
DE SANTIAGO
DE COMPOSTELA

Appendix F

MasterCode observables

F.1 Mass Spectrum

The electroweak symmetry breaking of the MSSM leads to 4 physical Higgs particles: a *CP*-odd scalar (A), two *CP*-even neutral scalars (h^0 and H^0) and two charged scalars ($H^\pm$), with masses given by

$$\begin{aligned} M_A^2 &= |\mu|^2 + m_{H_u}^2 + m_{H_d}^2 \\ M_{h^0,H^0}^2 &= \frac{1}{2}\left[M_A^2 + M_Z^2 \mp \sqrt{(M_A^2+M_Z^2)^2 - 4M_Z^2 M_A^2 \cos 2\beta^2}\right] \\ M_{H^\pm}^2 &= M_A^2 + M_W^2 \end{aligned} \tag{F.1}$$

As for the neutralinos, its mass matrix is given by

$$\mathbf{Y} = \begin{pmatrix} M_1 & 0 & -c_\beta s_W M_Z & s_\beta s_W M_Z \\ 0 & M_2 & c_\beta c_W M_Z & -s_\beta c_W M_Z \\ -c_\beta s_W M_Z & c_\beta c_W M_Z & 0 & -\mu \\ s_\beta s_W M_Z & -s_\beta c_W M_Z & -\mu & 0 \end{pmatrix} \tag{F.2}$$

where $s_\beta = \sin\beta$, $c_\beta = \cos\beta$, $c_W = \cos W$, $s_W = \sin W$. The four neutralino masses are obtained diagonalising F.2, $\mathbf{NYN^{-1}} = \mathrm{diag}(\mathrm{m}_{\tilde{\chi}_1^0}, \mathrm{m}_{\tilde{\chi}_2^0}, \mathrm{m}_{\tilde{\chi}_3^0}, \mathrm{m}_{\tilde{\chi}_4^0})$, where $m_{\tilde{\chi}_1^0} < m_{\tilde{\chi}_2^0} < m_{\tilde{\chi}_3^0} < m_{\tilde{\chi}_4^0}$.

In the case of the charginos, its mass matrix is:

$$\mathbf{X} = \begin{pmatrix} M_2 & \sqrt{2} s_\beta M_W \\ \sqrt{2} c_\beta M_W & \mu \end{pmatrix} \tag{F.3}$$

It is diagonalised by two unitary matrices, $\mathbf{U}$, $\mathbf{V}$ as $\mathbf{U^* X V^{-1}} = \mathrm{diag}(\mathrm{m}_{\tilde{\chi}_1^\pm}, \mathrm{m}_{\tilde{\chi}_2^\pm})$, where

$$m_{\tilde{\chi}_1^\pm}^2, m_{\tilde{\chi}_2^\pm}^2 = \frac{1}{2}\left\{|M_2|^2 + |\mu|^2 + M_W^2 \mp \sqrt{(|M_2|^2+|\mu|^2+2M_W^2)^2 - 4|\mu M_2 - M_W \sin 2\beta|^2}\right\} \tag{F.4}$$

For the sfermion, the mass terms are given in the MSSM Lagrangian by [275]:

$$\mathcal{L} = -\frac{1}{2}(\tilde{f}_L^\dagger, \tilde{f}_R^\dagger) \begin{pmatrix} M_L^2 + m_f^2 & m_f X_f^* \\ m_f X_f & M_R^2 + m_f^2 \end{pmatrix} \begin{pmatrix} \tilde{f}_L \\ \tilde{f}_R \end{pmatrix} \tag{F.5}$$

where

$$
\begin{aligned}
M_L^2 &= M_{\tilde{F}}^2 + M_Z^2 \cos 2\beta (I_3^f - Q_f s_W^2), \\
M_R^2 &= M_{\tilde{F}'}^2 + M_Z^2 \cos 2\beta Q_f s_W^2, \\
X_f &= A_f - \mu * \cot\beta, \tan\beta
\end{aligned}
\tag{F.6}
$$

$\cot\beta$ and $I_3^f = \frac{1}{2}$ ($\tan\beta$ and $I_3^f = -\frac{1}{2}$) correspond to up-type squarks (down-type squarks and sleptons) and $M_{\tilde{F},\tilde{F}'}$ denote the left-handed and right-handed soft SUSY breaking mass parameters respecitvely, and Q_f is the electromagnetic charge. The sfermion mass eigenstate can be obtained with unitary matrix, $\mathbf{U}_{\tilde{\mathbf{f}}}$, giving the eigenvalues:

$$
m_{\tilde{f}_{1,2}}^2 = m_f^2 + \frac{1}{2}\left[(M_L^2 - M_R^2)^2 + 4m_f^2 |X_f|^2\right] \tag{F.7}
$$

F.2 Dark Matter Relic Density

The cosmological dark matter density is one of two most important dark matter constraints. Its value is measured by Planck to be $\Omega_{\mathrm{CDM}} h^2 = 0.1186 \pm 0.0022_{\mathrm{EXP}} \pm 0.0024_{\mathrm{TH}}$ [271, 272, 301], where h is he reduced Hubble constant.Assuming the neutralino to be the supersymmetric DM candidate and the only responsible for the DM relic density, different (co)annihilation mechanisms are suggested to bring the obtained density into the observed range. Some of these mechanisms (hereafter, DM mechanisms) are:

1. Bulk region: in the case where the neutralino is mostly Bino-like and at least one of the sfermions is not too heavy, the neutralino annihilates to a pair of SM particles (e.g., a pair of fermions) via t-channel exchange of a sfermion.

2. Sfermion coannihilation: it takes place when sfermions have nearly degenerate masses and the LSP is mostly Bino-like. The condition for stau and stop coannihilation ($\tilde{f}$) is:

$$
\left(\frac{m_{\tilde{f}}}{m_{\tilde{\chi}_1^0}} - 1\right) < 0.15 \tag{F.8}
$$

3. A/H, h and Z Funnels: in this mechanism, the neutralino is mostly Bino-like and $\left|\frac{M_{A,H,h}}{m_{\tilde{\chi}_1^0}} - 2\right| < 0.1$

4. Chargino coannihilation: fulfilled when the lightest chargino and neutralino are nearly degenerate: $\left(\frac{m_{\tilde{\chi}_1^\pm}}{m_{\tilde{\chi}_1^0}} - 2\right) < 0.25$, being the LSP either Higgsino-like (with very heavy neutralinos) or Bino-like.

5. Focus-point region: fulfilled when the LSP has an enhanced Higgsino component as a result of a near-degeneracy in the neutralino mass matrix, $\left(\frac{\mu}{m_{\tilde{\chi}_1^0}} - 1 < 0.3\right)$.

6. *Hybrid* regions: where more than one of the aforementioned DM mechanism dominate.

F.3 Neutralino Scattering off Nuclei

One of the most powerful ways in which to search for DM is to look for its scattering on nuclei in low-background underground experiments, both in direct (XENON1T [318], LUX [303], PandaX-II [302] ...) and indirect (IceCube [322], PICO [323]) dark matter detection experiments, that include searches for γ-rays, neutrinos, positrons or antiprotons from DM annihilations near the Galactic Center, Galactic Halo and in dwarf galaxies, and for highly energetic neutrinos produced by the annihilations of DM particles inside the Sun or Earth. In both cases, the signals are proportional to the local density of dark matter and the χ-nucleon cross-section. Within MSSM, four observables can contribute to this scattering: the spin-independent and dependent cross sections of neutralinos on protons and nucleons. These contributions appear in non velocity dependent part of the MSSM Lagrangian that addresses the χ-nucleon scattering:

$$\mathcal{L} = \alpha_{2i}\bar{\chi}\gamma^{\mu}\gamma^{5}\bar{q}_i\gamma_{\mu}\gamma^{5}q_i + \alpha_{3i}\bar{\chi}\chi\bar{q}_i q_i \tag{F.9}$$

where the coefficients sum over the quark generations, denoting i up-type ($i = 1$) and down-type ($i = 2$) quarks. The first term is spin-dependent, while the second part is spin-dependent. The cross-sections for these two parts are obtained from α_{3i} and α_{2i}, respectively.

F.3.1 Spin-Independent Term

The scalar or spin-independent (SI) part of the cross-section can be written in the zero-momentum-transfer limit as [287]

$$\sigma_{\mathrm{SI}} = \frac{4m_r^2}{\pi}[Zf_p + (A - Z)f_n]^2 \tag{F.10}$$

where m_r is the χ-nuclear reduced mass, Z the atomic number, A the atomic weight, and for $N = n$ or p

$$\frac{f_N}{m_N} = \sum_{q=u,d,s} f_{T_q}^{(N)}\frac{\alpha_{3q}}{m_q} + \frac{2}{27}f_{TG}^{(N)}\sum_{q=c,b,t}\frac{\alpha_{3q}}{m_q} \tag{F.11}$$

and

$$m_N f_{T_q}^{(N)} \equiv \langle N|m_q\bar{q}q\rangle \equiv m_q B_q^{(N)},\ f_{TG}^{(N)} = 1 - \sum_{q=u,d,s} f_{T_q}^{(N)} \tag{F.12}$$

The π-nucleon sigma term, $\Sigma_{\pi n}$, may be written as

$$\Sigma_{\pi n} \equiv \frac{1}{2}(m_u + m_d) \times (B_u^{(N)} + B_d^{(N)}) \tag{F.13}$$

It is related to the strange scalar density in the nucleon, y, by

$$y = 1 - \sigma_0/\Sigma_{\pi N} \tag{F.14}$$

F.3.2 Spin-Dependent Term

The scalar or spin-dependent (SD) part of the cross-section can be written in the zero-momentum-transfer limit as [287]

$$\sigma_{\mathrm{SD}} = \frac{32}{\pi}G_F^2 m_r^2 \Lambda^2 J(J+1) \tag{F.15}$$

where J is the spin of the nucleus and

$$\Lambda \equiv \frac{1}{J}(a_p \langle S_p \rangle + a_n \langle S_n \rangle) \tag{F.16}$$

and

$$a_p = \sum_q \frac{\alpha_{2q}}{\sqrt{2}G_f}\Delta_q^{(p)},\ a_n = \sum_i \frac{\alpha_{2q}}{\sqrt{2}G_f}\Delta_q^{(n)} \tag{F.17}$$

The factors $\Delta_q^{(N)}$ parametrize the quark spin contennt of the nucleon and are only significant for the light (u,d,s) quarks [287].

The biggest uncertainty in spin-independent scattering is due to the poor knowledge of the $\langle N|q\bar{q}|N\rangle$ matrix elements linked to the π-nucleon σ term, $\Sigma_{\pi N}$, followed by uncertainties in the SU(3) octet symmetry-breaking contribution to the nucleon mass, σ_0. The treatment of the spin-independent nuclear scattering matrix element within `MasterCode` is performed with `SSARD`.

Given the expressions in F.10 and F.15, experiments with heavy elements such as Ge and Xe are more sensitive to $\sigma_{\rm SI}$ (proportional to Z^2) than to $\sigma_{\rm SD}$. The SD cross sections are on the other hand nearly independent on the quark masses [287].

F.4 Anomalous Magnetic Moment of the Muon

The magnetic moment for a given lepton, l, is related to its intrinsic spin, $\vec{S}$, through the Dirac equation:

$$\vec{M} = g_l \frac{e}{2m_l}\vec{S} \tag{F.18}$$

Where m_l is the lepton mass and g_l is the gyromagnetic ratio. Quantum loop effects to the Dirac prediction are parameterized by the anomalous magnetic moment

$$a_l \equiv \frac{g_l - 2}{2} \tag{F.19}$$

While for the electron this quantity is the most precisely measured [324–326] and calculated [59] quantity in Nature, this is not the case for the muon. For this particle, $g_\mu = 2$, while

$$a_\mu^{\rm SM} = a_\mu^{\rm QED} + a_\mu^{\rm EW} + a_\mu^{\rm Had} \tag{F.20}$$

where photonic and leptonic contributions are embedded inside $a_\mu^{\rm QED}$, $W^\pm, Z$ or Higgs loops are accounted for in $a_\mu^{\rm EW}$ and $a_\mu^{\rm Had}$ contain hadronic (quark and gluon) loop contributions:

$$a_\mu^{\rm QED} = 116584718.95(0.08) \times 10^{-11} \tag{F.21}$$

where the main contribution to the uncertainty comes from the fine structure constant, α [327]

$$a_\mu^{\rm EW} = a_\mu^{\rm EW}[1-{\rm loop}] + {\rm a}_\mu^{\rm EW}[2-{\rm loop}] = 153.6(1.0) \times 10^{-11} \tag{F.22}$$

and

$$a_\mu^{\rm Had}[{\rm LO}] = 6931(33)(7) \times 10^{-11},\ {\rm a}_\mu^{\rm Had}[{\rm N(N)LO}] = 19(26) \times 10^{-11} \tag{F.23}$$

where the error is dominated by systematic uncertainties and perturbative QCD for Leading Order (LO), and by hadronic light-by-light uncertainty in (Next-to-)Next-Leading Order (N(N)NLO). Summing all these contributions give rise to the SM prediction:

$$a_\mu^{\rm SM} = 116591823(1)(34)(26) \times 10^{-11} \tag{F.24}$$

being the errors due to the electroeak, lowest-order hadronic and higher-order hadronic contributions, respectively. As it can be seen, the hadronic contribution to the anomalous magnetic moment dominates the uncertainty. The most precise measurement of this quantity has been made studying the precession of μ^+ and μ^- in a constant external magnetic field inside a confining storage ring by the E821 experiment at Brookhaven National Lab (BNL), yielding [327–331]:

$$a_\mu^{\rm exp} = 11659209.1(5.4)(3.3) \times 10^{-10} \tag{F.25}$$

where the first error is statistic and the second systematic. Therefore

$$\Delta a_\mu = a_\mu^{\rm exp} - a_\mu^{\rm SM} = 268(63)(43) \times 10^{-11} \tag{F.26}$$

where the first error is experimental and the second theoretical. Hence, there is a 3.5σ discrepancy between the experimental and SM results. Possible explanations for such difference arise in a Supersymmetric scenario, where there is an additional contribution:

$$a_\mu^{\rm SUSY} \simeq \pm 130 \times 10^{-11} \left(\frac{100{\rm GeV}}{m_\Lambda}\right)^2 \tan\beta \tag{F.27}$$

An alternative scenario that can give explanation to this disagreement is that with a *dark photon* [332], a relatively light vector boson from the dark matter sector that couples to the SM sector through mixing with the ordinary photon.

F.5 Electroweak Precision Observables

Electroweak precision observables (henceforth, EWPO), are known with high accuracy. Therefore, they serve as useful constraints in NP models. The EWPO that are used within the `MasterCode` framework are the following:

Inclusive Quantities: Cross-Sections and Partial Widths:

- Z mass, M_Z
- Total decay width, Γ_Z
- Hadronic pole cross-section $\sigma^0_{\rm had} \equiv \frac{12\pi}{M_Z^2}\frac{\Gamma_{ee}\Gamma_{\rm had}}{\Gamma_Z^2}$
- Ratio of hadronic to leptonic decay $R_l^0 \equiv \Gamma_{\rm had}/\Gamma_{ll}$
- Ratio of partial decay width into $q\bar{q}$ ($q = b, c$) to the total hadronic width $R_q^0 = \Gamma_{q\bar{q}}/\Gamma_{rmhad}$

Asymmetries and Effective Fermionic Weak Mixing Angle:

- Asymmetry parameters, $\mathcal{A}_f \equiv 2\frac{{\rm Re}({\rm g_{Vf}}7{\rm g_{Af}})}{1+{\rm Re}({\rm g_{Vf}}/{\rm g_{Af}})^2}$, where g_{Vf} and g_{Af} are the effective vector and axial couplings

- Forward backward asymmetries, $A_{\rm FB}^{0,f} = \frac{3}{4}\mathcal{A}_e\mathcal{A}_f$
- Effective fermionic weak mixing angle, $\sin\theta_{\rm eff}^{f\ 2}$

Observables with the superscript 0 are *pseudo-observables*, derived from measured quantities to facilitate the theoretical interpretation.

F.6 Flavour Physics Observables

Flavour Physics Observables (hereafter, FPO) are also included within the `MasterCode` framework, as their observables are also affected by NP. The B-meson decays $B_{s,d} \to \mu^+\mu^-$, $B \to X_s\gamma$, $B \to \tau\nu$, $B \to X_s ll$, the K-mesond decays $K \to \mu\nu$, $K \to \pi\nu\bar{\nu}$, observables related to $B - \bar{B}$ mixing ΔM_{B_s}, $\frac{\Delta M_{B_s}^{\rm EXP/SM}}{\Delta M_{B_d}^{\rm EXP/SM}}$ and $\Delta\epsilon_K$ are included.

Appendix G

ϕ_s phenomenological studies

G.1 $\mathcal{B}(B_s^0 \to \mu^+\mu^-)$ and $\mathcal{B}(B_d^0 \to \mu^+\mu^-)$

$$\mathcal{B}(B^0_{s,d} \to \mu^+\mu^-) = \tau_{B_s,B_d}\Gamma(B^0_{s,d} \to \mu^+\mu^-) = \tau_{B_s,B_d}\frac{f^2_{B_{s,d}} M^3_{B_{s,d}}\beta_\mu}{16\pi}\left(|A_{B_s,B_d}|^2 + \beta^2_\mu |B_{B_s,B_d}|^2\right), \tag{G.1}$$

where

$$\beta_\mu = \sqrt{1 - \frac{4m^2_\mu}{M^2_{B_{s,d}}}}. \tag{G.2}$$

and

$$A_{B_s,B_d} = \frac{m_s M_{B_s}}{m_{s,d} + m_b}\mathrm{Im}(C_P - \tilde{C}_P) + \frac{2m_\mu}{M_{B_s}}\mathrm{Im}(C_A - \tilde{C}_A), \tag{G.3}$$

$$B_{B_s,B_d} = \frac{2G^2_F M^2_W m_\mu}{\pi^2 M_{B_s}} B^\mu_{S\gamma\gamma} - \frac{m_s M_K}{m_{s,d} + m_b}\mathrm{Re}(C_S - \tilde{C}_S), \tag{G.4}$$

$$C_P = -C_S, \tilde{C}_P = \tilde{C}_S \tag{G.5}$$

G.1.1 $\mathcal{B}(B_s^0 \to \mu^+\mu^-)$

Within the SM, the Wilson coefficients are,

$$C_{A,\mathrm{SM}} = -\frac{[\alpha_2(M_Z)]^2}{2M^2_W}\left(V^*_{ts}V_{tb}Y_t + V^*_{cs}V_{cb}Y_c\right), \tag{G.6}$$

$$\tilde{C}_{A,\mathrm{SM}} = C_{S,\mathrm{SM}} = \tilde{C}_{S,\mathrm{SM}} = C_{P,\mathrm{SM}} = \tilde{C}_{P,\mathrm{SM}} \simeq 0, \tag{G.7}$$

where $Y_t = 0.963$ and $Y_c = 3.243 \times 10^{-4}$.

$$\tilde{C}_S = -\frac{2}{3}\frac{\alpha_s \alpha_2 m_\mu}{M_W^2}\frac{\mu M_3}{M_A^2 \tilde{m}_d^2}(\delta_d^{RR})_{32}\frac{\tan\beta^3}{(1+\epsilon_g \tan\beta)^2(1+\epsilon_l \tan\beta)}G(x_d^3, x_d^Q) \tag{G.8}$$

$$\begin{aligned} C_S = &-\frac{2}{3}\frac{\alpha_s \alpha_2 m_\mu}{M_W^2}\frac{\mu M_3}{M_A^2 \tilde{m}_Q^2}\left(\delta_d^{LL}\right)_{32}\frac{\tan^3\beta}{(1+\epsilon_g \tan\beta)^2(1+\epsilon_\ell \tan\beta)}G\left(x_Q^3, x_Q^d\right) \\ &+\frac{(\alpha_2)^2 m_\mu m_t^2}{8M_W^4}\frac{\mu A_t}{M_A^2 \tilde{m}_Q^2}V_{ts}^* V_{tb}\frac{\tan^3\beta[1+(\epsilon_g+\epsilon_Y y_t^2)\tan\beta]^2}{(1+\epsilon_g \tan\beta)^4(1+\epsilon_\ell \tan\beta)}F\left(x_Q^\mu, x_Q^u\right) \\ &+\frac{(\alpha_2)^2 m_\mu}{4M_W^2}\frac{\mu M_2}{M_A^2 \tilde{m}_Q^2}\left(\delta_u^{LL}\right)_{32}\frac{\tan^3\beta}{(1+\epsilon_g \tan\beta)^2(1+\epsilon_\ell \tan\beta)}G\left(x_Q^2, x_Q^\mu\right), \end{aligned} \tag{G.9}$$

with

$$\epsilon_g = \frac{2\alpha_s}{3\pi}\frac{\mu M_3}{\tilde{m}_Q^2}F\left(x_Q^3, x_Q^d\right), \tag{G.10}$$

$$\epsilon_Y = \frac{1}{16\pi}\frac{\mu A_t}{\tilde{m}_Q^2}F\left(x_Q^\mu, x_Q^u\right), \tag{G.11}$$

$$\epsilon_\ell \simeq -\frac{3\alpha_2}{16\pi}, \tag{G.12}$$

where $x_d^3 = M_3^2/\tilde{m}_d^2$, $x_d^Q = \tilde{m}_Q^2/\tilde{m}_d^2$, $x_Q^3 = M_3^2/\tilde{m}_Q^2$, $x_Q^d = \tilde{m}_d^2/\tilde{m}_Q^2$, $x_Q^\mu = \mu^2/\tilde{m}_Q^2$, $x_Q^u = \tilde{m}_u^2/\tilde{m}_Q^2$, $x_Q^2 = M_2^2/\tilde{m}_Q^2$, and $x_Q^\mu = \mu^2/\tilde{m}_Q^2$.

G.1.2 $\mathcal{B}(B_d^0 \to \mu^+\mu^-)$

Within the SM, the Wilson coefficients are,

$$C_{A,\mathrm{SM}} = -\frac{[\alpha_2(M_Z)]^2}{2M_W^2}\left(V_{td}^* V_{tb} Y_t + V_{cd}^* V_{cb} Y_c\right), \tag{G.13}$$

$$\tilde{C}_{A,\mathrm{SM}} = C_{S,\mathrm{SM}} = \tilde{C}_{S,\mathrm{SM}} = C_{P,\mathrm{SM}} = \tilde{C}_{P,\mathrm{SM}} \simeq 0, \tag{G.14}$$

where $Y_t = 0.963$ and $Y_c = 3.243 \times 10^{-4}$.

$$\tilde{C}_S = -\frac{2}{3}\frac{\alpha_s \alpha_2 m_\mu}{M_W^2}\frac{\mu M_3}{M_A^2 \tilde{m}_d^2}(\delta_d^{RR})_{31}\frac{\tan\beta^3}{(1+\epsilon_g \tan\beta)^2(1+\epsilon_l \tan\beta)}G(x_d^3, x_d^Q) \tag{G.15}$$

$$\begin{aligned} C_S = &-\frac{2}{3}\frac{\alpha_s \alpha_2 m_\mu}{M_W^2}\frac{\mu M_3}{M_A^2 \tilde{m}_Q^2}\left(\delta_d^{LL}\right)_{31}\frac{\tan^3\beta}{(1+\epsilon_g \tan\beta)^2(1+\epsilon_\ell \tan\beta)}G\left(x_Q^3, x_Q^d\right) \\ &+\frac{(\alpha_2)^2 m_\mu m_t^2}{8M_W^4}\frac{\mu A_t}{M_A^2 \tilde{m}_Q^2}V_{td}^* V_{tb}\frac{\tan^3\beta[1+(\epsilon_g+\epsilon_Y y_t^2)\tan\beta]^2}{(1+\epsilon_g \tan\beta)^4(1+\epsilon_\ell \tan\beta)}F\left(x_Q^\mu, x_Q^u\right) \\ &+\frac{(\alpha_2)^2 m_\mu}{4M_W^2}\frac{\mu M_2}{M_A^2 \tilde{m}_Q^2}\left(\delta_u^{LL}\right)_{31}\frac{\tan^3\beta}{(1+\epsilon_g \tan\beta)^2(1+\epsilon_\ell \tan\beta)}G\left(x_Q^2, x_Q^\mu\right), \end{aligned} \tag{G.16}$$

G.2 Wilson coefficients

G.2.1 $\Delta F = 1$ Processes

$$\epsilon = \frac{2\alpha_s \mu M_{\tilde{g}} F(x_Q^3, x_Q^d)}{3\pi \tilde{m}_Q^2} \tag{G.17}$$

(G.18)

where

$$x_Q^3 = \frac{M_{\tilde{g}}^2}{\tilde{m}_Q^2},\ x_Q^d = \frac{\tilde{m}_d^2}{\tilde{m}_d^2} \tag{G.19}$$

$$C_7^{\rm NP} = C_{7,8}^{H^\pm} + C_{7,8}^{\chi^\pm} + C_{7,8}^{\tilde{g}} \tag{G.20}$$

$$C_{7,8}^{H^\pm} \simeq \left(\frac{1-\epsilon\tan\beta}{1+\epsilon\tan\beta}\frac{1}{2}h_{7,8}(y_t)\right),\ y_t = m_t^2/M_{H^\pm}^2 \tag{G.21}$$

$$\frac{4G_F}{\sqrt{2}}C_{7,8}^{\chi^\pm} \simeq \frac{g_2^2}{\tilde{m}^2}\left[\frac{(\delta_u^{LL})_{32}}{V_{tb}V_{ts}^*}\frac{\mu M_2}{\tilde{m}^2}f_{7,8}^{(1)}(x_2,x_\mu) + \frac{m_t^2}{M_W^2}\frac{A_t\mu}{\tilde{m}^2}f_{7,8}^{(2)}(x_\mu)\right]\frac{\tan\beta}{(1+\epsilon\tan\beta)}\ x_2 = \frac{|M_2|}{\tilde{m}^2},\ x_\mu = \frac{|\mu|}{\tilde{m}^2} \tag{G.22}$$

$$\frac{4G_F}{\sqrt{2}}C_{7,8}^{\tilde{g}} \simeq \frac{g_s^2}{\tilde{m}^2}\left[\frac{M_{\tilde{g}}}{m_b}\frac{(\delta_d^{RL})_{32}}{V_{tb}V_{ts}^*}g_{7,8}^{(1)}(x_g) + \frac{M_{\tilde{g}}\mu}{\tilde{m}^2}\frac{\tan\beta}{(1+\epsilon\tan\beta)}\frac{(\delta_d^{LL})_{32}}{V_{tb}V_{ts}^*}g_{7,8}^{(2)}(x_g)\right],\ x_g = \frac{M_{\tilde{g}}^2}{\tilde{m}^2} \tag{G.23}$$

$$\frac{4G_F}{\sqrt{2}}\tilde{C}_{7,8}^{\tilde{g}} \simeq \frac{g_s^2}{\tilde{m}^2}\left[\frac{M_{\tilde{g}}}{m_b}\frac{(\delta_d^{LR})_{32}}{V_{tb}V_{ts}^*}g_{7,8}^{(2)}(x_g) + \frac{M_{\tilde{g}}\mu^*}{\tilde{m}^2}\frac{\tan\beta}{(1+\epsilon\tan\beta)}\frac{(\delta_d^{RR})_{32}}{V_{tb}V_{ts}^*}g_{7,8}^{(3)}(x_g)\right],\ x_g = \frac{M_{\tilde{g}}^2}{\tilde{m}^2} \tag{G.24}$$

G.2.2 $\Delta F = 2$ Processes

G.2.2.1 Gluino contributions

$$\begin{aligned} C_{\tilde{g}}^1 = &-\frac{\alpha_s^2}{\tilde{m}_Q^2}g_1(x_g^L)(\delta_d^{LL})_{23}(\delta_d^{LL})_{23} \\ &-\frac{1}{6}\alpha_2\alpha_s g_{g\tilde{w}}^{(1)}(x_g^L, x_{2L})\frac{1}{\tilde{m}_Q^2}(\delta_d^{LL})_{23}(\delta_d^{LL})_{23} \\ &-\frac{1}{8}\alpha_s^2 g_{\tilde{w}}^{(1)}(x_{2L})\frac{1}{\tilde{m}_Q^2}(\delta_d^{LL})_{23}(\delta_d^{LL})_{23} \\ ,&x_g^L = \frac{M_{\tilde{g}}^2}{\tilde{m}_Q^2}, x_{2L} = \frac{M_2^2}{\tilde{m}_Q^2} \end{aligned} \tag{G.25}$$

$$C_{\tilde{g}}^4 = -\frac{\alpha_s^2}{M_{\tilde{g}}^2} g_4(x_g^L, x_g^R)(\delta_d^{LL})_{23}(\delta_d^{RR})_{23}, x_g^L = \frac{M_{\tilde{g}}^2}{\tilde{m}_Q^2}, x_g^R = \frac{M_{\tilde{g}}^2}{\tilde{m}_d^2} \tag{G.26}$$

$$C_{\tilde{g}}^5 = -\frac{\alpha_s^2}{M_{\tilde{g}}^2} g_5(x_g^L, x_g^R)(\delta_d^{LL})_{23}(\delta_d^{RR})_{23}, x_g^L = \frac{M_{\tilde{g}}^2}{\tilde{m}_Q^2}, x_g^R = \frac{M_{\tilde{g}}^2}{\tilde{m}_d^2} \tag{G.27}$$

$$\tilde{C}_{\tilde{g}}^1 = -\frac{\alpha_s^2}{\tilde{m}_u^2} g_1(x_g^R)(\delta_d^{RR})_{23}(\delta_d^{RR})_{23}, x_g^R = \frac{M_{\tilde{g}}^2}{\tilde{m}_d^2} \tag{G.28}$$

$$C_{\tilde{g}}^2 = C_{\tilde{g}}^3 = \tilde{C}_{\tilde{g}}^2 = \tilde{C}_{\tilde{g}}^3 = 0 \tag{G.29}$$

G.2.2.2 Chargino contributions

$$C_{\tilde{\chi}}^1 = -\alpha_2^2 m_t^4 f_1(\mu^2/\tilde{m}_d^2) \frac{1}{8\tilde{m}_u^2 M_W^4} (V_{tb}V_{ts}^*)^2 \tag{G.30}$$

$$\tilde{C}_{\tilde{\chi}}^3 = -\frac{1}{8} A_t^2 \alpha_2^2 f_3(\frac{\mu^2}{\tilde{m}_Q^2}, \frac{\mu^2}{\tilde{m}_d^2}) m_t^4 \mu^2 \tan\beta^2 \frac{1}{\tilde{m}_Q^4 \tilde{m}_u^4 (1+\varepsilon\tan\beta)} \frac{(V_{tb}V_{ts}^*)^2}{(m_b+m_s)^2} \tag{G.31}$$

where

$$\varepsilon = 2\alpha_s \mu M_{\tilde{g}} F(x_g^L, \frac{\tilde{m}_d^2}{\tilde{m}_Q^2}) \frac{1}{3\pi\tilde{m}_Q^2} \tag{G.32}$$

$$C_{\tilde{\chi}}^2 = C_{\tilde{\chi}}^3 = C_{\tilde{\chi}}^4 = C_{\tilde{\chi}}^5 = \tilde{C}_{\tilde{\chi}}^1 = \tilde{C}_{\tilde{\chi}}^2 \tag{G.33}$$

G.2.2.3 Double Higgs penguin contribution

$$C_H^2 \simeq \tilde{C}_H^2 \simeq 0 \tag{G.34}$$

$$\begin{aligned} C_H^4 \simeq & -\frac{8\alpha_s^2\alpha_2}{9\pi} \frac{m_b^2}{M_W^2} \frac{\tan\beta^4}{(1+\varepsilon_g\tan\beta)^2[1+(\varepsilon_g+\varepsilon_Y y_t^2)\tan\beta]^2} \frac{|\mu|^2 M_3^2}{M_A^2 \tilde{m}_d^2 \tilde{m}_Q^2} \\ & \times (\delta_d^{LL})_{32}(\delta_d^{RR})_{32} G(x_d^3, x_d^Q) G(x_Q^3, x_Q^d) \\ & + \frac{\alpha_2^2\alpha_s}{6\pi} \frac{m_b^2}{M_W^2} \frac{\tan\beta^4}{(1+\varepsilon_g\tan\beta)^2[1+(\varepsilon_g+\varepsilon_Y y_t^2)\tan\beta]^2} \frac{|\mu|^2 M_3}{M_A^2 \tilde{m}_d^2} G(x_d^3, x_d^Q)(\delta_d^{RR})_{32} \\ & \times \left[\frac{m_t^2}{M_W^2} \frac{A_t}{\tilde{m}_Q^2} V_{tb}V_{ts}^* \frac{1+\varepsilon_g\tan\beta}{1+(\varepsilon_g+\varepsilon_Y y_t^2)\tan\beta} F(x_Q^\mu, x_Q^u) \right. \\ & \left. + \frac{2M_2}{\tilde{m}_Q^2} (\delta_u^{LL})_{32} G(x_Q^3, x_Q^\mu) \right. \end{aligned} \tag{G.35}$$

with

$$\varepsilon_g = \frac{2\alpha_s}{3\pi} \frac{\mu M_3}{\tilde{m}_Q^2} F(x_Q^3, x_Q^d) \tag{G.36}$$

$$\varepsilon_Y = \frac{1}{16\pi^2} \frac{\mu A_t}{\tilde{m}_Q^2} F(x_Q^\mu, x_Q^u) \tag{G.37}$$

$$y_t = \frac{m_t^2}{M_H^2} \tag{G.38}$$

$$x_d^3 = \frac{M_{\tilde{g}}^2}{\tilde{m}_d^2}, x_d^Q = \frac{\tilde{m}_Q^2}{\tilde{m}_d^2}, x_Q^3 = \frac{M_{\tilde{g}^2}}{\tilde{m}_Q 2}, x_Q^d = \frac{\tilde{m}_d^2}{\tilde{m}_Q^2}, x_Q^\mu = \frac{|\mu|^2}{\tilde{m}_Q^2}, x_Q^u = \frac{\tilde{m}_u^2}{\tilde{m}_Q^2}, x_Q^2 = \frac{M_2^2}{\tilde{m}_Q^2} \tag{G.39}$$

$$C_H^1 = C_H^3 = C_H^5 = \tilde{C}_H^1 = \tilde{C}_H^3 \tag{G.40}$$

G.2.3 Electric Dipole Moments

G.2.3.1 Gluino/squark contribution

$$\left\{\frac{d_{d_i}}{e}, d_{d_i}^c\right\}_{\tilde{g}} = -\frac{\alpha_s}{4\pi}\frac{m_b}{\tilde{m}^2}\frac{M_{\tilde{g}}\mu}{\tilde{m}^2}\frac{f_{\tilde{g}}^d(x_g)}{1+\epsilon\tan\beta}\mathrm{Im}\left[(\delta_d^{LL})_{i3}(\delta_d^{RR})_{3i}\right], x_g = \frac{M_{\tilde{g}}^2}{\tilde{m}^2} \tag{G.41}$$

where

$$\epsilon \simeq \frac{2\alpha_s}{3\pi}\frac{\mu M_{\tilde{g}}}{\tilde{m}^2} f(x_g) \tag{G.42}$$

$$\epsilon_R = \frac{\alpha_s \mu}{9\pi\tilde{m}} \tag{G.43}$$

$$\left\{\frac{d_u}{e}, d_u^c\right\}_{\tilde{g}} = -\frac{\alpha_s}{4\pi}\frac{m_{u_k}}{\tilde{m}^2}\frac{M_{\tilde{g}}A_{u_k}}{\tilde{m}^2} f_{\tilde{g}}^u(x_g)\mathrm{Im}\left[(\delta_u^{LL})_{1k}(\delta_u^{RR})_{k1}\right] \tag{G.44}$$

where $k = 2, 3,\ A_{u_2,u_3} = A_{c,t}$.

G.2.3.2 Charged Higgs contribution

$$\left\{\frac{d_{d_i}}{e}, d_{d_i}^c\right\}_{H^\pm} = -\frac{\alpha_2}{16\pi}\frac{m_b}{M_{H^\pm}}\frac{m_t^2}{M_W^2}\frac{(1-\epsilon\tan\beta)\epsilon_R\tan\beta}{3(1+\epsilon\tan\beta)^2}\mathrm{Im}\left[V_{3i}^*(\delta_d^{RR})_{3i}\right] f_{H_\pm}(y_t), y_t = \frac{m_t^2}{m_{H_\pm}} \tag{G.45}$$

G.2.3.3 Charged-Higgsino/squark contribution

$$\left\{\frac{d_{d_i}}{e}, d_{d_i}^c\right\}_{\tilde{H}^\pm} = -\frac{\alpha_2}{16\pi}\frac{m_b}{\tilde{m}^2}\frac{m_t^2}{M_W^2}\frac{A_t\mu}{\tilde{m}^2}\tan\beta\frac{\epsilon_R\tan\beta}{3(1+\epsilon\tan\beta)^2}\mathrm{Im}\left[V_{3i}^*(\delta_d^{RR})_{3i}\right] f_{\tilde{H}_\pm}(x_\mu), x_\mu = \frac{\mu^2}{\tilde{m}^2} \tag{G.46}$$

G.3 Loop functions

G.3.1 Loop functions for Electric Dipole Moments

$$f(x) = \frac{1}{1-x} + \frac{x}{(1-x)^2}\log x, f(1) = \frac{1}{2} \tag{G.47}$$

$$f_{\tilde{g}}^d(x) = \left\{-\frac{4}{9}f_0^{(3)}(x), -\frac{1}{6}f_0^{(3)}(x) + \frac{3}{2}f_1^{(3)}(x)\right\}, f_{\tilde{g}}^d(x) = \left\{\frac{4}{135}, \frac{11}{180}\right\} \tag{G.48}$$

$$f_{\tilde{g}}^u(x) = \left\{\frac{8}{9}f_0^{(3)}(x), -\frac{1}{6}f_0^{(3)}(x) + \frac{3}{2}f_1^{(3)}(x)\right\}, f_{\tilde{g}}^u(x) = \left\{-\frac{8}{135}, \frac{11}{180}\right\} \tag{G.49}$$

$$f_{H^\pm}(z) = \left\{ -f_0^{(0)}(z) + \frac{2}{3} f_1^{(0)}(z), f_1^{(0)}(z) \right\}, f_{H^\pm}(1) = \left\{ -\frac{7}{9}, -\frac{2}{3} \right\} \tag{G.50}$$

$$f_{\tilde{H}^\pm}(y) = \left\{ \frac{2}{3} f_0^{(1)}(y) - f_1^{(1)}(y), f_0^{(1)}(y) \right\}, f_{\tilde{H}^\pm}(1) = \left\{ -\frac{5}{18}, -\frac{1}{6} \right\} \tag{G.51}$$

$$f_0^{(0)}(x) = \frac{1 - x^2 + 2x \log x}{(1-x)^3} \tag{G.52}$$

$$f_0^{(1)}(x) = \frac{-1 - 4x + 5x^2 - 2x(x+2) \log x}{(1-x)^4} \tag{G.53}$$

$$f_0^{(2)}(x) = \frac{1 + 9x - 9x^2 - x^3 + 6x(x+1) \log x}{(1-x)^5} \tag{G.54}$$

$$f_0^{(3)}(x) = \frac{-3 - 44x + 36x^2 + 12x^3 - x^4 - 12x(3x+2) \log x}{3(1-x)^6} \tag{G.55}$$

$$f_1^{(0)} = \frac{3 - 4x + x^2 + 2 \log x}{(1-x)^3} \tag{G.56}$$

$$f_1^{(1)} = \frac{-5 + 4x + x^2 - 2(1+2x) \log x}{(1-x)^4} \tag{G.57}$$

$$f_1^{(2)} = \frac{2(3 - 3x^2 + (1 + 4x + x^2) \log x)}{(1-x)^5} \tag{G.58}$$

$$f_1^{(3)} = 2 \frac{-10 - 9x + 18x^2 + x^3 - 3(1 + 6x + 3x^2) \log x}{3(1-x)^6} \tag{G.59}$$

G.3.2 $\Delta F = 1$ Processes

$$h_7(x) = -\frac{5x^2 - 3x}{12(1-x)^2} - \frac{3x^2 - 2x}{6(1-x)^3} \log x \tag{G.60}$$

$$h_8(x) = -\frac{x^2 - 3x}{4(1-x)^2} - \frac{x}{2(1-x)^3} \log x \tag{G.61}$$

$$f_7^{(2)}(x) = -\frac{13 - 7x}{24(1-x)^3} - \frac{3 + 2x - 2x^2}{12(1-x)^4} \log x \tag{G.62}$$

$$f_8^{(2)}(x) = \frac{1 + 5x}{8(1-x)^3} + \frac{x(2+x)}{4(1-x)^4} \log x \tag{G.63}$$

$$f_{7,8}^{(1)}(x,y) = \frac{2}{x-y} (f_{7,8}^2(x) - f_{7,8}^2(y)) \tag{G.64}$$

$$g_7^{(1)}(x) = -\frac{2(1+5x)}{9(1-x)^3} - \frac{4x(2+x)}{9(1-x)^4}\log x \tag{G.65}$$

$$g_8^{(1)}(x) = -\frac{11+x}{3(1-x)^3} - \frac{9+16x-x^2}{6(1-x)^4}\log x \tag{G.66}$$

$$g_7^{(2)}(x) = -\frac{2(1+10x+x^2)}{9(1-x)^4} - \frac{4x(1+x)}{3(1-x)^5}\log x \tag{G.67}$$

$$g_8^{(2)}(x) = -\frac{53+44x-x^2}{12(1-x)^4} - \frac{3+11x+2x^2}{2(1-x)^5}\log x \tag{G.68}$$

G.3.3 $\Delta F = 2$ Processes

$|\Delta S| = 2$ gluino box contributions

$$g_1(x) = -\frac{11+144x+27x^2-2x^3}{108(1-x)^4} - \frac{x(13+17x)}{18(1-x)^5}\ln x \tag{G.69}$$

$$\begin{aligned} g_4(x,y) = &-\frac{x^2 y\ln x}{3(x-y)^3(1-x)^3}\left\{x^2(5+7x)+y\left[2+7(x-3)x\right]\right\} \\ &-\frac{y^2 x\ln y}{3(y-x)^3(1-y)^3}\left\{y^2(5+7y)+x\left[2+7(y-3)y\right]\right\} \\ &+\frac{xy}{3(1-x)^2(1-y)^2(x-y)^2}\left(x+y-13x^2-13y^2+8xy+15x^2y+15xy^2-14x^2y^2\right) \end{aligned} \tag{G.70}$$

$$\begin{aligned} g_5^{(1)}(x,y) = &-\frac{x^2 y\ln x}{9(x-y)^3(1-x)^3}\left[x^2(11+x)+(x-5)(x+2)y\right] \\ &-\frac{y^2 x\ln y}{9(y-x)^3(1-y)^3}\left[y^2(11+y)+(y-5)(y+2)x\right] \\ &-\frac{xy}{9(1-x)^2(1-y)^2(x-y)^2}\left(5x+5y+7x^2+7y^2-32xy+3x^2y+3xy^2+2x^2y^2\right). \end{aligned} \tag{G.71}$$

G.3.3.1 Wino and Higgsino contributions

The loop functions $g_{\tilde{g}\tilde{w}}^{(1)}$, $g_{\tilde{w}}^{(1)}(x)$, $f_1(x)$ and $f_3(x,y)$ are given by

$$\begin{aligned} g_{\tilde{g}\tilde{w}}^{(1)}(x,y) = &-\sqrt{xy}\left[\frac{x\ln x}{(x-y)(1-x)^4}+\frac{y\ln y}{(y-x)(1-y)^4}\right. \\ &\left.+\frac{11-7(x+y)+2(x^2+y^2)-10xy+5xy(x+y)-x^2y^2}{6(1-x)^3(1-y)^3}\right] \\ &-\frac{x^2\ln x}{2(x-y)(1-x)^4}-\frac{y^2\ln y}{2(y-x)(1-y)^4} \\ &-\frac{2+5(x+y)-(x^2+y^2)-22xy+5xy(x+y)+2x^2y^2}{12(1-x)^3(1-y)^3}, \end{aligned} \tag{G.72}$$

$$g_{\tilde{w}}^{(1)}(x) = \frac{-5 - 67x - 13x^2 + x^3}{12(1-x)^4} - \frac{x(3+4x)}{(1-x)^5}\ln x \tag{G.73}$$

G.3.4 Chargino and double Higgs penguin contribution

$$f_1(x) = -\frac{x+1}{4(1-x)^2} - \frac{x}{2(1-x)^3}\ln x \tag{G.74}$$

$$\begin{aligned} f_3(x,y) = &-\frac{x^2[x(1+x+y)-3y]}{(x-y)^3(1-x)^3}\ln x - \frac{y^2[y(1+x+y)-3x]}{(y-x)^3(1-y)^3}\ln y \\ &- 2\frac{x^2+y^2-xy-x^2y-xy^2+x^2y^2}{(1-x)^2(1-y)^2(x-y)^2} \end{aligned} \tag{G.75}$$

$$f_3(x) = \frac{x^2-8x-17}{6(1-x)^4} - \frac{3x+1}{(1-x)^5}\ln x \tag{G.76}$$

$$F(x,y) = \frac{x\ln x}{(x-1)(x-y)} + \frac{y\ln y}{(y-1)(y-x)} \tag{7.77}$$

$$G(x,y) = \frac{x\ln x}{(x-1)^2(x-y)} + \frac{y\ln y}{(y-1)^2(y-x)} + \frac{1}{(x-1)(y-1)} \tag{7.78}$$

Bibliography

[1] Particle Data Group, C. Patrignani *et al.*, *Review of Particle Physics*, Chin. Phys. **C40** (2016), no. 10 100001.

[2] P. W. Higgs, *Broken symmetries and the masses of gauge bosons*, Phys. Rev. Lett. **13** (1964) 508.

[3] M. Maltoni, T. Schwetz, M. A. Tortola, and J. W. F. Valle, *Status of global fits to neutrino oscillations*, New J. Phys. **6** (2004) 122, arXiv:hep-ph/0405172.

[4] *Elementary particles of the standard model, open content*, https://en.wikipedia.org/wiki/Standard_Model#Particle_content.

[5] LHCb, R. Aaij *et al.*, *Observation of $J/\psi p$ Resonances Consistent with Pentaquark States in $\Lambda_b^0 \to J/\psi K^- p$ Decays*, Phys. Rev. Lett. **115** (2015) 072001, arXiv:1507.03414.

[6] ATLAS, G. Aad *et al.*, *Observation of a new particle in the search for the Standard Model Higgs boson with the ATLAS detector at the LHC*, Phys. Lett. **B716** (2012) 1, arXiv:1207.7214.

[7] CMS, S. Chatrchyan *et al.*, *Observation of a new boson at a mass of 125 GeV with the CMS experiment at the LHC*, Phys. Lett. **B716** (2012) 30, arXiv:1207.7235.

[8] P. Kooijman and N. Tuning, *Lectures on CP Violation*, 2015.

[9] J. M. Cline, *Baryogenesis*, in *Les Houches Summer School - Session 86: Particle Physics and Cosmology: The Fabric of Spacetime Les Houches, France, July 31-August 25, 2006*, 2006. arXiv:hep-ph/0609145.

[10] A. D. Sakharov, *Violation of CP Invariance, C asymmetry, and baryon asymmetry of the universe*, Pisma Zh. Eksp. Teor. Fiz. **5** (1967) 32, [Usp. Fiz. Nauk161,no.5,61(1991)].

[11] P. Huet and E. Sather, *Electroweak baryogenesis and standard model CP violation*, Phys. Rev. **D51** (1995) 379, arXiv:hep-ph/9404302.

[12] N. P. Vogt, M. P. Haynes, T. Herter, and R. Giovanelli, *M/L, H-alpha rotation curves, and HI measurements for 329 nearby cluster and field spirals. 1. Data*, Astron. J. **127** (2004) 3273, arXiv:astro-ph/0402649.

[13] R. Massey, T. Kitching, and J. Richard, *The dark matter of gravitational lensing*, Rept. Prog. Phys. **73** (2010) 086901, arXiv:1001.1739.

[14] R. D. Peccei and H. R. Quinn, *Constraints imposed by* CP *conservation in the presence of pseudoparticles*, Phys. Rev. D **16** (1977) 1791.

[15] S. Weinberg, *A new light boson?*, Phys. Rev. Lett. **40** (1978) 223.

[16] F. Wilczek, *Problem of strong p and t invariance in the presence of instantons*, Phys. Rev. Lett. **40** (1978) 279.

[17] Y. B. Zel'dovich and I. D. Novikov, *The Hypothesis of Cores Retarded during Expansion and the Hot Cosmological Model*, **43** (1966) 758.

[18] `http://www.theo-physik.uni-kiel.de/~bonitz/public/nobel04/public.html`.

[19] J. R. Ellis, J. Hisano, M. Raidal, and Y. Shimizu, *A New parametrization of the seesaw mechanism and applications in supersymmetric models*, Phys. Rev. **D66** (2002) 115013, `arXiv:hep-ph/0206110`.

[20] F. Jegerlehner and A. Nyffeler, *The Muon g-2*, Phys. Rept. **477** (2009) 1, `arXiv:0902.3360`.

[21] LHCb, R. Aaij *et al.*, *Angular analysis of the* $B^0 \to K^{*0}\mu^+\mu^-$ *decay using 3* fb^{-1} *of integrated luminosity*, JHEP **02** (2016) 104, `arXiv:1512.04442`.

[22] LHCb, R. Aaij *et al.*, *Test of lepton universality with* $B^0 \to K^{*0}\ell^+\ell^-$ *decays*, JHEP **08** (2017) 055, `arXiv:1705.05802`.

[23] KamLAND-Zen, A. Gando *et al.*, *Search for Majorana Neutrinos near the Inverted Mass Hierarchy Region with KamLAND-Zen*, Phys. Rev. Lett. **117** (2016), no. 8 082503, `arXiv:1605.02889`, [Addendum: Phys. Rev. Lett.117,no.10,109903(2016)].

[24] GERDA, M. Agostini *et al.*, *Improved Limit on Neutrinoless Double-*β *Decay of* ^{76}*Ge from GERDA Phase II*, Phys. Rev. Lett. **120** (2018), no. 13 132503, `arXiv:1803.11100`.

[25] R. D. Peccei, *The Strong CP problem and axions*, Lect. Notes Phys. **741** (2008) 3, `arXiv:hep-ph/0607268`, [,3(2006)].

[26] T. Kaluza, *On the Unification Problem in Physics*, Sitzungsber. Preuss. Akad. Wiss. Berlin (Math. Phys.) **1921** (1921) 966, `arXiv:1803.08616`.

[27] O. Klein, *Quantentheorie und fünfdimensionale relativitätstheorie*, Zeitschrift für Physik **37** (1926) 895.

[28] L. Randall and R. Sundrum, *Large mass hierarchy from a small extra dimension*, Phys. Rev. Lett. **83** (1999) 3370.

[29] M. Tanabashi *et al.*, *Review of Particle Physics*, Phys. Rev. **D98** (2018), no. 3 030001.

[30] V. Sanz and J. Setford, *Composite Higgs Models after Run 2*, Adv. High Energy Phys. **2018** (2018) 7168480, `arXiv:1703.10190`.

[31] S. Coleman and J. Mandula, *All possible symmetries of the s matrix*, Phys. Rev. **159** (1967) 1251.

[32] S. S. AbdusSalam *et al.*, *Benchmark Models, Planes, Lines and Points for Future SUSY Searches at the LHC*, Eur. Phys. J. **C71** (2011) 1835, arXiv:1109.3859.

[33] S. L. Glashow and S. Weinberg, *Natural conservation laws for neutral currents*, Phys. Rev. D **15** (1977) 1958.

[34] E. A. Paschos, *Diagonal neutral currents*, Phys. Rev. D **15** (1977) 1966.

[35] D. Z. Freedman, P. van Nieuwenhuizen, and S. Ferrara, *Progress Toward a Theory of Supergravity*, Phys. Rev. **D13** (1976) 3214.

[36] J. R. Ellis, K. A. Olive, and Y. Santoso, *The MSSM parameter space with nonuniversal Higgs masses*, Phys. Lett. **B539** (2002) 107, arXiv:hep-ph/0204192.

[37] A. Datta, A. Kundu, and A. Samanta, *New bounds on slepton and Wino masses in anomaly mediated supersymmetry breaking models*, Phys. Rev. **D64** (2001) 095016, arXiv:hep-ph/0101034.

[38] E. Bagnaschi *et al.*, *Likelihood Analysis of the Minimal AMSB Model*, Eur. Phys. J. **C77** (2017), no. 4 268, arXiv:1612.05210.

[39] S. P. Martin, *A Supersymmetry primer*, arXiv:hep-ph/9709356, [Adv. Ser. Direct. High Energy Phys.18,1(1998)].

[40] Super-Kamiokande, H. Nishino *et al.*, *Search for Proton Decay via $p \to e^+\pi^0$ and $p\mu^+\pi^0$ in a Large Water Cherenkov Detector*, Phys. Rev. Lett. **102** (2009) 141801, arXiv:0903.0676.

[41] A. Masiero and J. W. F. Valle, *A model for spontaneous r parity breaking*, Physics Letters B **251** (1990), no. 2 273 .

[42] J. C. Romão, C. A. Santos, and J. W. F. Valle, *How to spontaneously break r parity*, Physics Letters B **288** (1992), no. 3 311 .

[43] D. K. Ghosh, G. Senjanovic, and Y. Zhang, *Naturally Light Sterile Neutrinos from Theory of R-parity*, Phys. Lett. **B698** (2011) 420, arXiv:1010.3968.

[44] *Summary plots from the atlas supersymmetry physics group*, https://atlas.web.cern.ch/Atlas/GROUPS/PHYSICS/CombinedSummaryPlots/SUSY/.

[45] *Cms supersymmetry physics results*, https://twiki.cern.ch/twiki/bin/view/CMSPublic/PhysicsResultsSUS.

[46] GAMBIT, P. Athron *et al.*, *Combined collider constraints on neutralinos and charginos*, arXiv:1809.02097.

[47] GAMBIT, P. Athron *et al.*, *A global fit of the MSSM with GAMBIT*, Eur. Phys. J. **C77** (2017), no. 12 879, arXiv:1705.07917.

[48] GAMBIT, P. Athron *et al.*, *Global fits of GUT-scale SUSY models with GAMBIT*, Eur. Phys. J. **C77** (2017), no. 12 824, arXiv:1705.07935.

[49] E. Bagnaschi *et al.*, *Likelihood Analysis of Supersymmetric SU(5) GUTs*, Eur. Phys. J. **C77** (2017), no. 2 104, arXiv:1610.10084.

[50] E. Bagnaschi *et al.*, *Likelihood Analysis of the Minimal AMSB Model*, Eur. Phys. J. **C77** (2017), no. 4 268, arXiv:1612.05210.

[51] E. Bagnaschi *et al.*, *Likelihood Analysis of the pMSSM11 in Light of LHC 13-TeV Data*, Eur. Phys. J. **C78** (2018), no. 3 256, arXiv:1710.11091.

[52] J. C. Costa *et al.*, *Likelihood Analysis of the Sub-GUT MSSM in Light of LHC 13-TeV Data*, Eur. Phys. J. **C78** (2018), no. 2 158, arXiv:1711.00458.

[53] P. Paradisi and D. M. Straub, *The SUSY CP Problem and the MFV Principle*, Phys. Lett. **B684** (2010) 147, arXiv:0906.4551.

[54] W. Altmannshofer, A. J. Buras, and D. Guadagnoli, *The MFV limit of the MSSM for low tan(beta): Meson mixings revisited*, JHEP **11** (2007) 065, arXiv:hep-ph/0703200.

[55] G. D'Ambrosio, G. F. Giudice, G. Isidori, and A. Strumia, *Minimal flavor violation: An Effective field theory approach*, Nucl. Phys. **B645** (2002) 155, arXiv:hep-ph/0207036.

[56] C. Csaki, Y. Grossman, and B. Heidenreich, *MFV SUSY: A Natural Theory for R-Parity Violation*, Phys. Rev. **D85** (2012) 095009, arXiv:1111.1239.

[57] D. M. Straub, *MFV and the SUSY CP Problem*, AIP Conf. Proc. **1200** (2010) 904, arXiv:0909.3296.

[58] A. J. Buras *et al.*, *Universal unitarity triangle and physics beyond the standard model*, Phys. Lett. **B500** (2001) 161, arXiv:hep-ph/0007085.

[59] C. P. et al. *The Review of Particle Physics (2017)*, Chin. Phys. **C40** (2016 and 2017 update) 100001.

[60] G. Isidori, *B Physics in the LHC Era*, in *Proceedings, 65th Scottish Universities Summer School in Physics: LHC Physics (SUSSP65): St. Andrews, UK, August 16-29, 2009*, pp. 69–109, 2010. arXiv:1001.3431. doi: 10.1201/b11865-5.

[61] http://ckmfitter.in2p3.fr/www/results/plots_summer18/ckm_res_summer18.html.

[62] J. Bernigaud, B. Herrmann, S. F. King, and S. J. Rowley, *Non-minimal flavour violation in $A_4 \times SU(5)$ SUSY GUTs with smuon assisted dark matter*, arXiv:1812.07463.

[63] S. Jager, *Supersymmetry beyond minimal flavour violation*, Eur. Phys. J. **C59** (2009) 497, arXiv:0808.2044.

[64] C. T. Hill, *Topcolor assisted technicolor*, Phys. Lett. **B345** (1995) 483, arXiv:hep-ph/9411426.

[65] S. Heinemeyer, W. Hollik, F. Merz, and S. Penaranda, *Electroweak precision observables in the MSSM with nonminimal flavor violation*, Eur. Phys. J. **C37** (2004) 481, arXiv:hep-ph/0403228.

[66] https://indico.cern.ch/event/280883/contributions/635264/attachments/515295/711048/LHCb_Kaons.pdf.

[67] CMS, S. Chatrchyan *et al.*, *Observation of a new boson at a mass of 125 GeV with the CMS experiment at the LHC*, Phys. Lett. **B716** (2012) 30, arXiv:1207.7235.

[68] ATLAS, G. Aad *et al.*, *Observation of a new particle in the search for the Standard Model Higgs boson with the ATLAS detector at the LHC*, Phys. Lett. **B716** (2012) 1, arXiv:1207.7214.

[69] M. Grabalosa and M. Musy, *Flavour Tagging developments within the LHCb experiment*, Mar, 2012. Presented 15 May 2012.

[70] ATLAS, W. W. Armstrong *et al.*, *ATLAS: Technical proposal for a general-purpose p p experiment at the Large Hadron Collider at CERN*, .

[71] CMS, *CMS, the Compact Muon Solenoid: Technical proposal*, .

[72] *ALICE: Technical proposal for a large ion collider experiment at the CERN LHC*, .

[73] LHCb, S. Amato *et al.*, *LHCb technical proposal*, .

[74] LHCb collaboration, A. A. Alves Jr. *et al.*, *The LHCb detector at the LHC*, JINST **3** (2008) S08005.

[75] LHCb, R. Aaij *et al.*, *LHCb Detector Performance*, Int. J. Mod. Phys. **A30** (2015), no. 07 1530022, arXiv:1412.6352.

[76] LHCb VELO Group, R. Aaij *et al.*, *Performance of the LHCb Vertex Locator. Performance of the LHCb Vertex Locator*, JINST **9** (2014) P09007. 61 p, Comments: 61 pages, 33 figures.

[77] LHCb Outer Tracker group, R. Arink *et al.*, *Performance of the LHCb Outer Tracker*, JINST **9** (2013) P01002. 30 p, Comments: 30 pages, 20 figures.

[78] LHCb RICH group, M. Adinolfi *et al.*, *Performance of the LHCb RICH detector at the LHC*, Eur. Phys. J. C **73** (2012) 2431. 25 p.

[79] J. Alves, A.Ã. *et al.*, *Performance of the LHCb muon system*, JINST **8** (2012) P02022. 32 p.

[80] R. Aaij *et al.*, *The LHCb Trigger and its Performance in 2011*, JINST **8** (2012) P04022. 31 p.

[81] https://www2.physics.ox.ac.uk/research/lhcb/the-lhcb-detector.

[82] A. A. Alves, Jr. *et al.*, *Performance of the LHCb muon system*, JINST **8** (2013) P02022, arXiv:1211.1346.

[83] https://lhcb-public.web.cern.ch/lhcb-public/en/Data%20Collection/Triggers2-en.html.

[84] V. V. Gligorov, *A single track HLT1 trigger*, LHCb-PUB-2011-003.

[85] R. Fruhwirth, *Application of Kalman filtering to track and vertex fitting*, Nucl. Instrum. Meth. **A262** (1987) 444.

[86] LHCb, R. Aaij *et al.*, *Physics case for an LHCb Upgrade II - Opportunities in flavour physics, and beyond, in the HL-LHC era*, arXiv:1808.08865.

[87] Belle II, W. Altmannshofer *et al.*, *The Belle II Physics Book*, arXiv:1808.10567.

[88] LHCb, R. Aaij *et al.*, *Test of lepton universality using $B^+ \to K^+\ell^+\ell^-$ decays*, Phys. Rev. Lett. **113** (2014) 151601, arXiv:1406.6482.

[89] LHCb, R. Aaij *et al.*, *Measurement of CP asymmetry in $B_s^0 \to D_s^\mp K^\pm$ decays*, JHEP **03** (2018) 059, arXiv:1712.07428.

[90] LHCb Collaboration, *Update of the LHCb combination of the CKM angle γ using $B \to DK$ decays*, Tech. Rep. LHCb-CONF-2017-004. CERN-LHCb-CONF-2017-004, CERN, Geneva, Jul, 2017.

[91] LHCb, R. Aaij *et al.*, *Measurement of CP violation in $B^0 \to J/\psi K_S^0$ and $B^0 \to \psi(2S)K_S^0$ decays*, JHEP **11** (2017) 170, arXiv:1709.03944.

[92] LHCb, R. Aaij *et al.*, *Precision measurement of CP violation in $B_s^0 \to J/\psi K^+K^-$ decays*, Phys. Rev. Lett. **114** (2015), no. 4 041801, arXiv:1411.3104.

[93] LHCb, R. Aaij *et al.*, *Measurement of the CP-violating phase ϕ_s in $\bar{B}_s^0 \to D_s^+D_s^-$ decays*, Phys. Rev. Lett. **113** (2014), no. 21 211801, arXiv:1409.4619.

[94] LHCb, R. Aaij *et al.*, *Measurement of CP violation in $B_s^0 \to \phi\phi$ decays*, Phys. Rev. **D90** (2014), no. 5 052011, arXiv:1407.2222.

[95] LHCb, R. Aaij *et al.*, *Measurement of the CP asymmetry in $B_s^0 - \overline{B}_s^0$ mixing*, Phys. Rev. Lett. **117** (2016), no. 6 061803, arXiv:1605.09768, [Addendum: Phys. Rev. Lett.118,no.12,129903(2017)].

[96] LHCb, R. Aaij *et al.*, *Determination of the quark coupling strength $|V_{ub}|$ using baryonic decays*, Nature Phys. **11** (2015) 743, arXiv:1504.01568.

[97] LHCb, R. Aaij *et al.*, *Measurement of the $B_s^0 \to \mu^+\mu^-$ branching fraction and effective lifetime and search for $B^0 \to \mu^+\mu^-$ decays*, Phys. Rev. Lett. **118** (2017), no. 19 191801, arXiv:1703.05747.

[98] LHCb, R. Aaij *et al.*, *Measurement of the ratio of branching fractions $\mathcal{B}(\bar{B}^0 \to D^{*+}\tau^-\bar{\nu}_\tau)/\mathcal{B}(\bar{B}^0 \to D^{*+}\mu^-\bar{\nu}_\mu)$*, Phys. Rev. Lett. **115** (2015), no. 11 111803, arXiv:1506.08614, [Erratum: Phys. Rev. Lett.115,no.15,159901(2015)].

[99] LHCb, R. Aaij *et al.*, *Test of Lepton Flavor Universality by the measurement of the $B^0 \to D^{*-}\tau^+\nu_\tau$ branching fraction using three-prong τ decays*, Phys. Rev. **D97** (2018), no. 7 072013, arXiv:1711.02505.

[100] LHCb, R. Aaij *et al.*, *Measurement of the ratio of branching fractions $\mathcal{B}(B_c^+ \to J/\psi\tau^+\nu_\tau)/\mathcal{B}(B_c^+ \to J/\psi\mu^+\nu_\mu)$*, Phys. Rev. Lett. **120** (2018), no. 12 121801, arXiv:1711.05623.

[101] LHCb, R. Aaij *et al.*, *Measurement of the difference of time-integrated CP asymmetries in $D^0 \to K^-K^+$ and $D^0 \to \pi^-\pi^+$ decays*, Phys. Rev. Lett. **116** (2016), no. 19 191601, arXiv:1602.03160.

[102] LHCb, R. Aaij *et al.*, *Measurement of the CP violation parameter A_Γ in $D^0 \to K^+K^-$ and $D^0 \to \pi^+\pi^-$ decays*, Phys. Rev. Lett. **118** (2017), no. 26 261803, arXiv:1702.06490.

[103] LHCb, R. Aaij *et al.*, *Updated determination of D^0-$\overline{D}^0$ mixing and CP violation parameters with $D^0 \to K^+\pi^-$ decays*, Phys. Rev. **D97** (2018), no. 3 031101, arXiv:1712.03220.

[104] L. Collaboration, *LHCb Trigger and Online Upgrade Technical Design Report*, .

[105] X. Llopart *et al.*, *Timepix, a 65k programmable pixel readout chip for arrival time, energy and/or photon counting measurements*, Nuclear Instruments and Methods in Physics Research Section A: Accelerators, Spectrometers, Detectors and Associated Equipment **581** (2007), no. 1 485 , VCI 2007.

[106] L. Collaboration, *LHCb VELO Upgrade Technical Design Report*, Tech. Rep. CERN-LHCC-2013-021. LHCB-TDR-013, Nov, 2013.

[107] LHCb SciFi Tracker, P. Hopchev, *SciFi: A large Scintillating Fibre Tracker for LHCb*, in *5th Large Hadron Collider Physics Conference (LHCP 2017) Shanghai, China, May 15-20, 2017*, 2017. arXiv:1710.08325.

[108] P. Mato, *Gaudi-architecture design document*, Tech. Rep. LHCb-98-064, CERN, Geneva, Nov, 1998.

[109] *The MOORE project*, http://lhcb-release-area.web.cern.ch/LHCb-release-area/DOC/moore/.

[110] *The BRUNEL project*, http://lhcbdoc.web.cern.ch/lhcbdoc/brunel/.

[111] *The ALIGNMENT project*, http://lhcbdoc.web.cern.ch/lhcbdoc/alignment/.

[112] https://twiki.cern.ch/twiki/bin/view/LHCb/DaVinci.

[113] https://gitlab.cern.ch/lhcb/Erasmus.

[114] C. Eck *et al.*, *LHC computing Grid: Technical Design Report. Version 1.06 (20 Jun 2005)*, Technical Design Report LCG, CERN, Geneva, 2005.

[115] http://lhcbdoc.web.cern.ch/lhcbdoc/gauss/.

[116] T. Sjöstrand, S. Mrenna, and P. Skands, *PYTHIA 6.4 physics and manual*, JHEP **05** (2006) 026, arXiv:hep-ph/0603175.

[117] A. Ryd *et al.*, *EvtGen: A Monte Carlo Generator for B-Physics*, .

[118] S. Agostinelli *et al.*, *Geant4 simulation toolkit*, Nuclear Instruments and Methods in Physics Research Section A: Accelerators, Spectrometers, Detectors and Associated Equipment **506** (2003), no. 3 250 .

[119] R. Aaij *et al.*, *Tesla : an application for real-time data analysis in High Energy Physics*, Comput. Phys. Commun. **208** (2016) 35, arXiv:1604.05596.

[120] D. Derkach *et al.*, *LHCb trigger streams optimization*, J. Phys. Conf. Ser. **898** (2017), no. 6 062026, arXiv:1702.05262.

[121] https://lhcb.github.io/starterkit-lessons/first-analysis-steps/run-2-data-flow.html.

[122] S. Benson, V. Gligorov, M. Anton Vesterinen, and J. Michael Williams, *The lhcb turbo stream*, Journal of Physics: Conference Series **664** (2015) 082004.

[123] LHCb, R. Aaij *et al.*, *Search for the rare decay $K_S \to \mu^+\mu^-$*, JHEP **01** (2013) 090, arXiv:1209.4029.

[124] C. Hamzaoui, M. Pospelov, and M. Toharia, *Higgs mediated FCNC in supersymmetric models with large tanβ*, Phys. Rev. **D59** (1999) 095005, arXiv:hep-ph/9807350.

[125] K. S. Babu and C. F. Kolda, *Higgs mediated $B^0 \to \mu^+\mu^-$ in minimal supersymmetry*, Phys. Rev. Lett. **84** (2000) 228, arXiv:hep-ph/9909476.

[126] P. H. Chankowski and L. Slawianowska, *$B^0_{d,s} \to \mu^-\mu^+$ decay in the MSSM*, Phys. Rev. **D63** (2001) 054012, arXiv:hep-ph/0008046.

[127] C. Bobeth, T. Ewerth, F. Kruger, and J. Urban, *Analysis of neutral Higgs boson contributions to the decays $\bar{B}(s^) \to \ell^+\ell^-$ and $\bar{B} \to K\ell^+\ell^-$*, Phys. Rev. **D64** (2001) 074014, arXiv:hep-ph/0104284.

[128] G. Isidori and A. Retico, *Scalar flavor changing neutral currents in the large* $\tan\beta$ *limit*, JHEP **11** (2001) 001, arXiv:hep-ph/0110121.

[129] G. Isidori and A. Retico, *$B_{s,d} \to l^+l^-$ and $K_L \to l^+l^-$ in SUSY models with nonminimal sources of flavor mixing*, JHEP **09** (2002) 063, arXiv:hep-ph/0208159.

[130] A. Crivellin, *Effective Higgs Vertices in the generic MSSM*, Phys. Rev. **D83** (2011) 056001, arXiv:1012.4840.

[131] A. Crivellin, L. Hofer, and J. Rosiek, *Complete resummation of chirally-enhanced loop-effects in the MSSM with non-minimal sources of flavor-violation*, JHEP **07** (2011) 017, arXiv:1103.4272.

[132] A. Crivellin and C. Greub, *Two-loop supersymmetric QCD corrections to Higgs-quark-quark couplings in the generic MSSM*, Phys. Rev. **D87** (2013) 015013, arXiv:1210.7453, [Erratum: Phys. Rev.D87,079901(2013)].

[133] S. R. Choudhury and N. Gaur, *Dileptonic decay of B_s meson in SUSY models with large* $\tan\beta$, Phys. Lett. **B451** (1999) 86, arXiv:hep-ph/9810307.

[134] C.-S. Huang, W. Liao, Q.-S. Yan, and S.-H. Zhu, *$B_s \to$ lepton + lepton - in a general 2 HDM and MSSM*, Phys. Rev. **D63** (2001) 114021, arXiv:hep-ph/0006250, [Erratum: Phys. Rev.D64,059902(2001)].

[135] Z. Xiong and J. M. Yang, *B meson dileptonic decays enhanced by supersymmetry with large* $\tan\beta$, Nucl. Phys. **B628** (2002) 193, arXiv:hep-ph/0105260.

[136] A. Dedes, H. K. Dreiner, and U. Nierste, *Correlation of* $B_s \to \mu^+\mu^-$ *and (g-2)* (μ) *in minimal supergravity*, Phys. Rev. Lett. **87** (2001) 251804, arXiv:hep-ph/0108037.

[137] C. Bobeth, T. Ewerth, F. Kruger, and J. Urban, *Enhancement of B(anti-B(d)* $\to \mu^+\mu^-$*) / B(anti-B(s)* $\to \mu^+\mu^-$*) in the MSSM with minimal flavor violation and large tan beta*, Phys. Rev. **D66** (2002) 074021, arXiv:hep-ph/0204225.

[138] S. Baek, P. Ko, and W. Y. Song, *Implications on SUSY breaking mediation mechanisms from observing* $B_s \to \mu^+\mu^-$ *and the muon (g-2)*, Phys. Rev. Lett. **89** (2002) 271801, arXiv:hep-ph/0205259.

[139] A. Dedes, H. K. Dreiner, U. Nierste, and P. Richardson, *Trilepton events and* $B_s \to \mu^+\mu^-$ *: No lose for mSUGRA at the Tevatron?*, arXiv:hep-ph/0207026.

[140] J. K. Mizukoshi, X. Tata, and Y. Wang, *Higgs mediated leptonic decays of* B_s *and* B_d *mesons as probes of supersymmetry*, Phys. Rev. **D66** (2002) 115003, arXiv:hep-ph/0208078.

[141] S. Baek, P. Ko, and W. Y. Song, *SUSY breaking mediation mechanisms and (g-2)* (μ), $B \to X_s\gamma$, $B \to X_s\ell^+\ell^-$ *and* $B_s \to \mu^+\mu^-$, JHEP **03** (2003) 054, arXiv:hep-ph/0208112.

[142] C. Bobeth and A. J. Buras, *Leptoquarks meet* ε'/ε *and rare Kaon processes*, JHEP **02** (2018) 101, arXiv:1712.01295.

[143] G. Ecker and A. Pich, *The Longitudinal muon polarization in* $K_L \to \mu^+\mu^-$, Nucl. Phys. **B366** (1991) 189.

[144] G. Isidori and R. Unterdorfer, *On the short distance constraints from* $K_{L,S} \to \mu^+\mu^-$, JHEP **01** (2004) 009, arXiv:hep-ph/0311084.

[145] G. D'Ambrosio and T. Kitahara, *Direct CP Violation in* $K \to \mu^+\mu^-$, Phys. Rev. Lett. **119** (2017), no. 20 201802, arXiv:1707.06999.

[146] R. Aaij *et al.*, *Improved limit on the branching fraction of the rare decay* $k_S^0 \to \mu^+\mu^-$, The European Physical Journal C **77** (2017) 678.

[147] D. Martinez Santos. LHCb-TALK-2017-164, at FPCP 2017.

[148] LHCb, D. M. Santos, *A strange program for LHCb*, EPJ Web Conf. **179** (2018) 01013.

[149] L. J. Hall, V. A. Kostelecky, and S. Raby, *New flavor violations in supergravity models*, Nuclear Physics B **267** (1986), no. 2 415 .

[150] F. Mescia, C. Smith, and S. Trine, $K_L \to \pi^0 e^+ e^-$ *and* $K_L \to \pi^0\mu^+\mu^-$*: A Binary star on the stage of flavor physics*, JHEP **08** (2006) 088, arXiv:hep-ph/0606081.

[151] G. Isidori, C. Smith, and R. Unterdorfer, *The Rare decay* $K_L \to \pi^0\mu^+\mu^-$ *within the SM*, Eur. Phys. J. **C36** (2004) 57, arXiv:hep-ph/0404127.

[152] D. Gomez Dumm and A. Pich, *Long distance contributions to the K(L) $\to \mu^+\mu^-$ decay width*, Phys. Rev. Lett. **80** (1998) 4633, arXiv:hep-ph/9801298.

[153] M. Knecht, S. Peris, M. Perrottet, and E. de Rafael, *Decay of pseudoscalars into lepton pairs and large N(c) QCD*, Phys. Rev. Lett. **83** (1999) 5230, arXiv:hep-ph/9908283.

[154] Particle Data Group, C. Patrignani *et al.*, *Review of Particle Physics*, Chin. Phys. **C40** (2016), no. 10 100001.

[155] A. Pich and E. de Rafael, *Weak K amplitudes in the chiral and $1/N_c$ expansions*, Phys. Lett. **B374** (1996) 186, arXiv:hep-ph/9511465.

[156] J.-M. Gerard, C. Smith, and S. Trine, *Radiative kaon decays and the penguin contribution to the $\Delta I = 1/2$ rule*, Nucl. Phys. **B730** (2005) 1, arXiv:hep-ph/0508189.

[157] M. Gorbahn and U. Haisch, *Charm Quark Contribution to $K_L \to \mu^+\mu^-$ at Next-to-Next-to-Leading*, Phys. Rev. Lett. **97** (2006) 122002, arXiv:hep-ph/0605203.

[158] G. Colangelo, R. Stucki, and L. C. Tunstall, *Dispersive treatment of $K_S \to \gamma\gamma$ and $K_S \to \gamma\ell^+\ell^-$*, Eur. Phys. J. **C76** (2016), no. 11 604, arXiv:1609.03574.

[159] G. Colangelo and G. Isidori, *Supersymmetric contributions to rare kaon decays: Beyond the single mass insertion approximation*, JHEP **09** (1998) 009, arXiv:hep-ph/9808487.

[160] A. J. Buras *et al.*, *Connections between ϵ'_K/ϵ_K and rare kaon decays in supersymmetry*, Nucl. Phys. **B566** (2000) 3, arXiv:hep-ph/9908371.

[161] M. Endo, S. Mishima, D. Ueda, and K. Yamamoto, *Chargino contributions in light of recent ϵ'_K/ϵ_K*, Phys. Lett. **B762** (2016) 493, arXiv:1608.01444.

[162] W. Altmannshofer *et al.*, *Anatomy and Phenomenology of FCNC and CPV Effects in SUSY Theories*, Nucl. Phys. **B830** (2010) 17, arXiv:0909.1333.

[163] J. Rosiek, *Complete set of Feynman rules for the MSSM: Erratum*, arXiv:hep-ph/9511250.

[164] B. C. Allanach *et al.*, *SUSY Les Houches Accord 2*, Comput. Phys. Commun. **180** (2009) 8, arXiv:0801.0045.

[165] A. Crivellin, G. D'Ambrosio, T. Kitahara, and U. Nierste, *$K \to \pi\nu\overline{\nu}$ in the MSSM in light of the ϵ'_K/ϵ_K anomaly*, Phys. Rev. **D96** (2017), no. 1 015023, arXiv:1703.05786.

[166] T. Blum *et al.*, *The $K \to (\pi\pi)_{I=2}$ Decay Amplitude from Lattice QCD*, Phys. Rev. Lett. **108** (2012) 141601, arXiv:1111.1699.

[167] T. Blum *et al.*, *Lattice determination of the $K \to (\pi\pi)_{I=2}$ Decay Amplitude A_2*, Phys. Rev. **D86** (2012) 074513, arXiv:1206.5142.

[168] T. Blum *et al.*, *$K \to \pi\pi$ $\Delta I = 3/2$ decay amplitude in the continuum limit*, Phys. Rev. **D91** (2015), no. 7 074502, arXiv:1502.00263.

[169] RBC, UKQCD, Z. Bai *et al.*, *Standard Model Prediction for Direct CP Violation in $K \to \pi\pi$ Decay*, Phys. Rev. Lett. **115** (2015), no. 21 212001, arXiv:1505.07863.

[170] E. Pallante, A. Pich, and I. Scimemi, *The Standard model prediction for ϵ'_K/ϵ_K*, Nucl. Phys. **B617** (2001) 441, arXiv:hep-ph/0105011.

[171] T. Hambye, S. Peris, and E. de Rafael, *$\Delta I = 1/2$ and ϵ'_K/ϵ_K in large N_c QCD*, JHEP **05** (2003) 027, arXiv:hep-ph/0305104.

[172] H. G. Mullor, *Updated standard model prediction for the kaon direct CP-violating ratio ϵ'_k/ϵ_k*, 10, 2017. Talk given at IX CPAN DAYS.

[173] G. D'Ambrosio, G. Ecker, G. Isidori, and H. Neufeld, *Radiative non-leptonic kaon decays*, in *2nd DAPHNE Physics Handbook:265-313*, pp. 265–313, 1994. arXiv:hep-ph/9411439.

[174] SWME, Y.-C. Jang, W. Lee, S. Lee, and J. Leem, *Update on ϵ_K with lattice QCD inputs*, in *35th International Symposium on Lattice Field Theory (Lattice 2017) Granada, Spain, June 18-24, 2017*, 2017. arXiv:1710.06614.

[175] M. Endo *et al.*, *Gluino-mediated electroweak penguin with flavor-violating trilinear couplings*, JHEP **04** (2018) 019, arXiv:1712.04959.

[176] T. Kitahara, U. Nierste, and P. Tremper, *Singularity-free next-to-leading order $\Delta S = 1$ renormalization group evolution and ϵ'_K/ϵ_K in the Standard Model and beyond*, JHEP **12** (2016) 078, arXiv:1607.06727.

[177] S. Descotes-Genon, L. Hofer, J. Matias, and J. Virto, *Global analysis of $b \to s\ell\ell$ anomalies*, Journal of High Energy Physics **2016** (2016) 92.

[178] ATLAS, M. Aaboud *et al.*, *Search for additional heavy neutral Higgs and gauge bosons in the ditau final state produced in 36 fb^{-1} of pp collisions at $\sqrt{s}$ = 13 TeV with the ATLAS detector*, arXiv:1709.07242.

[179] R. Barbieri, R. Contino, and A. Strumia, *ϵ'_K from supersymmetry with nonuniversal A terms?*, Nucl. Phys. **B578** (2000) 153, arXiv:hep-ph/9908255.

[180] A. J. Buras, M. Gorbahn, S. Jäger, and M. Jamin, *Improved anatomy of ϵ'_K/ϵ_K in the Standard Model*, JHEP **11** (2015) 202, arXiv:1507.06345.

[181] A. J. Buras and J.-M. Gérard, *Upper bounds on ϵ'_K/ϵ_K parameters $B_6^{(1/2)}$ and $B_8^{(3/2)}$ from large N QCD and other news*, JHEP **12** (2015) 008, arXiv:1507.06326.

[182] A. J. Buras and J.-M. Gerard, *Final state interactions in $K \to \pi\pi$ decays: $\Delta I = 1/2$ rule vs. ϵ'_K/ϵ_K*, Eur. Phys. J. **C77** (2017), no. 1 10, arXiv:1603.05686.

[183] L. Lellouch and M. Luscher, *Weak transition matrix elements from finite volume correlation functions*, Commun. Math. Phys. **219** (2001) 31, arXiv:hep-lat/0003023.

[184] G. Colangelo, J. Gasser, and H. Leutwyler, *$\pi\pi$ scattering*, Nucl. Phys. **B603** (2001) 125, arXiv:hep-ph/0103088.

[185] R. Garcia-Martin *et al.*, *The Pion-pion scattering amplitude. IV: Improved analysis with once subtracted Roy-like equations up to 1100 MeV*, Phys. Rev. **D83** (2011) 074004, arXiv:1102.2183.

[186] G. Colangelo. Talk given at the NA62 Physics Handbook MITP Workshop.

[187] T. Kitahara, U. Nierste, and P. Tremper, *Supersymmetric Explanation of CP Violation in $K \to \pi\pi$ Decays*, Phys. Rev. Lett. **117** (2016), no. 9 091802, arXiv:1604.07400.

[188] A. L. Kagan and M. Neubert, *Large $\Delta I = 3/2$ contribution to ϵ'_K/ϵ in supersymmetry*, Phys. Rev. Lett. **83** (1999) 4929, arXiv:hep-ph/9908404.

[189] V. Cirigliano, A. Pich, G. Ecker, and H. Neufeld, *Isospin violation in ϵ'_K*, Phys. Rev. Lett. **91** (2003) 162001, arXiv:hep-ph/0307030.

[190] V. Cirigliano, G. Ecker, H. Neufeld, and A. Pich, *Isospin breaking in $K \to \pi\pi$ decays*, Eur. Phys. J. **C33** (2004) 369, arXiv:hep-ph/0310351.

[191] SWME, J. A. Bailey, Y.-C. Jang, W. Lee, and S. Park, *Standard Model evaluation of ϵ_K using lattice QCD inputs for $\hat{B}_K$ and V_{cb}*, Phys. Rev. **D92** (2015), no. 3 034510, arXiv:1503.05388.

[192] Y. Amhis *et al.*, *Averages of b-hadron, c-hadron, and τ-lepton properties as of summer 2016*, arXiv:1612.07233.

[193] D. Bigi, P. Gambino, and S. Schacht, *A fresh look at the determination of $|V_{cb}|$ from $B \to D^* \ell\nu$*, Phys. Lett. **B769** (2017) 441, arXiv:1703.06124.

[194] B. Grinstein and A. Kobach, *Model-Independent Extraction of $|V_{cb}|$ from $\bar{B} \to D^* \ell\overline{\nu}$*, Phys. Lett. **B771** (2017) 359, arXiv:1703.08170.

[195] F. U. Bernlochner, Z. Ligeti, M. Papucci, and D. J. Robinson, *Tensions and correlations in $|V_{cb}|$ determinations*, Phys. Rev. **D96** (2017), no. 9 091503, arXiv:1708.07134.

[196] A. Bevan *et al.*, *Standard Model updates and new physics analysis with the Unitarity Triangle fit*, Nucl. Phys. Proc. Suppl. **241-242** (2013) 89.

[197] KLOE, F. Ambrosino *et al.*, *Determination of CP and CPT violation parameters in the neutral kaon system using the Bell-Steinberger relation and data from the KLOE experiment*, JHEP **12** (2006) 011, arXiv:hep-ex/0610034.

[198] A. Crivellin and M. Davidkov, *Do squarks have to be degenerate? Constraining the mass splitting with Kaon and D mixing*, Phys. Rev. **D81** (2010) 095004, arXiv:1002.2653.

[199] F. Gabbiani, E. Gabrielli, A. Masiero, and L. Silvestrini, *A Complete analysis of FCNC and CP constraints in general SUSY extensions of the standard model*, Nucl. Phys. **B477** (1996) 321, arXiv:hep-ph/9604387.

[200] A. J. Buras, D. Guadagnoli, and G. Isidori, *On ϵ_K Beyond Lowest Order in the Operator Product Expansion*, Phys. Lett. **B688** (2010) 309, arXiv:1002.3612.

[201] RBC/UKQCD, N. Garron, R. J. Hudspith, and A. T. Lytle, *Neutral Kaon Mixing Beyond the Standard Model with $n_f = 2 + 1$ Chiral Fermions Part 1: Bare Matrix Elements and Physical Results*, JHEP **11** (2016) 001, arXiv:1609.03334.

[202] J. A. Bagger, K. T. Matchev, and R.-J. Zhang, *QCD corrections to flavor changing neutral currents in the supersymmetric standard model*, Phys. Lett. **B412** (1997) 77, arXiv:hep-ph/9707225.

[203] D. M. S. et al. *Ipanema-β: tools and examples for hep analysis on gpu*, arXiv:1706.01420.

[204] J. Brest *et al.*, *Self-Adapting Control Parameters in Differential Evolution: A Comparative Study on Numerical Benchmark Problems*, IEEE Transactions on Evolutionary Computation **10** (2006) 646.

[205] P. A. R. Ade *et al.*, *Planck 2015 results xiii. cosmological parameters*, Astronomy & Astrophysics **594** (2016) .

[206] E. A. Bagnaschi *et al.*, *Supersymmetric Dark Matter after LHC Run 1*, Eur. Phys. J. **C75** (2015) 500, arXiv:1508.01173.

[207] A. Cuoco, J. Heisig, M. Korsmeier, and M. Krämer, *Constraining heavy dark matter with cosmic-ray antiprotons*, arXiv:1711.05274.

[208] J. Hisano *et al.*, *Non-perturbative effect on thermal relic abundance of dark matter*, Phys. Lett. **B646** (2007) 34, arXiv:hep-ph/0610249.

[209] M. Ibe, S. Matsumoto, and R. Sato, *Mass Splitting between Charged and Neutral Winos at Two-Loop Level*, Phys. Lett. **B721** (2013) 252, arXiv:1212.5989.

[210] M. Bauer, S. Casagrande, U. Haisch, and M. Neubert, *Flavor Physics in the Randall-Sundrum Model: II. Tree-Level Weak-Interaction Processes*, JHEP **09** (2010) 017, arXiv:0912.1625.

[211] G. D'Ambrosio, G. Ecker, G. Isidori, and J. Portoles, *The Decays $K \to \pi l^+ l^-$ beyond leading order in the chiral expansion*, JHEP **08** (1998) 004, arXiv:hep-ph/9808289.

[212] G. Buchalla, G. D'Ambrosio, and G. Isidori, *Extracting short distance physics from K(L,S) —¿ pi0 e+ e- decays*, Nucl. Phys. **B672** (2003) 387, arXiv:hep-ph/0308008.

[213] NA48/1, J. R. Batley *et al.*, *Observation of the rare decay $K_S \to \pi^0 \mu^+ \mu^-$*, Phys. Lett. **B599** (2004) 197, arXiv:hep-ex/0409011.

[214] H. Voss, A. Hoecker, J. Stelzer, and F. Tegenfeldt, *TMVA - Toolkit for Multivariate Data Analysis*, PoS **ACAT** (2007) 040.

[215] A. Hoecker *et al.*, *TMVA 4 — Toolkit for Multivariate Data Analysis. Users Guide.*, arXiv:physics/0703039.

[216] D. J. Lange, *The evtgen particle decay simulation package*, Nuclear Instruments and Methods in Physics Research Section A: Accelerators, Spectrometers, Detectors and Associated Equipment **462** (2001), no. 1-2 152, BEAUTY2000, Proceedings of the 7th Int. Conf. on B-Physics at Hadron Machines.

[217] M. Williams, *Numerical Object Oriented Quantum Field Theory Calculations*, Comput. Phys. Commun. **180** (2009) 1847, arXiv:0805.2956.

[218] E. L. A. *et al*, *Measurement of trigger efficiencies and biases*, LHCb public note CERN-LHCB-2008-073 (2008).

[219] R. Armenteros and J. Podolanski, *Analysis of V-events*, Phil. Mag. **45** (1954) 13.

[220] D. Martinez Santos, *Study of the very rare decay Bs-¿mumu in LHCb*, PhD thesis, Universidade de Santiago de Compostela, 2010, CERN-THESIS-2010-068.

[221] D. Martínez Santos and F. Dupertuis, *Mass distributions marginalized over per-event errors*, Nucl. Instrum. Meth. **A764** (2014) 150, arXiv:1312.5000.

[222] J. Charles *et al.*, *Predictions of selected flavour observables within the Standard Model*, Phys. Rev. **D84** (2011) 033005, arXiv:1106.4041.

[223] M. Kobayashi and T. Maskawa, *CP violation in the renormalizable theory of weak interaction*, Prog. Theor. Phys. **49** (1973) 652.

[224] N. Cabibbo, *Unitary symmetry and leptonic decays*, Phys. Rev. Lett. **10** (1963) 531.

[225] A. J. Buras, *Flavour theory: 2009*, PoS **EPS-HEP2009** (2009) 024, arXiv:0910.1032.

[226] C.-W. Chiang *et al.*, *New physics in $B_s^0 \to J/\psi\,\phi$: a general analysis*, JHEP **04** (2010) 031, arXiv:0910.2929.

[227] F. Feroz, M. P. Hobson, and M. Bridges, *MultiNest: an efficient and robust Bayesian inference tool for cosmology and particle physics*, Mon. Not. Roy. Astron. Soc. **398** (2009) 1601, arXiv:0809.3437.

[228] Heavy Flavour Averaging Group, Y. Amhis et al. , *Averages of b-hadron, c-hadron, and τ-lepton properties as of summer 2017*, arXiv:1612.07233, http://www.slac.stanford.edu/xorg/hfag/osc/summer_2017/.

[229] X. Liu, W. Wang, and Y. Xie, *Penguin Pollution in $B \to J/\psi V$ Decays and Impact on the Extraction of the $B_s - \bar{B}_s$ mixing phase*, arXiv:1309.0313.

[230] I. Belyaev *et al.*, *Handling of the generation of primary events in* Gauss*, the LHCb simulation framework*, Nuclear Science Symposium Conference Record (NSS/MIC) **IEEE** (2010) 1155.

[231] D. J. Lange, *The EvtGen particle decay simulation package*, Nucl. Instrum. Meth. **A462** (2001) 152.

[232] P. Golonka and Z. Was, *PHOTOS Monte Carlo: a precision tool for QED corrections in Z and W decays*, Eur. Phys. J. **C45** (2006) 97, arXiv:hep-ph/0506026.

[233] GEANT4 collaboration, S. Agostinelli *et al.*, *GEANT4: A simulation toolkit*, Nucl. Instrum. Meth. **A506** (2003) 250.

[234] GEANT4 collaboration, J. Allison *et al.*, *Geant4 developments and applications*, IEEE Trans. Nucl. Sci. **53** (2006) 270.

[235] M. Clemencic *et al.*, *The LHCb simulation application,* GAUSS*: design, evolution and experience*, J. of Phys. : Conf. Ser. **331** (2011) 032023.

[236] L. Anderlini *et al.*, *The PIDCalib package*, Tech. Rep. LHCb-PUB-2016-021. CERN-LHCb-PUB-2016-021, CERN, Geneva, Jul, 2016.

[237] M. Pivk and F. R. Le Diberder, *SPlot: A Statistical tool to unfold data distributions*, Nucl. Instrum. Meth. **A555** (2005) 356, arXiv:physics/0402083.

[238] Y. Xie, *Some physics and technical issues in analysis of the decay* $B_s^0 \to J/\psi K^+K^-$, LHCb-INT-2012-017.

[239] LHCb, R. Aaij *et al.*, *Resonances and CP violation in* B_s^0 *and* $\overline{B}_s^0 \to J/\psi K^+K^-$ *decays in the mass region above the* $\phi(1020)$, JHEP **08** (2017) 037, arXiv:1704.08217.

[240] LHCb, R. Aaij *et al.*, *Measurement of resonant and CP components in* $\bar{B}_s^0 \to J/\psi\pi^+\pi^-$ *decays*, Phys. Rev. **D89** (2014), no. 9 092006, arXiv:1402.6248.

[241] S. M. Flatté, *Coupled-channel analysis of the and* kk^- *systems near* kk^- *threshold*, Physics Letters B **63** (1976), no. 2 224 .

[242] G. Breit and E. Wigner, *Capture of slow neutrons*, Phys. Rev. **49** (1936) 519.

[243] LHCb collaboration, R. Aaij *et al.*, *Tagged time-dependent analysis of* $B_s^0 \to J/\psi\, K^+K^-$ *and* $B_s^0 \to J/\psi\,\pi^+\pi^-$ *decays with 1.0* fb^{-1}, LHCb-ANA-2012-067.

[244] R. Aaij *et al.*, *Measurements of the* B^+, B^0, B_s^0 *meson and* Λ_b^0 *baryon lifetimes*, submitted to JHEP (2014) arXiv:1402.2554.

[245] Heavy Flavour Averaging Group, Y. Amhis et al. , *Averages of b-hadron, c-hadron, and* τ*-lepton properties prepared for the PDG 2018 Review of Particle Physics*, , http://www.slac.stanford.edu/xorg/hflav/osc/PDG_2018/.

[246] LHCb collaboration, R. Aaij *et al.*, *Measurement of the polarization amplitudes in* $B^0 \to J/\psi K^*(892)^0$ *decays*, Phys. Rev. **D88** (2013) 052002 CERN-PH-EP-2013-104, LHCb-PAPER-2013-023, arXiv:1307.2782.

[247] LHCb collaboration, R. Aaij *et al.*, *Precision measurement of CP violation in* $B_s^0 \to J/\psi\, K^+K^-$ *decays*, Phys. Rev. Lett. **114** (2015) 041801 LHCb-PAPER-2014-059, CERN-PH-EP-2014-271, arXiv:1411.3104.

[248] B. Efron and R. J. Tibshirani, *An introduction to the bootstrap*, Mono. Stat. Appl. Probab., Chapman and Hall, London, 1993.

[249] F. Feroz, M. P. Hobson, E. Cameron, and A. N. Pettitt, *Importance Nested Sampling and the MultiNest Algorithm*, arXiv:1306.2144.

[250] LHCb, R. Aaij *et al.*, *Determination of the sign of the decay width difference in the* B_s *system*, Phys. Rev. Lett. **108** (2012) 241801, arXiv:1202.4717.

[251] Y. A. *et al.* , *Averages of b-hadron, c-hadron, and tau-lepton properties as of summer 2016*, arXiv:1612.07233.

[252] B. Graner, Y. Chen, E. G. Lindahl, and B. R. Heckel, *Reduced limit on the permanent electric dipole moment of* ^{199}Hg, Phys. Rev. Lett. **116** (2016) 161601.

[253] L. Lavoura, J. P. Silva, and G. Castelo Branco, *Cp violation*, 1999. Oxford University Press.

[254] C. Bobeth *et al.*, $B_{s,d} \to l^+ l^-$ *in the Standard Model with Reduced Theoretical Uncertainty*, Phys. Rev. Lett. **112** (2014) 101801, arXiv:1311.0903.

[255] BaBar, J. P. Lees *et al.*, *Measurements of direct CP asymmetries in* $B \to X_s$ *decays using sum of exclusive decays*, Phys. Rev. **D90** (2014), no. 9 092001, arXiv:1406.0534.

[256] C. A. Baker *et al.*, *Improved experimental limit on the electric dipole moment of the neutron*, Phys. Rev. Lett. **97** (2006) 131801.

[257] B. C. Allanach, *SOFTSUSY: a program for calculating supersymmetric spectra*, Comput. Phys. Commun. **143** (2002) 305, arXiv:hep-ph/0104145.

[258] G. Degrassi *et al.*, *Towards high precision predictions for the MSSM Higgs sector*, Eur. Phys. J. **C28** (2003) 133, arXiv:hep-ph/0212020.

[259] S. Heinemeyer, W. Hollik, and G. Weiglein, *FeynHiggs: A Program for the calculation of the masses of the neutral CP even Higgs bosons in the MSSM*, Comput. Phys. Commun. **124** (2000) 76, arXiv:hep-ph/9812320.

[260] S. Heinemeyer, W. Hollik, and G. Weiglein, *The Masses of the neutral CP - even Higgs bosons in the MSSM: Accurate analysis at the two loop level*, Eur. Phys. J. **C9** (1999) 343, arXiv:hep-ph/9812472.

[261] M. Frank *et al.*, *The Higgs Boson Masses and Mixings of the Complex MSSM in the Feynman-Diagrammatic Approach*, JHEP **02** (2007) 047, arXiv:hep-ph/0611326.

[262] T. Hahn *et al.*, *High-Precision Predictions for the Light CP -Even Higgs Boson Mass of the Minimal Supersymmetric Standard Model*, Phys. Rev. Lett. **112** (2014), no. 14 141801, arXiv:1312.4937.

[263] P. Z. Skands *et al.*, *SUSY Les Houches accord: Interfacing SUSY spectrum calculators, decay packages, and event generators*, JHEP **07** (2004) 036, arXiv:hep-ph/0311123.

[264] B. C. Allanach *et al.*, *SUSY Les Houches Accord 2*, Comput. Phys. Commun. **180** (2009) 8, arXiv:0801.0045.

[265] F. Mahmoudi, *SuperIso: A Program for calculating the isospin asymmetry of B —¿ K* gamma in the MSSM*, Comput. Phys. Commun. **178** (2008) 745, arXiv:0710.2067.

[266] F. Mahmoudi, *SuperIso v2.3: A Program for calculating flavor physics observables in Supersymmetry*, Comput. Phys. Commun. **180** (2009) 1579, arXiv:0808.3144.

[267] D. Eriksson, F. Mahmoudi, and O. Stal, *Charged Higgs bosons in Minimal Supersymmetry: Updated constraints and experimental prospects*, JHEP **11** (2008) 035, arXiv:0808.3551.

[268] A. Crivellin *et al.*, *SUSY_FLAVOR v2: A Computational tool for FCNC and CP-violating processes in the MSSM*, Comput. Phys. Commun. **184** (2013) 1004, arXiv:1203.5023.

[269] J. D. Hunter, *Matplotlib: A 2d graphics environment*, Computing In Science & Engineering **9** (2007), no. 3 90.

[270] A. Buckley, *PySLHA: a Pythonic interface to SUSY Les Houches Accord data*, Eur. Phys. J. **C75** (2015), no. 10 467, arXiv:1305.4194.

[271] G. Belanger, F. Boudjema, A. Pukhov, and A. Semenov, *micrOMEGAs_3: A program for calculating dark matter observables*, Comput. Phys. Commun. **185** (2014) 960, arXiv:1305.0237.

[272] Information about this code is available from K. A. Olive: it contains important contributions from J. Evans, T. Falk, A. Ferstl, G. Ganis, F. Luo, A. Mustafayev, J. McDonald, K. A. Olive, P. Sandick, Y. Santoso, V. Spanos, and M. Srednicki.

[273] G. Isidori and P. Paradisi, *Hints of large tan(beta) in flavour physics*, Phys. Lett. **B639** (2006) 499, arXiv:hep-ph/0605012.

[274] G. Isidori, F. Mescia, P. Paradisi, and D. Temes, *Flavour physics at large tan(beta) with a Bino-like LSP*, Phys. Rev. **D75** (2007) 115019, arXiv:hep-ph/0703035.

[275] S. Heinemeyer *et al.*, *Precise prediction for M(W) in the MSSM*, JHEP **08** (2006) 052, arXiv:hep-ph/0604147.

[276] S. Heinemeyer, W. Hollik, A. M. Weber, and G. Weiglein, *Z Pole Observables in the MSSM*, JHEP **04** (2008) 039, arXiv:0710.2972.

[277] P. Bechtle *et al.*, *HiggsSignals: Confronting arbitrary Higgs sectors with measurements at the Tevatron and the LHC*, Eur. Phys. J. **C74** (2014), no. 2 2711, arXiv:1305.1933.

[278] P. Bechtle *et al.*, *Probing the Standard Model with Higgs signal rates from the Tevatron, the LHC and a future ILC*, JHEP **11** (2014) 039, arXiv:1403.1582.

[279] P. Bechtle *et al.*, *HiggsBounds: Confronting Arbitrary Higgs Sectors with Exclusion Bounds from LEP and the Tevatron*, Comput. Phys. Commun. **181** (2010) 138, arXiv:0811.4169.

[280] P. Bechtle *et al.*, *HiggsBounds 2.0.0: Confronting Neutral and Charged Higgs Sector Predictions with Exclusion Bounds from LEP and the Tevatron*, Comput. Phys. Commun. **182** (2011) 2605, arXiv:1102.1898.

[281] P. Bechtle *et al.*, HiggsBounds – 4*: Improved Tests of Extended Higgs Sectors against Exclusion Bounds from LEP, the Tevatron and the LHC*, Eur. Phys. J. **C74** (2014), no. 3 2693, arXiv:1311.0055.

[282] P. Bechtle *et al.*, *Applying Exclusion Likelihoods from LHC Searches to Extended Higgs Sectors*, Eur. Phys. J. **C75** (2015), no. 9 421, arXiv:1507.06706.

[283] M. Muhlleitner, A. Djouadi, and Y. Mambrini, *SDECAY: A Fortran code for the decays of the supersymmetric particles in the MSSM*, Comput. Phys. Commun. **168** (2005) 46, arXiv:hep-ph/0311167.

[284] F. Feroz *et al.*, *Challenges of Profile Likelihood Evaluation in Multi-Dimensional SUSY Scans*, JHEP **06** (2011) 042, arXiv:1101.3296.

[285] *Lep 2 joint susy working group aleph, delphi, l3, opal experiments.*, http://lepsusy.web.cern.ch/lepsusy/.

[286] ATLAS, M. Aaboud *et al.*, *Search for Minimal Supersymmetric Standard Model Higgs bosons H/A and for a Z' boson in the $\tau\tau$ final state produced in pp collisions at $\sqrt{s} = 13$ TeV with the ATLAS Detector*, Eur. Phys. J. **C76** (2016), no. 11 585, arXiv:1608.00890.

[287] J. R. Ellis, K. A. Olive, and C. Savage, *Hadronic Uncertainties in the Elastic Scattering of Supersymmetric Dark Matter*, Phys. Rev. **D77** (2008) 065026, arXiv:0801.3656.

[288] ATLAS, CDF, CMS, D0, *First combination of Tevatron and LHC measurements of the top-quark mass*, arXiv:1403.4427.

[289] Tevatron Electroweak Working Group, CDF, DELPHI, SLD Electroweak and Heavy Flavour Groups, ALEPH, LEP Electroweak Working Group, SLD, OPAL, D0, L3, L. E. W. Group, *Precision Electroweak Measurements and Constraints on the Standard Model*, arXiv:1012.2367.

[290] Gfitter, M. Baak, *Review of electroweak fits of the SM and beyond, after the Higgs discovery – with Gfitter. After the Higgs: status and prospects of the electroweak [U+FB01]t of the Standard Model and beyond*, PoS **EPS-HEP2013** (2014) 203. 6 p.

[291] SISSA, , (Trieste), SISSA, 2013.

[292] ATLAS, CMS, G. Aad *et al.*, *Combined Measurement of the Higgs Boson Mass in pp Collisions at $\sqrt{s} = 7$ and 8 TeV with the ATLAS and CMS Experiments*, Phys. Rev. Lett. **114** (2015) 191803, arXiv:1503.07589.

[293] M. Misiak *et al.*, *Updated NNLO QCD predictions for the weak radiative B-meson decays*, Phys. Rev. Lett. **114** (2015), no. 22 221801, arXiv:1503.01789.

[294] LHCb, CMS, V. Khachatryan *et al.*, *Observation of the rare $B_s^0 \to \mu^+\mu^-$ decay from the combined analysis of CMS and LHCb data*, Nature **522** (2015) 68, arXiv:1411.4413.

[295] ATLAS, M. Aaboud *et al.*, *Study of the rare decays of B_s^0 and B^0 into muon pairs from data collected during the LHC Run 1 with the ATLAS detector*, Eur. Phys. J. **C76** (2016), no. 9 513, arXiv:1604.04263.

[296] BaBar Collaboration, J. P. Lees *et al.*, *Measurement of the $b \to X_s\ell^+\ell^-$ branching fraction and search for direct cp violation from a sum of exclusive final states*, Phys. Rev. Lett. **112** (2014) 211802.

[297] W. J. Marciano, *Precise determination of $|V_{us}|$ from lattice calculations of pseudoscalar decay constants*, Phys. Rev. Lett. **93** (2004) 231803.

[298] A. J. Buras, D. Buttazzo, J. Girrbach-Noe, and R. Knegjens, *$K^+ \to \pi^+ \nu\overline{\nu}$ and $K_L \to \pi^0 \nu\overline{\nu}$ in the Standard Model: status and perspectives*, JHEP **11** (2015) 033, arXiv:1503.02693.

[299] L. L. Joao Paulo Silva Gustavo Castelo Branco, *CP Violation*, Oxford University Press, 1999.

[300] A. J. Buras *et al.*, *epsilon-prime / epsilon and rare K and B decays in the MSSM*, Nucl. Phys. **B592** (2001) 55, arXiv:hep-ph/0007313.

[301] Planck, P. A. R. Ade *et al.*, *Planck 2013 results. XVI. Cosmological parameters*, Astron. Astrophys. **571** (2014) A16, arXiv:1303.5076.

[302] PandaX-II, A. Tan *et al.*, *Dark Matter Results from First 98.7 Days of Data from the PandaX-II Experiment*, Phys. Rev. Lett. **117** (2016), no. 12 121303, arXiv:1607.07400.

[303] LUX, D. S. Akerib *et al.*, *Results from a search for dark matter in the complete LUX exposure*, Phys. Rev. Lett. **118** (2017), no. 2 021303, arXiv:1608.07648.

[304] CMS, V. Khachatryan *et al.*, *Search for neutral MSSM Higgs bosons decaying to a pair of tau leptons in pp collisions*, JHEP **10** (2014) 160, arXiv:1408.3316.

[305] P. Cushman *et al.*, *Working Group Report: WIMP Dark Matter Direct Detection*, in *Proceedings, 2013 Community Summer Study on the Future of U.S. Particle Physics: Snowmass on the Mississippi (CSS2013): Minneapolis, MN, USA, July 29-August 6, 2013*, 2013. arXiv:1310.8327.

[306] LUX, D. S. Akerib *et al.*, *Results from a search for dark matter in the complete LUX exposure*, Phys. Rev. Lett. **118** (2017), no. 2 021303, arXiv:1608.07648.

[307] PandaX-II, A. Tan *et al.*, *Dark Matter Results from First 98.7 Days of Data from the PandaX-II Experiment*, Phys. Rev. Lett. **117** (2016), no. 12 121303, arXiv:1607.07400.

[308] J. Billard, L. Strigari, and E. Figueroa-Feliciano, *Implication of neutrino backgrounds on the reach of next generation dark matter direct detection experiments*, Phys. Rev. **D89** (2014), no. 2 023524, arXiv:1307.5458.

[309] GAMBIT, P. Athron *et al.*, *Global fits of GUT-scale SUSY models with GAMBIT*, Eur. Phys. J. **C77** (2017), no. 12 824, arXiv:1705.07935.

[310] GAMBIT, P. Athron *et al.*, *GAMBIT: The Global and Modular Beyond-the-Standard-Model Inference Tool*, Eur. Phys. J. **C77** (2017), no. 11 784, arXiv:1705.07908, [Addendum: Eur. Phys. J.C78,no.2,98(2018)].

[311] A. Sommerfeld, *Über die Beugung und Bremsung der Elektronen*, Ann. Phys. **403** (1931), no. 257.

[312] ATLAS, M. Aaboud *et al.*, *Study of the rare decays of B_s^0 and B^0 into muon pairs from data collected during the LHC Run 1 with the ATLAS detector*, Eur. Phys. J. **C76** (2016), no. 9 513, arXiv:1604.04263.

[313] ATLAS, CMS, G. Aad *et al.*, *Combined Measurement of the Higgs Boson Mass in pp Collisions at $\sqrt{s} = 7$ and 8 TeV with the ATLAS and CMS Experiments*, Phys. Rev. Lett. **114** (2015) 191803, arXiv:1503.07589.

[314] E. Bagnaschi *et al.*, *Likelihood Analysis of Supersymmetric SU(5) GUTs*, Eur. Phys. J. **C77** (2017), no. 2 104, arXiv:1610.10084.

[315] H. Baer, V. Barger, and D. Mickelson, *Direct and indirect detection of higgsino-like WIMPs: concluding the story of electroweak naturalness*, Phys. Lett. **B726** (2013) 330, arXiv:1303.3816.

[316] D. Barducci *et al.*, *Uncovering Natural Supersymmetry via the interplay between the LHC and Direct Dark Matter Detection*, JHEP **07** (2015) 066, arXiv:1504.02472.

[317] M. Badziak *et al.*, *Detecting underabundant neutralinos*, JHEP **11** (2015) 053, arXiv:1506.07177.

[318] XENON, E. Aprile *et al.*, *Physics reach of the XENON1T dark matter experiment*, JCAP **1604** (2016), no. 04 027, arXiv:1512.07501.

[319] D. C. Malling *et al.*, *After LUX: The LZ Program*, arXiv e-prints (2011) arXiv:1110.0103, arXiv:1110.0103.

[320] DARWIN Consortium, L. Baudis, *DARWIN: dark matter WIMP search with noble liquids*, J. Phys. Conf. Ser. **375** (2012) 012028, arXiv:1201.2402.

[321] R. Harnik, D. T. Larson, H. Murayama, and A. Pierce, *Atmospheric neutrinos can make beauty strange*, Phys. Rev. **D69** (2004) 094024, arXiv:hep-ph/0212180.

[322] IceCube, M. G. Aartsen *et al.*, *Search for annihilating dark matter in the Sun with 3 years of IceCube data*, Eur. Phys. J. **C77** (2017), no. 3 146, arXiv:1612.05949.

[323] PICO, C. Amole *et al.*, *Dark Matter Search Results from the PICO-60 C_3F_8 Bubble Chamber*, Phys. Rev. Lett. **118** (2017), no. 25 251301, arXiv:1702.07666.

[324] G. Gabrielse *et al.*, *New determination of the fine structure constant from the electron g value and qed*, Phys. Rev. Lett. **97** (2006) 030802.

[325] G. Gabrielse *et al.*, *Erratum: New determination of the fine structure constant from the electron g value and qed [phys. rev. lett. 97, 030802 (2006)]*, Phys. Rev. Lett. **99** (2007) 039902.

[326] D. Hanneke, S. Fogwell, and G. Gabrielse, *New measurement of the electron magnetic moment and the fine structure constant*, Phys. Rev. Lett. **100** (2008) 120801.

[327] P. J. Mohr, B. N. Taylor, and D. B. Newell, *Codata recommended values of the fundamental physical constants: 2010*, Rev. Mod. Phys. **84** (2012) 1527.

[328] Muon (g-2) Collaboration, G. W. Bennett *et al.*, *Measurement of the positive muon anomalous magnetic moment to 0.7 ppm*, Phys. Rev. Lett. **89** (2002) 101804.

[329] Muon (g-2) Collaboration, G. W. Bennett *et al.*, *Publisher's note: Measurement of the positive muon anomalous magnetic moment to 0.7 ppm [phys. rev. lett. 89, 101804 (2002)]*, Phys. Rev. Lett. **89** (2002) 129903.

[330] Muon (g-2) Collaboration, G. W. Bennett *et al.*, *Measurement of the negative muon anomalous magnetic moment to 0.7 ppm*, Phys. Rev. Lett. **92** (2004) 161802.

[331] Muon g-2 Collaboration, G. W. Bennett *et al.*, *Final report of the e821 muon anomalous magnetic moment measurement at bnl*, Phys. Rev. D **73** (2006) 072003.

[332] M. Pospelov, *Secluded u(1) below the weak scale*, Phys. Rev. D **80** (2009) 095002.